Transactions of the ASME

Technical Editor
ARTHUR J. WENNERSTROM
Senior Associate Editor
G. K. SEROVY
Associate Editors
Advanced Energy Systems
S. I. FREEDMAN
Environmental Control
H. E. HESKETH
Fuels and Combustion Technologies
R. E. BARRETT
Gas Turbine
S. KUO
Internal Combustion Engine
K. J. SPRINGER
Nuclear Engineering
S. M. CHO
Power
R. W. PORTER

BOARD ON COMMUNICATIONS
Chairman and Vice-President
K. N. REID, JR.

Members-at-Large
W. BEGELL
J. T. COKONIS
M. FRANKE
W. G. GOTTENBERG
M. KUTZ
F. LANDIS
J. R. LLOYD
T. C. MIN
R. E. NICKELL
R. E. REDER
F. W. SCHMIDT

President, **N. D. FITZROY**
Executive Director,
PAUL ALLMENDINGER
Treasurer, **ROBERT A. BENNETT**

PUBLISHING STAFF
Mng. Dir., Publ., **J. J. FREY**
Dep. Mng. Dir., Pub.,
JOS. SANSONE
Managing Editor,
CORNELIA MONAHAN
Sr. Production Editor,
VALERIE WINTERS
Editorial Prod. Asst.,
MARISOL ANDINO

Transactions of the ASME, Journal of Turbomachinery (ISSN 0889-504X) is published quarterly (Jan., Apr., July, Oct.,) for $85 per year by The American Society of Mechanical Engineers, 345 East 47th Street, New York, NY 10017. Second class postage permission pending at New York, NY and additional mailing offices. POSTMASTER: Send address change to The Journal of Turbomachinery, c/o The AMERICAN SOCIETY OF MECHANICAL ENGINEERS, 22 Law Drive, Box 2300, Fairfield, NJ 07007-2300."

CHANGES OF ADDRESS must be received at Society headquarters seven weeks before they are to be effective. Please send old label and new address.

PRICES: To members, $24.00, annually; to nonmembers, $85.00.
Add $6.00 for postage to countries outside the United States and Canada.

STATEMENT from By-Laws. The Society shall not be responsible for statements or opinions advanced in papers or ... printed in its publications (B 7.1, para. 3).

COPYRIGHT © 1987 by the American Society of Mechanical Engineers. Reprints from this publication may be made on condition that full credit be given the TRANSACTIONS OF THE ASME – JOURNAL OF TURBOMACHINERY, and the author, and date of publication be stated.

INDEXED by Engineering Information

Journal of Turbomachinery

Published Quarterly by The American Society of Mechanical Engineers

VOLUME 109 • NUMBER 1 • JANUARY 1987

TECHNICAL PAPERS

Contents continued on page 9

Downloaded 01 Jun 2010 to 171.66.16.52. Redistribution subject to ASME license or copyright; see http://www.asme.org/terms/Terms_Use.cfm

(Contents Continued)

Downloaded 01 Jun 2010 to 171.66.16.52. Redistribution subject to ASME license or copyright; see http://www.asme.org/terms/Terms_Use.cfm

A Critical Evaluation of Three Centrifugal Compressors With Pedigree Data Sets: Part 5—Studies in Component Performance

D. Japikse
Concepts ETI, Inc.,
Norwich, VT 05055

A series of three centrifugal compressor data sets, each passing rigorous tests for quality, has been completed. Using this data base, single-zone and two-zone modeling is thoroughly critiqued in order to judge the appropriateness of such modeling and, hence, to set guidelines for subsequent design optimization using either single-zone or two-zone modeling.

Introduction

Attempts to match computational methods for turbomachinery performance against selected data sets are fairly common throughout the turbomachinery industry. However, attempts to evaluate the fundamental integrity of a basic modeling concept against pedigreed data are quite rare. A principal cause of this shortcoming is the general lack of high-quality data to support an in-depth, comprehensive evaluation of fundamental modeling procedures. During the middle 1970s, Dr. Dietrich Eckardt carried out a systematic study of three different centrifugal compressors using pneumatic probes, hot-wire anemometry, high-response pressure transducers, and laser two-focus velocimetry. The pneumatic information is of a type which can be taken in any industrial organization if desired. Unfortunately, such data have only been taken, in industry, on a qualitative basis, and extensive quantitative comparisons have not been published (specifically including a thorough evaluation of the mass average values of total pressure and flow angle).

In a companion study, Part 3 of this series [1], a critical evaluation of Level II and Level III performance modeling was presented with a comparison against Eckardt's data for the radial impeller at 14,000 rpm. Using a Level II (or single-zone) modeling approach, rotor efficiency and rotor slip factor are correlated in order to have a performance prediction system for a centrifugal compressor (or pump) rotor. The correlations of rotor efficiency and slip factor may depend on numerous additional parameters, but only these two fundamental parameters are used to describe the stage performance. An optional case, used by a minority of designers, wherein an impeller exit blockage is also correlated as part of the Level II approach, has been rejected as fundamentally inaccurate and significantly in error with respect to impeller exit flow angle. Level III modeling uses a two-zone description of the flow processes wherein an isentropic core flow is recognized and a residual flow of lower (nonisentropic) flow exists as the second zone. In some cases, the second zone may be an actual wake, in keeping with the early modeling philosophy of the jet/wake model. However, in other cases, there may be no separation, or no wake, but there are, of course, low-momentum, nonisentropic stream tubes which are represented by the two-zone modeling. Early descriptions of the two-zone modeling of the equations were presented by Johnston and Dean [2] and by Dean et al. [3]. There were, however, errors in these presentations and a correct derivation on a time-dependent basis was presented by Japikse [1].

It is the purpose of the present study to extend the evaluation of Level II and Level III modeling to the full sets of data taken by Eckardt for the three different impellers. To accomplish this objective, the complete data sets were obtained from one of the original sponsors and extensive discussions were held with Dr. Eckardt to establish a precise understanding of the method by which data were taken, the instruments which were used, and the procedures by which data reduction should be pursued. Approximately 5000 pieces of data were manually entered into the computer and then processed in order to carry out full integrations of the traverse profiles. Consequently, mass average total pressure, mass average flow angle, and mass average static pressure were obtained at both the inner and outer traverse location for each test point. Numerous questions had to be resolved concerning the possibilities of flow field distortion, measurement error, and basic data interpretation. The assistance of Dr. Eckardt in these matters is gratefully acknowledged and appreciated.

The Eckardt Data Set

Three sets of comprehensive data are available for one radial and two backward swept centrifugal compressor im-

Contributed by the Gas Turbine Division of THE AMERICAN SOCIETY OF MECHANICAL ENGINEERS and presented at the 31st International Gas Turbine Conference and Exhibit, Düsseldorf, Federal Republic of Germany, June 8-12, 1986. Manuscript received at ASME Headquarters February 11, 1986. Paper No. 86-GT-194.

© 1986 Concepts ETI, Inc.

Copyright © 1987 by ASME

Downloaded 01 Jun 2010 to 171.66.16.57. Redistribution subject to ASME license or copyright; see http://www.asme.org/terms/Terms_Use.cfm

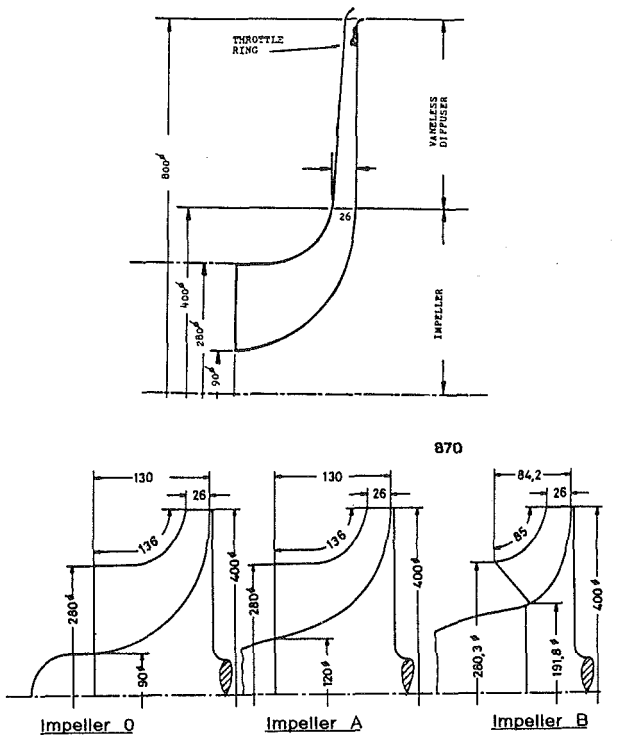

β_{1tb} = - 63° β_{1tb} = - 63° β_{1tb} = - 60°
β_{2b} = 0° β_{2b} = - 30° β_{2b} = - 40°

Fig. 1 Meridional cross section of Eckardt's centrifugal compressor stages; dimensions in mm

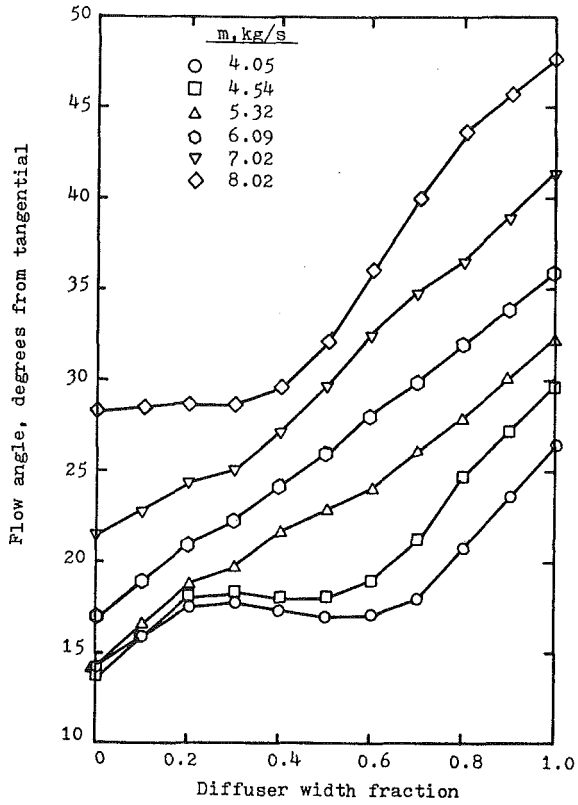

Fig. 2 Eckardt angle traverses, impeller O, 14,000 rpm, m = 5.32 kg/s at a radius of r = 1.075 r_2

pellers tested by Eckardt. His various investigations [4–6] include data taken by laser two-focus velocimetry, high-frequency pressure transducers, and conventional pneumatic probes. In this study, only the pneumatic probe information will be employed.

The stages considered by Eckardt are shown in Fig. 1. It may be observed that the same vaneless diffuser and shroud part are used for all the impellers, and that the stages differ only by modifications of blading and hub contour for the three different configurations. The impellers and vaneless diffuser are of a very common type and form a representative example of large-scale industrial compressors. The stage was tested without a volute (a collector dump was used) and with a clean inlet flow.

These three sets of data are particularly unique because of the completeness and overall accuracy of the data. No other set of data, including such detailed flow traverses, is known to be available for any centrifugal compressor. These data include static pressure taps at the impeller inlet, along the impeller shroud, and at the impeller exit, and diffuser taps through the vaneless diffuser. These taps were located at various meridional positions and at numerous circumferential locations. Furthermore, detailed traverses were taken at four different radial locations in the vaneless diffuser. The traverses were made with a small Cobra probe, thus permitting the determination of total pressure and flow angle in the flow field, while wall static pressures were recorded at the same location. The nearest traverse to the impeller tip was at a radius ratio of 1.075 (7.5 percent greater radius than the impeller tip radius) and the furthest radial (outward) traverse was at a radius ratio of 1.6875. Both the inner and outer traverse data were used for the present study. Over 5000 measured pieces of data were processed for the present study.

The basic traverse data from Eckardt have been systematically integrated to determine the mass average total pressure, the mass average flow angle, and of course the mass flow rate. Mass average calculations have been carried out according to the following equation:

$$(\text{parameter})_{\text{mass ave.}} = \int_0^b (\text{parameter}) dm / \int_0^b dm$$

where $dm = \rho C_m 2\pi r dx$. In general, there is excellent agreement between Eckardt's measured orifice mass flow rate and the mass flow rate deduced from integrated traverses. The discrepancy is usually a few percent for traverses close to the impeller tip and at nominal flows. However, for very high

Nomenclature

b = passage width
C_m = meridional velocity
m = mass flow rate
m_w/m = mass fraction in impeller secondary or wake flow
MR_2 = Mach number diffusion ratio = $M_{rel,1t}/M_{rel,2j}$
MR_{2i} = ideal Mach number ratio
p = static pressure
p_0 = stagnation pressure
r = radius
R = r/r_2
T_0 = total temperature
W_x = specific work
x = axial coordinate
Z = blade number
α = gas angle from the meridional plane
β_b = blade angle from the meridional plane
$\delta\eta$ = efficiency increment
η = efficiency
π = stage pressure ratio
ρ = density
σ = standard deviation

Subscripts

1 = impeller inlet location
2 = impeller exit location
4 = traverse location
b = blade conditions

Downloaded 01 Jun 2010 to 171.66.16.57. Redistribution subject to ASME license or copyright; see http://www.asme.org/terms/Terms_Use.cfm

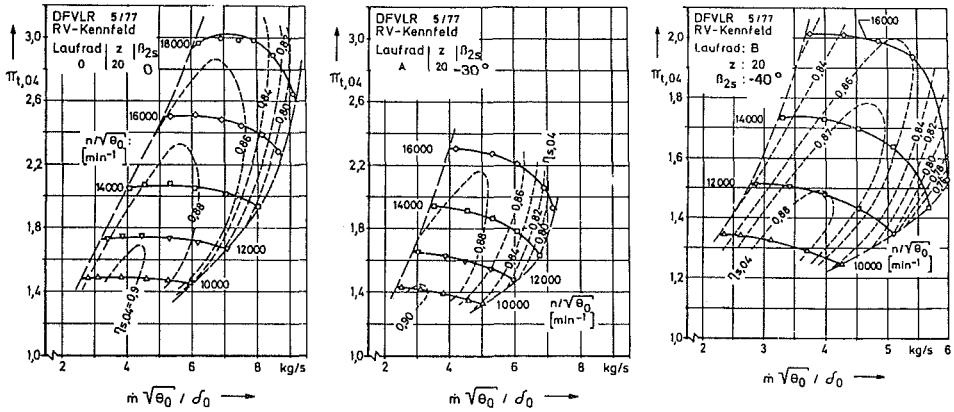

Fig. 3 Compressor maps for impellers O, A, and B

flow rates and occasionally low flow rates, the errors get larger. The errors are distinctly larger at the greater radius location and errors on the order of 10 percent may be found. It was known in the experimental investigation that some distortions from downstream elements were being fed into the vaneless diffuser. Eckardt was able to substantially eliminate these distortions by the use of a throttle ring, which may be observed in Fig. 1. However, some residual distortion still exists and this, presumably, accounts for some of the discrepancy between measured orifice mass flow rate and that which is obtained by integrating the traverse profiles. To account for the uncertainty which is introduced by using traverses which occasionally depart from a reasonable accuracy level, all data processed in this report are broken into quality data and marginal data. In subsequent plots, boundaries are drawn between the data which can be considered to be high quality and data which are more or less marginal.

It is also necessary to study the traverse data to see if any indication of backflow (recirculation) exists. Sample yaw-angle traverses are shown in Fig. 2. It may be observed that there is no evidence of backflow at the radius ratio of 1.075. In other words, the angles are distinctly above the tangential, and reverse flow to the impeller tip is not suggested by this figure. In addition, Eckardt (in a personal communication) indicated that laser measurements at the impeller inlet did not reveal any unusual turbulence intensities which should accompany inlet recirculation. Thus, one may conclude that inlet, or impeller exit, recirculation is either nonexistent or comparatively small for these impellers. However, if a small degree of recirculation has gone undetected, then the work input balance in any flow analysis will be slightly in error.

The Eckardt data sets appear to be the most comprehensive sets of data ever taken for centrifugal compressors. As a rule, compressor development specialists have been content to correlate or predict the stage overall performance (see for example the overall performance maps for these three stages shown in Fig. 3, giving the pressure ratio and efficiency characteristics for the three stages), and occasionally they have attempted to model, or predict, the impeller tip static pressure. On very rare occasions, a casual check may be made against a traverse total pressure but rarely, if ever, are these total pressures systematically integrated from traverse data whose integrals show agreement with orifice mass flow rate. Such comparisons have invariably excluded examination of the impeller exit flow angle. It is the objective of this study to test several prediction models for their ability to match *all* of the impeller tip conditions including the impeller tip static pressure, the mass average total pressure, the mass average flow angle, and the total temperature rise of the stage plus the mass flow rate and speed.

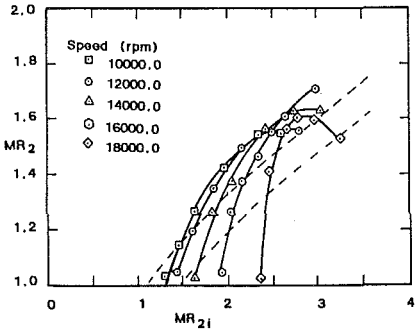

Fig. 4 Relative diffusion of impeller O showing performance above the reference band; $MR_2 = MR_{rel\ 1t}/M_{rel\ 2j}$; $MR_{2i} = M_{rel\ 1t}/M_{rel\ 2,s}$

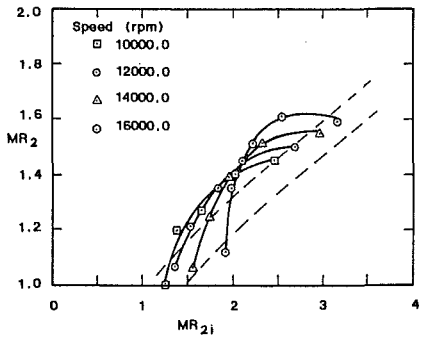

Fig. 5 Relative diffusion of impeller A showing performance above the reference band

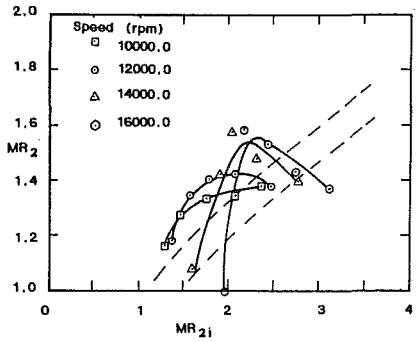

Fig. 6 Relative diffusion of impeller B showing performance above the reference band; note the highly peaked characteristic of the higher speeds

There are, of course, some limitations to the analysis. Firstly, it is impossible to know how much of the total temperature rise through the impeller is due to the work input to the gas flow and how much of it is due to shear stresses, either along

Downloaded 01 Jun 2010 to 171.66.16.57. Redistribution subject to ASME license or copyright; see http://www.asme.org/terms/Terms_Use.cfm

the front cover (front cover friction) or along the rear disk (rear disk friction). This is a fundamental question of any evaluation study. Shear stresses on the impeller backface or along the cover would generate heat which is carried away either by conduction or by convection. On the rear disk, if the heat is carried away by conduction, it is then conducted through the impeller and into the gas flow on the opposite side. If it is carried away by convection, it may be convected back to the gas path or down to a leakage point along the shaft, or it may be convected to the rear of the cavity where the heat is rejected by conduction to the back cavity face. Likewise, along the front cover, some of the heat generated by shear stresses can be conducted through the front cover. Hence, in principle, it is impossible to know exactly how all of the temperature rise to the flow path actually occurs. For this particular test series, a vacuum pump was used on the bearing chamber which kept the chamber pressure to approximately 0.9 bar. Eckardt felt that this implied a rear disk suction from rotor tip to the chamber for most nominal operating points. Thus, the rear cavity situation should be one of convection with little or no cavity friction influencing the main gas path temperature rise. Of course, since the front wall was carefully insulated, much of the front cover friction would enter the gas path. Eckardt estimated that 60 to 80 percent of the front cover friction would enter the flow path.

Finally, it is important to note a remark offered by Inoue and Cumpsty [7] regarding the tests by Eckardt. Since Eckardt carried out his work at a comparatively low speed on an impeller originally intended for higher speed operation, the basic structure of the important secondary flow processes in the impeller passage may have been affected. These authors point out that a better approach would have been to trim the cover so as to establish the same relative velocity ratio that was intended for design point operation. Since this was not done, Inoue and Cumpsty argue that the secondary flow process was artificially stabilized in a fixed position. Under different operating conditions, the secondary flow process would migrate around the impeller passage and different velocity distributions around the impeller exit would result. The present results are still of general interest to the turbomachinery industry, but could be affected by this test/modeling choice. The observation of Inoue and Cumpsty is relevant. However, far more research on the performance of centrifugal compressors must be completed before this hypothesis can be rigorously confirmed.

In spite of the few limitations and slight difficulties in interpretation, the Eckardt data set remains the most valuable and comprehensive data set on centrifugal compressors. Unfortunately, it has never been used to test one-dimensional performance models (with the exception of data presented in Part 3 of this study), and it should become a standard for evaluating performance models.

Basic Data Evaluation

In Part 3 of this study series, seven different cases were evaluated and compared against the 14,000 rpm line data for the Eckardt radial impeller. Both Level II and Level III modeling were used as explained previously. For the present case, three of the seven comparisons can be eliminated based on the prior critical evaluation. For the Level II modeling, which relies on a determination of a rotor efficiency and a slip factor in order to determine all remaining parameters, the option where tip blockage is additionally employed was eliminated from further study since it is fundamentally incorrect and leads to enormous errors in impeller exit mixed-out flow angle. Likewise, the two-zone modeling, which recognizes an isentropic core flow and a residual nonisentropic flow zone, will be evaluated here using the lower value of a mass fraction in the secondary zone ($m_w/m = 0.15$). The higher value of $m_w/m = 0.25$ was evidently somewhat excessive according to the prior Part 3 study. Thus, only the four remaining cases are given here for detailed comparison. These include the Level II modeling (single zone) with a total temperature and also with a total pressure match with the experimental data and the two-zone modeling with the total temperature match and the total pressure match to experimental data.

For each of the four cases, the validity of the modeling process can be tested by comparing the deduced impeller exit flow angle with the measured data from Eckardt and also by comparing the alternate experimental measurement of either total temperature or total pressure. For example, if a total temperature match is effected, then one can determine how well the resultant total pressure agrees with the experimental data. In all cases, the static pressure is always matched in the processing of the data.

An important distinction should be made at this point. The evaluation presented here, concerning the appropriateness of either Level II or Level III flow modeling, has nothing whatsoever to do with any correlated loss system or flow modeling correlations from any design group. This is not a test of the appropriateness of loss correlations from design group A versus design group B, etc. This is a fundamental test of the appropriateness of using either a Level II or Level III modeling procedure. The resultant parameters from the present evaluation, either Level II or Level III, could be used by any group to develop special correlations and form the basis of their specific design system. Whether such a choice would be sensible or not is reflected in the final level of accuracy obtained here. In other words, a fundamental question is being raised: What level of accuracy can be obtained if one wishes to develop a design modeling system using a correlated rotor efficiency (by any method whatsoever of correlation) and a slip factor on the one hand, or by a somewhat more comprehensive modeling system using a two-zone description of the flow process in the impeller, on the other hand?

In all cases, the measurements for total pressure and flow angle are at a radius of 1.075 and the analytical values which must be compared are the mixed-out total parameters for an infinitesimal control volume which is located at the impeller tip. Thus it is always necessary to integrate from the impeller tip to the traverse location by taking into account shear stresses along the sidewalls of the vaneless diffuser. This has been done by using the familiar Stanitz equations [8] for the vaneless diffuser and a skin friction correlation based on past studies for vaneless diffusers in centrifugal compressors. The value employed is $C_f = 0.010\ (\mathrm{Re}/100{,}000)^{0.2}$. This correlation and approach are open to debate.

It is recognized that an average skin friction coefficient might not be the ideal approach. Hence, an alternate friction coefficient, as a function of Reynolds number and distance from the impeller tip, was also evaluated; however, the results changed only slightly. The latter approach is intended to represent the developing nature of the boundary layers in the vaneless diffuser inlet. A further alternative is to use two coefficients to describe both skin friction and dissipation coefficient as proposed by Traupel [9]. The examination of these alternatives has yielded the important conclusion that the analytical modeling and fundamental flow calculation in vaneless diffusers should be completely reviewed from the earliest contributions through the present time in a subsequent paper. However, the integration in this case is over a very small distance, and it is expected that the answers will be only slightly affected regardless of the computational system.

Finally, original data accuracy has been checked with Eckardt. Flow rate is measured to ± 1.0 percent, speed to ± 3 min^{-1}, temperature to $\pm 0.07°\mathrm{C}$ baseline or $\pm 0.20°\mathrm{C}$ with recovery factor error, geometry at impeller exit or diffuser inlet to ± 2 percent on area, pressures to ± 0.25 percent nominal or ± 0.5 percent for $r/r_2 < 1.1$ and angles to ± 0.25 deg

Downloaded 01 Jun 2010 to 171.66.16.57. Redistribution subject to ASME license or copyright; see http://www.asme.org/terms/Terms_Use.cfm

Table 1 Impeller modeling parameters

Case	Model level	m_w/m	$p_{0,\text{traverse}}$	$T_{0,\text{coll}}$	α_{traverse}	p_2
1-O	II	–	D	M	D	M
2-O	II	–	M	D	D	M
3-O	III	0.15	D	M	D	M
4-O	III	0.15	M	D	D	M
1-A	II	–	D	M	D	M
2-A	II	–	M	D	D	M
3-A	III	0.15	D	M	D	M
4-A	III	0.15	M	D	D	M
1-B	II	–	D	M	D	M
2-B	II	–	M	D	D	M
3-B	III	0.15	D	M	D	M
4-B	III	0.15	M	D	D	M

Note: M = measured parameter used in evaluation
D = deduced parameter resulting from the evaluation

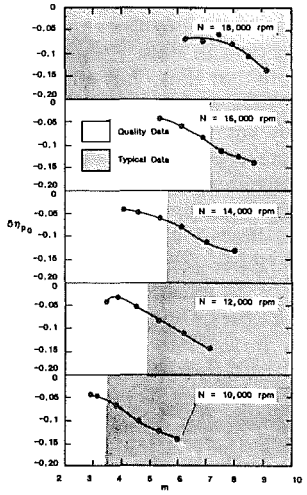

Fig. 7(a)

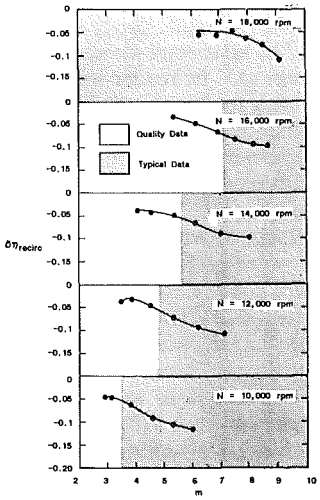

Fig. 7(b)

Fig. 7 Rotor O performance evaluation; Level II modeling: (*a*) based on matching N, m, p_2, T_{coll}, and computing $\delta p_0 = p_{0\ \text{traverse}} - p_0$ computed in terms of rotor efficiency decrement; (*b*) based on matching, N, m, p_2, $p_{0\text{traverse}}$, and computing $\delta T_0 = T_{\text{coll}} - T_{02\text{m}}$ in terms of rotor efficiency decrement

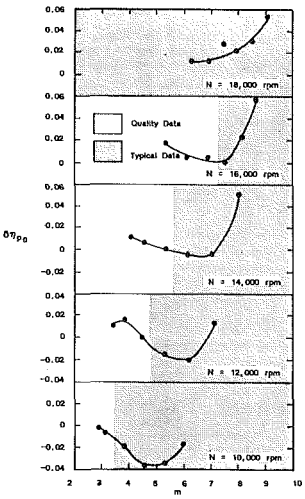

Fig. 8(a)

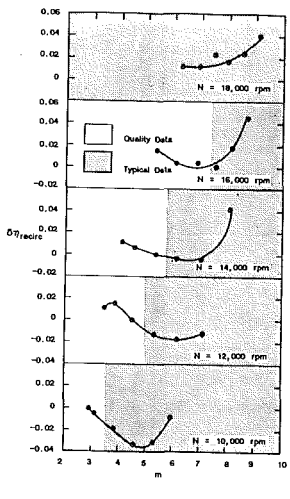

Fig. 8(b)

Fig. 8 Rotor O performance evaluation; Level III modeling: (*a*) based on matching N, m, p_2, T_{coll}, and computing $\delta p_0 = p_{0\ \text{traverse}} - p_0$ computed in terms of rotor efficiency decrement; (*b*) based on matching N, m, p_2, $p_{0\ \text{traverse}}$, and computing $\delta T_0 = T_{\text{coll}} - T_{02\text{m}}$ in terms of rotor efficiency decrement

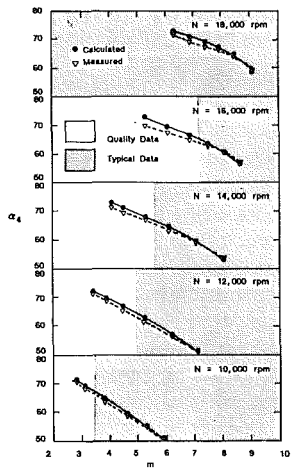

Fig. 9(a)

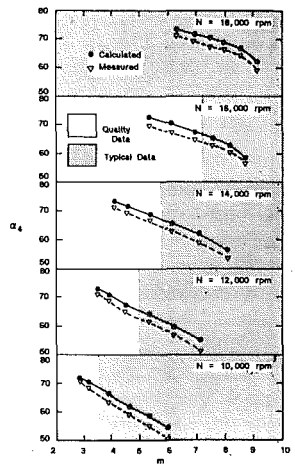

Fig. 9(b)

Fig. 9 Rotor O mass average flow angle at $R = 1.075$; Level II modeling: (a) T_0 match; (*b*) p_0 match

nominal or ± 0.5 deg for $r/r_2 < 1.1$, hence meeting or exceeding common research standards.

Impeller Diffusion Data

The basic data processing of this study utilizes the measured mass flow rate, rotational speed, and impeller tip static pressure. In addition, either a mass average total pressure or total temperature is used, as discussed elsewhere in this paper. For design purposes, static pressures cannot be taken as given and, hence, equivalent information is necessary. Most frequently, diffusion information is provided which directly implies the level of impeller tip static pressure. Thus, as an interesting aside to the present investigation of modeling accuracy, a common measure of impeller diffusion can be presented which is implied by the impeller tip static pressure from the Eckardt impellers. This is presented in the form of MR_2 versus $MR_{2\,\text{id}}$ data. The proper representation of this information into a prediction system is presented elsewhere in this paper series (Part 2, 1986 and Part 6, 1986). For completeness, the diffusion data described in the Eckardt impellers is presented here. This diffusion information is not employed in the present paper. The tip static pressure is used in all experimental evaluations as a direct input.

Impeller diffusion data of the type MR_2 ($= M_{\text{rel 1t}}/M_{\text{rel 2j}}$) versus the ideal Mach number ratio is presented in Figs. 4–6 for the three different stages. Substantial background on the use of this diffusion rating technique has been presented previously by Young [10], and in Parts 3 and 6 of this series (see [1] and [11]). These three stages are particularly unique in that they all show a data backbone (see Part 6) which is higher than the reference band from previous investigations. Yet, they are an industrial type of stage. Reasons for the differences might be explained in part by the series diffusion model presented in Part 7 of this series where the 14,000 rpm speed line from Fig. 4 was evaluated.

Although each of the three stages shows diffusion above the reference level, there are differences in the characteristics. Both Stages O and A have very similar inlet designs and the MR_2 versus MR_{2i} characteristics are comparatively similar, although the shape of individual speed lines differs as can be seen by comparing the two figures. Stage O shows less overlap of the individual speed lines than found for Stage A, thus

Downloaded 01 Jun 2010 to 171.66.16.57. Redistribution subject to ASME license or copyright; see http://www.asme.org/terms/Terms_Use.cfm

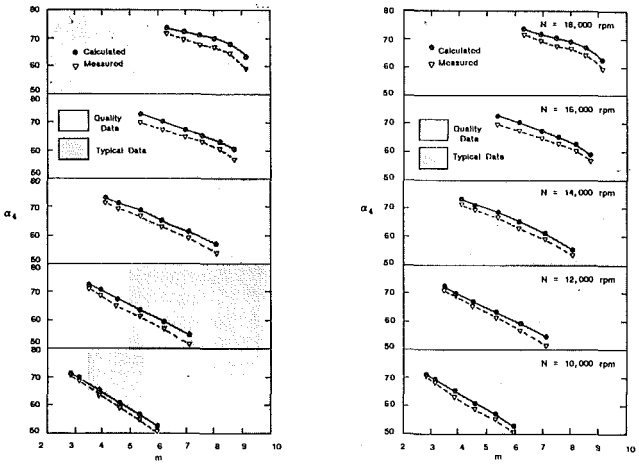

Fig. 10(a) Fig. 10(b)

Fig. 10 Rotor O mass average flow angle at $R = 1.075$; Level III modeling: (a) T_0 match; (b) p_0 match

revealing a tendency for the higher speed lines to break away from the backbone and show lower diffusion levels. Similar examples have been found for other stages in Part 6 of this series. The data for Stage B is somewhat different than the other stages and, in fact, the inlet is designed quite differently as illustrated in Fig. 2. Presently there is no explanation for this particular change in diffusion characteristics.

Model Evaluation

Available data permit the evaluation of the basic velocity triangles and thermodynamics of the stage while using some of the data as known parameters to be input to the calculation and using other parameters as deduced, based on the governing equations. The equations are shown in detail in Part 3 of this series and a summary of the various cases is shown as Table 1. As a consequence of this evaluation, three basic parameters are available for critical examination. Firstly, when the total temperature is matched at the impeller exit, there is a resultant deduction of the mixed-out total pressure from the stage. This mixed-out total pressure can be compared against the mass average total pressure, after a suitable adjustment for wall shear stresses between the impeller tip and the traverse location. In this case, some level of total pressure disagreement (between deduced and measured) will exist and can be plotted. In order to present the data in a meaningful pattern, the total pressure discrepancy has been converted into a $\delta\eta$ to represent the points of stage efficiency that the total pressure discrepancy would yield. This is accomplished by using the hydraulic equivalent so that $\delta\eta_{p_0} = \delta p_0/\rho/W_x$. In the second case, the total pressure is matched and the resultant discrepancy in total temperature is inevitable. This is readily converted to a difference in efficiency and, if the predicted total temperature from the velocity triangle work is less than the measured total temperature, then one would anticipate recirculation work as the culprit. However, it is possible due to experimental inaccuracies, or inaccuracies in thermodynamic modeling, that the opposite would result and this is physically impossible. Thus one would expect that $\delta\eta_{T_0}$ is always positive, and negative values would be a reflection of modeling or data errors. Furthermore, since no supporting evidence exists for recirculation, it would be expected that this discrepancy should be close to zero. Indeed, either a total pressure or a total temperature discrepancy should be very close to zero for acceptable modeling. The third physical parameter for examination is the mixed-out flow angle which is always a deduced parameter and can be critically examined by comparing the deduced value against the experimental value. Many other parameters could be plotted, but they are not of fundamental significance. Those chosen are absolutely essential for good fluid dynamic prediction of stage performance.

A thorough examination of the traverse data showed that distortions are probably present in the flow field since some of the traverses do not yield a mass flow rate which agreed with the orifice. In general, the traverses close to the impeller tip are good to within a few percent, with occasional exceptions which might drift up by 5 percent or a bit more. However, traverses far removed from the impeller tip, near the outer diameter of the vaneless diffuser, frequently have discrepancies of 10 percent or more. As a measure of the level of distortion in the stage, the average mass flow discrepancy at the innermost and outermost traverses is noted for reference. All data which have an average flow rate agreement (with the orifice mass flow level) of 5 percent or better are judged to be "quality" data, data which show less satisfactory agreement (5 to 10 percent discrepancy) are deemed "typical" data, and a few points which exceed 10 percent are marked as "marginal." The range of accuracy is shown in all of the figures to guide the reader in forming conclusions.

The efficiency matching data is shown in Figs. 7 and 8 for Stage O. The reader will quickly note that Figs. 7(*a*) and 7(*b*) appear to be virtually identical, and Figs. 8(*a*) and 8(*b*) appear to be virtually identical. The first pair represents the efficiency decrement associated with a total pressure mismatch when the total temperature is forced into a match agreement, whereas the second figure in the pair is the efficiency decrement associated with a total temperature mismatch when the total pressure is forced into agreement. Since the measurements were completely independent, there is no reason why the two must be exactly the same, and in fact they are not. However, the discrepancies are comparatively small. This was also true for Stages A and B and therefore nearly redundant plots for the latter stages are omitted from this paper. By examining Figs. 7(*a*) and 7(*b*), it will be observed that the single-zone (Level II) modeling invariably has an error between -0.05 and -0.15. This means that either the total pressure or the total temperature is mismatched by 5 to 15 points of stage efficiency when the opposite parameter is used in data reduction. Again, this has nothing to do with any loss prediction system. It is simply the direct result of using the basic thermodynamic and velocity triangle relationships according to the level of modeling employed. Figures 8(*a*) and 8(*b*) are directly equivalent to Figs. 7(*a*) and 7(*b*) but apply to the two-zone modeling (or Level III). In this case, the discrepancies range from approximately -0.04 to $+0.06$. Clearly, the discrepancies are much closer to physical reality with the Level III model than with the Level II model.

Figures 9(*a*), 9(*b*), 10(*a*), and 10(*b*) show the deduced flow angle values compared with the measured flow angle values at the first traverse location. In all cases, the trends are excellent. Only in the first case is the quantitative agreement really very good. In other words, when the total temperature match was used with single-zone modeling, the flow angle deduced is quite close to the measured values shown in Fig. 9(*a*). However, when the same modeling is used with a total pressure match, then the flow angle shows a greater discrepancy, on the order of 3 or 4 deg, see Fig. 9(*b*). Level III modeling is about the same but not quite as good as the Fig. 9(*a*) results. In general, the angle errors are on the order of 2 or 3 deg with the Level III two-zone modeling.

The results for Stage A are shown in Figs. 11(*a*) and 11(*b*), 12(*a*), and 12(*b*). Figures 11(*a*) and 11(*b*) contrast the efficiency discrepancies from total temperature matching and, as noted above, the efficiency discrepancies resulting from total pressure matching are quite similar. For Fig. 11(*a*), the efficiency discrepancy falls between approximately -3 and -18 percent. For the Level III analysis shown in Fig. 11(*b*), the er-

Downloaded 01 Jun 2010 to 171.66.16.57. Redistribution subject to ASME license or copyright; see http://www.asme.org/terms/Terms_Use.cfm

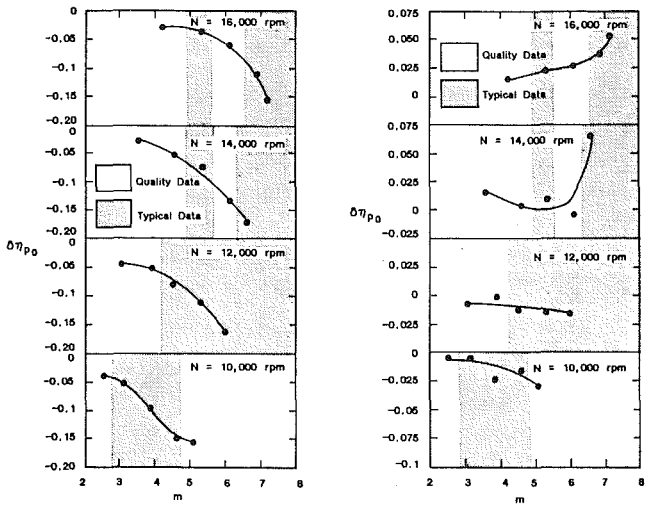

Fig. 11(*a*) Fig. 11(*b*)

Fig. 11 Rotor A performance evaluation based on matching N, m, p_2, T_{coll} and computing $\delta p_0 = p_{0\,\text{traverse}} - p_{0\,\text{computed}}$ in terms of rotor efficiency decrement: (*a*) Level II modeling; (*b*) Level III modeling

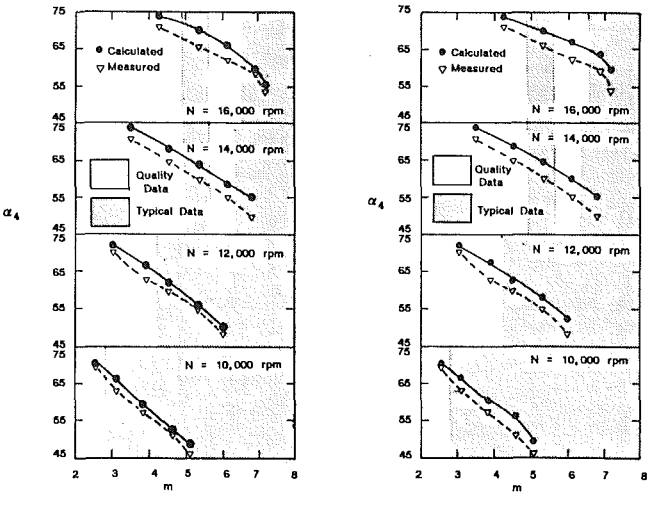

Fig. 13(*a*) Fig. 13(*b*)

Fig. 13 Rotor B performance evaluation based on matching N, m, p_2, T_{coll} and computing $\delta p_0 = p_{0\,\text{traverse}} - p_{0\,\text{computed}}$ in terms of rotor efficiency decrement: (*a*) Level II modeling; (*b*) Level III modeling

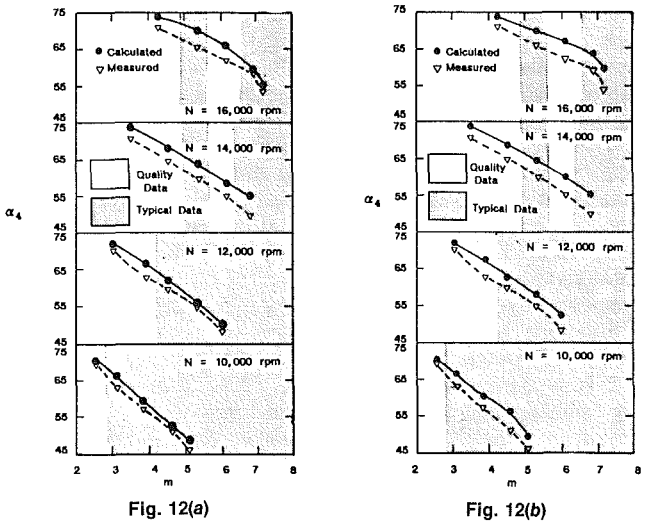

Fig. 12(*a*) Fig. 12(*b*)

Fig. 12 Rotor A mass average flow angle at $R = 1.075$ using T_0 match: (*a*) Level II modeling; (*b*) Level III modeling

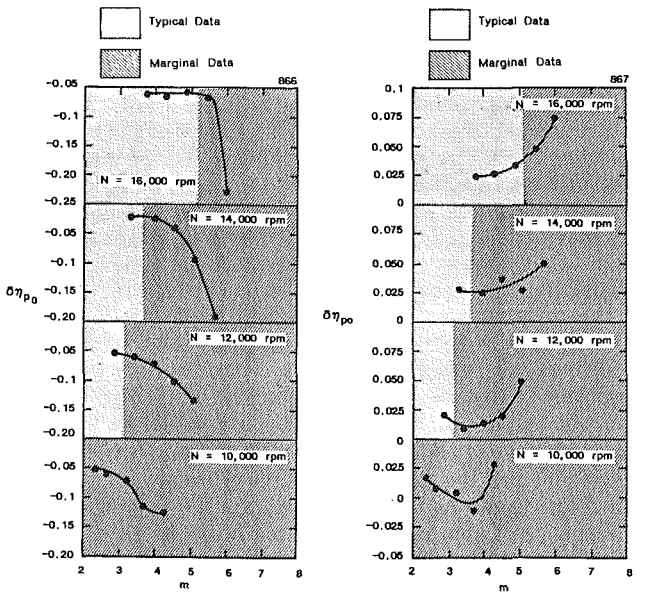

Fig. 14(*a*) Fig. 14(*b*)

Fig. 14 Rotor B mass average flow angle at $R = 1.075$ using T_0 match: (*a*) Level II modeling; (*b*) Level III modeling

ror falls between approximately -3 and $+5$ percent. Incidentally, an error of 0.1 on Fig. 11(*a*) or 11(*b*) is equivalent to approximately 2.3 percent of the impeller exit kinetic energy or 7.5 percent of the total pressure rise of the rotor.

Figures 12(*a*) and 12(*b*) contrast the angle predictions for single-zone and two-zone modeling, respectively. These results are for the total temperature match case with rather similar results being obtained for the total pressure match. When both matching techniques are considered together, there is virtually no difference in the level of agreement for the two different modeling procedures.

The evaluation results for Stage B are shown in Figs. 13(*a*), 13(*b*), 14(*a*) and 14(*b*). By comparing Figs. 13(*a*) and 13(*b*), one can observe the efficiency decrement for the total temperature match case by the two different techniques. In this case, the Level II single-zone modeling procedure shows discrepancies of -0.05 to -0.25, whereas the two-zone modeling shows discrepancies in the range of -0.02 to $+0.07$. Once again, the two-zone modeling is significantly better than the single-zone modeling but there are still residual errors which are undesirable. The pertinent angle data are shown in Figs. 14(*a*) and 14(*b*) for the single-zone and two-zone modeling, respectively. Truly excellent agreement is found for the single-zone modeling and very reasonable agreement is shown for the two-zone modeling in Fig. 14(*b*). Errors in the first case are approximately ± 1 deg and in the second case the errors are approximately $+1$ deg and -3 deg. When the additional data for total pressure matching are included, then both the Level II and Level III modeling show almost exactly the same level of agreement.

Table 2 shows a detailed comparison of the discrepancies found in the total pressure, total temperature, and flow angle for each case evaluated. This has been done on a statistical basis to guide readers in a critical evaluation of the appropriateness of both Level II and Level III modeling. Three types of data are included in Table 2. Firstly, the approximate

Downloaded 01 Jun 2010 to 171.66.16.57. Redistribution subject to ASME license or copyright; see http://www.asme.org/terms/Terms_Use.cfm

Table 2 Statistical summary of computed errors

Case	Approximate range of $\delta\eta$	$\overline{\delta\eta}$	$\sigma_{\delta\eta}$	Approximate range of $\delta\alpha$	$\overline{\delta\alpha}$	$\sigma_{\delta\alpha}$	No. of points
1-O	−0.05 to −0.15	−0.086	0.038	−0.5 to +2.5 deg	1.03 deg	0.69 deg	30
2-O	−0.03 to −0.12	−0.069	0.026	+1.0 to +3 deg	2.74 deg	0.57 deg	30
3-O	−0.04 to +0.06	+0.0075	0.023	+1.0 to +3 deg	2.51 deg	0.82 deg	30
4-O	−0.04 to +0.04	+0.0057	0.019	+1.0 to +3 deg	2.42 deg	0.57 deg	30
1-A	−0.03 to −0.17	−0.091	0.051	+1.0 to +3.5 deg	2.05 deg	1.04 deg	20
2-A	−0.03 to −0.17	−0.092	0.049	+2.5 to +6.5 deg	4.46 deg	1.14 deg	20
3-A	−0.03 to +0.06	+0.0077	0.025	+1.5 to +6.5 deg	3.82 deg	1.25 deg	20
4-A	−0.03 to +0.05	+0.0067	0.024	+1.0 to +3 deg	3.66 deg	0.96 deg	20
1-B	−0.02 to −0.25	−0.087	0.051	−2.0 to +0.5 deg	0.84 deg	0.71 deg	20
2-B	−0.05 to −0.25	−0.110	0.061	+0.5 to +8 deg	2.02 deg	1.96 deg	20
3-B	−0.01 to +0.06	+0.026	0.018	−0.5 to +8 deg	2.00 deg	2.05 deg	20
4-B	−0.02 to +0.06	+0.028	0.020	−0.5 to +6 deg	1.34 deg	1.64 deg	20

range of the match parameters from minimum to maximum value is given. Secondly, the mean value of the discrepancy is presented, and finally the variance, in the form of a standard deviation, is presented. All of these measures are of significance in understanding the accuracy of impeller performance modeling. By examining the range from minimum to maximum of any value, one can immediately appreciate the scope of the discrepancy under consideration. For example, the range of variation in $\delta\alpha$ for Level II total temperature T_0 matching invariably less than p_0 matching at Level II for either matching technique for Level III. The mean value is of paramount significance because it shows how far in error the modeling is for any particular parameter for the entire performance map on an average basis. However, many old-time designers have learned to compensate for mean value errors and may be tempted to compensate based on the example of mean values shown in Table 2. Therefore the variance in the tabulated discrepancies is also important, which is presented in the form of one standard deviation σ. Clearly, if the variance is very small, then one can make a correction in a modeling system according to the level of error reflected in the mean value. However, if the variance is large, then any correction will be poor at best. Thus effective model building requires small errors *and small variances* in the errors.

Examine first the mean values of the efficiency discrepancy. For rotors O and A, Level III evaluation shows a mean value discrepancy of approximately one-tenth that of Level II. For rotor B, the mean value of the Level III discrepancy is approximately one-third of the Level II discrepancy. In addition, the variance, as indicated by one standard deviation, for Level III is approximately one-half that for Level II (in some cases a bit less and in other cases quite a bit more favorable).

The fundamental accuracy on flow angle is nearly the same for both Levels II and III. As indicated above from the observation of the range of variation, the use of total temperature matching with a Level II approach (quite common throughout industry) is quite interesting because it does, in fact, show the lowest mean discrepancy value of any of the modeling attempts and the lowest variance. However, when the same level of modeling is used but applied to total pressure matching, then the exact opposite is obtained with the highest mean value of the discrepancy and a significant level of statistical variance. On the other hand, Level III modeling is pretty constant, giving a mean value of discrepancy that is approximately 2 to 3 deg high and a variance of approximately 1 to 2 deg. When all combinations are considered together, it appears that Level II and Level III modeling of flow angle are almost the same with perhaps a very slight bias toward the Level II modeling. The fact that the comparison is virtually a draw should not be surprising. Impeller exit flow angle is principally dependent on impeller tip speed and the mass flow rate as primary variables with only a weak secondary effect on other factors such as deviations, losses, etc.

Conclusions

Both single-zone and two-zone modeling provide effective means of representing the performance of a centrifugal compressor stage. By using the three comprehensive data sets from Eckardt, it has been possible to test this accuracy and determine relative levels of capability. Based on this examination, the following conclusions have been reached:

1 Single-zone modeling (representing the performance of a stage with a rotor efficiency and a slip factor) provides very good prediction of the impeller mixed-out flow angle but gives very poor prediction of the total pressure and/or total temperature leaving the rotor. As a consequence, the errors in total temperature or total pressure, when converted to increments of rotor efficiency, amount to 3 to 25 percent. These evaluations were made while satisfying rotor speed, mass flow, and impeller exit static pressure.

2 In a companion study (Part 3), the technique of improving single-zone modeling by the use of an additional parameter – the impeller exit mixed-out state blockage – was also tested for appropriateness and found to be fundamentally incorrect and significantly in error with respect to the impeller exit flow angle. Consequently, the use of single-zone modeling can only be accepted for approximate calculations of the detailed thermodynamic and fluid-dynamic conditions leaving a rotor.

3 Two-zone modeling, when applied to the three Eckardt data sets, gives impeller exit flow angles approximately comparable to the single-zone modeling but with a substantially reduced error in total temperature and/or total pressure leaving the rotor. Rotor efficiency errors in the range of 0.04 to +0.06 are found for all three stages at all speed lines. These evaluations have been, once again, carried out while matching rotor speed, mass flow, and impeller exit static pressure. For two-zone modeling, an assumption has also been made concerning the strength of the nonisentropic flow within the rotor. Based on results shown in Part 3, a value of $m_w/m = 0.15$ has been employed.

4 The diffusion characteristics of these impellers were interesting. Although they were all nominally designed to pass the same flow rate, the specific diffusion characteristics varied depending on whether a radial element inlet was employed or a swept-back inlet was utilized. All three stages showed relative diffusion which exceeded a traditional reference band. The stages must be evaluated further to determine exactly what contributes to the remarkable relative diffusion. A preliminary evaluation was included in Part 7 of this series [12].

Downloaded 01 Jun 2010 to 171.66.16.57. Redistribution subject to ASME license or copyright; see http://www.asme.org/terms/Terms_Use.cfm

Acknowledgments

The author has pursued this modeling companion over a period of years while acquiring data and preparing calculations. The assistance of Dr. Eckardt throughout this effort is greatly appreciated and acknowledged.

References

1 Japikse, D., "Assessment of Single- and Two-Zone Modeling of Centrifugal Compressors, Studies in Component Performance: Part 3," ASME Paper No. 85-GT-73, 1985.

2 Johnston, J. P., and Dean, R. C., Jr., "Losses in Vaneless Diffusers of Centrifugal Compressors and Pumps," ASME *Journal of Basic Engineering*, 1965, pp. 1–12.

3 Dean, R. C., Jr., Wright, D. D., and Runstadler, P. W., Jr., "Fluid Mechanics Analysis of High-Pressure-Ratio Centrifugal Compressor Data," USAAVLABS Technical Report 69-76, Feb. 1970.

4 Eckardt, D., "Instantaneous Measurements in the Jet-Wake Discharge Flow of a Centrifugal Compressor Impeller," ASME JOURNAL OF ENGINEERING FOR POWER, Vol. 97, 1975, pp. 337–346.

5 Trultzsch, K.-J., and Eckardt, D., "Radialverdichter, Forschungsberichte Verbrennungskraftmaschinen," Heft 237, 1977.

6 Eckardt, D., "Flow Field Analysis of Radial and Backswept Centrifugal Compressor Impellers, Part 1: Flow Measurements Using a Laser Velocimeter," *Performance Prediction of Centrifugal Pumps and Compressors*, ASME 25th Annual International Gas Turbine Conference, New Orleans, Mar. 9–13, 1980, pp. 77–86.

7 Inoue, M., and Cumpsty, N. A., "Experimental Study of Centrifugal Impeller Discharge Flow in Vaneless and Vaned Diffusers," ASME JOURNAL OF ENGINEERING FOR GAS TURBINES AND POWER, Vol. 106, 1984, pp. 455–467.

8 Stanitz, J. D., "One-Dimensional Compressible Flow in Vaneless Diffusers of Radial- and Mixed-Flow Centrifugal Compressors, Including Effects of Friction, Heat Transfer and Area Change," National Advisory Committee for Aeronautics Technical Note 2610, Jan. 1952.

9 Traupel, W., *Thermische Turbomaschinen*, Springer-Verlag, Berlin, 1977.

10 Young, L. R., "Discussion of Rodgers' Paper," ASME *Journal of Fluids Engineering*, Vol. 99, No. 1, 1977, pp. 94–95.

11 Japikse, D., and Osborne, C., "Design Optimization of Advanced Centrifugal Compressors," ASME Paper No. 86-GT-222.

12 Japikse, D., "A Critical Evaluation of Stall Concepts for Centrifugal Compressors and Pumps, Studies in Compressor Performance: Part 7," 1984.

Downloaded 01 Jun 2010 to 171.66.16.57. Redistribution subject to ASME license or copyright; see http://www.asme.org/terms/Terms_Use.cfm

Effect of Area Ratio on the Performance of a 5.5:1 Pressure Ratio Centrifugal Impeller

L. F. Schumann

D. A. Clark

Propulsion Directorate,
U.S. Army Aviation Research and
Technology Activity—AVSCOM,
Lewis Research Center,
Cleveland, OH 44135

J. R. Wood

NASA Lewis Research Center,
Cleveland, OH 44135

A centrifugal impeller which was initially designed for a pressure ratio of approximately 5.5 and a mass flow rate of 0.959 kg/s was tested with a vaneless diffuser for a range of design point impeller area ratios from 2.322 to 2.945. The impeller area ratio was changed by successively cutting back the impeller exit axial width from an initial value of 7.57 mm to a final value of 5.97 mm. In all, four separate area ratios were tested. For each area ratio a series of impeller exit axial clearances was also tested. Test results are based on impeller exit surveys of total pressure, total temperature, and flow angle at a radius 1.115 times the impeller exit radius. Results of the tests at design speed, peak efficiency, and an exit tip clearance of 8 percent of exit blade height show that the impeller equivalent pressure recovery coefficient peaked at a design point area ratio of approximately 2.748 while the impeller aerodynamic efficiency peaked at a lower value of area ratio of approximately 2.55. The variation of impeller efficiency with clearance showed expected trends with a loss of approximately 0.4 points in impeller efficiency for each percent increase in exit axial tip clearance for all impellers tested. The data also indicated that the impeller would probably separate at design area ratios greater than 2.748. An analysis was performed with a quasi-three-dimensional inviscid computer code which confirmed that a minimum velocity ratio was attained near this area ratio thus indicating separation. These data can be used to verify impeller flow models which attempt to account for very high diffusion and possible separation.

Introduction

In the design of centrifugal impellers, several geometric parameters must be specified. Some of these, such as impeller inlet and exit radii, are fixed by design constraints of pressure ratio, mass flow, and any geometric limits imposed by the configuration. Others such as impeller exit blade height, impeller exit blade sweepback, number of blades, and impeller rotative speed can be chosen by the designer in order to optimize the particular stage within limits dictated by stress or turbine matching considerations. Studies have been done in the past which indicate the trends of impeller efficiency with specific speed [1, 2], with impeller backsweep [2], and with impeller relative velocity distribution [3].

The subject of this paper is the variation of impeller performance with impeller area ratio. The data should be useful for evaluating the ability of an advanced computer code to calculate the outlet flow field of a series of impellers which have only a single geometric parameter varied. The area ratio was varied over a large range because data were desired that would include the effect of a large global separation in the impeller. This type of data would be useful in developing flow models that can describe the flow behavior in an impeller that approaches or operates with large amounts of separation. The data on clearance effects should also be useful for checking clearance models.

The equivalent area ratio is defined as the geometric area ratio needed to provide the equivalent amount of relative diffusion for a rotating impeller as in a nonrotating diffuser. Thus a change in equivalent area ratio is indicative of a change in relative velocity ratio. For a low diffusion impeller (i.e., a low ratio of inlet tip relative Mach number to exit relative Mach number), the boundary layer growth in the impeller will be small but the Mach number levels will be high. Also, since less diffusion is done in the impeller, more diffusion must be done in the diffusing system to achieve the same static pressure level.

On the other hand, for high diffusion impellers, although Mach number levels and clearance losses may be less, the impeller boundary layer growth may be large. For excessively large area ratios, the impeller boundary layers may separate and cause a decrease in impeller performance and, thus, a negative effect of diffuser performance. Therefore, the tradeoffs involved in choosing between low diffusion and high diffusion indicate that an optimum area ratio may exist.

For this study, the exit passage width of an impeller with a nominal total pressure ratio of 5.5 was successively cut back while maintaining the same tip contour. This effectively reduced the equivalent area ratio of the impeller from an initial

Contributed by the Gas Turbine Division of THE AMERICAN SOCIETY OF MECHANICAL ENGINEERS and presented at the 31st International Gas Turbine Conference and Exhibit, Düsseldorf, Federal Republic of Germany, June 8–12, 1986. Manuscript received at ASME Headquarters March 7, 1986. Paper No. 86-GT-303.

Copyright © 1987 by ASME

Downloaded 01 Jun 2010 to 171.66.16.57. Redistribution subject to ASME license or copyright; see http://www.asme.org/terms/Terms_Use.cfm

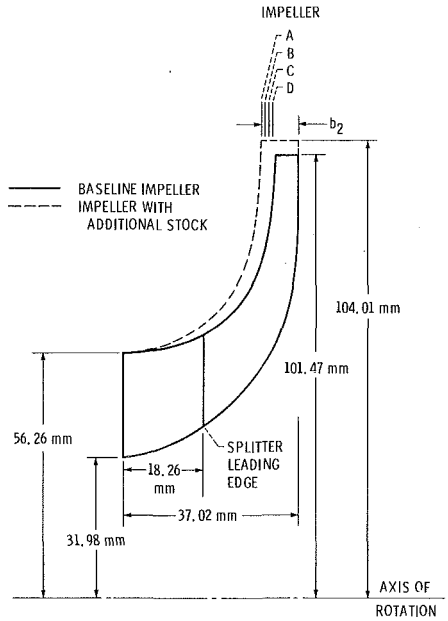

Fig. 1 Impeller configurations and geometry

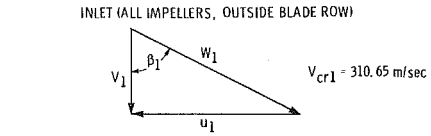

	u_1/V_{cr1}	V_1/V_{cr1}	W_1/W_{cr1}	β_1	P_1'/P_{STD}	T_1'/T_{STD}
HUB	0.494	0.398	0.597	51.11	1.0	1.0
MEAN	.730	.487	.827	56.27	1.0	1.0
TIP	.872	.562	.977	57.21	1.0	1.0

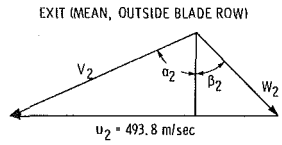

IMPELLER	u_2/V_{cr2}	V_2/V_{cr2}	W_2/W_{cr2}	α_2	β_2	P_2'/P_1'	T_2'/T_1'
D	1.239	0.989	0.455	75.63	48.83	5.162	1.683
C	1.236	.990	.427	77.13	50.84	5.269	1.690
B	1.234	.994	.404	78.28	52.20	5.385	1.697
A	1.231	.998	.383	79.25	53.32	5.501	1.704

Fig. 2 Design point impeller velocity diagrams at design mass flow rate

value of 2.945 to a final value of 2.322. For each of the four impeller configurations, three values of the impeller exit tip clearance were tested to establish the effect of clearance on overall performance and on the flow profiles at impeller exit.

Comparisons were made among the four impeller exit spanwise survey measurements to determine the effect of area ratio and clearance on impeller performance. Comparisons are based on derived impeller exit total pressure and efficiency and mass-averaged performance parameters at the downstream survey location.

Impeller Aerodynamic Design

The baseline impeller is a scaled-up (scale factor = 1.2588) version of an impeller designed for use in an automotive gas turbine engine. The original version of the impeller had 18 blades and its aerodynamic design is described in [4]. The impeller was subsequently modified to include a splitter blade in order to reduce impeller blade loading. This modified impeller was also reduced in exit radius in order to maintain the same work input; however, the impeller main blade shapes and hub and shroud contours were not changed. The splitter blade leading edge was biased toward the suction surface of the main blade in order to equalize the mass flow rate in the splitter channels. The splitter blade shape was then faired into the

Nomenclature

A = geometric area, m^2
AR = impeller equivalent area ratio at design flow rate $= \dfrac{P_2''}{P_1''}\sqrt{\dfrac{T_{1T}''}{T_2''}}\dfrac{A_2}{A_{1T}}$
A_{1T} = impeller inlet tip flow area = $\dot{m}/\rho_{1T}W_{1T}$
A_2 = impeller exit geometric area = $2\pi r_2 b_2 \cos\beta_{2b} - z_2 t_{n2}$
b = impeller blade height, mm
CL = impeller exit tip clearance, mm
CP_{imp} = impeller equivalent static pressure recovery coefficient $= \left(\dfrac{P_2}{P_{1T}}\dfrac{P_{1T}''}{P_2''} - 1\right)\Big/\left(\dfrac{P_{1T}''}{P_{1T}} - 1\right)$
h = enthalpy, J/kg
$\dot{m}$ = mass flow rate, kg/s
N_s = specific speed = $\omega\sqrt{\dot{m}/\rho_0'}/\Delta h_{id}^{3/4}$
P = pressure, Nt/m^2
r = radius, mm
t_n = blade normal thickness
T = temperature, K
U = wheel speed, m/s
V = absolute velocity, m/s
W = relative velocity, m/s
z = axial coordinates, mm
z = blade number
α = absolute flow angle, deg
β = relative flow angle, deg
Δ_{CL} = impeller exit tip deflection, mm
δ = ratio of inlet total pressure to U.S. standard sea level pressure
η = efficiency
θ = ratio of inlet total temperature to U.S. standard sea level temperature
ρ = density, kg/m^3
ω = impeller angular velocity, 1/s

Subscripts

a = average
b = blade
cr = conditions at the critical state
des = design
H = hub
id = ideal
IMP = impeller
M = mean
STD = U.S. standard sea level pressure, 101,325 Nt/m^2 and temperature, 288.15 K
T = tip
0 = station at bellmouth inlet (ambient)
1 = impeller inlet
2 = impeller exit
3 = survey location
4 = downstream measuring station
1-14 = shroud static tap numbers

Superscripts

$'$ = absolute total conditions
$''$ = relative total conditions

Downloaded 01 Jun 2010 to 171.66.16.57. Redistribution subject to ASME license or copyright; see http://www.asme.org/terms/Terms_Use.cfm

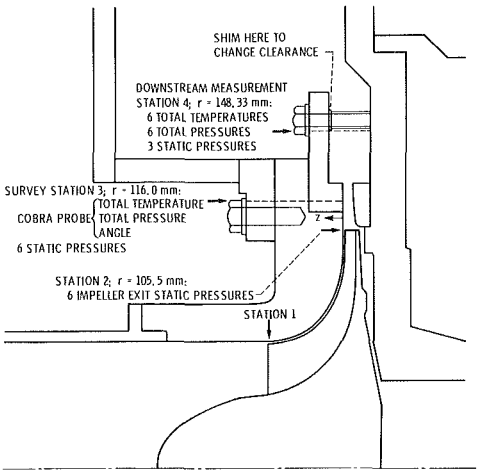

SHROUD STATIC TAP NUMBER	LOCATION r(mm)	z(mm)
1	56.58	33.95
2	57.00	27.23
3	58.47	20.63
4	61.47	14.53
5	65.86	9.38
6	71.46	5.59
7	77.75	3.10
8	84.36	1.55
9	91.09	.67
10	97.90	.18
11	104.71	0
12	105.51	0
13	116.03	0
14	148.34	0

Fig. 3 Compressor flow path and instrumentation stations

main blade shape at a specified distance downstream from the splitter leading edge. The computer code of [5] was used to determine the bias and fairing schedule that would produce reasonable splitter leading edge velocities with an equal mass flow rate split. The detailed blade coordinates and impeller mechanical design for the baseline impeller are presented in [6].

The initial build of the impeller had an exit radius and exit blade height 2.54 mm larger than the baseline impeller (Fig. 1). The blade shape was obtained by extrapolating the baseline blade. The overall geometry of the initial build of the impeller was as follows:

Number of main blades/splitter blades	18/18
Inlet tip diameter, mm	112.52
Inlet hub/tip ratio	0.568
Exit tip diameter, mm	208.02
Exit blade height, mm	7.57
Backsweep angle, deg	30.20
Design axial clearance/exit blade height	0.034

Estimated performance characteristics for Impeller A are as follows:

Equivalent mass flow rate, $\dot{m}\sqrt{\theta}/\delta$, kg/s	0.959
Impeller total pressure ratio, P_2'/P_0'	5.50
Impeller static pressure ratio, P_2/P_0'	2.85
Impeller inlet aerodynamic blockage	0.02
Impeller total efficiency, η_2	0.903
Equivalent speed, $N/\sqrt{\theta}$, rpm	45,337.0
Specific speed, Ns	0.518

The impeller design point velocity diagrams for the four impellers are shown in Fig. 2. A meridional view of the flow path and instrumentation locations is shown in Fig. 3. The flow from the backswept centrifugal impeller is reduced in velocity in a constant area vaneless space before being dumped into a plenum at a radius ratio of $r/r_2 = 1.177$. The width of both the vaneless space and dump region change as the exit blade height of the impeller is changed and as the clearance is changed.

Apparatus, Instrumentation, and Procedure

Test Facility. A schematic of the test facility is shown in Fig. 4. The compressor and turbine are on a common shaft. Compressor mass flow rate was measured with a calibrated

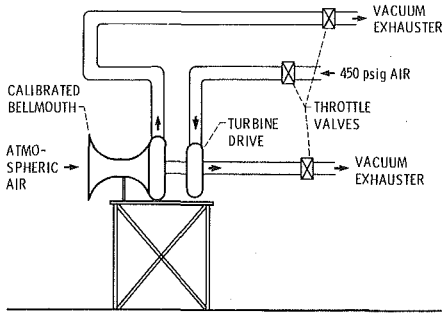

Fig. 4 Small centrifugal compressor facility

Table 1 Impeller configurations

Impeller	b_2/r_2	AR_{IMP} design point	Clearance	CL/b_2 design speed
A	0.0728	2.945	Small	0.023
			Medium	.057
			Large	.090
B	.0679	2.748	Small	.047
			Medium	.083
			Large	.115
C	.0630	2.550	Small	.054
			Medium	.093
			Large	.128
D	.0574	2.322	Small	.072
			Medium	.115
			Large	.153

bellmouth on the compressor inlet. Compressor discharge pressure was manually controlled with a remotely operated valve in the compressor discharge line. Drive turbine speed was manually controlled by a valve on the turbine inlet line. Turbine discharge pressure was manually controlled by a remotely operated valve in the turbine discharge line.

Instrumentation. The compressor instrumentation stations are shown in Fig. 3. Since ambient air enters the compressor inlet, local barometric pressure was used for the inlet total pressure. Inlet total temperature was measured with three bare-wire copper-constantan thermocouples spaced 120 deg apart and attached to the bellmouth. The downstream measurement station 4 was instrumented with six combination total temperature and total pressure probes evenly spaced about the circumference. The thermocouples were bare-wire chromel-alumel probes which were calibrated for Mach number effects. The total pressure tubes were chamfered to decrease angle sensitivity. The probes were set at an angle of approximately 80 deg from radial so as to be oriented in the approximate direction of the highly swirling flow.

Static pressures were measured along the impeller shroud and through the vaneless space to the dump. A single row of taps was used on the shroud with an additional five taps spaced 6 deg apart circumferentially just downstream of the impeller trailing edge ($r/r_2 = 1.014$). At station 3 ($r_3/r_2 = 1.115$) where survey data were taken, six static taps were spaced 6 deg apart. Three static pressure taps were equally spaced at the downstream measurement station 4. The radial locations of the static taps are shown on Fig. 3.

Survey data at station 3 were taken using a miniature combination probe having total pressure, total temperature, and angle sensors. The pressure tubes were made from 0.508-mm-dia tubing and the total temperature probe was made from a

Downloaded 01 Jun 2010 to 171.66.16.57. Redistribution subject to ASME license or copyright; see http://www.asme.org/terms/Terms_Use.cfm

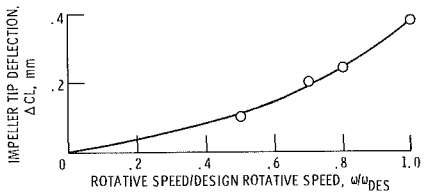

Fig. 5 Impeller tip deflection versus rotative speed

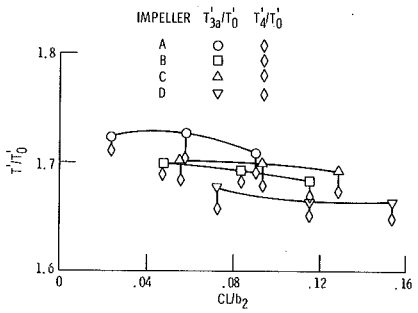

Fig. 6 Impeller temperature rise versus clearance; 100 percent design speed; $\dot{m}/\dot{m}_{des} = 0.90$

0.16-mm-dia chromel-alumel bare wire. The probe was nonnulling so it was necessary to calibrate it in a flow tunnel to determine corrections for total pressure, angle, and temperature versus indicated pressures from the angle sensor. The thermocouple was also calibrated for Mach number.

All thermocouple readings are referenced to an ice-bath temperature and are accurate to within ±0.5°F. Pressures were measured with a scanivalve system and were dynamically calibrated with a dead weight tester. The measured pressures should be accurate to within ±0.06 Nt/cm^2. For this study, repeatability of measurements is more important than absolute accuracy since trends are the desired result. Repeatability was judged to be good for this test.

Impeller Configurations. The impeller diffusion ratio was varied by changing the impeller exit blade height (b width) and thus equivalent area ratio. This was done by successively modifying the impeller as shown in Fig. 1. The exit b width was changed by axially translating the fabricating template for the impeller tip contour thus maintaining the same tip contour for all configurations. In all, four impeller exit b widths were tested corresponding to four impeller diffusion ratios as shown in Fig. 1. In order to maintain the same impeller exit clearance, the shroud shims (shown in Fig. 3) had to be changed for each impeller exit b width. Thus the vaneless diffuser width and the dump region width changed as the impeller b width changed. The impeller exit clearance was also changed using the shroud shims. For each impeller b width tested, three impeller exit clearances were tested. A list of the four impeller configurations tested along with the calculated area ratios and clearances tested for each impeller is shown in Table 1.

Tip Clearance. Impeller exit tip clearance was measured using graphite rub probes. The impeller tip deflected toward the shroud as impeller rotative speed increased. A plot of impeller deflection versus rotative speed is shown in Fig. 5. The actual clearance was obtained by subtracting the impeller deflection from the cold setup clearance. The deflection versus rotative speed curve was the same for all configurations tested.

Impeller Test. Ambient test cell air was used for the working fluid for all tests. Therefore, the inlet pressure was barometric and the inlet temperature was approximately 295 K. Data were taken at speeds of 50, 80, 90, and 100 percent of the design rotative speed. Mass flow rate was varied from open throttle to surge. Surge was indicated by an audible noise from the test cell. At 50 percent speed, no audible noise was detected and therefore surge could not be accurately determined.

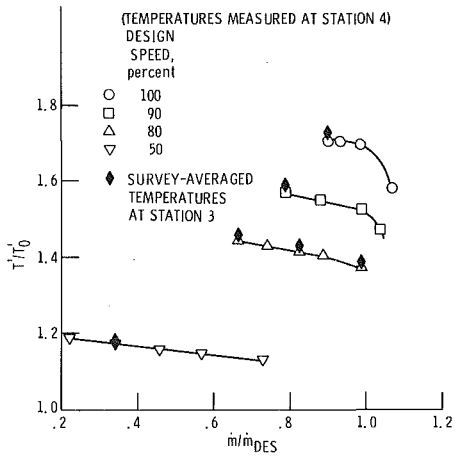

Fig. 7(*a*) Temperature ratio

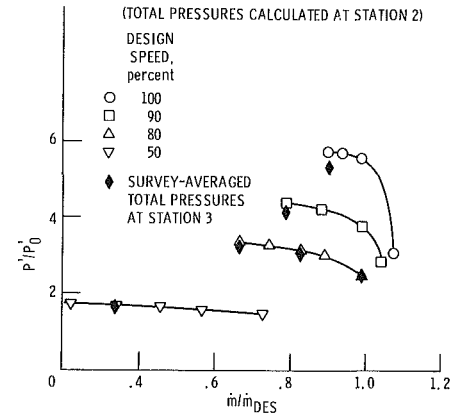

Fig. 7(*b*) Total pressure ratio

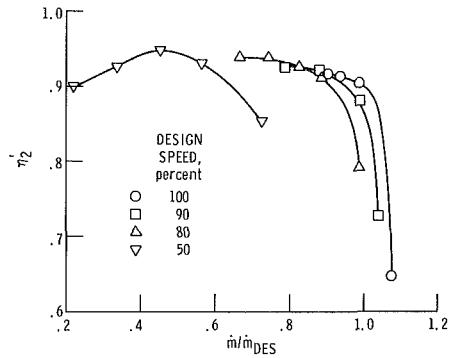

Fig. 7(c) Total efficiency

Fig. 7 Performance characteristics for Impeller A ($CL/b_2 = 0.023$)

Surveys. Impeller exit surveys were taken at a location downstream of the impeller trailing edge ($r_3/r_2 = 1.115$). Data were taken every 0.51 mm from hub to tip; therefore more survey data points were taken for the high b-width impellers than for the low b-width impellers. Surveys were conducted at selected mass flow rates at speeds from 50 to 100 percent of design. Surveys were taken at approximately the same mass flow rates for each impeller configuration tested so that comparisons could be made. At each point in the survey, total temperature, total pressure, and flow angle were measured using the combination probe.

Downloaded 01 Jun 2010 to 171.66.16.57. Redistribution subject to ASME license or copyright; see http://www.asme.org/terms/Terms_Use.cfm

Impeller Performance Calculation Procedure

Based on Calculated Quantities. The overall impeller map was derived from a calculated total pressure at the impeller exit and the measured downstream total temperature. This procedure was used since the time required to complete one survey was considerable and overall performance could be reasonably compared using this method since all the data were taken on the same test rig using the same instrumentation. Consequently, trends observed from these measurements should be correct for the configurations described herein. The total pressure was calculated from the measured impeller exit static pressure (an arithmetic average of the values from six static pressure taps), the measured downstream total temperature, impeller exit annulus area, and continuity assuming no impeller exit aerodynamic blockage. Results obtained with the survey probes indicate a heat loss between the survey location and the downstream measurement station. The temperature difference for the three clearances measured at each of the four b widths varied from 0.5 to 1.5 percent of the mass average of the survey temperatures. The trends observed for temperature ratio versus area ratio and clearance were the same for both the mass average survey temperatures and measured downstream temperatures. A comparison of the temperatures measured at the downstream measurement station (station 4) and those based on mass-averaged data at the survey location (station 3) for the four impeller configurations at design speed is shown in Fig. 6.

Another measure of impeller performance is given by the equivalent pressure recovery coefficient. This quantity is a measure of the static pressure recovery of the impeller. It is defined in such a way as to remove the centrifugal contribution to the static pressure recovery and thus is a measure of the impeller's performance as a diffusing element. The equivalent pressure recovery coefficient is calculated for the tip streamline and thus values of the static pressure at the impeller inlet tip are required. These calculations were done using an axisymmetric duct calculation procedure at the impeller inlet. This procedure was also used in defining the impeller inlet tip flow area for use in the definition of impeller equivalent area ratio.

Based on Survey Measurements. Survey measurements of total temperature, total pressure, and flow angle were taken downstream of the impeller trailing edge ($r_3/r_2 = 1.115$). Static pressure was obtained from an arithmetic average of six static taps on the shroud side of the diffuser at the same radius as the survey probe. The static pressure was assumed to be constant across the diffuser passage at a constant radius. From the measured static and total pressures and total temperatures local values of velocity were obtained. These velocities together with the angle measurements from the survey and the geometric area allowed an integrated mass flow to be calculated. This integrated mass flow was compared to the measured mass flow and the measured flow angles were adjusted by a constant value across the passage until agreement was obtained. This was done since it was judged that the angle measurements were more uncertain than the other measurements taken. The amount of correction varied from 2.0 to 3.5 deg for all flow points surveyed. Local values of radial and tangential velocities were then calculated from the calculated velocities and the corrected flow angles. Local efficiencies were calculated from the measured total pressures and total temperatures using curve fits on tables of gas properties. Averaged values of total efficiency, total pressure, velocity, and angle were then calculated using procedures described in the Appendix. The effect of the angle correction on the averaged efficiency was less than 0.25 points (a point is 1 percent in efficiency) and 0.5 percent in total pressure.

Results and Discussion

Overall Measurements. For this investigation, four impeller configurations were tested. The configurations differed from each other only in the size of the exit b width. All of the remaining geometry remained the same. For each value of impeller exit b width, three separate values of impeller tip clearance were tested.

The overall impeller performance for the impeller with the highest b width (designated Impeller A) and smallest clearance is shown in Fig. 7. The performance maps for the other impeller configurations and other clearances are not shown since they are similar. The temperatures shown were for measurements at the downstream measurement station (station 4). Also shown are the mass-averaged temperatures from the survey probe located at station 3. These measurements were taken at selected mass flows and indicated temperatures which were up to 1-1/2 percent higher than those measured by the downstream thermocouples. The compressor was surged for each of the speed lines shown; however, at 50 percent speed no audible surge was detected and therefore some data points may lie in a stalled region of the map. The calculated total pressure ratio peaked at a value of 5.75 for Impeller A at a mass flow near surge (90 percent design mass flow rate) for the smallest clearance tested ($CL/b_2 = 0.023$) at 100 percent design speed. Calculated impeller efficiency at 100 percent design speed also peaked at this mass flow rate and clearance at a value of 0.915. For this reason all comparisons for impeller configurations were made at design speed and at a mass flow of 90 percent design mass flow. Also, comparisons at other mass flow rates and rotative speeds were found to be similar to those at the selected rotational speed and mass flow rate.

The variations of impeller efficiency and impeller equivalent pressure recovery coefficient with clearance and mass flow are shown in Figs. 8 and 9 for each of the four impeller configurations. The figures show an increase in pressure recovery coeffi-

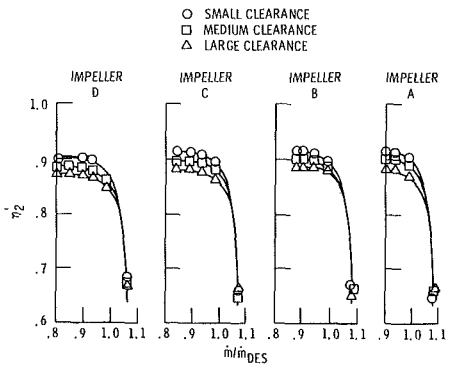

Fig. 8 Impeller total efficiency versus mass flow at design speed

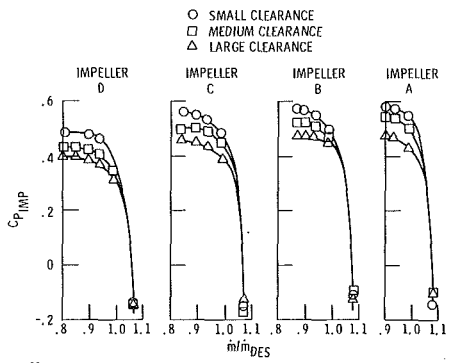

Fig. 9 Impeller equivalent static pressure coefficient versus mass flow at design speed

Downloaded 01 Jun 2010 to 171.66.16.57. Redistribution subject to ASME license or copyright; see http://www.asme.org/terms/Terms_Use.cfm

cient and efficiency with decreasing clearance for each of the four impellers tested. The figures also show an increase in flow range from a value of about 17 percent for Impeller A to a value of about 25 percent for Impeller D at 100 percent design speed. There is no appreciable change in flow range with clearance for any of the impellers tested.

The data from Figs. 8 and 9 are cross-plotted in Fig. 10 which shows the variation of efficiency and pressure recovery coefficient with clearance at a constant mass flow (near surge) for the four impeller configurations. The slopes of the curves

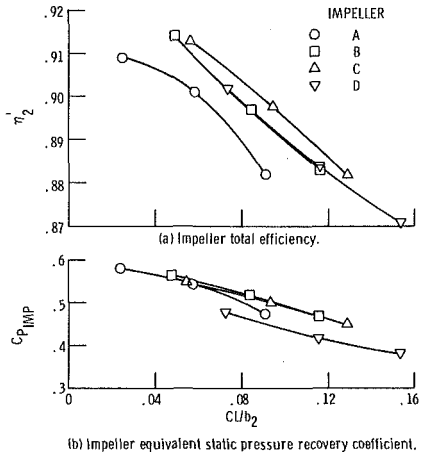

Fig. 10 Impeller performance characteristics versus clearance for design speed and $\dot{m}/\dot{m}_{des} = 0.90$

are nearly identical for the four impeller configurations. The slope of the impeller efficiency versus clearance curve shows a loss of approximately 0.4 points for every percent increase in tip clearance. This agrees well with the value obtained for a 6:1 pressure ratio impeller tested previously [7].

In order to compare the four impeller configurations, it is necessary to compare them at the same value of percent clearance at exit. Therefore, the data from the four impellers are cross-plotted to yield comparisons at nominal values of CL/b_2 of 0.08 and 0.06. The results of this procedure are shown in Fig. 11 where the following parameters are plotted as a function of area ratio: calculated impeller efficiency; impeller equivalent pressure recovery coefficient; total temperature ratio; static and total pressure ratio; total efficiency; and average flow angle. With the exception of the pressure recovery coefficient and calculated impeller efficiency, these parameters are obtained from averages of survey measurements at station 3.

The equivalent pressure recovery coefficient increases rapidly up to an area ratio of 2.55, continues to rise slightly up to an area ratio of 2.748, then decreases from an area ratio of 2.748 to 2.945. This is behavior typical for a stationary diffuser if area ratio is increased with no comparable increase in length. The pressure recovery coefficient increases rapidly until the diffuser approaches separation where peak recovery generally occurs. As area ratio continues to increase, pressure recovery falls as the diffuser experiences larger amounts of separation. From the equivalent pressure recovery curve, it can be concluded that global separation occurs in the impeller between the area ratios of 2.55 and 2.748. An examination of the temperature ratio plot also indicates a dramatic change in impeller behavior between these two area ratios (temperatures measured at station 4 were consistent with the averaged

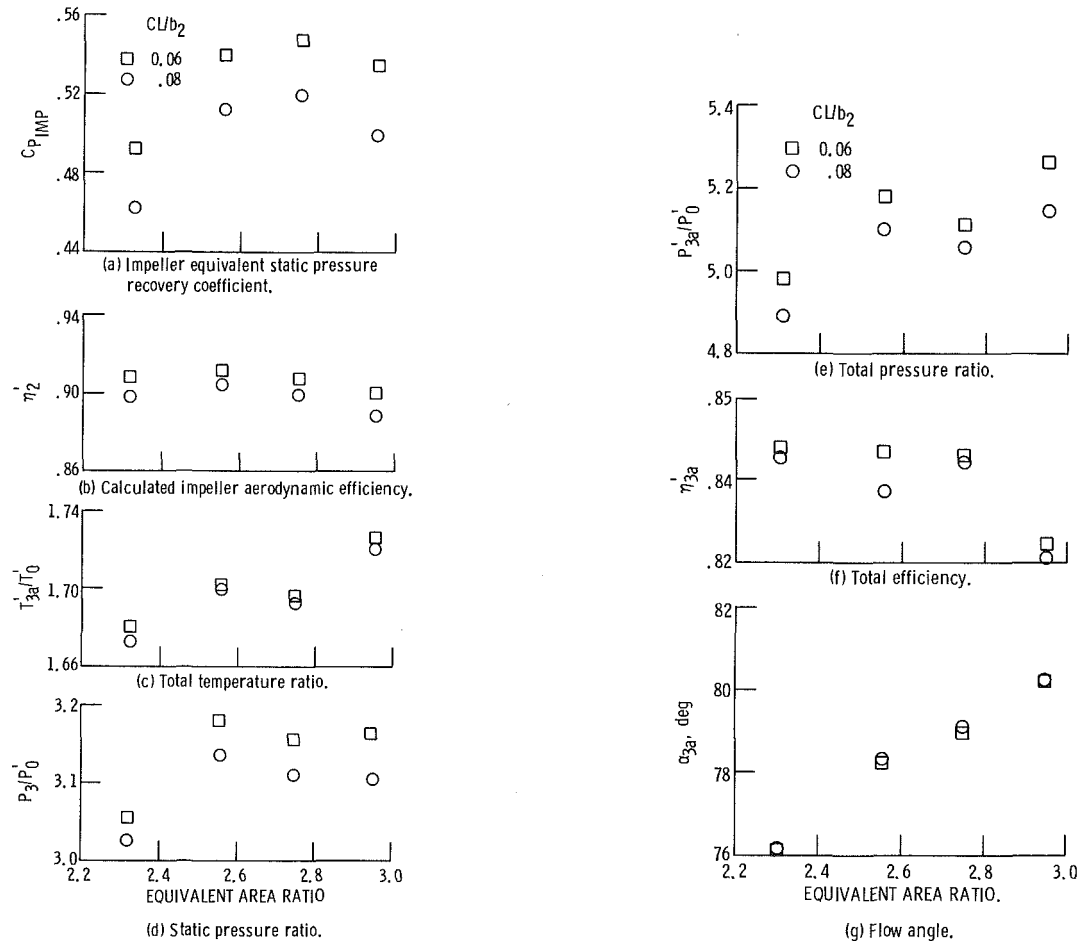

Fig. 11 Performance parameters for constant percent clearance versus impeller equivalent area ratio

Downloaded 01 Jun 2010 to 171.66.16.57. Redistribution subject to ASME license or copyright; see http://www.asme.org/terms/Terms_Use.cfm

temperatures obtained at station 3 and indicated that the observed trends were not a result of scatter in the data) which is consistent with the onset of global separation. The static and total pressure ratios measured at station 3 are consistent with this observation. A dramatic effect is also observed for the averaged efficiency at station 3 for the 2.55 area ratio impeller. The curve shows a drop of about 0.8 points between the 2.322 and 2.55 area ratio impellers at 8 percent clearance and then an increase by 0.7 points from 2.55 to 2.748 area ratio. This drop in efficiency does not occur for the 6 percent clearance case and the average efficiency is relatively constant from 2.322 to 2.748 area ratio and then drops by several points at the highest area ratio. This behavior indicates a stronger effect of clearance at 2.55 than for the other area ratios tested. The behavior manifests itself in the average efficiency at station 3 but does not appear to affect the calculated impeller efficiency. This implies one of two things: either (1) the vaneless space losses are more sensitive to clearance effects for this area ratio than they are for the other area ratios; or (2) the impeller, because of its proximity to its peak recovery point, is extremely sensitive to any perturbation such as an increased clearance and, since the calculated impeller efficiency is derived from the measured temperature and calculated impeller exit total pressure, the effect on calculated impeller efficiency is masked. The survey profiles for this area ratio indicate a dramatic effect with clearance as will be shown later. In Fig. 12 the impeller shroud static pressure is plotted versus mass flow ratio for the smallest clearance tested for each of the four impellers. Near the impeller exit, the plots for the two lower area ratio impellers (D and C) show a negative slope of pressure with mass flow rate while the plots for the higher area ratio impellers (A and B) show a zero slope near surge. In fact, the highest area ratio impeller shows a zero slope very close to the inducer region. This indicates that these two impellers may be separated at the low clearance.

Survey Measurements. The results of the surveys of total temperature, total pressure, and flow angle are shown in Figs. 13–16 for the four impellers tested. The comparison point was chosen to be 100 percent design speed at a mass flow of 90 percent design mass flow. The figures show the measured values of total temperature, total pressure, and flow angle as well as the derived values of efficiency, radial velocity, and tangential velocity for each of the three clearances tested.

The survey results for the lowest area ratio tested (Impeller D, Fig. 13) show profiles which are typical for nonseparated fully developed flow. There is an accumulation of low-momentum fluid along the shroud which increases as the impeller tip clearance is increased. This causes the profiles to be skewed toward the hub side of the channel. The flow angles show that the flow remains attached although separation may be imminent near the shroud. The axial clearance near the shroud drastically affects the flow total pressure and total temperature over 80 percent of the channel height.

For the next higher area tested (Impeller C, Fig. 14) the flow appears to remain attached for the smallest clearance tested although the flow along the hub has become more deficit causing a more symmetric profile. For the medium and large clearances, however, a large separation apparently occurs along the shroud which causes a large drop in total pressure

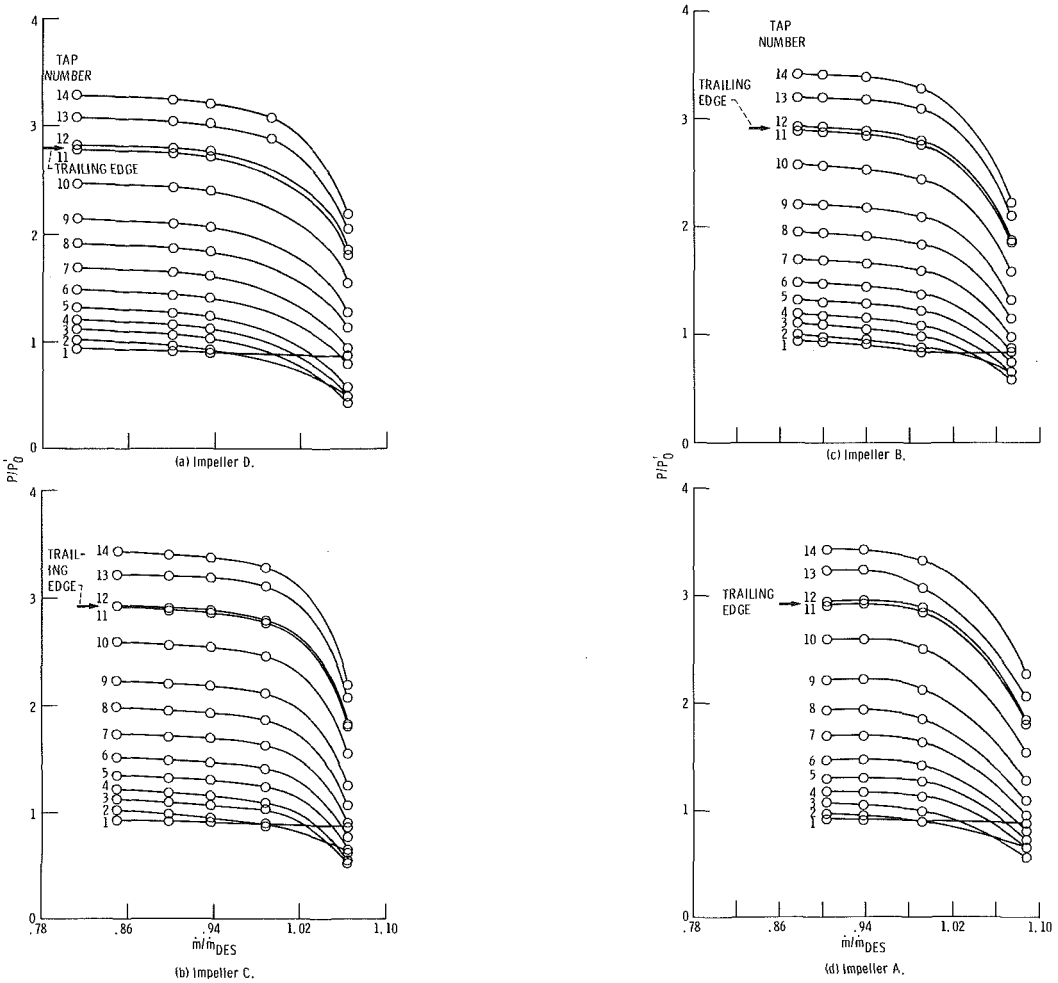

Fig. 12 Shroud static pressure distribution for design speed and small clearance

Downloaded 01 Jun 2010 to 171.66.16.57. Redistribution subject to ASME license or copyright; see http://www.asme.org/terms/Terms_Use.cfm

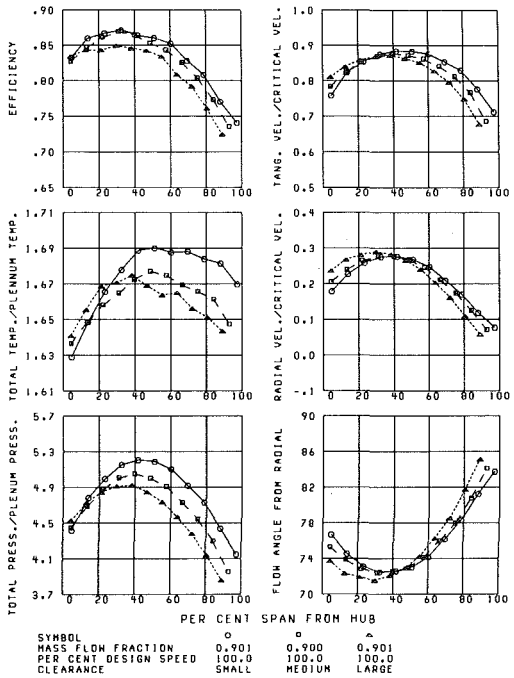

Fig. 13 Clearance comparison; 100 percent speed; Impeller D

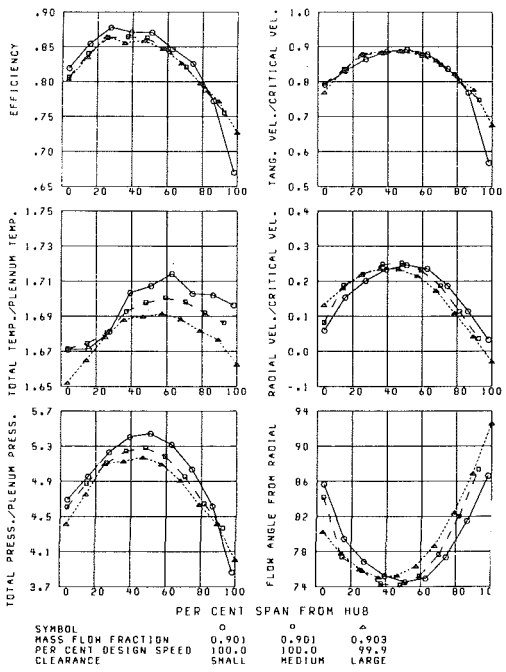

Fig. 15 Clearance comparison; 100 percent speed; Impeller B

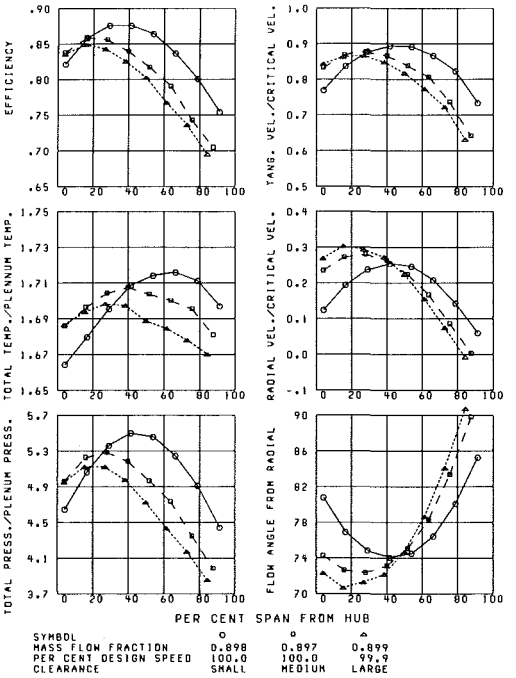

Fig. 14 Clearance comparison; 100 percent speed; Impeller C

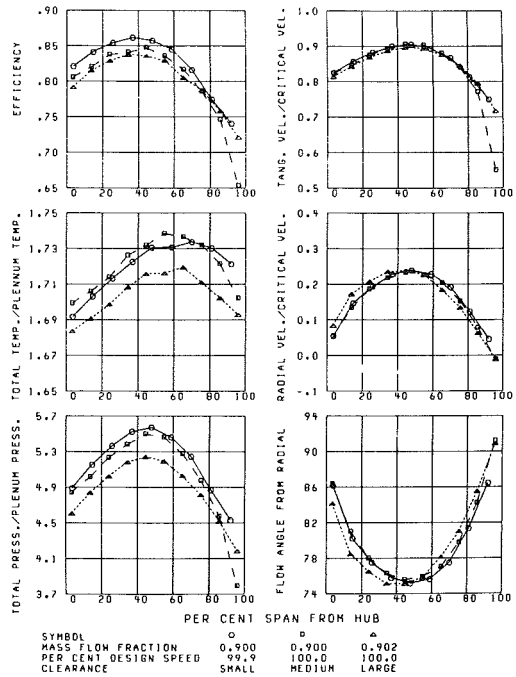

Fig. 16 Clearance comparison; 100 percent speed; Impeller A

and efficiency. This is probably what causes the large drop in efficiency in the cross-plotted data (Fig. 11(*f*)) going from Impeller D to Impeller C. If a smaller clearance had been chosen for the cross plot, this drop in efficiency would have been much less and may not have occurred at all.

The profiles for the impellers with the two highest area ratios tested (Impellers A and B) are similar. Both impellers show fairly symmetric profiles with some slight skewing toward the hub as clearance is increased. The flow angle measurements show no significant regions of separation although separation is probably imminent on both hub and shroud. Another possible explanation of the profiles is that impeller separation has already occurred on both the hub and shroud and turbulent mixing has caused the profiles to assume a symmetric character.

A comparison of the survey profiles for the four impellers at the smallest clearances tested is shown in Fig. 17. The profiles are similar for the four impellers tested although the hub becomes more deficit as the *b* width is increased. An examination of the temperature profiles shows that the temperature increases from Impellers D to C and also from Impellers B to A. This would be expected since an increased *b* width causes a decreased meridional velocity. For a backswept impeller with a constant deviation angle, this would cause the absolute tangential velocity to increase with increasing *b* width. From Euler's work equation, this would cause an increase in impeller temperature rise.

Downloaded 01 Jun 2010 to 171.66.16.57. Redistribution subject to ASME license or copyright; see http://www.asme.org/terms/Terms_Use.cfm

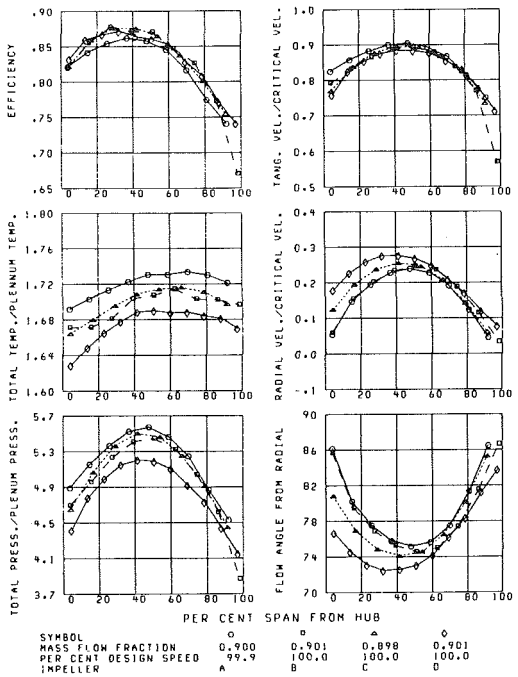

Fig. 17 Area ratio comparison; 100 percent speed; small clearance

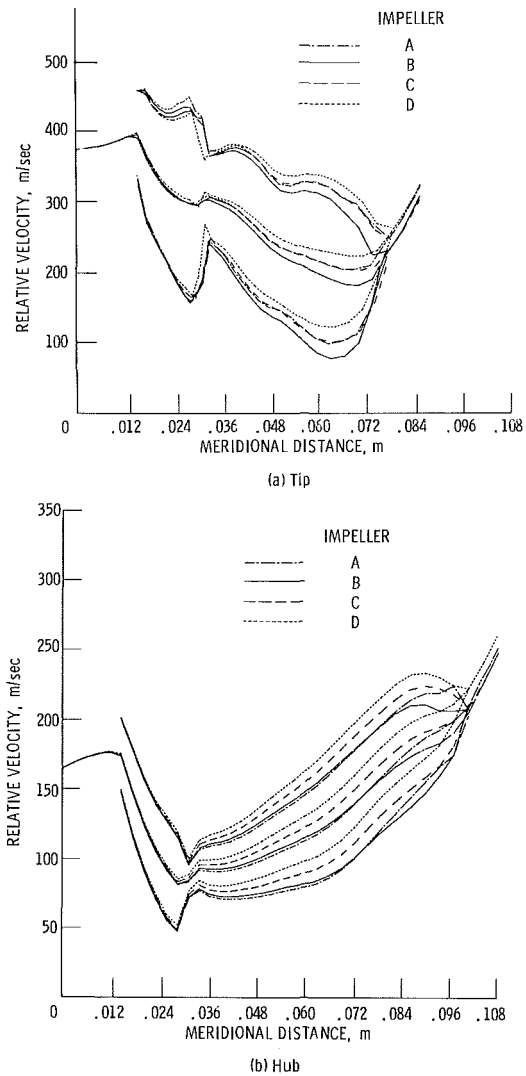

Fig. 18 Impeller loading diagrams for 100 percent design speed, $\dot{m}/\dot{m}_{des} = 0.9$, $CL/b_2 = 0.08$

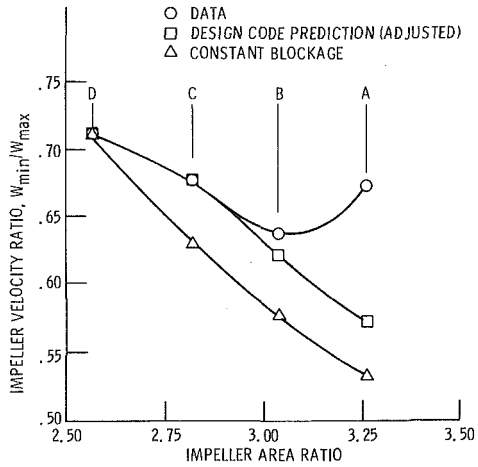

Fig. 19 Velocity ratio versus area ratio for design speed, $\dot{m}/\dot{m}_{des} = 0.90$, $CL/b_2 = 0.08$

However, going from Impellers C to B, there is actually a slight decrease in impeller temperature rise. This is probably due to a global impeller separation somewhere between an area ratio of 2.55 and 2.748 as discussed previously. An impeller separation would cause an increase in impeller losses and therefore an increased impeller exit mixed-out meridional velocity. Therefore, for the same reasoning as above, the temperature would decrease. As the impeller area ratio is further increased, the temperature would once again increase provided the separated zone did not increase in area. This is precisely the behavior observed.

Impeller Loading Diagrams. The hub and shroud loading diagrams for the four impellers at $CL/b_2 = 0.08$ are shown in Fig. 18. The flow point chosen for comparison was design speed at 90 percent of design flow. This corresponds to the flow points surveyed at design speed. The loading diagrams were obtained from the MERIDL code [8] and are representative of the inviscid core flow. The exit conditions for MERIDL (total pressure, absolute swirl, and blockage) were obtained by assuming an ideal core flow which produced the same static pressure rise and aerodynamic blockage as was obtained from the experiment. The ideal relative velocity at the exit of the impeller was calculated from the measured exit static pressure and the ideal relative total pressure. The ideal relative flow angle was calculated by assuming that the slip velocity of the inviscid core was the same as that for the mixed-out state at impeller exit as described under data reduction. The impeller exit aerodynamic blockage was then obtained from one-dimensional continuity. The MERIDL code was modified to accept an input aerodynamic blockage by reducing the tangential spacing between the blades by a blockage factor which was assumed to vary linearly between the leading and trailing edges. No total pressure loss was assumed for the core flow.

The impeller exit blockages calculated for the four impellers varied from 60.7 percent for Impeller A to 49.7 percent for Impeller D. The calculated exit ideal relative critical velocity ratios varied from 0.570 for Impeller A to 0.591 for Impeller D. The shroud static pressures from leading to trailing edge calculated by MERIDL using this method agreed with the experimental values everywhere within 3 percent.

Although these blockages seem high, they are typical for fully developed flow at impeller exit. For example, for a fully developed flow with a power law velocity profile exponent of 1/2 (shape factor = 2) in both axial and tangential directions, the blockage would be 55.6 percent. This would correspond to a nearly separated flow.

If impeller separation did not occur, it would be expected

Downloaded 01 Jun 2010 to 171.66.16.57. Redistribution subject to ASME license or copyright; see http://www.asme.org/terms/Terms_Use.cfm

that the impeller deceleration would increase uniformly as the impeller area ratio is increased. The loading diagrams for the shroud show that this is not the case for this impeller. The diagrams show that a limiting value of deceleration is reached. For this impeller configuration, the limiting velocity ratio along the midpitch line at the shroud (W_{min}/W_{1t}) is reached for Impeller B at a value of 0.64. The shroud loading diagrams seem to indicate that global impeller separation does not occur for Impellers D and C, possibly occurs for Impeller B and probably occurs for Impeller A since the minimum velocity attained decreases from Impellers D to B then increases for Impeller A. The trend is somewhat the same for the hub loading diagram but the minimum midpitch velocity for Impellers B and A is about the same. The minimum velocity ratios attained would seem to imply that calculations that yield lower values of the midpitch velocity ratio may have conditions at exit that are too optimistic. Obviously, the values of minimum velocity ratio quoted for this impeller may not be generally applicable and confirmation of some limiting ratio would require analysis of a range of impellers with different geometries and design conditions.

In order to determine how much the minimum velocity change was affected by the increased viscous effects and separation as area ratio increased, the MERIDL code was run twice more for each area ratio. For the first variation the intent was to determine how the minimum velocity varied only as a result of the area ratio change from Impellers D to A. The blockage calculated for Impeller D was used with the slip velocity determined experimentally for Impellers C, B, and A to establish the downstream input conditions for the MERIDL code. The second variation was to estimate the increase in viscous losses due to increased diffusion but eliminate the effects of separation. A centrifugal compressor design code which utilized internal boundary layer calculations to estimate viscous losses was used without a separation criterion (the shape factor used to indicate separation was set to a high value) to establish the slope in total temperature and static pressure rise from Impellers D to A. The predictions were normalized with the experimental values obtained for Impeller D (the predicted values were close to the experimental values for Impeller D). MERIDL exit conditions for Impellers C, B, and A were then obtained from the adjusted total temperature and static pressure. These two variations as well as the results obtained with the test data are shown in Fig. 19 as curves of minimum midpitch velocity at the shroud divided by the inlet midpitch velocity. This ratio should be representative of the amount of global diffusion attained in the impeller passages. As expected the trend obtained with the blockage held constant shows the velocity ratio continually decreasing with increasing area ratio. The trend obtained with the total temperature and static pressure estimated with the design code for Impellers B and A also shows a continually decreasing velocity ratio but not as fast as for the constant blockage case. The differing levels of minimum velocity ratio for these two variations gives an idea of the effect that the increased viscous losses have on the diffusion attainable in the impeller. The third trend which was obtained from the actual data shows the velocity ratio decreasing to a minimum value for Impeller B and then increasing for Impeller A. The deviation of these ratios from those calculated with the design code estimates indicates the possible effect of flow separation on the aerodynamic blockages calculated for Impellers B and A.

Summary of Results

This paper has presented the results of an experimental study of the affect of equivalent area ratio on impeller performance. Surveys of total pressure, total temperature, and flow angle were taken downstream of a backswept impeller operating with a vaneless diffuser. The data indicate the following:

1 For the impeller tested the equivalent pressure recovery coefficient and impeller efficiency reached maximum values at area ratios of 2.748 and 2.55, respectively.

2 The impeller efficiency decreases about 0.4 point for every 1 percent increase in exit clearance. The clearance effect on impeller efficiency is relatively insensitive to area ratio changes.

3 The efficiency measured at the survey station indicates the aerodynamic losses are strongly dependent upon clearance for the next to smallest area ratio tested. The clearance effect on these losses at the other area ratios is small.

4 Application of a quasi-three-dimensional computer code to the impellers using the experimentally determined exit conditions determined that the minimum shroud midpitch velocity was attained at the next to highest area ratio tested.

5 The experimental data indicate that the highest area ratio impeller tested experienced a global separation of the impeller.

References

1 Balje, O. E., "A Study On Design Criteria and Matching of Turbomachines; Part B – Compressor and Pump Performance and Matching of Turbocomponents," ASME JOURNAL OF ENGINEERING FOR POWER, Vol. 84, 1962, pp. 103–114.

2 Rodgers, C., "Specific Speed and Efficiency of Centrifugal Impellers," in: *Performance Prediction of Centrifugal Pumps and Compressors*, ASME, New York, 1980, pp. 191–200.

3 Mishina, H., and Nishida, H., "Effect of Relative Velocity Distribution on Efficiency and Exit Flow of Centrifugal Impellers," ASME Paper No. 83-GT-74, Mar. 1983.

4 Galvas, M. R., "A Compressor Designed for the Energy Research and Development Agency Automotive Gas Turbine Program," NASA TM-X-71719, 1975.

5 Katsanis, T., and McNally, W. D., "Fortran Program for Calculating Velocities and Streamlines on a Blade-to-Blade Stream Surface of a Tandem Blade Turbomachine," NASA TN-D-5044, 1969.

6 Pampreen, R. C., "Splitter-Bladed Centrifugal Compressor Impeller Designed for Automotive Gas Turbine Application," NASA CR-135237, 1977.

7 Klassen, H. A., Wood, J. R., and Schumann, L. F., "Experimental Performance of a 16.10-Centimeter-Tip-Diameter Sweptback Centrifugal Compressor Designed for a 6:1 Pressure Ratio," NASA TM-X-3552, 1977.

8 Katsanis, T., and McNally, W. D., "Revised Fortran Program for Calculating Velocities and Streamlines on the Hub-Shroud Midchannel Stream Surface of an Axial-, Radial-, or Mixed-Flow Turbomachine or Annular Duct: Part I – User's Manual," NASA TN-D-8430, 1977.

9 Glassman, A. J., "Turbine Design and Application," NASA SP-290, Vol. I, 1972.

APPENDIX

Averaging Procedure for Survey Quantities

The purpose of the integrated average values was to obtain single quantities that represented the energy transfer and inefficiency associated with the compression process. A procedure is described below which restricts the quantities averaged to extensive properties only. Other quantities are derived from these two averages so that the resultant averaged velocity triangle is representative of the energy transferred to the fluid and continuity. Overall mass flow rate was calculated by determining the mass flux, $\rho V \cos \alpha$, at each spanwise location. This quantity was set equal to zero at the walls and a cubic spline used to integrate the fluxes across the span to obtain the mass flow rate. Total enthalpy and ideal total enthalpy (obtained from the measured total pressure) were mass averaged in order to get overall quantities representative of the flow. Average total temperature was obtained from the average total enthalpy and average total pressure was obtained from the average ideal total enthalpy. Static pressure was assumed constant across the channel and was used with the averaged total pressure to calculate an average critical velocity ratio (see equations (1)–(61) of [9]). Average static density was calculated from the average critical velocity ratio, average total pressure, and average total temperature. With the known integrated mass flow rate, a flow angle consistent with continuity could be obtained.

Downloaded 01 Jun 2010 to 171.66.16.57. Redistribution subject to ASME license or copyright; see http://www.asme.org/terms/Terms_Use.cfm

Three-Dimensional Flowfield Calculation of High-Loaded Centrifugal Compressor Diffusers

I. Teipel

A. Wiedermann

Institute of Mechanics,
University of Hannover,
Hannover, Federal Republic of Germany

In this paper a method for calculating inviscid three-dimensional flowfields in vaned diffusers of high-loaded centrifugal compressors will be considered. Following the classical theory of Wu different kinds of streamsurfaces have been introduced. The complete three-dimensional result is approximated by a combination of blade-to-blade streamsurfaces (S_1 surface) and S_2 surfaces between the side walls of the diffuser. The geometry of each of the stream sheets depends on the others. A special curvilinear coordinate system has been introduced to take into account the twisted shape of the surfaces. Because of the expected transonic flow pattern due to the high loading of the considered units, a time-marching procedure is applied for solving the conservative form of the governing equations in each kind of streamsurface. To demonstrate the capability of the described calculation procedure, the flow pattern in a radial diffuser with twisted vanes has been considered. The impeller speed is assumed to be so large that the flow may become transonic behind the impeller exit. Shock waves may therefore occur in front of the diffuser vanes. Pressure distributions have been calculated in several stream sheets and have been compared with available experimental data. Also integral results predicted by this theory have been compared with measured performance maps. A simple method to estimate a diffuser blockage factor will be given. As a conclusion it will be indicated that a good agreement between theory and experiment justifies the application of an inviscid three-dimensional method for calculating essential details of the pressure field in radial diffusers. However, a coupling of inviscid theory and boundary layer theory does not provide a sufficient prediction of the losses.

Introduction

High-stage efficiency and loading are desired properties of today's centrifugal compressor units. They can be achieved by increasing the rotational speed of the impeller. As a consequence the kinetic energy at the impeller exit will become so large that vaneless diffusers will no longer be suited for efficient pressure recovery [1]. Therefore compressors have to be equipped with vaned diffusers. The blades might be formed with respect to aerodynamic rules [2].

Due to a very strong interaction between the impeller and diffuser, there are several facts to be taken into account for designing the diffuser vanes. Firstly supersonic regions including shock waves might occur in front of the blades. The requirements for calculating transonic flowfields can be completed by introducing a time-marching procedure as has been done by Jeske and Teipel [3]. Secondly the appearance of secondary flow motion in the impeller passages produces an energy gradient from hub to tip which leads to a variation of the flow angle between the diffuser side walls at the impeller exit as shown by measurements performed by Jansen [4]. In order to fit the geometry of the blades to the varying stream directions Jansen designed a three-dimensionally twisted blade passage shown in Fig. 1. As can be seen the value of the blade angle at the leading edge reaches from nearly 0 to 33 deg. In order to calculate the three-dimensional flow pattern Wiedermann [5] recently applied a quasi-three-dimensional method based on a general theory first given by Wu [6].

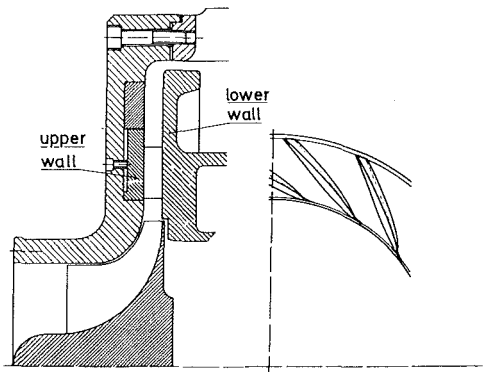

Fig. 1 Design of the twisted diffuser (Jansen [4])

Contributed by the Gas Turbine Division of THE AMERICAN SOCIETY OF MECHANICAL ENGINEERS and presented at the 31st International Gas Turbine Conference and Exhibit, Düsseldorf, Federal Republic of Germany, June 8–12, 1986. Manuscript received at ASME Headquarters February 10, 1986. Paper No. 86-GT-187.

Copyright © 1987 by ASME

Downloaded 01 Jun 2010 to 171.66.16.57. Redistribution subject to ASME license or copyright; see http://www.asme.org/terms/Terms_Use.cfm

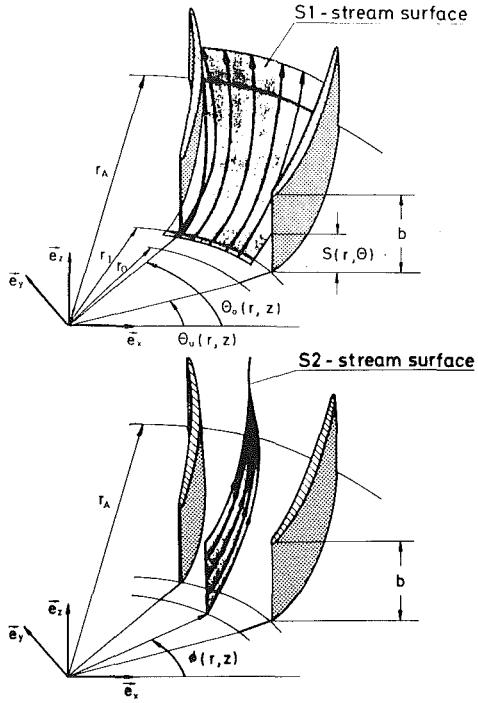

Fig. 2 S_1 and S_2 streamsurfaces in a centrifugal compressor diffuser

Description of the Method

Although modern vector computers like the CRAY 1 or CYBER 205 are becoming available for more and more research laboratories, the calculation of complete three-dimensional flowfields with complex boundaries has remained a time-consuming process. Therefore several attempts for an approximate solution procedure of the flowfield have been made. One of the most common approaches was published by Wu in 1952 [6]. Wu suggested describing the complete three-dimensional flow as a number of two-dimensional flowfields. He introduced S_1 streamsurfaces (blade-to-blade surfaces) and S_2 stream sheets between the side walls. The location of the different stream sheets in a centrifugal diffuser passage is illustrated in Fig. 2. As the geometries of the different kinds of streamsurfaces depend on each other one obtains an approximate solution of the three-dimensional flowfield. Matrix methods [6–8] as well as streamline curvature methods [9, 10] have been developed for solving the governing equations in each kind of streamsurface. Krimerman and Adler [11] and Hirsch [12] were among the first who succeeded in applying the complete theory of Wu. Hirsch replaced the flow along the S_2 surfaces by the calculation of the exact mass-averaged–pitch-averaged flow in a meridional plane whereas Krimerman and Adler used several twisted S_2 streamsurfaces, the shapes of which had been determined by the results in various S_1 stream sheets. They calculated the flowfield in a centrifugal impeller using a finite element procedure. Recently also Wang et al. [13] published a complete quasi-three-dimensional method for predicting subsonic flowfields.

In the present method the application of Wu's theory has been preferred to a complete three-dimensional approach because it was the authors' purpose to avoid large computer storage and CP-time requirements. The results obtained in three S_1 and three S_2 streamsurfaces have been coupled to build up an approximate solution of the three-dimensional flowfield in Jansen's twisted diffuser channel. The stream sheets are arranged as shown in Fig. 2. The structure of the complete calculation procedure is demonstrated in Fig. 3. First the pressure fields in plane blade-to-blade surfaces at different axial locations will be calculated. Then the shapes of the three S_2 stream sheets are given by the streamlines obtained in each S_1 streamsurface. In general they are twisted in a complicated manner. The last step of a convergence cycle is the calculation of the flowfields in the corrected S_1 stream sheets. Theoretically the loop can be repeated until a sufficient convergence limit is reached; but due to immense CPU times on a conventional CDC-CYBER 76 the calculation procedure was stopped after the S_1 streamsurfaces had been improved once.

Governing Equations

In order to calculate transonic flowfields which include shock waves a conservative formulation of the governing equations is desirable. Due to the complicated twisted shape of

Nomenclature

b = diffuser width, m
c_p = pressure recovery coefficient
e = specific energy, J/kg
$\mathbf{F}$ = vector, defined in equations (1) and (4)
$\mathbf{G}$ = vector, defined in equations (1) and (4)
$\mathbf{F}^*$ = vector, defined in equations (1) and (4)
$\mathbf{G}^*$ = vector, defined in equations (1) and (4)
h = specific enthalpy, J/kg
h_t = total enthalpy, J/kg
$\dot{m}_D$ = dimensionless mass flux, defined in equation (9)
$\underline{M}_1$ = diagonal matrix, defined in equations (1) and (4)
$\underline{M}_2$ = diagonal matrix, defined in equations (1) and (4)
$\underline{M}_3$ = diagonal matrix, defined in equations (1) and (4)
n_{red} = rotational speed, red. to norm condition
$\mathbf{P}$ = vector, defined in equations (1) and (4)
p = pressure, bar
p_t = total pressure, bar
r = radius, m
S = function of the S_1 streamsurface
t = time, s
$\mathbf{U}$ = vector, defined in equations (1) and (4)
$\mathbf{u}$ = velocity vector, m/s
u_x = x component of velocity, m/s
u_y = y component of velocity, m/s
u_r = radial velocity component, m/s
u_θ = tangential velocity component, m/s
u_z = axial velocity component, m/s
z = axial coordinate, m
γ = ratio of specific heats
ϕ = function of the S_2 streamsurface
θ = angle
λ = diffuser radius ratio = r/r_{IE}
λ, ν = angles of the S_1 stream sheet, rad
μ, ω = angles of the S_2 stream sheet, rad
π = 3.1415 . . .
ρ = density, kg/m^3
ρ_t = total density, kg/m^3
σ = thickness of the S_1 stream sheet, m
τ = angle, proportional to the thickness of the S_2 stream sheet, rad

Subscripts

IE = impeller exit
DE = diffuser exit
S_1 = S_1 stream sheet
S_2 = S_2 stream sheet

Downloaded 01 Jun 2010 to 171.66.16.57. Redistribution subject to ASME license or copyright; see http://www.asme.org/terms/Terms_Use.cfm

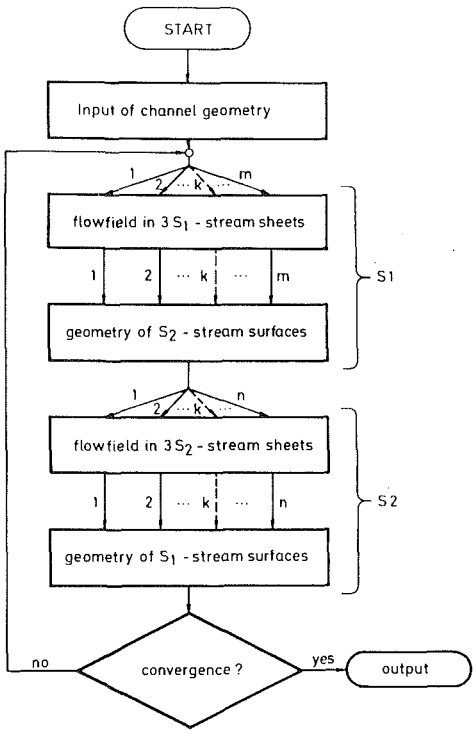

Fig. 3 Computational scheme of the applied quasi-three-dimensional procedure

the stream sheets the equations contain a large number of geometric parameters. Using cylindrical coordinates the governing equations for calculating flowfields in S_1 stream sheets can be written in a conservative form

$$\frac{\partial \mathbf{U}_{S_1}}{\partial t}+\frac{\partial \mathbf{F}_{S_1}}{\partial r}+\frac{\partial \mathbf{G}_{S_1}}{\partial \theta}+\underline{M}_1\left[\frac{\partial \mathbf{F}^*_{S_1}}{\partial r}+\frac{\partial \mathbf{G}^*_{S_1}}{\partial \theta}\right]+\underline{M}_2\frac{\partial \mathbf{P}_{S_1}}{\partial r}+\underline{M}_3\frac{\partial \mathbf{P}_{S_1}}{\partial \theta}=\mathbf{0} \tag{1}$$

with the matrices

$$\mathbf{U}_{S_1}=\begin{bmatrix} r\sigma\rho \\ r\sigma\rho[u_x+u_z(\tan\lambda\cos\theta-\tan\nu\sin\theta)] \\ r\sigma\rho[u_y+u_z(\tan\lambda\sin\theta+\tan\nu\cos\theta)] \\ r\sigma\rho\left[e+\frac{1}{2}\,\mathbf{u}\cdot\mathbf{u}\right] \end{bmatrix}$$

$$\mathbf{F}_{S_1}=\begin{bmatrix} r\sigma\rho u_r \\ r\sigma\rho u_x u_r \\ r\sigma\rho u_y u_r \\ r\sigma\rho u_r\left[h+\frac{1}{2}\,\mathbf{u}\cdot\mathbf{u}\right] \end{bmatrix}$$

$$\mathbf{G}_{S_1}=\begin{bmatrix} \sigma\rho u_\theta \\ \sigma\rho u_x u_\theta \\ \sigma\rho u_y u_\theta \\ \sigma\rho u_\theta\left[h+\frac{1}{2}\,\mathbf{u}\cdot\mathbf{u}\right] \end{bmatrix}$$

$$\mathbf{F}^*_{S_1}=\begin{bmatrix} 0 \\ r\sigma\rho u_z u_r \\ r\sigma\rho u_z u_r \\ 0 \end{bmatrix}\quad \mathbf{G}^*_{S_1}=\begin{bmatrix} 0 \\ \sigma\rho u_z u_\theta \\ \sigma\rho u_z u_\theta \\ 0 \end{bmatrix}\quad \mathbf{P}_{S_1}=\begin{bmatrix} 0 \\ p \\ p \\ 0 \end{bmatrix}$$

$$\underline{M}_1=\begin{bmatrix} 0 & 0 & 0 & 0 \\ 0 & \tan\lambda\cos\theta-\tan\nu\sin\theta & 0 & 0 \\ 0 & 0 & \tan\lambda\sin\theta+\tan\nu\cos\theta & 0 \\ 0 & 0 & 0 & 0 \end{bmatrix}$$

$$\underline{M}_2=r\sigma\begin{bmatrix} 0 & 0 & 0 & 0 \\ 0 & \cos\theta & 0 & 0 \\ 0 & 0 & \sin\theta & 0 \\ 0 & 0 & 0 & 0 \end{bmatrix} \tag{2}$$

$$\underline{M}_3=\sigma\begin{bmatrix} 0 & 0 & 0 & 0 \\ 0 & -\sin\theta & 0 & 0 \\ 0 & 0 & \cos\theta & 0 \\ 0 & 0 & 0 & 0 \end{bmatrix}$$

The angles λ and ν are given by

$$\lambda=\arctan\left(\frac{\partial S}{\partial r}\right)$$
$$\nu=\arctan\left(\frac{1}{r}\,\frac{\partial S}{\partial \theta}\right) \tag{3}$$

where $z = S(r, \theta)$ means the function of the S_1 streamsurface. σ is a factor which is proportional to the axial stream sheet thickness. As the S_1 surfaces are only slightly curved the angles λ and ν can be neglected.

For the S_2 streamsurfaces, which are strongly twisted in general, the conservative form of the governing equations yields

$$\frac{\partial \mathbf{U}_{S_2}}{\partial t}+\frac{\partial \mathbf{F}_{S_2}}{\partial r}+\frac{\partial \mathbf{G}_{S_2}}{\partial z}+\underline{M}_1\left[\frac{\partial \mathbf{F}^*_{S_2}}{\partial r}+\frac{\partial \mathbf{G}^*_{S_2}}{\partial z}\right]+\underline{M}_2\frac{\partial \mathbf{P}_{S_2}}{\partial r}+\underline{M}_3\frac{\partial \mathbf{P}_{S_2}}{\partial z}=\mathbf{0} \tag{4}$$

with the matrices

$$\mathbf{U}_{S_2}=\begin{bmatrix} r\tau\rho \\ r\tau\rho(u_x+\tan(\mu+\phi)u_y) \\ r\tau\rho\left(u_z+\frac{\tan\omega}{\cos\phi-\sin\phi\tan\mu}\,u_y\right) \\ r\tau\rho\left[e+\frac{1}{2}\,\mathbf{u}\cdot\mathbf{u}\right] \end{bmatrix}$$

$$\mathbf{F}_{S_2}=\begin{bmatrix} r\tau\rho u_r \\ r\tau\rho u_x u_r \\ r\tau\rho u_z u_r \\ r\tau\rho u_r\left[h+\frac{1}{2}\,\mathbf{u}\cdot\mathbf{u}\right] \end{bmatrix}$$

Downloaded 01 Jun 2010 to 171.66.16.57. Redistribution subject to ASME license or copyright; see http://www.asme.org/terms/Terms_Use.cfm

$$\mathbf{G}_{S_2} = \begin{bmatrix} r\tau\rho u_z \\ r\tau\rho u_x u_z \\ r\tau\rho u_z{}^2 \\ r\tau\rho u_z\left[h+\frac{1}{2}\,\mathbf{u}\cdot\mathbf{u}\right] \end{bmatrix}$$

$$\mathbf{F}^*_{S_2} = \begin{bmatrix} 0 \\ r\tau\rho u_y u_r \\ r\tau\rho u_y u_r \\ 0 \end{bmatrix} \quad \mathbf{G}^*_{S_2} = \begin{bmatrix} 0 \\ r\tau\rho u_y u_z \\ r\tau\rho u_y u_z \\ 0 \end{bmatrix} \quad \mathbf{P}_{S_2} = \begin{bmatrix} 0 \\ p \\ p \\ 0 \end{bmatrix}$$

$$\underline{M}_3 = \begin{bmatrix} 0 & 0 & 0 & 0 \\ 0 & 0 & 0 & 0 \\ 0 & 0 & r\tau & 0 \\ 0 & 0 & 0 & 0 \end{bmatrix} \tag{5}$$

$$\underline{M}_1 = \begin{bmatrix} 0 & 0 & 0 & 0 \\ 0 & \tan(\mu+\phi) & 0 & 0 \\ 0 & 0 & \dfrac{\tan\omega}{\cos\phi-\sin\phi\tan\mu} & 0 \\ 0 & 0 & 0 & 0 \end{bmatrix}$$

$$\underline{M}_2 = r\tau \begin{bmatrix} 0 & 0 & 0 & 0 \\ 0 & \dfrac{\cos\phi}{+\sin\phi\tan(\mu+\phi)} & 0 & 0 \\ 0 & 0 & \dfrac{\tan\omega}{\cot\phi-\tan\mu} & 0 \\ 0 & 0 & 0 & 0 \end{bmatrix}$$

μ and ω are angles describing the curvature of the stream sheet, given as derivatives of the streamsurface function $\theta = \phi(r, z)$ by

$$\mu = \arctan\left(r\frac{\partial\phi}{\partial r}\right)$$
$$\omega = \arctan\left(r\frac{\partial\phi}{\partial z}\right) \tag{6}$$

The angle τ is proportional to the angular thickness of the S_2 stream sheet.

The different rows of the matrices denote the continuity equation, the two remaining independent components of the momentum equation in the considered surface kind, and the energy equation. Assuming isoenergetic flow condition the fourth row of equations (1) and (4) can be replaced by an algebraic energy relation. For an ideal gas one gets

$$h_t = \frac{\gamma}{\gamma-1}\frac{p_t}{\rho_t} = \frac{\gamma}{\gamma-1}\frac{p}{\rho} + \frac{\mathbf{u}\cdot\mathbf{u}}{2} \tag{7}$$

The solutions of equations (1) and (4) are obtained by applying an explicit MacCormack scheme in its original version published in 1969 [14]. To fulfill the boundary conditions a body-fitted coordinate system is introduced. At the solid walls the flowfield variables are calculated in a special coordinate system. At the inlet and outlet section of the computational domain characteristic relations are applied. Further details are outlined in [5].

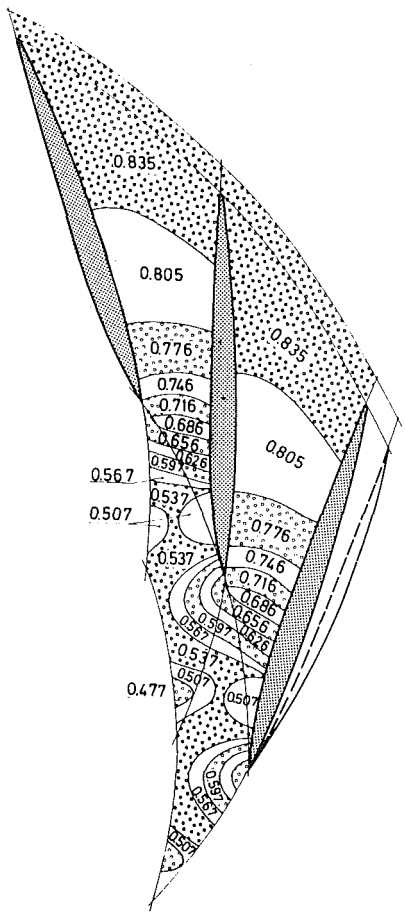

Fig. 4 Regions of constant pressure p/p_t at the upper side wall; measurements by Jansen et al. [4, 15]; n_{red} = 18,000 rpm

The modeling of the complicated fluid flow pattern at the impeller exit has to be considered very carefully because of its important influence on the flowfield in the vaneless region of the diffuser. As only the steady-state solution is of interest the time-dependent jet-wake structure has not been taken into account. However, the gradient of the total pressure between the diffuser side walls due to secondary flow motion in the impeller passage can be simulated by prescribing a function for p_t which has been derived from experiment. As a consequence the distribution of the flow variables is not uniform in the circumferential as well as in the axial direction.

Comparison of Predicted and Measured Flowfields

Now the range of application of the described method will be proved by comparing theory with experimental data. The measurements were carried out at the Institute of Turbomachinery at the University of Hannover and reported in [4, 15].

Measured pressure fields obtained at an impeller rotational speed of 18,000 rpm near the upper and the lower side wall are shown in Figs. 4 and 5. The considered operating point is located near the surge line. The graphs contain domains of constant pressure which are related to the maximum total pressure at the impeller exit. The average absolute Mach number at the impeller outlet was about 1.25. The measured isobars indicate a strong pressure rise in the vaneless and semivaned region in front of the throat of the diffuser channel while the pressure recovery is only small further downstream. There is an especially strong pressure gradient at the suction

Downloaded 01 Jun 2010 to 171.66.16.57. Redistribution subject to ASME license or copyright; see http://www.asme.org/terms/Terms_Use.cfm

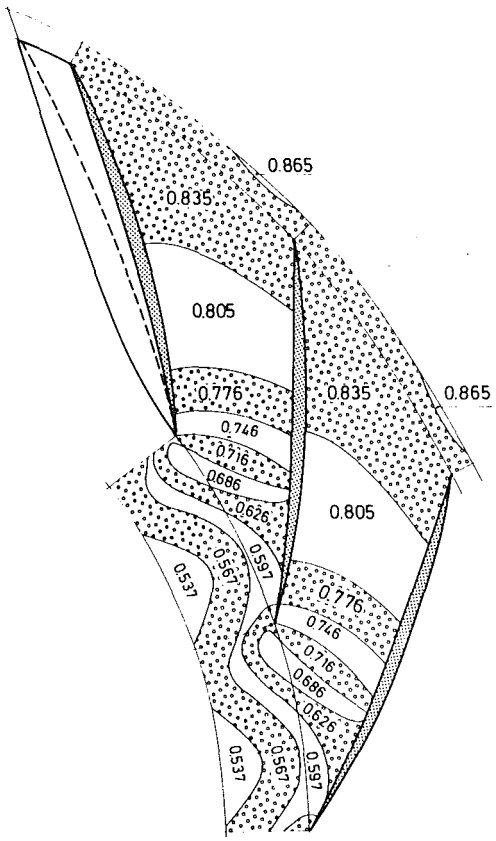

Fig. 5 Regions of constant pressure p/p_t at the lower side wall; measurements by Jansen et al. [4, 15]; n_{red} = 18,000 rpm

side near the leading edge at the upper side wall (Fig. 4) where high loading at the blades occurs. The predicted isobar contours (Figs. 6 and 7) calculated along the corrected stream sheets after one convergence cycle as shown in Fig. 3 correspond well with the measured pattern. The curved shape of the isobars in the vaneless region is in especially close agreement with experiment. As indicated by measurements the essential part of the pressure recovery is predicted to take place in front of the throat. At the lower side wall the wavy contour of pressure lines is well predicted by theory. However, the calculated isobars accumulate strongly in front of the blades while there is no shock observed by experiment. Nevertheless, essential details of the flowfield can be given by applying the present inviscid theory.

In Fig. 8 the isobars in the projection of the three S_2 streamsurfaces into the meridional plane have been plotted. As in the S_1 surface nearly all the predicted pressure rise occurs in the vaneless region between $\lambda = 1.0$ and $\lambda = 1.15$. The accumulation of the isobars in front of the vanes coincides well with both the predicted data in the S_1 sheets and experiment. Due to the energy gradient at the impeller exit there is a rise of static pressure from lower to upper wall, where the energy is lowest.

A further advantage of the present method is the fact that also velocity and isobar profiles in a θ, z plane can be constructed by combining several stream sheet solutions. A comparison of measured and predicted flow patterns is given in the next four pictures, Figs. 9 to 12. If an impeller rotational speed of 14,600 rpm is chosen the measured distribution of the absolute flow angle will provide a strong gradient from the lower ($z/b = 1$) to the upper wall ($z/b = 0$). After having introduced a variation of the total pressure at the impeller exit from the experiment as one boundary condition at the entrance one gets a close agreement between measured and predicted profiles. However, the very small numbers of the

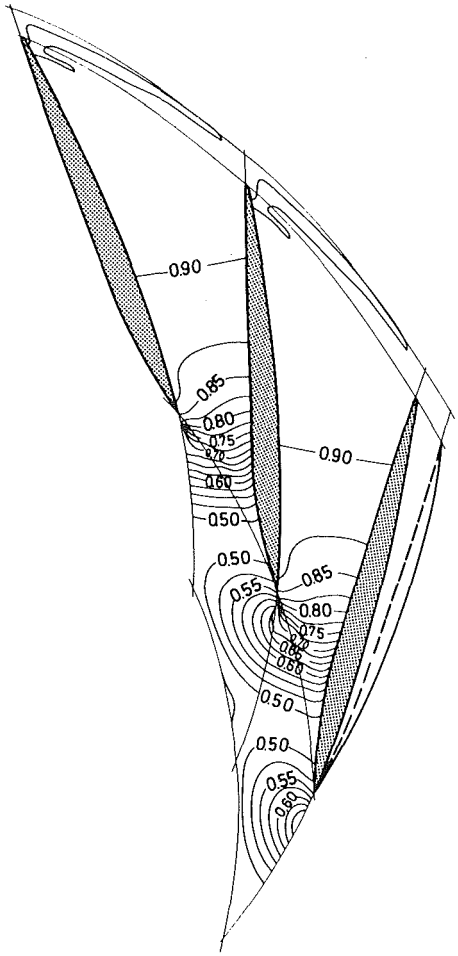

Fig. 6 Calculated isobars p/p_t at the upper side wall; n_{red} = 18,000 rpm

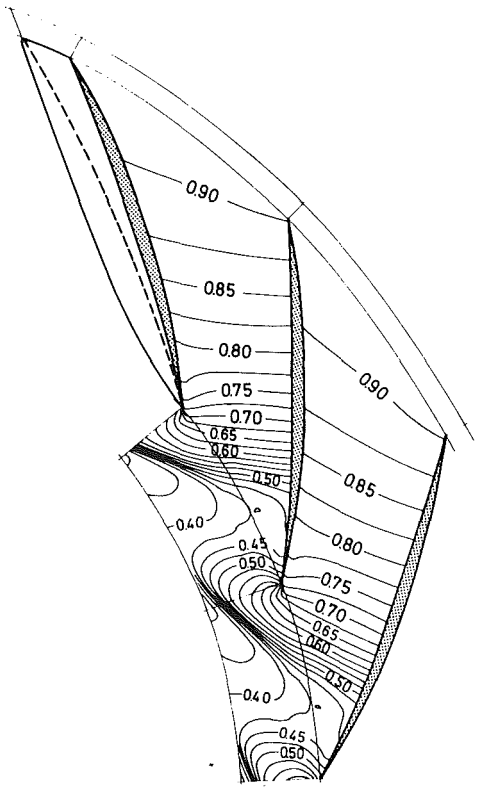

Fig. 7 Calculated isobars p/p_t at the lower side wall; n_{red} = 18,000 rpm

Downloaded 01 Jun 2010 to 171.66.16.57. Redistribution subject to ASME license or copyright; see http://www.asme.org/terms/Terms_Use.cfm

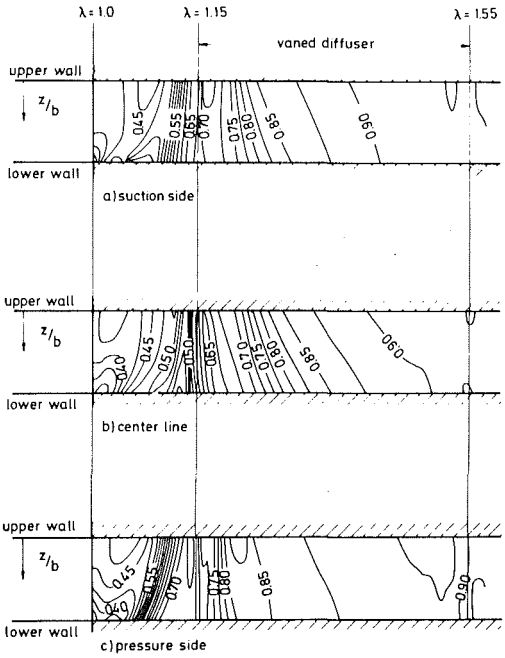

Fig. 8 Calculated isobars p/p_t in the S_2 streamsurfaces projected into the meridional plane

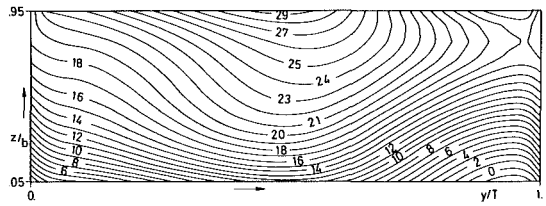

Fig. 9 Measured distribution of the absolute flow angles at $\lambda = 1.1$; $n_{red} = 14{,}600$ rpm

flow angle near the upper wall cannot be calculated satisfactorily by the present theory because of the absence of any friction terms.

Also the comparison of predicted and measured Mach line contours in front of the vaned diffuser offers a reasonably good agreement as shown in Figs. 11 and 12. It is noticeable that especially the location of the maximum and the minimum of the profile corresponds well with experiment. Due to the neglect of friction forces the calculated Mach number is too high.

Comparison of Measured and Predicted Performance Maps

For practical purposes the evaluation of integral results of the considered unit is more essential than flowfield calculations. To characterize the diffuser efficiency a pressure recovery coefficient c_p, defined by

$$c_p = \frac{\bar{p}_{DE} - \bar{p}_{IE}}{\bar{p}_t - \bar{p}_{IE}} \tag{8}$$

where $\bar{p}_{IE}$ and $\bar{p}_{DE}$ are average pressure values at the impeller and diffuser exit and $\bar{p}_t$ is the total pressure, is plotted versus a nondimensional mass flux defined by

$$\dot{m}_D = \frac{1}{2\pi r_{IE} b \sqrt{p_t \rho_t}} \int_0^b \int_0^{2\pi} r \cdot \rho u_r \, d\theta \, dz \tag{9}$$

A comparison of a predicted and measured performance map is shown in Fig. 13. For high-loaded machines the choking and suction line are determined by the vaned diffuser. Therefore the performance map of the diffuser gives interesting information about the operating range of the unit. It was found previously that there exists a correlation between numerical and physical instabilities near the surge line [16].

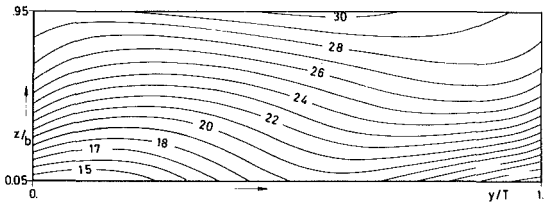

Fig. 10 Predicted distribution of the absolute flow angles at $\lambda = 1.1$; $n_{red} = 14{,}600$ rpm

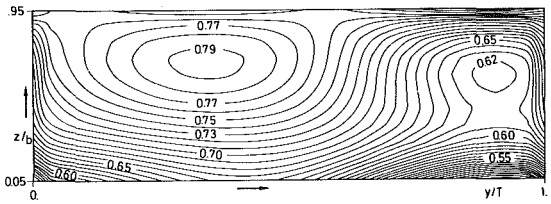

Fig. 11 Measured distribution of the Mach numbers at $\lambda = 1.1$; $n_{red} = 14{,}600$ rpm

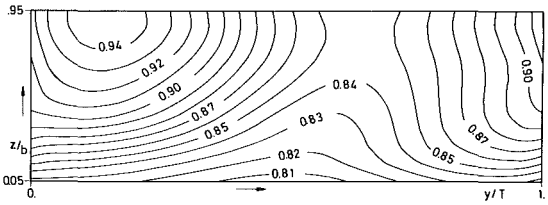

Fig. 12 Predicted distribution of the Mach numbers at $\lambda = 1.1$; $n_{red} = 14{,}600$ rpm

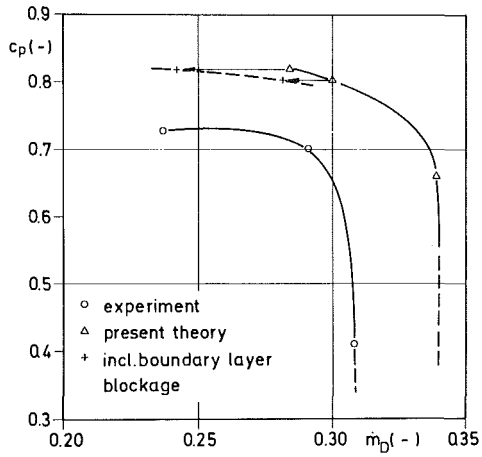

Fig. 13 Measured and predicted performance map of Jansen's twisted diffuser

As friction is neglected pressure recovery and maximum mass flux are estimated too large compared with measured data. One can improve the results of the inviscid theory by applying boundary layer theory along the intersecting lines between the blades and the S_1 streamsurface as well as between the side walls and the S_2 streamsurface. After calculating a blockage factor in the throat with the values of displacement thickness obtained by an entrainment method [17] one gets the results connected by a dotted line (Fig. 13). In spite of a better agreement there is still a large defect left. As a consequence it has to be stated that a coupling of inviscid theory and boundary layer programs is not able to provide a better prediction of the phenomena in diffuser passages.

Downloaded 01 Jun 2010 to 171.66.16.57. Redistribution subject to ASME license or copyright; see http://www.asme.org/terms/Terms_Use.cfm

As the numerical integration of the complete or parabolized Navier–Stokes equations in connection with complex boundaries has remained a time-consuming process, even if a vector computer is available, one can improve the results by employing a simple loss model as given by, e.g., Horlock [18]. However, the solution depends strongly on measured loss figures at special operating points and, therefore, one will only get reliable information about the loss mechanism in those cases where experimental data are available.

Concluding Remarks

In this paper a method for calculating inviscid three-dimensional flowfields in vaned diffuser passages is described. For this purpose a quasi-three-dimensional approach first given by Wu has been employed. The present procedure consisting of several FORTRAN programs has been applied for predicting the three-dimensional flow pattern in a diffuser with twisted vanes. A comparison of calculated and measured data shows good agreement. The diffuser performance map can also be determined by the method within certain limits. The application of boundary layer theory, however, is not able to predict all the losses in the diffuser channel. Nevertheless, the described method provides valuable results for a better understanding of some important flow phenomena in radial diffusers.

References

1 Kenny, D. P., "Supersonic Radial Diffusers," in: *Advanced Compressors*, AGARD Lecture Series 39, 1970.

2 Japikse, D., "Centrifugal Compressor Design," *Concepts ETI*, Course No. 2, 1981.

3 Jeske, H. O., and Teipel, I., "A Theoretical Investigation of Transonic Flows in Radial Compressor Diffusers," ASME JOURNAL OF ENGINEERING FOR POWER, Vol. 105, 1983, pp. 452–456.

4 Jansen, M., "Untersuchung an beschaufelten Diffusoren eines hochbelasteten Radialverdichters," Ph.D. Thesis, Hannover, 1982.

5 Wiedermann, A., "Die raeumliche reibungslose Stroemung in Diffusoren eines Radialverdichters bei transsonischer Anstroemung," Ph.D. Thesis, Hannover, 1985.

6 Wu, Ch.-H., "A General Theory of Three-Dimensional Flow in Subsonic and Supersonic Turbomachines of Radial-, Axial- and Mixed Flow Types," NACA TND 2604, 1952.

7 Marsh, H., "A Digital Computer Program for the Through-flow Fluid Mechanics in an Arbitrary Turbomachine Using a Matrix Method," ARC R&M No. 3509, 1968.

8 Bosman, C., and El-Shaarawi, M. A. I., "Quasi-Three-Dimensional Numerical Solution of Flow in Turbomachines," ASME *Journal of Fluids Engineering*, Vol. 99, 1977, pp. 132–140.

9 Wilkinson, D. H., "Calculation of Blade-to-Blade Flow in a Turbomachine by Streamline Curvature," ARC R&M No. 3704, 1972.

10 Novak, R. A., "Streamline Curvature Computing Procedures for Fluid-Flow Problems," ASME JOURNAL OF ENGINEERING FOR POWER, Vol. 89, 1967, pp. 478–490.

11 Krimerman, Y., and Adler, D., "The Complete Three-Dimensional Calculation of the Compressible Flowfield in Turbo Impellers," *Journal of Mechanical Engineering Science*, Vol. 20, 1978, pp. 149–158.

12 Hirsch, C., and Warzee, G., "An Integrated Quasi-3D Finite Element Calculation Program for Turbomachinery Flows," ASME Paper No. 78-GT-56, 1978.

13 Wang, Q., Zhu, G., and Wu, Ch.-H., "Quasi-Three-Dimensional and Full Three-Dimensional Rotational Flow Calculations in Turbomachines," ASME JOURNAL OF ENGINEERING FOR GAS TURBINES AND POWER, Vol. 107, 1985, pp. 277–285.

14 MacCormack, R. W., "The Effect of Viscosity in Hypervelocity Impact Cratering," AIAA Paper No. 69-354, 1969.

15 Jansen, M., and Rautenberg, M., "Design and Investigations of a Three Dimensional Twisted Diffuser for a Centrifugal Compressor," ASME Paper No. 82-GT-102, 1982.

16 Teipel, I., and Wiedermann, A., "The Influence of Different Geometries for a Vaned Diffuser on the Pressure Distribution in a Centrifugal Compressor," ASME Paper No. 84-GT-68, 1984.

17 Green, J. E., Weeks, D. J., and Brooman, J. W. F., "Prediction of Turbulent Boundary Layers and Wakes in Compressible Flow by a Lag-Entrainment Method," ARC R&M No. 3791, 1973.

18 Horlock, J. H., "On Entropy Production in Adiabatic Flow in Turbomachines," ASME *Journal of Basic Engineering*, Vol. 93, 1971, pp. 587–593.

Downloaded 01 Jun 2010 to 171.66.16.57. Redistribution subject to ASME license or copyright; see http://www.asme.org/terms/Terms_Use.cfm

I. Ariga
Professor.

S. Masuda
Associate Professor.

Faculty of Science & Technology,
Keio University,
Yokohama, Japan

A. Ookita
Ishikawajima Harima Heavy
Industries Co., Ltd.,
Mass-Produced Machinery Division,
Rokyo, Japan

Inducer Stall in a Centrifugal Compressor With Inlet Distortion

The effects of inlet distortion on the inducer stall in a centrifugal compressor are investigated. Cases of both radial and circumferential distortion are investigated. It is shown that the rotating stall onset is amplified by radial distortions, and restrained by circumferential distortions. These results are compared with calculations based on the small disturbance theory. The authors find that the stall onset is governed by the characteristic parameters related to the lower flow rate region for radial distortions, but affected by those of the higher flow rate region for circumferential distortion. It is shown that the process of stall is different for each distortion pattern. Existence of inlet distortion reduces compressor performance characteristics and strongly influences the stability margin.

Introduction

Flow nonuniformity at the impeller inlet of centrifugal compressors, termed "inlet distortion," can be caused by inlet flowpath restrictions in equipment such as turbochargers, small-sized gas turbines, and multistage compressors.

Only a small amount of data has been collected, concerning such inlet distortions in centrifugal compressors and the consequent deterioration of compressor performance [1]. There is also a need to clarify compressor performance over the whole operating range, given that inlet distortion tends to be accompanied by impeller stall and surge at higher flow rates than without distortion.

This paper investigates the effects of inlet distortion on the inducer stall and surge in a centrifugal compressor, over the range from stall to the initial surge point. Inlet distortions increase the inducer stall flow rate, and reduce the surge margin, because some parts of the blades in the distorted flow through an impeller are considered to be working under more unfavorable conditions than in a nondistorted flow. The influence of inlet distortions on stall phenomena has been previously reported [2–5], and the extensive concepts of stall and surge have also been discussed [6–8]. In particular, Greitzer [6] has promoted a better understanding of the mechanisms and processes of these phenomena.

Inducer stall has been observed in a few flow conditions characterized by distinctive recirculations, and is commonly referred to as "rotating stall." In the present paper, two types of rotating stall are defined as follows, to clarify its progressive process.

(*i*) Small stall; the flow condition in which some small recirculations (termed "cells") rotate in the opposite direction relative to the impeller rotation.

(*ii*) Large stall; the flow condition in which one or two large recirculations rotate, as the fluctuating component of inlet velocity increases abruptly.

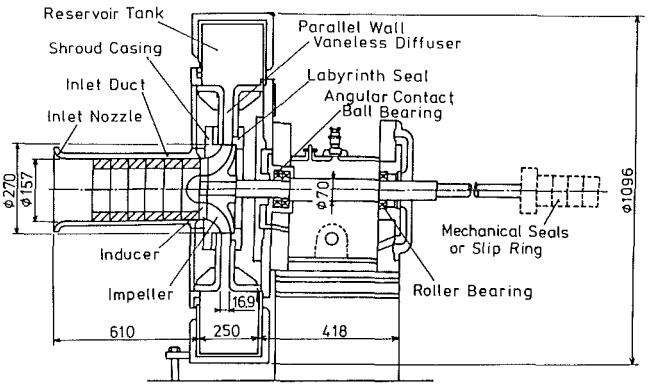

Fig. 1 Compressor configuration

Measurements are performed with covered hot-wire probes and an anemometer. The analyses of these measurements give some information concerning stall and surge. It is hoped that the results will contribute to an improved understanding of the part-load characteristics of centrifugal compressors as influenced by inlet distortions and aid the development of future compressor design and operation.

Test Facilities and Instrumentation

Experimental Equipment. The present investigation was carried out on a low-pressure centrifugal compressor rig, as shown in Fig. 1. This compressor is the same as used in [1] and is driven at a continual corrected speed N_0 = 5000 rpm. Each inducer has 12 blades, forming a parabolic camber line, and is designed to produce shockless inlet-flow conditions at the leading edge.

Inlet distortions are generated through the honeycombs and meshes installed at the locations upstream of an inducer, as shown in Fig. 2. Honeycombs alter the flow resistance in the inlet duct, and produce the specific pressure loss for the dif-

Contributed by the Gas Turbine Division of THE AMERICAN SOCIETY OF MECHANICAL ENGINEERS and presented at the 31st International Gas Turbine Conference and Exhibit, Düsseldorf, Federal Republic of Germany, June 8–12, 1986. Manuscript received at ASME Headquarters January 27, 1986. Paper No. 86-GT-139.

Copyright © 1987 by ASME

Downloaded 01 Jun 2010 to 171.66.16.57. Redistribution subject to ASME license or copyright; see http://www.asme.org/terms/Terms_Use.cfm

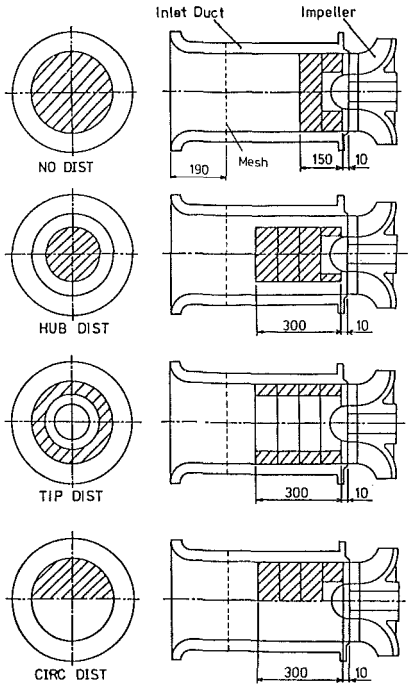

Fig. 2 Setting location of distortion generator

ferent kinds of distortions; however, honeycombs do not allow the pressure loss to reach the same level. Thus, by using meshes which are mounted upstream of their honeycombs, the inlet pressure loss can be adjusted to the same drop for each kind of distortion.

Kinds of distortion are shown in Table 1. Inlet distortion is divided mainly into two radial distortions and one circumferential distortion in this paper. Radial distortions are represented by Tip dist (tip distortion) and Hub dist (hub distortion). Circumferential distortion is designated as Circ dist, which is generated through the honeycombs inserted at a circumferential location between 0 deg and 180 deg.

The blocked area ratio in Table 1 is calculated by the following expression

$$\text{Blocked area ratio} = \frac{\text{Area of honeycombs}}{\text{Area of inlet duct}} \quad (1)$$

Table 1 Kinds of distortion

DISTORTION PATTERN	BLOCKED AREA RATIO	DISTORTION GENERATOR
NO DIST (No Distortion)	0	No Honeycomb
	1	Honeycomb at All Area
HUB DIST (Hub Distortion)	1/2	Cylindrical Honeycomb at the Hub Side
	2/3	
TIP DIST (Tip Distortion)	1/2	Cylindrical Honeycomb at the Shroud Side
	2/3	
CIRC DIST (Circumferential Distortion)	1/2	Fan-Shaped Honeycomb

At present, these values are indicated in all figures together with the kinds of distortion patterns.

No dist (no distortion) means almost uniform flow, but honeycombs are installed into the inlet duct, to equal the pressure loss such as No dist 1.

Measuring Methods of Fluctuating Flow. For the measurements of the rotating stall and surge, covered hot-wire probes are employed as shown in Fig. 3. On the inflow side of the cylindrical cover, there is a 1.2-mm-dia hole, which is as large as the length of the uncoppered part of the copper-plated tungsten wire. On the opposite side, the hole is about ten times the size of the inlet hole and houses 60 (in.$^{-1}$) meshes.

Therefore, the angular response of the probe is derived in the sharp form of curves where the pitch angle γ occurs over the range of 120 deg, and the output of reverse flow is attenuated by meshes. Such probes are mounted perpendicularly to the center line of ducts, at the following four points (Fig. 4(*a*)):

Nomenclature

C_{1m} = axial velocity, m/s
H = total head, m
h = length along blade height, m
DI = distortion index
Δh_{in} = shock loss at the inducer, m
ht = distance from hub to shroud along quasi-orthogonal line, m
i = incidence angle, deg
ic = number of cells
K = the ratio of inducer shock loss to impeller total loss, kg/s
m = mass flow rate
N_0 = corrected rotational speed $= N/\sqrt{T_{a,0}/T_a}$, rpm
P_a = atmospheric pressure, Pa
Pr = pressure ratio
P_t = total pressure, Pa
P_s = static pressure, Pa
SP = stability parameter $= (\partial Pr/\partial m)/Pr$, s/kg
Δt = time lag between two probes, s
t_s = periodicity of rotating stall, s
u = fluctuating component of inflow velocity
U_2 = average value of inflow velocity
U = rotational speed at the outlet of impeller, m/s
Z = total pressure loss coefficient of impeller
Z_i = number of inducer blades
γ = pitch angle, deg
α = inlet angle of diffuser, deg
β = relative incidence angle of rotating cascade, deg
β^* = relative incidence angle, deg
ζ_{in} = shock loss coefficient = 0.6
δ = yaw angle
θ = circumferential angle, deg
Θ^* = inducer inlet angle, deg
φ = flow coefficient
φ_{part} = mean velocity coefficient in the partial area $= \frac{A_1}{A_2}\frac{\rho_1}{\rho_2}\frac{C_{1m,\,part}}{U_2}$ (A = section area, ρ = density)
ω_0 = angular rotational speed of impeller, rad/s
ω_s = angular propagation speed of rotating stall, rad/s

Subscripts

1 = inducer inlet condition
2 = impeller outlet condition
loss = loss component
part = partially averaged component
tip = tip-area averaged component

Downloaded 01 Jun 2010 to 171.66.16.57. Redistribution subject to ASME license or copyright; see http://www.asme.org/terms/Terms_Use.cfm

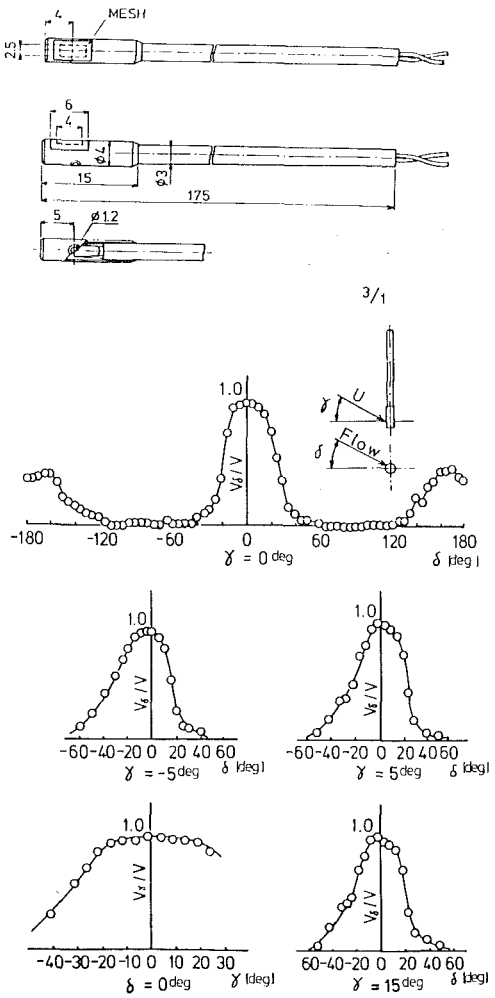

Fig. 3 Covered hot-wire probe and its calibration

Table 2 Characteristics of rotating stall (measuring station *b*)

NO DIST 1

Flow Condition	Measured Point	Flow Coefficient	Peak Frequency	Rotating Velocity	Number of Cells
Design	A	0.40	1000 (Hz)	–	–
Stall Onset	B	0.254	1000,390,455	–	0 – 1
Small Stall	C	0.229	280,1000	0.435	0 – 3
	D	0.216	285, 225	0.625	3 – 4
	E	0.204	225, 285	0.625	3 – 4
	F	0.193	230	0.667	4
	G	0.183	230	0.667	4
	H	0.174	225	0.667	4
	I	0.164	225	0.667	4
Large Stall	J	0.154	21.5	0.333	1
Near V. S.	K	0.123	21.5	0.286	1
Hysteresis	L	0.158	21.5	0.286	1
	M	0.166	21.5	0.250	1
	N	0.177	21.5	0.250	1

* V.S. : Violent Surge

(*a*) 40 mm upstream of inducer
(*b*) 5 mm upstream of inducer
(*c*) 5 mm downstream of impeller
(*d*) near diffuser outlet (= radius ratio of 1.70)

Three probes are placed at each point:

$h/ht = 11/13$ (in the tip area)
$= 7/13$ (in the middle area)
$= 3/13$ (in the hub area)

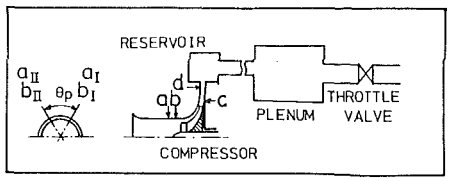

(a) Compression System and Measuring Station

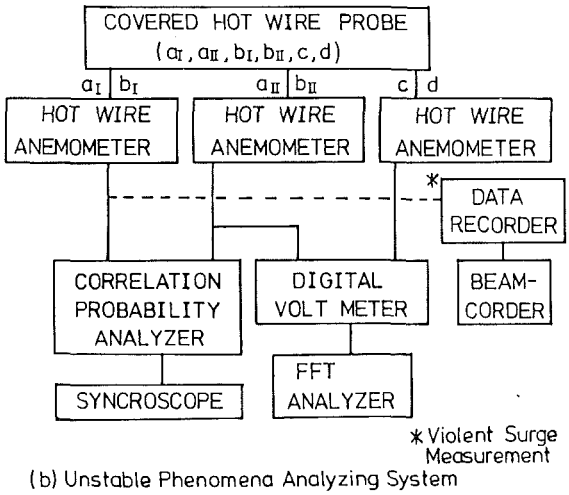

(b) Unstable Phenomena Analyzing System

Fig. 4 Measuring system

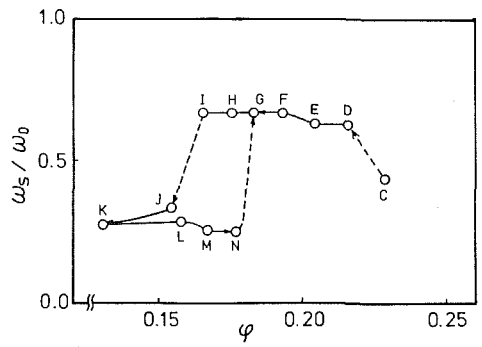

Fig. 5 Variation of absolute propagation speed with flow coefficient

Figure 4(*b*) shows the analyzing system for unstable phenomena. Each anemometer signal is linearized, and analyzed by a correlation probability analyzer and a Fast Fourier Transform (FFT) analyzer, to determine the phase shift between two different locations and the frequency spectrum of each station. Flow perturbations rotating in the inducer will generate periodic signals at a_{I} and a_{II}, or b_{I} and b_{II} with period t_s. Due to the angle difference θ_p (= 60 deg) in the circumferential position, there will be a time lag Δt between the signals from two probes, which is the determination of the angular propagation speed ω_s and the number of cells i_c.

$$\frac{\omega_s}{\omega_0} = \frac{t_0}{i_c t_s}, \qquad i_c = \frac{360 \text{ deg}}{\theta_p \text{ deg}} \cdot \frac{\Delta t}{t_s} \tag{2}$$

These data, however, are given by the final result averaged under the following sampling conditions, with a 500 Hz low-pass filter.

ω_s/ω_0	Sampling rate (ms)	Sampling size (words)
0.5-1	0.2	2^{16}-2^{17}
0-0.5	1	2^{10}-2^{14}

Downloaded 01 Jun 2010 to 171.66.16.57. Redistribution subject to ASME license or copyright; see http://www.asme.org/terms/Terms_Use.cfm

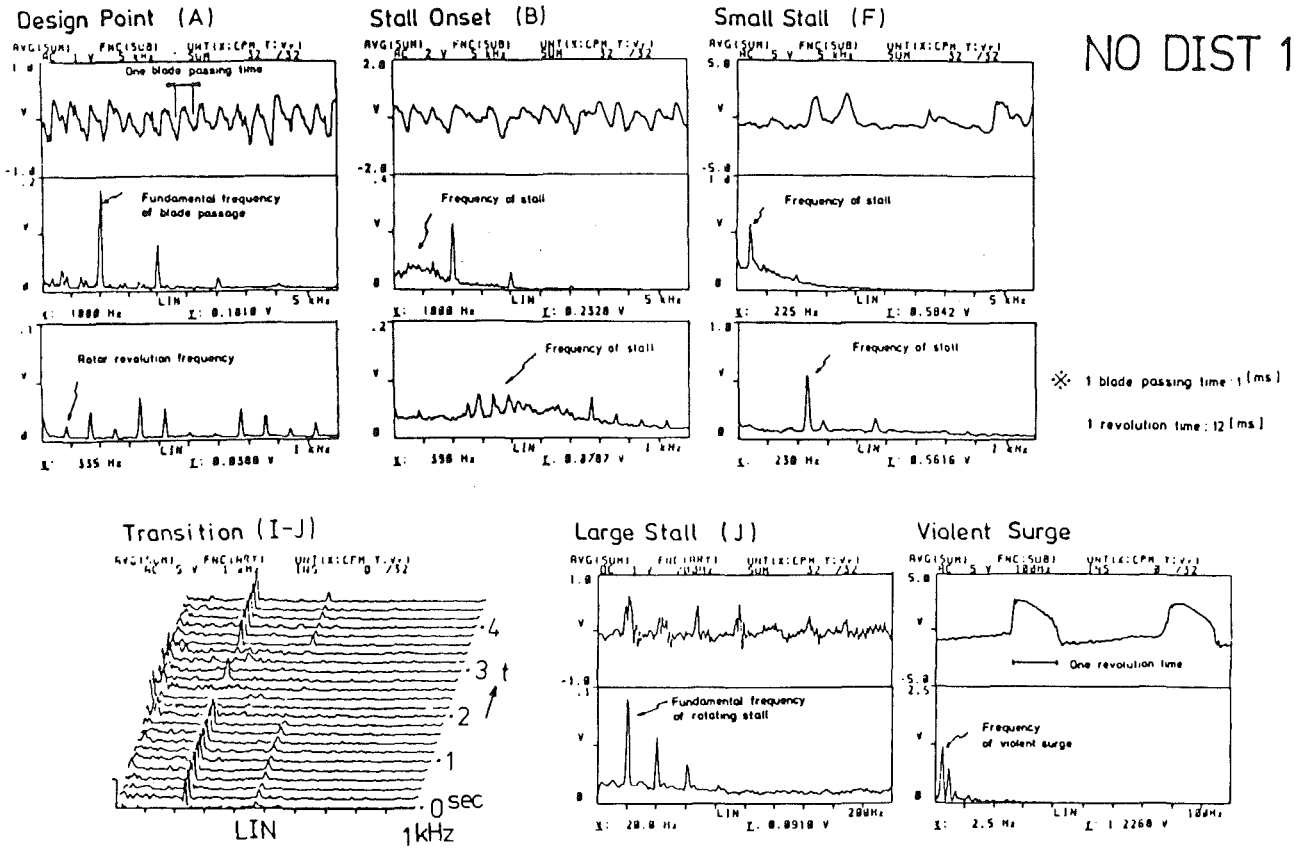

Fig. 6 The power spectra for inlet velocity

Fluctuating Flow Phenomenon of No Distortion

Prior to attempting to investigate the inducer stall for each distortion, it is worthwhile to understand any stall conditions for no distortion. The data of fluctuating flow phenomenon under unstable operation are described as follows in the case of No dist 1 (no distortion).

Unstable Flow Conditions. Table 2 shows the flow conditions under a lower flow rate operation than at the design point. These measurements were performed with covered hot-wire probes at a location 5 mm upstream from the inducer.

The operating points are indicated by $A \rightarrow N$, where B presents the stall onset point and C to N the points under the rotating stall conditions, revealed by fixed peak frequencies of power spectrum analysis. These stall conditions are obtained by using the analyzing system in Fig. 4, and equation (2).

Figure 5 shows the variation of the stall propagation speed ω_s at reduced flow coefficient. Figure 6 also shows the frequency spectrum, visualized on the scope of an FFT analyzer. The ranges, however, are shown at 5 kHz and 1 kHz for the flow rates of A, B, and F, to compare the signal level between the rotating stall and the fluctuating flow induced into the blades. The latter frequency is

$$Z_i(=12)\times 5000\ \text{rpm}/60 = 1000\ \text{Hz}$$

Thus, the detailed explanation can be described as follows.

At the design point A, the observed dominating frequency is 1000 Hz. As the flow rate decreases, a weak frequency appears, which is attributed to a self-excited vibration, over the range of 390 to 450 Hz. The fluctuating components of velocity are gradually increased around the flow rate B, and the level of power spectrum of 1000 Hz is reduced. These data can corroborate a destabilization of the inducer flow. The operating point B, where the reappearance of such conditions is confirmed, is considered to be the onset of rotating stall.

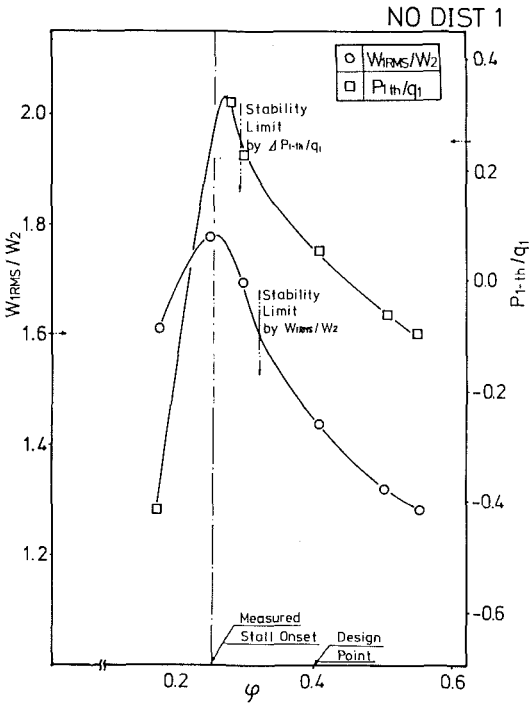

Fig. 7 Stability limit due to inducer stall onset

At point F, the peak frequency of 240 Hz can be clearly detected. Four stall cells are found to rotate at an absolute propagation speed $\omega_s = 0.677\ \omega_0$. The fluctuating flows around the point F seem to generate a few small recirculations along the inducer blade.

Another observation is that the stalled flow is observed to

Downloaded 01 Jun 2010 to 171.66.16.57. Redistribution subject to ASME license or copyright; see http://www.asme.org/terms/Terms_Use.cfm

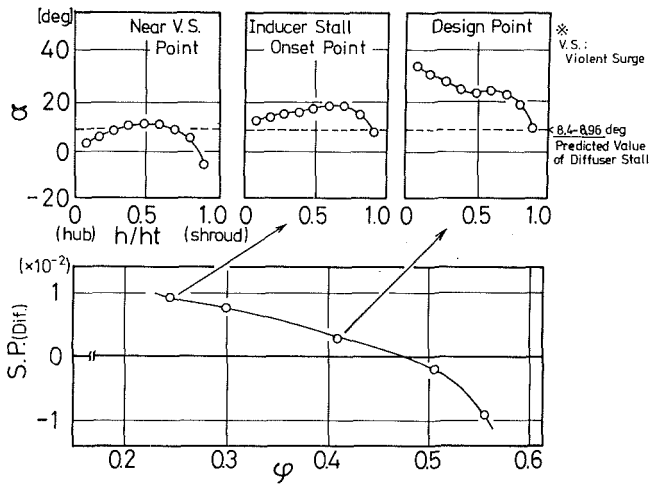

Fig. 8 Variation of inlet angle and stability parameter (SP) of diffuser

be a single large recirculation at the further reduced flow rate J, which rotates at a propagation speed $\omega_s = 0.333\omega_0$. There are likely to be two patterns of the rotating stall in this compressor, as shown in Fig. 5. One is a small stall, observed between C and I, another is a large stall measured below J. The hysteresis loop exists over the transition process.

The transition from I to J occurs as a very unsteady phenomenon, as shown in Fig. 6. In this condition both frequencies of the small stall and the large stall appear with random periodicity. This abrupt development of the stalled flow is not considered to develop directly at the inducer, but to be triggered by a diffuser stall according to the following facts.

Initially, the data for rotating stall onset, which occurs when the ratio of inlet and outlet relative velocities is 1.78, and the static pressure ratio of inducer throat and inducer inlet is 0.26, should correspond to the stability margins of the impeller recommended by Rodgers [9] and Yoshinaka [10]. These values in the present experiment are almost the same as Rodger's experimental value 1.6 and Yoshinaka's 0.25 as shown in Fig. 7.

On the other hand, near the violent surge point whose flow rate is almost the same at the transition point of large stall conditions, the mean flow angle of the diffuser inlet is around 6.5 deg from the circumferential direction as shown in Fig. 8. This angle is nearly equal to the predicted one, which was obtained by Senoo's experiments [11]. He has proposed that the inlet angle of the onset of diffuser rotating stall is 0.75–0.8 times as large as that calculated for the induction of reverse flow. In this study, the latter value was 11.7 deg, and thus the diffuser stall onset was predicted to occur at an inlet angle of 8.4–8.96 deg. Furthermore, the flow conditions of the diffuser are liable to become instable in the lower flow rate range where the value of stability parameter (SP) is positive and increases as shown in Fig. 8.

Based on these facts diffuser stall will probably occur.

Flow Visualization. The complicated flow around the transition point can be confirmed by the tuft visualization technique. Figure 9 shows the tuft reactions 36.5 to 68.5 mm upstream of the inducer at the midpoint between *I-J*. A large circulation shifts to the same direction of inducer rotation once every 45.5-msec period. This result corresponds to the frequency of 21.5 Hz, measured 40 mm upstream of the inducer.

In conclusion, the developmental process of rotating stall generated within an inducer may be illustrated as shown in Fig. 10. Thus, rotating stall is generated from the tip side (in small stall) and becomes a large recirculation over the whole area (in large stall), and further, inflow cannot be charged in the tip area (in near violent surge conditions).

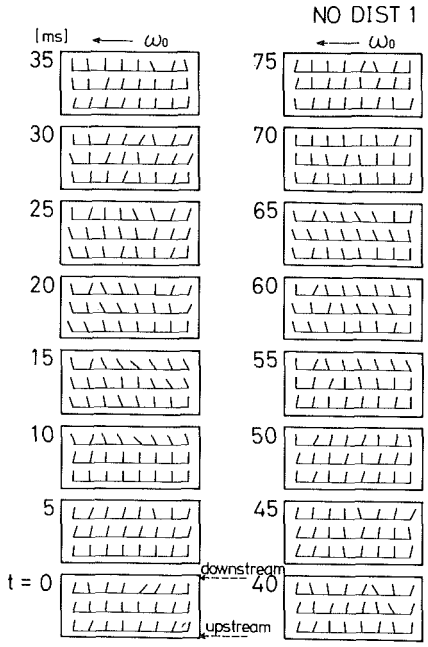

Fig. 9 Tuft reactions upstream of inducer (visualization test)

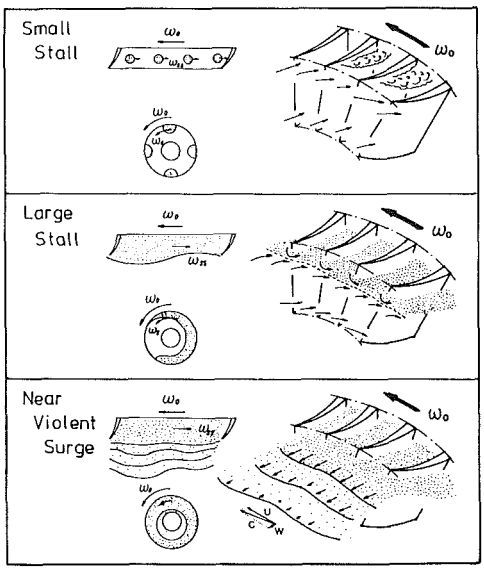

Fig. 10 Flow conditions of inducer rotating stall

Effects of Inlet Distortion

The existence of inlet distortion is considered to cause partial flow separation at larger flow rates than conditions of nondistorted inflow. It is clarified how the transition occurs and how the impeller gets into and recovers from rotating stall on the basis of the variation of the case of No dist 1 in the following items:

(*i*) the progressive process of inducer rotating stall, with inlet distortions;
(*ii*) the correlation of the occurrence of inducer stall with the factors governing inlet flow conditions.

Inlet Conditions. Figure 11 shows the distributions of axial velocity for radial distortions, which were measured 5 mm upstream of the inducer inlet. The flow patterns in stable region were almost the same as those at the design point. At the onset point of inducer rotating stall, which was detected at

Downloaded 01 Jun 2010 to 171.66.16.57. Redistribution subject to ASME license or copyright; see http://www.asme.org/terms/Terms_Use.cfm

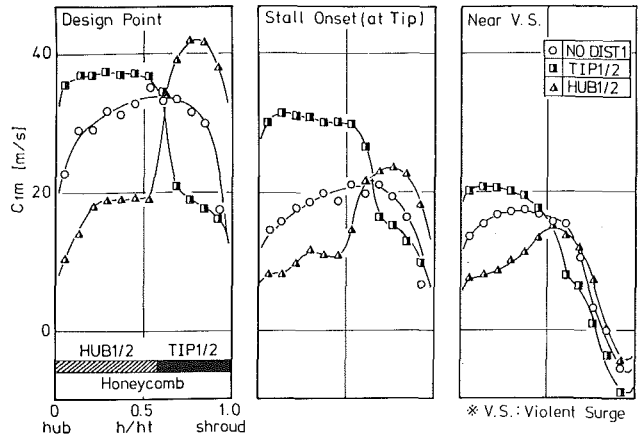

Fig. 11 Axial velocity distributions for radial distortions at the inducer inlet

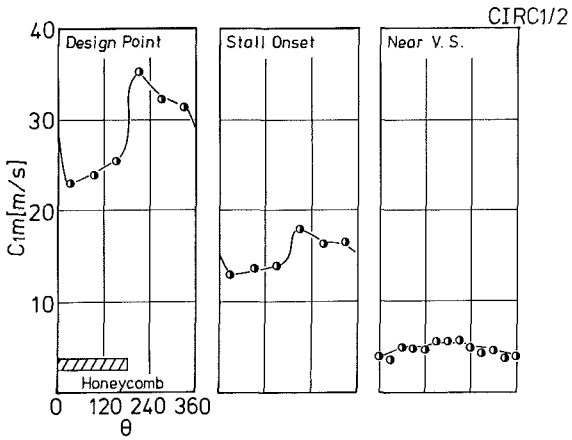

Fig. 12 Axial velocity distributions for circumferential distortion at the inducer inlet

the tip side by means of a covered hot wire, the tip velocity for each distortion pattern tends almost to be equal.

Furthermore, reverse flow is generated steadily at reduced flow rates termed as "near violent surge (VS)" where the velocity distributions in the tip area are almost the same as ones in any distortions.

Figure 12 shows the velocity distributions for circumferential distortion, and Fig. 13 presents the variations of the corresponding incidence angles. When inducer rotating stall occurs, the incidence angles in the area without honeycombs are increased under the influence of low-velocity flow generated through the honeycombs. This peculiar tendency is also observed just before the surge point (Near VS point). Although large reverse flow occurs near the shroud, its remaining areas near the hub appear to be affected by the propagating flow toward the direction of inducer rotation, and as a result the incidence angles in the area without honeycombs are increased.

Overall Performance and Stall Onset. The impeller performances under different inlet conditions are shown in Fig. 14. The deterioration of performances increases in the order: tip distortion (Tip 1/2), circumferential distortion (Circ 1/2), and hub distortion (Hub 1/2), as has been previously reported [1].

Some of the arrows in this figure indicate the onset point of inducer rotating stall. A full line shows the flow rate of rotating stall detected at the tip side, and a broken line is at the hub side. The rotating stall onset point is shifted to the greater flow rate in the case of radial distortions of Tip 1/2 and Hub 1/2. Both stalls in the tip distortion and hub distortion appear

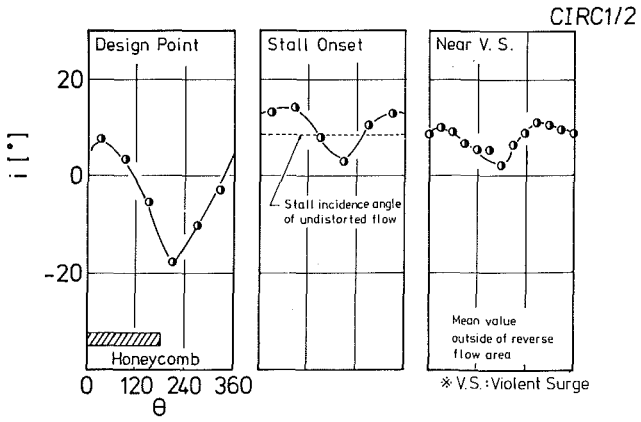

Fig. 13 Incidence angle distributions for circumferential distortion at the inducer inlet

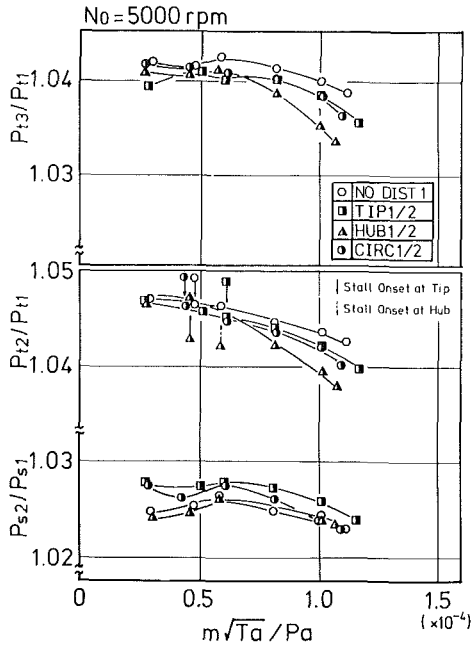

Fig. 14 Comparison of performance curves and onset points of inducer rotating stall with various distortions

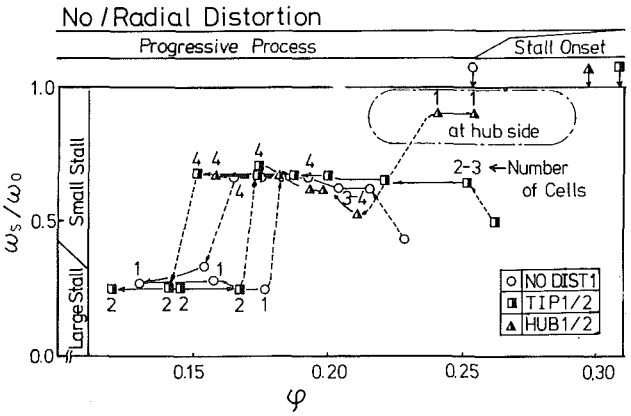

Fig. 15 Variation of absolute propagation speed with flow coefficient for radial distortion

near the wall where the low velocity inflows exist. Moreover, the case of Hub 1/2 possesses other characteristics of rotating stall observed in the tip area, after the first occurrence of rotating stall in the hub area, too.

In the cases of Circ 1/2, the onset point is at a flow rate just

Downloaded 01 Jun 2010 to 171.66.16.57. Redistribution subject to ASME license or copyright; see http://www.asme.org/terms/Terms_Use.cfm

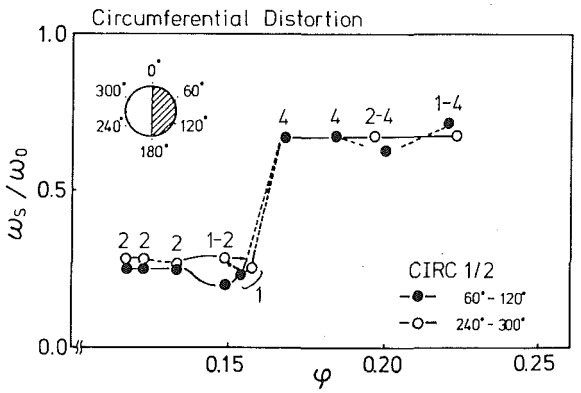

Fig. 16 Variation of absolute propagation speed with flow coefficient for circumferential distortion

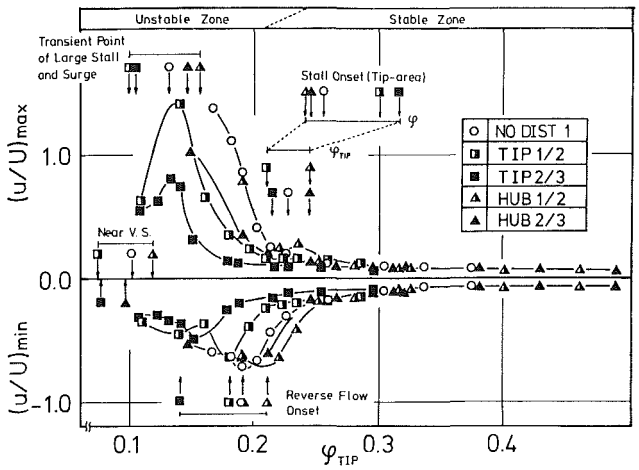

Fig. 17 Relation of the fluctuating components of inlet velocity to the averaged flow coefficient in tip area in the case of radial distortions

lower than No dist 1. The mechanism of the rotating stall is more complicated than one in the cases of other inlet distortions.

Progressive Process of Inducer Rotating Stall. Figure 15 shows both of the variations of stall propagation speed and the number of stall cells detected in the tip area. There are no differences in the form of rotating stall itself among all distortions, except for their onset points and the rapid process of their growth. There are about four cells at the speed of $\omega_s = 0.667\omega_0$ near the onset points, and one or two cells at the speed of $\omega_s = 0.333\omega_0$ near the point of violent surge. The former corresponds to a small stall, and the latter, a large stall according to the case of No dist 1.

Hub 1/2, however, has different characteristics from No dist 1, and Tip 1/2 from the only subsequent view point. It is impossible exactly to measure rotating stall at the transition point between small and large stalls, because a fairly large fluctuating flow is generated abruptly. This fact may be the reason that the hysteresis loop is not shown in this figure. However, on the FFT analyzer scope, a frequency of 40 Hz is obtained over all areas upstream of the inducer. In addition, the rotating stall detected at the hub side can be found near the onset point as mentioned in the preceding section. Its propagation speed ω_s is 0.909 ω_0 and may exist in very small single cells.

With Circ 1/2, the variation is shown in Fig. 16. Its number of cells and propagation speed look like the cases of no distortion or radial distortions, but it is remarakable that a hysteresis loop does not exist. This fact is based on the reason that the increase in incidence angle due to the circumferential existence of honeycombs permits the spanwise loading to shift

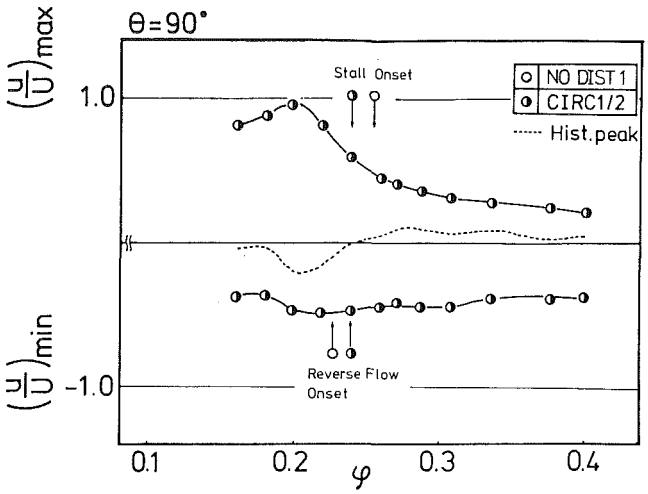

Fig. 18 Relation of the fluctuating components of inlet velocity for the averaged flow coefficient in tip area in the case of circumferential distortion

greatly over the whole span in opposition to the cases of no distortion or radial distortions.

Fluctuating Component. Figure 17 shows the comparison of the fluctuating component with the mean flow coefficient in the tip area. The stepwise process of growth in rotating stall is indicated, together with the variation of the fluctuating component and explanatory notes.

Stall onset and the transition to large stall is detected by frequency analysis, and the occurrence of local reverse flow in rotating stall is obtained by an internal function of the FFT analyzer: histogram of the probability density.

The reverse flow in rotating stall is nearly all in the circumferential direction, and the wave of the covered hot-wire output becomes flat. Then the peak of the histogram on the scope of probability density mode shifts across the point of the mean value of the density. So the onset of reverse flow can be checked too.

From these points, the development of the Tip 1/2 situation is slower than in No dist 1, obviously. On the contrary, with Hub 1/2, the fluctuating component varies gradually.

Figure 18 shows the variation of fluctuating component for the situation Circ 1/2. In this case the situation is different from that of No dist 1, and radial distortions, in that the reverse flow is detected simultaneously, as soon as the rotating stall occurs. The occurrence of rotating stall is at a lower flow coefficient than radial distortions, and its development is more abrupt. This is caused by the difference of the mechanism of how the rotating stall occurs, which is as follows.

Mechanism of Rotating Stall Onset. There exist some differences in the process to stall onset, between the radial and circumferential distortion. As a result, the rotating stall appears in the lower velocity region at the inlet area in all radial distortion patterns, and its onset position is moved to the larger flow rate. However, in the case of hub distortion, the large fluctuations of flow caused by the stall are observed in the tip area such as in no distortion as the flow rate decreases, while the rotating stalls are simultaneously detected near a hub side, which are qualitatively different from the one in the tip area.

In general, the pressure losses within an impeller tend to be more remarkable in the shroud side area, as shown from the results by Mizuki et al. [12], and the rotating stalls in this area are apt to appear, whether any distortion exists or not. In view of these facts, the data are arranged in this section under the consideration that the large pressure losses, which lead to surge as its trigger, are due to the tip rotating stall.

Downloaded 01 Jun 2010 to 171.66.16.57. Redistribution subject to ASME license or copyright; see http://www.asme.org/terms/Terms_Use.cfm

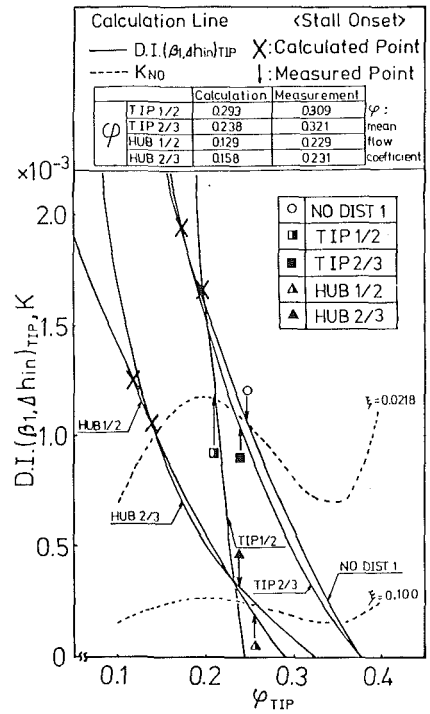

Fig. 19 Distortion index DI and predicted points of rotating stall onset for radial distortions

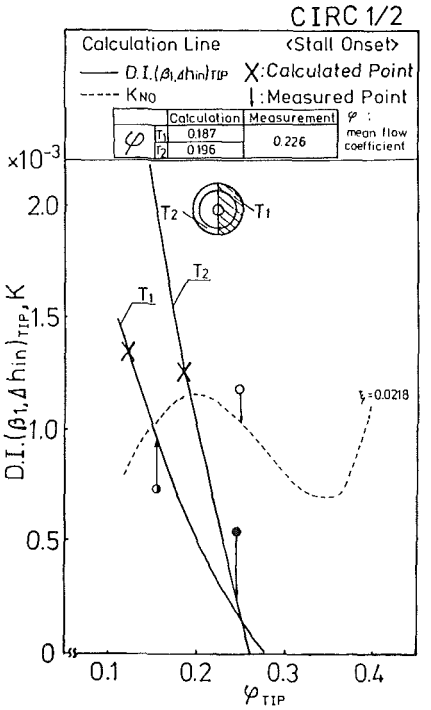

Fig. 20 Distortion index DI and predicted points of rotating stall onset for circumferential distortion

The knowledge of local characteristics at an impeller inlet is useful in predicting rotating stall onset. Thus, it will be useful to investigate the differences in the mechanisms of rotating stall, between nondistorted inflow and distorted inflow conditions. The distortion index, which was derived from the two-dimensional cascade analysis by Takata [13] based on the small perturbation method, was introduced in the following process. Specifically, Takata proposed that rotating stall occurs when the following expression holds

$$\frac{\partial Z}{\partial(\tan\beta_1)} = Z' = 2 \cdot \frac{Z + \sec^2\beta_2}{\tan\beta_1} \tag{3}$$

where, provided that no flow separation occurs prior to stall onset, and the fluid passes through an impeller along the blades, the relative outlet air angle β^* nearly equals 0 deg.

Equation (3) is rewritten in the following form

$$Z' \cdot \frac{\tan\beta_1}{2} - Z = 1 \tag{4}$$

Within a certain small range of the flow rate, the total pressure loss within an inducer and the shock loss at the inducer leading edges are related to

$$\Delta h_{in}/H = K \cdot Z \tag{5}$$

where K is the proportional constant. The total pressure loss coefficient Z is described in the following expression, using the impeller total loss coefficient ξ $(= \Delta H_{\text{loss}}/U_2^2/2g)$

$$\frac{1}{2}\frac{\partial(\Delta h_{in}/H_1)}{\partial\tan\beta_1} \cdot \tan\beta_1 - \frac{\Delta h_{in}}{H_1} = K\left(C_{1m}, \frac{\Delta h_{in}}{H_1}, \xi\right) \tag{6}$$

Even in the present test compressor, the rotating stall onset is presupposed when equation (6) holds, in which the left side presents the diffusion index DI (β_1, Δh_{in}), where K is regarded as the parameter consisting of the ratio of inducer shock loss to impeller total loss.

Figure 19 shows the results of calculation for radial distortion, where the full lines in the figure represent the values of DI, using the incidence measured at the site upstream of the inducer, and the broken lines correspond to the ratio of total pressure loss to the loss under no distortion K. When both values of the two parameters are equal, rotating stall should theoretically occur.

Therefore, the following consideration may be possible: Provided that the rotating stall appears under the assumption of the same magnitude of total pressure loss within the impeller, the stall onset positions for each distortion pattern might be predicted, using the value of total pressure loss at the stall onset, in No dist 1, $\xi = 0.0218$. The table in Fig. 19 shows the predicted values, which are converted into by the marked ones as $\times$ points in the figure.

The remarkable difference between the calculated results and experimental ones on the ordinate is caused by the different loss ratio K. At the onset point of rotating stall from the direct measurement, the value of shock loss is smaller than the theoretically predicted one. Namely, there exist the losses within an impeller caused by the other reasons, and the rotating stall is generated probably at a larger flow rate than the predicted one.

Provided that $\xi = 0.100$ as the total loss, the experimental result and the calculated one in the hub distortion are in good agreement with each other. In this case, it is conceivable that the secondary loss and the loss caused by the rotating stall at the hub side are included, compared with no distortion.

Figure 20 shows the circumferential distortion. In a comparison of the experimental and calculated results, the same tendency is also observed, having a strong dependence on the higher velocity regions. However, the loss from the flow separation is promoted by the existence of a low-velocity region, since the deviation on the ratio of loss K is larger there than in the high-velocity region.

Conclusion

Experimental investigations concerning the effect of inlet distortions on the instability phenomenon of centrifugal compressors existing at lower flow rates were conducted. The stall onset mechanisms and their progressive process, as well as some parameters governing the inlet distortion, were clarified. As a result, the following was concluded:

1 The existence of radial distortion in the inflow to an im-

Downloaded 01 Jun 2010 to 171.66.16.57. Redistribution subject to ASME license or copyright; see http://www.asme.org/terms/Terms_Use.cfm

peller makes the rotating stall onset point move to a higher flow rate, but there exist qualitative differences between the stalls in the tip and the hub areas, with the latter stall occurring under largely fluctuating velocity conditions.

2 The conditions for stall onset with tip inflow distortion may be predicted provided that its velocity defect exists in a certain region near the shroud, using the inlet parameters for no-distortion conditions, and the stall onset flow rate grows gradually.

3 With hub distortion, the stall at the tip develops rapidly under the stimulus of secondary flow caused by the distorted form of flow, and a weak stall near the hub. This tip stall is qualitatively different from the hub stall, and also induces a violent surge.

4 With circumferential distortion, the stability of the whole compressor system is kept to the critical value of stall onset in the same magnitude of uniform inflow as the higher velocity region, and the progressive process is remarkable, such as in hub distortion.

Acknowledgments

The authors are grateful to the financial support of Scientific Research Fund from the Ministry of Education of Japan.

References

1 Ariga, I., Kasai, N., Masuda, A., Watanabe, Y., and Watanabe, I., "The Effect of Inlet Distortion on the Performance Characteristics of a Centrifugal Compressor," ASME JOURNAL OF ENGINEERING FOR POWER, Vol. 105, 1983, pp. 223–230.

2 Graber, E. J., and Braithwaite, W. M., "Summary of Recent Investigations of Inlet Flow Distortion Effects on Engine Stability," AIAA Paper No. 74-236, 1974.

3 Baghdadi, S., and Lueke, J. E., "Compressor Stability Analysis," ASME *Journal of Fluids Engineering*, Vol. 104, 1982, pp. 242–249.

4 Maekawa, A., Higashi, T., and Tanaka, S., "Performance of Rotating Cascades Under the Inlet-Distortion Flow (1st Report, Performance Under the Radial Inlet-Distortions)" (in Japanese), *Trans. JSME*, Vol. 44, No. 383, 1978, pp. 2304–2313.

5 Seoo, N., Nakatani, T., and Tanaka, S., "Performance of Rotating Cascade Under the Inlet-Distortions (2nd Report, Performance Under the Circumferential Distortions)" (in Japanese), *Trans. JSME*, Vol. 46, No. 408, 1980, pp. 1363–1371.

6 Greitzer, E. M., "The Stability of Pumping Systems – The 1980 Freeman Scholar Lecture," ASME *Journal of Fluids Engineering*, Vol. 103, 1981, pp. 193–242.

7 Breugelmans, F. A. E., Lambropoulos, L., and Mathioudakis, K., "Measurement of the Radial Flow Along a Low Speed Compressor Blading During Unstalled and Stalled Operation," GTSJ, 83-TOKYO-IGTC-79.

8 Das, D. K., and Jiang, H. K., "An Experimental Study of Rotating Stall in a Multistage Axial-Flow Compressor," GTSJ, 83-TOKYO-IGTC-79.

9 Rodgers, C., "A Diffusion Factor Correlation for Centrifugal Impeller Stalling," ASME JOURNAL OF ENGINEERING FOR POWER, Vol. 100, 1978, pp. 592–602.

10 Yoshinaka, T., "Surge Responsibility and Characteristics of Centrifugal Compressor," Tokyo Joint G. T. Congress, Paper No. 46, 1977.

11 Kinoshita, Y., and Senoo, Y., "Influences of Inlet Flow Conditions and Geometries of Centrifugal Vaneless Diffusers on Critical Flow Angle for Stall" (in Japanese), *Trans. JSME*, Vol. 42, No. 362, 1976, pp. 3169–3176.

12 Mizuki, S., et al., "Investigation Concerning Rotating Stall and Surge Phenomena Within Centrifugal Compressor Channel," ASME Paper No. 78-GT-9.

13 Takata, H., and Okazaki, I., "Rotating Stall in Multistage Axial Compressors" (in Japanese), *Trans. JSME*, Vol. 26, No. 171, 1970, pp. 1598–1619.

Downloaded 01 Jun 2010 to 171.66.16.57. Redistribution subject to ASME license or copyright; see http://www.asme.org/terms/Terms_Use.cfm

A New Technique for Stabilizing the Flow and Improving the Performance of Vaneless Radial Diffusers

A. N. Abdel-Hamid
Professor of Mechanical Engineering,
The American University in Cairo,
Cairo, Egypt

Experiments were conducted to investigate the effects of using small exit vanes on the characteristics of an otherwise vaneless radial diffuser of outer radius and width-to-inlet radius ratios of 1.75 and 0.116, respectively. The steady and unsteady characteristics of the diffuser were evaluated as the angle of the vanes was varied continuously at several diffuser inlet conditions. The measurements showed that the influence of the adjustable exit vanes on the diffuser flow field increased as the diffuser inlet flow angle was decreased. Elimination of the self-excited flow oscillations in the diffuser was possible for all operating conditions by appropriate setting of the exit vane angle. Moreover for the diffuser investigated here and with optimum setting of the exit vanes angle the static pressure rise coefficient was significantly improved compared to the case of a pure vaneless diffuser and was found to remain almost constant at low values of diffuser inlet angles. Relative to other techniques for controlling flow instability in vaneless diffusers the proposed method offers mechanical simplicity and improved overall performance.

Introduction

Self-excited flow oscillations in vaneless radial diffusers have always been of major concern to centrifugal compressor designers and users because of their serious effects on machine performance and mechanical integrity. In recent years, various aspects of the phenomena have been analytically and experimentally investigated [1–8]. Based on the results presented to date it is now accepted that the triggering of the flow oscillations is dependent on the flow distribution in the entire vaneless diffuser and the dynamic coupling between the diffuser and the upstream and downstream components of the compression system [3, 8].

Several techniques have been suggested in the past to delay the occurrence of flow oscillations in the vaneless diffuser at reduced flow rates. A moving diffuser ring at inlet, a moving diffuser wall, and recently a moving control ring at diffuser exit [6] were all found to be effective in suppressing the triggering of the flow oscillations. Diffuser performance at low inlet flow angles however remains unsatisfactory because of the low values of achieved static pressure rise coefficient.

Based on the previously obtained theoretical [3] and experimental [6] results, which demonstrated the strong influence of the diffuser exit boundary conditions on the onset of self-excited flow oscillation in the diffuser, a new technique to stabilize the flow in vaneless radial diffusers is proposed.

In this new technique the diffuser flow field and the boundary conditions at diffuser exit have been modified through the use of adjustable vanes of limited extent near the exit of the otherwise vaneless diffuser. By proper adjustment of the angle of the vanes, elimination of self-excited flow oscillations and

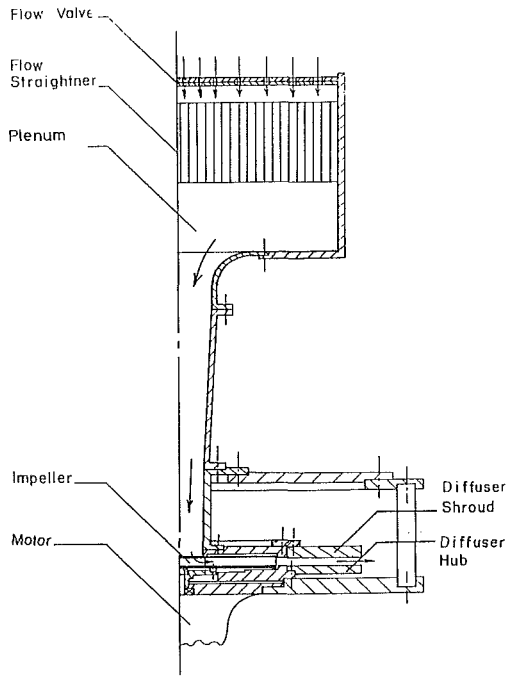

Fig. 1 Schematic of the experimental test facility

Contributed by the Gas Turbine Division of the THE AMERICAN SOCIETY OF MECHANICAL ENGINEERS and presented at the 31st International Gas Turbine Conference and Exhibit, Düsseldorf, Federal Republic of Germany, June 8–12, 1986. Manuscript received at ASME Headquarters January 24, 1986. Paper No. 86-GT-128.

Copyright © 1987 by ASME

Downloaded 01 Jun 2010 to 171.66.16.57. Redistribution subject to ASME license or copyright; see http://www.asme.org/terms/Terms_Use.cfm

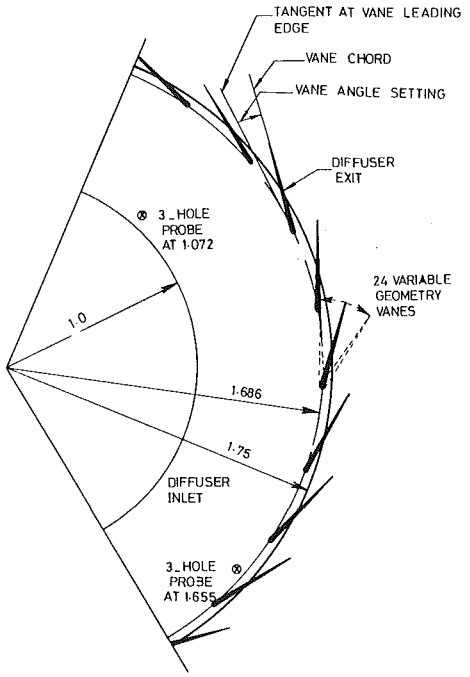

Fig. 2 Schematic of the diffuser with exit vanes

significant improvement of the diffuser performance was possible for all flow conditions. Possible mechanisms responsible for the success of the proposed technique are discussed.

Experimental Facility

The facility used in the present investigations was similar to the one used earlier to study the effects of a diffuser exit ring on flow oscillations [6]. A schematic diagram of the facility is shown in Fig. 1. The shrouded impeller overall geometry was:

Impeller exit diameter	233 mm
Height to exit radius ratio	0.116
Inlet to exit radius ratio	0.287
Number of blades	24
Blade exit angle	60 deg

The radial diffuser, which was originally vaneless, has the following geometry:

Diffuser radius ratio r_o/r_i	1.75
Diffuser width to inlet radius ratio W/r_i	0.116

The flow conditions in the diffuser exit were changed using a set of 24 vanes. The vanes were hinged at the leading edge at a radius ratio r/r_i of 1.686 as shown in Fig. 2. The ratio between the chord of the vanes and the diffuser inlet radius was 0.5. The vane angle setting relative to the tangential direction was varied in a continuous manner at different flow conditions.

The volume flow rate through the system was calculated from measurements of the total and static pressures upstream of the impeller. The flow angle at diffuser inlet and exit were determined using two traversed three-hole probes which were located at radius ratios r/r_i of 1.072 and 1.655, respectively. The diameter of each probe was 3 mm and both were introduced to the flow through the shroud wall. Since the spacing between the diffuser walls was 13.5 mm possible interference between the probe and the diffuser flow was minimal. The distributions of flow magnitude and direction were measured using the probes at 11 equally spaced points between the hub and the shroud. For each flow condition in the diffuser the mass flow rate evaluated from the measured velocity profile was compared with the one evaluated from measurements upstream of the impeller inlet. The measured flow angles at diffuser inlet were corrected to ensure equality between the two values of the mass flow rates. Typically the magnitude of these corrections was less than one degree. The performance of the diffuser was determined from measurements of the static pressures at diffuser inlet, exit vane inlet, and outlet.

Self-excited flow oscillations in the diffuser were measured using piezoelectric dynamic pressure transducers. The transducers were flush mounted with the shroud wall at a radius ratio r/r_i of 1.05 and a circumferential separation of 41 deg. The dynamic signals from the pressure transducers were analyzed in the frequency domain to accurately identify the onset of the oscillations.

Test Procedure

Based on the results obtained in the earlier investigations [5, 6], it was decided to run the test facility at a number of flow coefficients ϕ, covering the stable and unstable ranges of the original vaneless diffuser. For each flow coefficient the vane angle setting β, measured from the tangential direction, was gradually increased. The flow coefficient was kept constant during vane setting changes using the flow valve upstream of the bellmouth. For each flow coefficient and vane setting the velocity profiles at diffuser inlet and exit were measured using the three-hole probes. The vane angle setting β for each flow coefficient was increased until flow oscillations were observed in the diffuser. Through the entire test program the impeller was run at a constant speed of 5000 rpm.

The recorded pressure values were later manipulated to yield the nondimensional characteristics of the diffuser for different vane settings. The flow rate and the diffuser static pressure rise values were nondimensionalized with respect to the product of the impeller tip speed and impeller exit area, and the dynamic pressure at diffuser inlet, respectively. The velocity magnitudes were divided by the impeller tip speed. The density was assumed constant since the flow Mach number at impeller tip was less than 0.2 for all flow conditions.

Results and Discussion

Effect of Vane Angle on Overall Pressure Rise Coefficient

Nomenclature

C_v = vane chord
p_i = static pressure at diffuser inlet
p_o = static pressure just upstream of vanes
Q = volume flow rate
r = radius at a point in diffuser space
r_i = diffuser inlet radius
r_o = diffuser exit radius
U = mechanical velocity at impeller tip
V_i = flow velocity at diffuser inlet
V_v = flow velocity just upstream of vane
W = spacing between hub and shroud
X = axial distance of a point in the diffuser measured from the hub
α_i = flow angle at diffuser inlet, measured from tangential direction
α_v = flow angle just upstream of vane
β = vane angle measured from tangential direction
ρ = fluid density
ϕ = flow coefficient $\equiv Q/(2\pi r_i W U)$
ψ = diffuser pressure rise coefficient $\equiv (p_o - p_i)/(\frac{1}{2}\rho U^2)$
ψ_v = vane pressure rise coefficient $\equiv (p_o - p_v)/(\frac{1}{2}\rho U^2)$

Downloaded 01 Jun 2010 to 171.66.16.57. Redistribution subject to ASME license or copyright; see http://www.asme.org/terms/Terms_Use.cfm

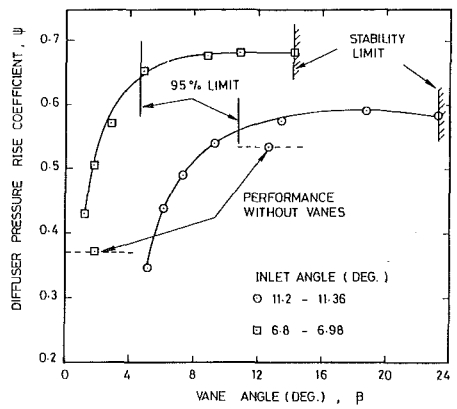

Fig. 3 Effect of vane angle on diffuser static pressure rise coefficient

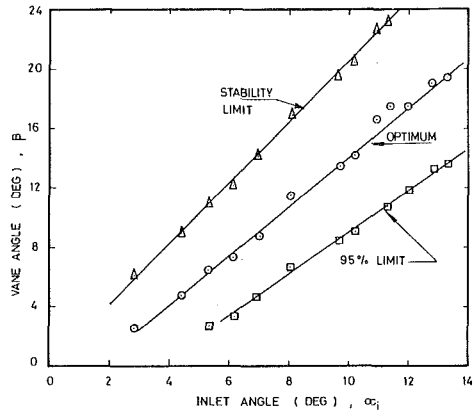

Fig. 5 Variation of optimum vane angle with diffuser inlet angle

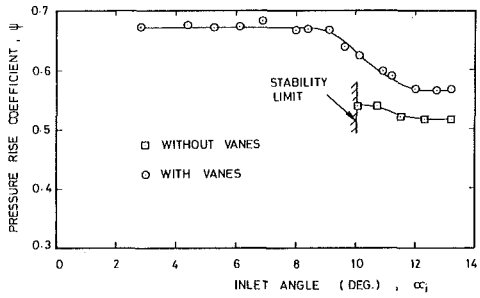

Fig. 4 Optimum performance of diffuser-vane combination

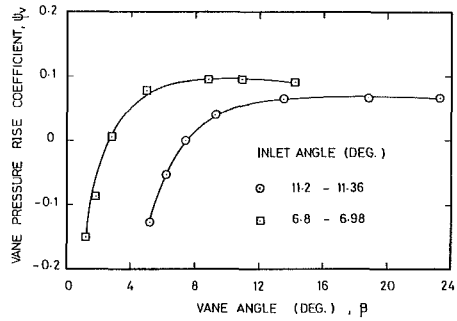

Fig. 6 Effect of vane angle on static pressure rise across the vanes

at Constant Flow Rate Coefficient. Figure 3 shows the typical variation of the diffuser pressure rise coefficient with vane angle for flow coefficients ϕ of 0.08 and 0.128. The corresponding average flow angles at diffuser inlet α_i for these two flow coefficients were 6.9 and 11.3 deg, respectively.

The diffuser pressure rise coefficient ψ initially increased sharply and then tapered off to an almost constant value as the vane angle β was increased. The trend continued until further increase in vane angle β resulted in the onset of self-excited flow oscillations in the diffuser.

For an inlet flow angle α_i of 6.9 deg a diffuser flow without the exit vanes was unstable and the pressure rise coefficient ψ under these conditions was limited to 0.37 [6]. The use of exit vanes set at an angle less than 14.2 deg stabilized the diffuser flow and resulted in significant improvement in diffuser performance. The maximum pressure rise coefficient ψ increased to 0.67 and the peak of the pressure rise coefficient was flat to the extent that the range of vane angles for which the pressure rise coefficient was at least 95 percent of the maximum value was 4.7–14.2 deg.

Without the exit vanes the diffuser flow for an inlet angle α_i of 11.3 deg was stable and the pressure rise coefficient ψ was 0.54 [6]. The use of the exit vanes with settings between 9 and 23.3 deg slightly improved the diffuser performance and the pressure rise coefficient reached a maximum of 0.59. The peak of the pressure rise coefficient was also flat and pressure rise coefficients larger than 95 percent of the maximum value were obtained in the vane angle range 10.8–23.3 deg. Beyond a vane setting of 23.3 deg however, the flow became unstable and periodic flow oscillations were observed in the diffuser. The nature of these self-excited flow oscillations is discussed further below in relation to the measured velocity profiles near diffuser inlet and exit.

The same behavior was observed for every other flow condition tested in the present study. The vane angle at which the maximum pressure rise coefficient was observed for a given inlet flow angle is termed here the optimum vane angle for this particular inlet flow conditions.

Optimum Diffuser Performance. Figure 4 shows a comparison between the diffuser performances with and without diffuser exit vanes. For each inlet flow angle, the exit vanes were set at the optimum value. Without the exit vanes the diffuser pressure coefficient ψ reached a maximum value of 0.54 and a critical inlet flow angle, at which the diffuser flow became unstable, of 10.0 deg. With the vanes set at the optimum positions, self-excited flow oscillations were eliminated and the diffuser performance was significantly improved for all flow conditions.

Most dramatic is the attainment of a diffuser pressure rise coefficient of 0.67 for all inlet flow angles less than 9.0 deg. This performance is superior to the performance of a vaneless diffuser with diffuser exit control ring [6]. With the control ring the maximum value of the pressure rise coefficient ψ was 0.58 at a diffuser inlet flow angle α_i of 8.0 deg. For lower inlet flow angles and optimum control ring positions the pressure rise coefficient decreased considerably although the flow remained stable.

Variation of Optimum Vane Angle With Diffuser Inlet Flow Angle. Figure 5 shows the variation of the optimum angle of the exit vanes with diffuser inlet flow angle. The optimum vane angles increased linearly with the diffuser inlet flow angle. Also shown in Fig. 5 are the boundaries corresponding to the 95 percent and stability limits as obtained from results similar to those shown in Fig. 3. The wide range of vane angles between these two boundaries for a given inlet flow angle α_i emphasizes the suitability of diffuser exit vanes for significant improvements in radial diffuser performance.

Effect of Vane Angle on Pressure Rise Across the Vanes. Although the main purpose of using the diffuser exit vanes was to stabilize the flow in the diffuser, the exit vanes also proved to be effective in diffusing the flow for a wide range of operating conditions despite their limited extent. Figure 6 shows the variation of the vane pressure rise coefficient ψ_v with vane angle β for two different flow coefficients. At very low vane angle settings the static pressure rise across the vanes was negative and the vanes behaved as a throttle.

Downloaded 01 Jun 2010 to 171.66.16.57. Redistribution subject to ASME license or copyright; see http://www.asme.org/terms/Terms_Use.cfm

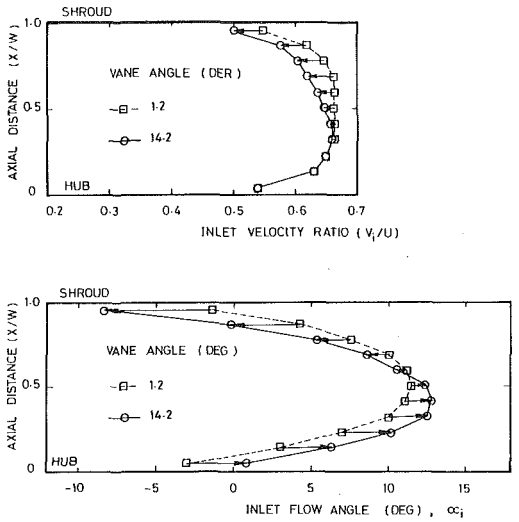

Fig. 7 Range of inlet velocity profiles for different vane angle settings; flow rate coefficient = 0.08

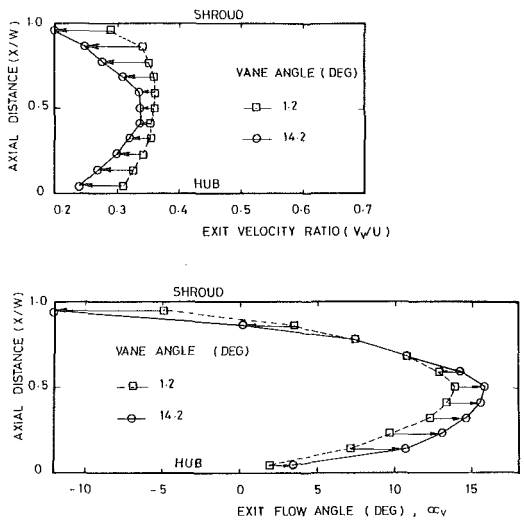

Fig. 8 Range of exit velocity profiles for different vane angle settings; flow rate coefficient = 0.08

For higher settings of vane angles, however, the static pressure across the vanes became positive.

The vane static pressure rise coefficient ψ_v showed a flat maximum as the vane angle β was increased for a constant flow coefficient ϕ. For a flow coefficient of 0.08 the maximum value of vane pressure rise coefficient ψ_v was 0.095 while for a flow coefficient of 0.128 the vane pressure rise coefficient was 0.07. For comparison purposes the pressure rise across a vaneless space extending from the position of the leading edge of the vanes to the diffuser exit was 0.054 at a flow coefficient of 0.128.

The results shown in Fig. 6 also indicate that onset of flow instability in the diffuser was not triggered by the changing of the performance of the exit vanes from throttlelike to diffuserlike. For the data shown in Fig. 6 such a change occurred at vane angles of 2.8 and 7.4 deg for flow coefficients of 0.08 and 0.128, respectively. Flow oscillations were observed at vane settings of 14.2 and 23.3 for the same respective flow coefficients.

In a recent publication [9], the improved stability margin of a radial compressor stage was attributed to the use of a closely coupled throttle at the exit of a vaned diffuser. The results presented here, however, indicate that an improvement in the stability margin of vaneless radial diffusers can be obtained even with diffusion through added exit vanes.

Effect of Exit Vane Setting on Velocity Profiles Near Diffuser Inlet and Exit. Figure 7 shows the extent of inlet velocity profile change for the range of exit vane settings between 1.2 and 14.2 deg. The flow coefficient was kept constant and was equal to 0.08. The corresponding inlet flow angle α_i varied in the range 6.8–6.98 deg.

Starting from the 1.2-deg vane setting, which corresponded to flow throttling by the vanes, the profile of the inlet velocity magnitude was fairly uniform and the flow angle distribution was almost symmetric about the midplane of the radial diffuser. Limited flow reversal zones occurred at both walls of the diffuser at inlet. As the setting of the vane angle was increased the velocity profile was gradually skewed toward the hub in terms of magnitude and direction. At a vane setting β of 14.2 deg, which corresponds to flow diffusion by the vanes, the flow reversal zone at the shroud was more than doubled with no flow reversal at the hub. The diffuser flow was marginally stable under this condition.

Velocity profile near diffuser exit is shown in Fig. 8 for the same flow coefficient and range of vane settings. The velocity magnitude decreased at the diffuser walls more than at the middle of the flow passage as the vane angle β was increased from 1.2 to 14.2 deg. The flow reversal zone which existed at the shroud wall was not significantly affected by the vane setting. There was no flow reversal zone at the diffuser exit near the hub under these conditions. The flow angle distribution was more skewed toward the hub at 14.2 deg than at 1.2 deg vane setting.

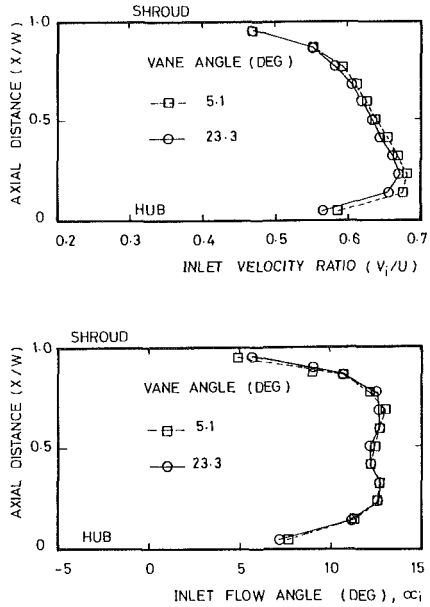

Fig. 9 Range of inlet velocity profiles for different vane angle settings; flow rate coefficient = 0.128

Figure 9 shows the effect of vane setting on the inlet velocity profile for a flow coefficient ϕ of 0.128 and a range of vane angle setting β of 5.1–23.3 deg. The corresponding inlet flow angle α_i varied in the range 11.2–11.36 deg. Under these conditions the vane setting virtually had no effect on the inlet velocity profile. The velocity magnitude profile was skewed toward the hub while the flow direction profile was almost symmetric. No flow reversal zones were present at the hub or the shroud. The flow was marginally stable at a vane setting of 23.3 deg.

Near the diffuser exit, however, the velocity profile did change with vane setting. As shown in Fig. 10 the velocity magnitude decreased across the entire passage and the flow angle distribution was more skewed toward the shroud for a vane setting of 23.3 deg than for 5.1 deg. A slight flow reversal

Downloaded 01 Jun 2010 to 171.66.16.57. Redistribution subject to ASME license or copyright; see http://www.asme.org/terms/Terms_Use.cfm

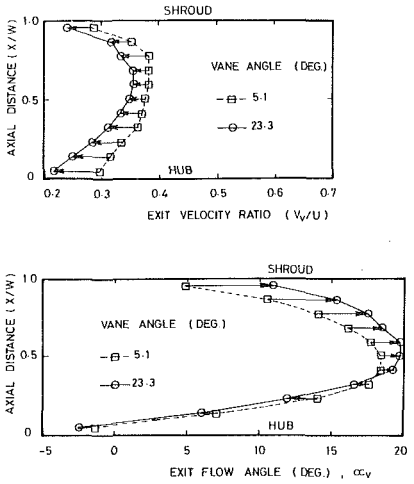

Fig. 10 Range of exit velocity profiles for different vane angle settings; flow rate coefficient = 0.128

zone existed at the diffuser exit near the hub for all vane settings and this flow coefficient.

For the lower flow coefficients, for which the original vaneless diffuser flow would normally be unstable, the exit vanes modified the flow field in the entire diffuser and imposed a new dynamic boundary condition at exit. Both of these parameters affect the onset of the oscillations in the diffuser [3]. Flow oscillations in the diffuser were triggered, as the vane setting was increased at constant flow rate, when the overall damping of the coupled flow in the vaneless space and the exit vanes became negative. The nonuniform flow in the vaneless space was the source of energy required to sustain the flow oscillations. It should be noted again that onset of flow oscillations did not coincide with the changing of the vane performance from a throttler to a diffuser.

For the higher flow coefficients, for which the vaneless diffuser flow would normally be stable, the source of the observed flow oscillations, when the setting of the vane angle was increased at constant flow rate, is believed to be rotating stall associated with the exit vanes. The suggestion is supported by the fact that the measured velocity profiles in the diffuser for a vane setting β of 23.3 deg were very similar to the one measured for a stable flow in a vaneless diffuser without exit vanes [6]. In other words, the flow in the vaneless space of the diffuser, which extended to a radius ratio r/r_i of 1.686, was stable and oscillations were triggered by increased incidence angles and eventual stall of the exit vanes as the vane setting was increased.

Conclusions

1 Onset of rotating nonuniform flow patterns in vaneless radial diffusers can be affected by flow field modifications at the diffuser exit.

2 The influence of small diffuser exit vanes on the diffuser flow field increased as the diffuser inlet flow angle was decreased.

3 For each flow rate through the diffuser there was an exit vane angle setting below which self-excited diffuser flow oscillations were not triggered. Throttling the flow at diffuser exit was not a necessary condition for delaying the onset of the oscillations.

4 For each flow rate through the diffuser the static pressure rise coefficient showed a maximum at an optimum vane angle setting. For the diffuser investigated here the optimum vane setting varied linearly with diffuser inlet flow angle.

5 For the given diffuser geometry the use of adjustable diffuser exit vanes increased the maximum pressure rise coefficient, eliminated flow instability, and maintained high static pressure rise coefficients over a very wide flow range.

6 Fixed diffuser vanes can be set to increase the stable range of an otherwise vaneless diffuser to a specified extent.

Acknowledgments

This research was partially supported by the National Science and Engineering Research Council of Canada under Grant No. A7429 and by a research grant from the American University in Cairo.

References

1 Abdel-Hamid, A. N., Colwill, W. H., and Barrows, J. F., "Experimental Investigation of Unsteady Phenomena in Vaneless Radial Diffusers," ASME JOURNAL OF ENGINEERING FOR POWER, Vol. 101, 1979, pp. 52–60.

2 Abdel-Hamid, A. N., and Bertrand, J., "Distinctions Between Two Types of Self Excited Flow Oscillations in Vaneless Radial Diffusers," *Canadian Aeronautics and Space Journal*, Vol. 26, No. 2, 1980, pp. 105–117; also ASME Paper No. 79-GT-58.

3 Abdel-Hamid, A. N., "Analysis of Rotating Stall in Vaneless Diffusers of Centrifugal Compressors," *Canadian Aeronautics and Space Journal*, Vol. 28, No. 2, 1980, pp. 118–128; also ASME Paper No. 80-GT-184.

4 Van den Braembussche, R. A., Frigne, P., and Roustan, M., "Rotating Non-uniform Flow in Radial Compressors," AGARD Conference Reprint 282, Paper No. 12, May 1980.

5 Abdel-Hamid, A. N., "Effects of Vaneless Diffuser Geometry on Flow Instability in Centrifugal Compression Systems," *Canadian Aeronautics and Space Journal*, Vol. 29, No. 3, 1983, pp. 259–288; also ASME Paper No. 81-GT-10.

6 Abdel-Hamid, A. N., "Control of Self Excited Flow Oscillations in Vaneless Diffusers of Centrifugal Compression Systems," *Canadian Aeronautics and Space Journal*, Vol. 29, No. 4, 1983, pp. 336–345; also ASME Paper No. 82-GT-188.

7 Kinoshita, Y., and Senoo, Y., "Rotating Stall Induced in Vaneless Diffusers of Very Low Specific Speed Centrifugal Blowers," ASME JOURNAL OF ENGINEERING FOR GAS TURBINES AND POWER, Vol. 107, 1985, pp. 514–521.

8 Frigne, P., and Van den Braembussche, R., "A Theoretical Model for Rotating Stall in the Vaneless Diffuser of a Centrifugal Compressor," ASME JOURNAL OF ENGINEERING FOR GAS TURBINES AND POWER, Vol. 107, 1985, pp. 507–513.

9 Railly, J. W., and Ekerol, H., "Influence of a Closely Coupled Throttle on the Stalling Behavior of a Radial Compressor Stage," ASME JOURNAL OF ENGINEERING FOR GAS TURBINES AND POWER, Vol. 107, 1985, pp. 522–527.

Downloaded 01 Jun 2010 to 171.66.16.57. Redistribution subject to ASME license or copyright; see http://www.asme.org/terms/Terms_Use.cfm

Improvements in Performance Characteristics of Single-Stage and Multistage Centrifugal Compressors by Simultaneous Adjustments of Inlet Guide Vanes and Diffuser Vanes

H. Simon
Head of Development and Analysis.

T. Wallmann
Head of Aerodynamics R & D.

T. Mönk
R & D Engineer.

Mannesmann Demag,
Compressors and Pneumatic Equipment,
Duisburg, Germany

Nowadays, multistage geared centrifugal compressors are most often equipped with three-dimensional impellers and adjustable inlet guide vane cascades, at least upstream of the first stage. Optimum stage efficiencies are made possible by optimum axial in-flow into each stage and freely selectable pinion shaft speeds. Combined with intercooling of the medium, the result is high machine efficiency with good operating ranges. Additional increases in efficiency can be achieved by means of vaned diffusers. Due to the attendant restriction to the working range, this solution is not common in production compressors. Nevertheless, the working range can be distinctly expanded by adjusting the diffuser vanes. In addition, the combination of simultaneous adjustment to inlet guide vanes and diffuser vanes enables an increase in machine efficiency over the entire operating range as compared with regulation using only inlet guide vanes or diffuser vanes. This paper reports on the development of centrifugal compressor stages equipped with vaned diffusers. The impellers have backward-curved blades. Experimental determination of suitable schedules for simultaneous adjustment of both inlet guide vanes and diffuser vanes, depending on the desired performance characteristic, will be dealt with in detail. Furthermore, some examples of the overall performance maps for multistage intercooled geared compressors will be shown as a result of combining the performance characteristic curves of the individual stages. The operating ranges and regions of maximum efficiency are optimally matched to the requirements in question by means of suitable adjustment schedules.

Introduction

Geared compressors (Fig. 1) offer a number of advantages. Optimum stage efficiencies can be achieved thanks to favorable axial intake and freely selectable pinion shaft speeds. Combined with intercooling of the fluid, this permits high degrees of overall efficiency and favorable operating ranges. Nowadays, many of these compressors are fitted with backward-curved three-dimensional impeller blades.

Figure 2 shows two examples from a series of impellers, which have recently been developed for use in geared compressors with exit angles of $\beta_2 = 50$ and 65 deg. Impellers with outlet angles of $\beta_2 = 50$ deg are designed as closed impellers because of the efficiency advantages. For higher pressure ratios, impellers with steeper outlet angles and, thus, greater head rise coefficients are employed. They are operated at greater circumferential speeds and are, therefore, designed as semi-open impellers.

This new series covers the required flow coefficient range of $0.025 \leq \phi \leq 0.125$. All impeller types feature three-dimensionally twisted blades, as opposed to the previous design, which provided two-dimensional blades for lower flow coefficients. Apart from improving maximum efficiency, another objective was to achieve the widest possible operating range.

In order to handle the entire volume flow with good efficiency, several types of impellers are provided. The high specific speed versions are equipped with splitter blades. Adaptation of the flow within the range assigned to each type is provided by trimming the shroud contour. The impellers were designed with the help of quasi-three-dimensional flow calculations and finite element stress analyses. Systematic stage experiments helped to check and further optimize the performance characteristics.

Contributed by the Gas Turbine Division of THE AMERICAN SOCIETY OF MECHANICAL ENGINEERS and presented at the 31st International Gas Turbine Conference and Exhibit, Düsseldorf, Federal Republic of Germany, June 8–12, 1986. Manuscript received at ASME Headquarters January 24, 1986. Paper No. 86-GT-127.

Copyright © 1987 by ASME

Downloaded 01 Jun 2010 to 171.66.16.57. Redistribution subject to ASME license or copyright; see http://www.asme.org/terms/Terms_Use.cfm

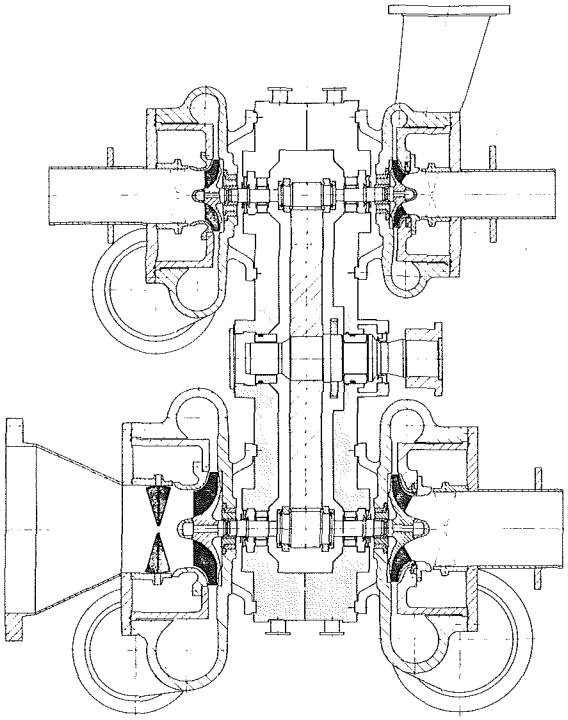

Fig. 1 Cross section through a four-stage geared compressor

Fig. 2(a) Closed impeller with outlet angle $\beta_2 = 50$ deg, flow coefficient $\phi = 0.08$

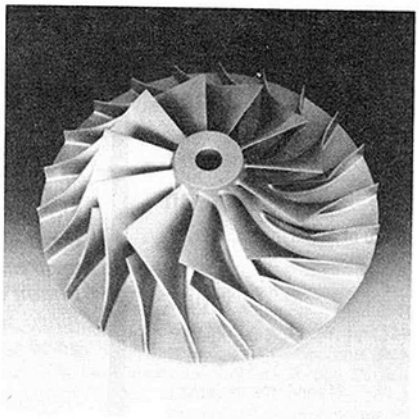

Fig. 2(b) Semi-open impeller with outlet angle $\beta_2 = 65$ deg, flow coefficient $\phi = 0.10$

Standard regulation of the compressors driven by electric motors is provided through an adjustable inlet guide vane cascade upstream of the first stage. For higher operating range requirements, all stages are equipped with such inlet guide vanes.

Further efficiency increases are possible with vaned diffusers. Because of the resulting limitation of the operating range, however, this solution has rarely been implemented to date for production units.

On the other hand, such disadvantages can be avoided by fitting adjustable vanes, especially when this coincides with matching adjustment of the inlet guide vanes. The following text provides information on research conducted in this direction.

The vaned diffusers used in these studies were designed by applying the results obtained from tests with channel diffusers [1–3]. They have aerodynamically shaped profiles.

Test Compressor

The single-stage test compressor is shown in Figs. 3 and 4. The flow-wetted components correspond largely to those found on existing geared compressors. Adjustable inlet guide vanes permit continuous change in inlet swirl and the fluid leaves the compressor via a spiral collector. The setup of the test compressor stage allows quick change of the impellers and stator elements under investigation. Both semi-open and closed impellers can be tested. Because of the modular construction, the vaneless diffuser can be set to any width. As an alternative, adjustable vaned diffusers can be fitted. There are several scrolls available permitting a high degree of adaptation to the volume flow of the impeller installed.

The test stand has been designed for an impeller diameter of $d_2 = 0.300$ m. The compressor is powered by a variable-speed electric motor with a power of 1000 kW. With a gear, the speed may be increased to $n = 32{,}000\ \text{min}^{-1}$.

To measure the overall performance of the stage, two combined temperature and pressure probes each are inserted in the discharge nozzle and in the suction nozzle upstream of the *IGV* row. They are staggered at 90 deg intervals around the circumference and, if necessary, can be moved over the cross section to allow reliable averaging of the measured values. The mean flow velocity in the measuring planes at design speed amounts to about 6 percent of the impeller tip speed.

Additional probes are inserted at different radial positions and peripheral angles on the vaneless diffuser, permitting measurement across the width of the diffuser. Static pressure

Nomenclature

d_2 = impeller tip diameter
d_3 = diffuser inlet diameter
d_4 = diffuser exit diameter
Δh_s = isentropic specific head
Δh_t = specific head (total)
M_{u2} = tip speed Mach number
n = rotational speed
q_t = head rise coefficient $= \Delta h_t / u^2$
u = impeller tip speed
V = volume flow (at inlet)
z = number of blades
α_{DV} = vaned diffuser inlet angle in degrees (relative to tangential direction)
α_{IGV} = inlet guide vane exit angle in degrees (relative to meridional direction)
β_2 = blade exit angle in degrees (relative to tangential direction)
η = efficiency
π = pressure ratio
ϕ = flow coefficient $= V/(d_2^2 \cdot u)$

Downloaded 01 Jun 2010 to 171.66.16.57. Redistribution subject to ASME license or copyright; see http://www.asme.org/terms/Terms_Use.cfm

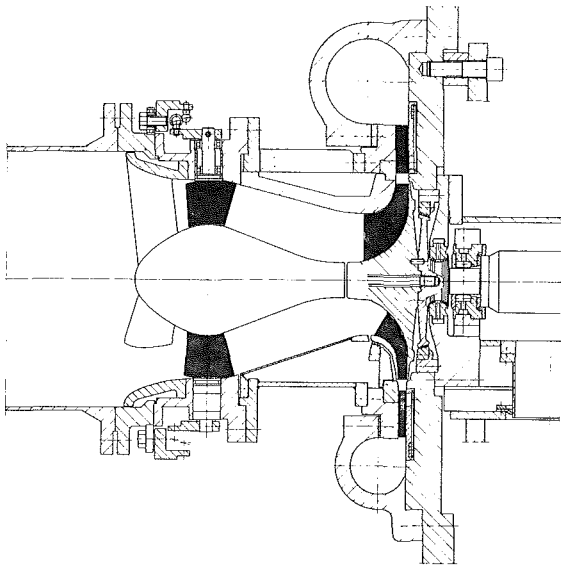

Fig. 3 Cross section through the test compressor with semi-open and closed impeller

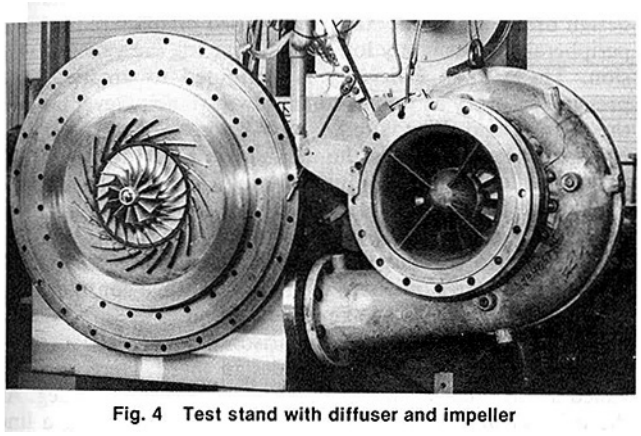

Fig. 4 Test stand with diffuser and impeller

taps are provided in the side walls of the diffuser. In the case of semi-open impellers, the casing walls are also provided in part with shroud static pressure taps to assess impeller performance. Two capacitive pickups are used to determine the tip clearance in the impeller inlet and near the trailing edge during operation. The weight flow is determined by means of two orifices arranged at the suction and discharge nozzles.

To approach an adiabatic condition during operation, the stage is insulated. The absolute measurement uncertainties of the isentropic head Δh_s can be supposed to be about $\pm$ 0.5 percent of the head coefficient q_t, the efficiency η about $\pm$ 0.8 percent, about 1 percent for the volume flow, and $\pm$ 1 deg for the vane angles. The uncertainties in measurement reproduction of the performance data are about half of those values.

Stage Configuration

The following sections provide a comparison between the performance maps of compressor stages equipped with vaneless and with continuously adjustable vaned diffusers. The single stages compared were equipped with the same impeller. In the example shown here the exit angle was $\beta_2 = 50$ deg.

The diffuser diameter ratio from the inlet to the spiral-shaped volute is $d_4/d_2 = 1.6$. In the vaneless diffuser stage, the width of the diffuser, which has been optimized by systematic variations in the course of previous experimental research, is less than that of the impeller outlet. In its design position, the inlet diameter of the adjustable vaned diffuser is

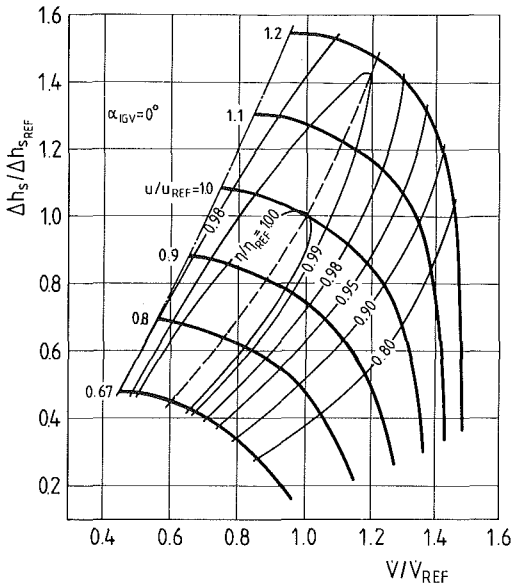

Fig. 5 Performance map of reference test compressor stage with vaneless diffuser

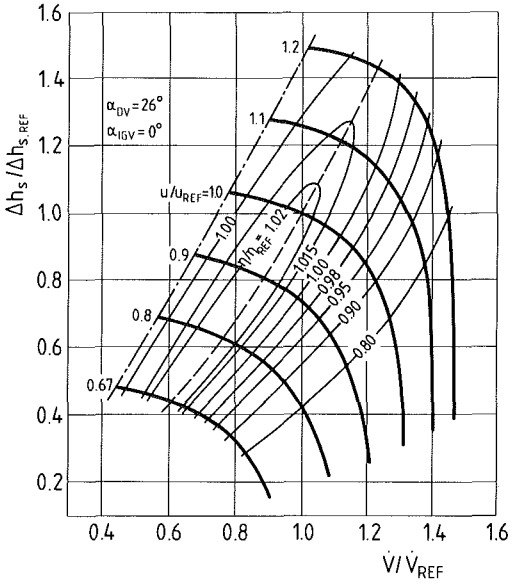

Fig. 6 Performance map of test compressor stage with vaned diffuser; fixed vaned diffuser angle $\alpha_{DV} = 26$ deg

approximately $d_3/d_2 = 1.1$. The clearance at each side amounts to 1 percent of the vane height. The center of rotation has been chosen so as to prevent the diffuser vanes in any possible position from interfering with the impeller. The volutes are designed assuming constant angular momentum via the cross section [4], which indicates that stages equipped with a vaned diffuser require larger cross sections. Adaptation of the volute in such cases is done according to the design setting of the vaned diffuser. The most important stage parameters are shown in Table 1.

Comparison of Performance Maps of Stages With Fixed Diffuser Angle

The results will be demonstrated using as an example a test compressor stage equipped with a $\beta_2 = 50$ deg impeller of moderate flow coefficient. For comparison purposes, the characteristics of the stage configuration with a vaneless dif-

Downloaded 01 Jun 2010 to 171.66.16.57. Redistribution subject to ASME license or copyright; see http://www.asme.org/terms/Terms_Use.cfm

Table 1 Data of tested stage

Impeller		Diffuser	
d_2(m)	= 0.3	d_3/d_2	= 1.1
M_{u2}	= 0.9	d_4/d_2	= 1.6
z	= 17	z	= 20
β_2(deg)	= 50	α_{DV}(deg)	= 26
ϕ	= 0.08	(design angle)	

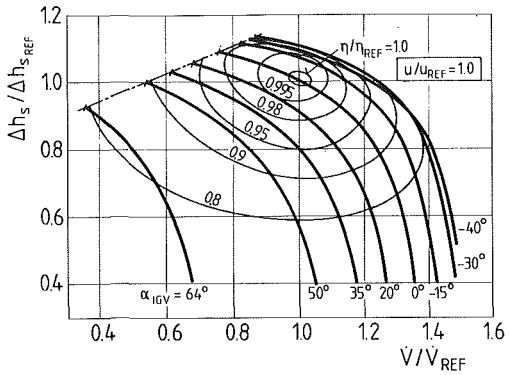

Fig. 7 Performance map with variable inlet swirl of test compressor stage with vaneless diffuser

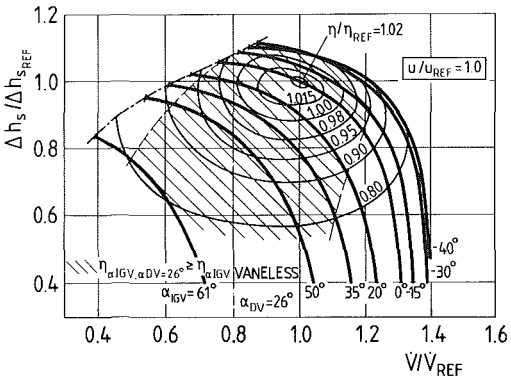

Fig. 8 Performance map with variable inlet swirl of test compressor stage with vaned diffuser; fixed diffuser angle α_{DV} = 26 deg

fuser and a vaned diffuser with fixed vane angle are shown first (Figs. 5 and 6).

The diffuser vane angle setting is $\alpha_{DV} = 26$ deg. At this angle, the volume flow with the maximum efficiency at design speed $u/u_{\text{REF}} = 1.0$ is the same as in the case of the vaneless diffuser.

All the single-stage maps in this paper are therefore standardized on the basis of this volume flow. The isentropic enthalpy rises refer to the respective values assigned to this volume flow. The enthalpy rises of all further single-stage maps in this paper at other angle settings refer to that same enthalpy rise of the $\alpha_{DV} = 26$ deg line.

From the performance characteristics at design speed, the operating range of the stage equipped with a vaned diffuser, when compared with that of the vaneless version, is reduced at both the compressor surge and choke limits. Thus, surge point and choke limit are influenced by the type of diffuser. In this case, the largest stage operating range for a fixed vaned diffuser is obtained.

The stage efficiencies shown in this and in the following single-stage characteristics charts relate to the maximum value for the vaneless version at design speed. It can be seen that, with the vaned diffuser, this value is approximately 2 percent higher. There was no evidence of any influence of the vaned

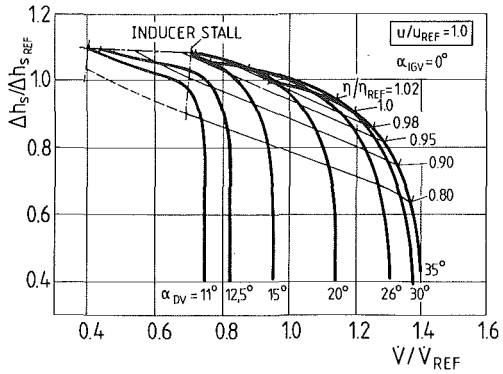

Fig. 9 Performance map with variable inlet angle of diffuser blades, swirl-free inflow, $\alpha_{IGV} = 0$ deg

diffuser on the impeller performance. Thus, the increase in stage efficiency coincides with an increase in the resulting stage pressure ratio. This increased pressure ratio should not be taken from the nondimensional charts applying to the vaned diffuser version, due to standardization to the respective isentropic enthalpy changes (as mentioned above).

The given design point objective therefore permits the design of a compressor stage with vaned diffuser requiring a peripheral speed slightly lower than that for the vaneless version. The gain in efficiency is attributed to greater static pressure recovery as well as to the lower velocity level both in the diffuser and the volute.

For off-design speeds, the angle setting of the vaned diffuser is no longer the optimum solution. At higher speeds, the choke limit is determined by the natural choke limit of the impeller. In this case the operating range of the compressor can be extended to the surge line by smaller diffuser angles. At lower speeds, the surge lines of the vaned stage configuration coincide with those of the vaneless version.

Figures 7 and 8 show a comparison of characteristics obtained with variable inlet swirl at design speed. Here, too, the vaned diffuser has a constant inlet angle of $\alpha_{DV} = 26$ deg. At the diffuser angle selected, the turndown range along a line $\Delta h_s/\Delta h_{s\text{REF}} = 1.0$ is reduced both within the positive swirl range ($\alpha_{IGV} > 0$) toward the surge line and the counterswirl range ($\alpha_{IGV} < 0$) toward the choke limit. The shaded area on the charts indicates those zones where efficiency gains were possible in comparison with the vaneless version. Also, the maximum obtainable efficiency within range of the characteristic optima is about 2 percent higher.

Adjustment of the Vaned Diffuser

Figure 9 shows a performance map with adjusted diffuser vanes with the *IGV* angle set at 0 deg. When the diffuser angle is reduced, the vaned diffuser determines the choke limit, so that the characteristic curves are displaced in general toward lower volume flows. At low angle settings, the curves extend into the volume flow ranges below the surge limit flow volume for the vaneless version.

Operation within this range is possible only at reduced efficiency accompanied in addition by a distinct change in the noise made by the machine, so that it must be assumed that the inducer is operating in the stalled condition. It is possible to considerably undershoot this stalling limit because of the characteristic of the vaned diffuser, the pressure recovery of which continues to increase toward smaller volume flows. The curves of constant efficiency are proportional to the overall enthalpy change in the impeller which increases with decreasing volume flow due to the backward curvature of the impeller blades. As long as the flow does not fall below the stalling limit, this tendency is also present in the upper regime of the performance map. The maximum efficiency of the

Downloaded 01 Jun 2010 to 171.66.16.57. Redistribution subject to ASME license or copyright; see http://www.asme.org/terms/Terms_Use.cfm

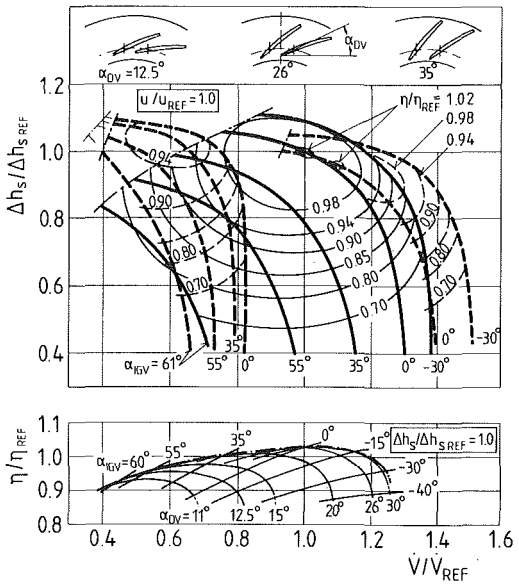

Fig. 10 Performance maps with variable inlet swirl for different diffuser vane angles and efficiencies for various α_{IGV} and α_{DV} combinations at $\Delta h_s/\Delta h_{sREF}$ = 1.0

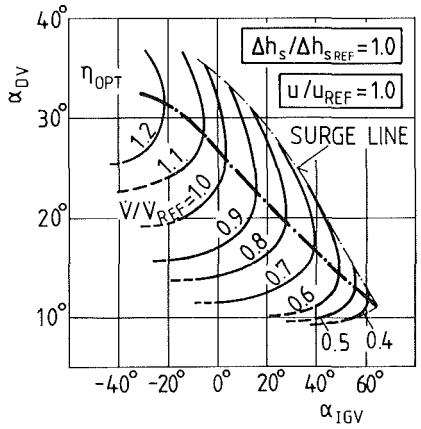

Fig. 11 Possible diffuser, inlet guide vane angle combinations for $\Delta h_s/\Delta h_{sREF}$ = 1.0, and optimum adjustment schedule

characteristics at diffuser angles between 20 deg $\leq \alpha_{DV} \leq$ 35 deg is higher than the maximum value possible on the vaneless version. The maximum gain with optimal diffuser vane setting angle amounts to 2 percent.

Combined Adjustment of Inlet Guide Vanes and Diffuser Vanes

Optimum Turndown Range $\Delta h_s/\Delta h_{sREF}$ = 1.0. Figure 10 compares excerpts from three performance maps with variable inlet swirl. These are obtained with the diffuser vanes set at various angles. It becomes apparent that the characteristic curves overlap extensively so that identical operating points can be operated at different diffuser angles and inlet guide vane angles.

Thus, for instance, at $\Delta h_s/\Delta h_{sREF}$ = 1.0, the volume flow V/V_{REF} = 0.75 can be operated with the combination α_{DV} = 12.5 deg and α_{IGV} = 0 deg, but also with the combination α_{DV} = 26 deg and α_{IGV} = 25 deg. However, while the relative efficiency in the former instance is only η/η_{REF} = 92 percent, it is η/η_{REF} = 0.97 in the latter instance.

Where the diffuser blades are adjusted in small increments and, at the same time, there is variation of the inlet swirl, any number of angle combinations can be determined which would allow operation at $\Delta h_s/\Delta h_{sREF}$ = 1.0. These angle combinations have been entered as groups of parameters in the bottom half of the η/η_{REF}, V/V_{REF} diagram shown in Fig. 10. It can be seen that there is an optimum efficiency curve with volume flow, which is described by the contour of the parameter map. The points of intersection of the parameter curves at constant diffuser and swirl angles on the contour permit determination of the optimum adjustment combination for the operating line $\Delta h_s/\Delta h_{sREF}$ = 1.0. The optimum angle schedule of *IGV* and diffuser vane for u/u_{REF} = 1.0 is illustrated in Fig. 11. This diagram shows the diffuser angle as a function of the inlet guide vane angle. Besides the optimum combination, an infinite number of alternate settings along the operating line $\Delta h_s/\Delta h_{sREF}$ = 1.0 are possible. Optimum efficiency occurs at the maximum *IGV* setting for each flow rate.

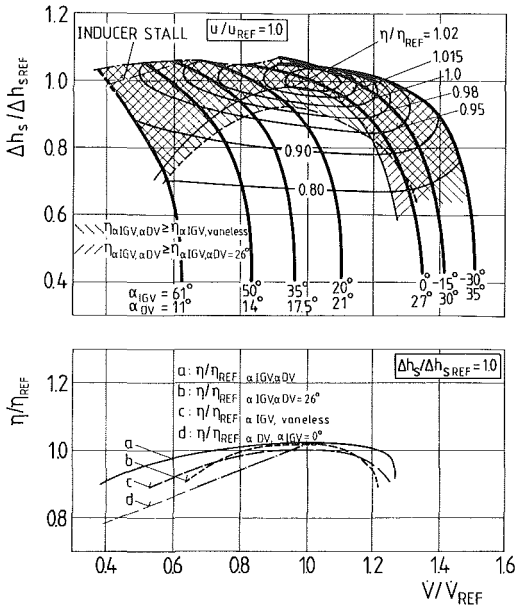

Fig. 12 Head-capacity curves for optimum adjustment schedule at $\Delta h_s/\Delta h_{sREF}$ = 1.0

The combinations corresponding to the curves representing V/V_{REF} = const do not affect the operating point flow and head but they do influence the efficiency and, under certain circumstances, the distance to the compressor surge line. Comparison with Fig. 10 shows that the angle combination α_{DV} = 26 deg and α_{IGV} = 32 deg results in an operating point at the surge line of the corresponding characteristic swirl map. Accordingly, this combination is located on the top edge of the adjustment range shown in Fig. 11 marked "surge line."

At low flows, the optimum curve gets closer to this limiting curve. Here, further decrease of the diffuser inlet angle does not allow further reduction of the volume flow, as a limiting minimum possible volume flow of the impeller has been reached. This latter, on the other hand, can be delivered only with a great positive inlet swirl. In the range of large volume flows, the optimum adjustment combination approaches a constant diffuser angle. Matching to changing volume flows in this case is provided primarily by adjusting the inlet guide vanes.

Since the adjustment schedule can be approximated largely through a linear relation between the inlet stator angle and the diffuser vane angle, Fig. 12 shows the head capacity curves resulting from implementation of the adjustment law optimized for the line $\Delta h_s/\Delta h_{sREF}$ = 1.0. Those areas in which efficiency advantages and an expansion of the operating range have been attained as opposed to the stage configuration with a vaneless diffuser and adjustable inlet vanes (Fig. 7), or with fixed vane diffuser and adjustable inlet stator (Fig. 8), are shown with different shading.

The gains are particularly clearly demonstrated in the bot-

Downloaded 01 Jun 2010 to 171.66.16.57. Redistribution subject to ASME license or copyright; see http://www.asme.org/terms/Terms_Use.cfm

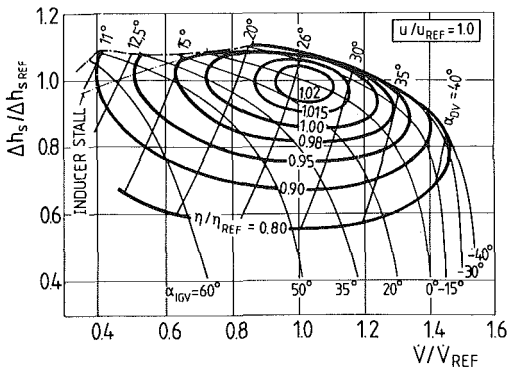

Fig. 13 Efficiencies obtainable with optimum angle combination at each head-capacity point

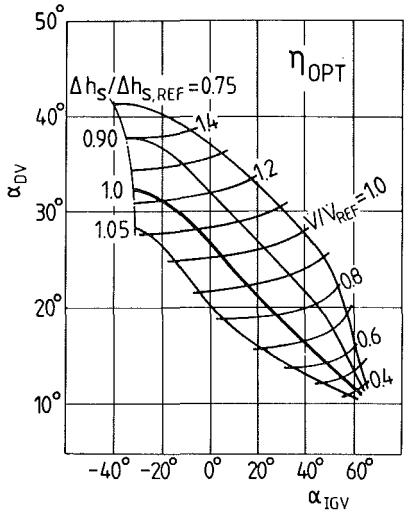

Fig. 14 Optimum α_{IGV} and α_{DV} combinations as a function of the operating point $\Delta h_s/\Delta h_{sREF}$, V/V_{REF}

tom diagram in Fig. 12. This graph shows the efficiencies along the operating curve $\Delta h_s/\Delta h_{sREF} = 1.0$ for the first three configurations studied, as well as for the example with adjusted diffuser vanes without inlet swirl.

Thus, for optimum adjustment, a pronounced widening of the operating range is noted. The operating range is between 38 and 126 percent of the reference volume flow, but with inducer stall within the 38 to 45 percent range. The operating range for the vaneless diffuser version, on the other hand, is only from 53 to 124 percent. The efficiency gain of 2 percent at the reference point can be increased considerably in the partial load and overload range (up to 6 percent).

The stage with fixed vaned diffuser reaches high degrees of efficiency at the reference point but can only produce an operating range of 62 to 122 percent. Despite the pronounced efficiency drop in the partial load and overload ranges, efficiencies between 70 and 117 percent are still higher than those for the vaneless version.

A decidedly less favorable situation is created by adjusting the vaned diffuser, if no adjustment of the inlet stator is made. Efficiency drops sharply in the partial load range. There is no appreciable operating range for overload volume flow. This is due to the characteristic of the impeller with backward-curved blades, which only allows favorable operating conditions to be expected if an operating curve has been matched to this characteristic.

In the range of small enthalpy rises at moderate volume flows, the advantages of the combined adjustment law mentioned above are lost, since it has been optimized especially along the curve $\Delta h_s/\Delta h_{sREF} = 1.0$. Higher efficiencies can be obtained by a law of adjustment optimized particularly for this range.

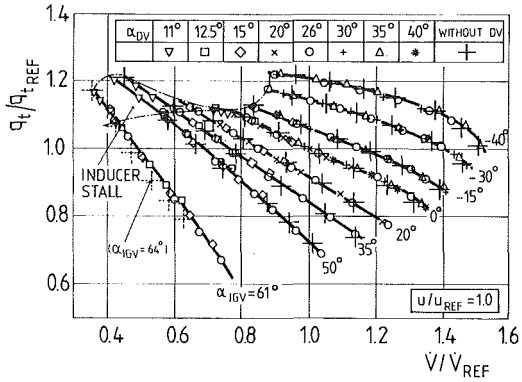

Fig. 15 Dimensionless total enthalpy change of the impeller as a function of the *IGV* angle setting

Optimum Efficiency Over the Whole Operating Range. The concept of an optimum adjustment schedule for $\Delta h_s/\Delta h_{sREF} = 1.0$ as explained in the context of Fig. 10 may also be applied to other constant enthalpy rise curves. Such an assessment is given in Fig. 13 by the scalloped contours of constant efficiency in a $\Delta h_s/\Delta h_{sREF}$, V/V_{REF} field. These curves can also be obtained by plotting enveloping rings of identical efficiency around the contours of the individual performance maps for various diffuser blade angles.

Figure 13 shows which maximum efficiency can be obtained at any given operating point for $u/u_{REF} = 1.0$, if an optimum diffuser angle/inlet guide vane angle combination is chosen. This optimum combination can be determined by using the plotted parameter curves of constant diffuser angle or inlet guide vane angle. Figure 14 shows a schedule of optimum angle combinations for parameter curves $\Delta h_s/\Delta h_{sREF} = \text{const}$ and $V/V_{REF} = \text{const}$. The curve for $\Delta h_s/\Delta h_{sREF} = 1.0$ is identical to the optimum curve shown in Fig. 11.

It is obvious from the above that the diffuser will have to be set for larger angles if optimum operating conditions are to be obtained with low enthalpy ratios and a given inlet volume flow ratio. This is attributable to the fact that the flow angle at the diffuser inlet increases because of the lower compression in the impeller.

If an arbitrary combination of inlet guide vane angle and diffuser angle is not practicable—e.g., in the case of mechanical coupling of adjusting mechanisms—this graph permits an approximation of the optimum adjustment law for a given operating curve.

By an optimal combination of the angles in a given case, the efficiencies obtained over the entire range exceed those obtained with other configurations. The performance of the impeller is not influenced by the vaned diffuser. This can be taken from Fig. 15. It shows the dimensionless total enthalpy change of the impeller, estimated by temperature measurements. The total enthalpy change is only a function of the volume flow and the inlet swirl at the given speed ratio $u/u_{REF} = 1.0$ but not of the diffuser vane setting angle. Therefore, the increase on the isentropic head with the attendant extension to the operating range can be attributed in every case to the efficiency gain caused by the vaned diffuser.

Multistage Geared Compressors

The results obtained on single-stage compressors are used to calculate the performance of four-stage geared compressors with intercooling, designed for a pressure ratio of 7.6. The compressor in this example is equipped with four impellers fitted with backward-curved blades at $\beta_2 = 50$ deg. The impeller diameter graduation as well as the speed settings for the two pinion shafts permit stage designs exhibiting optimum possible flow coefficients.

The map for the overall machine is determined by combining all the head-capacity curves obtained for the individual

Downloaded 01 Jun 2010 to 171.66.16.57. Redistribution subject to ASME license or copyright; see http://www.asme.org/terms/Terms_Use.cfm

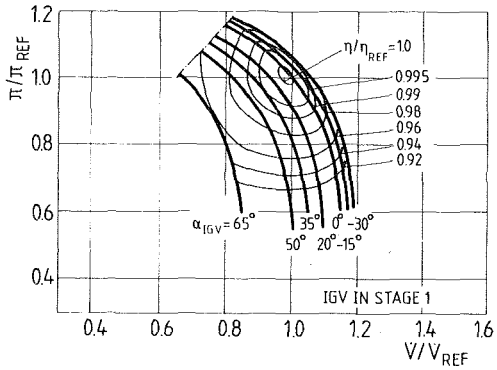

Fig. 16 Overall performance of a four-stage geared compressor with variable inlet swirl to the first stage and vaneless diffusers, $4 \times \beta_2 = 50$ deg

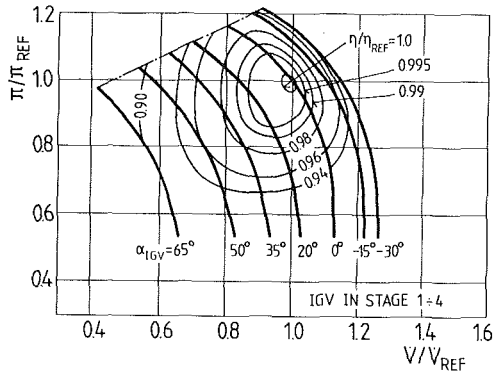

Fig. 17 Overall performance of a four-stage geared compressor with variable inlet swirl to all four stages and vaneless diffusers, $4 \times \beta_2 = 50$ deg

stages, with the expected leakage and cooler pressure losses taken into account. The design point for the overall machine—shown as $V/V_{REF} = 1.0$ and $\pi/\pi_{REF} = 1.0$—marks the point where the individual stages reach their maximum efficiency point of operating on the $\alpha_{IGV} = 0$ deg map.

Figure 16 shows the map with only adjustable inlet guide vanes upstream of the first stage, corresponding to the standard configuration of the compressor. This map is compared with that for adjustable guide vanes in front of each of the four stages (cf. Fig. 17). The swirl angles of the individual stages were chosen to permit the maximum operating range along curve $\pi/\pi_{REF} = 1.0$.

It can be seen that the operating range can be considerably enlarged by adjustment of four guide vane rows, both within the partial load and overload ranges. The pronounced increase in head rise at smaller flow ranges, resulting from the backward curvature of the blades, also has its full effect on the operation of multistage compressors. The operating range obtainable along the $\pi/\pi_{REF} = 1.0$ curve is identical to the smallest single-stage operating range.

To calculate the overall performance with combined inlet and diffuser adjustment, an individually optimized adjustment schedule along curve $\Delta h_s/\Delta h_{sREF} = 1.0$ has been taken as a basis for each individual stage (cf. Fig. 18). As with the single stage, the operating range in the four-stage compressor with intercooling has again been improved in comparison with inlet swirl adjustment alone.

The shaded area indicates that range in which the efficiency can be improved. At the reference point, the improvement is 2 percent. With a flow rate of $V/V_{REF} = 0.55$ and at the reference pressure ratio, the relative isothermal efficiency is $\eta/\eta_{REF} = 97$ percent as opposed to 90 percent in the case of inlet stator adjustment alone.

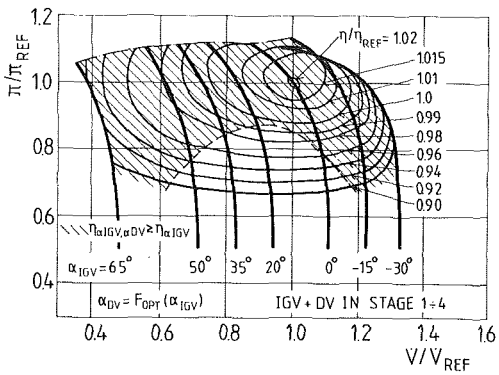

Fig. 18 Overall performance of a four-stage geared compressor with adjustable diffuser and inlet guide vanes at optimum adjustment law for $\pi/\pi_{REF} = 1.0$, $4 \times \beta_2 = 50$ deg

Conclusions

1 By matched adjustment of variable inlet guide and diffuser vanes, the operating range of centrifugal flow compressors with backward-curved impeller blades can be extended (Figs. 17 and 18).

2 For backswept impellers with $\beta_2 = 50$ deg backward curvature, mere adjustment of the diffuser blades does not produce any favorable efficiency curves along constant pressure ratio operating lines (Fig. 12).

3 Compared with the reference test compressor stage equipped only with adjustable inlet guide vanes, the efficiency gains with combined adjustment of the two stators at the reference point amount to approximately 2 percent, and up to 6 percent, for example, along the operating curve $\Delta h_s/\Delta h_{sREF} = 1.0$. The optimum efficiency occurs at the maximum possible *IGV* setting angle for each flow rate (Fig. 11).

4 The optimum combination of diffuser and swirl angles is a function of the flow ratio and pressure ratio for a given speed ratio. For a given schedule—i.e., a fixed correlation—improvement in efficiency can be obtained only over sections of the entire map. The full potential of possible improvements can be exploited only with freely selectable adjustment combinations.

5 In the case of the compressor stages tested, no influence of the vaned diffuser on impeller performance was observed. The increase in isentropic enthalpy rise with its attendant expansion of the operating range is therefore attributable to gains in efficiency. Additional expansion of the operating range is brought about by the fact that the stage equipped with a vaned diffuser can also be partially operated in a stable manner within such ranges where inducer stall occurs.

Acknowledgments

The authors wish to thank Mannesmann Demag AG for their permission to publish this paper.

References

1 Runstadler, P. W., Dolan, F. X., and Dean, R. G., "Diffuser Data Book," *Creare Tech. Note 1986, Hanover, NH, 1975.*

2 Sprenger, H., "Experimentelle Untersuchungen an geraden und gekrümmten Diffusoren," Diss. ETH Zürich, Leemann, Zürich, 1959.

3 Japikse, D., "Turbomachinery Diffuser Design Technology," DTS-1, *Concepts ETI Inc., Norwich, VT, 05055, 1984.*

4 Eckert, B., and Schnell, E., "Axial- und Radialkompressoren," Springer, Berlin-Göttingen-Heidelberg, 1961.

5 "Radialverdichterwechselwirkung I und II," FVV, Hefte 337, 358, Frankfurt, 1983 and 1985.

6 Krain, H., "A Study on Centrifugal Impeller and Diffuser Flow," ASME JOURNAL OF ENGINEERING FOR POWER, Vol. 103, Oct. 1981.

7 Turanskyj, L., "On the Design and General Performance of a New Compressor," published at the Compressed Air Symposium at the South African Institute of Mechanical Engineers, Johannesburg, 1977.

Downloaded 01 Jun 2010 to 171.66.16.57. Redistribution subject to ASME license or copyright; see http://www.asme.org/terms/Terms_Use.cfm

Influence of a Circumferential Exit Pressure Distortion on the Flow in an Impeller and Diffuser

M. Th. Sideris

R. A. Van den Braembussche

von Karman Institute for Fluid Dynamics,
Chaussée de Waterloo, 72,
B-1640 Rhode Saint Genèse,
Belgium

Detailed velocity measurements, using Laser Doppler Anemometry (LDA) and static pressure measurements in the vaneless diffuser of a centrifugal compressor, are presented. They show the relation between the circumferential variation of the pressure and the local flow in the diffuser and at the impeller exit. Theoretical calculations using an impeller-diffuser interaction model have been made. A comparison between the theoretical results and experimental data allows an evaluation of the possibilities and shortcomings of such a calculation. It also illustrates the mechanisms by which the variation of the impeller outlet velocity is defined.

Introduction

There is only one operating point per constant-speed line for which the volute-type collector imposes a circumferentially uniform pressure at the diffuser outlet. At smaller mass flows, the volute acts like a diffuser resulting in a static pressure rise between the volute inlet (tongue) and the outlet. At larger mass flows, the volute is too small and the flow accelerates resulting in a decreasing pressure from the volute inlet to outlet.

In the case of a vaneless diffuser, this volute pressure distribution propagates upstream and results in periodic outlet conditions for the rotating impeller. In the absence of a diffuser, the volute pressure is directly applied to the impeller and has a similar effect.

The main effect of this circumferential pressure variation can be summarized as follows:

- Radial forces: the nonuniform outlet conditions impose a circumferential variation of blade loading and result in a net radial force acting on the impeller shaft. This has been primarily studied experimentally in [1–5].
- Vorticity: potential theory suggests that any circumferential variation of radial velocity at the exit of a backward leaned impeller leads to a decrease in required torque. Experiments do not confirm this. One can therefore conclude that the real flow is not irrotational and that an outlet pressure variation gives rise to a trailing edge vorticity [6].
- Losses: the unsteady rotor flow gives rise to extra losses and as such can have an important influence on the surge limit [4, 6–8].
- Noise and vibrations: they are strongly related to local pressure gradients as has been shown in [9].

The purpose of this paper is to provide a detailed set of experimental data and to evaluate a diffuser-impeller interaction model, which would allow the prediction of the first two effects mentioned above.

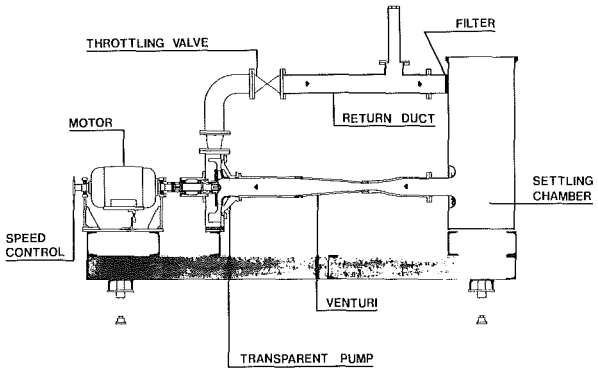

Fig. 1 Experimental facility

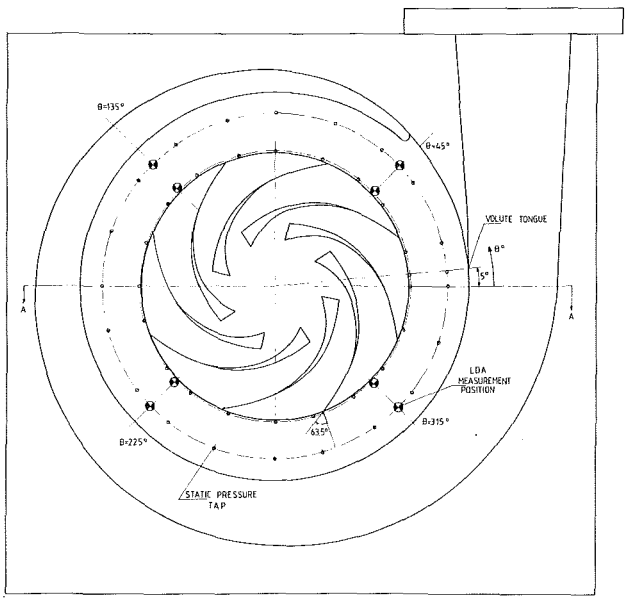

Fig. 2 Measuring locations

Contributed by the Gas Turbine Division of THE AMERICAN SOCIETY OF MECHANICAL ENGINEERS and presented at the 31st International Gas Turbine Conference and Exhibit, Düsseldorf, Federal Republic of Germany, June 8–12, 1986. Manuscript received at ASME Headquarters December 26, 1985. Paper No. 86-GT-9.

Copyright © 1987 by ASME

Downloaded 01 Jun 2010 to 171.66.16.57. Redistribution subject to ASME license or copyright; see http://www.asme.org/terms/Terms_Use.cfm

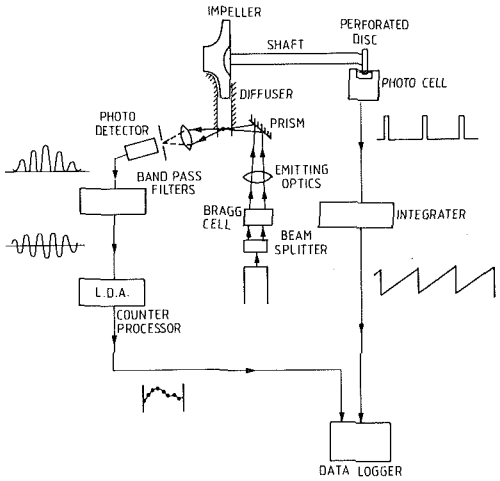

Fig. 3 LDA measuring system

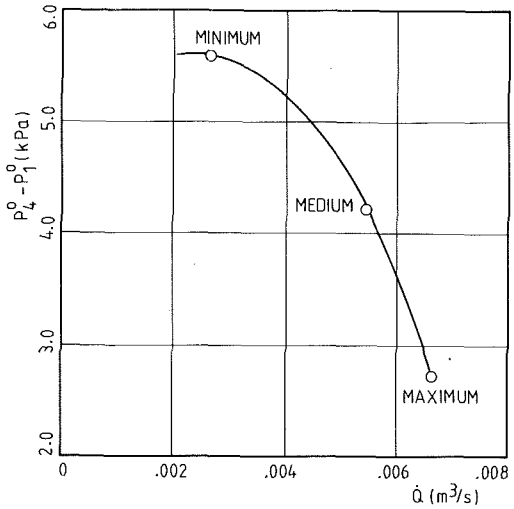

Fig. 4 Performance curve (300 rpm)

Experimental Facility and Instrumentation

All measurements have been performed on the P-1 test stand at the von Karman Institute (VKI) (Fig. 1). In this closed-loop facility, the impeller is driven by a variable speed d-c motor. The mass flow is measured at the inlet by a venturi and controlled at the outlet by means of a throttling valve.

This facility is operated with water and has been specially built for LDA measurements in centrifugal impellers, diffusers, and volutes. The shrouded mixed flow impeller has eight blades with 63.5 deg outlet lean angle (Fig. 2). The diffuser has parallel walls and is followed by a volute of rectangular cross section. The impeller and casing are manufactured of plexiglass. The back part of the casing has parallel walls and the front cover has a flat window which can be rotated at the position of the measuring point.

The diffuser is instrumented with 42 static pressure tappings on the shroud wall. They are located at the inlet ($R = 102$ mm) and outlet of the parallel part ($R = 128$ mm) (Fig. 2). These pressures are directly measured by water manometers.

An LDA measurement system is used to measure the radial and tangential velocity components in the diffuser (Fig. 3). As the velocity changes instantaneously when the blades are passing, one must also measure simultaneously the angular position of the blades. This is done by means of a perforated disk with eight holes (the same as the number of blades) and a photocell, which creates a pulse each time the impeller is rotated over one blade pitch. The output of the integrater is proportional to the time since the last pulse. At constant rpm it is a measure of the angular position of the impeller.

The LDA emitting system consists of a 15 mW He–Ne laser, beam splitter, bragg cell, and lens. The distance between the two parallel beams is 50 mm and the optical system can be rotated to measure each velocity component separately. The bragg cell is absolutely required for this type of measurement because of the possible change in flow direction for the radial velocity component. The two beams are focused by a lens with focal length of 305 mm, which results in a fringe spacing of 3.88 μm. One can show that the fringe spacing is independent of the medium (air or water). However, any axial displacement in air of the emitting optics results in a 1.332 times larger displacement of the probe volume in water. The bragg cell is oriented in such a way as to increase the measured velocity by 1.55 m/s.

Latex particles of 1–4 μm diameter are added to the water and the filter in the return duct takes out all particles larger than 10 μm.

The photodetector collects forward-scattered light and is fixed on the same moving table as the emitting optics. The filtered signal enters a counter processor system which verifies the quality of the signal and calculates the instantaneous velocity which is stored on a cassette logger together with the impeller circumferential position. 2000 data are taken per measurement point.

Experimental Results

The V_R and V_T velocity distributions have been measured in four circumferential positions at the diffuser inlet ($R = 102$ mm) and outlet ($R = 128$ mm) (Fig. 2). In each location, traverses are made at 300 rpm for the points of maximum, medium, and minimum mass flow, shown on the performance curve in Fig. 4. The velocity distributions are measured in 10 locations between hub and shroud, at 2 mm intervals starting at 1 mm from the hub wall.

The data reduction program divides the 2000 measurements into 20 groups, corresponding to 20 equal parts of one impeller pitch. After checking that a sufficient number of measurements are made in each part, a statistical analysis is

Nomenclature

A = cross-sectional area
B = diffuser width
EL = effective length
l = distance along a streamline
P = static pressure
R = radius
rms = root mean square
t = time
U = peripheral velocity
V = absolute velocity
W = relative velocity
α = absolute flow angle from radial direction
β = relative flow angle from radial direction
Δt = time step
$\Delta\theta$ = angular step
θ = circumferential angle
σ = standard deviation

Subscripts

1 = impeller inlet
2 = impeller exit or diffuser inlet
3 = diffuser exit
4 = volute exit
bl = blade value
j = discretization index along tangential direction
R = radial component
T = tangential component

Superscripts

$\bar{}$ = averaged
0 = total value
k = time level

Downloaded 01 Jun 2010 to 171.66.16.57. Redistribution subject to ASME license or copyright; see http://www.asme.org/terms/Terms_Use.cfm

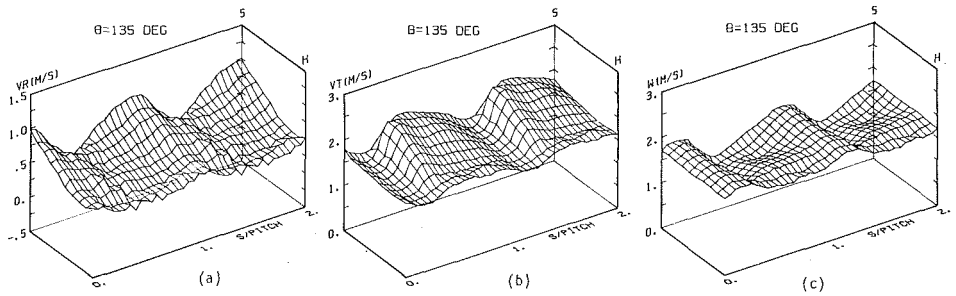

Fig. 5 Pitch- and spanwise distribution of V_{R2} (*a*), V_{T2} (*b*), and W_2 (*c*) for medium mass flow

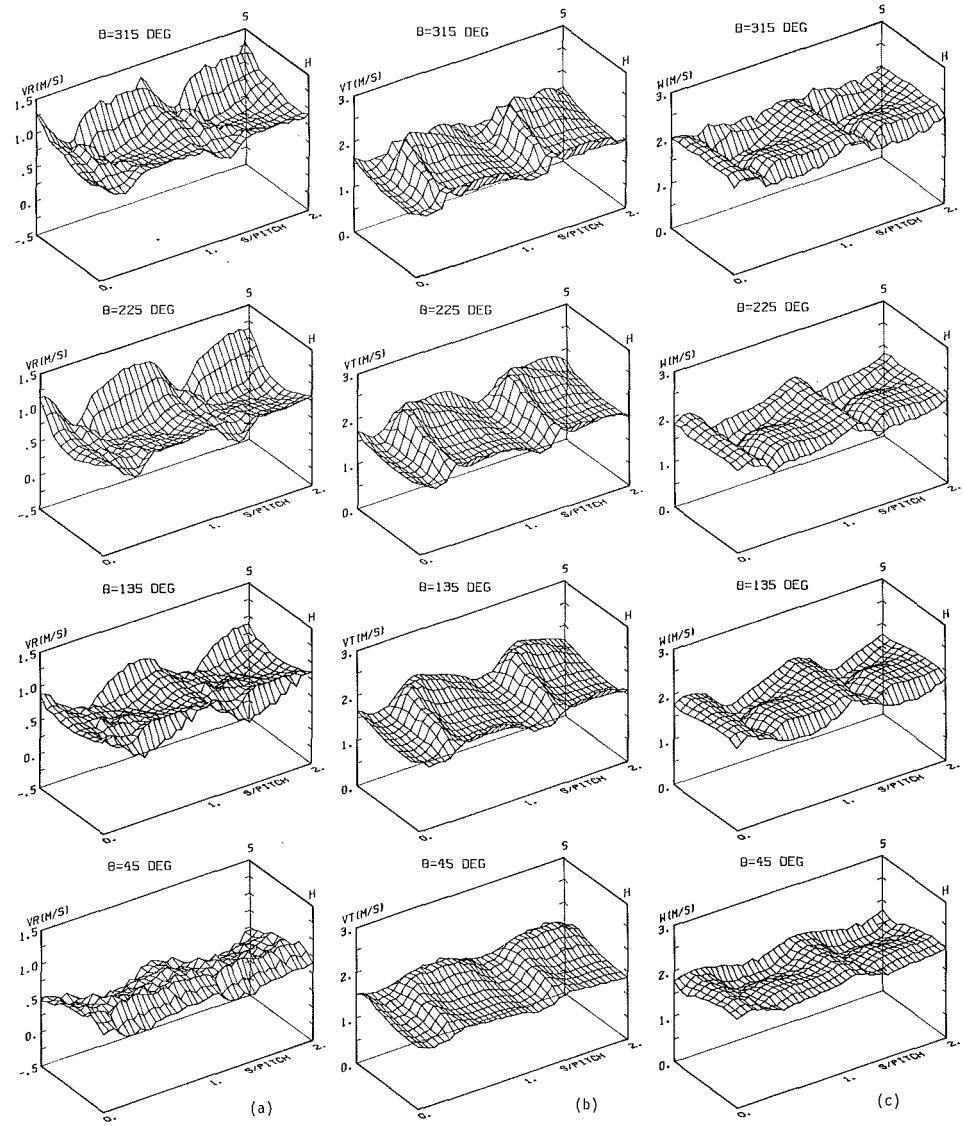

Fig. 6 Pitch- and spanwise distribution of V_{R2} (*a*), V_{T2} (*b*), and W_2 (*c*) for maximum mass flow

started. Data which fall more than 4σ from the mean value are removed, where σ is the standard deviation. The remaining points are used to calculate a linearized mean value distribution over one pitch. This allows the calculation of an rms value of the fluctuations which is independent of the local velocity gradient.

The measurement error is not only dependent on calibration and geometric parameters, but mainly on the statistical treatment which is applied to the data measured in an unsteady flow. These errors are very difficult to calculate. They have therefore been estimated by comparing the integrated radial velocity with the mass flow measured by the venturi. The absolute error was found to be ± 4 cm/s for all cases.

The measured velocity components, together with the peripheral velocity, allow the calculation of the absolute and relative velocity and flow angle.

Figures 5(*a*) and 5(*b*) show the radial and tangential velocity distribution measured at medium mass flow. On each figure the same velocity distribution is repeated over two pitches to illustrate the periodic variation of the flow. They are shown only at $\theta = 135$ deg, because the velocity distributions at the three other circumferential positions are almost identical. The

Downloaded 01 Jun 2010 to 171.66.16.57. Redistribution subject to ASME license or copyright; see http://www.asme.org/terms/Terms_Use.cfm

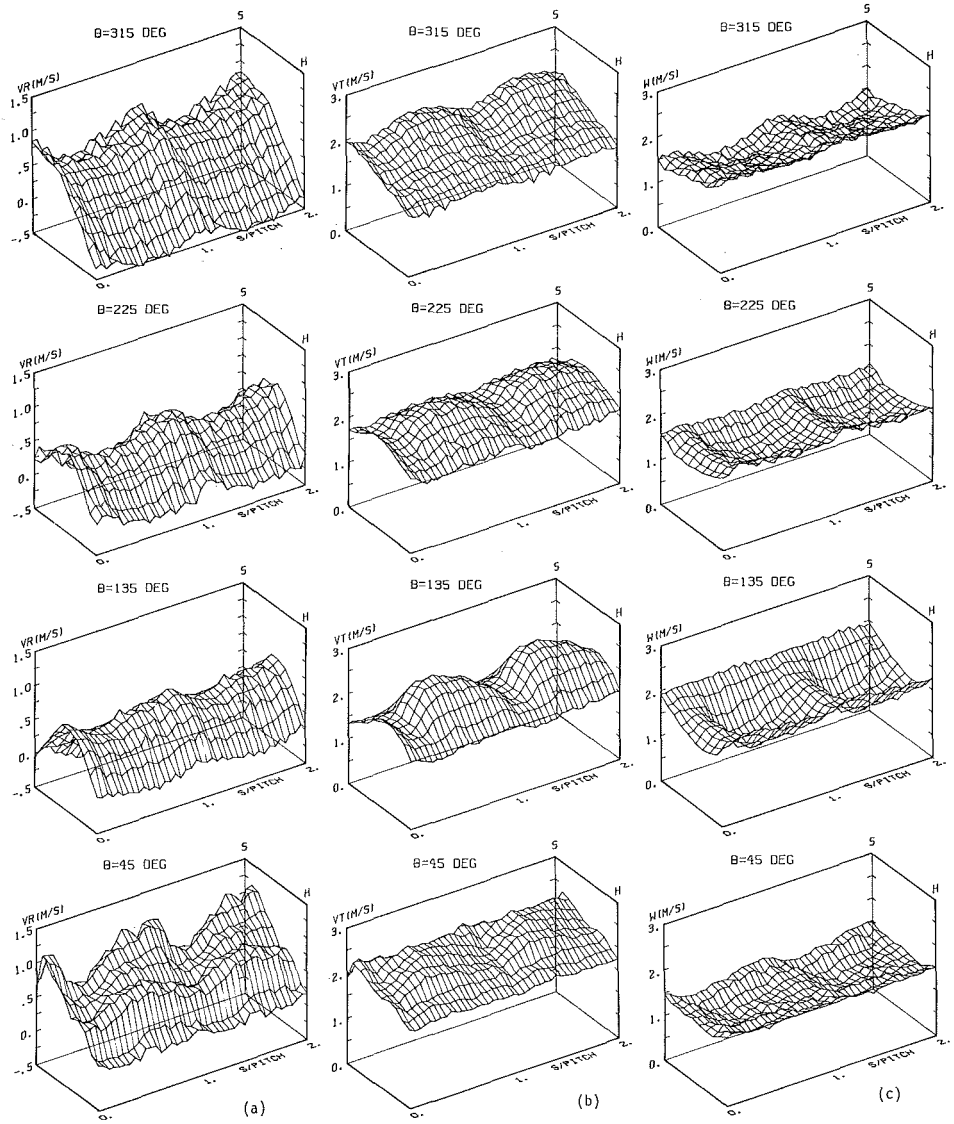

Fig. 7 Pitch- and spanwise distribution of V_{R2} (*a*), V_{T2} (*b*), and W_2 (*c*) for minimum mass flow

corresponding relative velocity (Fig. 5*c*) illustrates how the local velocity components are influenced by the spanwise variation of the jet and wake flow pattern.

Figures 6(*a*), 6(*b*), and 6(*c*) show the radial, tangential, and relative velocity distributions measured at maximum mass flow in the four circumferential positions at the rotor exit. The nonuniformity of the flow is now strongly dependent on the circumferential position.

The radial and tangential velocity distributions measured at minimum mass flow are shown on Figs. 7(*a*) and 7(*b*). Important circumferential variations of the velocity profile and velocity level are again observed. The hub-to-shroud velocity distribution is strongly dependent on the peripheral position, and an important zone of return flow is observed at the hub for $\theta = 315$ deg. The corresponding relative velocity is shown in Fig. 7(*c*) and illustrates the variation of the impeller relative velocity during one rotation. Calculated values of rms velocities show that the fluctuation of the absolute velocity in each measuring position increases with decreasing mass flow.

However, the way the measurements are performed does not allow the determination of the time-dependent evolution of the velocity. The illustrated data must be considered as time-averaged.

The pitchwise nonuniformity of the flow has fully disap-

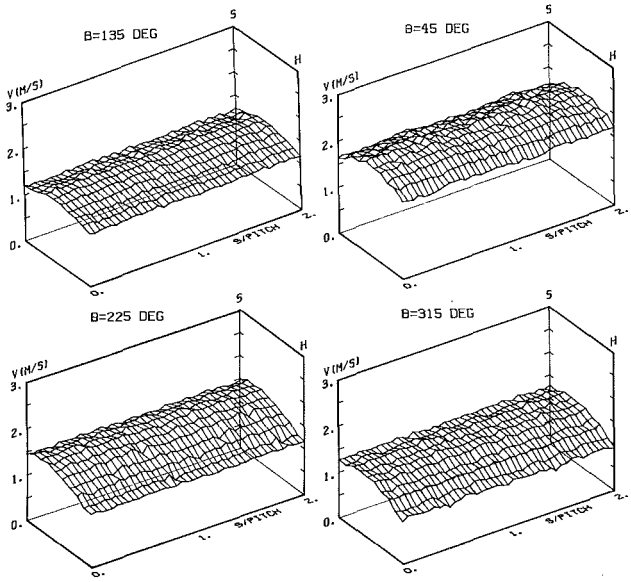

Fig. 8 V_3 distribution for minimum mass flow

Downloaded 01 Jun 2010 to 171.66.16.57. Redistribution subject to ASME license or copyright; see http://www.asme.org/terms/Terms_Use.cfm

peared at the diffuser exit (Fig. 8), but the circumferential variation is still present.

Volute Impeller Interaction

The nonuniformity of the flow along the impeller circumference results from the pressure distribution imposed by the volute. The static pressure distributions measured on the shroud side at diffuser inlet and outlet are shown in Fig. 9 for maximum, medium, and minimum mass flow. The pressure variation from volute tongue to volute outlet is similar to what can be expected for a decelerating, constant-velocity, or accelerating flow.

A comparison of the measurements at the diffuser inlet and outlet reveals that the amplitude of the circumferential pressure variation is increasing when it propagates upstream to the impeller exit. The pitchwise-averaged radial velocity profiles at diffuser inlet and outlet show the effect of the radial pressure gradient at different mass flows (Fig. 10).

At maximum mass flow, the nearly constant radial velocity distribution at impeller exit changes into a symmetric boundary layer type profile at the diffuser exit for $\theta = 135$ and 225 deg. At $\theta = 45$ and 315 deg the profile is asymmetric with return flow on the shroud and hub side, respectively. At medium mass flow, the nearly constant radial velocity distribution at the impeller discharge changes into a completely asymmetric one at the diffuser exit with return flow at the hub side. At minimum mass flow, return flow is already observed at the diffuser inlet and continues up to the diffuser exit. These observations are similar to the measurements of [10].

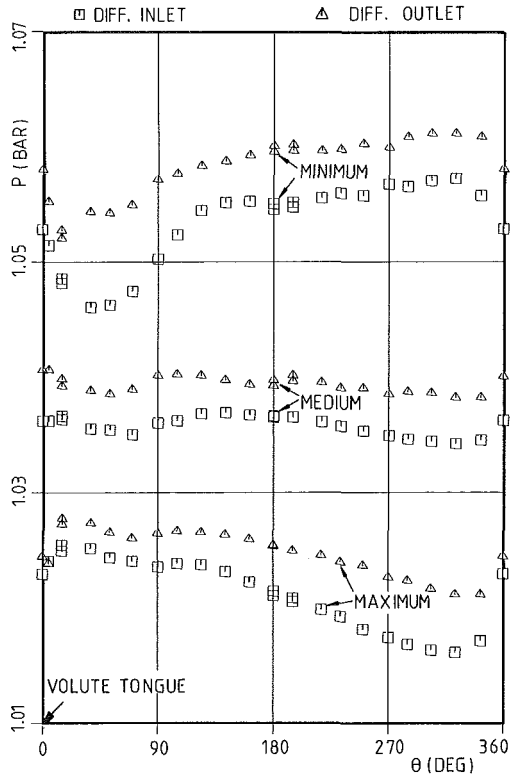

Fig. 9 Static pressure distribution

The LDA measurements also allow the evaluation of the effect of the circumferential pressure variations on the flow in the impeller. The pitch- and spanwise, mass-averaged values of radial and tangential velocity variations at the four LDA measuring positions are indicated on Figs. 11(*a*) and 11(*b*). Comparing these figures with Fig. 9, it can be observed that a local increase in outlet pressure results in a decrease of V_{R2} and that V_{T2} is almost unaffected.

Few theoretical models are available to predict the influence of outlet pressure distribution on the performance of a centrifugal pump impeller. The model evaluated in the present study is the impeller diffuser interaction model used in the rotating stall calculation method of [11]. This model assumes that the flow is two dimensional, incompressible, and inviscid. It allows the calculation of the time evolving variation of the radial velocity at the impeller outlet for a prescribed circumferential static pressure distribution $P_2(\theta)$. The following formula describes the abovementioned diffuser impeller interaction

$$\frac{\partial V_{R2}}{\partial t} = -U_2 \frac{\partial V_{R2}}{R_2 \partial \theta} + \frac{\cos \beta_{bl}}{EL}\left(U_2 V_{T2} - U_1 V_{T1} + \frac{P_1^0 - P_2(\theta)}{\rho} - \frac{V_{R2}^2 + V_{T2}^2}{2}\right) \tag{1}$$

EL is the effective length of the flow channel and is defined as

$$EL = \int_1^2 \frac{A_2}{A}\, dl \tag{2}$$

The model further assumes that the exit relative flow angle is constant, which allows the calculation of V_{T2}

$$V_{T2} = U_2 - V_{R2} \cdot \tan \bar{\beta}_2 \tag{3}$$

The radial velocity distribution can be obtained by a numerical integration in time using an explicit one-step Lax-Wendroff discretization scheme [12]

$$V_{R2j}^{k+1} = V_{R2j}^k - \frac{\mathrm{CFL}}{2}\left(V_{R2j+1}^k - V_{R2j-1}^k\right) + \frac{\mathrm{CFL}^2}{2}\left(V_{R2j+1}^k - 2V_{R2j}^k + V_{R2j-1}^k\right)$$

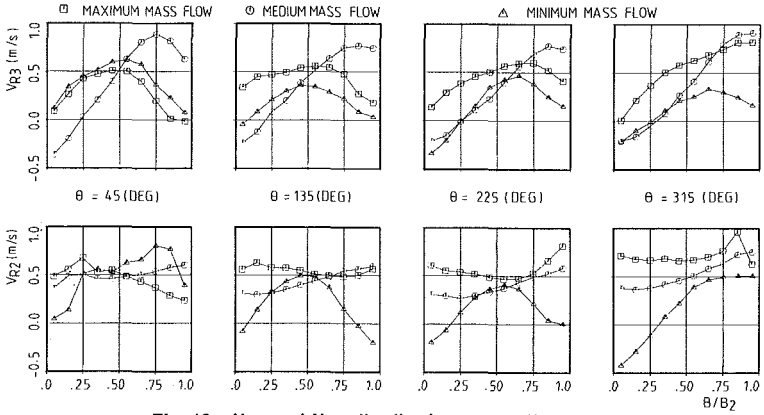

Fig. 10 V_{R2} and V_{R3} distribution over diffuser width

Downloaded 01 Jun 2010 to 171.66.16.57. Redistribution subject to ASME license or copyright; see http://www.asme.org/terms/Terms_Use.cfm

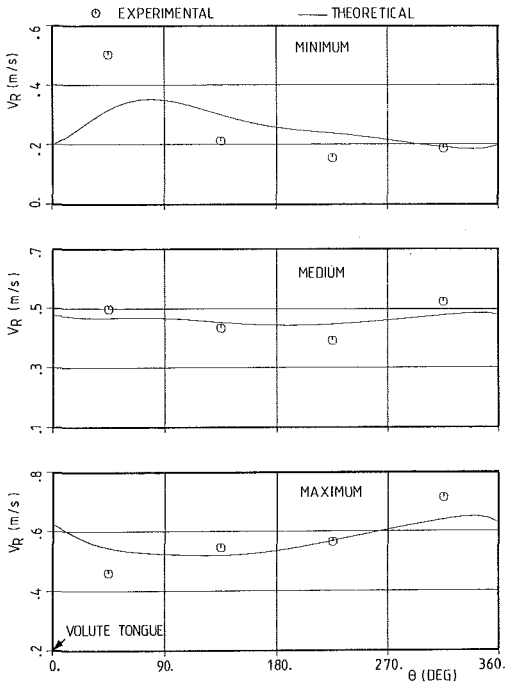

Fig. 11(*a*) Measured and calculated V_{R2} distribution (β_2 = const)

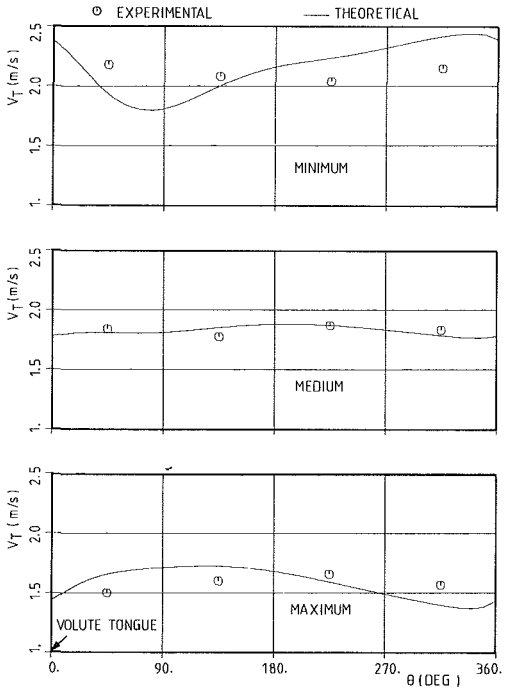

Fig. 11(*b*) Measured and calculated V_{T2} distribution (β_2 = const)

$$+\frac{\cos\beta_{bl}}{EL}\Delta t\left[U_2 V_{T2j}^k - U_1 V_{T1j}^k + \frac{P_1^0}{\rho} - \frac{P_{2j}^k}{\rho} + \frac{1}{2}\left(V_{R2j}^{k2} + V_{T2j}^{k2}\right)\right] \quad (4)$$

where CFL = $(U_2\Delta t)/(R_2\Delta\theta)$ must be smaller than one and allows the time step Δt to be defined.

The effective length used in the calculations is the real impeller channel length. This is only half the blade length because of the low solidity and high stagger. Figure 11(*a*) shows a comparison between the experimental and calculated V_{R2} distribution for the three mass flows tested. The shape of the curve agrees fairly well with the experimental data. However, the predicted amplitude of the velocity perturbation is smaller than the measured one. There are not enough experimental points to make a precise evaluation of the predicted V_{T2} distribution (Fig. 11*b*). However, it seems that the experimental V_{T2} is almost constant, whereas the theoretical one changes with V_{R2} according to (3).

The theoretical calculation is based on the assumption that the exit flow angle β_2 is constant. The varying pressure difference between impeller inlet and outlet results in an acceleration or deceleration of the relative velocity, and Figs. 11(*a*) and 11(*b*) show the corresponding variation of V_{R2} and V_{T2}.

In reality, the radial velocity also changes at constant W_2, because of a change in the slip factor ($\beta_2 \neq$ const). Calculations in which the experimental β_2 distribution (Fig. 12) is used to relate V_{R2} and V_{T2} result in very good agreement (Fig. 13). This proves that the outlet velocity variation is partly due to a change in relative velocity, according to the previously mentioned model, and partly due to a change in slip factor, for which a prediction method is not yet available.

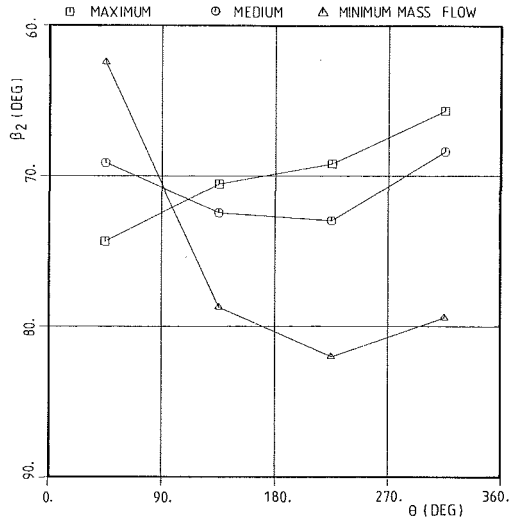

Fig. 12 Measured relative flow angle distribution

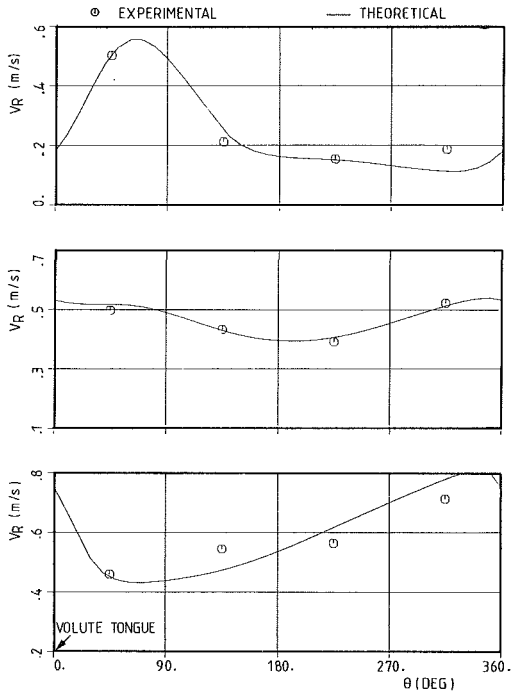

Fig. 13 Measured and calculated V_{R2} distribution ($\beta_2 \neq$ const)

Downloaded 01 Jun 2010 to 171.66.16.57. Redistribution subject to ASME license or copyright; see http://www.asme.org/terms/Terms_Use.cfm

Conclusions

The present LDA measurements provide a set of detailed experimental data describing the impeller response to a circumferential variation of the outlet pressure. These data reveal how the outlet volute influences the flow inside the impeller through the static pressure variation at the impeller exit and allow the evaluation of theoretical prediction methods.

The prediction method evaluated in this paper gives very good results if a correct variation of β_2 is used for the V_{T2} calculation. From this comparison one can also conclude that the velocity variations at the impeller exit are partly due to an unsteady acceleration or deceleration of the relative flow in the blade passage and partly due to a change in outlet flow angle β_2.

Acknowledgments

The authors wish to thank Miss H. Junker of Aalborg University and Mr. B. Vandenbosch of the University of Michigan for their help in the experimental part of this research.

References

1 Stepanoff, A. J., *Centrifugal and Axial Flow Pumps*, Wiley, New York, 1948, pp. 122–136.

2 Iversen, H., Rolling, R., and Carlson, J., "Volute Pressure Distribution, Radial Force on the Impeller, and Volute Mixing Losses of a Radial Flow Centrifugal Pump," ASME JOURNAL OF ENGINEERING FOR POWER, Vol. 82, No. 2, Apr. 1960, pp. 136–144.

3 Agostinelli, A., Nobles, D., and Mocridge, C. R., "An Experimental Investigation of Radial Thrust in Centrifugal Pumps," ASME JOURNAL OF ENGINEERING FOR POWER, Vol. 82, No. 2, Apr. 1960, pp. 120–126.

4 Worster, R. C., "Flow in the Volute of a Centrifugal Pump and Radial Forces on the Impeller," BHRA RR 543, Dec. 1956.

5 Chamieh, D. S., et al., "Experimental Measurements of Hydrodynamic Stiffness Matrices for a Centrifugal Pump Impeller," in: *Rotordynamic Instability Problems in High Performance Turbomachinery—1982*, NASA CP 2250, 1982, pp. 382–398.

6 Bowerman, R., and Acosta, A., "Effect of the Volute on Performance of a Centrifugal Pump Impeller," *Trans. ASME*, Vol. 79, No. 5, 1957, pp. 1057–1069.

7 Stiefel, W., "Experiences in the Development of Radial Compressors," in: *Advanced Radial Compressors*, von Karman Institute LS 50, May 1972.

8 McCutcheon, A., "Modern Developments in the Design and Performance of Turbocharger Compressors," in: *Turbochargers and Related Problems*, von Karman Institute LS 1982-01, Jan. 1982.

9 Yuasa, T., and Hinata, T., "Fluctuating Flow Behind the Impeller of Centrifugal Pump," *Bull. JSME*, Vol. 22, No. 174, Dec. 1979, pp. 1746–1753.

10 Rebernik, R., "Impeller and Diffusor Correlated Components of Radial Flow Pumps," IAHR-AIRH Symp., Rome 1972.

11 Frigne, P., and Van den Braembussche, R., "A Theoretical Model for Rotating Stall in the Vaneless Diffuser of a Centrifugal Compressor," ASME JOURNAL OF ENGINEERING FOR GAS TURBINES AND POWER, Vol. 107, No. 2, Apr. 1985, pp. 507–513.

12 Roache, P. J., *Computational Fluid Dynamics*, Hermosa Publ., Albuquerque, 1976.

Downloaded 01 Jun 2010 to 171.66.16.57. Redistribution subject to ASME license or copyright; see http://www.asme.org/terms/Terms_Use.cfm

Deterioration of Compressor Performance Due to Tip Clearance of Centrifugal Impellers

Y. Senoo
Professor,
Research Institute of Industrial Science,
Kyushu University,
Kasugashi, Fukuoka 816, Japan
Fellow ASME

M. Ishida
Professor,
Faculty of Engineering,
Nagasaki University,
Nagasaki, 852, Japan

The authors' theory on the tip-clearance loss of centrifugal impellers is modified to include the variation of slip coefficient of the impeller due to the tip clearance, by deriving a rational relationship between two empirical parameters in the theory. In order to compare experimental data in the literature with prediction, examination was made regarding accuracy of available data and the way to select corresponding flow rates of a compressor with different values of tip clearance. Good agreement between data and prediction was observed. These examples demonstrate the following tendency regarding effects of various parameters on the tip clearance loss. Efficiency drop due to the tip clearance of high-pressure-ratio compressors is less than that of low-pressure-ratio compressors if the tip clearance ratio at the impeller exit is equal. The magnitude of clearance loss becomes smaller as the flow rate is reduced and also at a reduced shaft speed in cases of high-pressure-ratio compressors. The equations in the theory clearly show these tendencies.

Introduction

In many turbomachines impellers are not shrouded and the performance is deteriorated by the pressure loss due to the clearance between the shroud casing and the tips of impeller blades. For the design of turbomachines, therefore, it is important to estimate effects of tip clearance correctly, and several empirical equations have been published in the literature. Pampreen [1] collected data of six different centrifugal impellers and correlated the efficiency drop to the tip-clearance ratio at the exit of impeller, and he drew an average correlation line with an inclination of 0.3 in Fig. 1. In the literature usually the relationship has been published as an empirical formula

$$-\frac{\Delta\eta}{\eta}=\frac{2ac}{b_1+b_2} \tag{1}$$

Eckert and Schnell [2] chose $a=0.9$ while Pfleiderer [3] recommended $a=1.5\sim3.0$. Pampreen's average line roughly agrees with Eckert and Schnell's equation providing that $b_1/b_2=4$ and $\eta=0.8$.

In Fig. 1 four broken lines are drawn to connect data which belong to respective impellers. Inclination of these lines is different from each other and all of them are considerably larger than that of Pampreen's full line. It is also noticed that none of these broken lines passes through the origin. In Fig. 1 the ordinate is the decrement of efficiency in comparison to the efficiency at zero clearance.[1] Since it is not possible to test an impeller at zero clearance, the reference efficiency at zero clearance is dubious, but the inclination of each broken line is not influenced by one particular datum of reference, therefore the inclination is reliable. Since the inclination of broken lines is different from one impeller to another, it is clear that the efficiency drop due to tip clearance can not be decided only by the parameter in the abscissa or the clearance ratio at the impeller exit.

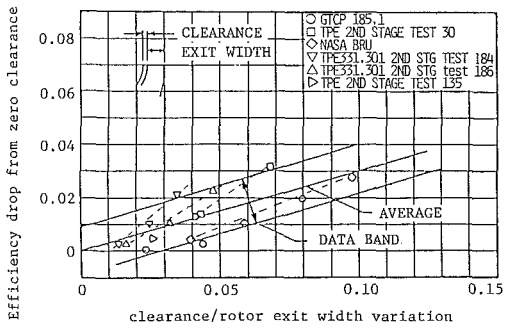

Fig. 1 Effect of tip clearance on efficiency drop in the literature [1]

In [5], the present authors have proposed a new approach regarding the tip-clearance loss. It consists of the pressure loss induced by the leakage flow through the clearance and the

[1] It is experimentally demonstrated that the performance of an unshrouded impeller with small tip clearance was superior to that of a shrouded impeller with identical geometry in a wide flow range except at a large flow rate [4]. It is generally understood that motion of the stationary shroud relative to the blade prevents boundary layer fluid from accumulating at the blade suction surface and consequently reduces pressure loss. Therefore, the performance of a shrouded impeller is different from the performance of an unshrouded impeller with zero tip clearance and the latter can be estimated only by extrapolating data of the impeller with different values of the tip clearance.

Contributed by the Gas Turbine Division of THE AMERICAN SOCIETY OF MECHANICAL ENGINEERS and presented at the 31st International Gas Turbine Conference and Exhibit, Düsseldorf, Federal Republic of Germany, June 8–12, 1986. Manuscript received at ASME Headquarters January 24, 1986. Paper No. 86-GT-123.

Copyright © 1987 by ASME
Downloaded 01 Jun 2010 to 171.66.16.57. Redistribution subject to ASME license or copyright; see http://www.asme.org/terms/Terms_Use.cfm

pressure loss for supporting fluid against the pressure gradient in the blade channels and against the pressure gradient in the thin annular clearance space generated by the rotating blade tip and the shroud. Predicted values agreed well with experimental data of seven axial impellers as well as data of two types of centrifugal blowers in the literature. More comparisons with experimental data of high-pressure-ratio centrifugal compressors are described.

The performance of a compressor is influenced by the tip clearance in two ways: change of the input power, and increase of the pressure loss, but the former was not discussed in [5]. In this paper an attempt is made to correlate the change of input power to the leakage flow, and the flow model in [5] is slightly modified so that the leakage flow, the pressure loss, and the change of input power due to tip clearance are interrelated.

Regarding experimental study it should be noted that variation of performance due to tip clearance is not large and an error of a fraction of one percent in head H or efficiency η may mask the correct relationship between ΔH or $\Delta\eta$ and the tip-clearance ratio λ_2. On the other hand it is very difficult to evaluate the total pressure correctly at the exit of impeller where the velocity is severely distorted and periodic. If the total pressure is measured at the exit of the diffuser, data are influenced by the performance of the diffuser; therefore, the difference of stage efficiencies of a compressor with two different values of tip clearance is not always equal to the difference of impeller efficiencies unless the pressure loss of the diffuser is identical. Since the diffuser performance is sensitive to the inlet condition to the diffuser, it is important that corresponding flow conditions of a compressor with different values of tip clearance are chosen so that the pressure loss of the diffuser is identical.

Modification of the Previous Theory on Tip-Clearance Loss

If there is a clearance between the edge of a loaded blade and a wall, near the edge the pressure difference across the blade is less than the ordinary value without clearance, and the defect of pressure difference is related to contraction of leakage flow through the clearance. At the same time the pressure distribution is related to the input head of the impeller and also to the pressure loss due to the tip clearance. The relationship among these variables is discussed here and consequently the previous theory on the tip-clearance loss is slightly modified.

Contraction Coefficient of Leakage Flow and Blade Loading of Impeller. In cases of flow through an orifice or a slit of width c on a big wall, the pressure along the wall falls toward the slit, and it is easily proved that the defect of the pressure force along the wall is equal to $(2\alpha-1)c$ times the undisturbed pressure difference across the wall where α is the contraction coefficient of jet through the slit.[2] Similarly in cases of leakage through a tip clearance of c, it is proper to assume that the blade loading or the pressure difference across a blade is not effective on a width of $(2\alpha-1)c$ from the blade tip. That is, the effective loading width of the blade is $b-(2\alpha-1)c$.

Near the tip of blade where the blade loading is smaller the mean through-flow velocity between a pitch of blades is also smaller in proportion to the blade loading; as a result the flow rate through the channel of impeller is also reduced or the effective width of flow passage is less than the blade width, although the physical passage width is made larger by the clearance. That is, for a given flow rate the mean velocity between blades is increased as follows

$$1+\frac{\Delta w}{w_0}=\frac{b}{b-(2\alpha-1)c}\simeq 1+\frac{c}{b}(2\alpha-1) \tag{2}$$

The input head of a centrifugal impeller is usually expressed as

$$\psi_i/2=1-k-\phi\cot\beta_{b2} \tag{3}$$

ϕ in the above equation is the dimensionless meridian component of velocity, and variation of ψ_i due to tip clearance $c_2/b_2=\lambda_2$ is expressed as

$$\Delta\psi_i/2\Delta\lambda_2=-(2\alpha-1)\phi\cot\beta_{b2} \tag{4}$$

It has been experimentally recognized [6] that $\Delta\psi_i/\Delta\lambda_2$ varies almost in proportion to $\cot\beta_{b2}$, but $\Delta\psi_i$ was not exactly zero for a radial impeller. It is presumed that equation (4) does not perfectly express the mechanics of flow, but in practice equation (4) is acceptable for most cases.

The contraction coefficient α varies depending upon the geometry of the slit, and α is usually between 0.6 and 0.8. In some literature $\Delta\psi_i/\Delta\lambda_2$ is experimentally measured, and we can estimate the contraction coefficient α using the data and equation (4). If the value is between 0.6 and 0.8, the experiment supports equation (4) and the hypothesis behind it. However, equation (4) should not be used to estimate α for cases of very small value of $\phi\cot\beta_{b2}$, because a small uncertainty in $\Delta\psi_i/\Delta\lambda_2$ results in a large error in α.

Flow Model. It is experimentally known that variation of blade loading with respect to flow rate is easily predictable based on equation (3) or one-dimensional flow analysis, i.e., it is not influenced much by blockage in the impeller. In cases of

[2] This relation is easily derived using a momentum equation and a Bernoulli equation. In many textbooks it is assumed for simplicity that the wall pressure is not changed by the flow, then $(2\alpha-1)c=0$ and $\alpha=0.5$. In reality $\alpha=0.61$ for an orifice with a sharp edge.

Nomenclature

a = coefficient
b = blade width
c = tip clearance
G = mass flow rate
k = slip coefficient
m = meridional distance along shroud
p = pressure
r = radial distance from axis
U = tip speed at impeller exit
v = component of leakage velocity normal to blade
w = mean through-flow velocity between a blade pitch
z = number of blades
α = contraction coefficient of leakage flow
β = flow angle, from circumference
β_b = blade angle
ϵ = pressure recovery coefficient
η = efficiency
λ = tip clearance ratio $=c/b_2$
ρ = density of fluid
σ = effectiveness of flow area
ϕ = flow coefficient at impeller exit
ψ = pressure coefficient of impeller
ψ_i = work input coefficient
ψ_l = pressure loss coefficient due to tip clearance
Ω = angular velocity of impeller

Subscripts

p = pressure surface
s = suction surface
0 = values for zero clearance
1 = impeller inlet
2 = impeller exit

Superscripts

$'$ = due to leakage
$''$ = due to pressure gradient on annular clearance
$'''$ = due to pressure gradient on blockage in channel

Downloaded 01 Jun 2010 to 171.66.16.57. Redistribution subject to ASME license or copyright; see http://www.asme.org/terms/Terms_Use.cfm

shrouded impellers or open impellers with very small tip clearance, the effective area of blade to support the blade loading is not influenced by the blockage, and the pressure difference across a blade is not influenced by the blockage either. Usually the pressure difference across a blade is expressed as follows

$$(p_p - p_s)/\rho = (w_s^2 - w_p^2)/2 = (w_s - w_p)(w_s + w_p)/2 = (w_s - w_p)w \tag{5}$$

where w is the mean velocity between a blade pitch; it is evaluated disregarding blockage in the impeller.

In cases of open impellers with a finite tip clearance, the effective width of a blade becomes narrower due to leakage and the flow model is equivalent to an impeller with a narrower width by a factor of σ, where $1-\sigma=(2\alpha-1)c/b$. As a result, the through-flow velocity is $w=w_0/\sigma$, and the effect of blockage on the blade loading is different from that in ordinary cases without leakage.

The blade loading of an impeller is related to the change of angular momentum of flow as follows

$$(p_p - p_s)r\sigma bz dm = \rho w(w_s - w_p)r\sigma bz dm$$

$$= 2\pi r b\sigma\rho w \sin\beta \frac{d}{dm}(r^2\Omega - rw\cos\beta)dm$$

Replacing $w=w_0/\sigma$ the above equation becomes

$$w_s - w_p = \frac{2\pi r}{z}\sin\beta\left\{2\Omega\frac{dr}{dm} + \frac{w_0}{\sigma^2}\cos\beta\frac{d\sigma}{dm} - \frac{1}{\sigma}\left(\frac{w_0}{r}\cos\beta\frac{dr}{dm} + \cos\beta\frac{dw_0}{dm} - w_0\sin\beta\frac{d\beta}{dm}\right)\right\} \tag{6}$$

This equation is identical to equation (12) of [5].

In [5] it was assumed that the effective width of the blade was b while the mean through-flow velocity was w_0. In the present flow model the effective width is σb while the mean through-flow velocity is w_0/σ. That is, according to equation (5) in the present flow model the pressure difference across a blade is larger by a factor of $1/\sigma$ but the blade force as a whole is identical to the model of [5]. Because of the larger pressure difference across a blade, the leakage velocity v is larger by a factor of $1/\sqrt{\sigma}$. Since σ is usually larger than 0.95, the leakage flow may be increased by about 2 percent based on the modified flow model providing that the contraction coefficient is identical. That is, the change of flow model hardly influences the results of prediction, but in the new model the blockage factor is directly related to the contraction coefficient of the leakage flow and there is less freedom to adjust prediction.

Working Equations. Working equations based on the new flow model are a little bit different from those in [5]. In [5] equations (1), (2), and the two equations in between, σ is replaced by unity, in equation (7) w_0 is changed to w_0/σ, and in equation (8) the first term $v/2U$ in the parentheses is multiplied by σ, while in equation (9) the term $d\sigma/dm$ is added. They are reproduced as follows

$$v = \sqrt{2(w_s - w_p)w_0/\sigma} \tag{7}$$

$$\psi_l' = \frac{z}{\pi r_2\phi}\int_{m_1}^{m_2}\frac{\rho\alpha\lambda}{\rho_2\sin\beta_b}\left(\frac{v}{U}\right)^2\left(\frac{v}{2U} - \frac{2\pi}{z}\frac{w_0}{\sigma U}\frac{dr}{dm}\right)dm \tag{8}$$

$$\psi_l'' + \psi_l''' = \frac{2}{r_2\phi}\int_{m_1}^{m_2}\frac{\rho}{\rho_2}\frac{r\lambda w_0}{\sigma U}\sin\beta\left\{-2\alpha\epsilon\frac{w_0}{\sigma U}\left(\frac{1}{\sigma U}\frac{dw_0}{dm} - \frac{w_0}{\sigma^2 U}\frac{d\sigma}{dm}\right) + \frac{2\Omega w_0}{\sigma U^2}\cos\beta\frac{dr}{dm} - \frac{w_0^2}{\sigma^2 U^2 r}\cos^2\beta\frac{dr}{dm}\right\}dm \tag{9}$$

The change of pressure coefficient ψ and the change of impeller efficiency η due to a change of tip clearance λ_2 are related to these parameters in the above equations and the relations are presented in equations (10) and (11) in [5]. They are

$$\psi_0 - \psi = \psi_{i0} - \psi_i - (\psi_{h0} - \psi_h) + \psi_l \tag{10}$$

$$\psi_l = \psi_l' + \psi_l'' + \psi_l'''$$

$$\eta_0 = 1 - (\psi_{h0}/\psi_{i0}), \qquad \eta = 1 - (\psi_h + \psi_l)/\psi_i$$

$$\frac{\eta_0 - \eta}{\lambda_2} = \frac{\psi_l}{\psi_i\lambda_2} - \frac{\psi_{h0} - \psi_h}{\psi_i\lambda_2} + (1-\eta_0)\frac{\psi_{i0} - \psi_i}{\psi_i\lambda_2} \tag{11}$$

where ψ_h is the hydraulic pressure loss other than the tip clearance loss, and the subscript 0 indicates the values for the case of zero clearance. $\psi_{h0} - \psi_h$ is almost zero but it may be negative at off-design conditions.

These parameters are calculated and listed in Table 1 for the experimental cases in the following chapter. In the first four lines of Table 1, the effects of flow rate at a constant speed are demonstrated for two compressors, where the parameters were calculated for the maximum and the minimum tip clearances at the specified identical flow rate and the difference of the parameters was divided by the difference of the tip clearances $\Delta\lambda_2$ at each flow rate. In the last six lines, the effects of shaft speed are demonstrated for two compressors, where the parameters were calculated for the maximum and the minimum tip clearances at slightly different flow rates so that the diffuser efficiencies were identical in the experiments and the difference of the parameters was divided by the difference of the tip clearances $\Delta\lambda_2$. The listed flow rates were the one at the minimum clearance. The flow rate was slightly less at the maximum clearance.

Table 1 Predicted pressure loss and efficiency drop due to tip clearance

Compressor	Ω, percent	G, kg/s	$\frac{\Delta\psi_l'}{\Delta\lambda_2}$	$\frac{\Delta\psi_l''}{\Delta\lambda_2}$	$\frac{\Delta\psi_l'''}{\Delta\lambda_2}$	$\frac{(\eta_0-1)\Delta\psi_i}{\psi_i\Delta\lambda_2}$	$\frac{-\Delta\eta}{\Delta\lambda_2}$
A	100	0.86	0.166	0.224	0.013	0.024	0.296
Fig. 7	100	0.80	0.162	0.193	0.009	0.020	0.26
C	90	0.86	0.204	0.173	0.012	0.025	0.302
Fig. 13	90	0.82	0.203	0.165	0.011	0.023	0.287
A	100	0.86	0.164	0.211	0.011	0.024	0.285
Fig. 5	80	0.574	0.126	0.132	0.004	0.028	0.209
	50	0.249	0.110	0.073	0.000	0.019	0.148
B	90	0.826	0.121	0.120	0.003	0.029	0.221
Fig. 11	70	0.516	0.103	0.082	0.000	0.032	0.179
	50	0.280	0.099	0.060	0.000	0.032	0.141

Downloaded 01 Jun 2010 to 171.66.16.57. Redistribution subject to ASME license or copyright; see http://www.asme.org/terms/Terms_Use.cfm

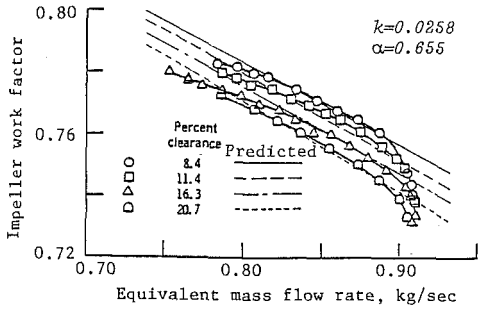

Fig. 2 Change of input head due to tip clearance, Compressor A [7]

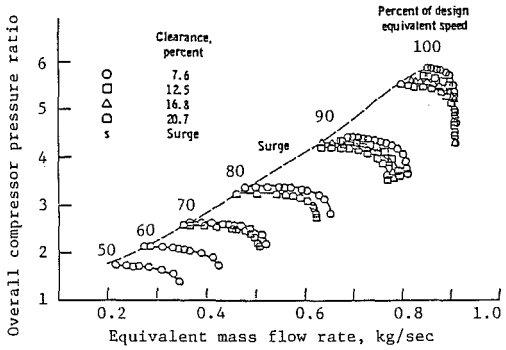

Fig. 3 Change of stage pressure ratio due to tip clearance, Compressor A [7]

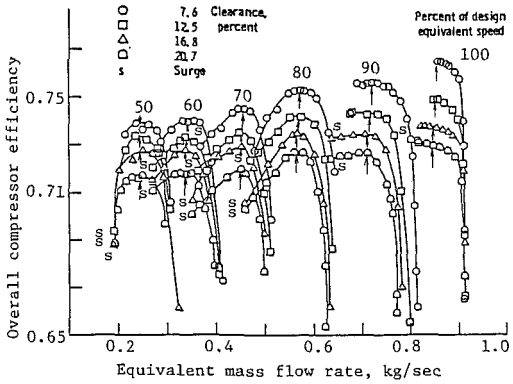

Fig. 4 Change of stage efficiency due to tip clearance, Compressor A [7]

Comparison With Experimental Data

Accuracy of Total Pressure. The relative flow pattern at the impeller exit is not axisymmetric due to blades and the pattern rotates with the impeller; therefore, the velocity relative to a fixed probe changes the magnitude and the direction periodically, and the measured time-mean total pressure is not equal to the mass-averaged total pressure. The axial distribution of velocity is also distorted. That is, the meridian component of velocity is very low in a thin layer near the shroud due to the effect of tip clearance of the impeller, and the layer changes the thickness with the tip clearance; therefore, it is quite difficult to measure the mass-averaged total pressure. The wall static pressure at the exit of the impeller may be the best parameter to accurately demonstrate the change of impeller performance due to tip clearance, but it is seldom presented in the literature.

Corresponding Flow Rates of a Compressor With Different Values of Tip Clearance. At the exit of diffuser, the flow is almost steady and the dynamic pressure is small; therefore, the stage performance including the diffuser can be easily and accurately measured. However, if the pressure loss in the diffuser is not equal for the tests with different values of tip clearance of the impeller, the variation of impeller performance due to tip clearance can not be evaluated from the stage performances. In order to minimize variation of the diffuser performance in different experiments, the inlet flow angle must be far from the angle for stall and far from the angle for choke, and furthermore the flow rate must be adjusted in different experiments so that the inlet flow angle to the diffuser is identical.

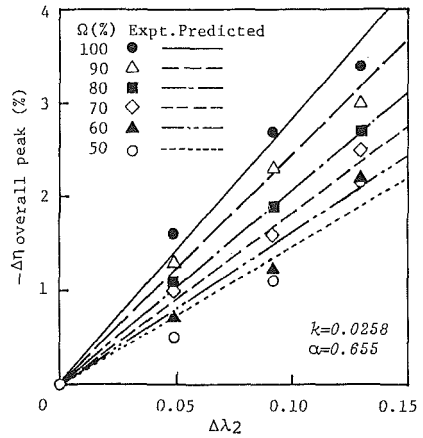

Fig. 5 Effect of shaft speed on tip-clearance loss, Compressor A

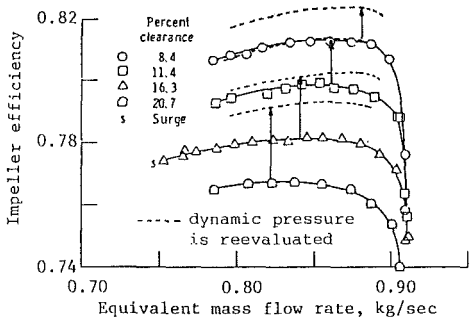

Fig. 6 Change of impeller efficiency due to tip clearance, Compressor A [7]

As the tip clearance increases, the blade loading and the tangential velocity component at the impeller exit decrease while the radial component increases because the gas density is lower and the blockage is larger, consequently the direction of flow tends to be away from the tangential direction. Therefore, in cases of high-pressure-ratio compressors, in order to keep a constant flow angle at the diffuser inlet, the mass flow rate should be slightly reduced as the tip clearance increases.

Test of Compressor A. A centrifugal compressor was tested with four different values of tip clearance [7]. It was designed for a pressure ratio of 6 and a specific speed of 0.769 at 80,000 rpm. The impeller diameter was 136.5 mm, the exit width was 4.67 mm, and there were 24 blades with an exit blade angle of 59.2 deg from circumference.

Variation of the input head due to change of the tip clearance is presented in Fig. 2 where four straight lines are prediction based on equation (2) assuming that $\alpha = 0.655$ or the blockage factor $1-\sigma = (2\alpha-1)\lambda_2 = 0.31\lambda_2$. The assumed value of k in equation (3) is 0.0258 which is smaller than the value usually adopted. That is, in this experiment the input power is considerably larger than what is usually expected and it may be the cause for the low efficiency of the impeller.

Figures 3 and 4 are characteristic of the compressor with a

Downloaded 01 Jun 2010 to 171.66.16.57. Redistribution subject to ASME license or copyright; see http://www.asme.org/terms/Terms_Use.cfm

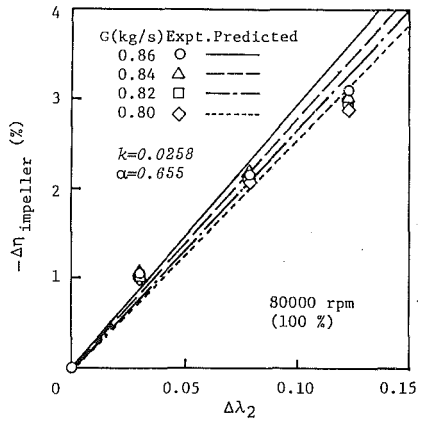

Fig. 7 Effect of flow rate on tip-clearance loss, Compressor A

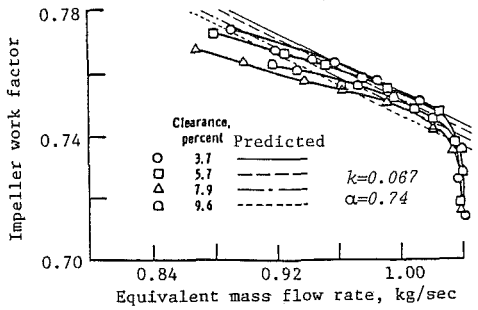

Fig. 8 Change of input head due to tip clearance, Compressor B [8]

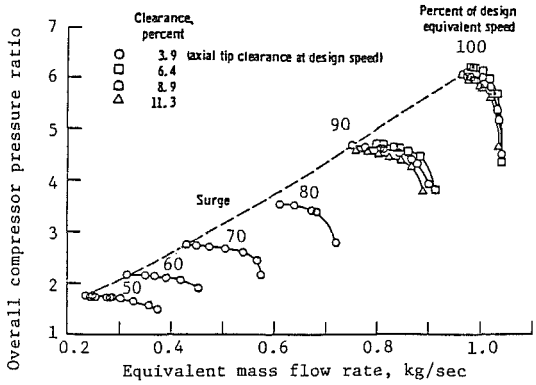

Fig. 9 Change of stage pressure ratio due to tip clearance, Compressor B [8]

vaned diffuser. It is clear that the tip clearance influences the compressor performance a great deal, but variation of the pressure ratio at a low speed is not apparent because the pressure ratio itself is very small. Therefore, comparison of experimental data with prediction is limited to only efficiency.

Regarding corresponding flow rates for different values of tip clearance, they are chosen near the flow rate for the maximum efficiency and furthermore the flow angle at the exit of impeller is made identical regardless of the tip clearance. These corresponding flow rates are indicated by arrows in Fig. 4.

Influence of Shaft Speed. The efficiency of the compressor with the minimum tip clearance is used as the base[3] and the decrement of the maximum efficiency due to the increment of tip clearance is experimentally determined at six different shaft speeds, which are indicated as different symbols in Fig. 5 while the predicted relationships are presented as straight lines. Some of the experimental data are not on the predicted straight lines, but they are located near the corresponding straight lines.

According to Fig. 5 for a given increment of tip clearance the decrement of measured efficiency becomes less as the shaft speed is lower, and the trend is also predicted. At a reduced speed the ratio ρ/ρ_2 is relatively large along the shroud, consequently w/U is small compared to the value at the design speed. According to equations (4), (5), and (6) a small value of w/U results in a small value of pressure loss similar to the case mentioned in the following section.

Influence of Flow Rate. If a centrifugal impeller is tested with a vaned diffuser the flow range is usually limited by stall and choke of the diffuser and the flow range is considerably narrower than the flow range of the impeller itself. Therefore, an impeller with backward-leaning blades is often tested with a vaneless diffuser in order to examine the characteristics of the impeller in the entire range of flow rate. The impeller efficiency of Compressor A is presented in Fig. 6 where the total pressure at the exit of impeller was estimated as the sum of the measured static pressure and the estimated dynamic pressure assuming that the flow was uniform in the width which covered the blade and the clearance. In reality, blockage increases with the tip clearance; therefore, in Fig. 6 the total pressure and the impeller efficiency were underestimated due to the assumptions of wider exit width and of no blockage.

If the efficiency of the vaned diffuser is estimated based on the difference between the maximum stage efficiency in Fig. 4 and the impeller efficiency at that flow rate in Fig. 6, the diffuser efficiency is higher for the case with a larger tip clearance. This means that a better pressure recovery is achieved when the blockage at the diffuser inlet is larger. The trend is against our knowledge on diffusers and the cause is attributed to the unsuitable way for estimating the dynamic pressure at the exit of impeller in Fig. 6.

Regarding the velocity distribution at the exit of impeller it may be proper to assume that there is no outward flow from the annulus of tip clearance and the outward flow is uniform only in the effective width of impeller. Assuming the above velocity distribution, the total pressure at the exit of impeller was re-evaluated from the data in Fig. 6, and the modified efficiencies were presented as dotted lines. Using the modified impeller efficiency, the relationship between $-\Delta\eta$ and $\Delta\lambda_2$ was examined for four flow rates between 0.80 and 0.86 kg/s and the results are presented in Fig. 7 together with the predicted lines.

Although the estimated total pressure may not be accurate, both the experimental data and the prediction demonstrate that the influence of tip clearance on the efficiency becomes weaker as the flow rate is reduced. One of the reasons is that the blade loading is reduced with the flow rate and the leakage flow rate is also reduced. That is, $\Delta\psi_l'/\Delta\lambda_2$ is smaller. More important is that at a reduced flow rate deceleration in the impeller is large only near the inducer, but the tip clearance of inducer is not much changed by axial movement of the shroud in the test, while deceleration along the rest of shroud is less. Consequently the tip-clearance loss based on deceleration $(\Delta\psi_l''+\Delta\psi_l''')/\Delta\lambda_2$ is small at a reduced flow rate.

Compressor B [8]. This compressor was designed for a pressure ratio of about 6 and a specific speed of 0.718 at 68,384 rpm. The diameter and the exit width of the impeller were 161 mm and 5.16 mm, respectively, and it had 19 blades with an exit blade angle of 55.3 deg.

Symbols in Fig. 8 show the relationship between the tip-

[3] The tip clearance did not remain constant due to flowering of the impeller toward the shroud as the speed was increased. Since the compressor with the minimum tip clearance is used as the base at each speed, $\Delta\lambda_2$ is the increment of tip clearance relative to that of the base compressor, and the variation of tip clearance of the base compressor due to the rotative speed is excluded for the comparison providing that $-\Delta\eta$ is almost proportional to $\Delta\lambda_2$.

Downloaded 01 Jun 2010 to 171.66.16.57. Redistribution subject to ASME license or copyright; see http://www.asme.org/terms/Terms_Use.cfm

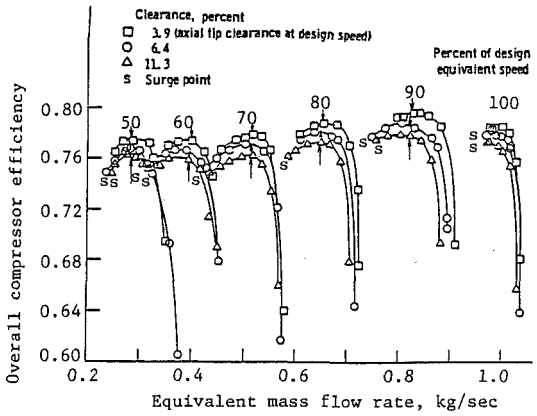

Fig. 10 Change of stage efficiency due to tip clearance, Compressor B [8]

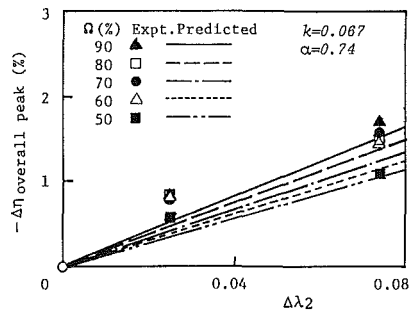

Fig. 11 Effect of shaft speed on tip-clearance loss, Compressor B

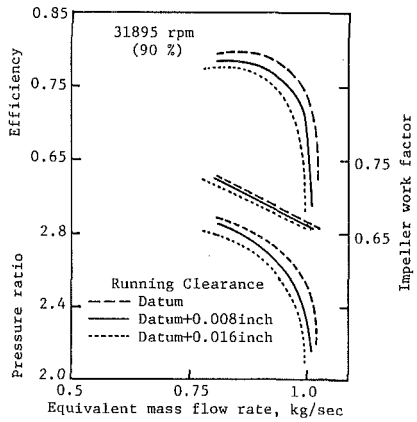

Fig. 12 Change of compressor performance due to tip clearance, Compressor C [9]

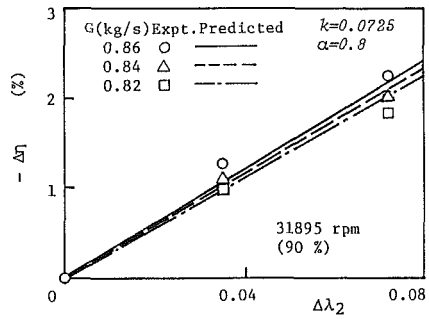

Fig. 13 Effect of flow rate on tip-clearance loss, Compressor C

clearance ratio and the input head of the impeller which was tested with a vaneless diffuser, while the four straight lines are predicted assuming $k=0.067$ and $\alpha=0.74$ in equations (3) and (4). It is puzzling that the input power of compressor with $\lambda_2=0.079$ is smaller than that with $\lambda_2=0.096$ for the identical flow rate.

Figures 9 and 10 are performances of the compressor with a vaned diffuser. At 100 percent speed the surge flow rate was close to the choke flow rate and the flow condition at the maximum efficiency was not identical for cases with different values of tip clearance; therefore they are omitted from the present discussion.

It is embarassing that in Fig. 9 the compressor with $\lambda_2=0.064$ has a higher pressure ratio than the compressor with $\lambda_2=0.039$, while in Fig. 10 the latter has a higher efficiency than the former has. The strange relation was not mentioned at all in the original paper and it could be a simple error on symbols. Otherwise, the inconsistent data in Figs. 8, 9, and 10 mean difficulty of reliable measurement which was accurate enough to compare the performances of a compressor with different values of tip clearance.

The efficiency of the compressor with the minimum tip clearance is used as the base, and the decrement of peak efficiency due to the increment of tip clearance is indicated in Fig. 11 using different kinds of symbols for each shaft speed while the prediction is indicated as different kinds of line for each shaft speed.

Compressor C [9]. This compressor was designed for a pressure ratio of about 3.6 and a specific speed of 0.485, and it was tested at 31,895 rpm which was 90 percent of the design speed. The characteristic curves of the compressor with three different values of tip clearance are presented in Fig. 12 without indicating experimental data. In the prediction, the contraction coefficient α is assumed as 0.80 based on the experimental data of the input head, and the relationship between the increment of tip clearance and the decrement of efficiency is predicted at three flow rates in Fig. 13 and compared with symbols which are deduced from the experimental data in Fig. 12. Good agreement is observed.

Compressors D and E. In [5] the theory was applied to a radial compressor D and a compressor E with 45 deg backward-leaning blades, and the experimental relationship between the decrement of efficiency and the increment of tip clearance was predicted fairly well by the theory in the range of $\lambda_2<0.1$. Those experiments covered a wide range of λ_2 and they demonstrated that $-d\eta/d\lambda_2$ became smaller as λ_2 was larger. In the present paper, the theory was modified, but as it was mentioned before, the predicted inclination $-\Delta\eta/\Delta\lambda_2$ did not change more than a few percent which was smaller than the uncertainty of experimental data. In order to predict the tip clearance loss in a wide range of λ_2, for estimating ψ_l'' and ψ_l''' it is necessary to include the effect of reduction of the radial pressure gradient due to the tip clearance.

Conclusions

The contraction coefficient of leakage flow through a tip clearance is related to the blade loading and to the blockage of flow in the channels between blades. Using the relationship, the change of input head and the change of pressure loss are quantitatively related to a change of tip clearance, and the authors' previous theory on the tip clearance is modified slightly. The theory not only predicts the relationship between the tip clearance and the pressure loss at the design condition, but also correctly predicts how the relationship varies at off-design flow rates and at off-design shaft speeds. They are summarized as follows:

1 The tip-clearance loss is almost proportional to the tip-clearance ratio in the range of $\lambda_2<0.1$.

2 The ratio $-\Delta\eta/\Delta\lambda_2$ becomes somewhat smaller as the flow rate is reduced.

3 If the tip-clearance ratio c_2/b_2 is equal, compressors with a higher design pressure ratio have smaller values of

Downloaded 01 Jun 2010 to 171.66.16.57. Redistribution subject to ASME license or copyright; see http://www.asme.org/terms/Terms_Use.cfm

$-\Delta\eta/\Delta\lambda_2$, because near the inlet the blade height is larger and the local tip-clearance ratio c/b is smaller.

4 If a high-pressure-ratio compressor is tested at a reduced shaft speed, $-\Delta\eta/\Delta\lambda_2$ is smaller than the value at the design speed.

Acknowledgments

When the authors submitted the manuscript of [5] to ASME, one of the reviewers suggested that the authors should apply the theory to data in [7, 8, 9]. The titles of these papers did not properly indicate the contents in spite of the comprehensive work on tip clearance. Without his suggestion these references were unknown to the authors and the present paper was not possible. The authors are grateful to the reviewer and also to Dr. C. Hah who served as the coordinator for review of the paper at that time.

References

1 Pampreen, R. C., "Small Turbomachinery Compressor and Fan Aerodynamics," ASME JOURNAL OF ENGINEERING FOR POWER, Vol. 95, July 1973, p. 251.

2 Eckert, B., and Schnell, E., *Axial- und Radial-Kompressoren*, 2nd ed., Springer-Verlag, 1961, pp. 192, 357.

3 Pfleiderer, C., *Die Kreisel Pumpen*, 5th ed., Springer-Verlag, 1961, p. 99.

4 Harada, H., "Performance Characteristics of Shrouded and Unshrouded Impellers of a Centrifugal Compressor," ASME JOURNAL OF ENGINEERING FOR GAS TURBINES AND POWER, Vol. 107, Apr. 1985, p. 528.

5 Senoo, Y., and Ishida, M., "Pressure Loss Due to the Tip Clearance of Impeller Blades in Centrifugal and Axial Blowers," ASME JOURNAL OF ENGINEERING FOR GAS TURBINES AND POWER, Vol. 108, Jan. 1986, pp. 32-37.

6 Ishida, M., and Senoo, Y., "On the Pressure Losses Due to the Tip Clearance of Centrifugal Blowers," ASME JOURNAL OF ENGINEERING FOR POWER, Vol. 103, Apr. 1981, p. 271.

7 Klassen, H. A., Wood, J. R., and Schumann, L. F., "Experimental Performance of a 13.65-centimeter-Tip-Diameter Tandem-Bladed Sweptback Centrifugal Compressor Designed for a Pressure Ratio of 6," NASA Technical Paper 1091, Nov. 1977.

8 Klassen, H. A., Wood, J. R., and Schumann, L. F., "Experimental Performance of a 16.10-centimeter-Tip-Diameter Sweptback Centrifugal Compressor Designed for a 6:1 Pressure Ratio," NASA Technical Memorandum X-3552, June 1977.

9 Beard, M. G., Pratt, C. M., and Timmis, P. H., "Recent Experience on Centrifugal Compressors for Small Gas Turbines," ASME Paper No. 78-GT-193, Apr. 1978.

Downloaded 01 Jun 2010 to 171.66.16.57. Redistribution subject to ASME license or copyright; see http://www.asme.org/terms/Terms_Use.cfm

S. Elfeki
Graduate Research Assistant.
Student Mem. ASME

W. Tabakoff

Professor.
Fellow ASME

Department of Aerospace Engineering
and Engineering Mechanics,
University of Cincinnati,
Cincinnati, OH 45221

Erosion Study of Radial Flow Compressor With Splitters

Gas turbine engines operating in areas where the atmosphere is polluted by small solid particles are examples of machines operating under particulate two-phase flow conditions. The presence of solid particles in the working media leads to erosion and loss of engine power. In the present paper, particle trajectories are calculated by direct integration of the particle equations of motion through a compressor impeller with two different size splitters. Particle collisions with the blade, hub, and casing surfaces are determined. Erosion caused by the particle collisions with the compressor surfaces is calculated.

Introduction

Aircraft engines flying in areas where the atmosphere is polluted by small solid particles and gas turbines used in coal industry are examples of turbomachines operating under particulate two-phase flow conditions. Under such flow conditions, gas and particles experience different degrees of turning as they flow through the bladed channels. Thus, the particles may collide with the blade surfaces causing erosion and roughness which have undesirable influences on the fluid flow. Therefore, the study of particle trajectories to predict the particle collision locations is very important. Most of the studies published in the open literature are for particle trajectories in axial flow machines [1-3], and for radial inflow turbines [4]. In this paper, an attempt is made to study particle trajectories and erosion through a radial compressor impeller with two different size splitters.

The presence of small solid particles in the flow causes blade surface erosion and compressor performance deterioration.

The subject of this paper is to study particle trajectories, and to determine the collision locations and the erosion on each blade surface as well as hub and casing for a compressor impeller with two different size splitters. The three-dimensional flow fields through such impellers are calculated [5] using the computer code "MERDIL" [6] and an improved panel method [7]. Data on the particle trajectories and erosion pattern are obtained for different particle sizes. It is well documented that the particle sizes have large effects on the trajectory, number of impacts, and erosion rate.

Analysis

The equations that govern the three-dimensional notion of solid particles suspended by a compressible gas flow through a rotating compressor impeller are formulated. The particles entering the flow field are subjected to aerodynamic and gravitational forces. In this analysis for compressor impeller, only the drag force is considered as an external force [5]. It is assumed that the solid particles have spherical geometry. The total drag force, acting on the spherical particles, moving in gas flow may be written as follows

$$\mathbf{D}=\frac{1}{2}\rho\bar{V}^2AC_D\sum_i\frac{V_i}{|\bar{V}|}\mathbf{e}_i \tag{1}$$

where

$$\bar{V}=\Sigma V_i\mathbf{e}_i, \qquad i=r,\theta,z$$

and $V_i=W_i-V_{Pi}$; V_p is particle velocity. For the case of steady rotation around the z axis with a rotating speed ω, the particle acceleration vector in the rotating reference frame may be given by

$$\mathbf{a}=\{\ddot{r}-r(\dot{\theta})^2-2\omega r\dot{\theta}-r\omega^2\}\mathbf{e}_r+\{r\ddot{\theta}+2\dot{r}\dot{\theta}+2\omega\dot{r}\}\mathbf{e}_\theta+\{\ddot{z}\}\mathbf{e}_z \tag{2}$$

Applying Newton's second law of motion to the particles, with the drag forces as the only external force affecting the particle motion, one obtains the following equation

$$\begin{aligned}\ddot{r}-r(\dot{\theta}+\omega)^2 &= GV_r\\ r\ddot{\theta}+2\dot{r}(\dot{\theta}+\omega) &= GV_\theta\\ \ddot{z} &= GV_z\end{aligned} \tag{3}$$

where $G=\frac{1}{2}\rho\bar{V}^2AC_D/m_p|\bar{V}|$. The drag coefficient C_D is considered for spherical particles. The value of C_D was found experimentally over a wide range of Reynolds numbers [5].

The particle trajectories were obtained by numerical integration of the particle equations of motion (3). The exact location of particle impact point with the surface was determined using the Newton-Raphson iteration technique. The particle was considered in collision with the solid surface when it was one particle diameter tolerance from the surface. The rebound characteristics of the particle (i.e., velocity direction and magnitude after collision) were determined using empirical correlation data [8]. In this study the particles are quartz and the target material is 410 stainless steel. These

Contributed by the Gas Turbine Division of THE AMERICAN SOCEITY OF MECHANICAL ENGINEERS and presented at the 31st International Gas Turbine Conference and Exhibit, Düsseldorf, Federal Republic of Germany, June 8-12, 1986. Manuscript received at ASME Headquarters February 23, 1986. Paper No. 86-GT-240.

Copyright © 1987 by ASME

Downloaded 01 Jun 2010 to 171.66.16.57. Redistribution subject to ASME license or copyright; see http://www.asme.org/terms/Terms_Use.cfm

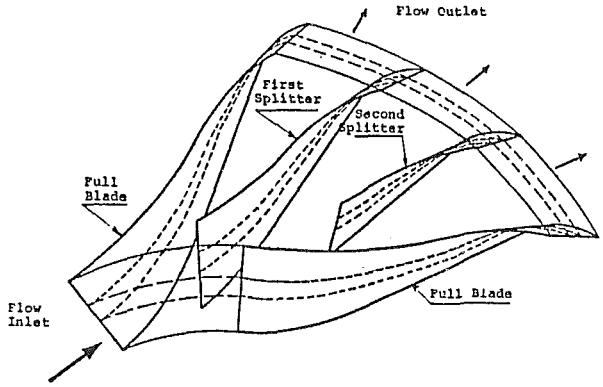

Fig. 1(*a*) Scheme of an impeller sector with two different size splitters

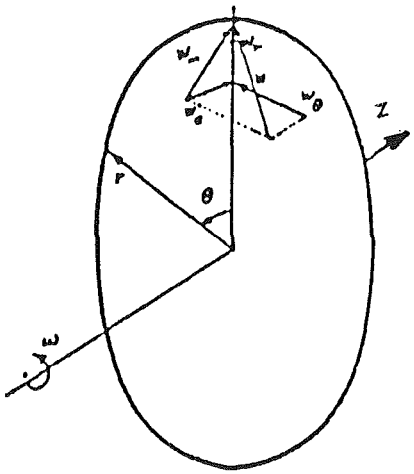

Fig. 1(*b*) Coordinate system (r, θ, z) used in the calculation

restitution ratio data were expressed as ratios of the rebounds from the surface after collision in tangential and normal velocity components and the incidence rebound angle ratio. They are given as

$$\frac{V_{n2}}{V_{n1}} = 1.0 - 0.4159\beta_1 - 0.4994\beta_1^2 + 0.292\beta_1^3$$

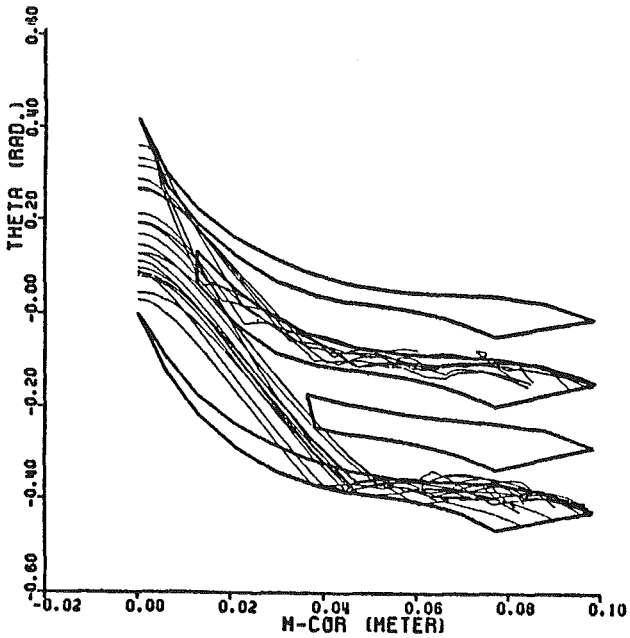

Fig. 2 (*a*)

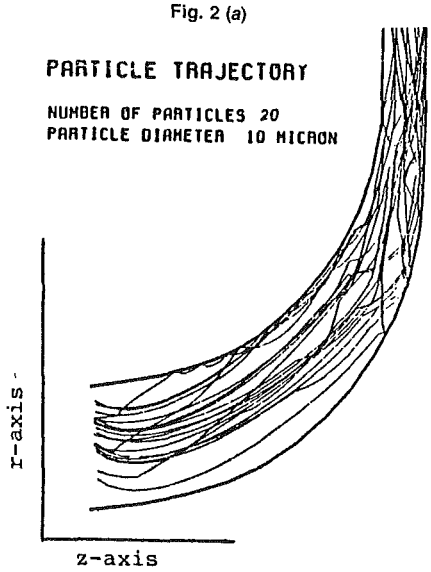

Fig. 2 (*b*)

Fig. 2 Sample of particle trajectories for 20 particles with particle diameter 10 μ in both (M-θ) and (r-z) planes

Nomenclature

A = cross-sectional area of the spherical particle, m^2
$\mathbf{a}$ = particle acceleration vector in the rotating frame, m/s
C_D = drag coefficient for spherical particle
$\mathbf{D}$ = drag force
E = erosion rate, mg of eroded material/g of colliding particles
$\mathbf{e}_r$, $\mathbf{e}_\theta$, $\mathbf{e}_z$ = unit vectors in the r, θ, and z directions
K_1, K_2, K_{12}, K_3 = constants defined in the erosion formula (5)
M = meridional coordinate, m
m_p = particle mass, kg
R_T = coefficient defined in the erosion rate correlation (5)
r, θ, z = radial, tangential, and axial coordinates
t = time, s
W = fluid velocity relative to the blade, m/s
β = the solid angle between the particle and the surface, rad
ρ = density, kg/m^3
ω = impeller rotational speed, rpm

Subscripts

n = normal to the solid surface
p = particle
t = tangential to the solid surface
1 = before collision
$2a$ = after collision

Superscripts

$\dot{}$ = first derivative with respect to time in the rotating frame, $\partial/\partial t$
$\ddot{}$ = second derivative with respect to time in the rotating frame, $\partial^2/\partial t^2$

Downloaded 01 Jun 2010 to 171.66.16.57. Redistribution subject to ASME license or copyright; see http://www.asme.org/terms/Terms_Use.cfm

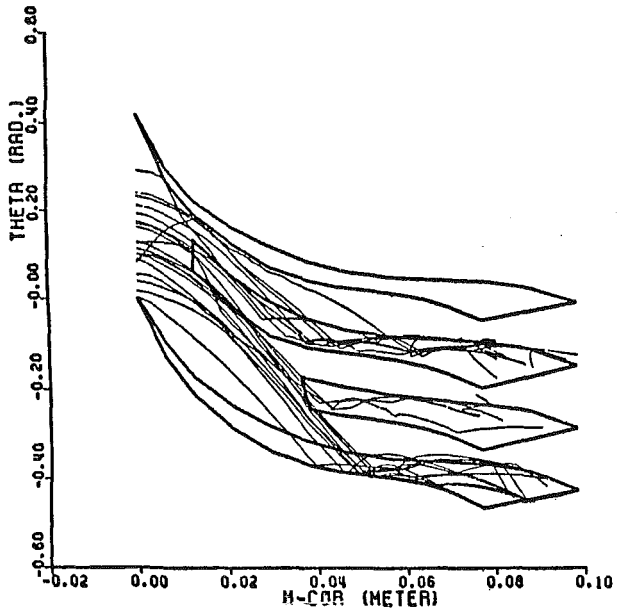

Fig. 3(a)

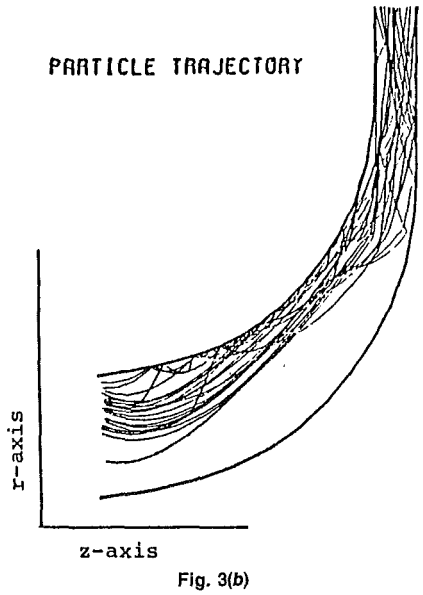

Fig. 3(b)

Fig. 3 Sample of particle trajectories for 20 particles with particle diameter 20 μ in both (M-θ) and (r-z) planes

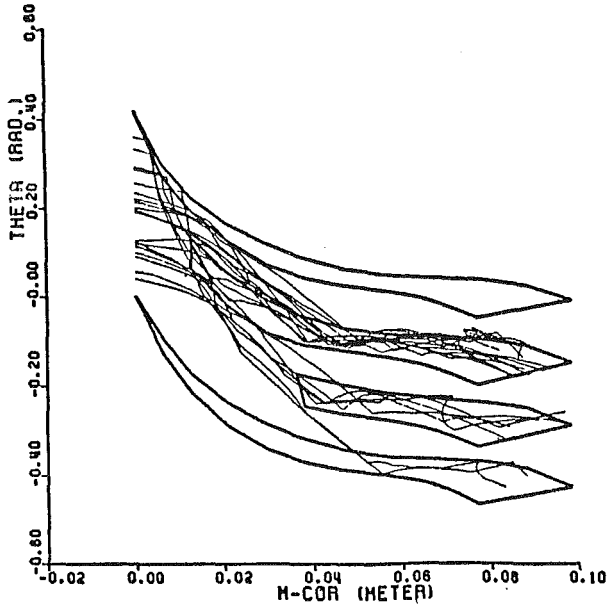

Fig. 4(a)

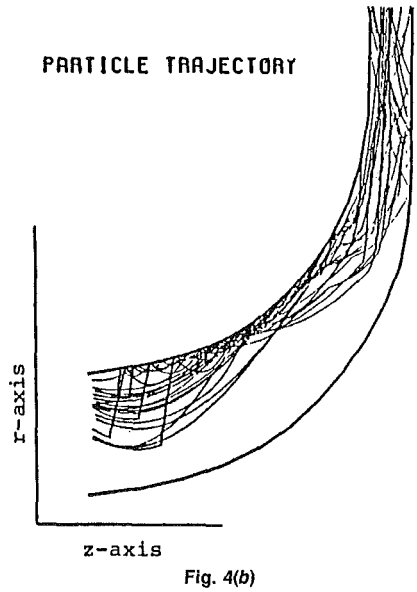

Fig. 4(b)

Fig. 4 Sample of particle trajectories for 20 particles with particle diameter 50 μ in both (M-θ) and (r-z) planes

$$\frac{V_{t2}}{V_{t1}} = 1.0 - 2.12\beta_1 + 3.0778\beta_1^2 - 1.1\beta_1^3$$

$$\frac{\beta_2}{\beta_1} = 1.0 + 2.6067\beta_1 - 5.708\beta_1^2 + 2.535\beta_1^3 \quad (4)$$

The erosion rates of the blades, hub, and casing surfaces were calculated using experimental data correlation [9]. These data represent the erosion rate as the ratio of target surface eroded mass to the mass of the impinging particles. It is well known that the erosion rate depends mainly on the particle velocity and impingement angles. Grant and Tabakoff [9] developed the following semi-empirical erosion equation

$$E = K_1 f_\beta V_{p_1}^2 \cos^2\beta_1 (1 - R_T^2) + K_3 V_{p_1}^4 \sin^4\beta_1 \quad (5)$$

where

$$f_\beta = \left\{1.0 + K_2\left[K_{12}\sin\left(\beta_1 \frac{90}{\beta_0}\right)\right]\right\}^2$$

$$R_T = 1.0 - 0.0017\, V_p \sin\beta_1$$

The values of the constants K_1, K_2, K_{12}, and K_3 for quartz particle impacting on 410 stainless steel target material are given as

$$K_1 = 6.07 \times 10^{-6}$$
$$K_{12} = 0.293328$$
$$K_3 = 5.56 \times 10^{-13}$$

The constant K_2 depends on the value of particle impingement angle β_1

$$K_2 = 1.0 \quad \text{for} \quad \beta_1 \le 2\beta_0$$
$$K_2 = 0.0 \quad \text{for} \quad \beta_1 > 2\beta_0$$

where β_0 is the impact angle where maximum erosion occurs.

Downloaded 01 Jun 2010 to 171.66.16.57. Redistribution subject to ASME license or copyright; see http://www.asme.org/terms/Terms_Use.cfm

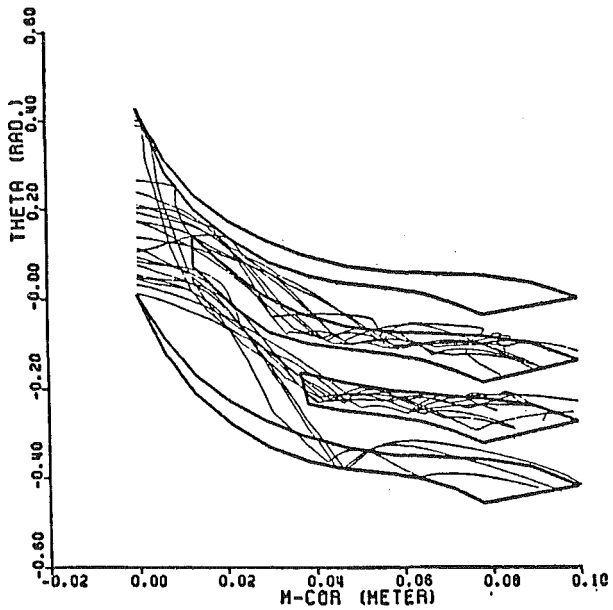

Fig. 5(*a*)

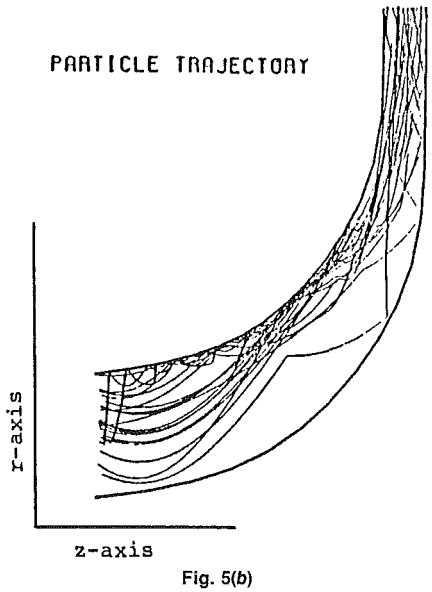

Fig. 5(*b*)

Fig. 5 Sample of particle trajectories for 20 particles with particle diameter 165 μ in both (M-θ) and (r-z) planes

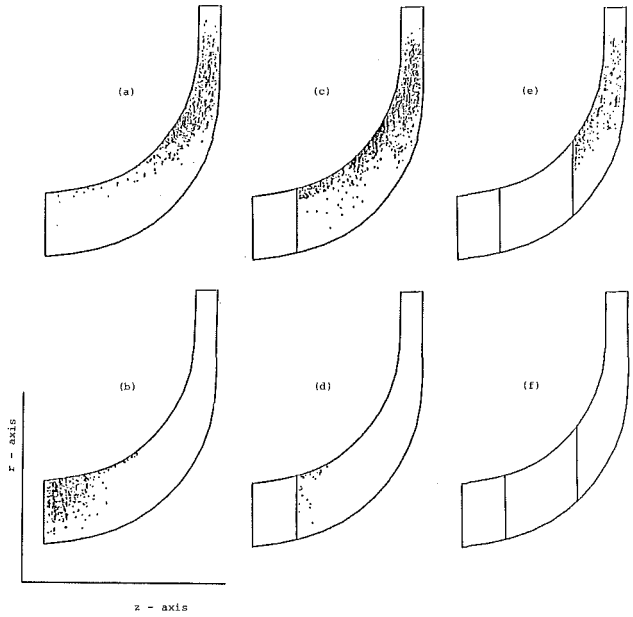

Fig. 6 Impact location on impeller blade for particles with diameter of 20 μ: (*a*) blade pressure surface; (*b*) blade suction surface; (*c*) first splitter pressure surface; (*d*) first splitter suction surface; (*e*) second splitter pressure surface; (*f*) second splitter suction surface

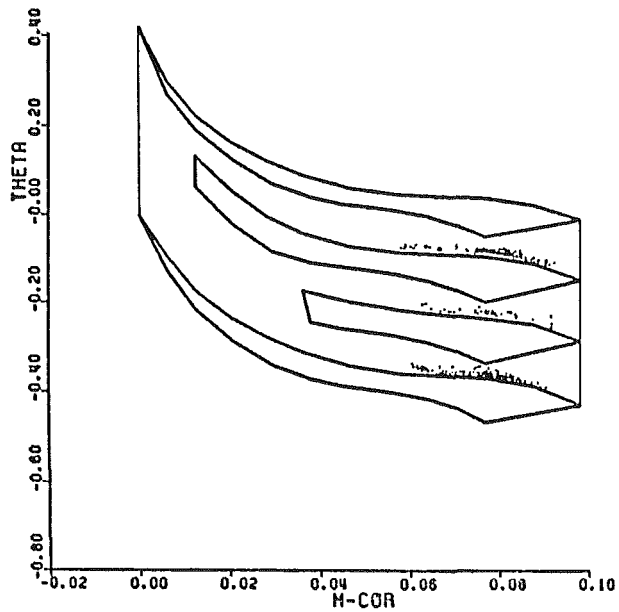

Fig. 7 Impact locations on impeller hub for 20 μ particle diameter

Results and Discussion

The particle trajectories through a compressor impeller with two different size splitters, as shown in Fig. 1, are calculated for different particle sizes. The following particle sizes are considered in the present analysis: 10, 20, 50, and 165 μ. All particles considered are quartz, with a specific mass of $\rho = 2680$ kg/m^3, and the impeller material is 410 stainless steel. The impeller's main data are:

Mass rate of air = 2.78 kg/s
Inlet inner radius = 0.04826 m
Inlet outer radius = 0.06587 m
Exit radius = 0.1193 m
Exit width = 0.0060 m
First splitter axial location = 0.0125 m
Second splitter axial location = 0.0332 m
Impeller axial width = 0.0481 m
Impeller rotational speed = 35,000 rpm

Particle trajectories were obtained for each size considering random particle distribution at impeller inlet. Also, inlet particle velocities were chosen at random.

The obtained particle trajectories for the above described impeller vary with the particle sizes. Figures 2–5 present a sample of the calculated trajectories for 20 particles of 10, 20, 50, and 165 μ. The centrifugal effect on larger particle sizes is more pronounced than that for the smaller particle sizes. Therefore, the particle trajectories are shifted to higher radii as the particle size increases especially in the axial part of the impeller channel. The smaller particle sizes are more affected by the gas flow field. This effect can be seen from the particle trajectory after the collision. Larger particle sizes have almost a straight path after the collision, while the smaller ones after the collision follow the main gas flow field. From the particle trajectory calculations the collision locations for different par-

Downloaded 01 Jun 2010 to 171.66.16.57. Redistribution subject to ASME license or copyright; see http://www.asme.org/terms/Terms_Use.cfm

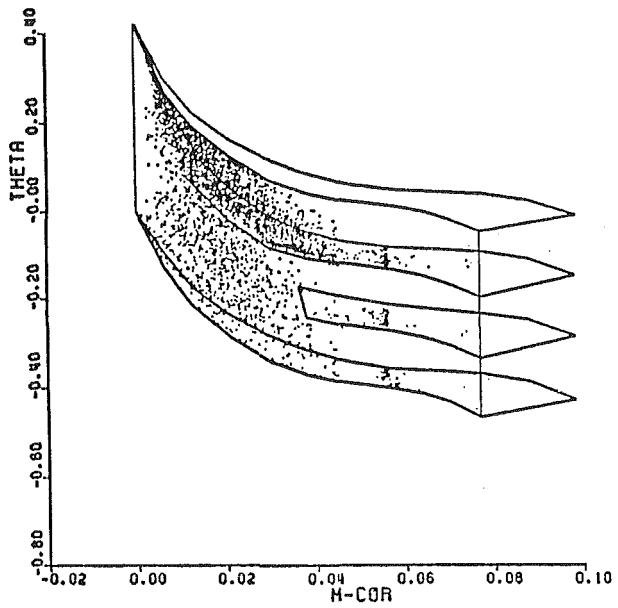

Fig. 8 Impact locations on impeller casing for 20 μ particle diameter

ticle sizes are determined. However, only a sample of collision locations with all impeller surfaces for particle diameter of 20 μ is presented. For this particle size, the trajectories and impact locations for 1824 particles entering the calculated impeller cascade segment, Fig. 1(*a*), were performed. The obtained impact locations are shown in Figs. 6–8 for each surface. Figure 6(*a*) shows the blade pressure surface particle impact. From inspection of this figure, it can be seen that the particle collisions on the blade pressure surface are distributed over the entire surface but with the largest impacts in the middle area. For the suction surface, as shown in Fig. 6(*b*), the collisions are mainly closer to the blade leading edge. Figures 6(*c–f*) show the particle collision locations on the two impeller splitters. Again the impacts are mostly on the splitter pressure sides. The impeller hub is subjected to fewer collisions than the impeller casing as shown in Figs. 7 and 8 correspondingly. This is due to the centrifugal effect on the particles. The impacts on the hub are concentrated at the impeller exit at the roots of the blade pressure surfaces and the impacts on the casing are concentrated on almost two thirds of the area starting from the gas entrance.

The surface erosion is calculated using the correlation data given in [9]. Each surface is divided into a set of mesh cells. The erosion caused by particle impacts within the cell is calculated and summed up. The erosion contours were obtained by linear interpolation of the erosion sums. In order to present the most affected part of the local surfaces, the erosion contours are calculated and plotted. The actual amounts of erosion from each surface for different particle size are presented in Tables 1–4. The erosion rates are calculated in mass rate (mg/g) and in volume rate (cm^3/g) of the material removed. Figures 9–12 present the erosion contours for each surface for 20 μ particles. The erosion rate, material actually removed from the blade surfaces, depends on the particle size, as shown in Tables 1–4. For the same particle size, it is observed from the tables that the pressure surfaces are more eroded than the suction surfaces. The pressure surfaces are eroded over the larger part of the blade middle areas as shown in Figs. 9(*a*), 10(*a*), and 11(*a*). The blade and splitter suction surfaces are mostly eroded closer to their leading edges, as illustrated in Figs. 9(*b*) and 10(*b*). The suction surface of the second splitter is almost not affected by the particle presence as shown in Fig. 11(*b*). This is due to the location of the second splitter. The erosion on the impeller hub is in the areas

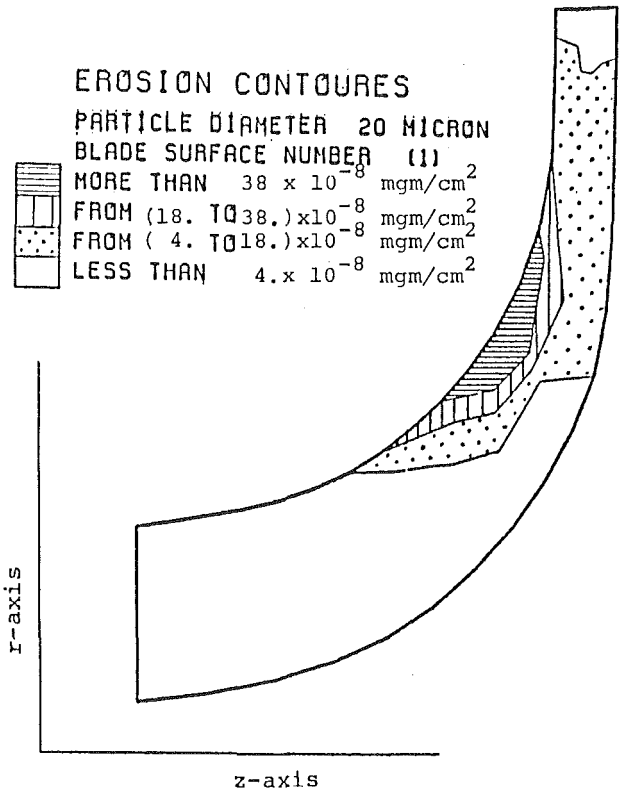

Fig. 9 (*a*)

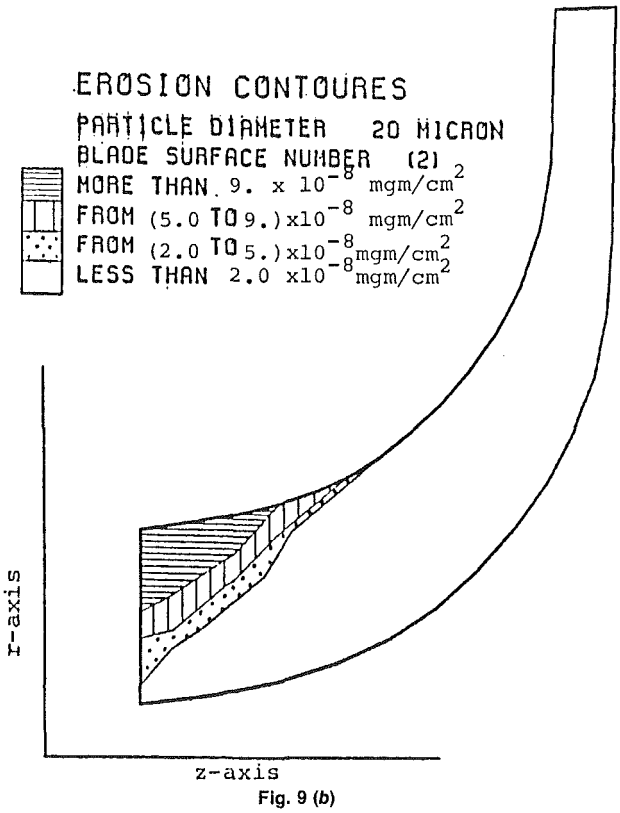

Fig. 9 (*b*)

Fig. 9 Erosion contours for impeller blade caused by 20 μ particles: (*a*) blade pressure surface; (*b*) blade suction surface

closer to the blade roots of the pressure surfaces in the radial part of the impeller channel as shown in Fig. 12(*a*), while the casing is mainly affected in the axial part of the channel and in the beginning of the radial part as shown in Fig. 12(*b*). From the data presented in Tables 1–4, it can be seen that the casing surface is more eroded than the hub surface.

Downloaded 01 Jun 2010 to 171.66.16.57. Redistribution subject to ASME license or copyright; see http://www.asme.org/terms/Terms_Use.cfm

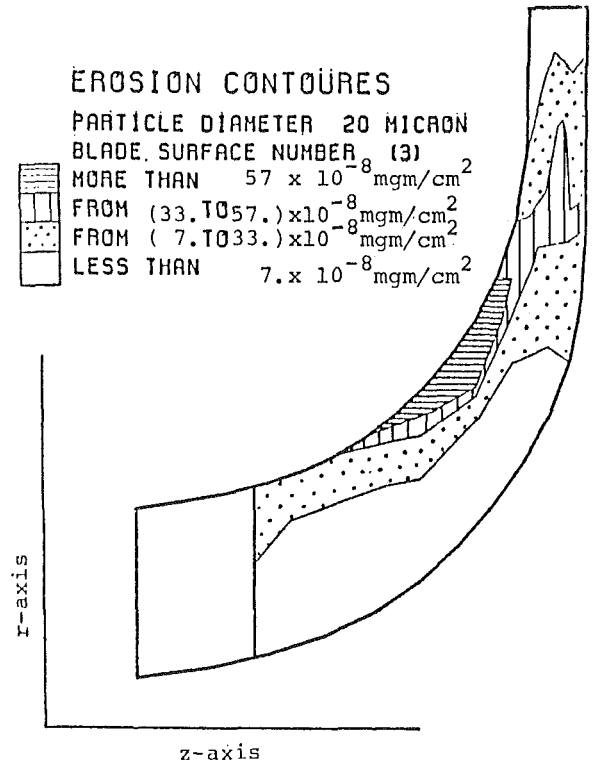

Fig. 10 (*a*)

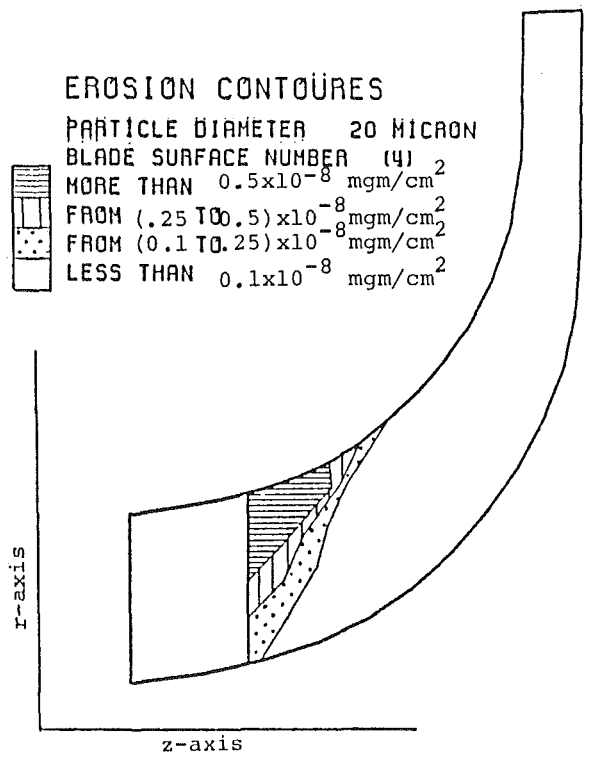

Fig. 10 (*b*)

Fig. 10 Erosion contours for impeller first splitter caused by 20 μ particles: (*a*) first splitter pressure surface; (*b*) first splitter suction surface

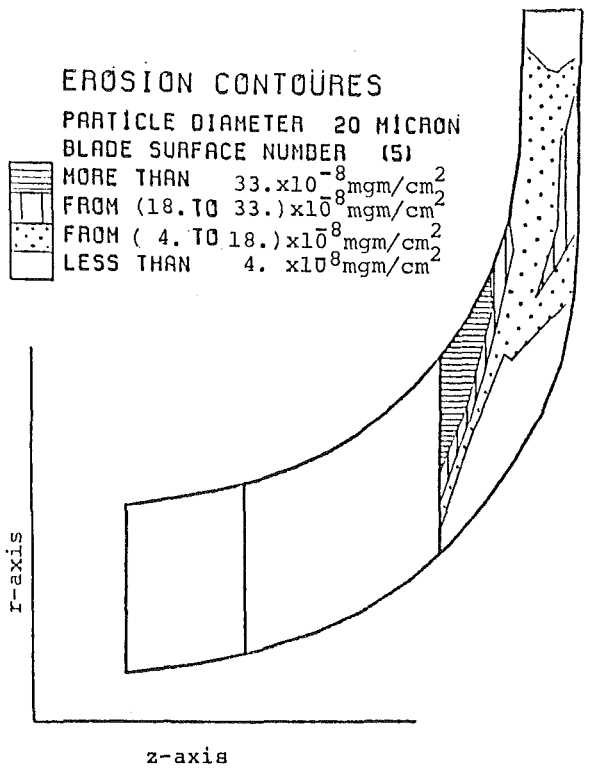

Fig. 11(*a*)

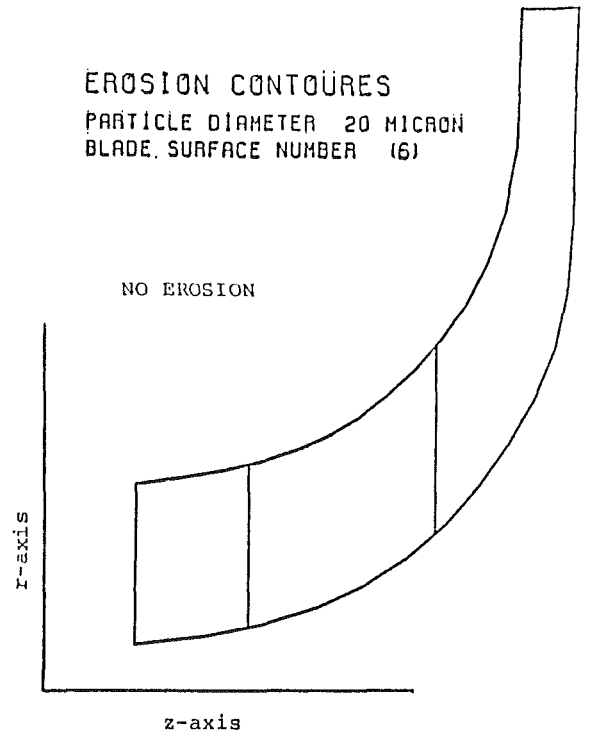

Fig. 11(*b*)

Fig. 11 Erosion contours for impeller second splitter caused by 20 μ particles: (*a*) second splitter pressure surface; (*b*) second splitter suction surface

Conclusion

Flow calculations were carried out through a centrifugal compressor impeller with two splitters. Particle trajectories were obtained for particles with different diameters. The collision locations for all surfaces of the impeller as well as for hub and casing were determined and the corresponding erosion rates calculated. All pressure surfaces were subjected to higher erosion rate than the suction surfaces. The erosion rate on the impeller hub area is mainly in the area connecting the blade and splitter pressure surfaces on the radial part of the impeller channel. The casing erosion rate is mainly in the axial impeller part area and is much more eroded than the hub area.

Downloaded 01 Jun 2010 to 171.66.16.57. Redistribution subject to ASME license or copyright; see http://www.asme.org/terms/Terms_Use.cfm

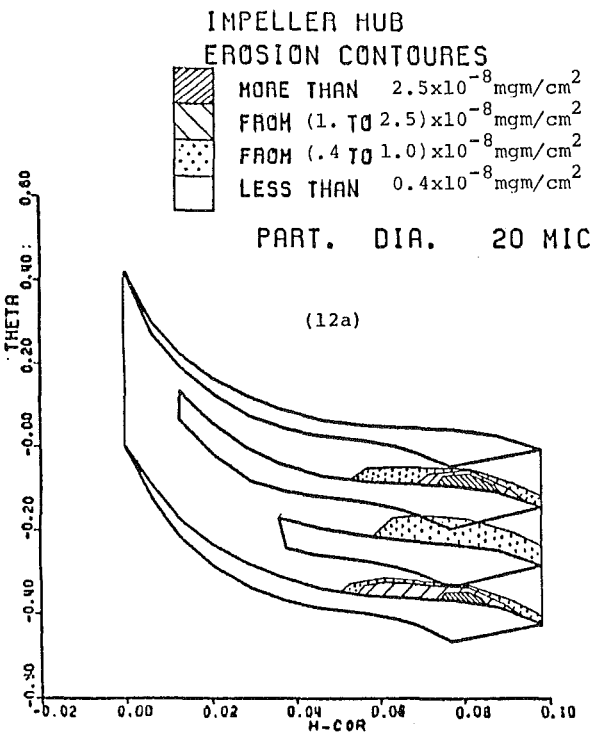

Fig. 12 (a)

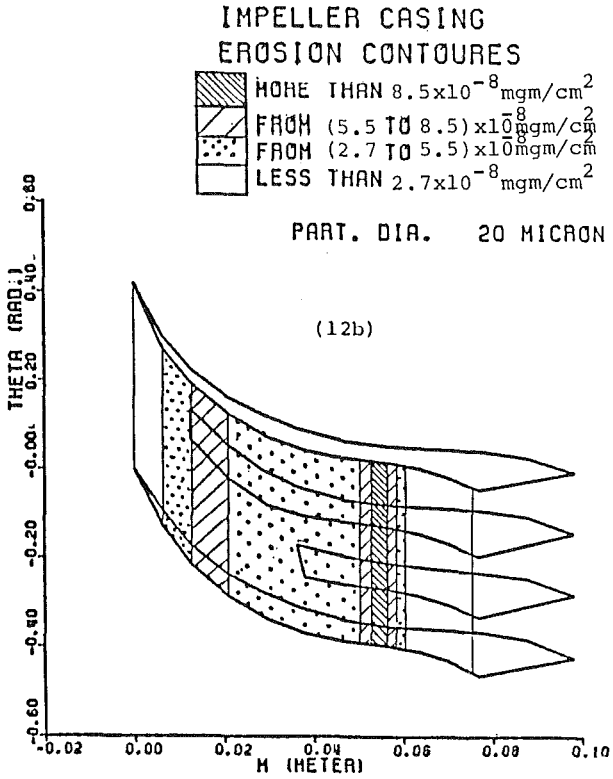

Fig. 12 (b)

Fig. 12 Erosion contours for impeller hub and casing caused by 20 μ particles: (a) hub; (b) casing

Table 1 Erosion rates for particle diameter, $D_p = 10\ \mu$

Surface	Mass erosion rates		Volume erosion rates		Percent of actual erosion
	$(mg/g)10^3$	$mg \times 10^6$	$(cm^3/g)10^6$	$cm^3 \times 10^{10}$	
Blade pressure surface	7.984	0.05772	1.01707	0.07353	31.386
Blade suction surface	1.872	0.00911	0.23847	0.01161	4.956
First splitter pressure surface	4.941	0.06723	0.62943	0.08564	36.559
First splitter suction surface	1.998	0.000135	0.25452	0.00017	0.073
Second splitter pressure surface	7.041	0.00577	0.89694	0.00735	3.138
Second splitter suction surface	–	–	–	–	–
Impeller hub	10.947	0.01055	1.39452	0.01344	5.737
Impeller casing	6.776	0.03339	0.86319	0.04254	18.160

Table 2 Erosion rates for particle diameter, $D_p = 20\ \mu$

Surface	Mass erosion rates		Volume erosion rates		Percent of actual erosion
	$(mg/g)10^3$	$mg \times 10^6$	$(cm^3/g)10^6$	$cm^3 \times 10^{10}$	
Blade pressure surface	13.498	0.2606	1.71945	0.33197	19.508
Blade suction surface	0.8371	0.0316	0.10664	0.04026	2.366
First splitter pressure surface	7.3691	0.3082	0.93874	0.39261	23.072
First splitter suction surface	1.8900	0.00191	0.24076	0.00243	0.143
Second splitter pressure surface	8.6928	0.0797	1.10736	0.10157	5.969
Second splitter suction surface	–	–	–	–	–
Impeller hub	15.891	0.05726	2.02433	0.07294	4.286
Impeller casing	8.783	0.5965	1.11885	0.75987	44.655

Table 3 Erosion rates for particle diameter, $D_p = 50\ \mu$

Surface	Mass erosion rates		Volume erosion rates		Percent of actual erosion
	$(mg/g)10^3$	$mg \times 10^6$	$(cm^3/g)10^6$	$cm^3 \times 10^{10}$	
Blade pressure surface	11.7476	2.6293	1.49651	3.34943	16.094
Blade suction surface	0.7781	0.5801	0.09912	0.73898	3.551
First splitter pressure surface	9.5331	4.7489	1.21441	6.04955	29.067
First splitter suction surface	1.1768	0.0900	0.14991	0.11465	0.551
Second splitter pressure surface	11.158	1.9944	1.42140	2.54064	12.208
Second splitter suction surface	–	–	–	–	–
Impeller hub	19.7718	1.2312	2.51870	1.56841	7.536
Impeller casing	6.2269	5.0636	0.79324	6.45045	30.994

Downloaded 01 Jun 2010 to 171.66.16.57. Redistribution subject to ASME license or copyright; see http://www.asme.org/terms/Terms_Use.cfm

Table 4 Erosion rates for particle diameter, $D_p = 165\ \mu$

Surface	Mass erosion rates		Volume erosion rates		Percent of actual erosion
	$(mg/g)10^3$	$mg \times 10^6$	$(cm^3/g)10^6$	$cm^3 \times 10^{10}$	
Blade pressure surface	13.5449	117.8260	1.72547	150.0968	16.955
Blade suction surface	0.8134	25.1386	0.10362	32.0237	3.617
First splitter pressure surface	9.4952	169.0864	1.20958	215.3967	24.330
First splitter suction surface	0.9826	3.9208	0.12517	4.9947	0.564
Second splitter pressure surface	12.1482	97.6357	1.54754	124.3767	14.050
Second splitter suction surface	3.000	0.0019	0.382172	0.00242	0.0024
Impeller hub	21.1947	50.1006	2.69996	63.8224	7.209
Impeller casing	6.4322	231.2332	0.81939	294.5646	33.273

Acknowledgments

This research was sponsored by the U.S. Army Research Office–Durham, under Contract No. DAAG29-82-K-0029.

References

1 Tabakoff, W., and Hussein, M. F., "Trajectories of Particles Suspended in Fluid Flow Through Cascades," *Journal of Aircraft*, Vol. 8, No. 1, 1971.

2 Grant, G., and Tabakoff, W., "Erosion Prediction in Turbomachinery Resulting From Enviromental Solid Particles," *Journal of Aircraft*, Vol. 12, No. 5, 1975.

3 Hamed, A., and Fowler, S., "Erosion Pattern of Twisted Blades by Particle Laden Flows," ASME JOURNAL OF ENGINEERING FOR POWER, Vol. 105, 1983, pp. 839–843.

4 Clevenger, W. B., and Tabakoff, W., "Erosion in Radial Inflow Turbines," Vol. I-V, NASA CR-134700, 1974.

5 Elfeki, S., and Tabakoff, W., "Particulate Flow Solutions Through Centrifugal Impeller With Two Splitters," ASME Paper No. 86-GT-130.

6 Katsanis, T., and McNally, W. D., "Revised Fortran Program for Calculating Velocities and Streamlines on the Hub–Shoud Midchannel Stream Surface of an Axial, Radial, or Mixed-Flow Turbomachine or Annular Duct," 2 volumes, NASA TND-8430 and TND-8431.

7 McFarland, E. R., "A Rapid Blade-to-Blade Solution for Use in Turbomachinery Design," ASME JOURNAL OF ENGINEERING FOR GAS TURBINES AND POWER, Vol. 106, 1984, pp. 376–382.

8 Ball, R., and Tabakoff, W., "An Experimental Investigation of the Particle Dynamics of Quartz Sand Impacting 6A1-4V Titanium and 410 Stainless Steel in an Erosive Environment," Report No. 74-43, Oct. 1974.

9 Tabakoff, W., "Erosion Rate for Quartz and 410 Stainless Steel," Internal Report, University of Cincinnati, Cincinnati, OH, 1981.

Downloaded 01 Jun 2010 to 171.66.16.57. Redistribution subject to ASME license or copyright; see http://www.asme.org/terms/Terms_Use.cfm

Laser Velocimeter Measurements in Shrouded and Unshrouded Radial Flow Pump Impellers

C. P. Hamkins
Development Engineer,
KSB AG,
Frankenthal, West Germany

R. D. Flack
Associate Professor,
Department of Mechanical and
Aerospace Engineering,
University of Virginia,
Charlottesville, VA 22901

Shrouded and unshrouded versions of a four-vaned radial flow impeller with a design flow coefficient of 0.063 were tested in a volute pump using a two-component frequency-shifted laser velocimeter. Velocity profiles were measured at six flow rates and at four radial and six circumferential positions in the volute. The variations of the velocity from blade to blade and in the axial direction were measured and are presented. A passage vortex caused by tip leakage and relative casing wall velocity was found in the unshrouded impeller. The tip leakage did not accumulate in the suction wake region; the suction wake region was only 30 to 50 percent as large in the unshrouded impeller as compared to the shrouded impeller. The slip was 30 percent higher in the unshrouded impeller and the variation of slip with flow rate is presented. At no measured position in the impellers did the slip factor reach unity; the closest approach was 0.90. Reverse loadings of the vanes at outer radii were found for flow rates below the impeller/volute matching point for both impellers.

Introduction

Unshrouded pump impellers are very sensitive to the tip clearance – when the clearance is increased, the head and efficiency decrease, and the absorbed power usually falls [1]. The dissipation of the tip leakage in a vortex is a direct energy loss resulting in lower delivered head. At the same time the blades unload and reduce the required torque.

A number of studies on the performance of centrifugal pump impellers and experimental methods have been reviewed, for example, in [2, 3]. All of these references are applicable to the present research. However, for the sake of brevity only the references covering the effects of impeller shrouding/unshrouding will be discussed.

Lakshminarayana [4] proposed a vortex model of the tip clearance leakage for axial flow machines. The leakage fluid was assumed to form an energy-dissipating vortex in the passage. The vortex strength is computed using an assumption for the blade unloading in the tip region. Flow deviation and energy losses due to the leakage can be calculated from the geometry of the vortex. Figure 1 shows the results of a test in a stationary cascade. There is good evidence for a vortex core in which the losses are concentrated.

Later Lakshminarayana et al. [5] performed a hot-wire anemometer survey of an axial flow compressor blade passage. The tip leakage was in the form of a jet within the blade row, and traveled farther from the suction side than in a stationary cascade. The jet rolled up between the midpassage and pressure surface near the tip region. An intense viscous and leakage flow interaction occurred in the 10 percent of the passage on the casing wall, with the highest turbulence in the region of largest velocity deficiency. The boundary layer on the wall was energized by the leakage.

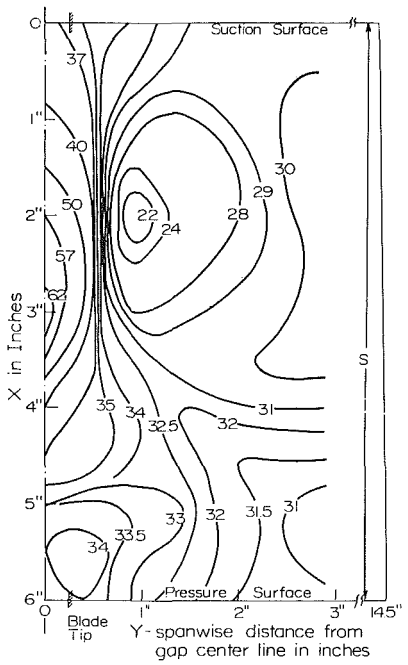

Fig. 1 Experimental flow deviation angles in a stationary cascade with tip leakage (deg from radial; from [4])

Hoshide and Nielsen [6] studied the effects of tip clearance for radial flow pumps. They postulated an energy loss in the clearance based on an orifice-type relationship. The flow deviation was accommodated by adding the leakage to the im-

Contributed by the Gas Turbine Division of THE AMERICAN SOCIETY OF MECHANICAL ENGINEERS and presented at the 31st International Gas Turbine Conference and Exhibit, Düsseldorf, Federal Republic of Germany, June 8–12, 1986. Manuscript received at ASME Headquarters January 24, 1986. Paper No. 86-GT-129.

 Copyright © 1987 by ASME

Downloaded 01 Jun 2010 to 171.66.16.57. Redistribution subject to ASME license or copyright; see http://www.asme.org/terms/Terms_Use.cfm

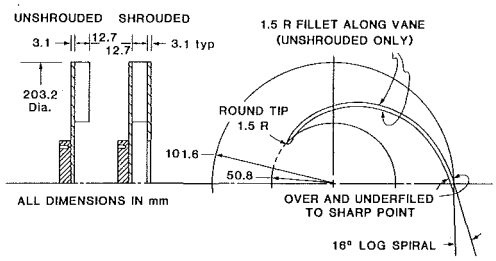

Fig. 2 Impeller geometry

peller throughflow. Although this approach approximates the overall pump performance, it is not solidly based on the mechanics of the leakage. Hoshide and Nielsen also did extensive pressure measurements on the blades which show an unloading with increasing clearance.

Howard and Kittmer [7] measured passage velocities in a radial impeller with shrouded and unshrouded configurations. In the shrouded version, boundary layer flow was swept along both shrouds from pressure to suction sides, creating two counterrotating passage vortices. In the unshrouded impeller, the tip leakage and relative wall motion caused only one large vortex.

The present research addresses the question of whether the axial flow models are applicable to low specific speed radial flow pump impellers. The effects which filled 10 percent of the axial machine passage width are likely to dominate in the narrow radial flow passage, and should have more drastic effects. To evaluate the effects a clear plexiglass pump with two different clear impellers was tested at different flow rates. A two-directional laser velocimeter (LV) was used to map the flow field in the impeller and volute regions. The differences between shrouded and unshrouded impellers in terms of velocity profiles, flow deviation, and angular momentum development are addressed and results are presented. The data are used to evaluate the slip factor and can also be used as benchmark data for computational methods currently under development.

Experimental Equipment and Procedures

Pump and Flow Loop. The centrifugal pump used in this study is a radial flow machine of constant flow width (12.7 mm). The geometry is shown in Figs. 2–4. The impeller (Fig. 2) has four blades with constant blade angles of 16 deg and discharges into a 7.0 deg log spiral volute of the same width. The pump was constructed of plexiglass and laser velocimeter measurements were possible in the windows shown in Fig. 3. The walls of the casing are 50.8 mm thick plexiglass except in the window regions, where the thickness is reduced to 9.5 mm to allow better transmission of the laser beams.

The volute of the pump is a separately adjustable insert. It can be adjusted off center to study an impeller operating eccentrically in the volute. For this study the volute was "centered" around the impeller so that the volute area was linearly increasing with circumferential position. The tip of the cutwater is at an angle $\theta = 7$ deg.

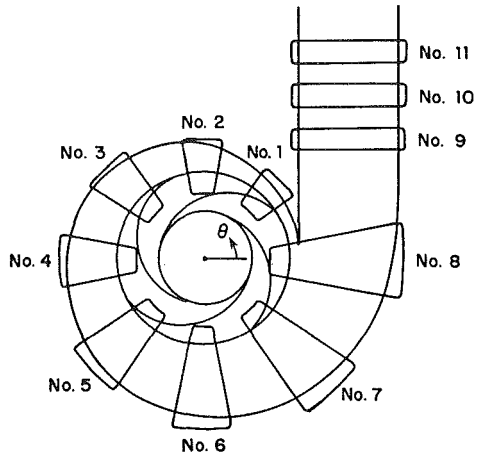

Fig. 3 Impeller/volute assembly

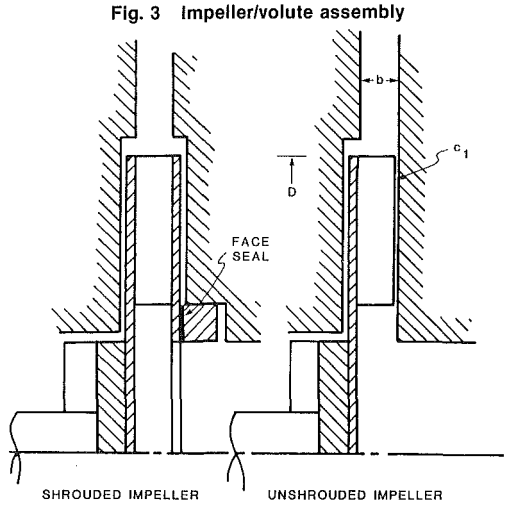

Fig. 4 Impeller/casing assembly

The flow loop is conventional and consists of a 76.2-mm-dia pipe connected to a tank open to the atmosphere. The flow rate was measured with an orifice plate downstream of the discharge. The total developed head was measured with static pressure taps located in the suction pipe 5 diameters upstream of the impeller and in the discharge of the volute just beyond window 11 in Fig. 3. The outputs of the taps were recorded with vertical water manometers. There are flow straighteners 19 pipe diameters before the pump suction side and 9 diameters before the orifice plate. The pump flow rate was set with a globe valve downstream of the orifice plate.

Nomenclature

A = passage area
b = passage width
c_1 = tip clearance
C = velocity in stationary frame
D = impeller diameter
H = total head produced by pump
h_0 = slip factor (defined in text)
N = rotational speed
N_s = specific speed $= NQ^{1/2}/H^{3/4}$
Q = net flow rate through impeller
r = radius
t = blade thickness
u = impeller peripheral speed
w = velocity in rotating frame
z = number of blades
β = blade angle
ζ = blade-to-blade parameter
θ = angular position, Fig. 3
ϕ = flow coefficient $= Q/2\pi r_2 b_2 u_2$
ψ = angular momentum parameter
$\psi_1 = r\tilde{C}_\theta/r_2 u_2$ (velocity plots)
$\psi_2 = gH/u_2^2$ (head plots)
ω = angular rotation frequency

Subscripts

p = pressure side
r = radial direction
s = suction side
t = volute throat
θ = tangential direction
1 = impeller inlet
2 = impeller exit

Superscripts

$\tilde{}$ = mass averaged across a blade passage
$\hat{}$ = area averaged across a blade passage

Downloaded 01 Jun 2010 to 171.66.16.57. Redistribution subject to ASME license or copyright; see http://www.asme.org/terms/Terms_Use.cfm

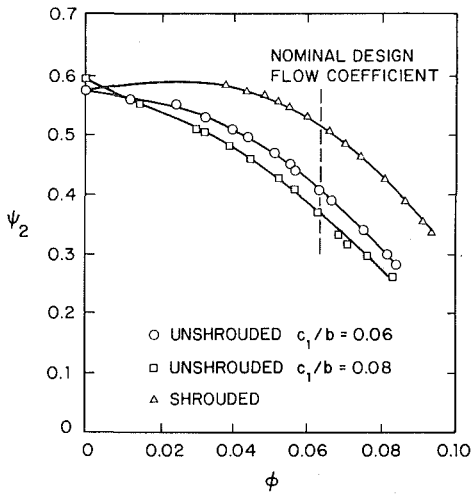

Fig. 5 Head-flow characteristics

The 25.4-mm drive shaft is supported by two ball bearings. Axial positioning and tip clearances (c_1, see Fig. 4) were set with an adjustable sleeve against the pump end (inboard) bearing inner race. The shaft was driven with a belt drive to an induction motor. The belt pulley was placed near the outboard bearing to eliminate transmitted deflections to the impeller. The shaft torque was not measured. The pump running speed is 620 rpm, and the nominal design flow rate is 31.5 l/s (ϕ = 0.063, N_s = 1200 US units).

Figure 5 shows the total head flow characteristics of the two impellers. Two tip clearances were tested for the unshrouded impeller (c_1/b = 0.06 and 0.08). The velocity head was computed using the average velocities at the pressure tap cross sections. For both clearances the unshrouded impeller produces significantly lower head than the shrouded version. For all of the following LV results a nondimensional tip clearance c_1/b of 0.06 was used. Further details of the pump can be found in Hamkins [8], Flack and Lanes [9], and Thomas et al. [3].

Laser Velocimeter and Shaft Encoder. The laser velocimeter is a four-beam frequency-shifted system, operated in a forward scatter mode. The basic system is shown in Fig. 6. Two pairs of beams create two sets of perpendicular interference fringes in the probe volume. The velocity of the fluid is determined by measuring the frequency of the light scattered by particles moving through the interference fringes. The entire optical system is mounted on a mill bed, so that positioning the probe volume in all three directions is possible.

In each beam pair the two beams have slightly different frequencies due to frequency shifting. An apparent motion of the fringes results and allows a measurement of the velocity direction as well as magnitude. Measuring velocities in regions of flow reversals is also possible. The frequency shifting is accomplished with a Bragg cell, which performs the dual functions of beam separation and frequency shifting. By rotating the Bragg cell through any angle the two sets of perpendicular fringes were also rotated through the same angle. Thus, the velocities in any two perpendicular directions (A and B) can be measured. The two sets of beams have different shift frequencies, so that the signal from a single photomultiplier tube can be separated electronically to simultaneously indicate the two perpendicular velocity components.

The velocity is determined from the frequency of scattered light pulses from particles passing through the fringes in the probe volume. The signal processing is accomplished with two burst-type processors having adjustable threshold levels and five/eight count comparisons with adjustable tolerances. Coincidence checking of the signals from each beam pair was done and only signals occurring simultaneously on both channels were considered valid.

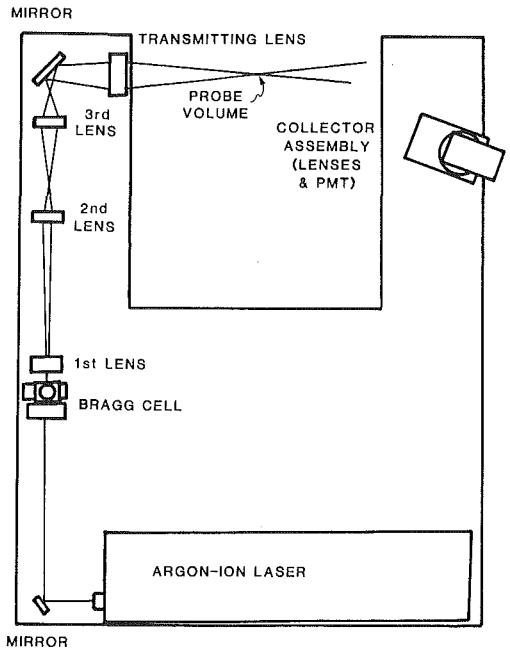

Fig. 6 Laser velocimeter schematic

The outputs of the two processors were two voltages calibrated to velocities. The impeller angular position was converted into voltage with a shaft encoder; the voltage varies linearly from 0 to 10 V as shaft angular position varies from 0 to 2π. When valid signals occurred simultaneously on both channels, three voltages were recorded: velocity for channel A, velocity for channel B, and the shaft angular position. Each set of data was stored with a dedicated microcomputer onto floppy disks for further processing.

To obtain LV signals of good quality, appropriate particle seeding in the flow must be present. Microscopic investigations indicated that tap water, after being filtered (using an odor and taste filter), contained particles 3 μm and less in diameter and of suitable scattering properties. The water in the test facility was filtered upon initial filling and then periodically recirculated through the filters. Valid signals with high visibilities were achieved using this method.

Data Reduction. In the data processing stage the following were performed:

1 The data were sorted into 256 separate groups each representing a particular shaft angular position.

2 For each group, the average velocity and turbulence intensity were computed and transformed to the standard (r, θ) coordinate system.

After the first two steps were performed the effective blade-to-blade velocity distribution was known for the impeller since an average velocity is associated with each shaft position from 0 to 2π. To obtain more accurate overall results for the blade-to-blade velocity profiles, passage averaging, step 3, was performed.

3 The profiles in the four impeller passages were averaged together (each has 64 groups) to obtain an average passage profile.

To obtain sufficient accuracy with a laser anemometer, a large sample size is required. In this study 5000 data points were collected at each measurement location. The signals occur at random angular positions of the shaft but are sorted into 256 "shaft angle bins" using the shaft encoder data so that the correct average could be computed for each shaft position. Hence, an average of 20 points was used to compute an average velocity for each shaft position.

After a separate average was computed for each of the 256 shaft angle bins, the velocity distributions of the four impeller

Downloaded 01 Jun 2010 to 171.66.16.57. Redistribution subject to ASME license or copyright; see http://www.asme.org/terms/Terms_Use.cfm

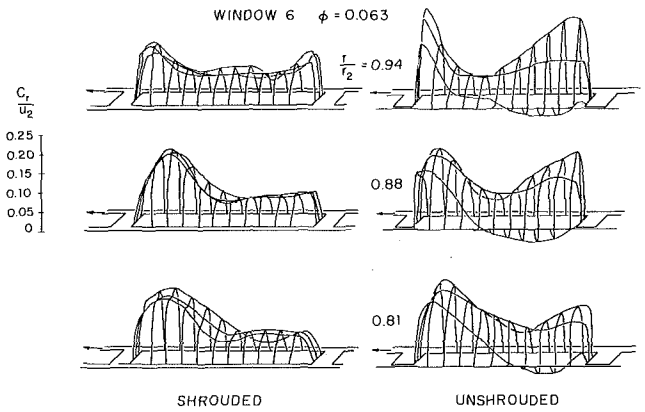

Fig. 7 Radial velocity for shrouded and unshrouded impellers

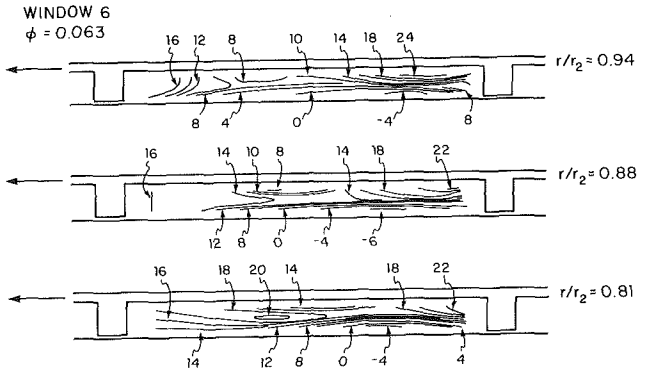

Fig. 8 Flow angle contours for the unshrouded impeller (deg from tangential)

channels were averaged together into a single average passage of 64 angle bins, each containing an average of 80 data signals to produce the profiles presented in this paper. Before averaging, the four profiles were identical to within the uncertainty of the data.

Overall area and mass-averaged velocities are computed from the velocity distribution across a blade passage at one particular position in the volute according to

$$\hat{C}_r = \frac{1}{2\pi}\int_0^{2\pi} C_r d\theta$$

$$\tilde{C}_\theta = \frac{\int_0^{2\pi} C_r C_\theta d\theta}{\int_0^{2\pi} C_r d\theta} \tag{1}$$

An angular momentum parameter defined by

$$\psi_1 = r\tilde{C}_\theta / r_2^2 \omega \tag{2}$$

and a slip factor following Busemann [10]

$$h_0 = \frac{Q \cot \beta}{\left(2\pi r - \frac{zt}{\sin \beta}\right) br\omega} + \frac{\tilde{C}_\theta}{r\omega} \tag{3}$$

are used to correlate the data. Usually, slip is only defined at the exit of an impeller. However, in a somewhat unorthodox usage, for this paper the slip factor is also defined and calculated in the interior of the impeller to show the development of the slip. Furthermore, the slip is calculated based on a mass flow averaged circumferential velocity across the blade passages and not the center span velocities.

Since measuring velocities exactly at the impeller exit was not possible, the slip factor at impeller exit was deduced from measurements just outside the impeller ($r/r_2 = 1.005$) according to:

$$h_{0_2} = \frac{Q \cot \beta}{\left(2\pi r_2 - \frac{zt_2}{\sin \beta_2}\right) b_2 r_2 \omega} + \frac{r\tilde{C}_\theta}{r_2^2 \omega} \tag{4}$$

Uncertainty. The probe volume could be positioned within an accuracy of 0.025 mm radially and 1.0 mm axially. The angular uncertainty of the laser beam orientation with respect to the reference axes was 0.6 deg; this is the limiting factor in computing flow direction. The uncertainty in average velocity components is approximately $0.013u_2$ with the sample sizes used. ψ is uncertain by 1.5 percent, the slip factor h_0 is uncertain by 1.0 percent, and the uncertainty in ϕ is 0.0006. These uncertainties do not include the effect of positional uncertainty in the presence of velocity gradients.

The position of the probe volume is uncertain, particularly in the axial direction. Since there are spatial velocity gradients, a misplaced probe volume will measure the incorrect velocity. The position uncertainty and velocity gradients result in an additional uncertainty of $0.014u_2$ in the radial component and $0.002u_2$ in the tangential component, yielding total uncertainties of $0.019u_2$ and $0.013u_2$ for the radial and tangential components, respectively.

Alternatively, the velocities are uncertain by $0.013u_2$, but the position at which to assign them is uncertain, as given above. Finally, the uncertainties in the pump construction itself are $D_2 \pm 0.02$ percent, $b \pm 2$ percent, impeller runout $\pm$ 0.2 percent of D_2, and front clearance $\pm$ 2 percent of b.

Discussion of Results

Blade-to-blade velocity profiles at the axial center of both impellers were measured in six different windows (1, 4, 5, 6, 7, and 8) for four radii and two flow rates. The angular positions of the measurements for the six windows were θ = 45, 180, 225, 270, 315, and 0 deg, respectively. In addition, blade-to-blade velocity profiles were measured at the axial center of window 6 for seven flow rates. Finally, axial traverses were performed in window 6. Only representative data are included herein.

Passage Vortex. Figure 7 shows the radial velocity profiles in window 6 at three radial positions for a flow rate at the design point of $\phi = 0.063$. Figure 7 shows a striking difference between the flow fields in the shrouded and unshrouded impellers. In the unshrouded impeller a strong axial gradient of velocity is present near the pressure side of the passage. The radial component of the velocity is much larger on the rear of the impeller than near the casing wall. This is an indication of a vortex in the passage. The shrouded impeller has no such strong gradient.

Figure 8 shows a contour plot of the flow angle for three radial positions for the unshrouded impeller. The flow angle is defined as the angle the relative velocity vector makes with the tangential direction. One should note the similarity to Lakshminarayana's data [4] in Fig. 1. The results in Fig. 1 were for an axial machine; as a result, Fig. 1 should be rotated -90 deg for a one-to-one comparison with the present data. Interestingly, the vortex seems to migrate from midpassage at a radius of $r/r_2 = 0.81$ to near the pressure side at the outer radii. Lakshminarayana's early results [4] were for a stationary cascade, but his later work [5] showed that in the rotating passage the wall velocity tends to carry the vortex to the pressure side. His results also showed a migration of the vortex to the pressure side of the passage. This migration has been confirmed here for a radial flow machine.

Finally, the tangential velocity did not vary greatly axially in

Downloaded 01 Jun 2010 to 171.66.16.57. Redistribution subject to ASME license or copyright; see http://www.asme.org/terms/Terms_Use.cfm

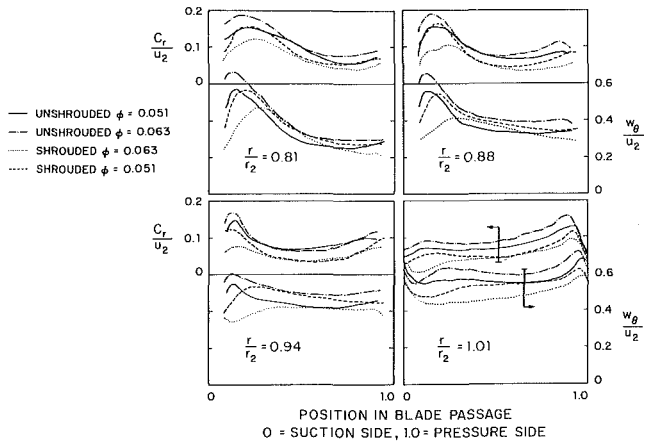

Fig. 9 Average velocity profiles from six windows at the axial center of the impeller

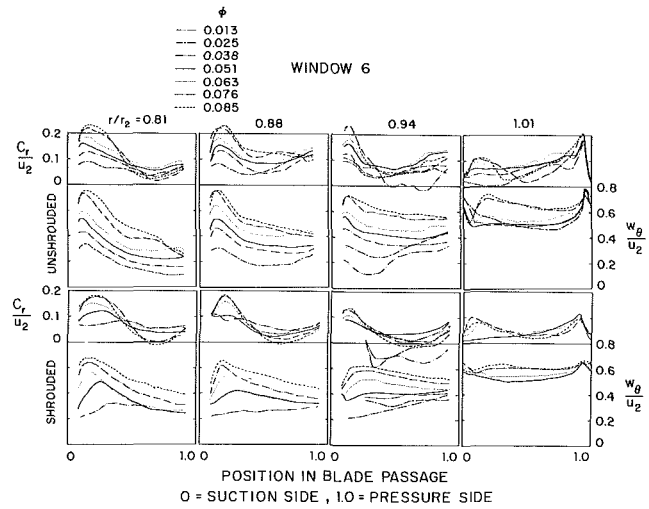

Fig. 10 Variation of velocity profiles with flow rate in window 6

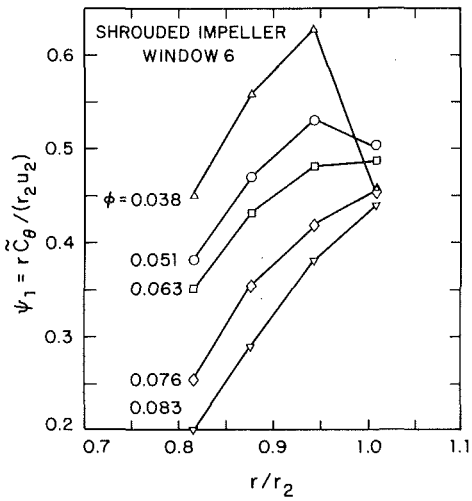

Fig. 11 Angular momentum distributions for the shrouded impeller in window 6

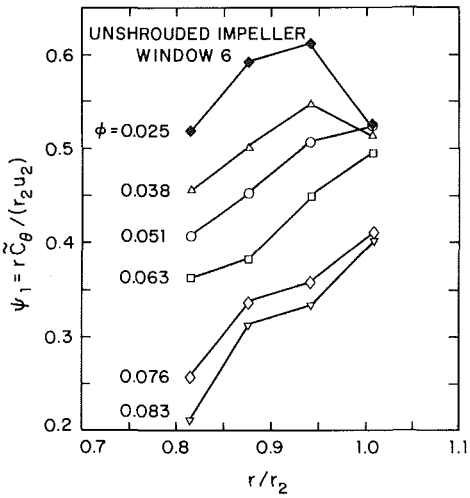

Fig. 12 Angular momentum distributions for the unshrouded impeller in window 6

either impeller. As a result, large axial gradients in flow angle for the unshrouded impeller were found, as shown in Fig. 8.

Before the present results were available, one may have postulated that the tip leakage would emerge as a low-energy fluid and accumulate in the suction side wake. This has been clearly disproved. Figure 9 shows the absolute radial and relative tangential velocities for both impellers at two flow rates ($\phi = 0.051$ and 0.063) near the nominal design point ($\phi = 0.063$) at the axial center of passage for four radius ratios. This figure is the result of averaging the profiles in the six accessible windows. Figure 9 shows that the unshrouded impeller has a smaller average suction side wake than the shrouded impeller. A greater distance from the suction side blade surface to the peak velocity is seen for the closed impeller than for the open impeller. In the shrouded impeller, transverse flow in the boundary layer on the front shroud feeds the wake; in the unshrouded impeller, the relative wall motion and leakage carry the fluid away from the wake. The leakage fluid emerges as a jet into the passage and causes the boundary layer fluid on the suction surface to mix back into the main flow.

Figure 10 indicates how the absolute radial and relative tangential velocity profiles at the axial centerplane change with flow rate in window 6. One should note the variation in velocity gradients from suction to pressure side, which indicate varying blade loadings at the different flow rates.

An estimate of the flow rate at which the impeller and volute are matched can be made by matching the angular momentum of the impeller exit and the angular momentum in the volute throat, i.e.

$$r_2 \tilde{C}_{\theta_2} = r_t \tilde{C}_t = r_t Q / A_t \tag{5}$$

where r_t is the radius of the centroid of the throat area and $\tilde{C}_t$ is the average throat velocity. Using equation (3), the measured slip factor, and $\tilde{C}_{\theta 2}$ from equation (5), the matching point is calculated to be $\phi = 0.060$ for the closed impeller and $\phi = 0.053$ for the unshrouded impeller. In the following discussion, "matching point" refers to these values.

Figures 11 and 12 show the angular momentum distributions in the center plane of window 6 for various flow rates. Similar trends were observed in other windows. One should note the reversal in angular momentum development near the impeller discharge for lower flow rates. Several interesting variations of the flow pattern can be noticed with changes in flow rate. For flows at or above the matching point, there is a uniform increase in angular momentum with radius. For low flow rates, however (i.e., $\phi = 0.051$ and 0.038 for the shrouded impeller; $\phi = 0.038$ for the unshrouded impeller), the angular momentum rises to a peak within the impeller, and then falls toward the outer diameter. For this trend to occur, the vanes must have reverse loading near the exit.

The reverse loading can also be inferred from Fig. 10. To maintain a normal loading, a gradient of relative velocity must exist across the passage that increases from pressure to suction side. For the shrouded impeller and for the inner radii in Fig. 10 the normal velocity gradient is present for the tangential

Downloaded 01 Jun 2010 to 171.66.16.57. Redistribution subject to ASME license or copyright; see http://www.asme.org/terms/Terms_Use.cfm

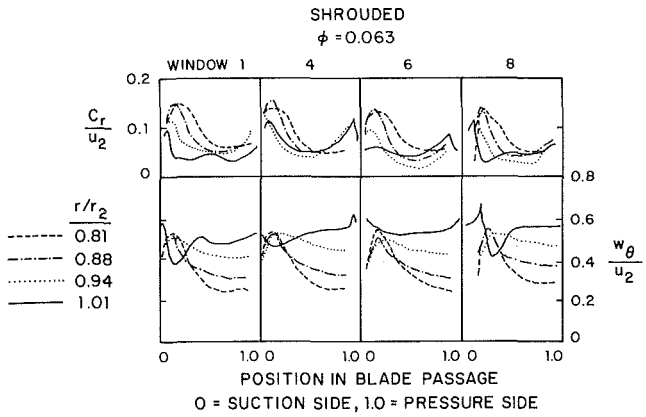

Fig. 13 Variation of velocity profiles in shrouded impeller with circumferential position

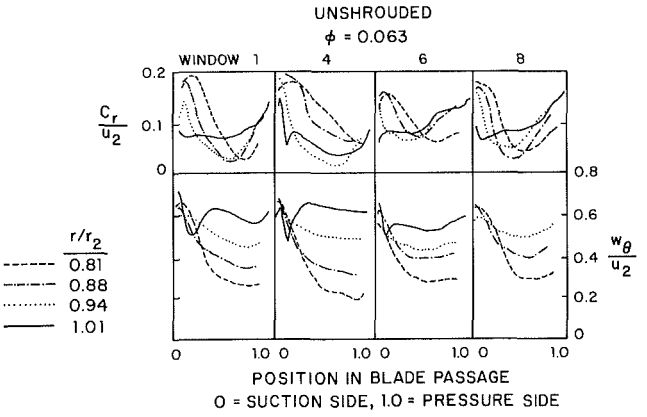

Fig. 14 Variation of velocity profiles in unshrouded impeller with circumferential position

velocity. However, for $r/r_2 = 0.94$ and 1.01 the gradient reverses for all below-matching-point flow rates. If the flow predominantly follows the blades in the interior of the impeller and deviates only near the exit, there can be "overshoot" of the angular momentum in the interior. This overshoot has been shown here to actually exist in the test pump. Plots of circumferentially averaged relative flow angles as functions of radius also indicated reverse loading near the impeller exit.

As indicated above, the reverse loading is present in both impellers. For the shrouded impeller it begins between flow coefficients of 0.063 and 0.051; for the unshrouded impeller it begins between 0.051 and 0.038. These inception flow rates are near the impeller/volute matching points for these impellers as calculated above using the experimental slip factor (0.060 and 0.053, respectively). Thus, the present data indicate that the reverse loading may be related to impeller/volute matching.

Variations With Circumferential Position. Velocities were measured in six windows as indicated earlier. For some data reduction averaging was performed over all six windows. For the readers' information and for benchmark usage, representative variations of the profiles are presented for four of the windows (1, 4, 6, and 8). These data are for $\phi = 0.063$, four radii, and both impellers (Figs. 13 and 14).

In some cases similar profiles at all windows are observed, for example, shrouded impeller at $r/r_2 = 0.81$. In other cases, however, much different profiles were observed in the different windows, for example, shrouded impeller at $r/r_2 = 1.01$. At an off-design flow rate ($\phi = 0.051$), more circumferential variations of the profiles were observed.

Slip. Figure 15 shows the results for the slip factor for two flow rates near the nominal design point, based on an average

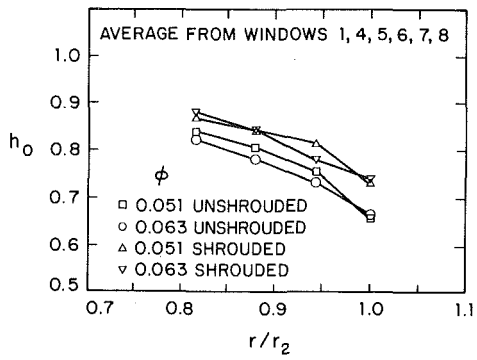

Fig. 15 Average slip factor variation from six windows with radius

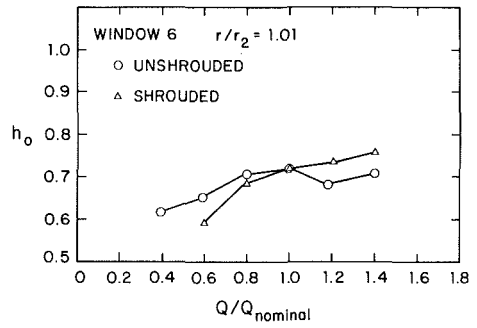

Fig. 16 Slip factor (at impeller exit) variation with flow rate (window 6)

of all six windows and at the axial centerplane. More slip is present in the unshrouded impeller. It is also interesting that the local slip factor h_0 does not approach 1.0 inside the impeller but rather approaches a smaller value. Figure 16 shows that the slip factor at the impeller exit decreases for lower flow rates.

It is often implied that when the flow follows the blades, slip does not occur in an impeller. This assumption is made implicitly in [11–14] in the calculation of the blade surface velocities. However, it is possible for the flow angle to be equal to the blade angle everywhere, and still to have slip, that is, to have h_0 less than unity. An analysis with simple linear velocity profiles shows that this is possible. If the blade-to-blade velocity profile is assumed to be linear

$$w = w_s(1-\zeta) + w_p\zeta \tag{6}$$

where ζ is a parameter ranging from zero on the suction side to one on the pressure side, and that the flow follows the blades everywhere

$$\begin{aligned} w_\theta &= w\cos\beta \\ w_r &= w\sin\beta \end{aligned} \tag{7}$$

then the mass and area-averaged velocities according to equation (1) are

$$\tilde{w}_\theta = 2\cos\beta(w_p^2 + w_p w_s + w_s^2)/[3(w_s + w_p)]$$

and

$$\hat{w}_r = [(w_s + w_p)\sin\beta]/2 \tag{8}$$

After noting that

$$\hat{w}_r = Q/((2\pi r - zt/\sin\beta)b) \tag{9}$$

the slip factor according to equation (3) becomes

$$h_0 = 1 - (w_{\theta s} - w_{\theta p})^2/[6u(w_{\theta s} + w_{\theta p})] \tag{10}$$

This expression indicates that if a velocity gradient exists across the passage, the slip factor will be lower than unity even if the flow follows the vanes.

In the results presented here, the local slip factor h_0 was always significantly less than unity, reaching a maximum of

Downloaded 01 Jun 2010 to 171.66.16.57. Redistribution subject to ASME license or copyright; see http://www.asme.org/terms/Terms_Use.cfm

about 0.9 in the interior of the impeller (Fig. 15). This result is contrary to assumptions sometimes made for simple blade-to-blade flow solutions, but is understandable in terms of the analysis just given. The most useful slip factor is one based on the mass-averaged tangential velocity as in equation (3), and this slip factor is not equal to unity when velocity gradients exist.

Summary and Conclusions

Velocities in shrouded and unshrouded versions of an impeller in a radial flow volute pump were measured at various positions and for various flow rates. Velocity profiles in the blade-to-blade and hub-to-shroud planes were obtained. The data were used to analyze tip clearance leakage, angular momentum through the impellers, and slip factors. The data can also be used for benchmarking ongoing prediction methods. The important conclusions are as follows:

1 The tip clearance leakage in combination with the relative wall motion causes a vortex in the unshrouded impeller. The vortex migrates from midpassage at the inner radii to near the pressure side at the outer radii. This was determined from the hub-to-shroud velocity profiles. The relative wall motion and tip leakage act to decrease the suction surface wake region in the unshrouded impeller. This indicates that the boundary layer fluid does not accumulate on the suction side blade surface as it does for a closed impeller. The leakage fluid is a jet into the passage, which mixes the boundary layer fluid back into the main flow. The data indicate the same type of tip leakage occurs as for previously studied axial flow machines.

2 At the impeller/volute matching point a uniform increase of angular momentum with increasing radius for both impellers was found. At low flow rates the angular momentum peaks inside the impeller and a reverse loading in the impeller exit region was found.

3 The slip factor varies from 0.8 to 0.9 in the interior of the impeller and approaches a lower value at the exit. At no position was a slip factor of unity measured. This variation of h_0 is predicted by a simple blade-to-blade flow analysis. The slip factor decreases with decreasing flow rate. Improved blade loading calculations and performance predictions could be made with these findings.

Acknowledgments

This work was sponsored in part by the NASA-Lewis Research Center under Contract No. NAG3-180, in part by the ROMAC Industrial Research Program at the University of Virginia, and in part by Goulds Pumps, Inc.

References

1 Japikse, D., *Introduction to Turbomachinery Analysis*, Concepts ETI, Hanover, NH, Aug. 1981.

2 Brownell, R. B., and Flack, R. D., "Flow Characteristics in the Volute and Tongue Region of a Centrifugal Pump," Paper No. 84-GT-82, ASME International Gas Turbine Conference, The Netherlands, 1984.

3 Thomas, R. N., Kostrzewsky, G. J., and Flack, R. D., "Laser Velocimeter Measurements in a Pump Volute With a Non-rotating Impeller," *International Journal of Heat and Fluid Flow*, in press.

4 Lakshminarayana, B., "Methods of Predicting the Tip Clearance Effects in Axial Flow Turbomachinery," ASME *Journal of Basic Engineering*, Vol. 92, No. 3, Sept. 1970, pp. 467–482.

5 Lakshminarayana, B., Pouagare, M., and Davino, R., "Three-Dimensional Flow Field in the Tip Region of a Compressor Rotor Passage – Part 1: Mean Velocity Profiles and Annulus Wall Boundary Layer," ASME JOURNAL OF ENGINEERING FOR POWER, Vol. 104, No. 4, Oct. 1982, pp. 760–771.

6 Hoshide, R. K., and Nielsen, C. E., "Study of Blade Clearance Effects in Centrifugal Pumps," NASA CR 120815, Nov. 1972.

7 Howard, J. H. G., and Kittmer, C. W., "Measured Passage Velocities in a Radial Impeller With Shrouded and Unshrouded Configurations," ASME JOURNAL OF ENGINEERING FOR POWER, Vol. 97, No. 2, Apr. 1975, pp. 207–213.

8 Hamkins, C. P., "Laser Velocimeter Measurements in a Shrouded and Unshrouded Radial Flow Pump Impeller," MS thesis, Department of Mechanical and Aerospace Engineering, University of Virginia, May 1985.

9 Flack, R. D., and Lanes, R. F., "Effects of Volute Geometry and Impeller Orbit on the Hydraulic Performance of a Centrifugal Pump," *Performance Characteristics of Hydraulic Turbines and Pumps*, ASME Publication H00280, 1983, pp. 127–133.

10 Busemann, A., "Das Folderhohen verhaltnis radialer Kreiselpumpen mit Logarithmischspiraligen Schaufeln," *Zeitschrift für Angewante Mathematik und Mechanik*, Vol. 8, No. 5, 1928, pp. 372–384.

11 Howard, J. H. G., and Osborne, C., "A Centrifugal Compressor Flow Analysis Employing a Jet-Wake Passage Flow Model," ASME *Journal of Fluids Engineering*, Vol. 99, No. 1, Mar. 1977, pp. 141–147.

12 Dallenbach, F., "The Aerodynamic Design and Performance of Centrifugal and Mixed Flow Compressors," *SAE Tech. Prog. Series*, Appendix C, Vol. 3, Jan. 1961, pp. 2–23.

13 Katsanis, T., and McNally, W. D., "Fortran Program for Calculating Velocities and Streamlines on the Hub, Shroud and Mid-channel Flow Surface of an Axial or Mixed Flow Turbomachine," NASA TN D-7343, 1973.

14 Gopalakrishnan, S., "Computer Based Hydraulic Design of Pumps," in: *Pumps, The Developing Needs*, 7th Technical Conference of The British Pump Manufacturers Association, York, Mar. 31–Apr. 2, 1981.

Downloaded 01 Jun 2010 to 171.66.16.57. Redistribution subject to ASME license or copyright; see http://www.asme.org/terms/Terms_Use.cfm

A Study on Unstable S-Shape Characteristic Curves of Pump Turbines at No-Flow

Y. Senoo
Professor.
Fellow ASME

M. Yamaguchi

Research Institute of Industrial Science,
Kyushu University,
Kasugashi, Fukuoka 816, Japan

A small model of a Francis-type pump turbine was tested without the rotating shroud and the radial distribution of pressure in the rotor was measured using pressure taps on the stationary shroud. The mean tangential velocity component in the rotor was measured with a laser velocimeter, and the flow pattern was visualized using a camera which rotated with the rotor. Comparing data at the no-flow condition in the turbine mode with those in the pump mode, the effect of semi-open spaces at the inlet and at the exit of blade rows on the difference of pressure rise between the two modes was recognized, and the flow patterns and the distributions of tangential velocity component in these zones were utilized to understand the phenomena. Furthermore, some discussion is included on the relationship between the design head coefficient in the turbine mode and the S-shape characteristics.

Introduction

As nuclear power stations are not suitable for operation at part-load conditions, pump-turbine power stations are often constructed in parallel to nuclear power stations to store excess energy or to deliver energy so that they balance demand of power to the output of nuclear stations.

In a pump-turbine station the rotor of a pump turbine rotates in one direction $n>0$ when it operates as a pump, and it rotates in the other direction $n<0$ when it serves as a turbine. In either case high efficiency is achieved in a wide range of head and flow rate. One of the serious problems to be solved is the unstable characteristic of some pump turbines in the lightly loaded turbine mode. The unstable characteristic is responsible for the following problems [1-11]. At startup to turbine operation, it is difficult to keep the shaft speed constant at no load. At turbine load rejection, an increase in the shaft speed results in a reverse pump operation and a high pressure occurs. At the runaway speed the system oscillates. If two or more turbines are connected to a common pipe line, the inlet pressure of a turbine drops temporarily by a sudden increase of the flow rate in another turbine and unexpectedly the turbine works as a pump absorbing a large power.

Figure 1 shows the complete four-quadrant characteristics of a Francis-type pump turbine, where the first quadrant represents the pump mode, the third quadrant represents normal operating conditions as a turbine, and the second quadrant represents conditions where the rotor rotates in the direction of turbine mode $n<0$ but it flows like a pump $Q>0$. The characteristic curves connecting the second and the third quadrant are S-shaped, and the positive inclination of the curves ($\partial Q/\partial n>0$) is responsible for the sudden jump of operating condition from the third quadrant to the second quadrant. In order to make the system safe from disturbance, it is desirable to increase $|n/\sqrt{H_{t0}}|$ at the no-through-flow condition relative to the value $|n\sqrt{H_t}|$ at the normal operating condition in the turbine mode.

In the case of pump turbines, the discharge head H_p in the pump mode must be higher than the available head in the turbine mode and the pump head at the no-flow condition is even higher. That is, the value of $|n/\sqrt{H_{p0}}|$ at the no-flow condition in the pump mode is smaller than the value of $|n/\sqrt{H_t}|$ at a normal operating condition as a turbine. At the no-flow condition, if the head H_{t0} developed by a pump turbine in the turbine mode is identical to that H_{p0} in the pump mode, the value of $|n/\sqrt{H_t}|$ at normal operating conditions in the turbine mode is larger than the value $|n/\sqrt{H_{t0}}|$ at the no-flow condition in the turbine mode, and the characteristic curve must have a positive gradient and the system may become unstable if a large perturbation occurs. In order to make the characteristic curves stable, the head H_{t0} developed by the

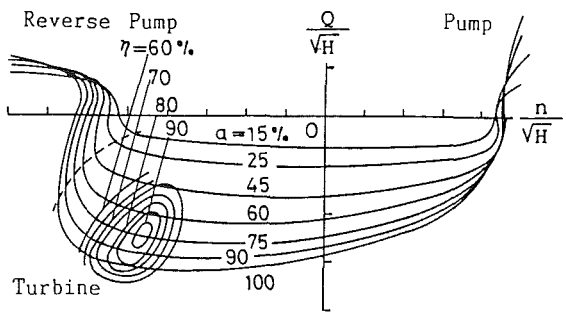

Fig. 1 Four quadrant characteristics of a pump turbine

Contributed by the Gas Turbine Division of THE AMERICAN SOCIETY OF MECHANICAL ENGINEERS and presented at the 31st International Gas Turbine Conference and Exhibit, Dusseldorf, Federal Republic of Germany, June 8-12, 1986. Manuscript received at ASME Headquarters December 26, 1985. Paper No. 86-GT-17.

Copyright © 1987 by ASME

Downloaded 01 Jun 2010 to 171.66.16.57. Redistribution subject to ASME license or copyright; see http://www.asme.org/terms/Terms_Use.cfm

pump turbine at the no-flow condition in the turbine mode must be much smaller than that H_{p0} at the no-flow condition in the pump mode.

Regarding the magnitude of $|n/\sqrt{H_0}|$ at no flow, it is noticed in Fig. 1 that the value $|n/\sqrt{H_{t0}}|$ in the turbine mode is considerably larger than the value $|n/\sqrt{H_{p0}}|$ in the pump mode, but it is not large enough to ensure stability. It is also noticed that the value is sensitive to the opening of guide vanes in the turbine mode but it is not so in the pump mode. The cause of difference in $|n/\sqrt{H_0}|$ in these cases may be clarified by comparing the condition of flow in the rotor in the pump mode and that in the turbine mode, and it is hoped that a method may be developed to increase the value of $|n/\sqrt{H_{t0}}|$ at the no-flow turbine mode relative to the value $|n/\sqrt{H_t}|$ at the normal operating condition. Then, it may be possible to design pump turbines which are safe from disturbance in the turbine mode.

Experimental Apparatus

According to the above discussion, the value of $|n/\sqrt{H_0}|$ is crucial at no-flow conditions. If the experiment is limited to no-flow conditions, the experimental apparatus is much simpler than an ordinary pump turbine. If there is no through-flow, the flow pattern must be very complicated and flow visualization is one of the best ways to understand the phenomena. On the other hand, the value of $|n/\sqrt{H}|$ depends upon the head rise; therefore, it is necessary to clarify the contributions of several components on the overall head rise, and finally it is desired to correlate the head rise in each component to the observed flow pattern.

In order to accomplish the above purposes, an experimental apparatus was made primarily for flow visualization, but it was also designed to be used for measurement of the pressure distribution. The experimental apparatus is shown in Fig. 2. The major parts of the apparatus were made of transparent plastic material for the purpose of flow visualization and also for velocity measurement using lasers. There was no cover over the rotor for simplicity of construction and for flow visualization. The diameter of the model rotor was 198 mm and it had eight blades which were backward leaning by 69 deg all the way from the inlet to the exit.

The axis of the rotor was vertical and it was driven by a motor in either direction in the pump mode and in the turbine mode, respectively. In either case, there was no through-flow and the free surface of water was adjusted so that it was just below the upper surface of the rotor disk. The head rise through the model pump turbine was measured as the difference between the mean pressure at the section B–B′ in the draft tube and the pressure at A, which was located outside the guide vanes where water was almost at a standstill.

In order to measure the radial distribution of pressure in the rotor, the rotor was made shroudless, and the axial clearance between the blade edge and the stationary shroud was 0.3 mm, which was about 2 percent of the blade height $b_2 = 18$ mm at the outer diameter. When it was tested with a clearance of 0.75 mm, there was very little change in the pressure distribution.[1]

The shaft speed was set at 85 rpm for the test of pressure distribution in order to insure good accuracy, while it was reduced to 20 rpm for taking pictures of path lines of relative flow with a camera which was rotating with the rotor. Although the Reynolds number $2b_2U/\nu$ was changed from 7.2×10^3 to 3×10^4, no significant change in the flow pattern was observed and the pressure difference between the inlet and the exit varied in proportion to the square of the shaft speed.

In order to avoid confusion, the inlet and the outlet of the rotor and of the guide vanes were named after those of the pump regardless of the direction of rotation, i.e., whether it was in the pump mode or in the turbine mode.

There were 20 guide vanes, which were made of a 5-mm-thick flat plate. The shape of the leading edges was semicircular and the vanes were pinned to the casing through the center of the semicircle so that the distance between the leading edge and the rotor remained constant regardless of the opening or the setting angle of guide vanes. The annular space is called the gap in this paper.

In this apparatus the shaft of the rotor passed through the draft tube, and the shaft was covered by a stationary tube. A pair of pressure taps, one on the wall of the draft tube and the other on the shaft cover, were used to indicate the intensity of swirl in the draft tube. Four pairs of them were located along the axis. In the present experiment there was no through-flow, and the draft tube was terminated at a length of about one diameter of the draft tube as shown in Fig. 2. The radial distribution of swirl velocity in the draft tube was measured using a cylindrical probe at the section B–B′ in Fig. 2.

Experimental Results and Discussion

Radial Distribution of Static Pressure. If the entire fluid rotates with the rotor, the radial pressure difference across the rotor is independent of the direction of rotation. As shown in Fig. 1, in cases of no flow the pressure difference is smaller in the turbine mode than that in the pump mode. By comparing the pressure distributions in the two cases, it is possible to find the zones which are the cause of the difference in pressure distribution and if the flow behavior in those zones is examined, the information may be useful to design a pump turbine which has a small value of $|n/\sqrt{H_{t0}}|$ at the no-flow condition in the turbine mode.

Influence of the Direction of Rotation. Radial distributions of static pressure are presented in Fig. 3, where closed symbols indicate data in the pump mode while open symbols indicate data in the turbine mode. Data at $r > 0.62r_2$ were measured along the stationary shroud while data at $r < 0.62r_2$, were measured in the draft tube at the section B–B′ using a cylindrical probe. For reference the chain line indicates the pressure

[1] As the loading of blades is very light at the no-flow condition, there is little leakage through the tip clearance of blades [12]. The friction force of the stationary shroud might have some effect on the pressure rise generated by the rotor.

Nomenclature

a = opening distance of guide vanes
b = width of blade
c_p = pressure coefficient = $2\Delta p/\rho U^2$
H = head
n = shaft speed, positive in pump mode
Q = flow rate, positive in pump mode
r = radius
t = pitch of guide vanes at leading edge
u = tangential component of velocity
U = tip speed of rotor
v = axial component of velocity positive toward rotor
α = opening angle of guide vanes = $\sin^{-1} a/t$
ψ = head coefficient = $2gH/U^2$
Ω = angular velocity of rotor

Subscripts

0 = at no through-flow
1 = inlet of rotor
2 = exit of rotor
m = at maximum efficiency
p = in pump mode
t = in turbine mode
v = leading edge of guide vanes

Downloaded 01 Jun 2010 to 171.66.16.57. Redistribution subject to ASME license or copyright; see http://www.asme.org/terms/Terms_Use.cfm

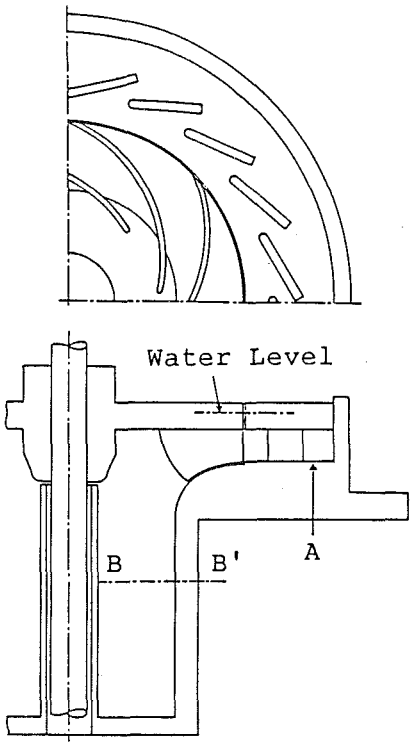

Fig. 2 Experimental apparatus of model pump turbine

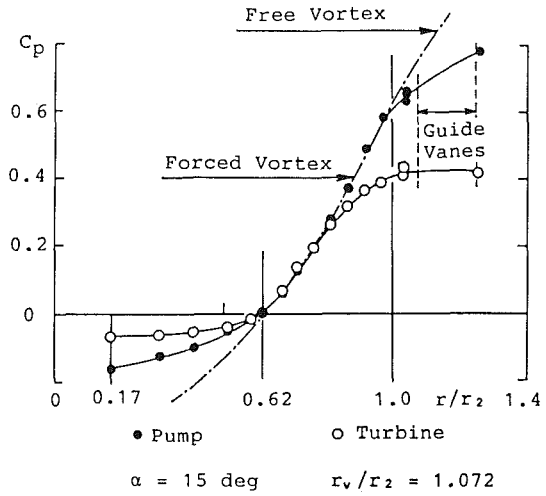

Fig. 3 Radial pressure distributions in pump mode and in turbine mode

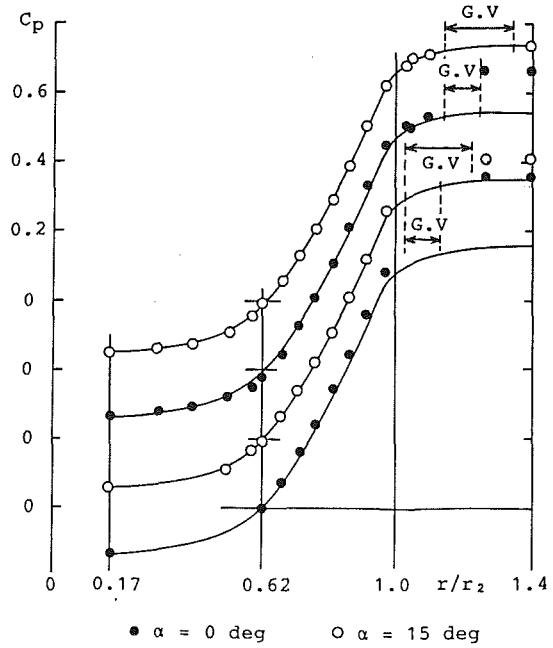

Fig. 4(a) Pump mode

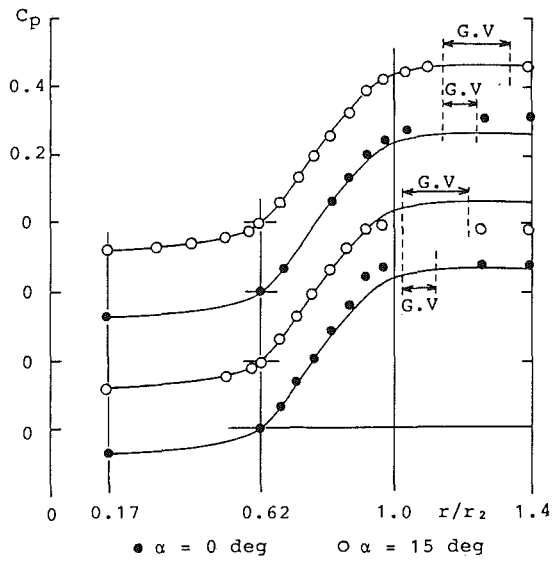

Fig. 4(b) Turbine mode

Fig. 4 Radial pressure distributions affected by guide vanes

distribution of a Rankine vortex, which is a forced vortex with an angular velocity of Ω at $r<r_2$ and a free vortex at $r>r_2$. It is noticed that the direction of rotation had a significant effect on the pressure gradient in the draft tube as well as on the pressure gradient in the rotor near the exit, and only the fluid in the inner half of the rotor blade row rotated with the angular velocity of the rotor in either direction.

Influence of Guide Vanes. The leading edges of guide vanes were set at two radial positions, and at each position the opening of guide vanes was changed in two steps. The pressure distributions in the pump mode are presented in Fig. 4(*a*), where the dotted lines indicate the locations of the leading edges and the trailing edges of guide vanes. For comparison identical solid lines are drawn for the four cases while symbols indicate experimental data. It is noticed that in the case of α = 0 deg the pressure at the exit of guide vanes was much higher than the static pressure in the gap, probably pretty close to the stagnation pressure of the flow near the leading edge of guide vanes, while in the case of α = 15.3 deg the pressure rise in the guide vanes was less.

Figure 4(*b*) shows the pressure distributions in the turbine mode. Four identical solid lines are drawn for comparison. Regarding the overall pressure rise, it was larger for guide vanes farther away from the rotor and also for smaller openings. Since the swirl did not flow toward the opening of the guide vanes, the dynamic pressure was hardly converted to the static pressure through the guide vanes.

Velocity Distribution. The distribution of the tangential velocity component in the rotor was measured with a laser-doppler velocimeter. The axis of the beam was parallel to the rotor axis and the depth of focus was about one-half of the depth of blades. It was focused at the middle of the depth. The

Downloaded 01 Jun 2010 to 171.66.16.57. Redistribution subject to ASME license or copyright; see http://www.asme.org/terms/Terms_Use.cfm

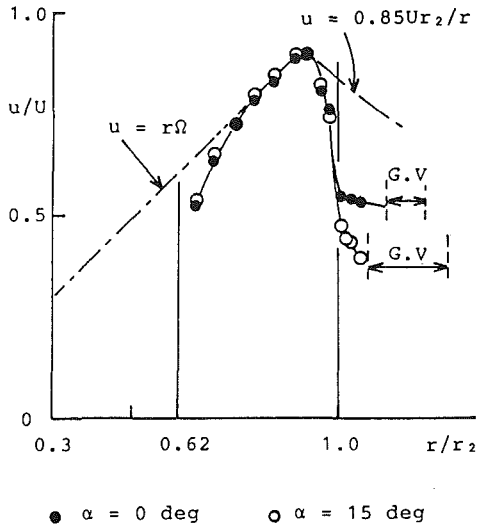

Fig. 5(a) Pump mode

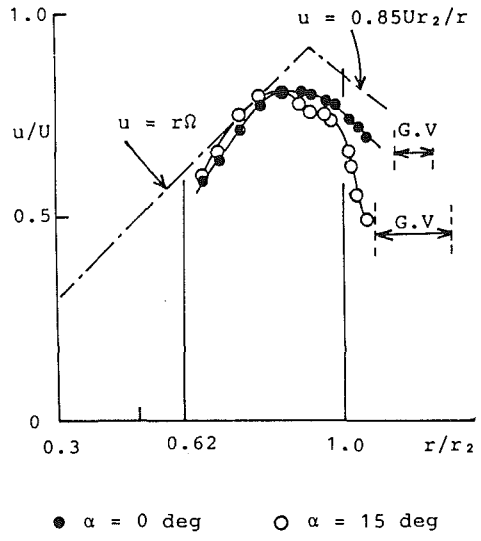

Fig. 5(b) Turbine mode

Fig. 5 Radial distributions of swirl velocity

data were taken only for the time-mean values, and the measured radial distributions are presented in Figs. 5(*a*) and 5(*b*) for the pump and the turbine modes, respectively.

The chain lines indicate a Rankine vortex, which has a core angular velocity of Ω and a slip coefficient of 0.85 at the exit of rotor. The measured distribution in the pump mode in Fig. 5(*a*) agrees well with the Rankine vortex except very near the exit of rotor. The dotted lines indicate the locations of the leading edges and the trailing edges of guide vanes. As the opening of guide vanes was larger and the leading edges were closer to the rotor, the swirl velocity in the gap between the rotor and the guide vanes was smaller, but their effects were hardly observed in the rotor. The difference in the swirl velocity at the two openings of guide vanes appeared in Fig. 4(*a*) as the difference in the pressure rise through the guide vanes.

It should be noted that the velocity in the gap was much smaller than the tangential velocity of fluid in the rotor. Obviously such distribution was unstable and there was a certain amount of recirculating flow between these two zones, but it was weak. Otherwise a big difference in the tangential velocity did not exist in the two zones.

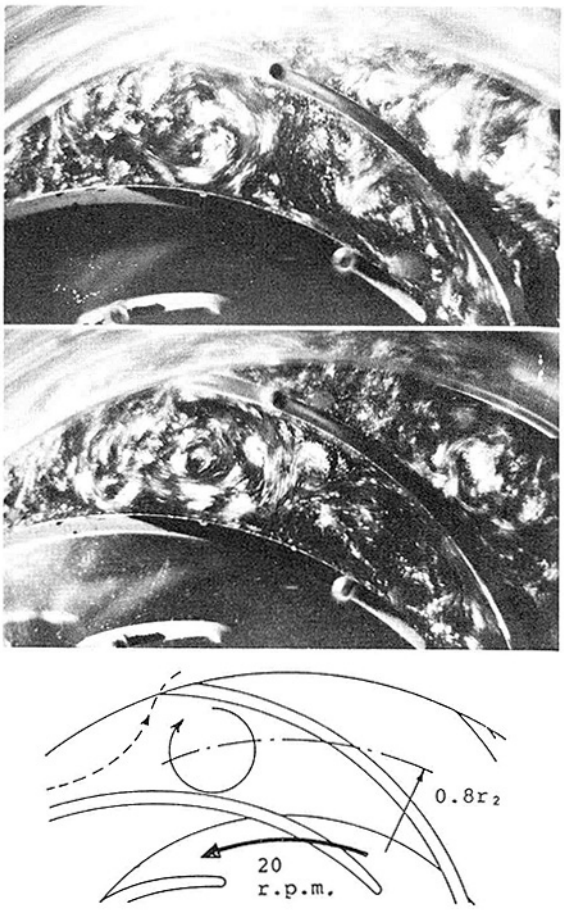

Fig. 6 Flow in the rotor in turbine mode

The tangential velocity component in the rotor in the turbine mode in Fig. 5(*b*) was considerably smaller than that in the pump mode, and furthermore the velocity distribution was influenced by the condition of guide vanes. These data mean that the recirculating flow between the gap and the rotor was strong. These velocity distributions support the pressure distributions observed in Figs. 4(*a*) and 4(*b*).

Flow Visualization in the Rotor. The photograph in Fig. 6 shows path lines of relative flow in the rotor in the turbine mode, where the rotor rotated counterclockwise. The photograph was taken at the middle depth. It is apparent that fluid outside the rotor flowed into the rotor along the convex surface of blades and then left at the edge of the adjacent blade after it moved about the semi-open space.

The flow induced a large clockwise vortex near the outer end of the blade channel. The two pictures in Fig. 6 show how the flow pattern in a channel varied while it rotated 180 deg. Apparently the vortex was three dimensional and the vortex in the plane of middle depth did not keep the strength while it moved about in the channel. That is, the vortex in the middle plane often changed strength and location. However, on average the center of vortex was located at $0.8r_2$ from the center of the rotor. Outside the center of the vortex it flowed toward the right relative to the rotor and the absolute tangential velocity was considerably smaller than the tip speed.

In the pump mode the rotor rotated clockwise in Fig. 7 and fluid outside the rotor moved counterclockwise relative to the rotor. Because of the inclination of rotor blades, fluid outside the rotor had little chance to flow into the rotor and it simply dragged fluid in the rotor near the outer diameter. As a result

Downloaded 01 Jun 2010 to 171.66.16.57. Redistribution subject to ASME license or copyright; see http://www.asme.org/terms/Terms_Use.cfm

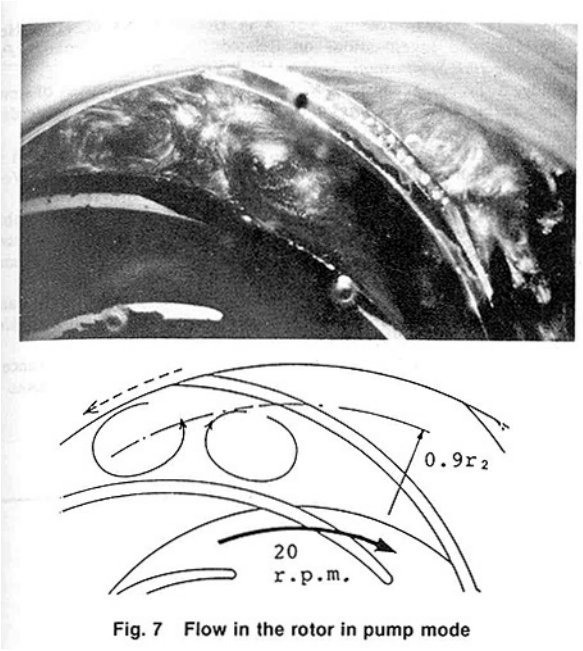

Fig. 7 Flow in the rotor in pump mode

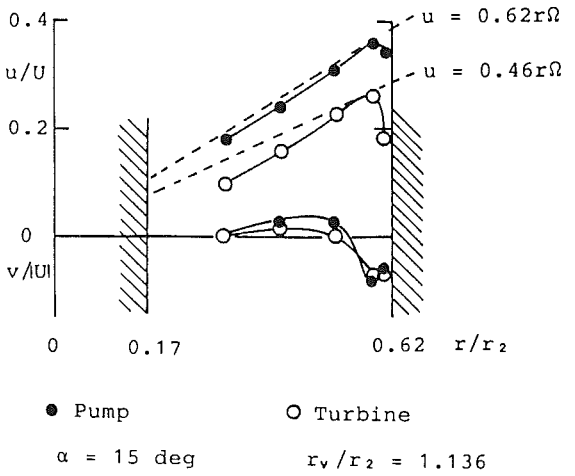

Fig. 8 Velocity distribution at draft tube inlet

a counterclockwise vortex was formed in the semi-open area and a clockwise vortex was induced in the channel between blades. The center of the outer vortex was located at $0.9r_2$ from the center of the rotor, and the only fluid outside the center of the vortex moved toward the left relative to the rotor, or that was the region where the tangential velocity was smaller than the velocity of rotor. The location of vortices in the turbine mode and in the pump mode in Figs. 6 and 7, respectively, agrees very well with the location of the maximum velocity observed in Figs. 5(*a*) and 5(*b*).

Flow in the Draft Tube. The pressure distributions in Fig. 3 clearly show that there was a swirl in the draft tube and the intensity varied depending upon the direction of rotation of the rotor. The velocity distributions measured at the section B–B′ are presented in Fig. 8. The swirl may be approximated as a solid body of rotation. Also it is observed that it flowed axially away from the rotor near the outer radius of the draft tube while it flowed axially toward the rotor near the center.

Since the radial position of the leading edges of rotor blades varied from the hub to the shroud as shown in Fig. 2, a certain amount of fluid was discharged from the blade row to the draft tube near the shroud, and the pumping action was greater in the pump mode because of the backward leaning blade angle at the inlet. If the kinetic energy of the swirl flow is recovered at the exit (larger end) of the draft tube, the mean pressure at the exit section is higher than that at the inlet section. In a real draft tube with noncircular cross section, the kinetic energy of swirl is not recovered well in the draft tube at the no-through-flow condition and the mean pressure at a section is not much different along the draft tube although a little pressure rise is expected in the conical zone near the inlet. That is, the difference between the wall pressure and the mean pressure at the inlet section of the draft tube would represent the pressure difference induced in the draft tube. As it is clearly observed in Fig. 3, the pressure difference in the turbine mode is considerably smaller than that generated by a rotating fluid with an angular velocity Ω. Therefore, a large diameter of the draft tube relative to the rotor diameter is favorable to reduce the head at the no-flow condition in the turbine mode.

Design Consideration. The head coefficient ψ_{tm} at the peak turbine efficiency depends upon the reaction rate (the ratio of the static head in the rotor to the overall head), and the relation is well known to designers. It is possible to increase ψ_{tm} considerably by reducing the design value of reaction rate while variation of ψ_{t0} is relatively small. As $|n/\sqrt{H}|$ is inversely proportional to $\sqrt{\psi}$, it is obvious in Fig. 1 that the larger the ratio ψ_{tm}/ψ_{t0} is, the safer the system would be from disturbance of the turbine head.

As the discharge head in the pump mode is larger than the design head in the turbine mode, the impeller blades must be backward leaning so that there is a higher theoretical head at a reduced flow rate. Also it is essential that the pump efficiency be high. Since the pressure recovery coefficient of diffusers is not very large, a pump impeller equipped with blades of a large backward-leaning angle or a high reaction rate is preferable. That is, unless the reaction rate is fairly large, a pump turbine cannot satisfy the requirement in the pump mode. However, for determining the reaction rate of a pump turbine, compromise is necessary considering safety from disturbance in the turbine mode.

Conclusions

In order to avoid unstable S-shape characteristics of pump turbines, the head at the no-flow condition in the turbine mode ψ_{t0} must be considerably smaller than the design head for the turbine ψ_{tm}.

At no through-flow, the pressure rise through a pump turbine was certainly considerably smaller in the turbine mode than that in the pump mode. The difference in pressure rise in these two modes occurred at three zones, the inlet and the exit of the rotor and the inlet of guide vanes, or the semi-open space of blade rows. That is, the inclination of blades relative to the direction of rotation has significant effects on the pressure rise. The number of blades, the inlet/exit radius ratio of the rotor as well as the gap between the rotor and the guide vanes, also have some effects on the pressure rise coefficient ψ_{t0}, but it is difficult to reduce ψ_{t0} by a large amount, because the geometry is mainly designed for normal operating conditions.

On the other hand, it is not so difficult to design a turbine with a large value of ψ_{tm} at normal operating conditions, providing that the reaction rate of the rotor is small. However, a pump turbine with a low reaction rate cannot develop a high head in the pump mode. Therefore, proper selection of the reaction rate is very important. If it is not allowed to adopt a relatively large value of ψ_{tm}, however, an effort is required to reduce ψ_{t0} in order to secure stable operation in the turbine mode without complicated control.

Downloaded 01 Jun 2010 to 171.66.16.57. Redistribution subject to ASME license or copyright; see http://www.asme.org/terms/Terms_Use.cfm

References

1 Swed, R. J., and Yang, K. H., "Experience on Startup and Trial Operation at Yards Creek Pumped Storage Project," ASME *Journal of Basic Engineering*, Vol. 91, 1969, p. 387.

2 Takoh, T., and Yamamoto, K., "The Rapid Progress of Pump-Turbine Design and Techniques," *Water Power*, 1972, p. 71.

3 Pejovic, S., et al., "Unstable Operation of High-Head Reversible Pump-Turbines," *Proceedings of the 8th IAHR Symposium*, Leningrad, 1976, Vol. 1-III-2, p. 283.

4 Tanaka, T., "Problems on Transient Phenomena of Pump-Turbines," *Turbomachinery* (in Japanese), Vol. 4, No. 7, 1976-1978, p. 457.

5 Tanaka, H., and Tsunoda, S., "The Development of High Head Single Stage Pump-Turbines," *Proceedings of the 10th IAHR Symposium*, Tokyo, 1980, Vol. 1, p. 429.

6 Oishi, A., and Yokoyama, T., "Development of High-Head Single- and Double-Stage Reversible Pump-Turbines," *Proceedings of the 10th IAHR Symposium*, Tokyo, 1980, Vol. 1, p. 441.

7 Murai, H., "Hydrodynamic Topics in Developments of High Head Pump-Turbines and Investigations on Related Problems in Japan," *Proceedings of the 10th Symposium*, Tokyo, 1980, Vol. 2, p. 17.

8 Boldy, A. P., and Walmsley, N., "Performance Characteristics of Reversible Pump Turbines," *Proceedings of the 11th IAHR Symposium*, Amsterdam, 1982, Vol. 2, pp. 60-61.

9 Klemm, D., "Stabilizing the Characteristics of a Pump-Turbine in the Range Between Turbine Part-Load and Reverse Pumping Operation," Voith Research and Construction, Vol. 28e, Paper 2, Reprint 2488e, 1982.

10 Pejovic, S., Gajic, A., and Obradovic, D., "Forms of Pump-Turbine Characteristics in Water Hammer Calculation," *Proceedings of Performance Characteristics of Hydraulic Turbines and Pumps*, ASME Winter Annual Meeting, 1983, p. 15.

11 Yang, C. S., "Performance of the Vertical Turbine Pumps as Hydraulic Turbines," *Proceedings of Performance Characteristics of Hydraulic Turbines and Pumps*, ASME Winter Annual Meeting, 1983.

12 Senoo, Y., and Ishida, M., "Pressure Loss Due to the Tip Clearance of Impeller Blades in Centrifugal and Axial Blowers," ASME JOURNAL OF ENGINEERING FOR GAS TURBINES AND POWER, Vol. 108, 1986, p. 32.

Downloaded 01 Jun 2010 to 171.66.16.57. Redistribution subject to ASME license or copyright; see http://www.asme.org/terms/Terms_Use.cfm

A Numerical Analysis of the Three-Dimensional Viscous Flow in a Transonic Compressor Rotor and Comparison With Experiment

W. N. Dawes
Whittle Laboratory,
Cambridge, United Kingdom

The numerical analysis of highly loaded transonic compressors continues to be of considerable interest. Although much progress has been made with inviscid analyses, viscous effects can be very significant, especially those associated with shock–boundary layer interactions. While inviscid analyses have been enhanced by the interactive inclusion of blade surface boundary layer calculations, it may be better in the long term to develop efficient algorithms to solve the full three-dimensional Navier–Stokes equations. Indeed, it seems that many phenomena of key interest, like tip clearance flows, may only be accessible to a Navier–Stokes solver. The present paper describes a computer program developed for solving the three-dimensional viscous compressible flow equations in turbomachine geometries. The code is applied to the study of the flowfield in an axial-flow transonic compressor rotor with an attempt to resolve the tip clearance flow. The predicted flow is compared with laser anemometry measurements and good agreement is found.

Introduction

The complex flowfield in a transonic axial compressor rotor represents a considerable challenge for flow prediction methods. Typically the relative inlet Mach number varies from about 0.8 at the hub to around 1.4 near the tip. Strong shock waves may be present, particularly toward the tip, with peak suction surface Mach numbers as high as 1.5. The blade suction surface boundary layers are usually very thick and cause considerable blockage. The shock–boundary layer interaction may lead to separation, even at the design point. The tip clearance flow is complex and may have a major effect on the performance and stability of the compressor. The strong coupling between the boundary layer flow and the core flow and the strong probability of boundary layer separation have led to two main approaches to the flow prediction problem. The first is the viscous-inviscid interactive method (e.g., [1, 2]) in which the boundary layer displacement effects are iteratively coupled to the main inviscid body of the flow. This is achieved either by computing and adding the boundary layer displacement thickness to the blade geometry [1] or by representing the displacement effects by transpiration of mass through blade surfaces [2].

The second approach to the flow prediction problem is the solution of the full compressible Navier–Stokes equations. There are several reasons why this is an attractive option. In principle there are no problems matching viscous and inviscid regions and no coupling problems. Also, features like boundary layer separation and shock–boundary layer interaction can be captured automatically. However, a Navier–Stokes solver is complicated to code and must be efficiently structured to avoid being too expensive for use in a design environment. Currently, much effort is being devoted to the development of three-dimensional Navier–Stokes solvers [3–5].

The current paper outlines an efficient implicit algorithm developed recently by the author for solving the compressible Navier–Stokes equations in turbomachinery geometries. The resulting code is applied to the study of the flowfield in a low hub–tip ratio axial-flow transonic compressor rotor.

Governing Equations

It is convenient to write the three-dimensional Reynolds averaged Navier–Stokes equations in finite volume form cast in the blade-relative frame using cylindrical coordinates (r, θ, x) [6]:

$$\frac{\partial}{\partial t}\oint_{\mathrm{VOL}} \bar{U} d\mathrm{VOL} = \oint \bar{H} \cdot d\overline{\mathrm{AREA}} + \oint \rho \bar{S} d\mathrm{VOL} \qquad (1)$$

where

$$\bar{U} = \begin{bmatrix} \rho \\ \rho W_x \\ r\rho W_\theta \\ \rho W_r \\ \rho E \end{bmatrix} \quad \bar{H} = \begin{bmatrix} \rho\bar{q} \\ \rho W_x \bar{q} + \bar{\bar{\tau}}\hat{i}_x \\ r\rho W_\theta \bar{q} + \bar{\bar{\tau}}\hat{i}_\theta \\ \rho W_r \bar{q} + \bar{\bar{\tau}}\hat{i}_r \\ \rho I\bar{q} \end{bmatrix} \quad \bar{S} = \begin{bmatrix} 0 \\ 0 \\ -2\Omega r W_r \\ \dfrac{W_\theta^2}{r} + r\Omega^2 + 2\Omega W_\theta \\ 0 \end{bmatrix}$$

Contributed by the Gas Turbine Division of THE AMERICAN SOCIETY OF MECHANICAL ENGINEERS and presented at the 31st International Gas Turbine Conference and Exhibit, Düsseldorf, Federal Republic of Germany, June 8–12, 1986. Manuscript received at ASME Headquarters December 26, 1985. Paper No. 86-GT-16.

 Copyright © 1987 by ASME

Downloaded 01 Jun 2010 to 171.66.16.57. Redistribution subject to ASME license or copyright; see http://www.asme.org/terms/Terms_Use.cfm

with $\bar{q} = W_x\hat{i}_x + W_r\hat{i}_r + W_\theta\hat{i}_\theta$, the relative velocity; Ω = rotation speed; $\bar{\bar{\tau}}$ = the stress tensor (containing both the static pressure and the viscous stresses); and $I = c_p T_{0_{\text{rel}}} - \frac{1}{2}(\Omega r)^2$, the rothalpy. The system is closed by an equation of state

$$p = \rho(\gamma - 1)(E - 0.5*(\bar{q}\cdot\bar{q} - (\Omega r)^2))$$

and a mixing length turbulence model patterned after Baldwin and Lomax [7].

Algorithm Development: Model Equation

The use of a centered difference approximation to represent the convection terms is desirable from the point of view of spatial symmetry, compactness, and simplicity. However, in convection-dominated flow, centered space differences lead to two main numerical difficulties. The first is the need to add artificial dissipation to prevent wiggles (i.e., odd-even point solution decoupling) and to permit shock capture. The second difficulty is simply that of devising a stable time-marching algorithm.

At high Reynolds number, explicit schemes such as the popular MacCormack algorithm [8] have very restrictive stability properties associated with the CFL time step limit and the fine mesh near blade boundaries. In principle, we can resolve this stability problem by using an implicit algorithm like the Beam–Warming or Briley–MacDonald schemes [9, 10]. For the model equation

$$\frac{\partial u}{\partial t} + A\frac{\partial u}{\partial x} = \nu\frac{\partial^2 u}{\partial x^2} \tag{2}$$

such an implicit algorithm takes the form

$$[I + \Delta t\{A\delta_x^0 - \nu\delta_{xx}^2\}]\Delta u = -\Delta t\{A\delta_x^0 u - \nu\delta_{xx} u\} = R \tag{3}$$

where δ_x^0 and δ_{xx}^2 are centered difference replacements for first and second derivatives and $\Delta u = u^{n+1} - u^n$ with n the time level. In the current work we define

$$\delta_x^0 u = (u_{i+1} - u_{i-1})/2\Delta X \quad \delta_{xx}^2 u = (u_{i+1} - 2u_i + u_{i-1})/\Delta X^2$$

In theory this algorithm has good stability properties, but in practice the ability to invert the left-hand side matrix is compromised by the loss of diagonal dominance associated with large time steps and high Reynolds numbers; large time steps must be used to pay for the increased operation count. The faithful mimicry of the right-hand side in the linearized left-hand side matrix simply perpetuates the basic problem of centered difference convection terms – lack of diagonal dominance.

In the present paper we derive an implicit algorithm by premultiplying the basic algorithm (3) by a preprocessing matrix:

$$[I - \Delta t\{A\delta_x^0 - \nu\delta_{xx}^2\}]$$

This gives

$$[I - \Delta t\{A\delta_x^0 - \nu\delta_{xx}^2\}][I + \Delta t\{A\delta_x^0 - \nu\delta_{xx}^2\}]\Delta u = R^*$$

where

$$R^* = [I - \Delta t\{A\delta_x^0 - \nu\delta_{xx}^2\}]R \tag{4}$$

The object of the present work is to obtain steady solutions and so we regard the left-hand matrix product as merely providing time-marching stability. Accordingly we multiply out the left-hand side and neglect terms which cannot be supported on a three-point molecule so that we retain the advantages of a tridiagonal structure. The basic preprocessed algorithm is therefore

$$[I - \epsilon\Delta t^2 A^2\delta_{xx}^2]\Delta u = R^* \tag{5}$$

where $\delta_x^0\delta_x^0$ has been replaced by a three-point δ_{xx}^2 and R^* is defined in equation (4). The diagonal dominance of the left-hand side of (5) is guaranteed for any time step and it can be shown that suitable choice of the free parameter ϵ guarantees stability.

The role of the left-hand side matrix is to enhance the stability of the time marching and so the simplified structure of the matrix has no impact on the accuracy of the converged steady solution (provided one can be obtained). The accuracy of the steady solution is determined by the accuracy to which the residue R^* is evaluated. Therefore it is important to take care with the evaluation of this residue. If the residue R^* in equation (4) was multiplied out, its evaluation would require a five-point molecule with the associated difficulties of maintaining accuracy near boundaries. In addition, the steady solution $R^* = 0$ would have a numerical viscosity error dependent on the time step size; this seems particularly inappropriate for an algorithm designed for use at large time steps.

Therefore to retain the compactness of a three-point molecule and to ensure the possibility of a steady solution independent of time step size and without numerical viscosity, we evaluate R^* by a two-step procedure

$$\begin{aligned} R &= -\Delta t\{A\delta_x^0 u - \nu\delta_{xx}^2 u\}^n \\ \tilde{u} &= u^n + R \\ R^* &= -\Delta t\{A\delta_x^0\tilde{u} - \nu\delta_{xx}^2\tilde{u}\} \end{aligned} \tag{6}$$

This two-step formation of R^* is analogous to the Brailovskaya scheme [11]. The steady solution is independent of the time step size since once R has become zero, then so too must R^*.

Application of the Algorithm to the Three-Dimensional Equations of Motion

Finite Volume Formulation. The governing equations (1) are written in integral conservation form and the numerical discretization is designed to mimic this. We divide the computational domain into hexahedral cells and store the variables $\bar{U} = (\rho, \rho W_x, r\rho W_\theta, \rho W_r, \rho E)$ at cell centers (ijk). The integrals in the equations are replaced by discrete summation around the faces of the computational cell

$$\frac{\Delta\bar{U}_{ijk}}{\Delta t}\Delta\text{VOL}_{ijk} = \sum_{\text{CELL}(ijk)} \bar{H}\cdot\Delta\overline{\text{AREA}} + \rho S_{ijk}\Delta\text{VOL}_{ijk} = \bar{F}(\bar{U})_{ijk} \tag{7}$$

Fluxes through cell faces are found by linear interpolation of density, velocity, etc., between cell centers and so the formal spatial accuracy is second order on smoothly varying meshes and global conservation is ensured. Viscous stresses are computed by defining a local curvilinear coordinate system and the chain rule.

Artificial Viscosity. An adaptive artificial viscosity term recommended by Jameson [12] is added to the discretized equations (7) to control odd-even point solution decoupling and to suppress oscillations in regions with strong pressure gradients. Equation (7) becomes

$$\frac{\Delta\bar{U}_{ijk}}{\Delta t}\Delta\text{VOL}_{ijk} = \bar{F}(\bar{U})_{ijk} + \bar{D}(\bar{U})_{ijk} \tag{8}$$

where $\bar{D}$ is the dissipative operator.

The artificial viscosity term has the form

$$\bar{D}(\bar{U}) = \bar{D}_I + \bar{D}_J + \bar{D}_K$$

where D_I, D_J, and D_K represent the contributions from each of the curvilinear coordinate directions. Each contribution is written in conservation form as, for example,

$$D_I = d_{i+1/2jk} - d_{i-1/2jk}$$

The right-hand side terms have the form

$$d_{i+1/2jk} = \frac{\Delta\text{VOL}}{\Delta t}\left\{\epsilon_{i+1/2jk}^{(2)}(U_{i+1jk} - U_{ijk}) - \epsilon_{i+1/2jk}^{(4)}(U_{i+2jk} - 3U_{i+1jk} + 3U_{ijk} - U_{i-1jk})\right\}$$

Downloaded 01 Jun 2010 to 171.66.16.57. Redistribution subject to ASME license or copyright; see http://www.asme.org/terms/Terms_Use.cfm

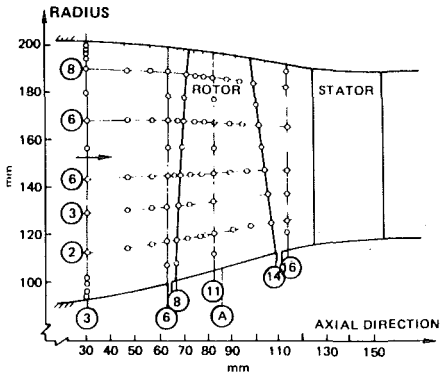

Fig. 1 Compressor flowpath with the laser velocimeter measuring stations

The coefficients $\epsilon^{(2)}$ and $\epsilon^{(4)}$ are determined by the flow in a self-adaptive manner

$$\epsilon^{(2)}_{i+1/2jk} = K^{(2)} A\text{MIN1}(0.5, (\pi_{ijk} + \pi_{i+1jk})*0.5)$$

$$\epsilon^{(4)}_{i+1/2jk} = A\text{MAX1}(0., (K^{(4)} - \alpha\epsilon^{(2)}_{i+1/2jk}))$$

where

$$\pi_{ijk} = |p_{i+1jk} - 2p_{ijk} + p_{i-1jk}|/(p_{i+1jk} + 2p_{ijk} + p_{i-1jk})$$

In the current effort we have used values for the constants of $K^{(2)} = 1$, $K^{(4)} = 0.01$, $\alpha = 2$. Numerical experimentation showed that the dissipation in directions normal to solid boundaries should be set to zero to avoid masking the physical viscosity.

Preprocessed Algorithm. We now define a preprocessed residue R^* to mimic that for the model equation (6), using the following two steps:

$$\bar{R}_{ijk} = \frac{\Delta t}{\Delta \text{VOL}_{ijk}} [\bar{F}^n_{ijk} + \bar{D}^n_{ijk}]$$

$$\tilde{\bar{U}}_{ijk} = \bar{U}^n_{ijk} + \bar{R}_{ijk}$$

$$\bar{R}^*_{ijk} = \frac{\Delta t}{\Delta \text{VOL}_{ijk}} [\tilde{\bar{F}}_{ijk} + \tilde{\bar{D}}_{ijk}]$$

We then extend the preprocessed algorithm from the model equation (5) to the three-dimensional set of equations (9) as follows

$$\left[I - \epsilon_I \frac{\Delta t^2}{\Delta \text{VOL}^2} \lambda_I^2 \delta_{II}^2\right]\left[I - \epsilon_J \frac{\Delta t^2}{\Delta \text{VOL}^2} \lambda_J^2 \delta_{JJ}^2\right]$$

$$\left[I - \epsilon_K \frac{\Delta t^2}{\Delta \text{VOL}^2} \lambda_K^2 \delta_{KK}^2\right]\Delta\bar{U} = \bar{R}^*$$

where ϵ_I, ϵ_J, and ϵ_K are free parameters (of order unity), λ_I, λ_J, and λ_K are the spectral radii of the Jacobians associated with the convective fluxes in the I, J, and K directions, and $\delta^2_{II}\phi$, for example, represents $(\phi_{I+1} - 2\phi_I + \phi_{I-1})$. The left-hand side is factored into three tridiagonal matrices for efficient inversion.

The use of spectral radii rather than the Jacobians themselves does not disrupt the formal accuracy or stability of the scheme but does allow a significant reduction of computer time per point per time step since a coupled 5×5 system is replaced by five scalar equations. Replacing the Jacobians with spectral radii clearly does reduce the nonlinear coupling between the equations. The implications of this for convergence rate have not been studied. Nevertheless, the computer cost per point per time step would be approximately a factor of five larger if a close-coupled Jacobian-based system were solved (using block tridiagonal inversion) rather than the spectral radius-based system (using scalar tridiagonals). It is suspected that this large increase in operation count would not be paid for by reduced time steps to convergence. In addition, the spectral radius-based system is much more straightforward to code.

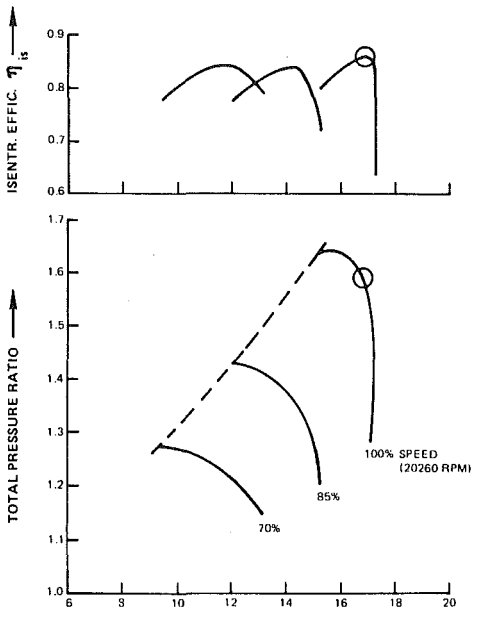

Fig. 2 Compressor stage performance

Although in principle the algorithm can be made stable for any size time step by suitable choice of the free parameters ϵ_I, ϵ_J, and ϵ_K, in practice it is found that there is an optimum range of time steps which leads to minimum number of steps to convergence. Extensive numerical experimentation for a range of geometries showed that larger time steps required larger values of ϵ for stability and that after a certain point the solutions became too smoothed during the transient, delaying convergence. It was found that CFL numbers in the range 2–5 were optimal with associated values of ϵ equal to unity. For the results presented in this paper, the CFL number was 3 and $\epsilon_I = \epsilon_J = \epsilon_K = 1$.

Boundary Conditions. A variety of boundary conditions is employed in the current study.

At inflow, total temperature and pressure are fixed and either flow angle or absolute swirl velocity held constant depending on whether the relative flow is subsonic or supersonic. At outflow the hub static pressure is fixed and radial variation derived from the simple radial equilibrium equation.

The finite volume mesh is constructed so that cell faces lie on solid surfaces (blades, hub, and casing) and along the periodic boundaries up and downstream of the blade row. Consequently, cells adjacent to periodic boundaries are updated just as if they were interior cells with the flux across the periodic boundary formed from linear interpolation between variables stored at the centers of the cells on either side of the boundary.

For cells adjacent to solid boundaries, zero fluxes of mass, momentum, and energy are imposed through the cell face aligned with the solid boundary. In addition, boundary conditions must be devised for the wall static pressure and wall shear stress; these two, acting on the wall cell face, are used in updating the momentum and energy equations for the cells adjacent to the solid walls. Wall static pressure is found by setting the derivative of pressure normal to the wall equal to zero. This is an accepted high Reynolds number approximation to solving the normal momentum equation. To prescribe the wall shear stress we use the velocities stored at cell centers adjacent to the wall and the known zero value of velocity on the wall to compute the velocity gradients at the wall. These gradients together with the wall viscosity are used with a locally defined curvilinear coordinate system to compute the wall shear

Downloaded 01 Jun 2010 to 171.66.16.57. Redistribution subject to ASME license or copyright; see http://www.asme.org/terms/Terms_Use.cfm

stresses. If the mesh spacing near the wall is too coarse to resolve the boundary layer then wall shear stresses are set to zero.

Application to the Compressor Rotor

The code is applied to the study of the three-dimensional flowfield in the axial flow single stage transonic compressor rotor tested using laser-two-focus velocimetry at the DFVLR [13, 14]. The compressor rotor has an inlet tip diameter of 0.4 m, a hub–tip ratio of 0.5, and tip solidity of 1.34. The design total pressure ratio is 1.626 with a mass flow of 17.1 kg/s at 20260 rpm. The compressor flow path with the laser velocimeter measuring stations is shown in Fig. 1; the compressor stage performance is shown in Fig. 2 with the maximum efficiency point indicated.

The computations were performed with an attempt to resolve the tip clearance flow. A 17 × 41 × 17 finite volume mesh was used, illustrated in Fig. 3. This mesh requires about 2 Mbytes of computer storage using 32-bit real numbers. The mesh is refined exponentially near blade suction and pressure surfaces and in the radial direction cells are concentrated near the casing and stretched away toward the hub. The blade tip is treated rather crudely by simply reducing the blade thickness smoothly to zero and then applying periodic boundary conditions between the tip itself and the casing. The tip clearance was taken to be 1.5 mm, i.e., 1.5 percent span; the actual value is not known. Only two cells are used in the clearance region because of computer storage constraints. Nevertheless it is believed that, at least to a first approximation, something of the nature of the clearance flow can be resolved. Again because of storage constraints, no attempt was made to model the hub boundary layer and an inviscid solid surface boundary condition imposed. It is believed that this will not affect the solution over the majority of the blade height but clearly may affect the computed mass flow–pressure rise characteristics of the stage. It is accepted that ideally this mesh

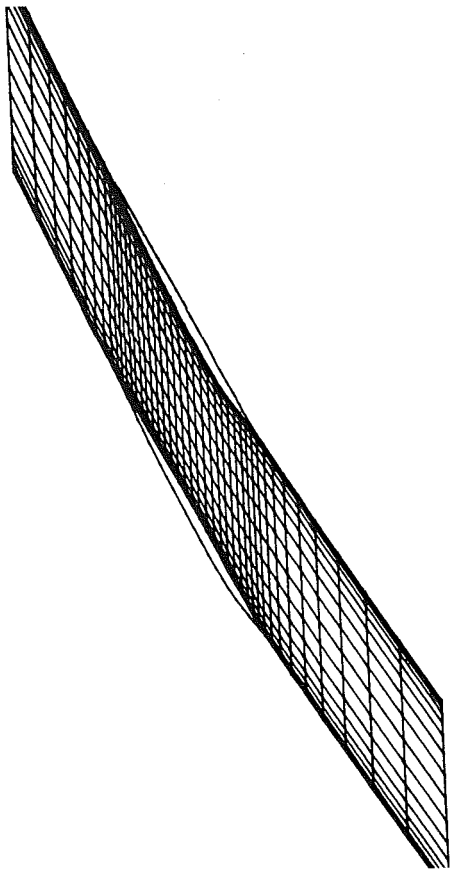

Fig. 3(c) Tip blade–blade plane

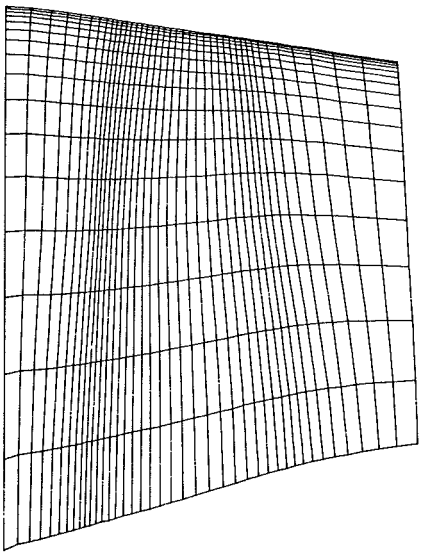

Fig. 3(a) Meridional plane

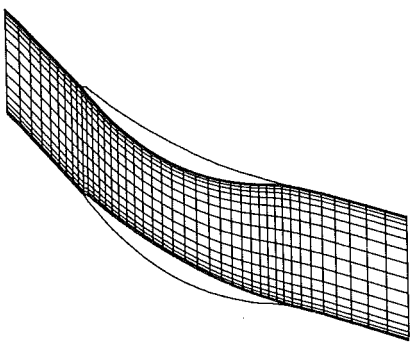

Fig. 3(b) Hub blade–blade plane

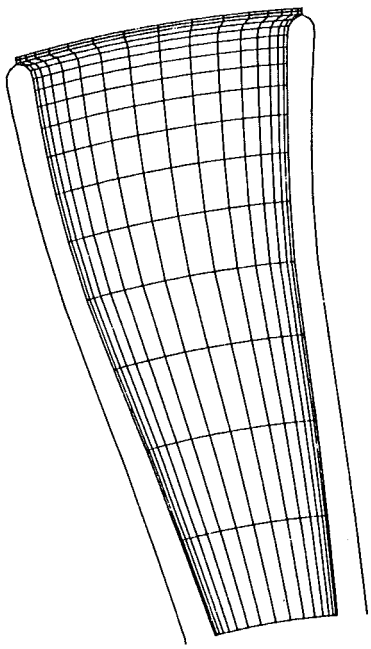

Fig. 3(d) Cross-flow plane

Fig. 3 Computational mesh

Downloaded 01 Jun 2010 to 171.66.16.57. Redistribution subject to ASME license or copyright; see http://www.asme.org/terms/Terms_Use.cfm

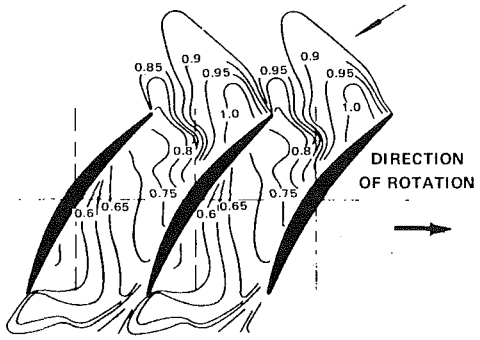

MEASURED

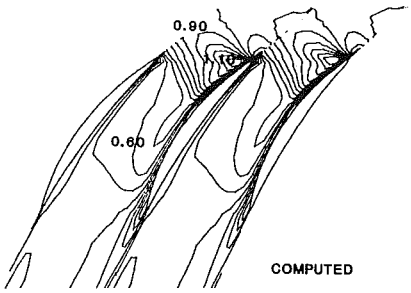

Fig. 4 Contours of relative Mach number at 18 percent span

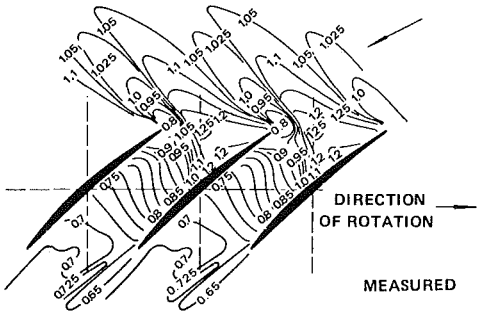

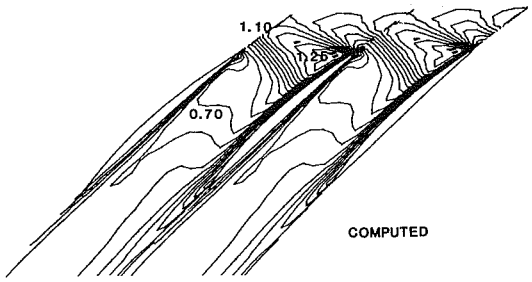

Fig. 5 Contours of relative Mach number at 45 percent span

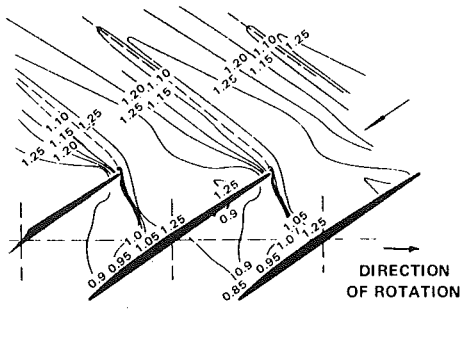

MEASURED

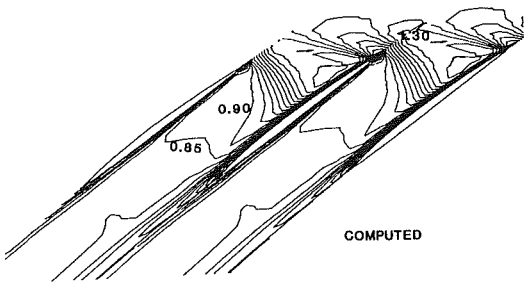

Fig. 6 Contours of relative Mach number at 68 percent span

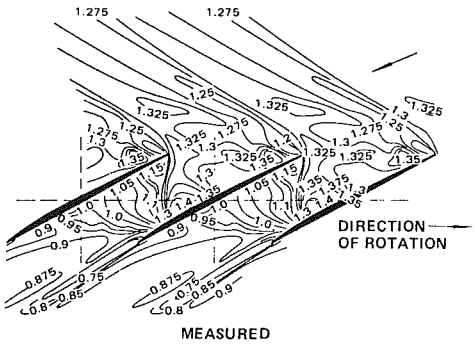

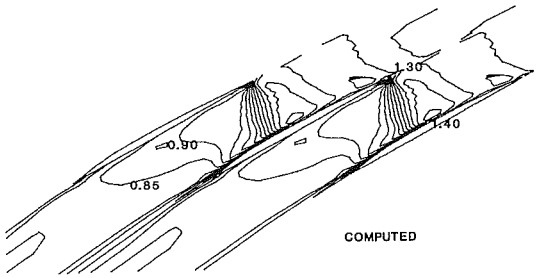

Fig. 7 Contours of relative Mach number at 89 percent span

should be denser. However, currently the author only has access to a minicomputer with severely constrained storage and refined mesh calculations cannot be attempted without configuring a virtual machine system with consequent increase in run times to an unacceptable degree. Nevertheless, the mesh spacing is fine enough near blade surfaces and casing for the centers of cells adjacent to the solid surfaces to be at $Y^+ \cong 10$. This gives marginally acceptable resolution.

The code executes at about 5×10^{-3}s per point per time step on a Perkin-Elmer 3230 minisystem ($= 5 \times 10^{-4}$s on an IBM 370). Using a spatially varying time step with CFL number around 3, 1000 time steps were used to achieve acceptable convergence (rms pointwise $\Sigma H(\rho W_x) \cdot d\text{AREA}$ less than 2×10^{-5}).

Figures 4–7 compare contours of computed relative Mach number with the laser measurements at each of four spanwise stations. The relative inflow Mach number varies from around 0.95 near the hub to about 1.3 toward the casing and there is a corresponding spanwise variation of flow character. At 18 percent span the flow accelerates to just sonic before shock-free compression. At 45 percent span the relative inflow is just supersonic and a well-resolved detached bow shock forms. At this point flow is spilling from one passage to the next and local incidence at the leading edge is high. Considering the coarseness of the computational mesh, the resolution of the expansion-shock pattern is considered to be good. At 68 percent span, the relative inflow Mach number is higher and the bow shock is now attached to the leading edge. Again on such a coarse mesh, the pattern of expansion waves and shock are adequately resolved. At 89 percent span the measurements indicate a weak oblique shock followed by diffusion to the subsonic exit flow whereas the computations show a rather stronger shock with somewhat less downstream diffusion.

In general, considering the complexity of the flow and the

Downloaded 01 Jun 2010 to 171.66.16.57. Redistribution subject to ASME license or copyright; see http://www.asme.org/terms/Terms_Use.cfm

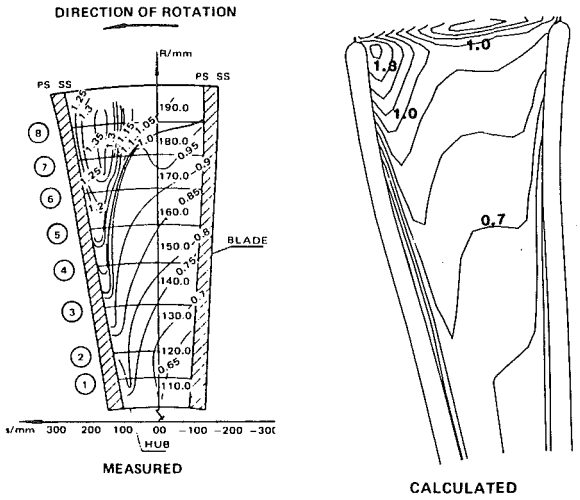

Fig. 8 Contours of relative Mach number in Plane 11

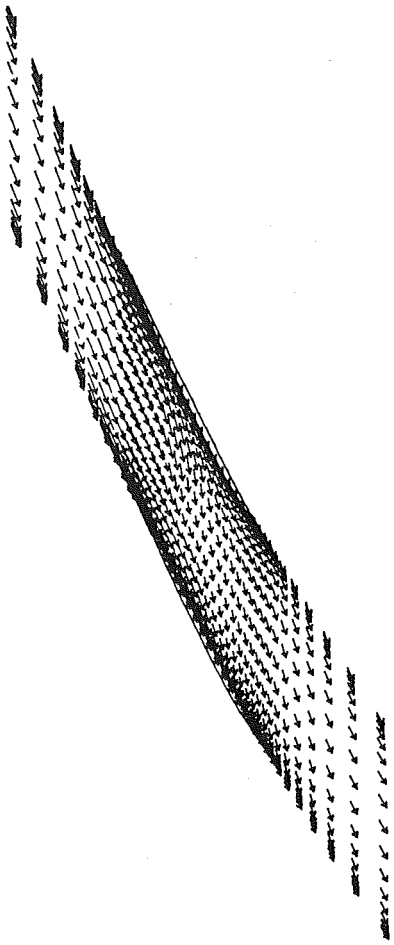

Fig. 10 Velocity vectors at 89 percent span

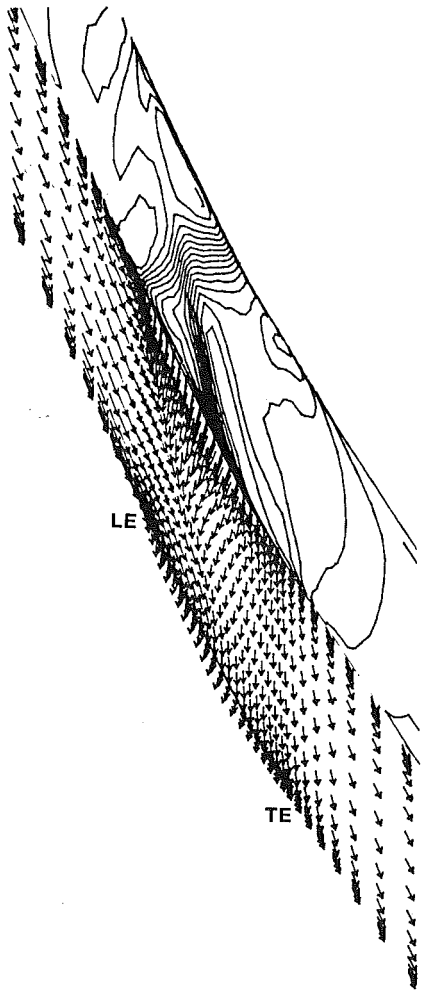

Fig. 9 Relative Mach number contours and velocity vectors in the clearance region

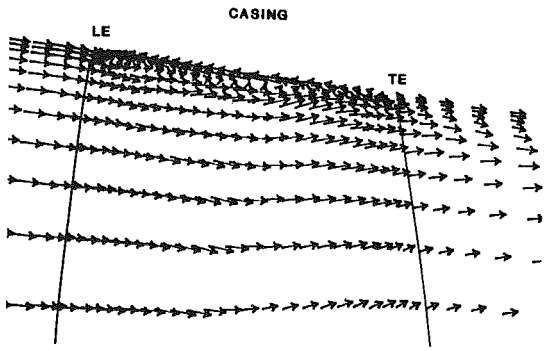

Fig. 11 Velocity vectors near the suction surface

coarseness of the mesh the level of agreement is considered to be encouraging. Toward the exit plane the computed Mach numbers tend to be lower than those measured, particularly toward the hub. This discrepancy is partly due to the coarse mesh underestimating the blockage. However, the discrepancy also arises because the mixing length turbulence model contains no correction for the stabilizing effect of convex curvature. Thus, toward the hub the turning is overpredicted and Mach number level too low.

The smearing of the computed shocks is of course large when compared with the near-discontinuous experimental data. However, in terms of the finite volume numerical approximation, the shocks are quite well resolved. Shocks passing obliquely across a coarse mesh are the most difficult type of shock to resolve but here they are still captured in 3–4 mesh cells.

Computed and measured contours of relative Mach number in the cross-flow plane near the blade stacking axis, plane 11 in Fig. 1, are compared in Fig. 8. The predicted high Mach number region in the casing-suction surface corner associated with the leakage jet is clearly resolved but smaller in spatial extent than that measured.

Figure 9 shows predicted contours of relative Mach number and relative velocity vectors in a blade–blade plane just near the casing actually in the clearance region. The bow shock causes a large pressure difference across the blade tip which

Downloaded 01 Jun 2010 to 171.66.16.57. Redistribution subject to ASME license or copyright; see http://www.asme.org/terms/Terms_Use.cfm

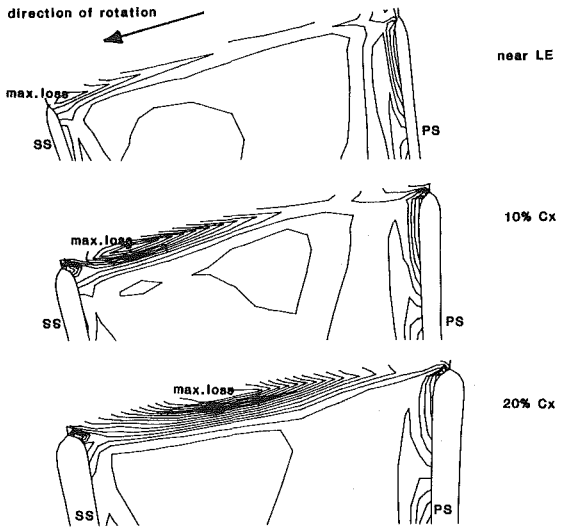

Fig. 12 Contours of entropy

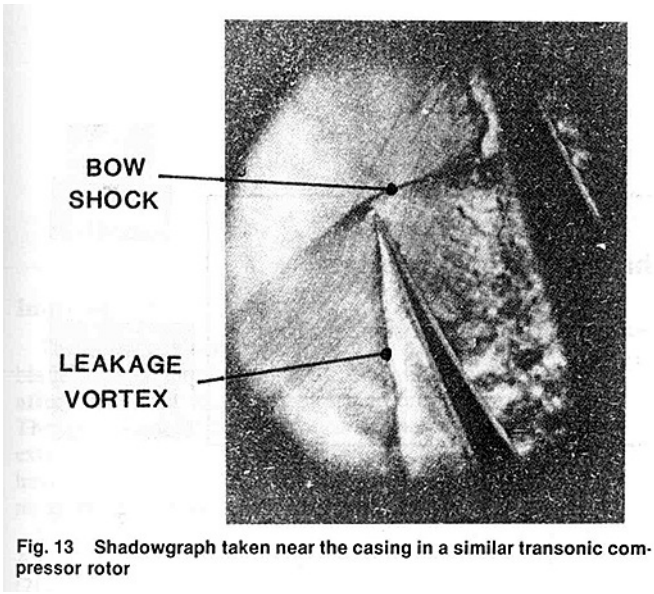

Fig. 13 Shadowgraph taken near the casing in a similar transonic compressor rotor

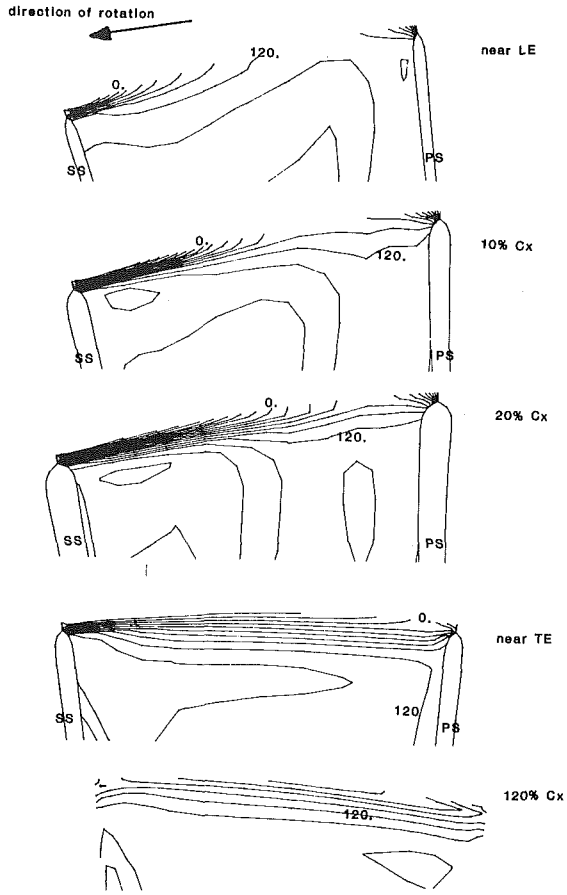

Fig. 14 Contours of axial velocity at several axial stations

drives a strong jet from the pressure side to the suction side starting at the leading edge. This jet meets and deflects the incoming flow along a clearly visible interaction zone passing from the leading edge to about midchord on the pressure surface. Over the aft half of the passage the flow is nearly circumferential representing a considerable axial blockage. Even at 89 percent span (Fig. 10) the influence of the clearance flow is causing visible distortion of the velocity vectors. Figure 11 shows velocity vectors just near the suction surface. This shows the strong vortex associated with the clearance flow and the strongly disturbed casing endwall boundary layer profile.

The interaction zone between the leakage flow and the incoming flow corresponds to the rollup of the tip leakage into a vortex whose core represents a region of high loss. Figure 12 shows predicted entropy contours at several axial stations starting at the leading edge. A loss core can be seen, moving across the pitch following the line of the interaction zone.

Figure 13 shows a shadowgraph taken in a plane near the casing of a similar transonic compressor rotor [15]. Labeled on the figure is the bow shock and the strong vortex arising from the tip clearance flow. A similar result and interpretation has been reported in [16]. This experimental evidence provides strong support for the physical realism of the present computed flow.

One of the key parameters in understanding the effect of clearance flows on compressor stability is the state of the casing endwall boundary layer [15]. Not only the circumferential average is of interest but also any local thickening. Figure 14 shows contours of axial velocitiy in axial stations from the leading edge to the wake. This gives a qualitative picture of the development of endwall blockage and shows that although downstream of the blade row (where conventional measurements are made) the axial blockage is more or less circumferentially uniform, within the blade passage substantial pitchwise variation exists.

Concluding Remarks

An efficient code solving the compressible Navier–Stokes equations in turbomachinery geometries has been described.

Results are presented for the flow in a low hub–tip transonic compressor rotor with an attempt to model the tip clearance flow. Despite using a relatively coarse mesh which supports only marginally acceptable resolution, generally good agreement with laser velocimeter measurements is obtained.

The influence of the clearance flow is found to extend over about 15 percent of the blade span. A strong tip leakage vortex is predicted in good qualitative agreement with experimental evidence. The predicted development of axial blockage on the casing endwall through the machine shows strong circumferential nonuniformity within the blade passage. It is believed that calculations of this type will provide valuable insight into problems in compressor stability.

References

1 Calvert, W. J., "Application of an Inviscid-Viscous Interaction Method to Transonic Compressor Cascades," NGTE Report R83001, Mar. 1983.

2 Singh, U. K., "A Computation and Comparison With Measurements of

Downloaded 01 Jun 2010 to 171.66.16.57. Redistribution subject to ASME license or copyright; see http://www.asme.org/terms/Terms_Use.cfm

Transonic Flow in an Axial Compressor Stage With Shock and Boundary Layer Interaction," ASME JOURNAL OF ENGINEERING FOR POWER, Vol. 104, 1982.

3 Moore, J., and Moore, J. E., "Performance Evaluation of Linear Turbine Cascades Using Three-Dimensional Viscous Flow Calculations," ASME JOURNAL OF ENGINEERING FOR GAS TURBINES AND POWER, Vol. 107, 1985, pp. 969-975.

4 Hah, C., "A Numerical Modelling of Endwall and Tip Clearance Flow of an Isolated Compressor Rotor," ASME JOURNAL OF ENGINEERING FOR GAS TURBINES AND POWER, Vol. 108, 1986, pp. 15-21.

5 Weinberg, B. C., Yang, R.-J., McDonald, H., and Shamroth, S. J., "Calculation of Two and Three-Dimensional Transonic Cascade Flow Fields Using the Navier-Stokes Equations," ASME JOURNAL OF ENGINEERING FOR GAS TURBINES AND POWER, Vol. 108, 1986, pp. 93-102.

6 Sarathy, K. P., "Computation of Three-Dimensional Flowfields Through Rotating Blade Rows and Comparison with Experiment," ASME JOURNAL OF ENGINEERING FOR POWER, Vol. 104, 1982.

7 Baldwin, B., and Lomax, H., "Thin Layer Approximation and Algebraic Model for Separated Turbulent Flows," AIAA Paper No. 78-257, 1978.

8 Purohoit, S. C., Strang, J. S., and Hankey, W. L., "Numerical Simulation of Flow Around a Three-Dimensional Turret," *AIAA Journal*, Vol. 21, No. 11, Nov. 1983.

9 Warming, R. F., and Beam, R. M., "On the Construction and Application of Implicit Factored Schemes for Conservation Laws," *SIAM-AMS Proceedings*, Vol. 11, 1978.

10 Weinberg, B. C., and McDonald, H., "Solution of Three-Dimensional Time-Dependent Viscous Flows," Eighth International Conference on Num. Methods in Fluid Dynamics, Aachen, 1982.

11 Roache, P. J., "Computational Fluid Dynamics," Hermosa Pub., Albuquerque, NM, 1971.

12 Jameson, A., and Baker, T. J., "Multigrid Solution of the Euler Equations for Aircraft Configurations," *AIAA Paper No. 84-0093, 1984.*

13 Weyer, H. B., and Dunker, R., "Laser Anemometry Study of the Flowfield in a Transonic Compressor Rotor," AIAA Paper No. 78-1, 1978.

14 Dunker, R., Strinning, P. E., and Weyer, H. B., "Experimental Study of the Flowfield Within a Transonic Axial Compressor Rotor by Laser Velocimetry and Comparison With Throughflow Calculations," ASME Paper No. 77-GT-28, 1977.

15 Freeman, C., "Tip Clearance Effects in Axial Turbomachines," VKI Lecture Series LS-05, 1985.

16 Kerrebrock, J. L., "Flow in Transonic Compressors," *AIAA Journal*, Vol. 19, No. 4, 1980.

Downloaded 01 Jun 2010 to 171.66.16.57. Redistribution subject to ASME license or copyright; see http://www.asme.org/terms/Terms_Use.cfm

Three-Dimensional Boundary Layer on a Compressor Rotor Blade at Peak Pressure Rise Coefficient

B. Lakshminarayana[1]
Distinguished Alumni Professor.
Fellow ASME

P. Popovski[2]
Visiting Assistant Professor.

Department of Aerospace Engineering,
The Pennsylvania State University,
University Park, PA 16802

A comprehensive study of the three-dimensional turbulent boundary layer on a compressor rotor blade at peak pressure rise coefficient is reported in this paper. The measurements were carried out at various chordwise and radial locations on a compressor rotor blade using a rotating miniature V configuration hot-wire probe. The data are compared with the measurement at the design condition. Substantial changes in the blade boundary layer characteristics are observed, especially in the outer 16 percent of the blade span. The increased chordwise pressure gradient and the leakage flow at the peak pressure coefficient have a cumulative effect in increasing the boundary layer growth on the suction surface. The leakage flow has a beneficial effect on the pressure surface. The momentum and boundary layer thicknesses increase substantially from those at the design condition, especially near the outer radii of the suction surface.

Introduction

The boundary layer developing on a turbomachinery rotor blade is three dimensional and turbulent and is significantly affected by rotation, curvature, and local pressure gradients. The measurement and prediction of these boundary layers are extremely difficult and, hence, very few systematic attempts have been made to understand these boundary layers through measurement and computation.

Some of the earlier investigations have been carried out by Anand and Lakshminarayana [1] on an inducer blade, Evans [2] and Pouagare et al. [3] on a compressor blade, Toyokura et al. [4] and Lakshminarayana et al. [5] on a fan blade, and Hodson [6] on a turbine blade. The boundary layers developing at various radii on a rotor blade are strongly coupled and, hence, a knowledge of the boundary layer behavior from hub to tip and from the leading edge to the trailing edge is essential for a detailed understanding of the nature and effects of viscous layers on rotor blades. An attempt was made [3] to provide such comprehensive data. The present paper is a continuation of this investigation and is concerned with a comprehensive understanding of the rotor blade boundary layer at the peak pressure rise (off-design) condition. The boundary layers at peak pressure rise coefficient develop under severe chordwise pressure gradient and are likely to be substantially different from those at the design condition. Such data have not been acquired previously. Hence, one of the major objectives of this investigation was to study the boundary layer developing on both surfaces of a compressor blade at the peak pressure rise coefficient. This should lead to a better understanding of the boundary layer at various operating conditions. An additional objective was to obtain a comprehensive set of data necessary for the validation of computer codes under development at various universities and research and industrial organizations.

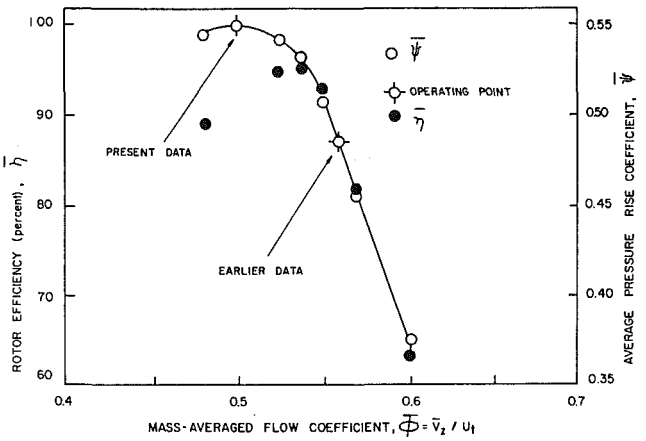

Fig. 1 Overall performance of the compressor rotor

The present program included detailed measurement of the blade boundary layers on rotor blades in a low-speed compressor and utilizes a rotating hot-wire probe. The measurement was carried out at large number of radial and axial locations on the blade and the boundary layer data are integrated with the laser-doppler measurement in the inviscid region presented in [7].

Experimental Facility and Program

The measurements were carried out in a single-stage axial flow compressor facility in the Department of Aerospace

[1] Director of Computational Fluid Dynamic Studies.
[2] Fulbright Scholar.

Contributed by the Gas Turbine Division of THE AMERICAN SOCIETY OF MECHANICAL ENGINEERS and presented at the 31st International Gas Turbine Conference and Exhibit, Düsseldorf, Federal Republic of Germany, June 8-12, 1986. Manuscript received at ASME Headquarters February 10, 1986. Paper No. 86-GT-186.

Copyright © 1987 by ASME

Downloaded 01 Jun 2010 to 171.66.16.57. Redistribution subject to ASME license or copyright; see http://www.asme.org/terms/Terms_Use.cfm

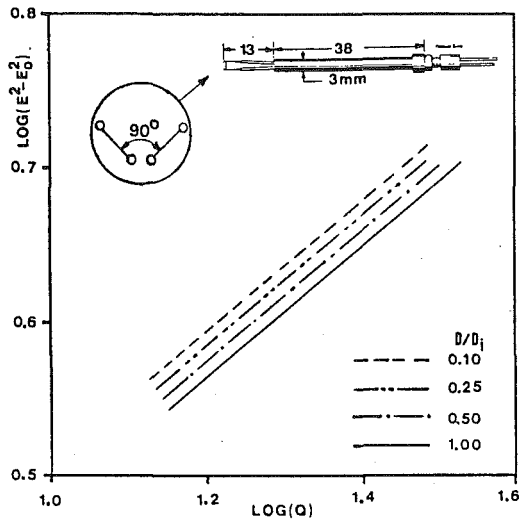

Fig. 2 Hot-wire calibration curve for the wall vicinity effect

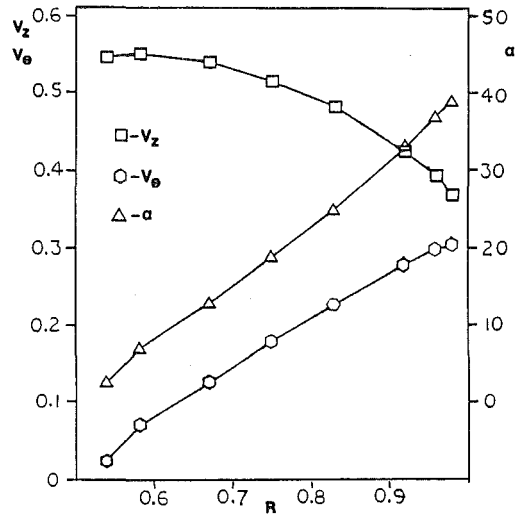

Fig. 3 Velocity profiles and angles inlet to the compressor ($Z = -0.35$), $\phi = 0.50$

Engineering at The Pennsylvania State University. A detailed description of the facility is given by Lakshminarayana [8]. The hub/outer annulus wall diameter ratio of the facility is 0.5, with the diameter of the outer annulus wall equal to 0.938 m. The inlet guide vane (IGV) row consists of 43 blades, and the rotor has 21 blades. The rotor is driven by a 37-kW variable-speed motor. The rotor is followed by a stator row of 25 blades. Downstream of the stator there is an axial flow fan with a variable blade setting for control of the pressure rise and mass flow through the facility. The overall performance of the rotor is shown in Fig. 1. The earlier data [3] were acquired at $\phi = 0.56$ and the present data were acquired at $\phi = 0.50$; both conditions are shown in Fig. 1. Other operating conditions are as follows: loading coefficient based on tip speed, $\psi = 0.55$ (peak value), rotor speed 1080 rpm; tip clearance 1.5 to 2 mm.

The rotating-probe traverse mechanism and the instrumentation system used for blade boundary layer measurements are described in detail in [8, 3]. All the velocity and turbulence measurements inside the blade boundary layer were taken with a miniature **V** configuration hot-wire probe (TSI model 1240). The sensors were 3-μm-dia platinum–tungsten wires with $l/d = 300$, located in the (s–r)-plane with their axes at 45 deg to the s axis. The probe was traversed normal to the blade surface. The signals from each of these wires were transmitted through a six-channel mercury slip-ring unit to two DISA 55D01 anemometers, a sum and difference circuit, and rms voltmeter. The present configuration, together with the relevant hot-wire equations [9], provides the value of the streamwise velocity U, radial velocity W, and the respective intensities $\overline{u^2}$ and $\overline{w^2}$ in the s, n, r system. The s coordinate is parallel to the blade surface lying on the cylindrical plane, n is the principal (outward) normal, and r is the radial direction. Since the flow traverse was done close to the blade surface, the component of the velocity in the n direction is assumed to be small.

Since the measurements were taken very close to the blade surface and the wire heat transfer characteristics are affected

Nomenclature

B = blockage coefficient
C = local chord length
D = distance between sensor and wall
D_i = reference distance between sensor and wall
E = voltage of the hot wire
E_0 = voltage of the hot wire at zero velocity
N = n/C
Q = calibration nozzle jet velocity
R = r/r_t
S = streamwise distance s normalized by the corresponding total arc length of the blade surface measured from the leading to the trailing edge of the blade
s, n, r = streamwise, normal, and radial directions (orthogonal to each other): $s = 0$ at the leading edge, $n = 0$ on the blade surface, $r = 0$ at the axis of the machine
t = blade spacing
u, v, w = fluctuating velocities in s, n, and r directions
V_z, V_θ = axial and tangential velocity normalized by the blade tip speed
U = streamwise relative velocity normalized by U_e
U_e = local free-stream (or edge) relative streamwise velocity normalized by blade tip speed
U_t = blade tip speed
W = radial velocity normalized by U_e
W_s = resultant of relative tangential and axial velocities normalized by the blade tip speed
Y = tangential distance normalized by the local distance from blade to blade ($Y = 0$ on suction side, $Y = 1$ on pressure side)
δ = boundary layer thickness normalized by the local blade chord
ϵ_w = limiting streamline angle
δ_1^*, θ_{11} = displacement and momentum thicknesses normalized by C
ϕ = average flow coefficient (average axial velocity at the inlet of the IGV divided by the blade tip speed)
$\bar{\eta}$ = mass-averaged efficiency
$\bar{\psi}$ = mass-averaged stagnation pressure rise coefficient normalized by $\rho U_t^2/2$

Subscripts

PS, SS = pressure and suction surfaces, respectively
TE = trailing edge
w, e = wall and edge, respectively
z = axial direction
t = tip

Downloaded 01 Jun 2010 to 171.66.16.57. Redistribution subject to ASME license or copyright; see http://www.asme.org/terms/Terms_Use.cfm

Table 1 Radial and streamwise measurement locations

S \ R	0.58	0.75	0.92	0.96	0.98
SS	0.52 0.66 0.82	0.56 0.72 0.87	0.60 0.78 0.94	0.61 0.79 0.96	0.62 0.80 0.97
PS	0.42 0.68 0.95	0.43 0.69 0.96	0.41 0.69 0.94	0.41 0.69 0.94	0.40 0.69 0.93
C (mm)	126	134	146	150	152
t (mm)	81	104	128	131	134

by the wall vicinity, the hot-wire probe was calibrated to derive corrections for the wall vicinity effect. A method of incorporating the correction to the wall vicinity effect, through calibration, is described in [3]. The calibration of the hot wire for the "wall vicinity" effect is shown in Fig. 2, where D_i is the distance (5 mm) beyond which the wall has a negligible effect on the heat transfer characteristics.

Experimental Results and Interpretation

The blade boundary layer measurements were carried out at an off-design condition corresponding to the maximum aerodynamic loading of the rotor. The radial variation of the flow properties measured at 0.35 chord length upstream of the rotor is shown in Fig. 3. The circumferential variation of flow properties at this location was found to be small.

The blade boundary layers were measured at five radial and three streamwise locations on both surfaces of the rotor blade. The streamwise and radial coordinates of these locations are listed in Table 1.

First, three radii were chosen to represent the blade boundary development near the hub, midspan, and tip

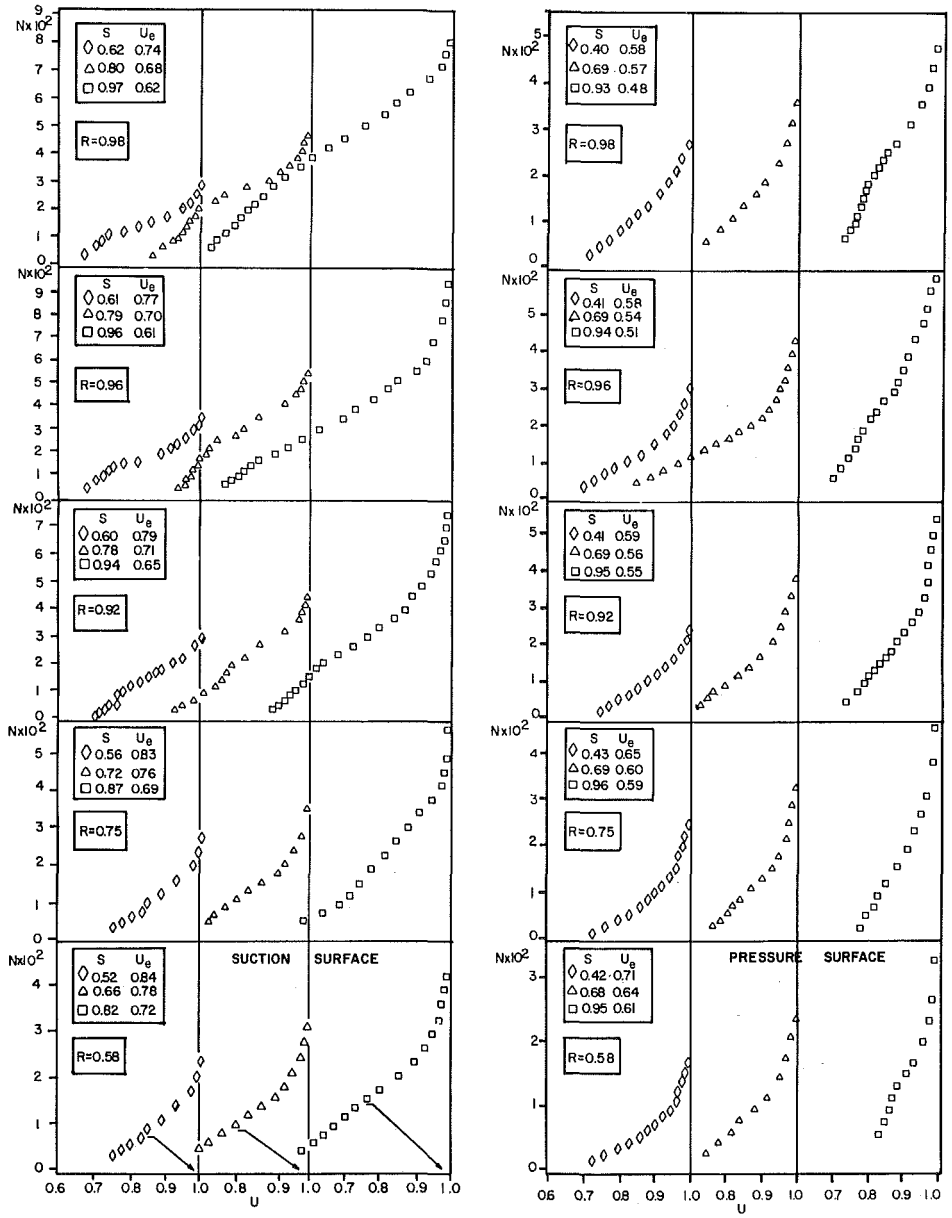

Fig. 4 Streamwise velocity profiles on pressure and suction surfaces, $\phi = 0.50$

Downloaded 01 Jun 2010 to 171.66.16.57. Redistribution subject to ASME license or copyright; see http://www.asme.org/terms/Terms_Use.cfm

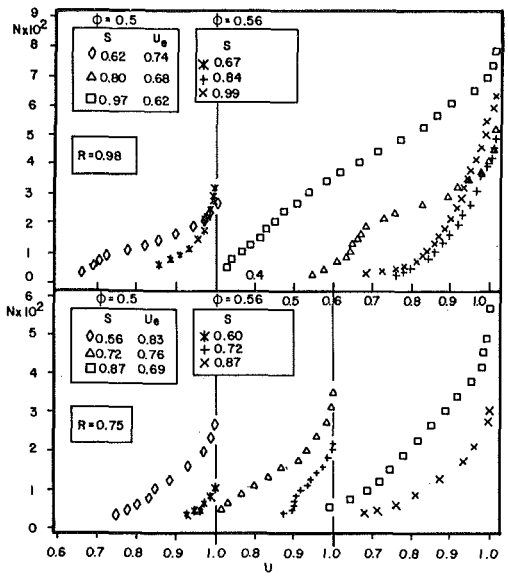

Fig. 5 Comparison of the streamwise velocity profiles at design and peak pressure rise coefficient on the suction side

regions. The last two radii, $R=0.96$ and $R=0.98$, are in the region affected by the tip clearance, and the data at these locations should show the influence of the tip-leakage flow on the blade boundary layers. In the streamwise direction, the measurement was performed at locations beyond $S=0.40$. Measurements showed that the blade boundary layer is very thin from the leading edge to about $S=0.40$. Since the accuracy of measurement is not good in very thin boundary layers, most measurements were taken from midchord to the trailing edge.

Streamwise Velocity Profile. The distribution of the streamwise velocity profiles at various axial and radial locations is shown plotted in Fig. 4. The development of the blade boundary layer in the streamwise and the radial directions on both the surfaces of the blade can be seen very clearly from this plot.

Close to the trailing edge of the suction surface, the boundary layer thickness increases with the radius, from 4.2 percent at $R=0.58$ to 9.4 percent of the local chord length at $R=0.96$. The corresponding figures on the pressure surface are 3.2 to 5.8 percent, respectively. Most of this increase occurs beyond the midspan region. The increase of δ in the tip regions can be explained by examining the three-dimensional nature of the blade boundary layer. The radial component of velocity is outward, and this transports low-momentum fluid toward the higher radii. The boundary layer profiles are well behaved on the suction side in regions away from the tip, up to $R=0.92$. The profiles are very similar at $R=0.583$ and 0.75. The profiles at $R=0.96$ and 0.98 show that it is either separated or about to separate beyond the chordwise location $s=0.62$. No such tendency was observed at $\phi=0.56$ [3]. A large boundary layer thickness near the tip, with an inner layer which is either separated or about to separate, indicates the effects of chordwise pressure gradient and the leakage flow and its interaction with the blade boundary layer. It is well known that the leakage flow and the leakage vortex induce radial outward flow and mixing near the blade vicinity, resulting in a substantial increase in boundary layer thickness. It is not clear which of these two effects dominates.

On the pressure surface, the boundary layers are well behaved at most locations, including the tip region, with the exception of locations very close to the trailing edge. The boundary layers at $R=0.98$ and $s=0.93$ show a tendency toward separation. Unlike the suction side, there is no dramatic increase in boundary layer thickness toward the outer radii.

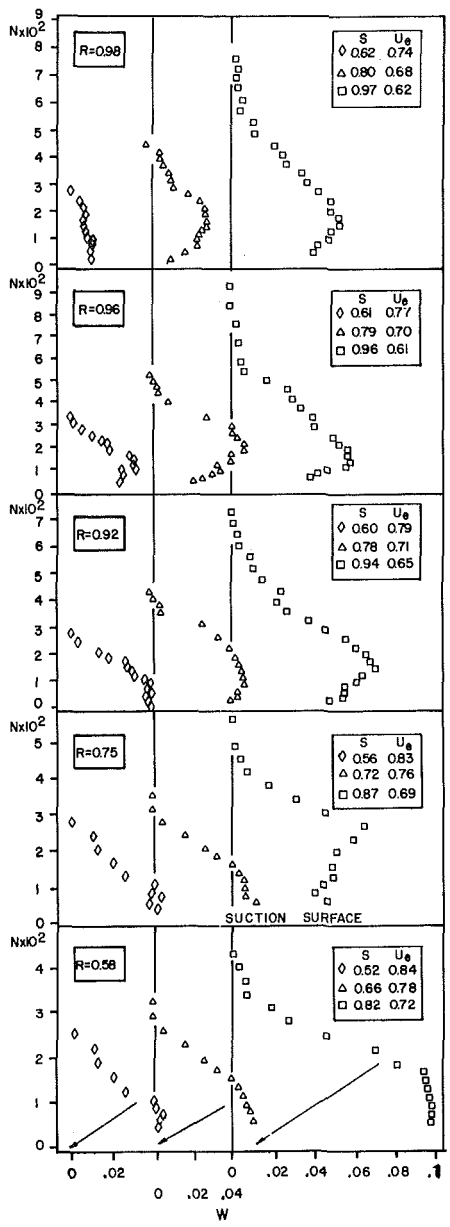

Fig. 6 Radial velocity profiles on the suction surface, $\phi=0.50$

There is an appreciable decrease (about 10–20 percent, depending on the radii) in the boundary layer thickness from 0.96 to 0.98. The chordwise pressure gradients at $R=0.98$ are lower than those at $R=0.96$ due to blade unloading at the tip, and this is likely to cause a reduction in boundary layer growth. In addition, the leakage flow has a tendency to decrease the growth of the boundary layer on the pressure side and increase the growth on the suction side. Hence, on the suction side the effects are cumulative, and on the pressure side the effects are subtractive. This explains the observed behavior.

A comparison of the blade boundary layer profile on the suction side for the off-design ($\phi=0.50$) and design conditions ($\phi=0.56$) at $R=0.75$ and 0.98 is shown in Fig. 5. The measurements are not available for the same chordwise location. Hence, comparisons are made for the closest available chordwise location. At $R=0.75$, the profiles are similar in both cases, but there is a substantial increase in the boundary layer thickness for $\phi=0.50$. For example, near the midchord and trailing edge locations, the boundary layer thickness is

Downloaded 01 Jun 2010 to 171.66.16.57. Redistribution subject to ASME license or copyright; see http://www.asme.org/terms/Terms_Use.cfm

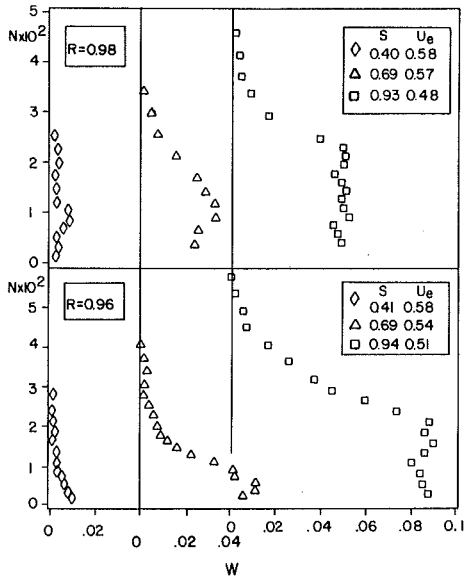

Fig. 7 Radial velocity profiles on the pressure surface, $\phi = 0.50$

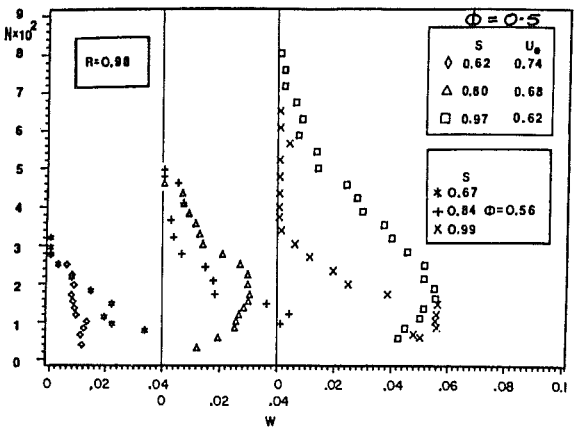

Fig. 8 Comparison of the radial velocity profiles at design and peak pressure rise coefficient on the suction side

nearly doubled and the profiles at both the flow coefficients show no tendency toward separation. The observed change between the flow coefficients is mainly caused by differential chordwise pressure gradients.

However, the comparison at $R = 0.98$, shown in Fig. 5, indicates the dramatic changes in the profiles observed at the two flow coefficients. The change in the profile can be attributed to two distinct effects. One of them is the chordwise pressure gradient, and the other is the magnitude of the leakage flow. More severe adverse pressure gradients exist at flow coefficient $\phi = 0.50$, and this gives rise to a nearly separated boundary layer at $s = 0.62$, even though the thickness of the boundary layer is about the same. The same trend is observed at $s = 0.80$. The outer layer is almost identical in both cases. The defect in velocity in the inner layer is much larger; this is caused by the severe pressure gradient. It is known that the leakage flow increases the suction pressures near the blade tip (due to the presence of a vortex), and its effect is clearly evident in the velocity profiles. The difference in velocity profiles is substantial near the trailing edge and the momentum defect is drastically increased. This is clear evidence of the effects of the leakage flow and the mixing, which are much higher for the lower flow coefficient. Hence, the combined effect of the chordwise pressure gradient and the increased leakage flow make the boundary layer profiles

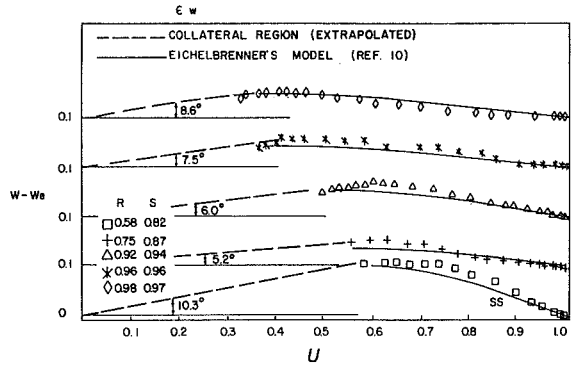

Fig. 9 Hodograph plot of velocity profiles on the suction side

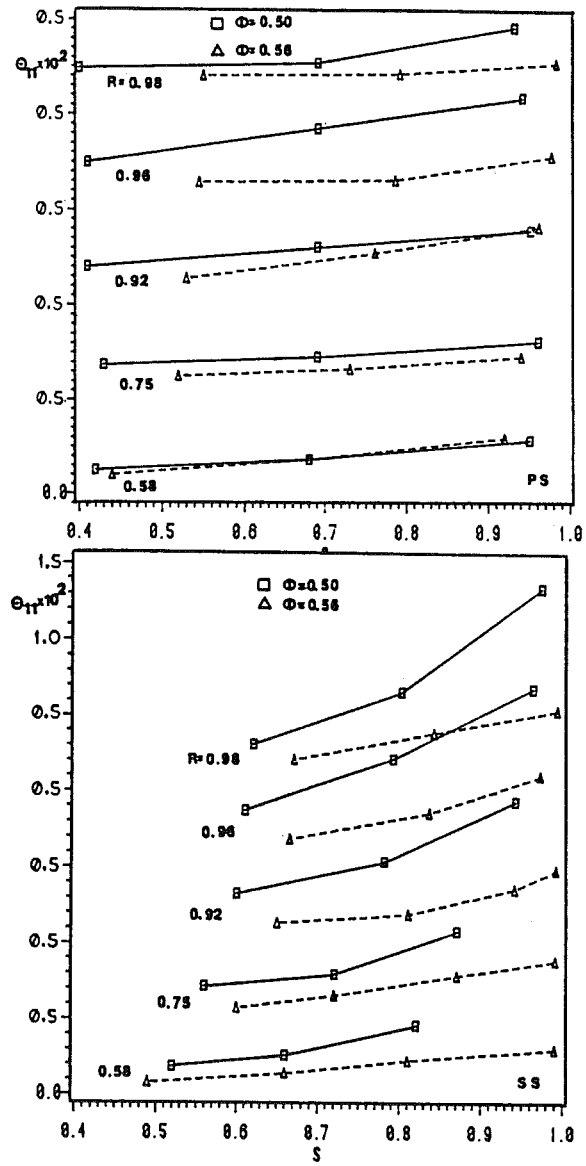

Fig. 10 Chordwise distribution of momentum thickness

substantially different. This also results in an appreciable increase in the momentum and the energy defects.

Analysis of the streamwise velocity profiles and a comparison with the power model

$$U = \left(\frac{n}{\delta}\right)^{1/m}$$

Downloaded 01 Jun 2010 to 171.66.16.57. Redistribution subject to ASME license or copyright; see http://www.asme.org/terms/Terms_Use.cfm

confirms the previous conclusion [3] that the exponent that gave the best fit varies from 1/4 to 1/8 on the suction surface and from 1/6 to 1/12 on the pressure surface. The power law gives poor representation of the profiles near the tip and trailing edge locations, particularly on the suction side.

Radial Velocity Profiles. The radial velocity profiles on the suction surface are shown in Fig. 6. The radial component of velocity starts developing at approximately 40 percent of the chord length and reaches its maximum value at the trailing edge. The radial velocities on the pressure side are found to be very small at most locations, except near the blade tip. Hence, the radial velocity profiles are shown for only two radial locations ($R = 0.96$ and 0.98) in Fig. 7.

The radial velocity distribution, shown in Fig. 6, indicates that the peak radial velocities near midchoard ($s = 0.5 \sim 0.6$) are nearly the same up to $R = 0.96$, beyond which a decrease in their value is observed. These peak velocities are less than 6 percent of the free-stream values. The peak radial velocities near the trailing edge location show values as high as 10 percent of the free-stream velocity near the hub, and about 6–7 percent at all other locations. It should be remarked that even though the peak velocities are highest at the hub location, the radial mass, momentum, and energy transport are highest near the tip region due to an increased boundary layer thickness. Higher values of radial velocities in the hub region are induced by the secondary flow inside the hub wall boundary layer. Both the secondary flow (radial component) and the radial velocity induced by rotation are in the same direction; hence, the observed higher values. The radial velocities, and hence the three dimensionality, are not large even at the peak pressure rise coefficient, but they will be substantially higher when the blades are stalled. One interesting observation from the radial velocity profiles shown in Fig. 6 is that the inner region (defined as the region from the surface to the location where the radial velocity peaks) of the three-dimensional boundary layer has been measured at R $\geq$ 0.75 for $\phi = 0.5$, but no such data are available at $\phi = 0.56$ [3]. This is because the boundary layers are thicker, about 9 percent of chord length at $R = 0.98$ with an inner layer of about 1 percent of chord length for $\phi = 0.5$. The radial velocity profiles are rather well behaved at most radial locations.

The radial velocities on the pressure surface boundary layers are found to be small up to $R = 0.92$, its magnitude being less than 2 to 3 percent of the free-stream velocity. Appreciable radial velocity is observed only near the tip region, as shown in Fig. 7. Some of the effects of leakage can be discerned by comparing the radial velocity distribution on the two surfaces at $R = 0.96$ and 0.98 (Figs. 6 and 7). The boundary layer on the pressure side is thinner than on the suction side, yet the peak radial velocity at $R = 0.96$ is higher on the pressure side. The "flat roof" type of distribution observed near the wall seems to indicate the presence of a strong radial jet caused by a strong radial pressure gradient (due to blade unloading). This effect is dominant at $R = 0.98$ on the pressure side. The distribution at $R = 0.96$ on the suction surface is more like a conventional three-dimensional boundary layer, caused mainly by the effects of Coriolis and centrifugal forces. In the case of the rotor, the leakage jet moves farther from the suction surface; hence, its influence is not dominant near the suction surface.

The radial velocity at $R = 0.98$ on the suction side is shown compared at $\phi = 0.50$ and 0.56 in Fig. 8. The major difference observed is near the trailing edge, where the peak radial velocities are about the same, but the radial velocities persist much farther from the wall due to a larger boundary layer thickness at $\phi = 0.50$.

An analysis of the radial velocity profile on the suction surface was carried out, and the best agreement was obtained

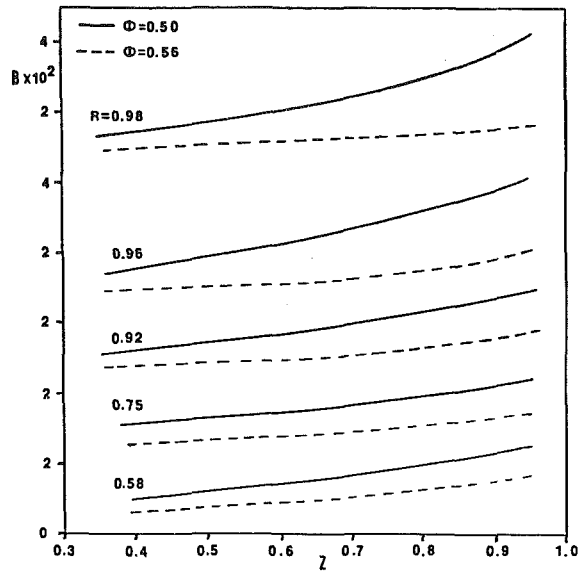

Fig. 11 Chordwise distribution of blade boundary blockage coefficient

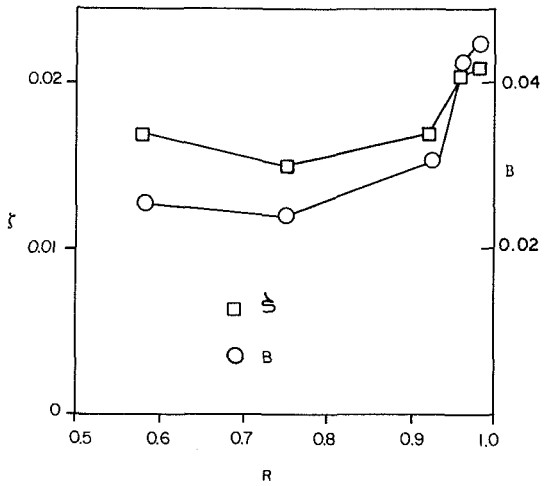

Fig. 12 Radial variation of ζ and B at the trailing edge

with Eichelbrenner's [10] model (fifth-order polynomial coupling of the radial and the streamwise velocity), given by

$$W - W_e = B\,U + \frac{1}{2}DU^2 - \left(6B + 4C + \frac{3}{2}D\right)U^3 + \left(8B + 7C + \frac{3}{2}D\right)U^4 - \left(3B + 3C + \frac{1}{2}D\right)U^5$$

where

$$B = \left(\frac{\partial W}{\partial U}\right)_w = \tan\,\epsilon_w,\quad C = \left(\frac{\partial W}{\partial U}\right)_e,\quad D = \left(\frac{\partial^2 W}{\partial U^2}\right)_w$$

Assuming that a collateral region exists near the wall, D is set equal to zero.

The experimental data near the trailing edge at various radial locations are plotted in Fig. 9 for the suction surface boundary layer. It can be seen from the graphs that Eichelbrenner's model gives very good predictions.

The presence of the inner region can be seen in Fig. 8. The limited data available at $R = 0.92$, 0.96, and 0.98 show that the inner region is nearly linear and a collateral region may exist in these three-dimensional boundary layers. It should be cautioned here that there is no conclusive evidence that such a region exists in these rotor boundary layers, even though it has

Downloaded 01 Jun 2010 to 171.66.16.57. Redistribution subject to ASME license or copyright; see http://www.asme.org/terms/Terms_Use.cfm

been observed in three-dimensional boundary layers on stationary bodies. The limiting streamwise angle derived from these measurements varies from 5.2 deg at $R = 0.75$ to 8.6 deg at $R = 0.98$, indicating that three dimensionality is mild. It should be remarked here that, even though the radial velocities inside the blade boundary layers are small, the data in the midpassage region at this location indicate large radial inward velocities, caused by the rollup of leakage flow as it travels from the suction to the pressure surface [11]. The limiting streamline angle is large near the hub ($R = 0.58$); this is caused by the combined effect of the secondary flow and the rotation, as explained earlier.

Boundary Layer Momentum Thickness. The momentum thickness is defined by

$$\theta_{11} = \frac{1}{C}\int_0^h U(1-U)\, dn; \qquad h > \delta$$

The values of θ_{11} derived from the experimental data are shown compared with the earlier data ($\phi = 0.56$) in Fig. 10.

On the pressure surface, θ_{11} varies almost linearly along the chordwise direction up to $R = 0.96$. The momentum thicknesses are small at both flow coefficients from hub to $R = 0.92$, with slightly higher values for $\phi = 0.50$. At $R = 0.96$, major changes are observed between the two flow coefficients. The momentum thickness at this location is almost doubled when ϕ is decreased from 0.56 to 0.5. This is caused by two related effects. A larger chordwise pressure gradient that exists at $\phi = 0.50$ causes the boundary layer thickness to increase from the values observed at $\phi = 0.56$, but not as much as observed. The other cause is the increased radial pressure gradient in the tip region when ϕ is decreased. This causes transport of the boundary layer toward the tip region and accounts for a large increase in θ_{11} observed at $R = 0.96$. But this trend is reversed as the tip of the blade is approached ($R = 0.98$).

The values of θ_{11} on the pressure surface at $R = 0.98$ are lower than those at $R = 0.96$ and are almost the same at both flow coefficients up to $s = 0.7$. This is caused by the leakage flow. The leakage flow has the same effect as "suction" on a boundary layer. Some of the low-momentum fluid is transported to the clearance region, thus decreasing θ_{11} from $R = 0.96$ to 0.98. Earlier investigations [11] have revealed that most of the leakage flow takes place from approximately 0.25 chord length to 0.75 chord length; hence, its effect should diminish as the trailing edge is approached. This is clear from the θ_{11} distribution from $s = 0.7$ to 0.9. Even though the θ_{11} values increase along the chord length, they are generally lower than those at $R = 0.96$. The values of θ_{11} near the trailing edge are 0.006 and 0.004 at $R = 0.96$ and 0.98, respectively, and the corresponding values are 0.004 and 0.0025 at $s = 0.7$.

The distribution on the suction surface indicates that the momentum thickness at $\phi = 0.5$ is substantially higher than the thicknesses observed at $\phi = 0.56$ at all radii. In the latter case, the increase in momentum thickness along the chordwise direction is almost linear. But the values of θ_{11} at $\phi = 0.50$ show a much larger rate of increase beyond midchord. The major influence of the blade loading is felt at $R > 0.92$. Here θ_{11} is nearly doubled at most locations, and nearly tripled near the trailing edge of the blade tip. The increases observed at $R = 0.58$, 0.75 are mostly caused by a larger adverse pressure gradient at $\phi = 0.50$. However, substantially higher values of θ_{11} from $R = 0.92$ to 0.98 are due to this effect as well as the leakage flow. The leakage flow, which moves farther into the passage toward the pressure surface and rolls up to form a vortex [11], tends to induce a large radial pressure gradient close to the blade suction surface near the tip. This effect is more pronounced at $\phi = 0.50$. The vortex tends to entrain mass and momentum, which thus introduces additional radial flows. Hence, the effect of leakage flow is opposite to that observed on the pressure side. The leakage flow and the radial transport of the boundary layer have a major influence in the dramatic increase in θ_{11} near the tip region when ϕ is decreased. The increase in θ_{11} is as much as 160 percent near the trailing edge at $R = 0.98$.

Blade Boundary Layer Blockage. The blade boundary layer blockage coefficient is defined as follows

$$B = \frac{(\delta_1^*)_{ss} + (\delta_1^*)_{ps}}{\cos \beta_c} \frac{C}{t} \tag{1}$$

where β_c is the blade camber angle.

The blade blockage coefficient derived from the experimental data is shown and compared with the data at $\phi = 0.56$ in Fig. 11. As expected, the blockage coefficient increases at all radii, with a substantially larger increase at $R = 0.96$ and 0.98. A detailed interpretation of this increase was given earlier. The suction surface boundary layer, which increases substantially at higher loading, has a major influence in increasing the blockage coefficient. The blockage coefficient is nearly constant from hub to $R = 0.92$ (2.3 to 3 percent) and increases rapidly to 4 percent at $R = 0.96$ and 0.98. The blockage coefficient at the trailing edge never exceeds 2 percent for the higher flow coefficient ($\phi = 0.56$).

Radial Variation of Loss and Blockage Coefficients. The aerodynamic losses at each radius can be estimated from the momentum thickness at the trailing edge using Speidel's [12] formula

$$\zeta = \frac{2[(\theta_{11})_{SS} + (\theta_{11})_{PP}]_{TE}}{\cos^3 \beta_2 \cos^{-2} \beta_1} \frac{C}{t} \tag{2}$$

where β_1 and β_2 are inlet and outlet relative air angle, respectively. The radial distribution of the loss coefficient derived from equation (2), based on measured values of θ_{11}, is shown in Fig. 12. Also shown plotted in this figure is the boundary layer blockage coefficient at the trailing edge derived from equation (1). The loss coefficients are found to be higher than those measured at the design condition (see Fig. 13, [3]) at most locations including the tip region. The percentage increase in the loss coefficient is much higher from hub to $R = 0.959$. The distributions of ζ and B are very similar, indicating a close correlation between the two.

It should be remarked here that Speidel's formula is based on two-dimensional analysis and it is only an approximation for three-dimensional flow.

Composite Velocity Profiles. The inviscid flow data acquired earlier with a laser-doppler velocimeter (LDV) are integrated with the boundary layer data to derive composite velocity profiles from blade-to-blade at various chordwise locations. The LDV data are presented and interpreted in [7]. Only the axial and tangential components were measured using the LDV system. Hence, the resultant of axial and tangential velocity $W_s = \sqrt{W_\theta^2 + V_Z^2}$, which is equivalent to U near the blade surface, is shown plotted. Furthermore, there was a slight difference in the axial location of the LDV measurement and some of the hot-wire measurements. In such a case, the data are interpolated.

The composite profiles at $R = 0.75$ and 0.96 are shown plotted in Figs. 13 and 14, respectively. Z is the chordwise distance normalized by the local chord. $Z = -0.02$ is upstream of the leading edge and $Z = 1.02$ is downstream of the trailing edge.

The results at $R = 0.75$ indicate that the inviscid flow dominates the leading edge region. The data at $Z = -0.02$ show the effect of the leading edge and the stagnation point in deceleration of the flow. The streamwise velocity gradients are large near the leading edge. For example, near the suction surface, the value of W_s increases from 0.53 at $Z = -0.02$ to 0.9

Downloaded 01 Jun 2010 to 171.66.16.57. Redistribution subject to ASME license or copyright; see http://www.asme.org/terms/Terms_Use.cfm

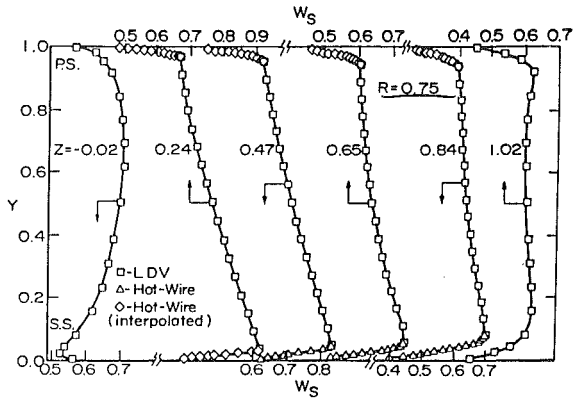

Fig. 13 Composite velocity profiles (W_S) at $R = 0.75$, $\phi = 0.50$

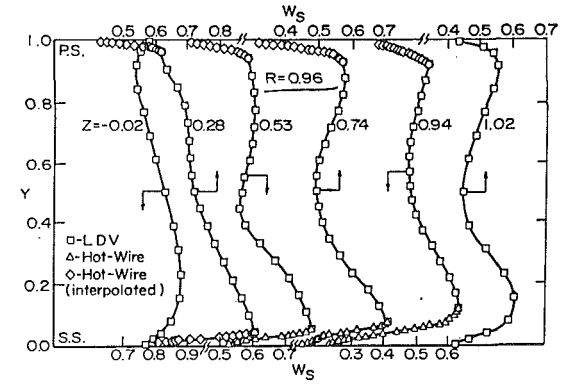

Fig. 14 Composite velocity profiles (W_S) at $R = 0.96$, $\phi = 0.50$

at $Z = 0.24$. As observed earlier, the boundary growth on the suction surface is higher than on the pressure surface, and the boundary layer grows rapidly near the trailing edge.

The composite profile at $R = 0.96$ (Fig. 14) shows several features that result from the leakage flow and the chordwise pressure gradient. The inviscid region (where W_s increases linearly from pressure to suction surface) is small and the distribution near midpassage shows the effect of mixing between leakage flow and the main stream, resulting in a wake type of profile. The boundary layer behavior has been interpreted earlier.

The features that make this boundary layer extremely complex and one which cannot be described by conventional profiles (law of the wall, power law, etc.) are clearly seen in this figure. The velocity profile has a peak close to the blade surface and a minimum at the center of the passage. The edge of the boundary layer cannot be defined. Such flows have to be treated by the entire Navier–Stokes equation, and the boundary layer approximations are not valid. The maximum defect in velocity inside the boundary layer is as much as the maximum defect in velocity near the midpassage at most locations beyond $Z = 0.28$.

Conclusions

The conclusions on the behavior of the boundary layer at the peak pressure rise coefficient are as follows:

1 Even at the peak pressure rise coefficient, the boundary layers are well behaved at most locations. One probable reason for this is that the end wall region is controlling the peak pressure rise coefficient. There is a substantial increase in the momentum and the boundary layer thicknesses near the tip region as the flow coefficient is decreased from its design value to the peak pressure rise coefficient condition.

2 Momentum thicknesses of the suction surface boundary layers are substantially higher than those on the pressure surface.

3 The boundary layer profile up to about 8 percent of span from the tip is either separated or shows a tendency to separate.

4 The leakage flow at higher loading coefficient increases the momentum and boundary layer thicknesses substantially on the suction surface. It has the opposite effect on the pressure side.

5 The blockage coefficient also increases substantially when the blade loading is increased, especially in the outer 8 percent of span from midchord to the trailing edge.

6 The composite velocity profiles show well-behaved inviscid and boundary layer flows at midradius, while the tip region shows complex features that include wake-type profiles away from the blade surfaces. Substantial boundary layer growth occurs on both surfaces at about 8 percent of the span from the blade tip. The pressure surface boundary layer momentum thickness decreases beyond this radius, while on the suction surface it increases beyond this radius.

7 The limiting streamline angles are found to be small, varying from 5 to 10 deg.

8 Radial velocities of maximum magnitude occur away from the surface and their values are usually small, except in the hub region where the peak value is found to be about 10 percent of the free-stream velocity.

Acknowledgments

This work was partially supported by NASA grant NSG 3212, with P. Sockol as the contract monitor and the International Exchange of Scholars (Grant No. 83-03827) through a Fulbright Scholar award to Dr. Popovski.

References

1 Anand, A. K., and Lakshminarayana, B., "Three-Dimensional Boundary Layer in a Rotating Helical Channel," ASME *Journal of Fluids Engineering*, Vol. 97, 1975, pp. 197–210.

2 Evans, R. L., "Turbulent Boundary Layers on Axial Flow Compressor Blades," Ph.D. Thesis, Cambridge University, 1973.

3 Pouagare, M., Galmes, J. M., and Lakshminarayana, B., "An Experimental Study of the Compressor Rotor Blade Boundary Layer," ASME JOURNAL OF ENGINEERING FOR GAS TURBINES AND POWER, Vol. 107, 1985, p. 366.

4 Toyokura, T., Kurokama, J., and Kimoto, Y., "Three-Dimensional Boundary Layer Flow on Rotating Blades," *Bulletin of the JSME*, Vol. 25, 1982, pp. 513–520.

5 Lakshminarayana, B., Hah, C., and Govindan, T. R., "Three-Dimensional Boundary Layer Development on a Fan Rotor Blade," *AIAA Journal*, Vol. 22, 1984, pp. 83–89.

6 Hodson, H. P., "The Development of Unsteady Boundary Layers on the Rotor of an Axial-Flow Turbine," AGARD-CP-351, 1983.

7 Popovski, P., and Lakshminarayana, B., "An Experimental Study of the Compressor Rotor Field at Off-Design Conditions Using Laser Doppler Velocimeter," *AIAA Journal*, Vol. 24, Aug. 1986, pp. 1337–1345.

8 Lakshminarayana, B., "An Axial Flow Research Compressor Facility Designed for Flow Measurement in Rotor Passages," ASME *Journal of Fluids Engineering*, Vol. 102, 1980, pp. 402–411.

9 Klatt, F., "The X Hot-Wire Probe in a Plane Flow Field," DISA Information, No. 8, July 1969.

10 Eichelbrenner, E. A., "Three Dimensional Boundary Layer," *Ann. Rev. Fluid Mech.*, Vol. 5, 1973, pp. 339–360.

11 Lakshminarayana, B., Pouagare, M., and Davino, R., "Three-Dimensional Flow Field in the Tip Region of a Compressor Rotor Passage – Part I and Part II," ASME JOURNAL OF ENGINEERING FOR POWER, Vol. 104, 1982, pp. 760–781.

12 Speidel, L., "Berechnung der Stromungverluste von Ungestaffelten Ebenen Schaufelgittern," *Ing. Arch*, Vol. 22, 1954, p. 295.

Downloaded 01 Jun 2010 to 171.66.16.57. Redistribution subject to ASME license or copyright; see http://www.asme.org/terms/Terms_Use.cfm

Blade Design of Axial-Flow Compressors by the Method of Optimal Control Theory—Physical Model and Mathematical Expression

Chuan-gang Gu
Postdoctoral Research Fellow.

Yong-miao Miao
Professor.

Department of Power Mechanical Engineering,
Xi'an Jiaotong University,
Xi'an, People's Republic of China

In the design of compressor blades we put forward an optimization flow-type problem which enables the designers to consider the optimization of specified performance index of the flow-type characteristics, such as that of work or efficiency of a compressor stage. The method of the diffusion factor flow-type design (DFFTD), presented by the authors [1], is taken here as a physical model. On the basis of optimal control theory a mathematical model of the optimal flow-type problem has been established and further recast into a typical form of optimal control problem with free initial conditions, terminal constraints, and state variable inequality constraints.

Introduction

In a turbomachine the flow is very complex, and many parameters usually have various equality or inequality constraints that cause great difficulty to optimization problem. However, the previous investigations and studies of optimization of blade design were restricted to use only the typical method in solving the limiting value of function or functional [6–8] and, thus, the various inequality constaints could not be treated. The optimization of a two-dimensional cascade in incompressible flow was resolved by means of optimal control theory [3]. The idea in the present work is to investigate the optimal flow-type problem, its theory and calculation, in the S_2 plane (which is close to the meridian plane of a turbomachine). Due to the complexity of the problem, only incompressible or subsonic flows are considered here.

It is well known that in aerodynamic blade design of a compressor stage the flow-type design in the vaneless clearance (also called the twist rule of blade) – i.e., the distribution of a certain flow parameter along the height of blade – represents a very important link. On the basis of this distribution the quasi-three-dimensional flow equation can be solved which gives the distributions of all parameters, including pressure ratio, efficiency, velocities, inlet and outlet angles, etc. This forms the base of blade design. At the present time the method of radial-equilibrium calculation and the method of equilibrium along quasi-orthogonal lines in the meridian plane are widely used.

Up to now, various flow types in design have been offered: free vortex ($T(r)=C_u r=\text{const}$); forced vortex ($T=\text{const}\cdot r^2$); equal C_u ($T/r=\text{const}$); or their combinations ($T=Ar+B$, $T=Ar^2+B$); and the specified distribution of α or β, etc. Recently, the inequable work design along the height of blade, e.g., the control vortex, equal total pressure ratio, etc., have been more and more adopted. To sum up, in principle, any one of the above flow types or their combinations can be considered as a degree of freedom in design. It is obvious that for a certain flow type the distributions of its parameter along the height of blade may also be variable but, at least, one of them may be optimal for the performance index; this forms the physical base of optimization of flow type. Generally, the present method can be used for any optimization problem in flow-type design but the degree of difficulty for solving the optimal problem, particularly with inequality state constraints, depends on the selection of flow type.

In [1] the author has selected the distribution of loads and the diffusion factor as basic parameters of specified flow type, and a new inequable work design – the diffusion factor flow-type design (DFFTD) – has been proposed, by means of which the blade load can directly be chosen as a degree of freedom in design. In other words, this method gives the designers a great versatility in design to fully develop the capacity of work done by blades; thus the limits of load can reasonably be controlled and the efficiency and the operation range of impeller can also be increased and expanded, respectively. Therefore this flow type is used as the base of the present paper.

Another reason for choosing the DFFTD as the physical model of optimizational problem in present work is to simplify the mathematical model of the optimal problem, to facilitate imposing the necessary constraints, and to select such an index function which can be directly used in design practices, as, for instance, the efficiency or the amount of load.

Basing on optimal control theory [5, 9], a mathematical model of optimal flow-type problem for rotor blade of a com-

Contributed by the Gas Turbine Division of THE AMERICAN SOCIETY OF MECHANICAL ENGINEERS and presented at the 31st International Gas Turbine Conference and Exhibit, Düsseldorf, Federal Republic of Germany, June 8–12, 1986. Manuscript received at ASME Headquarters February 7, 1986. Paper No. 86-GT-183.

Copyright © 1987 by ASME

Downloaded 01 Jun 2010 to 171.66.16.57. Redistribution subject to ASME license or copyright; see http://www.asme.org/terms/Terms_Use.cfm

pressor stage has been established and further recast in a typical form of optimal control problem with free initial conditions, terminal constraints, and inequality constraints of state variables.

Physical Model of an Optimal Problem in Rotor Blade Design

In the present work the radial momentum equation for vaneless clearance in S_2 flow planes is applied. Because the radial component F_r of $\bar{F}$ in S_2 flow planes can be neglected with sufficient accuracy in the vaneless clearance, the equation is similar to the radial-equilibrium equation of axial symmetric flow [1].

Supposing the flow to be nonisentropic, relatively steady, and neglecting the action of local viscous force, the increase in entropy is used to take account of the effects of viscosity and other losses, e.g., separation of boundary layer, leakage flow, etc. The continuity equation, r momentum equation, and the work-enthalpy equation are as follows

$$\frac{\partial C_r}{\partial r}+\frac{C_r}{r}+\frac{\partial C_z}{\partial Z}=0 \tag{1}$$

$$\left(\frac{g}{A}\right)\frac{\partial i^*}{\partial r}-\left(\frac{g}{A}\right)T\frac{\partial S}{\partial r}=\frac{C_u^2}{r}+\frac{1}{2}\frac{\partial C^2}{\partial r}-C_r\frac{\partial C_r}{\partial r}-C_z\frac{\partial C_r}{\partial Z} \tag{2}$$

$$H=\frac{i_2^*-i_1^*}{A}=\frac{C_{2u}U_2-C_{1u}U_1}{g} \tag{3}$$

Since no heat exchange takes place in the blade passage, the increase of entropy can be expressed as [2]

$$S_2-S_1=A\cdot R\cdot\ln\frac{1}{\left\{1-\dfrac{\bar{\omega}_R\left[1-\left(1+\dfrac{k-1}{2}(M_1')^2\right)^{-k/(k-1)}\right]}{1+\dfrac{k-1}{2}M_T^2\left[1-\left(\dfrac{\gamma_1}{\gamma_2}\right)^2\right]^{k/(k-1)}}\right\}} \tag{4}$$

where $\bar{\omega}_R$ is the total pressure loss coefficient in the rotor, which is an empirical formula including σ_R, β_2, and $D_R(r)$.

The equation of state for perfect gas is written as

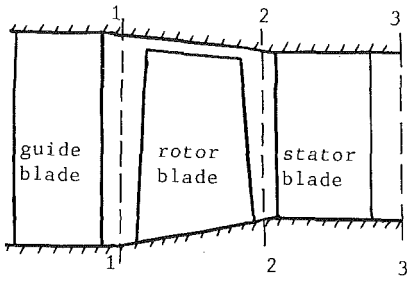

Fig. 1 Meridian flow passage (schematic)

$$P=\rho\cdot g\cdot R\cdot T \tag{5}$$

The formulation of the diffusion factor is

$$D_R=1-\frac{W_2}{W_1}+\frac{W_{1u}T_1-W_{2u}T_2}{\sigma_R W_1(r_1+r_2)} \tag{6}$$

Introducing equal-annular-area coordinates (see Appendix A), the calculation equations for all vaneless clearance sections, as shown in Fig. 1, can be expressed as

$$-\left(\frac{g}{A}\right)\frac{\partial i^*}{\partial r}+T\cdot\left(\frac{g}{A}\right)\frac{\partial S}{\partial r}+\frac{1}{2}\frac{\partial C_m^2}{\partial r}+\frac{1}{2}\frac{\partial C_u^2}{\partial r}+\frac{C_u^2}{r}+C_m^2\left(f_i+\frac{\sqrt{1+\tan^2\psi}}{R_m}\right)=0 \tag{7}$$

where

$$f_i=\left[\frac{2\mathrm{M}}{1+(\mathrm{M}r+N/r)^2}(\mathrm{M}r+N/r)\right]_i \qquad (i=1,\ 2)$$

The term f_i represents effect of slope of a streamline whereas $(\sqrt{1+\tan^2\psi}/R_m)$ represents that of curvature. R_m is the radius of a streamline.

The subscripts $i=1$, 2 denote inlet and outlet sections of a rotor, respectively.

It is known that there is one, and only one, freedom of choice in design for any section. In the present work the distributions of $C_u(r_1)$ and $D_R(r_2)$ have been chosen as freedoms of design (see Appendix B).

This indicates that with different distributions of $C_u(r_1)$ and $D_R(r_2)$, we will obtain different design results. The so-called optimal flow-type problem is to select one set of distributions which evolve optimal results.

Generally speaking, the larger the values of diffusion factor D_R are, the heavier the blade load would be and the bigger the entailed losses would be. Therefore, for a previously specified performance index there would be an optimal diffusion factor distribution.

Nomenclature

A = equivalent of heat = 1/427 kcal/kg-m
C = absolute velocity
D = diffusion factor
F = blade force
g = 9.81 m/s^2
H = amount of work
i = enthalpy
k = 1.4
M = Mach number
M_T = $\omega r/a_{01}'$
R = gas constant
S = entropy
s = control variable
U = peripheral velocity
W = relative velocity
w = angular velocity
β = angle between the relative velocity and axial direction
η = efficiency
ρ = density
σ = consistency of blading
ψ = angle between the coordinate line and axial direction (Fig. 2)
ω = total pressure loss coefficient

Subscripts

av = averaged
h = root of blade
m = streamline direction
pr = provided
R = rotor
r = radial direction or component
t = top of blade
u = peripheral direction or component
z = axial direction or component
0 = stagnation
1 = inlet of rotor
2 = outlet of rotor

Superscripts

= averaged for mass flow

Downloaded 01 Jun 2010 to 171.66.16.57. Redistribution subject to ASME license or copyright; see http://www.asme.org/terms/Terms_Use.cfm

Restrictive Conditions of the Optimal Flow Type

In order to make the optimal solution have realistic senses, we have to add the following restrictive conditions:

(*a*) As the flow condition at the blade tip is more complex, it is better for us to select a smaller value of diffusion factor there, usually a value of about 0.4.

(*b*) Because the peripheral velocity is lower at the blade roots, the ability to do work there being smaller, we have to put on a lower load at the roots, and this will help to improve the flow and efficiency conditions at the hub.

(*c*) In order to widen the operation range of a compressor, it is required that surging margin SM $\geq$ 15 percent, and thus average design value of D_{Rav} should be about 0.5 or less. At the same time, to make the blade's ability to do work fully developed, the diffusion factors in the intermediate part of flow passage should be approximately equal.

(*d*) The mass flow through all sections should be constant.

(*e*) An average value of consistency σ_{av} at the mean radius suggested in [4] is taken and the radial distribution of consistencies is given by

$$\sigma = \sigma_{av} \cdot (r_{1av} + r_{2av})/(r_1 + r_2) \tag{8}$$

(*f*) The values of other variables are free except for the mass flow.

Of course, the other constraint requirements and performance indexes demanded by the users should be met.

Thus, the optimal flow-type problem for rotor blade design of a stage can be expressed as: to find an optimal distribution of $C_u(r_1)$, $D_R(r_2)$ [or $H(r_1)$, $D_r(r_2)$] which, while satisfying all the constraint requirements, will make the efficiency (the total pressure ratio, or amount of work) attain its maximum.

Mathematical Expression of Optimal Flow-Type Problem

The system differential equations for the optimal flow-type problem are rather complex. They include various equality and inequality constraints.

Proper selection of state variables and control variables is critical for solving the optimal problem. We here take $C_u(r_1)$, $C_m(r_1)$, $G_1(r_1)$, $G_2(r_2)$, $C_u(r_2)$, and $D_R(r_2)$ as state variables and transform the above-mentioned physical model into a typical optimal control form. Besides, the constraints (*a*), (*b*), and (*c*) are also imposed.

Considering the indicated physical model and various constraints the mathematical expression for the optimal flow-type problem is written as follows:

Performance index for the system may be one of the following selections (other demanded requirements, of course, may further be provided)

$$(a)\ \bar{H} = \int_{r_n}^{r_t} (x_5 r_2 - x_2 r_1)(C_{2m} \cdot \cos\psi_2 \cdot \rho_2 \cdot g \cdot 2\pi r_2) dr_2 \rightarrow \max;$$

$$(b)\ \bar{\eta} = \int_{r_n}^{r_t} \eta(r_2) \cdot C_{2m} \cdot \cos\psi_2 \cdot \rho_2 \cdot g \cdot 2\pi r_2 dr_2 \rightarrow \max \tag{9};$$

(*c*) ensuring a given $\bar{\eta}$, $\bar{H} \rightarrow \max$ (i.e., satisfying $\bar{\eta} \geq \eta_{\min}$);

(*d*) ensuring a given $\bar{H}$, $\bar{\eta} \rightarrow \max$ (i.e., $\bar{H}$ satisfying $\bar{H} \geq \bar{H}_{\min}$).

The system differential equations are expressed as:

$$\frac{dx_1}{dr_2} = f_1(x_1, x_2, s_1, r_2) \tag{10}$$

$$\frac{dx_2}{dr_2} = s_1 \tag{11}$$

$$\frac{dx_3}{dr_2} = 2\pi r_1 \cdot \rho_1 \cdot g \cdot C_{1m} \cdot \cos\psi_1 \frac{dr_1}{dr_2} = f_3(x_1, x_2, r_2) \tag{12}$$

$$\frac{dx_4}{dr_2} = 2\pi r_2 \cdot \rho_2 \cdot g \cdot C_{2m} \cdot \cos\psi_2 = f_4(x_1, x_2, x_5, x_6, r_2) \tag{13}$$

$$\frac{dx_5}{dr_2} = f_5(x_1, x_2, x_5, x_6, s_1, s_2, r_2) \tag{14}$$

$$\frac{dx_6}{dr_2} = s_1 \tag{15}$$

The six-dimensional state variable $\bar{X}$ and two-dimensional control variable $\bar{S}$ are expressed as:

$$\bar{X} = (x_1, x_2, x_3, x_4, x_5, x_6)^T = (C_{1m}, C_{1u}, G_1, G_2, C_{2u}, D_r)^T \tag{16}$$

$$\bar{S} = (s_1, s_2)^T \tag{17}$$

where G_1 and G_2 denote the mass flow through sections 1 and 2, respectively (see Fig. 1).

Equations (10) and (14) are derived, respectively, from equation (7) on sections 1 and 2. Equations (12) and (13) are differential forms of mass conservation. Note that control varuables s_1 and s_2 have been introduced in equations (11) and (15).

The system is subject to the following conditions and constraint:

Initial conditions are

$$\begin{cases} x_1(r_h),\ x_2(r_h),\ x_5(r_h),\ x_6(r_h),\ \text{free} \\ x_3(r_h) = x_4(r_h) = 0 \end{cases} \tag{18}$$

Terminal conditions are

$$\begin{cases} x_1(r_t),\ x_2(r_t),\ x_5(r_t),\ x_6(r_t),\ \text{free} \\ x_3(r_t) = x_4(r_t) = G_{pr} \end{cases} \tag{19}$$

The inequality constraint on state variable is

$$x_6(r_2) \leq D_{pr}(r_2) \tag{20}$$

where D_{pr} is the constraint on diffusion factor provided by the designer.

Thus, the optimal problem for rotor blade design can be expressed as: Determine an optimal control variable distribution $\bar{S} = (s_1, s_2)^T$ which, transferring state variables from initial condition equation (18) to terminal equation (19), maximizes the performance index for the system [equation (9)], satisfying the constraint equation (20).

This is a typical form of an optimal problem with free initial conditions, terminal constraints, and an inequality constraint on a state variable. The optimal trajectory thus obtained is just the required optimal flow type.

Conclusions

Basing on the optimal control theory, the physical model of optimal flow-type problem for rotor blade design of a compressor stage with many constraints, as well as its mathematical expression, has been presented. It has been recast into a typical form of an optimal control problem. These methods can be extended conveniently to optimal design problem of other flow types. They appear suitable also for optimal problems with other performance indices and constraints than equation (9), e.g., requirements of total pressure, inlet or exit angles, efficiency, power, etc.

Downloaded 01 Jun 2010 to 171.66.16.57. Redistribution subject to ASME license or copyright; see http://www.asme.org/terms/Terms_Use.cfm

References

1 Gu Chuan-gang, "Theory, Application and Optimization of the Diffusion Factor Flow-Type Design for Axial-Flow and Mixed-Flow Compressors," *Chinese Journal of Mechanical Engineering*, Vol. 19, No. 2, 1983, pp. 87–94.

2 "Aerodynamic Design of Axial-Flow Compressors," NASA SP 36, 1965.

3 Liu, Gao-Lian, "A New Theory of Two-Dimensional Airfoil Cascades Optimized Aerodynamically via a Generalized Maximum Principle," *ACTA Mechanics Sinica*, Vol. 12, No. 2, 1980, pp. 337–346.

4 Liu, Gao-Lian, "Optimization of Consistency of Plane Cascade" [in Chinese], *Turbomachinery*, No. 1, 1979.

5 Ho, A. E. B., and Ho, Y. C., *Applied Optimal Control*, Hemisphere Publishing Corporation, New York, 1979.

6 Shubenko-Shubin, L. A., *Heatenergy* [in Russian], No. 7, 1976.

7 Shubenko-Shubin, L. A., *Powermachinery* [in Russian], No. 5, 1977.

8 Rzheznikov, Yu. V., *Heatenergy* [in Russian], No. 4, 1972.

9 Sage, A. P., and White, C. C. III, *Optimal System Control*, Prentice-Hall, New York, 1977.

APPENDIX A

The Equal-Annular-Area Coordinate

As shown in Fig. 2, the top and bottom coordinate lines are laid in the walls of the passage. Considering equal-annular-area for any coordinate line, we have

$$\frac{r_1^2 - r_{1h}^2}{r_{1t}^2 - r_{1h}^2} = \frac{r^2 - r_h^2}{r_t^2 - r_h^2} \tag{21}$$

$$\therefore r^2 = r_h^2(Z) + [r_t^2(Z) - r_h^2(Z)]\left(\frac{r_1^2 - r_{1h}^2}{r_{1t}^2 - r_{1h}^2}\right) \tag{22}$$

$$\tan\psi = \frac{dr}{dZ}\bigg|_t = \mathrm{M}\cdot r + N/r \tag{23}$$

where

$$\mathrm{M} = \frac{1}{r_t^2 - r_h^2}\,(r_t \cdot \tan\psi_t - r_h \cdot \tan\psi_h)$$

$$N = \frac{r_h \cdot r_t}{r_t^2 - r_h^2}\,(r_t \tan\psi_h - r_h \tan\psi_t)$$

APPENDIX B

The calculational methods in equation (7) have been explained in [1]. The brief of the calculation on section 2-2 of the rotor (see Fig. 1) is written as follows:

According to the distribution of $C_u(r_1)$, the parameters of section 1-1 (see Fig. 1) are yielded. Then, all the dependent unknown variables are transformed to the functions of $C_{2u}r_2$, so we have a first-order nonlinear differential equation

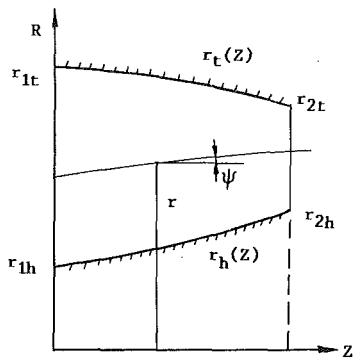

Fig. 2

$$\frac{dC_{2u}r_2}{dr_2}(C_{2u}r_2 + R_1) + R_2(C_{2u}r_2)^2 + R_3(C_{2u}r_2) + R_4 + T_2\left(\frac{g}{A}\right)\sigma_R^2(r_1 + r_2)^2\,\frac{dS_2}{dr_2} = 0 \tag{24}$$

where

$$R_1 = A_2 \cdot \sigma \cdot (r_1 + r_2)$$

$$R_2 = \left[\frac{2}{\sigma_R(r_1 + r_2)}\,\frac{d}{dr_2}\left(\frac{1}{\sigma_R(r_1 + r_2)}\right) + \frac{B_2}{\sigma_R^2(r_1 + r_2)^2} + \frac{2}{r_2^3} - \frac{B_2}{r_2^2}\right]\frac{\sigma_R^2(r_1 + r_2)^2}{2}$$

$$R_3 = \left[2A_2\,\frac{d}{dr_2}\left(\frac{1}{\sigma_R(r_1 + r_2)}\right) + \frac{2}{\sigma_R(r_1 + r_2)}\,\frac{dA_2}{dr_2} + \frac{2A_2B_2}{\sigma_R(r_1 + r_2)} + 2B_2\omega\right]\frac{\sigma_R^2(r_1 + r_2)^2}{2}$$

$$R_4 = \left[2A_2\,\frac{dA_2}{dr_2} - 2r_2\omega^2 + A_2^2B_2 + 2\omega\,\frac{d(C_{1u}r_1)}{dr_2} - B_2r_2^2\omega^2 - \frac{di_1^*}{dr_2} \cdot g\right]\frac{\sigma_R^2(r_1 + r_2)^2}{2}$$

$$A_2 = \left[(1 - D_R)W_1 - \frac{C_{1u}r_1}{\sigma_R(r_1 + r_2)} + \frac{\omega}{\sigma_R}(r_1 - r_2)\right]$$

$$B_2 = \frac{4\mathrm{M}(\mathrm{M}\cdot r + N/r)}{1 + (\mathrm{M}\cdot r + N/r)^2} + \frac{2\cdot\sqrt{1 + \tan^2\psi_2}}{R_{m2}}$$

When the distribution of $D_R(r_2)$ is provided, the parameters of section 2-2 can be calculated by solving the above equation. It is well known that different results are obtained for different distributions of $D_R(r_2)$. In the calculation of the term (dS_2/dr_2), the values of C_{2u} and β_2 must be used but they are unknown before; therefore the iteration method for β_2 is applied.

Downloaded 01 Jun 2010 to 171.66.16.57. Redistribution subject to ASME license or copyright; see http://www.asme.org/terms/Terms_Use.cfm

Blade Design of Axial-Flow Compressors by the Method of Optimal Control Theory—Application of Pontryagin's Maximum Principles, a Sample Calculation and Its Results

Chuan-gang Gu
Postdoctoral Research Fellow.

Yong-miao Miao
Professor.

Department of Power Mechanical Engineering,
Xi'an Jiaotong University,
Xi'an, People's Republic of China

Using the continual transformation technique [3] and the augmented penalty function method, the typical optimal control problem with various constraints proposed in the paper [2] has been converted to a new equivalent optimal control problem with no constraint. This enables the application of Pontryagin's maximum principle. Further, by means of the conjugate gradient method an example of the calculation is shown and the corresponding program is developed. A satisfactory optimal diffusion factor distribution has been obtained.

Introduction

In the previous paper [2] the optimal flow-type design problem with many equality constraints has been recast into a typical form of optimal control problem with free initial conditions, terminal conditions, and an inequality constraint on state variables. These constraints will involve great difficulties in solving the problem. In order to be able to apply the Pontryagin's maximum principle [3, 4] the problem has to be treated specially. In the present work by means of a continual transformation technique [3] the problem with inequality constraints on state variables can be converted to a new problem without constraint. In treating the terminal conditions, use has been made of the augmented penalty function method which is a combination of the penalty function and Lagrange's multiplier, so the original problem with terminal conditions is transformed to a new problem with new performance index and free terminal conditions. Therefore, a new optimal control problem with no constraint is established. In the numerical computation the conjugate gradient method has been utilized so that a faster approach to the optimal control and trajectory is possible.

As an example, the calculation and programming of optimal diffusion factor flow type for a rotor of single-stage compressor have been carried out. In the present situation, the initial values of diffusion factors (as a state variable) are arbitrarily given, after four–five iterations, the optimal trajectories, including an optimal distribution of diffusion factor, are obtained, while satisfying the constraints, the maximum value of the performance index has been reached. The results are satisfactory. It shows that the calculation method and computational program have good accuracy and convergence.

Treatments and Methods of Calculation

(*a*) Treatment of the Terminal Condition – Augmented Penalty Function Method. It is well known that the original penalty function method has been used frequently in optimization problems. However, in some cases it often fails to approach the optimal point in the state space. The reason for this is as follows: The new performance index, with large penalty parameter N, has a long narrow "valley" containing the optimal point at the "bottom". Gradient procedures for finding this point tend to go back and forth, from one side of the narrow valley to the other side. If N is very large, the "width" of the valley may become comparable to the numerical accuracy of the calculation, and the gradient procedure breaks down completely [6].

Therefore, the penalty function method combined with the Lagrange multiplier method, namely the augmented penalty method, has been introduced.

For a terminal condition of $\psi_j[x(r_f), r_f] = 0$, introducing a j-dimension multiplier and a penalty parameter N, a new performance index $\tilde{J}$ is formed as

$$\tilde{J} = J + \frac{N}{2}\psi^T \cdot \psi + \mu^T \cdot \psi[x(r_f), r_f] \tag{1}$$

Contributed by the Gas Turbine Division of THE AMERICAN SOCIETY OF MECHANICAL ENGINEERS and presented at the 31st International Gas Turbine Conference and Exhibit, Düsseldorf, Federal Republic of Germany, June 8–12, 1986. Manuscript received at ASME Headquarters February 7, 1986. Paper No. 86-GT-182.

Copyright © 1987 by ASME

Downloaded 01 Jun 2010 to 171.66.16.57. Redistribution subject to ASME license or copyright; see http://www.asme.org/terms/Terms_Use.cfm

Values of μ_j are obtained as

$$\mu_j^{(k+1)} = \mu_j^{(k)} + N^{(k)} \psi_j^{(k)}[x(r_f), r_f] \tag{2}$$

where (k) denotes the number of iterations. When $k=0$, if we let $\mu^{(0)} = 0$, then equation (2) reduces to the original penalty function method.

Thus, the original optimal control problem with performance index J and terminal conditions is converted to a new problem with new index $\tilde{J}$, equation (1), and a free terminal condition.

(b) Continual Transformation Technique [3]. Using the continual transformation technique the problem with inequality constraint on state variable can be transformed into one with no constraint. This, however, would increase the number of state variables, and new control variables are introduced.

The inequality constraint on state variable is assumed as $M(x, r) \leq 0$. Introducing a relaxational variable $\alpha(r)$, the inequality constraint becomes an equality as follows

$$M(x, r) + \frac{1}{2}\alpha^2(r) = 0 \tag{3}$$

where $r \in [r_0, r_f]$.

Since $\alpha^2(r)$ is not less than 0, $M(x, r) \leq 0$ is always satisfied.

Taking the Pth derivative of equation (3) with respect to r, as soon as the control variable s appears in the Pth derivative, the inequality constraint is then called the P-order constraint and the control variable s can be written as

$$s = s(x, \alpha_{p-1}, \alpha_{p-2}, \ldots, \alpha_1, \alpha, \alpha_p, r) \tag{4}$$

where $\alpha_1 = \dfrac{d\alpha}{d\gamma}, \ldots, \alpha_p = \dfrac{d^p\alpha}{dr^p}$.

Substituting equation (4) into the original state equations and equation of performance index, equation (1), $\alpha, \alpha_1, \ldots, \alpha_{p-1}$, are obtained as new additional state variables, and α_p is considered as a new control variable.

(c) Conjugate Gradient Method. In the calculation procedure the conjugate gradient method has been applied in order to reach the optimal point much faster.

Mathematical Expression for an Optimal Flow-Type Design of Rotor Blades

A problem which maximizes the amount of work done by the rotor blades with a prespecified distribution of $C_u(r_1)$ has been calculated. As $C_u(r_1) = F(r_1)$ is known, the parameters (including mass flow G_1) are determined in section 1 and the equations in section 2 of the previous paper [2] are simplified. However, the entropy gradient term in equation (14) in the paper [2] is so complex that C_{2m} is made to be a new state variable. The number of equations increases by one, but the deducing process and final equation forms are simpler.

The performance index is

$$J_1 = \int_{r_h}^{r_t} C_{2u} r_2 (C_{2m} \cos\psi_2 \cdot \rho_2 \cdot g \cdot 2\pi r_2) dr_2$$

$$= \int_{r_h}^{r_t} x_1 r_2 g_3 dr_2 \rightarrow \max \tag{5}$$

The system differential equations (i.e., equation of state variables) are

$$\begin{cases} \dfrac{dx_1}{dr_2} = g_1(x_1, x_2, x_4, s, r_2) \\ \dfrac{dx_2}{dr_2} = g_2(x_1, x_2, x_4, s, r_2) \\ \dfrac{dx_3}{dr_2} = x_2 \cdot \cos\psi_2 \rho_2 g \cdot 2\pi r_2 = g_3(x_1, x_2, x_4, r_2) \\ \dfrac{dx_4}{dr_2} = s \end{cases} \tag{6}$$

where the state variable vector is

$$\mathbf{X} = (x_1, x_2, x_3, x_4)^T = (C_{2u}, C_{2m}, G_2, D_r)^T \tag{7}$$

and the control vector is

$$\mathbf{S} = S \tag{8}$$

The system is subject to the conditions and constraints as follows:

Initial conditions are

$$\begin{cases} x_1(r_h),\ x_2(r_h),\ x_4(r_h),\ \text{free} \\ x_3(r_h) = 0 \end{cases} \tag{9}$$

The relationship between $x_1(r_h)$, $x_2(r_h)$, and $x_4(r_h)$ is written as

$$x_2 = \sqrt{\left[(1-x_4)W_1 + \frac{x_1 r_2 - C_{1u} r_1}{\sigma(r_1 + r_2)} + \frac{\omega}{\sigma}(r_1 - r_2)\right]^2 - (x_1 - r_2\omega)^2} \tag{10}$$

so only two of these terms are independent.

Terminal conditions are:

$$\begin{cases} x_1(r_t),\ x_2(r_t),\ x_4(r_t),\ \text{free} \\ x_3(r_t) = G_1 \end{cases} \tag{11}$$

Nomenclature

C = absolute velocity
D = diffusion factor
G = mass flow
$g^{(k)}$ = the gradient of Hamilton's function with respect to control variable, equation (41)
G_k = the inner product of $g^{(k)}$
G_{z0} = the gradient of performance index with respect to initial value of state variable, equation (33)
G_z = the inner product of g_{z0}
H = Hamilton's function
J = performance index
N = penalty parameter
s = control variable
W = relative velocity
x = state variable
β = conjugate coefficient
ϵ_1 = new control variable
μ = Lagrange multiplier
ψ = terminal condition
ω = angular velocity

Subscripts

h = root of blade
i = ith state variable
j = j dimension
m = streamline direction
pr = provided
r = radius direction
R = rotor
t = top of blade
1 = inlet of rotor
2 = outlet of rotor

Superscripts

(k) = Kth iteration

Downloaded 01 Jun 2010 to 171.66.16.57. Redistribution subject to ASME license or copyright; see http://www.asme.org/terms/Terms_Use.cfm

The constraint on the state variable is

$$x_4(r_2) \le D_{pr}(r_2) \tag{12}$$

The optimal problem would be expressed as: Determine an optimal control variable $s(r_2)$ which, after transferring state variables from initial condition equation (9) to the terminal equation (11), maximizes the performance index equation (5), satisfying the constraint equation (12).

Calculation Procedure

Using the methods above, the calculation procedure is as follows:

(*a*) Using the augmented penalty function method, a new performance index is obtained as

$$J = \int_{r_h}^{r_t} -x_1 \cdot r_2 \cdot g_3 dr_2 + \frac{N}{2}[x_3(r_t) - G_1]^2 + \mu \cdot [x_3(r_t) - G_1] \tag{13}$$

Then the terminal condition $x_3(r_t)$ becomes free (see equation (11)), and the original maximum problem of J_1, equation (5), turns into minimum problem of J, equation (13).

(*b*) Introducing a relaxation variable $\epsilon(r_2)$ and using the continual transformation technique, the inequality constraint of the state variable can be eliminated. Equation (12) is written as

$$x_4 - D_{pr}(r_2) + \frac{1}{2}\epsilon^2(r_2) = 0 \tag{14}$$

Taking the derivative of equation (14) with respect to r_2 and substituting it in the fourth equation of equation (6), we get

$$s - \frac{dD_{pr}}{dr_2} + \epsilon \cdot \epsilon_1(r_2) = 0 \tag{15}$$

where $\epsilon_1 = d\epsilon/dr_2$.

Therefore, the constraint of the state variable, equation (12), is first order.

Substituting equation (15) in equations (5) and (6) and eliminating the original control variable s, the ϵ_1 is now taken as a new control variable, while an additional state variable ϵ appears and its equation is written as

$$\frac{d\epsilon}{dr_2} = \epsilon_1 \tag{16}$$

Initial values of (r_2) are obtained from equation (15). Then the original optimal control problem has turned into an equivalent problem with no constraint on state variable and free terminal conditions. After this, the Pontryagin's maximum principle can be utilized.

The expression of the new problem is rewritten as follows:

The system differential equations are

$$\frac{dx_1}{dr_2} = \frac{-\xi_1}{Q_1} = f_1(x_1, x_2, x_4, x_5, \epsilon_1, r_2) \tag{17}$$

$$\frac{dx_2}{dr_2} = \frac{\xi_2}{Q_2} = f_2(x_1, x_2, x_4, x_5, \epsilon_1, r_2) \tag{18}$$

$$\frac{dx_3}{dr_2} = g \cdot x_2 \cos\psi_2 \cdot \rho_2 \cdot 2\pi r_2 = f_3(x_1, x_2, x_4, r_2) \tag{19}$$

$$\frac{dx_4}{dr_2} = \frac{dD_{pr}}{dr_2} - x_5 \cdot \epsilon_1 = f_4(x_5, \epsilon_1, r_2) \tag{20}$$

$$\frac{dx_5}{dr_2} = \epsilon_1 = f_5 \tag{21}$$

where the state and control vector are, respectively,

$$\mathbf{X} = (x_1, x_2, x_3, x_4, x_5)^T = (C_{2u}, C_{2m}, G_2, D_r, \epsilon)^T \tag{22}$$

$$\mathbf{S} = \epsilon_1 \tag{23}$$

and the detailed formulation of equations (17)–(21) is explained in the Appendix.

Initial conditions are

$$\begin{cases} x_1(r_h),\ x_2(r_h),\ x_4(r_h),\ x_5(r_h),\ \text{free} \\ x_3(r_h) = 0 \end{cases} \tag{24}$$

Terminal conditions are

$$x_1(r_t),\ x_2(r_t),\ x_3(r_t),\ x_4(r_t),\ x_5(r_t),\ \text{free} \tag{25}$$

(*c*) For the application of Pontryagin's maximum principle we introduce

$$\lambda = (\lambda_1, \lambda_2, \lambda_3, \lambda_4, \lambda_5)^T \tag{26}$$

Hamilton's function is formed as

$$\mathrm{H} = -x_1 f_3 r_2 + \lambda_1 f_1 + \lambda_2 f_2 + \lambda_3 f_3 + \lambda_4 f_4 + \lambda_5 f_5 \tag{27}$$

Adjoint equations are:

$$\frac{d\lambda_1}{dr_2} = -\frac{\partial \mathrm{H}}{\partial x_1} = -\left(-f_3 r_2 - x_1 r_2 \frac{\partial f_3}{\partial x_1} + \lambda_1 \frac{\partial f_1}{\partial x_1} + \lambda_2 \frac{\partial f_2}{\partial x_1} + \lambda_3 \frac{\partial f_3}{\partial x_1}\right)$$

$$\frac{d\lambda_2}{dr_2} = -\frac{\partial \mathrm{H}}{\partial x_2} = -\left(-x_1 r_2 \frac{\partial f_3}{\partial x_2} + \lambda_1 \frac{\partial f_1}{\partial x_2} + \lambda_2 \frac{\partial f_2}{\partial x_2} + \lambda_3 \frac{\partial f_3}{\partial x_2}\right)$$

$$\frac{d\lambda_3}{dr_2} = -\frac{\partial \mathrm{H}}{\partial x_3} = 0$$

$$\frac{d\lambda_4}{dr_2} = -\frac{\partial \mathrm{H}}{\partial x_4} = -\left(-x_1 r_2 \frac{\partial f_3}{\partial x_4} + \lambda_1 \frac{\partial f_1}{\partial x_4} + \lambda_2 \frac{\partial f_2}{\partial x_4} + \lambda_3 \frac{\partial f_3}{\partial x_4}\right)$$

$$\frac{d\lambda_5}{dr_2} = -\frac{\partial \mathrm{H}}{\partial x_5} = -\left(\lambda_1 \frac{\partial f_1}{\partial x_5} + \lambda_2 \frac{\partial f_2}{\partial x_5} + \lambda_4 \frac{\partial f_4}{\partial x_5}\right) \tag{28}$$

Terminal values $\lambda_i(r_t)$ are determined by

$$\lambda_i(r_t) = \frac{\partial \Phi}{\partial X_i}\bigg|_{r_t} \tag{29}$$

where $\Phi = (N/2)[x_3(r_t) - G_1]^2 + \mu[x_3(r_t) - G_1]$.

Therefore we have

$$\begin{cases} \lambda_1(r_t) = \lambda_2(r_t) = \lambda_4(r_t) = \lambda_5(r_t) = 0 \\ \lambda_3(r_t) = N \cdot [x_3(r_t) - G_1] + \mu \end{cases} \tag{30}$$

(*d*) In determining the initial value of the state variable, we rewrite equation (13) in the following form

$$\mathbf{J} = \frac{N}{2}[x_3(r_t) - G_1]^2 + \mu \cdot [x_3(r_t) - G_1] + \int_{r_h}^{r_t} (\mathrm{H} - \lambda^T \cdot \dot{X}) dr_2 \tag{31}$$

where H is Hamilton's function.

Substituting for **J**, we get

$$\delta \mathbf{J} = \{N \cdot [x_3(r_t) - G_1] + \mu\}_{r_t} \delta x_3(r_t) - [\lambda^T \delta x]_{r_t} + [\lambda^T \delta x]_{r_h} + \int_{r_h}^{r_t} \left[\frac{\partial \mathrm{H}}{\partial \epsilon_1} \delta\epsilon_1 + \left(\frac{\partial \mathrm{H}}{\partial x}\right)^T \delta x + \dot{\lambda}^T \delta x\right] dr_2 \tag{32}$$

The gradient of performance index with respect to initial value, $g_{z0,i}^{(k)}$, becomes

$$g_{z0,i}^{(k)} = \lambda_i(r_h) \qquad (i = 1, 2, 3, 4, 5) \tag{33}$$

Because only two of the initial values for x_1, x_2, x_4, x_5 are independent, we take x_1 and x_5 as independent variables.

Downloaded 01 Jun 2010 to 171.66.16.57. Redistribution subject to ASME license or copyright; see http://www.asme.org/terms/Terms_Use.cfm

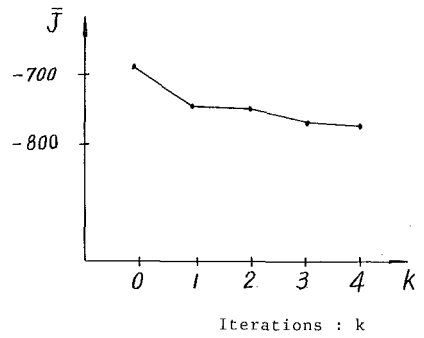

Fig. 1 J versus iteration number (schematic)

Taking variation of equations (10)–(14) and after deduction, we get

$$\lambda^T \delta x \Big|_{r_h} = \zeta_1 \delta x_1(r_h) + \zeta_5 \delta x_5(r_h) \tag{34}$$

where $\zeta_1 = \lambda_1(r_h) + \dfrac{\lambda_2(r_h)}{\sqrt{W^2 - (x_1 - r_2\omega)^2}} \left[\dfrac{W_2 r_2}{\sigma(r_1 + r_2)} - (x_1 - r_2\omega) \right]$; $\zeta_5 = \dfrac{\lambda_2(r_h)}{\sqrt{W^2 - (x_1 - r_2\omega)^2}} W_2 W_1 x_5(r_h) - \lambda_4(r_h) x_5(r_h) + \lambda_5(r_h)$.

For this problem to minimize **J**, in every iteration each initial value must make $\delta \mathbf{J} < 0$ and $|\delta \mathbf{J}|$ a maximum. The directions of iterations of initial values are determined from equation (34) as

$$\begin{cases} \delta x_1(r_h) \lessgtr 0 & \text{for } \zeta_1 \gtrless 0 \\ \delta x_5(r_h) \lessgtr 0 & \text{for } \zeta_5 \gtrless 0 \end{cases} \tag{35}$$

A new set of values at the $(k+1)$th iteration is given by

$$x_i^{(k+1)}(r_h) = x_i^{(k)}(r_h) + \delta x_i^{(k)}(r_h) \qquad (i = 1, 5) \tag{36}$$

and $x_2^{(k+1)}(r_h)$ and $x_4^{(k+1)}(r_h)$ are determined from equations (10) and (14).

Values of $x_i(r_h)$ in equation (36) are also established by the conjugate gradient method as follows:

The direction for seeking optimum at kth iteration $P_{z0,i}^{(k)}$ is given by

$$P_{z0,i}^{(k)} = -g_{z0,i}^{(k)} + \beta_{z0,i}^{(k)} \cdot P_{z,i}^{(k-1)} \tag{37}$$

where the conjugate coefficient

$$\beta_{z0}^{(k)} = \begin{cases} \dfrac{(g_{z0}^{(k)}, g_{z0}^{(k)})}{(g_{z0}^{(k-1)}, g_{z0}^{(k-1)})} & k > 0 \\ 0 & k = 0 \end{cases}$$

$$\delta x_i^{(k)}(r_h) = C^{(k)} \cdot P_{z0,i}^{(k)} \tag{38}$$

where $C^{(k)}$ is the optimal length of step.

(*e*) Evaluation of control variables in iterational computations proceeds as follows:

The direction for seeking optimum in the kth iteration $p^{(k)}$ is given by

$$P^{(k)} = -g^{(k)} + \beta^{(k)} \cdot P^{(k-1)} \tag{39}$$

where the conjugate coefficient

$$\beta^{(k)} = \begin{cases} \dfrac{(g^{(k)}, g^{(k)})}{(g^{(k-1)}, g^{(k-1)})} & k > 0 \\ 0 & k = 0 \end{cases}$$

The value of the control variable in the $(k+1)$th iteration is given by

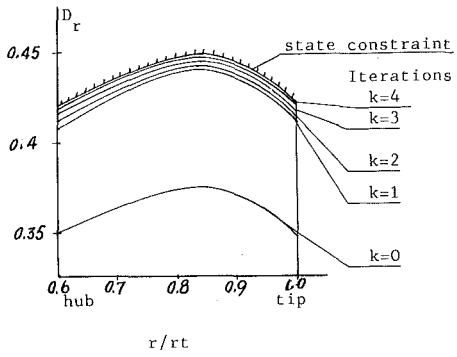

Fig. 2 D_r versus r/r_t (uncertainty in $D_r = 0.001$, in $r/r_t = 0.01$)

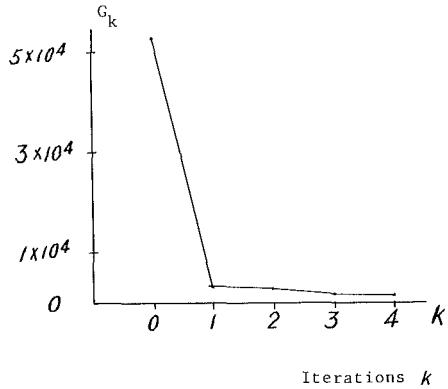

Fig. 3 G_k versus iteration number (schematic)

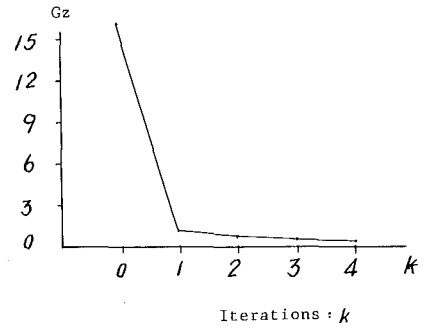

Fig. 4 G_z versus iteration number (schematic)

$$\epsilon_1^{(k+1)} = \epsilon_1^{(k)} + \alpha^{(k)} \cdot P^{(k)} \tag{40}$$

where $\alpha^{(k)}$ is optimal length of the step and $g^{(k)}$ is the gradient

$$g^{(k)} = \frac{\partial H}{\partial \epsilon_1}\Big|_{\epsilon_1 = \epsilon_1^{(k)}(r_2)} = \lambda_1 \frac{\partial f_1}{\partial \epsilon_1} + \lambda_2 \frac{\partial f_2}{2\partial \epsilon_1} - \lambda_4 x_5 + \lambda_5 \tag{41}$$

(*f*) The length of the optimal step $C^{(k)}$ and $\alpha^{(k)}$ is usually established by using a two-dimensional optimum seeking C and α. However, it is more convenient in present work to assume $C^{(k)} = \alpha^{(k)}$. The length of the optimal step is determined by using a one-dimensional optimum seeking method in which the curve-fitting method is applied.

Results and Discussion

Employing the distribution $C_{1u}(r_1) = 0.75/r_1 + 100 r_1$ suggested in [1], optimal distribution of diffusion factor in a rotor, maximizing the amount of work, has been computed.

In the calculation, the initial value of the new control variable is taken as $\epsilon_1 = 0$; penalty parameter $N = 70$. After four iterations, the relative error of performance index between the last two iterations has been less than 0.001 (Fig. 1) and the optimal distributions of diffusion factor (Fig. 2) and other parameters are obtained, while the flow rate is conservative: The relative error of flow rate deviation between section 1 and section 2 is less than 0.003.

Downloaded 01 Jun 2010 to 171.66.16.57. Redistribution subject to ASME license or copyright; see http://www.asme.org/terms/Terms_Use.cfm

In Fig. 2 the optimal distribution of diffusion factor is quite close to the constraint of state variable. This result is compatible with the physical meaning of this problem, i.e., to make the blades develop the maximum amount of work. The optimal work is 5.5 percent higher than the quoted values, calculated in [1].

In Fig. 3 is shown the relationship between the inner product of the gradient $g_k = (\partial H/\partial \epsilon_i)|_{\epsilon_1=\epsilon_1^{(k)}(r)}$ (equation (41)), and the number of iterations (k). In Fig. 4 the relationship between G_Z, the inner product of the gradient of initial value ζ_1 and ζ_5, and the number of iterations (k) is indicated.

From the third to the fourth iteration, both G_k and G_z have approached zero. This shows that optimal control and state variables are conceivable and accurate.

Calculations show that the augmented penalty function method has the advantage of good convergence and application convenience. In this calculation a constant value of 70 for the penalty parameter N has always been taken up until convergence. However, in the original penalty function method N always has to be increased, so that numerical solution difficulties occur in case of large N.

Therefore, the continual transformation technique is an available method for the optimal problem with inequality constraints on state variables, but the number of dimensions of the state equations is increased.

Conclusions

Using the augmented penalty function method and the continual transformation technique, the typical optimal control problem with various constraints proposed in the previous paper [2] has been converted to a new equivalent optimal control problem without any constraints. Pontryagin's maximum principle can now be utilized to solve the problem. In the calculation process the conjugate gradient method is used to accelerate the approach to the optimal control and trajectory. A sample calculation of optimal diffusion factor flow-type for a rotor blade design has been carried out. The results of calculation show that the method and the program applied in this paper are satisfactory in accuracy and convergence. These methods can be extended conveniently to optimal problems in various flow-type designs and appear also to be suitable for optimal problems with other performance indices [2] and constraints, e.g., requirements of total pressure, inlet or exit angle, efficiency, and power.

References

1 Gu, Chuan-gang, "Theory, Application and Optimization of the Diffusion Factor Flow-Type Design for Axial-Flow and Mixed-Flow Compressors," *Chinese Journal of Mechanical Engineering*, Vol. 19, No. 2, 1983, pp. 87-94.

2 Gu, Chuan-gang, and Miao, Yong-miao, "Blade Design of Axial-Flow Compressors by the Method of Optimal Control Theory – Physical Model and Mathematical Expression," ASME JOURNAL OF TURBOMACHINERY, this issue.

3 Jacobson, D. H., and Lele, M. M., "A Transformation Technique for Optimal Control Problems With a State Variable Inequality Constraint," *IEEE Trans. on Automatic Control*, Vol. AC-14, No. 5, 1969.

4 Liu Gao-lian, "A New Theory of Two-Dimensional Airfoil Cascades Optimized Aerodynamically via a Generalized Maximum Principle," *ACTA Mechanics Sinica*, Vol. 12, No. 2, 1980, pp. 337-346.

5 Sage, A. P., and White, C. C., III, *Optimum System Control*, Prentice-Hall, New York, 1977.

6 Noton, M., *Modern Control Engineering*, Pergamon Press, New York, 1972.

APPENDIX

The concrete formulas of equations (17)-(21) are written as follows:

$$\xi_1 = \left(\frac{dD_{pr}}{dr_2} - x_5\epsilon_1\right)\left[k_3 + T_2k_7\left(k_5 - k_6 \cdot x_2 \cdot W_1 - k_6W_2\frac{k_3}{x_2}\right)\right] + \left\{k_4 + \frac{x_1^2}{r_2} + x_2^2\left(\tilde{f}_2 + \frac{\sqrt{1+\tan^2\psi_2}}{Rm_2}\right)\right.$$
$$\left. - \left[x_1\omega - \frac{d(C_{1u}u_1)}{dr_2}\right] - T_2k_7 \cdot (k_6W_2\frac{k_4}{x_2} + k_6x_2k_9 + k_0) + T_2k_8\right\},$$

$$Q_1 = k_2 + x_1 - u_2 + T_2k_7k_6\left(\frac{x_2r_2}{C} - \frac{k_2W_2}{x_2}\right),$$

$$\xi_2 = \left(\frac{dD_{pr}}{dr_2} - x_5\epsilon_1\right)\left[k_3\frac{x_1}{k_2} - \frac{k_3u_2}{k_2} - T_2k_7(k_5 - k_6x_2W_1) + T_2k_7k_6\frac{k_3r_2x_2}{k_2C}\right] + \left[\frac{x_1k_4}{k_2} - \frac{x_1^2}{r_2} - x_2^2\left(\tilde{f}_2 + \frac{\sqrt{1+\tan^2\psi_2}}{Rm_2}\right) + x_1\omega - \frac{d(C_{1u}u_1)}{dr_2} - \frac{k_4u_2}{k_2} + T_2k_6k_7x_2\left(\frac{k_4r_2}{k_2C} - k_9\right) - T_2k_7k_0 - T_2k_8\right],$$

$$Q_2 = x_2\left(1 + \frac{x_1}{k_2}\right) - \frac{x_2u_2}{k_2} + T_2k_6k_7\left(\frac{x_2^2r_2}{k_2C} - W_2\right),$$

$$f_3 = x_2\cos\psi_2 g\rho_2 \cdot 2\pi r_2 = 2\pi r_2\cos\psi_2 \cdot \frac{P_{01}}{R}\frac{x_2B_2}{T_2}\left(\frac{B_1}{B_3}\right)^{\frac{k}{k-1}},$$

$$C = \sigma_{av}(r_{1av} + r_{2av}),$$

$$T_2 = T_{10} + \frac{A}{2gc_p}(u_2^2 - 2c_{1u}u_1 - W_2^2),$$

$$W_2 = k_1 - x_4W_1 + \frac{r_2}{C}x_1,$$

$$B_1 = 1 + \frac{(x_1r_2 - c_{1u}r_1)\omega A}{c_pT_{01}g}, \quad B_2 = 1 - \tilde{\omega}_R\left(\frac{Q_I}{P_I}\right),$$

$$B_3 = 1 + \frac{k-1}{2}\left(\frac{x_1^2 + x_2^2}{gkRT_2}\right), \quad k_1 = W_1 - \frac{c_{1u}r_1}{C} + \frac{\omega}{\sigma}(r_1 - r_2),$$

$$k_2 = \frac{r_2W_2}{C} - x_1 + u_2, \quad k_3 = -W_2W_1,$$

$$k_4 = W_2k_9 + x_1\omega - u_2\omega, \quad \tilde{\omega}_R = k_6W_2x_2,$$

$$k_5 = \frac{2\sigma W_2}{x_2}(0.02375 - 0.1x_4 + 0.375x_4^2),$$

$$k_6 = \frac{2\sigma}{x_2^2}(0.003 + 0.02375x_4 - 0.05x_4^2 + 0.125x_4^3),$$

$$k_7 = gR\left(\frac{Q_I}{P_I}\right)\Big/\left[1 - \left(\frac{Q_I}{P_I}\right)k_6W_2x_2\right],$$

$$k_8 = gR(k_6W_2x_2)\frac{\alpha}{\alpha r_2}\left(\frac{Q_I}{P_I}\right)\Big/\left[1 - \left(\frac{Q_I}{P_I}\right)k_6W_2x_2\right],$$

$$k_9 = \frac{\alpha k_1}{\alpha r_2} - x_4\frac{\alpha w_1}{\alpha r_2} + \frac{x_1}{C},$$

$$k_0 = -\left(1 + \frac{\alpha r_1}{\alpha r_2}\right)(k_6W_2x_2)/(r_1 + r_2)$$

The above W_1, C_{1u}, Q_I, P_I, P_{01} have been calculated for section 1. The $\tilde{f}_2$ is f_i ($i = 2$) in equation (7) of [2], which is only a function of the coordinates as is cos ψ_2.

Downloaded 01 Jun 2010 to 171.66.16.57. Redistribution subject to ASME license or copyright; see http://www.asme.org/terms/Terms_Use.cfm

Numerical Solution of Inviscid Two-Dimensional Transonic Flow Through a Cascade

J. Fořt
National Research Institute
for Machine Design

K. Kozel
Department of Applied Mathematics,
Faculty of Mechanical Engineering, ČVUT,
Prague, Czechoslovakia

The paper presents a method of numerical solution of transonic potential flow through plane cascades with subsonic inlet flow. The problem is formulated as a weak solution with combined Dirichlet's and Neumann's boundary conditions. The numerical procedure uses Jameson's rotated difference scheme and the SLOR technique to solve a system of difference equations. Numerical results of transonic flow are compared with experimental data and with other numerical results for both compressor and turbine cascades near choke conditions.

1 Introduction

The potential transonic flow is a sufficient physical model, if we deal with inviscid transonic flow with weak shock waves. The answer to problems of internal or external aerodynamics described by this potential model of flow is based on numerical solution of full potential equations. These methods employ:

(*a*) a nonconservative form of equation and Jameson's rotated difference scheme [3]. The system of difference equations is solved by an iteration procedure based on SLOR or multigrid techniques.

(*b*) a conservative equation form and certain difference schemes published by Jameson [2], Ballhaus and Holst [12], and Murmann, Hafez, and South [4]. The alternating direction method (ADI) or other method based on artifical time analysis is usually used to solve the system of difference equations.

In contrast to problems of external aerodynamics published in profusion, relatively few methods have been devoted to more complicated problems of internal flow.

Our method uses a modification of Jameson's rotated difference scheme and SLOR technique. The numerical method is described in more detail in [10, 11]. In the final section of this paper, numerical results for technical applications are compared with experimental data and numerical results of other authors, considering transonic flows through compressor cascades with embedded and detached bow shock waves as well as through turbine cascades near choke conditions.

2 Mathematical Formulation of the Problem

A steady irrotational isentropic flow is fully described by a quasilinear partial differential equation of mixed (elliptic-hyperbolic) type for a velocity potential

$$(A^2-\varphi_x^2)\varphi_{xx}-2\varphi_x\varphi_y\varphi_{xy}+(A^2-\varphi_y^2)\varphi_{yy}=0$$

$$A^2=\mathrm{M}_\infty^{-2}+\frac{\kappa-1}{2}(1-\varphi_x^2-\varphi_y^2) \tag{1}$$

where $\varphi=\Phi/w_\infty$, $A=a/w_\infty$. Φ is a flow velocity potential ($\mathbf{w}$ = grad φ), $\mathbf{w}$ = velocity vector, a = local speed of sound, M = w/a = local Mach number, κ = Poisson's constant. The index ∞ denotes the quantities of the inlet flow. We assume the existence of weak shock waves as curves of discontinuity of the first derivatives φ_x, φ_y. A weak solution is assumed in class $K(\Omega)$, where Ω is the domain of solution (see Fig. 1)

$$K(\Omega)=\{\varphi\in C^{(2)}(\Omega\backslash B)\cap C(\Omega);\forall \mathbf{x}\in\Omega,$$

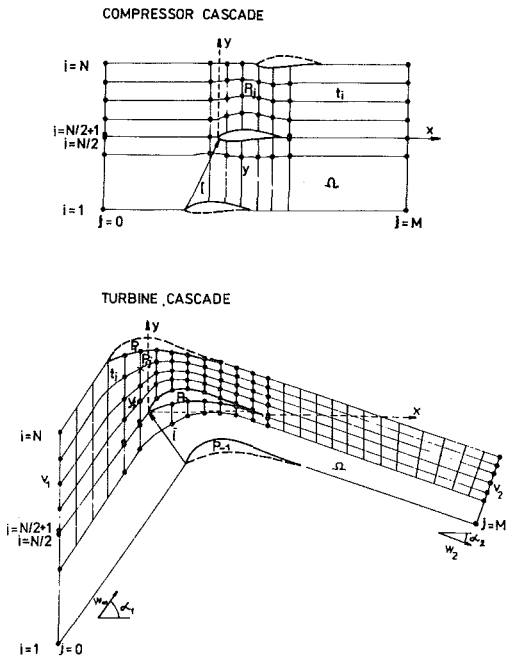

Fig. 1 Domain of solution; scheme of grid used for numerical solution

Contributed by the Gas Turbine Division of THE AMERICAN SOCIETY OF MECHANICAL ENGINEERS and presented at the 31st International Gas Turbine Conference and Exhibit, Düsseldorf, Federal Republic of Germany, June 8–12, 1986. Manuscript received at ASME Headquarters December 26, 1985. Paper No. 86-GT-19.

Copyright © 1987 by ASME

Downloaded 01 Jun 2010 to 171.66.16.57. Redistribution subject to ASME license or copyright; see http://www.asme.org/terms/Terms_Use.cfm

$$\forall \mathbf{x} + k \bullet \mathbf{l} \in \Omega;\ \varphi(\mathbf{x} + k \bullet \mathbf{l}) = \varphi(\mathbf{x}) + k \bullet C_1 \}$$

B is set of a finite number of smooth curves, $\mathbf{l}$ a periodicity vector of the cascade (see Fig. 1), C_1 a known constant and $k = 0, \pm 1, \pm 2, \ldots$.

The function $\varphi \in K(\Omega)$ must satisfy the equation

$$\oint_c \rho \varphi_x dy - \rho \varphi_y dx = 0$$

$$\rho = \rho_0 \bullet \left[1 + \frac{\kappa - 1}{2} M_\infty^2 \bullet \left(\frac{1 - \varphi_x^2 - \varphi_y^2}{1 + \frac{\kappa - 1}{2} M_\infty^2} \right)^{\frac{1}{\kappa - 1}} \right] \tag{2}$$

(ρ_0 is a positive constant) for an arbitrary positively oriented Jordan's curve c with its interior lying in Int Ω. For a sufficiently smooth function φ equation (2) is equivalent to (1).

For a subsonic inlet and outlet flow the problem is formulated by the following boundary conditions. On the inlet boundary v_1 (see Fig. 1) Dirichlet's condition ($\mathbf{w} = \mathbf{w}_\infty$) is prescribed, on the profile contour Neumann's condition of nonpermeability ($\partial\varphi/\partial\mathbf{n} = 0$), and on the outlet boundary v_2 also Neumann's condition ($\mathbf{w} = \mathbf{w}_2$), $\mathbf{w}_2$ being a constant determined uniquely by the value of circulation velocity around one of the profiles of cascade γ. Potential φ still satisfies the Kutta–Youkovski condition on the trailing edge of the profile. The value of quantity γ so far unknown is determined during the iteration process of the numerical solution.

3 Numerical Solution

The problem is solved by a finite difference method. The mesh is generated by a profile contour (see Fig. 1). The mesh in Fig. 1(*a*) is used to compute the compressor cascade flow. If the profile is more cambered (turbine cascades), the mesh on Fig. 1(*b*) is used.

The potential equation can be written in a canonical form in local coordinates s, n (s = streamline, n = normal)

$$(1 - M^2)\varphi_{ss} + \varphi_{nn} = 0 \tag{3}$$

where

$$M^2 = \frac{\varphi_s^2}{M_\infty^{-2} + \frac{\kappa - 1}{2}(1 - \varphi_s^2)} \tag{4}$$

is the local Mach number.

The angle of coordinate t_i will be denoted ϵ in mesh point P_{ij}. The angle of the local streamline s at point P_{ij} will be further denoted ϑ, and local distances of the mesh points will be denoted l_1, l_2, l_3, h_2 (see Fig. 2).

Both terms of equation (6) will be transformed independently into coordinates of mesh

$$(1 - M^2)\varphi_{ss} = A_1\varphi_{tt} + B_1\varphi_{ty} + C_1\varphi_{yy} + D_1\varphi_t + E_1\varphi_y \tag{5}$$

$$\varphi_{nn} = A_2\varphi_{tt} + B_2\varphi_{ty} + C_2\varphi_{yy} + D_2\varphi_t + E_2\varphi_y \tag{6}$$

Then equation (3) can be written as

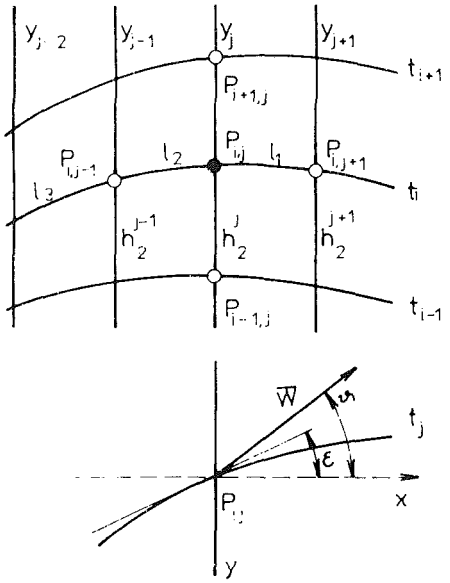

Fig. 2 Local grid parameters

$$[A_1\varphi_{tt} + B_1\varphi_{ty} + C_1\varphi_{yy}] + [A_2\varphi_{tt} + B_2\varphi_{ty} + C_2\varphi_{yy}] + (D_1 + D_2)\varphi_t + (E_1 + E_2)\varphi_y = 0 \tag{7}$$

where

$$A_1 = (1 - M^2)\left(\frac{\cos\vartheta}{\cos\epsilon}\right)^2$$

$$B_1 = -2(1 - M^2)\frac{\cos\vartheta}{\cos\epsilon}(\cos\vartheta\tan\epsilon - \sin\vartheta)$$

$$C_1 = (1 - M^2)(\cos\vartheta\tan\epsilon - \sin\vartheta)^2$$

$$A_2 = \left(\frac{\sin\vartheta}{\cos\epsilon}\right)^2 \tag{8}$$

$$B_2 = -2\frac{\sin\vartheta}{\cos\epsilon}(\sin\vartheta\tan\epsilon + \cos\vartheta)$$

$$C_2 = (\sin\vartheta\tan\epsilon + \cos\vartheta)^2$$

$$(D_1 + D_2) = (\sin^2\vartheta - (1 - M^2)\cos^2\vartheta)\sin\epsilon\, t''$$

$$(E_1 + E_2) = (\sin^2\vartheta + (1 - M^2)\cos^2\vartheta)t''$$

and further

$$t'' = \frac{d^2t(x)}{dx^2},\quad \sin\vartheta = \frac{\varphi_y}{\varphi_s}$$

$$\cos\vartheta = (\varphi_t - \varphi_y\sin\epsilon)\bullet(\varphi_s\bullet\cos\epsilon)^{-1} \tag{9}$$

$$\varphi_s = (\varphi_t^2 - 2\varphi_t\varphi_y\sin\epsilon + \varphi_y^2)^{1/2}\bullet(\cos\epsilon)^{-1}$$

The first derivatives φ_t, φ_y are approximated by central differences

Nomenclature

a = speed of sound
$\mathbf{w}$ = velocity vector
$\mathbf{l} = (x_p, y_p)$ = periodicity vector
M = Mach number
n = normal direction
P_{ij} = grid point
s = streamline direction
t_i, y_j = grid coordinates
$\mathbf{x} = (x, y)$ = a point in Ω
α = angle of inlet velocity
α_2 = angle of outlet velocity
ϵ = angle of grid coordinate t
φ = normalized potential function
κ = Poisson's constant
ϑ = angle of streamline
Ω = domain of solution

Subscripts

x = partial derivative on x
∞ = quantity of inlet flow

Superscript

n = number of iteration

Downloaded 01 Jun 2010 to 171.66.16.57. Redistribution subject to ASME license or copyright; see http://www.asme.org/terms/Terms_Use.cfm

$$\varphi_{t/ij}=\frac{l_2}{l_1(l_1+l_2)}\varphi^{(n)}_{i,j+1}\frac{l_1-l_2}{l_1l_2}\varphi^{(n)}_{i,j}$$

$$-\frac{l_1}{l_2(l_1+l_2)}\varphi^{(n+1)}_{i,j-1}+0(q^2),\qquad l_1,l_2<q \tag{10}$$

$$\varphi_{y/i,j}=\frac{1}{2h_2}(\varphi^{(n)}_{i+1,j}-\varphi^{(n)}_{i-1,j})+0(h_2^2),$$

where the index $(n+1)$ denotes values in the calculated iteration and (n) those in the previous iteration.

The coefficients of equation (7) and the value of Mach number M_{ij} are then determined by relations (8), (9), and (4).

For $M_{ij}<1$ (elliptic point) all second derivatives of φ in both terms (5), (6) are approximated by central differences of the second order

$$\varphi_{tt/ij}=2\cdot\left[\frac{1}{l_1(l_1+l_2)}\varphi^{(n)}_{i,j+1}-\frac{1}{l_1l_2}\varphi^{(n+1)}_{i,j}\right.$$

$$\left.+\frac{1}{l_2(l_1+l_2)}\varphi^{(n+1)}_{i,j-1}\right]+0(q^2),\qquad l_1,l_2<q$$

$$\varphi_{yy/ij}=\frac{1}{h_2^2}\left[\varphi^{(n+1)}_{i+1,j}-2\varphi^{(n+1)}_{i,j}+\varphi^{(n+1)}_{i-1,j}\right]+0(h_2^2)$$

$$\varphi_{ty/ij}=\frac{1}{2}\left[\frac{l_2}{l_1(l_1+l_2)}\frac{1}{h_2^{(i+1)}}\left(\varphi^{(n)}_{i+1,j+1}-\varphi^{(n)}_{i-1,j+1}\right)\right.$$

$$+\frac{l_1-l_2}{l_1l_2}\frac{1}{h_2^{(j)}}\left(\varphi^{(n+1)}_{i+1,j}-\varphi^{(n+1)}_{i-1,j}\right)$$

$$\left.-\frac{l_1}{l_2(l_1+l_2)}\frac{1}{h_2^{(j-1)}}\left(\varphi^{(n+1)}_{i+1,j-1}-\varphi^{(n+1)}_{i-1,j-1}\right)\right]$$

$$+0(q^2),\qquad l_1,l_2,h_2^{(j-1)},h_2^{(j)},h_2^{(j+1)}<q \tag{11}$$

For $M_{ij}>1$ (hyperbolic point) this approximation is used for terms (6). For second derivatives of φ in (5) we then use the following approximation (upwind differences)

$$\varphi_{tt/ij}=2\cdot\left[\frac{1}{l_3(l_2+l_3)}\varphi^{(n)}_{i,j-2}-\frac{1}{l_2l_3}\varphi^{(n)}_{i,j-1}\right.$$

$$\left.+\frac{1}{l_2(l_2+l_3)}\varphi^{(n+1)}_{i,j}\right]+0(q),\qquad l_2,l_3<q \tag{12}$$

In approximations φ_{ty} and φ_{yy} we distinguish two cases in the relationship on mutual position of velocity vector and coordinate t_i in given mesh point.

For $\tan\vartheta\le\tan\epsilon$ (see (9) and Fig. 2) we approximate

$$\varphi_{yy/ij}=\frac{1}{h_2^2}(2\varphi^{(n+1)}_{ij}-\varphi^{(n)}_{ij}-2\varphi^{(n+1)}_{i+1,j}$$

$$+\varphi^{(n)}_{i+2,j})+0(h_2)$$

$$\varphi_{ty/ij}=\frac{1}{h_2}\cdot\left[\frac{1}{l_2^{(i+1,j)}}\left(\varphi^{(n+1)}_{i+1,j}-\varphi^{(n)}_{i+1,j-1}\right)\right.$$

$$\left.-\frac{1}{l_2^{(i,j)}}\left(\varphi^{(n+1)}_{i,j}-\varphi^{(n)}_{i,j-1}\right)\right]$$

$$+0(q),\qquad l_2^{(i+1,j)},l_2^{(i,j)},h_2<q \tag{13}$$

For $\tan\vartheta>\tan\epsilon$ then

$$\varphi_{yy/ij}=\frac{1}{h_2^2}\left(\varphi^{(n)}_{i-2,j}-2\varphi^{(n+1)}_{i-1,j}+2\varphi^{(n+1)}_{i,j}\right.$$

$$\left.-\varphi^{(n)}_{i,j}\right)+0(h_2)$$

$$\varphi_{ty/ij}=\frac{1}{h_2}\cdot\left[\frac{1}{l_2^{(i,j)}}\left(\varphi^{(n+1)}_{ij}-\varphi^{(n)}_{i,j-1}\right)\right.$$

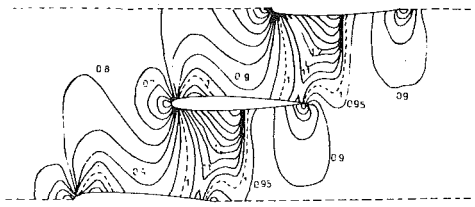

Fig. 3(a)

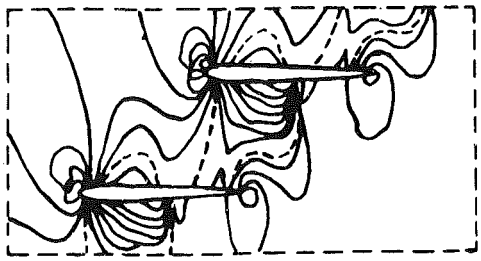

Fig. 3(b)

Fig. 3 Iso-Mach lines; profile NACA 0012: (a) presented method: backpressure; $M_\infty=0.85$, $\alpha=0$ deg, $M_2=0.89$, - - - - = sonic line; (b) results of [6]: finite element method; $M_\infty=0.85$, $\alpha=0$ deg, $M_2=0.86$

$$-\frac{1}{l_2^{(i-1,j)}}\cdot\left(\varphi^{(n+1)}_{i-1,j}-\varphi^{(n)}_{i-1,j-1}\right)$$

$$+0(q),\qquad l_2^{(i,j)},l_2^{(i-1,j)},h_2<q \tag{14}$$

In the elliptic point we use the difference scheme of the second order of accuracy, in hyperbolic point only of the first order.

The boundary condition of nonpermeability on the profile contour can be written as

$$\varphi_y\cdot\left(1+\frac{df_{h,d}(x)}{dx}\right)^{1/2}-\varphi_t\frac{df_{h,d}(x)}{dx}=0 \tag{15}$$

where $f_h(x)$, $f_d(x)$ are functions describing the upper and/or lower side of profile.

The derivative φ_t in (15) is approximated by

$$\varphi_{t/ij}=\frac{l_2}{l_1(l_1+l_2)}\varphi^{(n)}_{i,j+1}+\frac{l_1-l_2}{l_1l_2}\varphi^{(n+1)}_{ij}$$

$$-\frac{l_1}{l_2(l_1+l_2)}\varphi^{(n+1)}_{i,j-1}+0(q^2),\qquad l_1,l_2<q \tag{16}$$

and the derivative φ_y by

$$\varphi_{y/ij}=\frac{1}{2h_2}\left(-5\varphi^{(n+1)}_{ij}+2\varphi^{(n)}_{ij}\right.$$

$$\left.+4\varphi^{(n+1}_{i+1,j}-\varphi^{(n)}_{i+2,j}\right)+0(h_2^2) \tag{17}$$

in point P_{ij} lying at the upper side of the profile and

$$\varphi_{y/ij}=\frac{1}{2h_2}\left(\varphi^{(n+1)}_{i-2,j}-4\varphi^{(n+1)}_{i-1,j}\right.$$

$$\left.+5\varphi^{(n+1)}_{i,j}-2\varphi^{(n)}_{i,j}\right)+0(h_2^2) \tag{18}$$

in point P_{ij} lying at the lower side of the profile.

The form of approximation viscosity introduced by applying upwind difference approximation for $M_{ij}>1$ can be determined from the first differential approximation of difference scheme, i.e. (for $\tan\vartheta>\tan\epsilon$),

$$(1-M^2)\varphi_{ss}+\varphi_{nn}$$

$$=\frac{1}{a^2}\left(\frac{a^2}{w^2}-1\right)\frac{(\varphi_t-\varphi_y\sin\epsilon)^2}{\cos^2\epsilon}\left[\frac{1}{\cos^2\epsilon}\frac{2l_2+l_3}{3}\varphi_{ttt}\right.$$

$$+\frac{\tan\vartheta-\tan\epsilon}{\cos\epsilon}\left(\frac{l_2^{(i,j)}-l_2^{(i-1,j)}}{4}\varphi_{tty}+\frac{h_2}{2}\varphi_{tyy}\right)$$

$$\left.+(\tan\vartheta-\tan\epsilon)^2h_2\varphi_{yyy}\right] \tag{19}$$

Downloaded 01 Jun 2010 to 171.66.16.57. Redistribution subject to ASME license or copyright; see http://www.asme.org/terms/Terms_Use.cfm

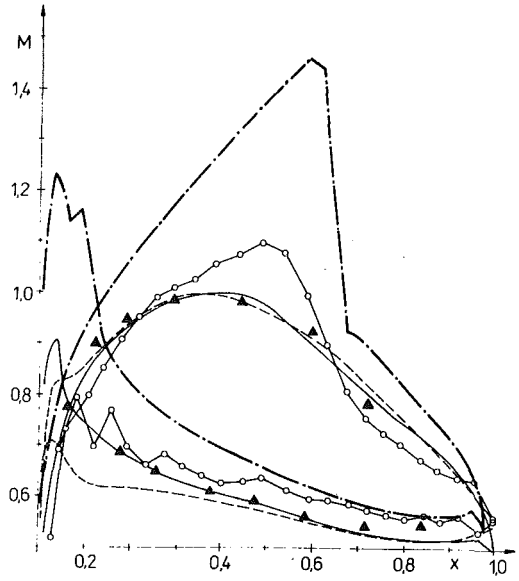

Fig. 4(a)

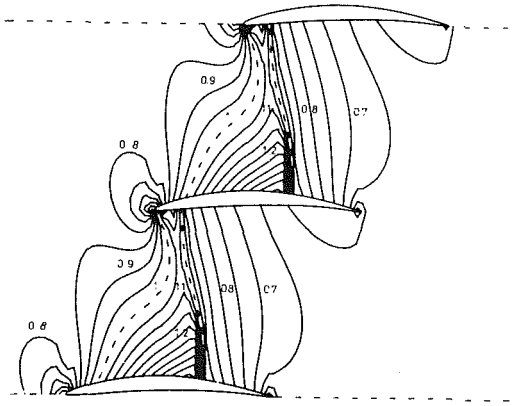

Fig. 4(b)

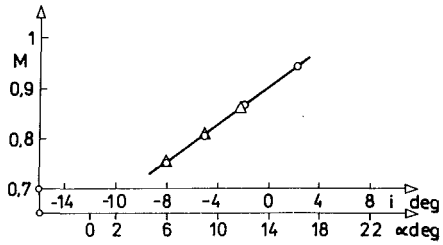

Fig. 4(c)

Fig. 4 Compressor cascade; profile of NACA 65 series: (*a*) distribution of Mach number along the profile; ——— presented method, $M_\infty = 0.7$, $\alpha = 9$ deg; - - - - method [8], $M_\infty = 0.7$, $\alpha = 9$ deg; — ○ — ○ — method [7], $M_\infty = 0.7$, $\alpha = 9$ deg; ▲ experimental data [7], $M_\infty = 0.7$, $\alpha = 9$ deg; —·—·— presented method, $M_\infty = 0.83$, $\alpha = 9$ deg; (*b*) iso-Mach lines; increment $\Delta M = 0.05$; (*c*) dependence of Mach number of choke on incidence angle; — ○ — experiment; Δ calculation

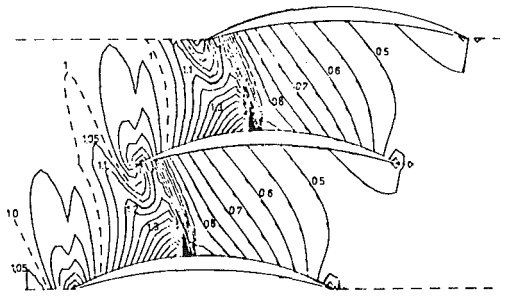

Fig. 5(a)

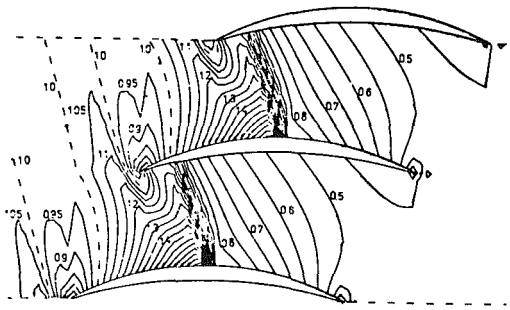

Fig. 5(b)

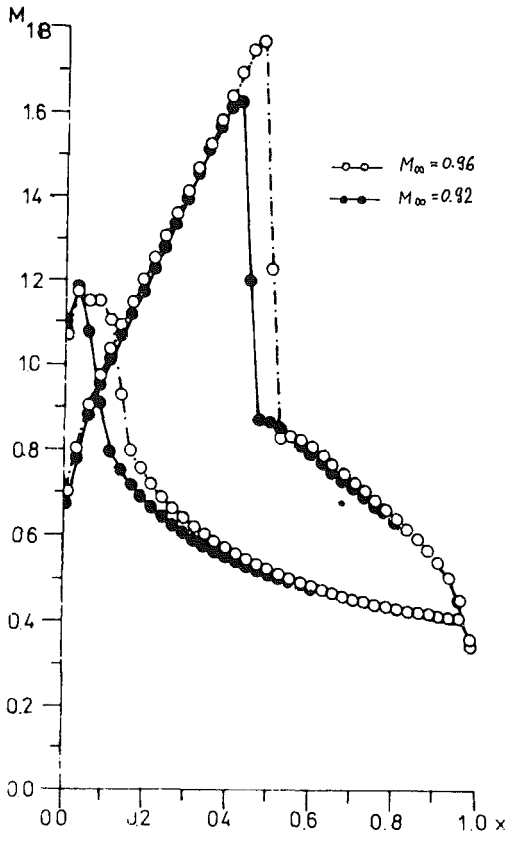

Fig. 5(c)

Fig. 5 Compressor cascade; DCA profile: (*a*) iso-Mach lines, $M_\infty = 0.92$, $\alpha = 19.5$ deg; (*b*) iso-Mach lines, $M_\infty = 0.96$, $\alpha = 19.5$ deg; (*c*) distribution of Mach number along profile

The iteration process uses the SLOR method. The system of equations given by difference approximation (7) in points P_{ij_0}, $i = 1, 2, \ldots, N$ is solved in one iteration step. We proceed in direction of rising value j_0, i.e., approximately in the flow direction. The system of difference equations is transferred to the right side of the equation. The matrix of the system has generally nonzero coefficients on line i by $\varphi_{i-1,j_0 i}\ \varphi_{i,j_0 i}\ \varphi_{i+1,j_0}$, by $\varphi_{1,j_0 i}\ \varphi_{2,j_0 i}\ \varphi_{3,j_0}$ on line 1, and $\varphi_{N-2,j_0}, \varphi_{N-1,j_0}, \varphi_{N,j_0}$ on line N. The system has been solved by recurrent modification of the Gauss method and the solution qualified by Jacobi's iteration method (one iteration).

Relaxation parameter ω has been chosen as follows

$$\omega = 1.7 \text{ for } (M_{i,j_0} < 1, i = 1,2, \ldots, N) \wedge$$

$$\wedge (y_{j_0} \cap \partial P = \phi) i \tag{20}$$

$\omega = 1$ in the other cases,

where y_{j_0} is mesh coordinate and ∂P is used to denote the profile contour.

Downloaded 01 Jun 2010 to 171.66.16.57. Redistribution subject to ASME license or copyright; see http://www.asme.org/terms/Terms_Use.cfm

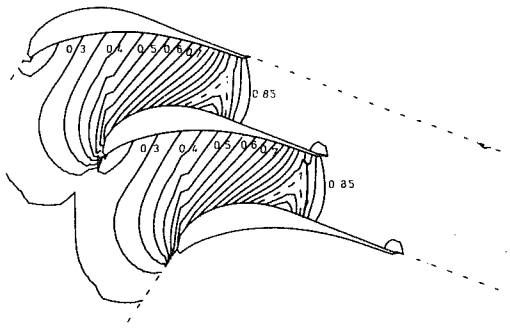

Fig. 6(a)

Fig. 6(b)

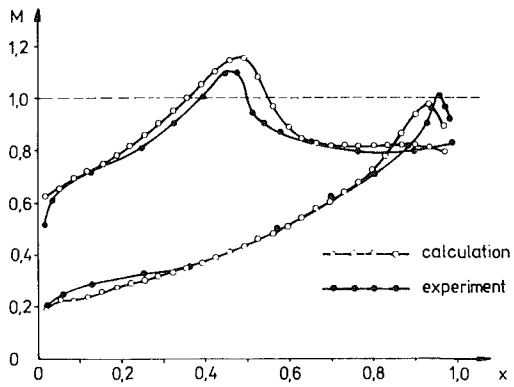

Fig. 6(c)

Fig. 6 Turbine cascade: (a) iso-Mach lines, $M_\infty = 0.334$, $M_2 = 0.809$, - - - sonic line; (b) experiment [9], $M_2 = 0.793$; (c) distribution of Mach number along profile

Always after several iterations, the value γ has been determined as a difference of potentials in the last points of the mesh at the upper and lower side of the profile and so have the coefficients of the boundary condition in ϑ_2.

4 Some Numerical Results

Figure 3 compares the flow field (iso-Mach lines) for a cascade consisting of NACA 0012 profiles with the results of Akay and Eccer [7] for $M_\infty = 0.85$, $\alpha = 0$ deg. The computation using this method (Fig. 3*a*) was performed with consideration of the back-pressure effect, i.e., with the value of outlet Mach number $M_2 = 0.89$ prescribed. A reasonable agreement can be observed both in the shape of domain of local supersonic flow and in the shape of corresponding iso-Mach lines.

The numerical method was further tested on several types of compressor cascades. Figure 4(*a*) compares the distribution of Mach number along profile surface for a cascade with NACA profiles of the 65 series at about critical Mach number $M_\infty = 0.7$, $\alpha = 9$ deg. The chosen values of inlet flow quantities enabled us to compare the results with the method [8] currently employed in subsonic flow calculations, and also with method [7], based on time-dependent concept of solution of Euler equations, and experiment [7]. The numerical results [7] appear to be considerably influenced by the crude mesh across the blade channel. More conspicuous differences between our results, the experiment [7] and the results [8] can be observed on the pressure side of the profile. Figure 4(*a*) also shows the results for $M_\infty = 0.83$ (dot-and-dash line). For this value of M_∞ the cascade is choked, as can be seen from the iso-Mach lines of the flow field in Fig. 4(*b*). Figure 4(*c*) shows the dependence of the Mach number of the choke on the incidence angle. There is a good agreement between numerical and experimental results.

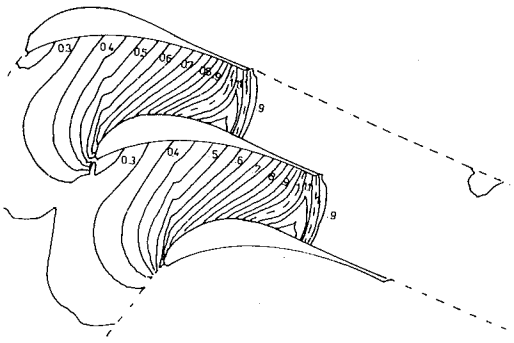

Fig. 7(a)

Fig. 7(b)

Fig. 7 Turbine cascade: (a) iso-Mach lines, $M_\infty = 0.334$, $M_2 = 0.906$, - - - sonic line; (b) experiment [9], $M_2 = 0.906$

Figures 5(*a–c*) show numerical results of the flow through a compressor cascade consisting of DCA profiles. Figures 5(*a*, *b*) are the iso-Mach lines of the calculated flow for two high subsonic inlet Mach numbers $M_\infty = 0.92$, $M_\infty = 0.96$. Both cases show a complicated structure of the flow field in the area before the leading edge of the profile. The result shown in Fig. 5(*b*) can be interpreted as a rise of detached shock wave. Figure 5(*c*) shows the distribution of Mach number along the profile.

The computation of flow through a turbine cascade with more cambered profiles uses the mesh as shown in Fig. 1(*b*). Figures 6(*a*, *b*) compare the calculated flow field with the interferogram [9]. About 2.5 interferogram strips correspond to increment $\Delta M = 0.05$ between iso-Mach lines. This comparison, as well as comparison of Mach number distribution along the profile in Fig. 6(*c*), suggests reasonable qualitative and quantitative agreement. Figures 7(*a*, *b*) are a comparison of calculation and experiment for higher $M_\infty = 0.906$. In both cases closing of the channel by the sonic line can be observed.

The computing time for one case – about 100 iterations – takes approximately 60 min CPU for the mesh shown in Fig. 1(*a*) – 150 × 36 grid points – and approximately 90 min CPU for the mesh shown in Fig. 1(*b*). The computing times are that long, because the computer, an EC 1033, is relatively very slow.

5 Conclusion

The comparisons show that the method can be used in practical computations of both compressor and turbine cascades in inviscid transonic flow. A more detailed comparison of com-

Downloaded 01 Jun 2010 to 171.66.16.57. Redistribution subject to ASME license or copyright; see http://www.asme.org/terms/Terms_Use.cfm

pressor cascade data suggests that the numerical method based on the potential flow model can be in some cases a satisfactory approximation of real flow in the vicinity of the choke within a certain range of incidence angles. This can be expected when the effect of the boundary layer is not very significant, i.e., the boundary layer is not separated and does not affect the main part of the potential flow in the blade channel. The described method can thus serve as a basis to determine some aerodynamic cascade characteristics.

References

1 Murman, E. M., and Cole, J. D., "Calculations of Plane Steady Transonic Flow," *AIAA Journal*, Vol. 9, No. 1, Jan. 1971, pp. 114–121.

2 Jameson, A., "Numerical Computation of Transonic Flow with Shock Waves," Symposium Transonicum II, Götingen 1975, Springer-Verlag, Berlin, 1976.

3 Jameson, A., "Iterative Solution of Transonic Flow Over Airfoils and Wings, Including Flow at Mach 1," *Communications of Pure and Applied Mathematics*, Vol. 27, 1974, pp. 283–309.

4 Hafez, M., South, J. C., and Murman, E. M., "Artificial Compressibility Methods for Numerical Solution of Transonic Full Potential Equation," *AIAA Journal*, Vol. 17, Aug. 1979, pp. 838–844.

5 Dulikravich, G. S., "Numerical Calculation of Inviscid Transonic Flow Through Rotors and Fans," Ph.D. Thesis, Cornell University, Jan. 1979.

6 Akay, H. U., and Ecer, A., "Finite-Element Analysis of Transonic Flow in Highly Staggered Cascades," *AIAA Journal*, Vol. 20, No. 3, Mar. 1982, pp. 410–416.

7 Petrovský, I., "Numerical Solution of Transonic Flow Through a Plane Cascade" (in Czech), Ph.D. Thesis, ÚT ČSAV, Praha, 1977.

8 Lakomý, C., "Theoretical Solution of High Subsonic Flow Past Two-Dimensional Cascades of Airfoils," ASME Paper No. 74-GT-91.

9 Dvořák, R., and Šafařík, P., "An Experimental Study of High Speed Flow in Turbine Cascades," Conf. Steam Turbines of the Large Output, Karlovy Vary, 1984.

10 Fořt, J., and Kozel, K., "Numerical Solution of Potential Transonic Flow Through Plane Cascades" (in Czech) Strojnicky časopis, Vol. 35, No. 3, 1984, pp. 375–389.

11 Fořt, J., and Kozel, K., "Calculation of Transonic Flow Through a Compressor and Turbine Cascade by Using the Relaxation Method for a Full Potential Equation," International Conference on Numerical Methods and Applications, Sofia, 1984.

12 Holst, T. L., and Ballhaus, W., "Fast, Conservative Schemes for the Full Potential Equation Applied to Transonic Flows," *AIAA Journal*, Vol. 17, No. 2, Feb. 1979, pp. 143–152.

Downloaded 01 Jun 2010 to 171.66.16.57. Redistribution subject to ASME license or copyright; see http://www.asme.org/terms/Terms_Use.cfm

Performance Prediction of Straight Compressor Cascades Having an Arbitrary Profile Shape

J. Citavý
Head of Fluid Mechanics Department,
National Research Institute for Machine Design (SVÚSS),
Prague, Czechoslovakia

A semi-analytical method of predicting losses and deviation angle for an arbitrary straight compressor cascade has been derived. The method has been developed at SVÚSS and is based upon the solution of the direct cascade problem using the following sources: (i) a potential flow calculation; (ii) attached boundary layer techniques; and (iii) experimental cascade data for separated flow. As an example of an application of the method, simple relations between geometric and aerodynamic cascade parameters have been derived by doing a systematic set of calculations for about 100 cascade configurations which had a 65-series blade profile and were run at low speed. The derived semi-analytical correlation has been compared to the published semi-empirical method of NASA for 65-series aerofoils, to experiments on cascades, and to results from a low-speed compressor.

Introduction

Two-dimensional cascade correlations in current use have their origin either directly in experiments (i.e., empirical data) or from experiments with potential flow using boundary layer theories as a frame (i.e., semi-empirical data). Extensive sets of cascade data have been obtained from systematic experiments in a wind tunnel with solid side walls at NGTE with a basic C4 profile [1, 2] and for a five-digit series CT airfoil profile at SVÚSS [3]. NACA/NASA performed systematic experiments on a 65-series profile [4] in a tunnel with porous walls, where the axial velocity ratio (AVR) was unity. The results from these experiments are suitable for comparison with two-dimensional flow calculation methods.

Theoretical results have been used to a limited extent previously, e.g., Carter [2] in extending a deviation rule and Lieblein [5] for a qualitative analysis of incidence angle, deviation, and loss correlations.

The present state of knowledge and current computers makes it possible to apply purely theoretical methods in predicting cascade performance, at least at design conditions and when the boundary layer is attached. Calculation of separated cascade flow, e.g., at off-design conditions, is not yet reliable and the use of experimental data is preferable. Some of the recent results concerning cascade aerodynamics have been summarized by Gostelow [6].

In this paper, a semi-analytical method of predicting the loss and deviation angle of an arbitrary straight compressor cascade is studied. The method consists of using available codes for calculating the potential flow and attached boundary layer for a cascade together with experimental data for separated cascade flow. Emphasis is given to the long-term research results obtained at the Fluid Mechanics Department of SVÚSS (National Research Institute for Machine Design) e.g., [7–13].

Basic Flow Model

The cascade notation is defined and the performance shown in Fig. 1. From a dependence of loss coefficient and deviation (outlet flow angle with some reference incidence) inlet flow angle is defined, e.g., nominal l_0 [1], l_* at the maximum lift-drag ratio [2], or l_r for minimum loss [5]. In this paper we will use a so-called smooth inlet condition l_0 or $(\alpha_1)_0$ which is defined from the potential flow calculation [10] as the incidence with minimum velocity peaks on both suction and pressure surfaces.

The reference value for a given cascade depends on several parameters: Reynolds and Mach numbers, AVR, turbulence intensities, etc. It is assumed that the effect of the various parameters can be determined by using Prandtl's hypothesis of superimposing the potential flow and boundary layer, providing no separation occurs. The general two-dimensional cascade flow model is then constructed from the attached or locally separated boundary layer and from the separated flow due to high incidence angle, low Re, and high Ma

$$\begin{aligned} \delta &= \delta_0 + \delta_i + \delta_{\mathrm{Re}} + \delta_{\mathrm{Ma}} \\ \xi_p &= \xi_{p0} + \xi_{pi} + \xi_{\mathrm{Re}} + \xi_{\mathrm{Ma}} \end{aligned} \tag{1}$$

where δ_0, ξ_{p0} are the reference values at high Re and low Ma; δ_i, ξ_{pi} are values due to the change of incidence from its reference value; δ_{Re}, ξ_{Re} and δ_{Ma}, ξ_{Ma} are values due to the low Re and high Ma, respectively.

For simplicity, an incompressible (or subsonic) flow at high Re is assumed here. The effect of compressibility on δ_0 and ξ_{p0} is assumed as a change of velocity distribution with Ma $<$ $(\mathrm{Ma})_{cr}$.

Contributed by the Gas Turbine Division of THE AMERICAN SOCIETY OF MECHANICAL ENGINEERS and presented at the 31st International Gas Turbine Conference and Exhibit, Düsseldorf, Federal Republic of Germany, June 8–12, 1986. Manuscript received at ASME Headquarters January 27, 1986. Paper No. 86-GT-140.

Copyright © 1987 by ASME

Downloaded 01 Jun 2010 to 171.66.16.57. Redistribution subject to ASME license or copyright; see http://www.asme.org/terms/Terms_Use.cfm

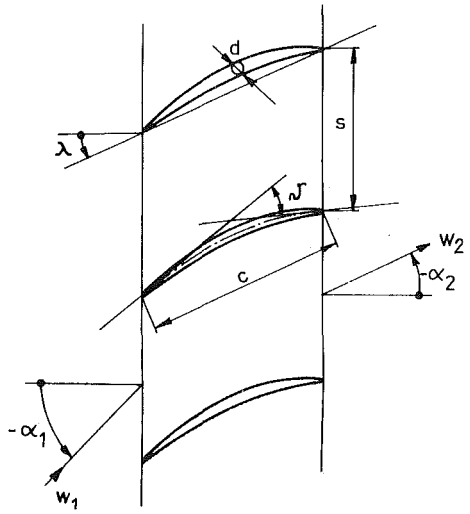

Fig. 1(a) Cascade notation

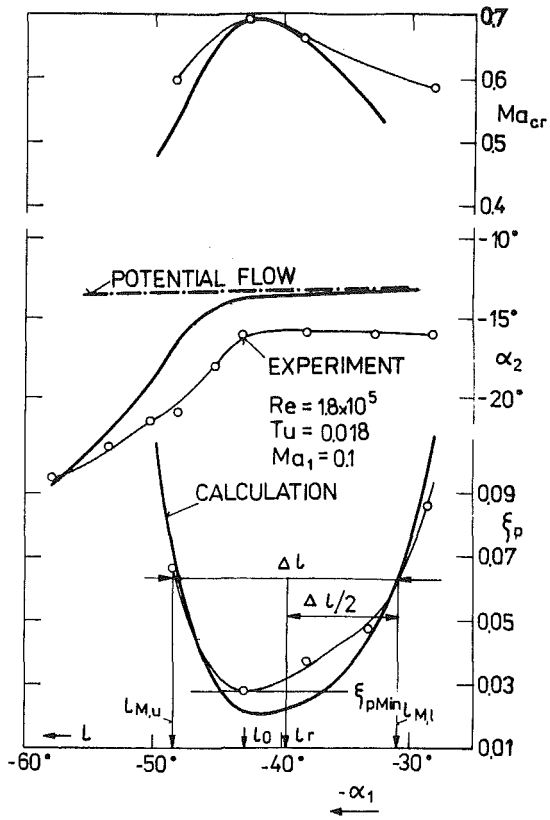

Fig. 1(*b*) Aerodynamic performance of a cascade

According to the physics of the flow, a rational method of cascade performance prediction should proceed as follows:

A Determination of reference values from potential flow and boundary layer theories
  1 Reference incidence and deviation angles
  2 Velocity distribution over the cascade blade
  3 Critical Mach number
  4 Momentum thickness and loss coefficient
  5 Correction of the deviation angle for viscosity (displacement) effect, AVR, etc.

B Prediction of off-design performance from a combination of theoretical (i.e., potential flow and boundary layer) and experimental results
  1 Deviation angle and velocity distribution (from potential flow calculations) for various incidence angles
  2 Critical Ma
  3 Position of boundary layer separation point (from calculations)
  4 Effect of separated layers on loss and deviation angle from experimental data
  5 Loss and deviation

The above steps represent the basis of a semi-analytical method. A brief description of the method is given below.

Method of Performance Prediction

The semi-analytical method for the performance prediction of a straight compressor cascade is described below. This method is based upon current analytical codes for the potential flow and boundary layers as well as on some experimental data for separated flow.

Potential Flow Code. The singularity method of Polášek [10] is used at SVÚSS for calculating incompressible flow. The method is valid for an airfoil of arbitrary camber and for a maximum thickness up to 20 percent. The singularities are distributed along the profile mean line. The outlet flow angle is determined from the position of the rear stagnation point which is assumed to be at the intersection between the trailing edge circle and an extension of the mean line. An advantage of the prediction method is the determination of the reference incidence angle (denoted by index "0") from a simple condition with a physical interpretation. This angle is defined as the incidence with the minimum peaks of velocity distribution over both suction and pressure surfaces. This method also provides a simple means of approximate modeling of the profile displacement thickness and wake by means of the choice of a

Nomenclature

c = chord length
c_p = pressure coefficient
d = maximum thickness
D = diffusion parameter = w_M/w_2
H = form parameter
Ma = Mach number
p_t = total pressure
P = pressure gradient
Re = Reynolds number
Re_θ = momentum thickness Reynolds number
s = blade spacing
Tu = turbulence intensity
w = velocity
w_M = maximum velocity on blade surface
x_M = position of maximum velocity
α_1, α_2 = inlet and outlet flow angles, deg
ϵ = flow deflection, deg
δ = deviation angle, deg
ϑ = blade-camber angle, deg
λ = stagger angle, deg
ξ_P = profile loss coefficient

$$= (p_{t_1} - p_{t_2}) / \frac{\rho}{2} w_1^2$$

i = incidence angle, deg.
θ = momentum thickness
LI = laminar instability

Subscripts

cr = critical
M = maximum
P = potential
r = reference (minimum loss)
s = separation
u = upper (suction) surface
0 = reference (smooth inlet)
1 = station at cascade inlet
2 = station at cascade outlet

Downloaded 01 Jun 2010 to 171.66.16.57. Redistribution subject to ASME license or copyright; see http://www.asme.org/terms/Terms_Use.cfm

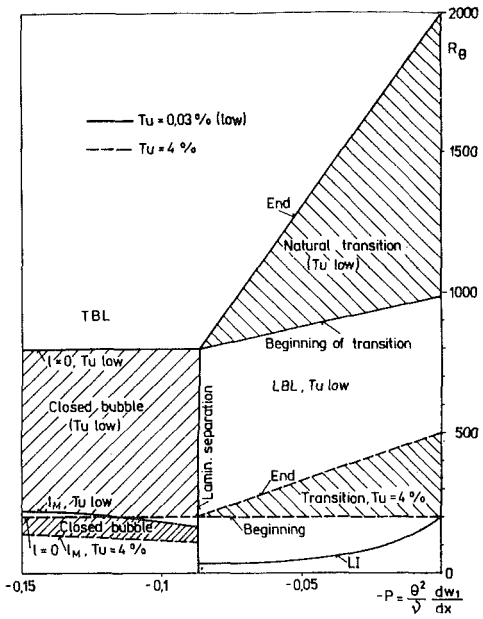

Fig. 2 Schematic presentation of boundary layer development using pressure gradient P and momentum thickness Reynolds number Re_θ at different turbulence intensities Tu

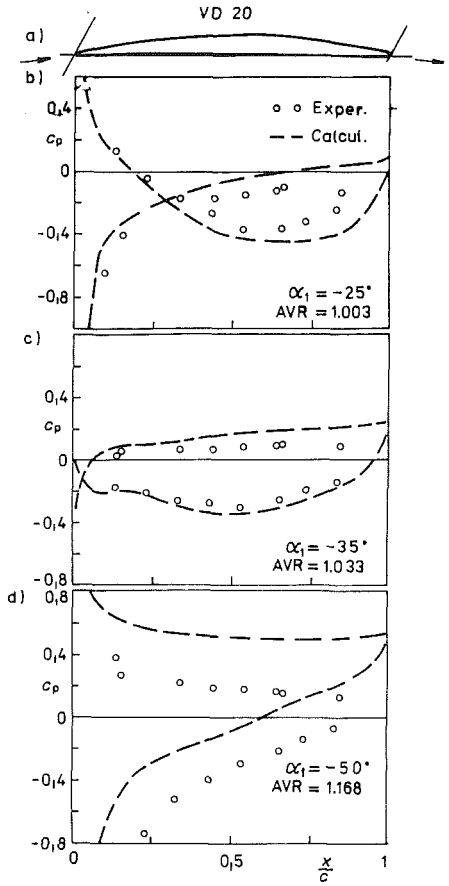

Fig. 3 Calculated and experimental pressure distribution at various incidence angles for VD 20 cascade

single coefficient A_0. The method has also been used and tested as an inverse (design) cascade code [11].

Results of calculations using this singularity method [10] have been compared to a series of experiments in order to test the validity of the predicted deviation angle and pressure distributions [11] (Figs. 3 and 4). For cases with attached

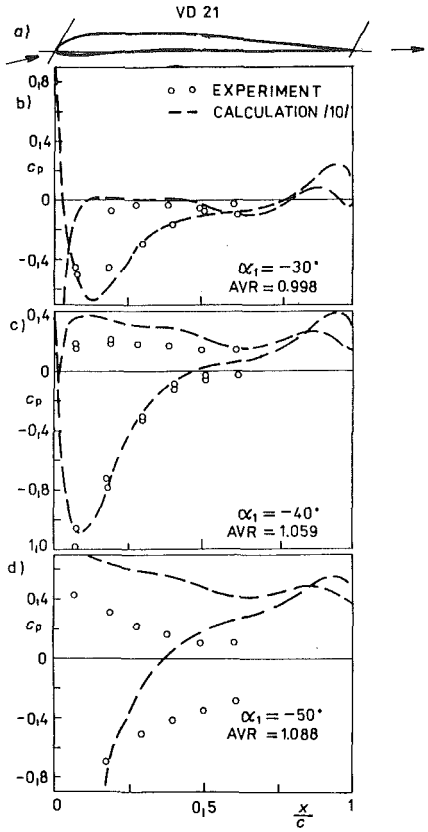

Fig. 4 Calculated and experimental pressure distribution at various incidence angles for VD 21 cascade

boundary layers the agreement is reasonable, providing AVR = 1.

The compressible subsonic velocity distribution is then calculated using a simple correction to the incompressible flow [12] based upon a locally linearized relation of the Prandtl-Glauert type. Since a code based on FEM has recently become available [13], an alternative analytical solution, at times, has been used up to the critical Ma. Transonic cascade flow is calculated using the full potential equation [9] or an artificial viscosity [13].

Boundary Layer Code. Calculation methods for both laminar and turbulent boundary layers in subsonic two-dimensional flow, as derived from basic research, have to be extended and modified for turbomachinery application. Real flow effects, for example a higher level of turbulence intensity, should be included. An even more difficult problem is encountered in the calculation of a transitional boundary layer for which only semi-empirical methods are presently available. More detailed calculation methods consider two ways of transition: (i) natural, as it occurs in an attached layer, e.g., a flat plate, and (ii) via a separation bubble. Thus, a complete boundary layer prediction model for a cascade blade consists of three parts: laminar, transitional (both natural transition and a closed separation bubble), and turbulent boundary layers. Such a model is denoted as a three-component one and uses an integral method for the laminar part with a modification at the separation point such that the value of P_{LS} is not a constant, but depends upon the detailed shape of the velocity distribution near the laminar separation point. For a transitional boundary layer empirical data in a physical plane built of two variables, P and Re, are used for both natural transition and a separation bubble [14, 18]. The effect of turbulence intensity Tu on the boundary layer is schematically shown in the P–Re_θ plane (Fig. 2).

Since a separation bubble is the more common case at low Re with an adverse pressure gradient, the semi-empirical

Downloaded 01 Jun 2010 to 171.66.16.57. Redistribution subject to ASME license or copyright; see http://www.asme.org/terms/Terms_Use.cfm

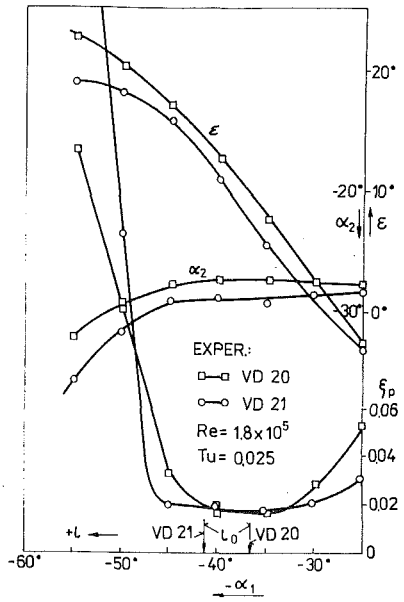

Fig. 5 Experimental results for cascades VD 20 and VD 21

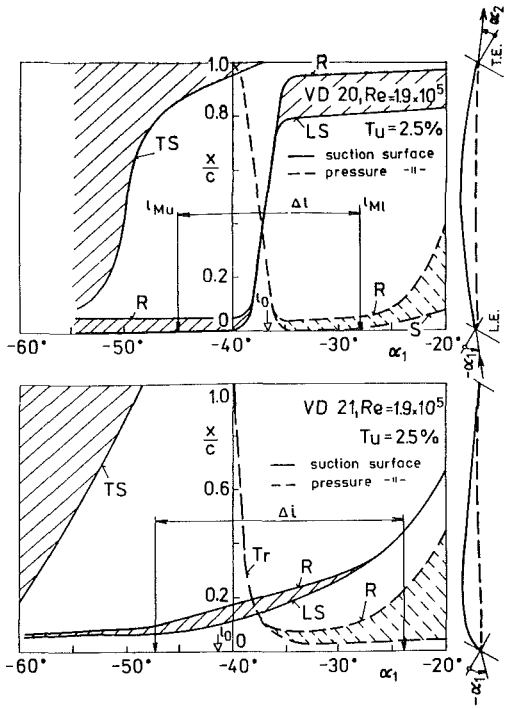

Fig. 6 Summary of boundary layer visualization on cascades VD 20 and VD 21

method of bubble prediction has been thoroughly tested on cascades [11, 14, 19, 23] and, in addition, on a circular cylinder [18].

The turbulent boundary layer calculation method of Head and Patel [15] or of Bradshaw [16] is applied either at the end of natural transition or shortly after the closed separation bubble. The initial conditions, i.e., Re_θ, H are provided from the calculation of the transitional boundary layer.

The presentation of boundary layer development in the Re_θ–P plane is similar to its presentation in a transformation plane H-Re_θ (so-called image plane) as suggested by LeFoll [17].

More details on cascade boundary layer calculations are given in [11, 14, 19, 21].

Experimental Data for Separated Flow. A complex theoretical and experimental investigation has been carried out

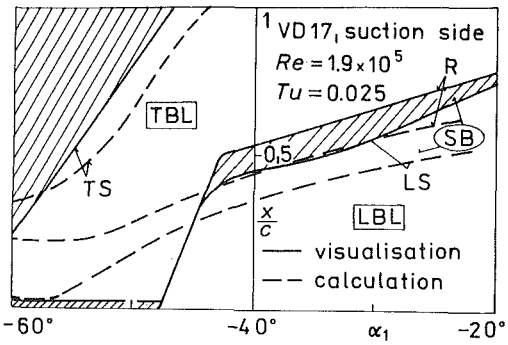

Fig. 7 Comparison between visualization and calculation of boundary layer development on the suction surface of VD 17 cascade [19]

on a series of compressor cascades, VD 17–21 [11], which have a prescribed velocity distribution (VD). Experiments and calculations have been performed and compared over a range of incidence angles (± 15 deg) at low speed. The effect of varying the shape of the design velocity distribution on the off-design performance characteristics has been studied. Figures 3 and 4 show two profile shapes with the corresponding predicted pressure distributions. Cascades VD 21 and VD 20, respectively, have a triangular and rectangular (roof-top) shaped velocity distribution at the design incidence angle, whereas cascade VD 17 is of intermediate shape. The stagger angle and space-chord ratio are the same for all of the cascades. Coordinates of the airfoils for cascades VD 20 and VD 21 are given in the Appendix.

Experimental pressure distributions at high-positive and high-negative incidence angles are compared with results from the potential flow calculations in Figs. 3 and 4. From these figures it follows that good agreement is obtained only at the design incidence angle (Figs. 3*c* and 4*c*), when the boundary layer is attached. Agreement between experiment and calculation at a high-negative incidence angle (i.e., at $\alpha_1 = -30$ deg; Figs. 3*b* and 4*b*) is better than at a high-positive incidence angle ($\alpha_1 = -50$ deg, Figs. 3*d* and 4*d*).

The measured performance of cascades VD 20 and VD 21 is shown in Fig. 5. It is clear that with increasing incidence, separation occurs sooner on cascade VD 21 than on VD 20.

The results of boundary layer visualization for cascades VD 20 and VD 21 are summarized in Fig. 6. The positions of laminar and turbulent separation (LS and TS) as well as the transition (Tr) and reattachment (R) on both suction and pressure surfaces are indicated in Fig. 6. The range of incidence angle (Δi) corresponding to low loss (from Fig. 5) is also shown in Fig. 6.

A similar relationship of x_s, x_R versus incidence angle has also been obtained from calculations. A comparison between experiment and calculation is illustrated in Fig. 7 for the suction surface of the VD 17 cascade [19]. In these calculations the potential flow velocity distributions have been used as an input. When using the experimental velocity distribution in boundary layer calculations, the agreement with experiment is improved, in particular at high incidence angles.

Correlation of Separated Cascade Flow. Several attempts along this line have been made in this field so far [1–3, 5, 6]. Because of the complexity of the separated cascade flow, no general solution to this problem has been obtained so far. The experimental results of Figs. 3–7 have been used to correlate the increase of loss and deviation at off-design conditions. These results clearly indicate that the increase of loss for incidence angles higher than the reference (l_0) depend on an upstream movement on the suction surface of the turbulent boundary layer separation point x_{TS}. Similarly, the increase of loss for negative incidence angles can be related to the

Downloaded 01 Jun 2010 to 171.66.16.57. Redistribution subject to ASME license or copyright; see http://www.asme.org/terms/Terms_Use.cfm

Table 1 Calculated cascade geometries

Profile	–	65-010	65-015
	65-600	65-610	65-615
	65-1200	65-1210	65-1215
	65-1800	65-1810	65-1815
	–	65-2410	–
Stagger angle	0	30 deg	60 deg
Space-chord ratio	0.5	1	1.5

downstream movement of the reattachment point x_R on the pressure surface.

Assuming that the length of the separated regions on both the upper and lower blade surfaces is proportional to loss, a correlation for the increase of loss and deviation angle due to separation at high-positive and negative incidence angles can be established from the experimental results and is shown in Fig. 8. This correlation uses positions of separation x_S and reattachment x_R estimated from the calculated potential velocity distribution together with the increase of loss ξ_{pi} and deviation angle δ_i as a function of the incidence angle from the VD 17-21 cascade experiments. The position (x_M) of maximum velocity $(w_M)_0$ on the suction surface appears as a parameter in the correlation. An explanation for this may be found in boundary layer theory. In the simplest case the separation and reattachment depend on the velocity distribution and Re. As argued earlier [11], the velocity distribution can be approximated by both the diffusion ratio D and the position of maximum velocity x_M. An estimation of the effect of x_M on the separation point x_S at various values of D can be obtained from the results of turbulent boundary layer calculations using Bradshaw's method and is shown in Fig. 9. As can be seen, different values of x_S are obtained at the same value of diffusion parameter D, but with different values of x_M.

The data from Fig. 8 are also used in Fig. 13 for a simplified prediction of off-design conditions.

Applications

Systematic calculations have been made for plane cascades with 65-series profiles in two-dimensional incompressible flow using the abovedescribed semi-analytical method. The extent of geometric parameters investigated is shown in Table 1. The combinations of parameters give in total about 100 cascade configurations. The extensive calculations have made it possible to derive a relationship between cascade geometric and calculated aerodynamic parameters.

Reference Conditions. An example of the potential flow calculation results is presented in Figs. 10 and 11 for 65-series profiles with a maximum thickness of 10 percent and with a stagger angle of 30 deg. In order to provide an extensive test of the semi-analytical calculation method relative to the experiments [4, 5], the results of the calculation have been evaluated using regression polynomials of the second order. However, for the reference incidence and deviation angle results, a linear dependence on the profile camber angle (of an equivalent circular arc) was found to be more suitable as shown in Fig. 10. Thus, the calculated reference incidence l_0 is approximated by:

$$l_0 = A_i + B_i \vartheta \tag{2}$$

where A_i and B_i depend upon the cascade geometry

$$A_i = [1.88 - 2.14 s/c + 0.68(s/c)^2]\lambda \cdot d/c \tag{3}$$

$$B_i = [(-0.65 d/c + 0.1833 \cdot s/c) + (0.0011 + 0.009 d/c) \cdot \lambda] \tag{4}$$

A similar type of relation has been used at NACA [5]; but the values A_i, B_i could not be correlated with the stagger angle, since the experiments at NACA were performed at constant inlet angles instead of the stagger angles.

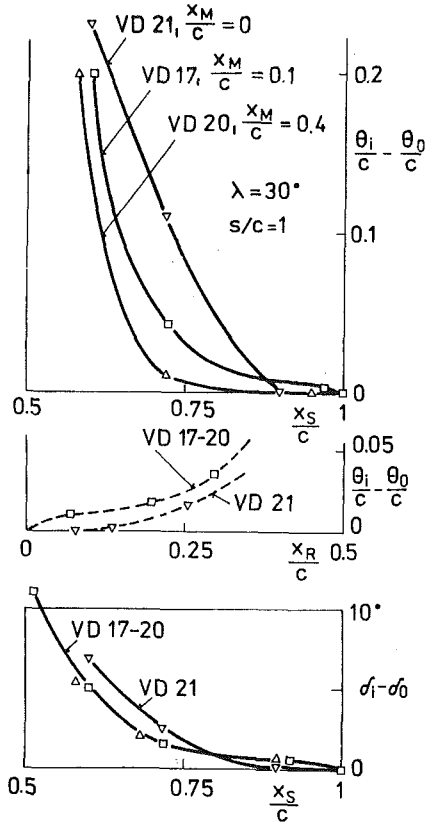

Fig. 8 Semi-empirical dependence of the increase of loss and deviation angle on the position of boundary layer separation x_S (suction surface) and reattachment x_R (pressure surface)

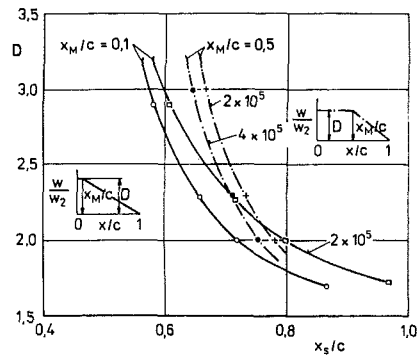

Fig. 9 The effect of the diffusion parameter, the position of the maximum velocity, and the Reynolds number on the separation point of a turbulent boundary layer

The reference deviation angle (uncorrected for viscosity effect) is similarly expressed by

$$\delta_{0P} = A_\delta + B_\delta \cdot \vartheta \tag{5}$$

where

$$A_\delta = [0.972 - 0.672 s/c + 0.104(s/c)^2]\lambda d/c \tag{6}$$

$$\begin{aligned} B_\delta = {} & (0.1722 - 0.000592\lambda + 0.000023\lambda^2) \\ & \times [(-0.3566 + 0.00098\lambda - 0.00024\lambda^2) \\ & + (1.6446 - 0.00276\lambda + 0.0004\lambda^2) s/c \\ & + (-0.288 + 0.00178\lambda - 0.00016\lambda^2) \\ & \times (s/c)^2] \cdot [1 + 0.1/(s/c)^3 - (d/c)/(s/c)^3] \end{aligned} \tag{7}$$

The reference deviation δ_0 is then determined from

$$\delta_0 = \delta_{0P} + \Delta\delta_D = \delta_{0P} + k_D \cdot D_0^n \tag{8}$$

where δ_{0P} is calculated from the potential flow theory [10];

Downloaded 01 Jun 2010 to 171.66.16.57. Redistribution subject to ASME license or copyright; see http://www.asme.org/terms/Terms_Use.cfm

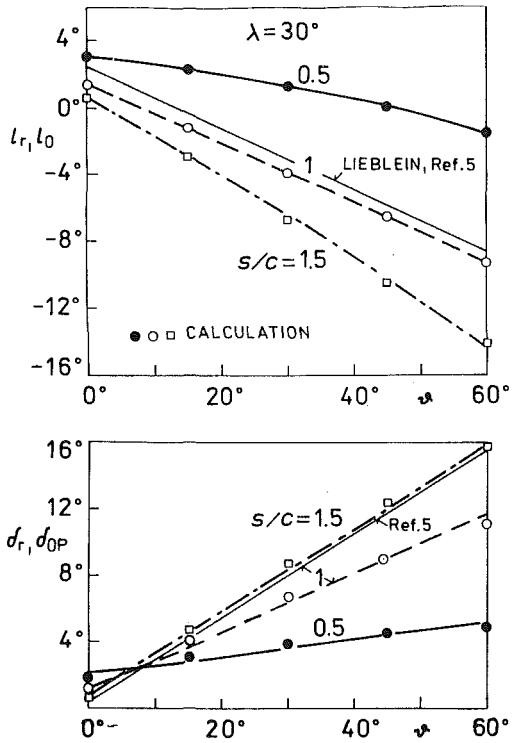

Fig. 10 An illustration of the calculated reference incidence and deviation angles for 65-series cascades with a maximum thickness of 10 percent

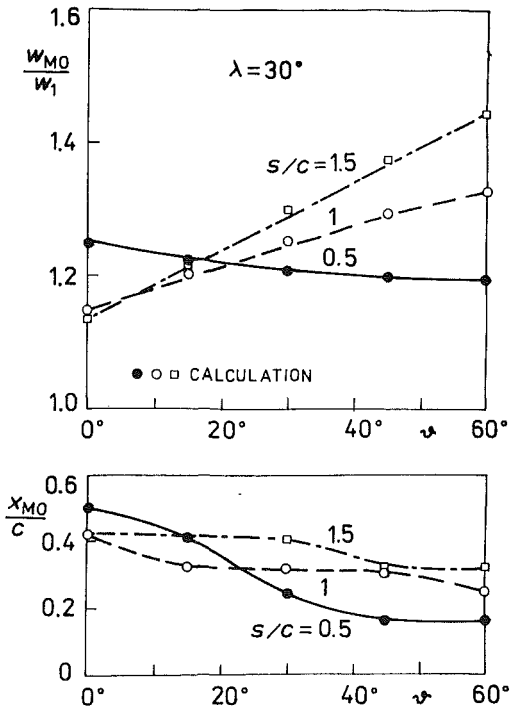

Fig. 11 Calculated maximum velocity and its position on the suction surface at the reference incidence angle for 65-series cascades with a maximum thickness of 10 percent

$\Delta\delta_D$ is a correction for the viscosity (displacement) effect. It can be determined from a relation between inviscid and viscous outlet flow angles

$$(\tan\alpha_2)_0 = F_\delta(\tan\alpha_2)_{0P}$$

obtained from an application of the momentum equation on cascade flow. Function F_δ depends on boundary layer thicknesses δ_1, θ, and also on space-chord ratio. This correction of outlet angle varies within a narrow range of 1 to 3 deg. It can therefore be approximated by

$$\Delta\delta_D = k_D \cdot D_0^n$$

where $n=2$ and K_D varies between 0.75 and 1.25.

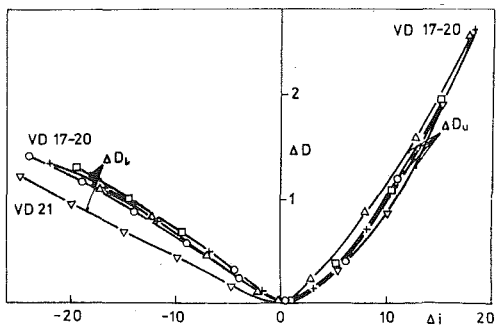

Fig. 12 Calculated difference of the diffusion parameters on the lower and upper blade surfaces versus the difference of the incidence angles

The calculated reference maximum velocity on the suction surface was found to depend upon cascade geometry as follows

$$\begin{aligned}\left(\frac{W_M}{W_1}\right)_0 = {} & 1.08304 - 0.0035\lambda - 0.107011 s/c \\ & + 3.149798 d/c + 0.000032\lambda^2 \\ & - 0.000048\lambda\cdot\vartheta + 0.006289\vartheta\cdot s/c \\ & - 0.019346\vartheta\cdot d/c + 0.002123\lambda\cdot s/c \\ & - 0.02271\lambda\cdot d/c - 0.61972 s/c\cdot d/c \end{aligned} \quad (9)$$

The diffusion parameter is given by

$$D_0 = \frac{W_M}{W_1}\cdot\frac{W_1}{W_2} \quad (10)$$

The position of the maximum velocity can also be expressed as a function of cascade geometry.

From boundary layer calculations of 65-series profiles, the momentum thickness at the trailing edge was determined to be dependent on the diffusion parameter

$$\left(\frac{\theta_2}{C}\right)_0 = f(D_0^3, \mathrm{Re}) = a + b(D_0^3 - e)\cdot k_{\mathrm{Re}} \quad (11)$$

The coefficients a, b, e are given in the interval $1 < D_0^3 < 5$ as follows

$$a = 0.006,\ b = 0.0017,\ e = -1$$

and in the interval $5 < D_0^3 \le 15$ by:

$$a = 0.0128,\ b = 0.0025,\ e = -5$$

The value of $k_{\mathrm{Re}} = 1 - 0.355\log(\mathrm{Re}/2.5\times10^5)$ is the same for both intervals. At $\mathrm{Re} \le \mathrm{Re}_{cr}$ the increase of loss ξ_{Re} and deviation δ_{Re} are estimated using a semi-empirical method [18, 21].

The profile loss coefficient is calculated from a simple relation

$$\xi_{P0} = 2\left(\frac{\theta_2}{c}\right)_0 \frac{1}{\frac{s}{c}\cos(\alpha_2)_0}\left(\frac{\cos\alpha_1}{\cos\alpha_2}\right)_0^2 \quad (12)$$

Off-Design Conditions. A simplification of the off-design prediction procedure has been suggested such that the differences $\Delta D_u = D_u - D_0$ for the airfoil suction (upper) and $\Delta D_l = D_l - D_0$ for the pressure (lower) surface are assumed to depend on the difference $\Delta l = l - l_0$ (Fig. 12).

These relations have been obtained for cascades VD 17-21 from the potential flow calculations. Since the separation position depends upon the values of D and X_M/c (Fig. 9), the

Downloaded 01 Jun 2010 to 171.66.16.57. Redistribution subject to ASME license or copyright; see http://www.asme.org/terms/Terms_Use.cfm

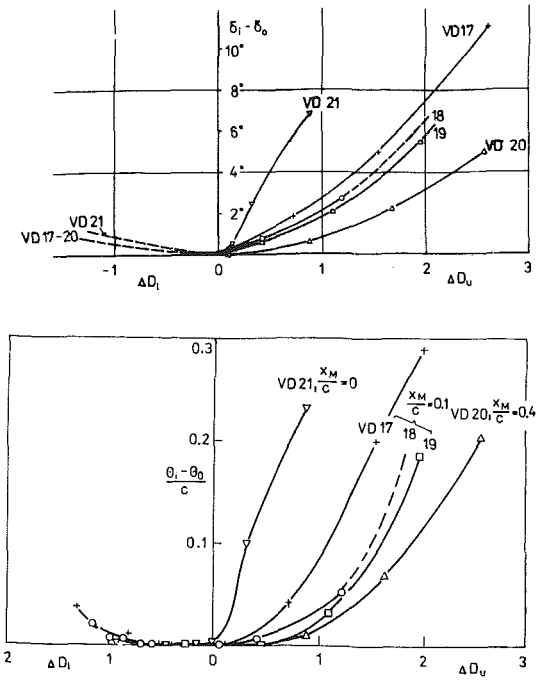

Fig. 13 Semi-empirical relation between the loss and deviation increase and the difference of the diffusion parameters on the upper (at positive l) and the lower (at negative l) blade surfaces; cascades VD 17-21

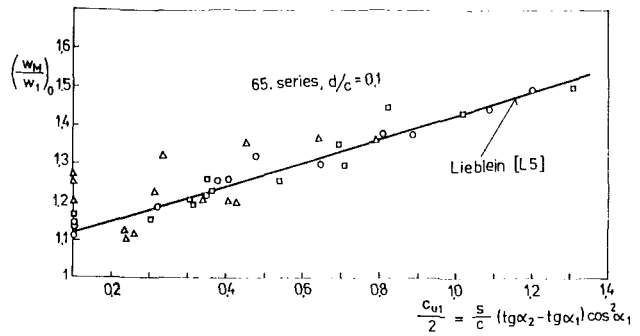

Fig. 14 Comparison of calculated maximum velocity with Lieblein's relationship

increase of loss and deviation angle (Fig. 8) can be correlated with the differences of the diffusion parameters. The result of the correlation for cascades VD 17-21 is shown in Figs. 12 and 13.

A simple program, MR 82, has been written which contains the polynomials for calculating the reference angles and loss, and uses the relations from Figs. 12 and 13 for predicting the off-design performance. Because of its simplicity, it can be employed in place of current cascade corelations in connection with a through-flow program.

Similar relations have been obtained with DCA airfoil profiles.

Comparisons

The above-described semi-analytical method of performance prediction has been tested using the following cases: (i) an alternative viscous flow model, (ii) cascade experiments at NACA [4] on 65-series profiles at reference conditions, (iii) cascade experiment at DFVLR on 65-612 cascade at off-design conditions, and (iv) rotor blade element experiments at SVÚSS on 65-series cascade.

Viscous Flow Model. Two-dimensional fully turbulent viscous flow code [20] has been used to predict the perfor-

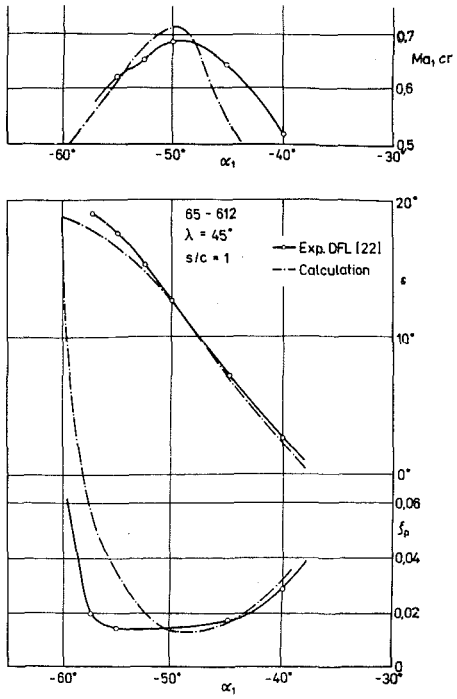

Fig. 15 Comparison between the measured [22] and simplified performance calculation of cascade 65-612

mance characteristic of RK3 cascade [11]. The predicted velocity distribution at off-design incidence angles agrees with experiment better than that obtained from the potential flow calculation. However, the development of the method for viscous flow calculation has not yet been finished to the extent that it can be used in a current design practice.

NACA 65-Series Cascade Experiments. Results of systematic calculations of 65-series profiles at reference conditions have been compared with Lieblein's correlation [5].

Reference Incidence Angle. A direct comparison between the reference incidence angles l_0 [10] and l_r [5] is complicated because of different definitions employed in the two methods. Nevertheless, the physical interpretations are rather similar. An example of the comparison between l_0 and l_r is shown in Fig. 10. The difference between the two incidence angles varies from 2 to 5 deg, depending on stagger angle and other geometric cascade parameters. In the extreme case of high camber, i.e., $\vartheta = 60$ deg, the linear dependence of l_0 (and also l_r) on camber is no longer in agreement with experiments at NGTE [2] and also at SVÚSS [3]. It appears that a separation occurs on highly cambered cascades even at the reference incidence angle and therefore the validity of Prandtl's model is rather limited in these cases.

Reference Deviation Angle. The uncorrected reference deviation angle δ_{0P}, which is defined as the value from the potential flow calculation, should be in general less than the δ_0 (corrected value) according to equation (8). However, δ_0 should be approximately the same as the reference value δ_r [5]. The values for δ_{0P} are from 1 to 8 deg less than those for δ_r except for the combination of $\vartheta = 60$ deg, $s/c = 0.5$ where extremely high differences (12 – 22 deg) occur. Although this is an extrapolated case, this large difference cannot be explained by boundary layer separation and therefore the potential flow calculation appears to be unreliable for this extreme cascade geometry.

Diffusion Factor. The calculated maximum velocity $(W_M/W_1)_0$ as a function of tangential force coefficient, C_{u1},

Downloaded 01 Jun 2010 to 171.66.16.57. Redistribution subject to ASME license or copyright; see http://www.asme.org/terms/Terms_Use.cfm

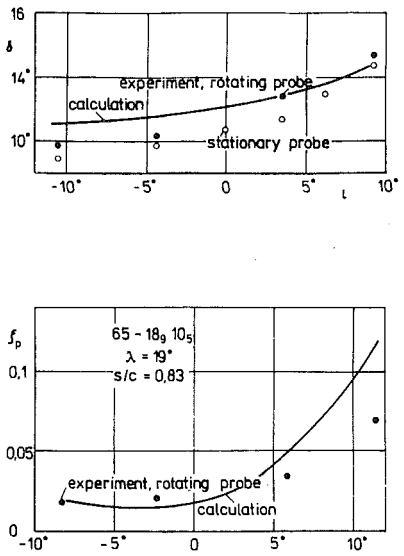

Fig. 16 Comparison of the simplified performance prediction with experiments on a rotor blade element [7]

has been compared to the linear relationship of Lieblein [5] (Fig. 14). The results of calculation have made it possible to extent Lieblein's relation in order to account for the effect of maximum thickness as follows

$$(W_M/W_1)_0 = (1 + 1.25d/c) + 0.61s/c(\tan\alpha_2 - \tan\alpha_1)\cos^2\alpha_1$$

DFL Cascade Experiment. A comparison of the performance prediction using this method with the experiments of DFL/DFVLR [22] is illustrated in Fig. 15. This is for the cascade 65-612 at low Ma and high Re. The simple program, MR 82, was used to calculate the design and off-design loss and flow deflection.

SVÚSS Rotor Blade Experiment. The simplified method of cascade performance prediction has been compared to experiments for a rotor blade element of an experimental compressor [7] (Fig. 16). From this comparison it follows that the simple semi-analytical method reasonably well agrees at the reference condition. For the prediction of the off-design conditions, however, the experimental data for separating flow are not sufficiently accurate and general; and therefore the validity is limited to moderately loaded cascades similar to those from which the data have been derived.

Summary

1 A semi-analytical method of performance prediction for an arbitrary straight compressor cascade has been developed. The method consists of two main parts: (i) theoretical prediction of loss and deviation angle at design (reference) incidence angle using verified codes for calculating potential flow and boundary layer development. Real flow effects are included either in potential flow (AVR, Ma) or in boundary layer (Re, *Tu*, Ma) methods, and (ii) combination of theoretical and experimental results for predicting loss and deviation angle at off-design condition. From complex experiments on series of the prescribed velocity distribution cascades VD 17-21 within a wide range of incidence angle, a correlation for the increase of loss and deviation angle with incidence angle (different from the reference one) has been suggested.

2 The semi-analytical method has been tested against the NACA/NASA experiments on 65-series at reference conditions and over a wide range of geometric cascade configuration (about 100 cascades). The off-design performance has been compared to a 65-series linear cascade experiment at DFL/DFVLR and also to a rotor blade element from an experimental compressor stage at SVÚSS. The semi-analytical method has also been applied to design and performance prediction of axial flow compressors.

3 Further improvement of the method is expected from the fully turbulent viscous flow model for predicting the separated flow at off-design conditions.

Acknowledgments

The work has been carried out at the Fluid Mechanics Department of SVÚSS (National Research Institute for Machine Design) for the ČKD Kompresory, Prague. The assistance of the Institute and ČKD Kompresory is gratefully acknowledged.

References

1 Howell, A. R., "The Present Basis of Axial Flow Compressor Design, Part 1 – Cascade Theory and Performance," ARC R and M 2095, 1942.

2 Carter, A. D. S., "The Low Speed Performance of Related Aerofoils in Cascade," Aeronautical Research Council, Current Paper No. 29, 1951.

3 Citavý, J., "Two-Dimensional Cascade Data," *Proceedings of the Second International JSME Symposium, Fluid Machinery and Fluidics*, Tokyo, Vol. I, Sept. 1972, pp. 1-9.

4 Herring, L. J., Emery, J. C., and Ervin, J. R., "Systematic Two-Dimensional Cascade Tests of NACA 65-Series Compressor Blades at Low Speeds," NACA TN 3916, 1956.

5 "Aerodynamic Design of Axial-Flow Compressors," NASA SP 36, 1965.

6 Gostelow, J. P., *Cascade Aerodynamics*, Pergamon Press, Oxford, 1984.

7 Cyrus, V., "Experimental Study of Three-Dimensional Flow in an Axial Compressor Stage," ASME Paper No. 86-GT-118, 1986.

8 Jílek, J., "An Experimental Investigation of the Three-Dimensional Flow Within Large Scale Turbine Cascades," ASME Paper No. 86-GT-170, 1986.

9 Fořt, J., and Kozel, K., "Numerical Solution of Inviscid Two-Dimensional Transonic Flow Through a Cascade," ASME JOURNAL OF TURBOMACHINERY, this issue.

10 Polášek, J., "Flügeprofil im inhomogenen Strömungsfeld," *Rewue Roumaine de Sciences Techniques, Mechanique Aplique*, Vol. 9, No. 3, 1964, pp. 617-666.

11 Citavý, J., "Two-Dimensional Compressor Cascades With Optimum Velocity Distribution Over the Blade," ASME JOURNAL OF ENGINEERING FOR POWER, 1975, pp. 101-110.

12 Citavý, J., "Two-Dimensional Compressor Cascades With Optimum Velocity Distribution Over the Blade" (in Czech), PhD Thesis, Prague, 1965.

13 Valchářová, J., "Application of Finite Element Method to Heat and Mass Transfer," *Monographs and Memoranda of SVUSS*, No. 30, Praha, 1981.

14 Citavý, J., and Norbury, J. F., "Some Features of Laminar Separation Bubbles on Blades in Cascades," *Proceedings of Symposium on Internal Flows*, Salford, Apr. 1971, pp. B109-B117.

15 Head, M. R., and Patel, V. C., "Improved Entrainment Method for Calculating Turbulent Boundary-Layer Development," ARC R and M 3634, 1968.

16 Bradshaw, P., Ferris, D. H., and Attvell, N. P., "Calculation of Boundary Layer Development Using Turbulent Energy Equation," *Journal of Fluid Mechanics*, Vol. 28, Part 3, 1967, pp. 593-616.

17 Le Foll, J., "A Theory of Representation of the Properties of Boundary Layers on Image Plane," Aeronautical Research Council 29240, 1967.

18 Citavý, J., "Prediction of the Separation Bubble on a Circular Cylinder," International Congress of IUTAM, Moscow, Aug. 1972, Book of Abstracts, p. 41.

19 Citavý, J., "The Effect of Incidence Angle and Free-Stream Turbulence on the Performance of Compressor Cascades," EUROMECH 72: Boundary Layers and Turbulence in Internal Flows, University of Salford, Mar. 30-Apr. 1, 1976.

20 Zuber, I., "Numerical Solution of the Turbulent Flow of an Incompressible Fluid in Curved Planar and Axially Symmetrical Channels," *Int. J. Heat and Fluid Flow*, Vol. 3, No. 2, 1982.

21 Citavý, J., "Design and Performance Prediction of Two-Dimensional Cascades" (in Czech), *Proceedings of Symposium on CAD of Turbomachines*, Prague, Mar. 1985, pp. 187-191.

22 Bahr, J., "Untersuchen über den Einfluss der Profildicke auf die kompressible ebene Strömung durch Verdichtergitter," *Forsch. Ing. -Wes.*, Vol. 30, No. 1, 1964, pp. 14-25.

23 Citavý, J., and Norbury, J. F., "The Effect of Reynolds Number and Turbulence Intensity on the Performance of a Compressor Cascade With Prescribed Velocity Distribution," *J. Mech. Eng. Sci.*, Vol. 19, No. 3, 1977.

Downloaded 01 Jun 2010 to 171.66.16.57. Redistribution subject to ASME license or copyright; see http://www.asme.org/terms/Terms_Use.cfm

APPENDIX

Coordinates for VD 20 and VD 21 blades (stagger angle $\lambda = 30$ deg, space-chord ratio $s/c = 1.0$)

VD 20				VD 21			
Suction side		Pressure side		Suction side		Pressure side	
x_u/c	y_u/c	x_l/c	y_l/c	x_u/c	y_u/c	x_l/c	y_l/c
-0.50098	0	-0.50098	0	-0.50312	0	-0.50312	0
-0.49443	0.00686	-0.49223	-0.00353	-0.50045	0.01288	-0.49047	-0.00226
-0.47230	0.01567	-0.46895	-0.00370	-0.48034	0.03456	-0.46498	0.00108
-0.43536	0.02476	-0.43190	-0.00175	-0.44117	0.05541	-0.42950	0.00497
-0.38516	0.03352	-0.38188	0.00085	-0.38654	0.06677	-0.38280	0.00726
-0.32348	0.04239	-0.32015	0.00326	-0.32183	0.06769	-0.32290	0.00812
-0.25210	0.05169	-0.24862	0.00540	-0.24944	0.06248	-0.25152	0.00883
-0.17286	0.06050	-0.16971	0.00729	-0.17021	0.05555	-0.17222	0.00930
-0.08795	0.06699	-0.08600	0.00871	-0.08577	0.04877	-0.08803	0.00785
-0.00009	0.06959	0.00009	0.00929	0.00128	0.04192	-0.00128	0.00391
0.08774	0.06796	0.08622	0.00886	0.08801	0.03448	0.08575	-0.00039
0.17269	0.06281	0.16992	0.00768	0.17177	0.02655	0.17040	-0.00206
0.25221	0.05495	0.24861	0.00572	0.25037	0.01863	0.24975	-0.00041
0.32389	0.04497	0.31984	0.00356	0.32157	0.01134	0.32127	0.00234
0.38550	0.03355	0.38152	0.00136	0.38307	0.00544	0.38298	0.00351
0.43511	0.02196	0.43182	-0.00055	0.43299	0.00171	0.43303	0.00253
0.47132	0.01184	0.46913	-0.00176	0.46984	0.00021	0.46986	0.00092
0.49325	0.00443	0.49221	-0.00178	0.49240	0.00001	0.49240	0.00009

Note. The origin of the Cartesian coordinate system x, y is at the blade midchord position.

Downloaded 01 Jun 2010 to 171.66.16.57. Redistribution subject to ASME license or copyright; see http://www.asme.org/terms/Terms_Use.cfm

The Use of Surface Static Pressure Data as a Diagnostic Tool in Multistage Compressor Development

H. D. Weingold
Senior Research Engineer.

R. F. Behlke
Project Engineer.

Engineering Division,
Pratt & Whitney,
United Technologies Corporation,
East Hartford, CT 06108

A technique has been developed to analyze static pressure distributions obtained from the surfaces of stators in a multistage compressor to determine incident Mach number and flow angle and the turning and streamtube contraction for the individual stator sections. This data analysis technique permits this nonintrusive type of pressure measurement to be used to optimize the design of stator airfoils during the development phase of a multistage compressor and, in the development of analytic compressor representations, to segregate rotor and stator performance and to improve the modeling of endwall blockage. The value of this technique has been demonstrated in cascade testing of compressor airfoils, in single-stage and three-stage rig testing, and in engine testing.

Introduction

A technique is presented which permits the use of nonintrusive instrumentation to provide data with which to determine, to an improved level of certainty, the flowfield present in multistage compressor blade rows. Standard instrumentation used in development testing of such compressors, stator leading edge total temperature and total pressure sensors and wall casing static pressure taps, do not provide sufficient information to establish uniquely the flowfields present. Usually, an axisymmetric throughflow analysis is used to model the flowfield, using the available data, and employing empirical assumptions to provide uniqueness. These assumptions include the loss split between rotors and stators, the deviation in turning for each blade row, and the blockage growth through the compressor.

The information derived from this analysis is the radial distribution of flow properties at the inlet and exit of each blade row, including Mach number, flow angle, and blockage. The last two are determined by the empirical assumptions made, i.e., the data do not uniquely distinguish between blockage and deviation. The flowfield model is employed to determine how each airfoil is performing, i.e., where it is located in its loss bucket, what its incidence range to surge is, and what its loss and deviation are. This informaton is used to modify the compressor, during development, to improve performance by restaggering stators or by compressor redesign. The effectiveness of this process can be improved if higher certainty is provided for the flow angles and Mach numbers incident upon the stator rows.

Earlier attempts to provide an improved flowfield description relied on intrusive measurements obtained with traversing probes or pole rakes inserted between leading and trailing edges of adjacent blade rows. Although these probes provided a means of measuring flow angle and rotor inlet total conditions, they tended to backpressure upstream blade rows in closely spaced compressors, influencing significantly in a complex pattern of pressure and temperature distortions the flow variables being measured [1]. Alternatively, nonintrusive optical measurements employing laser velocimetry can be used to measure flowfield properties, but require significant steady-state running at each operating condition to acquire the needed data. What is needed is a nonintrusive measurement that can acquire flowfield data for all stages in the time commensurate with a normal data scan of pneumatic and thermocouple instrumentation.

The technique described below uses the static pressure distribution of the stator itself, measured using distributions of surface static pressure taps, to determine the flow conditions incident upon it. A technique has been developed to rapidly analyze static pressure data to determine incident Mach number, incidence angle, exit angle, and streamtube contraction through the stator section. The technique employs a rapid transonic potential flow analysis, combined with an optimization technique, to determine the inlet and exit variables which provide a best analytical match to the experimental static pressure data. The technique has been validated using analytical distributions, cascade tunnel data, single-stage and three-stage rig data, and is being employed currently in the development of multistage compressors. Subsequent discussion will describe the methods used in the data analysis, the number and location selection for static taps, the relative uniqueness of the solution, the verification of the technique, and the utilization of the procedure in

Contributed by the Gas Turbine Division of THE AMERICAN SOCIETY OF MECHANICAL ENGINEERS and presented at the 31st International Gas Turbine Conference and Exhibit, Düsseldorf, Federal Republic of Germany, June 8–12, 1986. Manuscript received at ASME Headquarters December 13, 1985. Paper No. 86-GT-3.

Copyright © 1987 by ASME

Downloaded 01 Jun 2010 to 171.66.16.57. Redistribution subject to ASME license or copyright; see http://www.asme.org/terms/Terms_Use.cfm

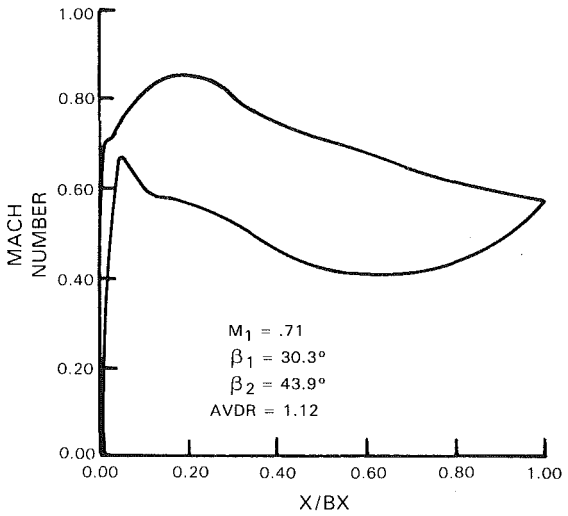

Fig. 1 Baseline Mach number distribution for cascade D

multistage compressor development and in the development of improved endwall loss and turning modeling for multistage compressors.

Analysis Technique

Airfoils With Attached Boundary Layers. One of the assumptions used in multistage compressor design is that, despite the three dimensionality of the flow field, airfoil sections can be designed using modified strip theory. This assumption permits the use of cascade data and infinite cascade analysis in the design, providing that proper modifications are made to account for streamtube contraction, streamtube radius change, and rotation effects. The transonic cascade analysis developed by Caspar et al. [2] is a finite area potential flow analysis which is extremely fast, lending itself to use in a data-matching iteration in the current analysis. This technique has been proven accurate and effective in the design of transonic compressor airfoils, which have verified their design pressure distributions in cascade and rotating rig testing [3]. When used in conjunction with a laminar/transitional boundary layer analysis [4] and wake mixing and base pressure corrections, this analysis is capable of predicting cascade performance (loss and turning) for airfoils with attached or slightly separated boundary layers. Data to be presented subsequently will verify that the assumption of modified strip theory is relatively good over a surprisingly large portion of the span in a multistage compressor.

In the current analysis, the Caspar analysis is used iteratively to match static pressure distributions measured on the surfaces of stators in a multistage compressor, using the total pressure and temperature measured with stator leading edge instrumentation. In addition to the upstream total conditions, the normal aerodynamic input to the Caspar analysis includes the upstream Mach number, inlet angle, exit angle, and streamtube contraction (AVDR—axial velocity density ratio). The exit angle can be replaced by a Kutta condition, imposed by requiring closure of the Mach number distribution at the trailing edge. In the current analysis, the above variables M_1, β_1, β_2, and AVDR are varied iteratively until a direct analysis of the static pressure distribution using the Caspar program best matches the measured static pressure distribution. This best match can be achieved automatically, using an optimization procedure, or manually by an engineer at a terminal, interactively varying the input to the program until graphical displays of analytical results and measured data achieve a reasonable correspondence. In the optimization procedure, the Kutta condition may be imposed indirectly by requiring a match to trailing edge static pressure data on both suction and pressure surfaces near the trailing edge, or directly by imposing a trailing edge Mach number closure requirement during optimization.

The automated matching procedure utilizes the COPES-CONMIN controlled optimization and minimization techniques developed by Masden and Vanderplaats [5, 6]. The ranges of the variables M_1, β_1, β_2, and ADVR are specified and each static pressure is identified with either the suction or pressure surface. The COPES-CONMIN optimization program minimizes the sum of the absolute differences between the measured and calculated static pressures. The option exists to weigh some static pressures more heavily than others. A preliminary search of the variable field has been found useful to find an effective initial guess for the optimization procedure. A typical automatic matching could require about ten iterations, each requiring seven evaluations of the static pressure distribution using the Caspar program. The total CPU time required, including an initial search, is on the order of 5 min on the IBM 3081.

In contrast, an engineer, manually iterating to a graphically equivalent best match, can achieve nearly equivalent results in far fewer function evaluations, with little loss in accuracy of the final set of aerodynamic variables. Therefore, the mode of operation depends on the volume of data to be analyzed and the speed with which the final results are desired. The procedure can be exercised manually on line during compressor testing to provide guidance in stagger optimization.

The accuracy of the procedure depends on the related questions of the uniqueness of the solution and the choice of location for the static taps. Because of the small size of compressor airfoils, the number of static taps possible is quite limited. In order to eliminate or reduce the effects of nonaxisymmetry in the compressor, it is desirable to place all static taps on one airfoil or, at worst, on two adjacent airfoils spanning one gap.

Nomenclature

AVDR = axial velocity density ratio or inlet to exit streamtube height ratio = $(\rho_2 C_{X2}/\rho_1 \cdot C_{X1}) = H_1/H_2$
C = velocity in absolute frame of reference
H = streamtube height
M = Mach number
P = pressure
R = radius
T = temperature
U = wheel speed at R
V = velocity
W = velocity in rotating frame of reference
X/BX = fraction of axial chord
Z = loss parameter $= \Delta P_T/(\frac{1}{2}\rho V^2)$
α = flow angle in absolute frame of reference (measured from tangential direction)
β = flow angle in rotating frame of reference (measured from tangential direction)
ρ = density
ω = rotational speed

Subscripts

For cascades
1 = inlet plane
2 = exit plane

For compressors
1 = rotor inlet station
2 = stator inlet station
3 = stator exit station
A = absolute frame of reference
R = rotating frame of reference
S = static
T = total
U = tangential direction
X = axial direction

Downloaded 01 Jun 2010 to 171.66.16.57. Redistribution subject to ASME license or copyright; see http://www.asme.org/terms/Terms_Use.cfm

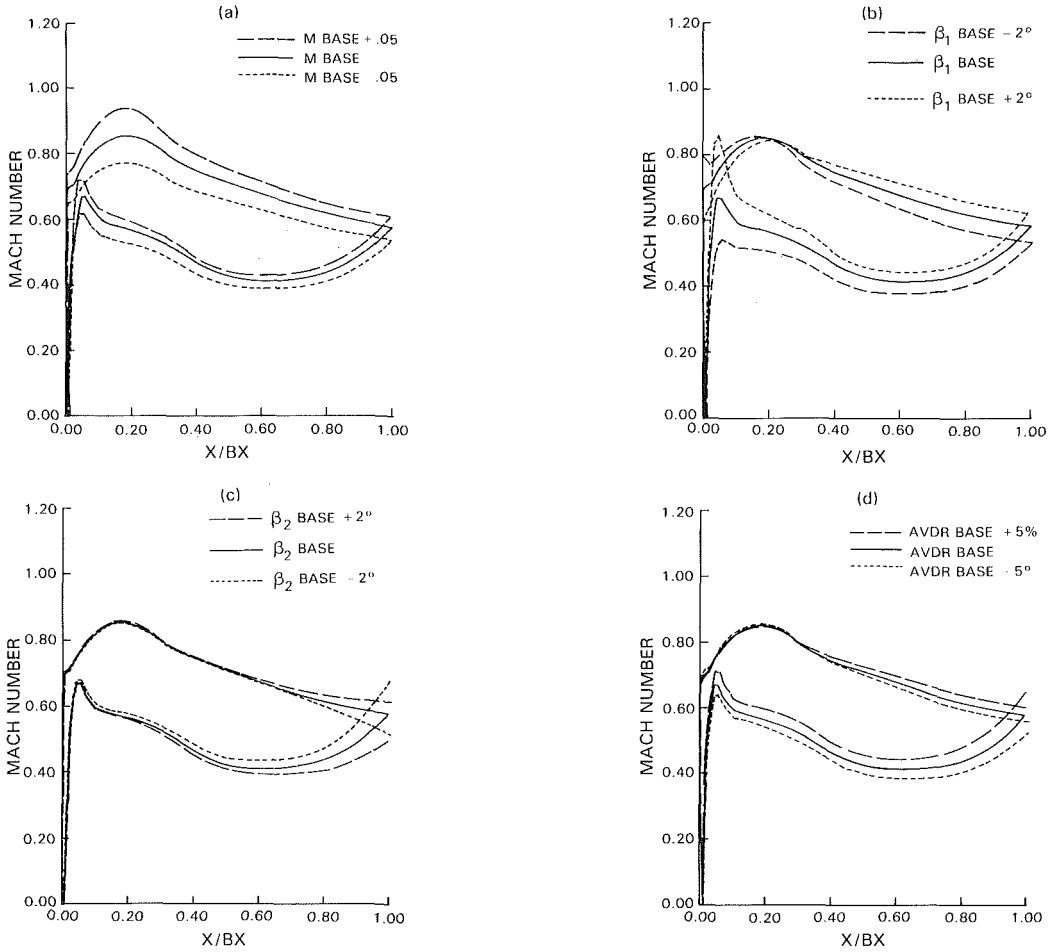

Fig. 2 Effects of individually varying (*a*) Mach number, (*b*) inlet angle, (*c*) exit angle, and (*d*) ADVR for cascade D

Thus it is necessary to carefully select the location of a limited number of static taps to provide the best chance of uniquely and accurately determining the aerodynamic variables.

Initially, the procedure was shown to accurately regenerate a set of input aerodynamic variables, when asked to match, using a large number of static pressure locations, a pressure distribution previously generated using the Caspar analysis. Then, smaller distributions of points were used to determine how the accuracy of the solution was affected by the number and distribution of static taps. It was found that a small number of strategically located taps would provide a good match to the known aerodynamic variables. This process also led to the method of choosing static tap locations for test data acquisition. In this and subsequent discussions, an adequate or good match is defined to be within 0.2 deg in flow angle, 0.005 in Mach number, and 0.005 in AVDR.

The initial step in the selection of static tap locations for an airfoil section to be tested is to perform a set of aerodynamic analyses for the section, varying the aerodynamic design variables independently over a range centering on their design values. Figure 1 illustrates a baseline Mach number distribution for Controlled Diffusion Airfoil cascade D, the performance of which was described in [3]. Figures 2(*a-d*) illustrate the effect on the calculated Mach number distribution as each of the variables M_1, β_1, β_2, and AVDR is independently varied.

As can be seen in Fig. 2(*a*), the principal effect of varying the upstream Mach number is to raise and lower the Mach number distribution nearly uniformly from leading edge to trailing edge. The effect of varying the inlet angle β_1, illustrated in Fig. 2(*b*), is to open or close the Mach number distribution in the forward portion of the airfoil, as the overspeed shifts from suction surface to pressure surface, while raising or lowering the Mach number distribution near the trailing edge. The result is that the suction surface Mach number distribution tends to rock about a stationary point, in this case near 20 percent axial chord. Thus, one might locate a static tap at this point mainly to determine Mach number since it is insensitive to inlet angle, while locating points on either side of it, say at 5 percent and 40 percent axial chord, to determine inlet angle.

Similarly, the effect of varying exit angle β_2, illustrated in Fig. 2(*c*), is to open or close the Mach number distribution over the rear portion of the airfoil. The effect of varying streamtube contraction AVDR, illustrated in Fig. 2(*d*), is to raise and lower the Mach number distributions of both suction and pressure surfaces approaching the trailing edge. Thus, static taps opposed to each other near the rear of the airfoil will tend to indicate exit angle by their difference and AVDR by their level. Because of the differing effects on the Mach number distribution of variations in each of the independent

Table 1 Cascade D aerodynamic parameters

	Design	Matched
Inlet Mach number, M_1	0.7110	0.7109
Inlet angle, β_1	30.3400 deg	30.4251 deg
Exit angle, β_2	43.8921 deg	43.8044 deg
AVDR	1.1218	1.1167

Downloaded 01 Jun 2010 to 171.66.16.57. Redistribution subject to ASME license or copyright; see http://www.asme.org/terms/Terms_Use.cfm

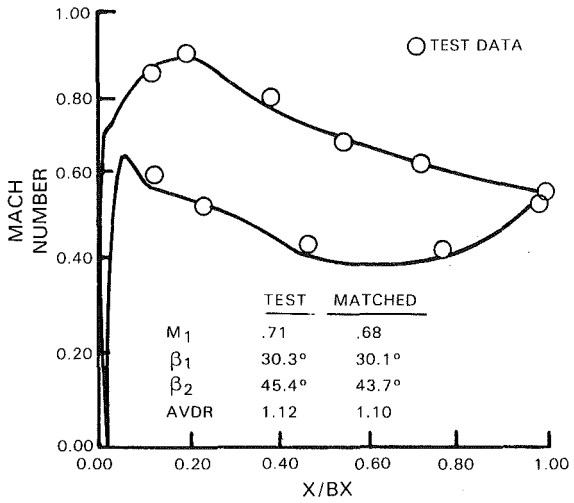

Fig. 3 Analytical match of cascade D static pressure data at a near-design condition

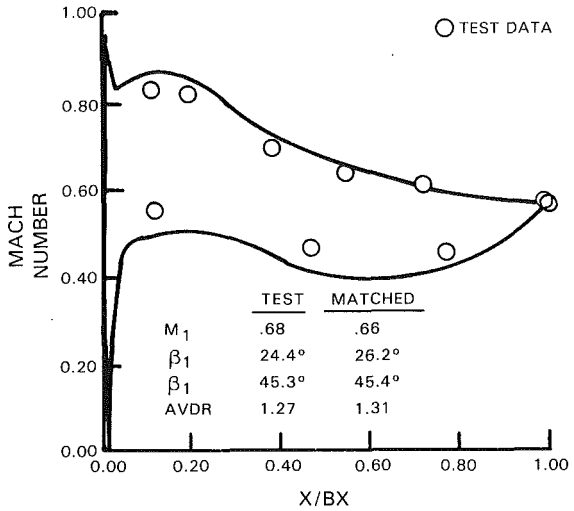

Fig. 4 Analytical match of cascade D static pressure data at a high-loss off-design condition

aerodynamic variables, a limited number of carefully chosen static taps can, in combination, uniquely determine the cascade aerodynamics. For most cases, five static taps on each surface are sufficient.

In the test of cascade D, ten static taps were used, six on the suction surface and four on the pressure surface of the airfoil. Table 1 illustrates the accuracy with which the procedure is capable of regenerating the design aerodynamic variables when asked to match static pressures interpolated to these ten locations from the analytic pressure distribution.

The ability to match static pressure data, using this technique, is illustrated in Fig. 3. The data were acquired in the United Technologies Research Center High Speed Cascade Tunnel at conditions close to the aerodynamic design condition for cascade D. For this low-loss, nonseparated airfoil, the procedure is able to closely match the experimental Mach number distribution. The remaining differences are probably due to the use of a linear distribution of streamtube contraction through the cascade in the analysis, while the physical distribution of AVDR may in reality be nonlinear. Table 2 illustrates the differences between the analytical values of the aerodynamic variables, necessary to match the static pressure distribution, and the values obtained from standard instrumentation located one chord length upstream and downstream of the cascade leading and trailing edges. This

Table 2 Cascade D data matched aerodynamic parameters

	Cascade data	Matched
Inlet Mach number, M_1	0.71	0.68
Inlet angle, β_1	30.3	30.1
Exit angle, β_2	45.4	43.7
AVDR	1.12	1.10

case illustrates that, even in the controlled environment of a cascade tunnel, the aerodynamic conditions incident upon the airfoil may differ from the measured values due to changes in endwall and top and bottom wall blockages from the instrumentation planes to the cascade edges, and due to the quality of the periodicity obtained in the finite linear cascade tunnel, using a limited number of physical controls. This effect was also observed in testing in the DFVLR transonic cascade tunnel, as reported by Stephens and Hobbs [7].

Analysis Technique for Airfoils With Separated Boundary Layers. The ability of an inviscid analysis to accurately match an experimental static pressure distribution depends on the magnitude of the viscous turning deviation. Since the force on the airfoil must correspond to the momentum change of the air, the area enclosed by the static pressure distribution is determined by the changes in the freestream aerodynamic variables from inlet to exit planes. For an airfoil with attached boundary layers, where viscous deviation is small, the inviscid force-momentum balance closely matches the physical force-momentum balance, permitting the inviscid analysis to closely match the experimental static pressure distribution. However, when significant boundary layer separation is present, the viscous turning deviation becomes significant. Since there is no mechanism in the inviscid analysis to introduce this deviation, the inviscid force-momentum balance cannot match that of the physical viscous flow. In this case, the application of the current technique results in a poor match to the experimental static pressure distribution, with the area of the experimental distribution being smaller than that of the analytical distribution due to the viscous reduction in lift. This is illustrated in Fig. 4 for cascade D at an off-design condition.

Thus, the first information gained by this analysis is that the airfoil may be separated. This is not always evident from the static pressure distribution since the classical flat pressure distribution for a separated region is often not evident in cascade or compressor airfoils. To better evaluate this situation, a boundary layer analysis is used, fitting a pressure distribution to the suction side static pressure data. This fitting can be done using the matching procedure for suction surface static pressure data only. Analysis of the boundary layer development on the suction surface is conducted using a modification of the McNally laminar/turbulent boundary layer program described in [4]. For most cases where the matching procedure fails to approximate the overall experimental static pressure distribution, the boundary layer analysis will show that separation is present.

It is not possible, using this technique, to determine accurately the aerodynamic variables for a separated airfoil. However, examination of the shape of the static pressure distribution, comparison to the design pressure distribution, and comparisons to separate matches of the suction and pressure surface static pressures can yield insight into the causes of the separation.

Application of the Technique to Multistage Compressor Development

In the development of multistage compressors, there are several areas where this technique can be applied as a supplement to traditional analysis methods to improve the understanding of the internal aerodynamics and facilitate the development process.

Downloaded 01 Jun 2010 to 171.66.16.57. Redistribution subject to ASME license or copyright; see http://www.asme.org/terms/Terms_Use.cfm

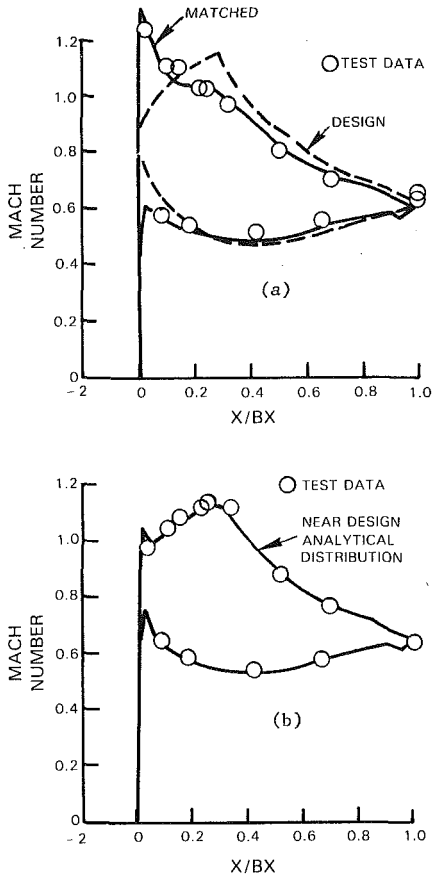

Fig. 5 Static pressure data for a low aspect ratio front stage Controlled Diffusion Stator 47 percent span section: (*a*) design flow, (*b*) high flow

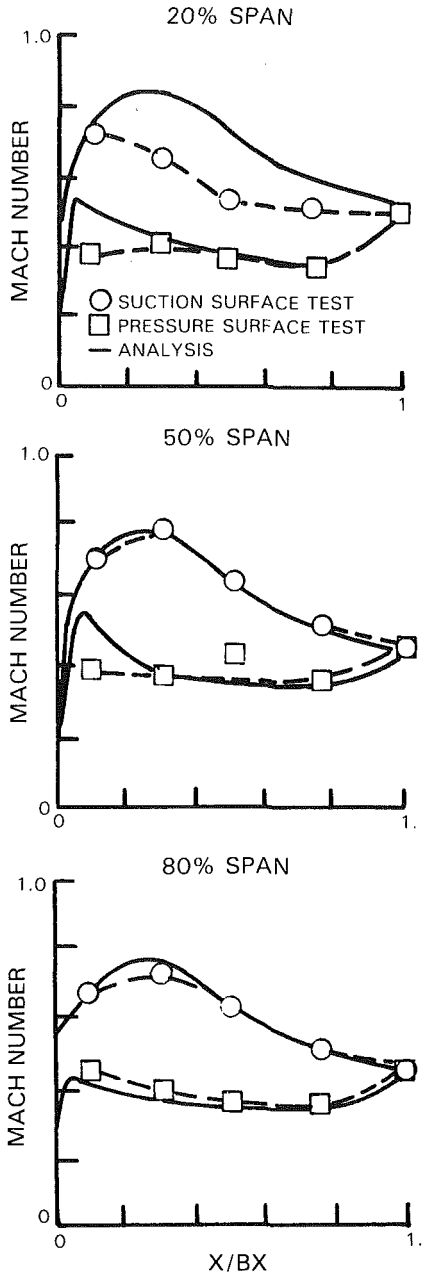

Fig. 6 Static pressure data for stator 2 of a three-stage research compressor

The simplest application is during the optimization of compressor performance using variable or adjustable stators. Traditional approaches to this task require the use of casing static pressures and stator leading edge instrumentation to construct stage characteristics, based on extensive testing of the compressor for a variety of stagger settings. Analysis of the stage characteristics ultimately leads to a selection of a set of stagger settings to optimize the compressor for efficiency and stability. Alternatively, a statistical approach can be used to analyze the trends in performance obtained from testing of a selected matrix of stagger settings, and an optimum set of settings deduced. Both approaches are expensive and time consuming and are not really based on an understanding of the compressor internal aerodynamics.

The examination of data obtained from rows of static pressure taps at several spanwise locations for each of the variable stators permits more insight into the stator aerodynamics for use in the optimization of stagger settings. Static pressure distributions can be examined "on line" and a manual matching used to determine incidence distributions for each stator. The aerodynamic effects of changes in stagger setting can be observed directly, and stators set to optimize stage performance.

This procedure was used during test of a low aspect ratio front stage Controlled Diffusion Airfoil stator, under Contract No. NAS3-22008 [8]. Rows of static pressure taps were installed at 16 and 47 percent span on the stator and data acquired at design stagger and at plus and minus 2 deg stagger. Analysis of the data indicated that, at the design stagger setting, the stator was operating at 2.25 deg of positive incidence and at higher AVDR than design intent (Fig. 5*a*). By restaggering the stator closed 2 deg, it was placed at a near-minimum loss incidence, with its static pressure distribution nearly matching design. This same effect is observed at the design stagger for a higher flow test point at design speed, where the incidence angle has decreased by 2.25 deg. At this condition, the static pressure distribution is near design (Fig. 5*b*).

A second application of this technique is to evaluate the operation of fixed stators relative to design intent. Data acquired at design speed on the compressor operating line can be compared to design pressure distributions to determine whether stators are operating at stalled or choked incidences or have significant regions of boundary layer separation. This type of evaluation can identify major design problems emanating from poor upstream blade row performance, radial mismatching between rotor and stator, or stator design problems. For example, data acquired in a highly loaded three-stage research compressor (Fig. 6) indicate that the second stator is operating close to design intent from midspan to the tip, but that severe boundary layer separation is present at 20 percent span. Analysis indicated that this section is operating at high incidence due to higher than anticipated root

Downloaded 01 Jun 2010 to 171.66.16.57. Redistribution subject to ASME license or copyright; see http://www.asme.org/terms/Terms_Use.cfm

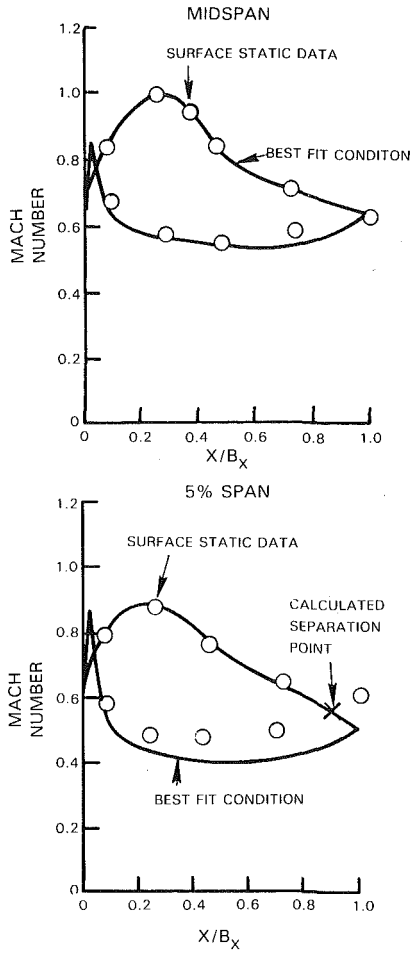

Fig. 7 Static pressure data for stator 2 of a four-stage low-pressure compressor

losses and lower root turning in upstream blade rows. In contrast, data acquired during engine testing of a four-stage low-pressure compressor indicate that over much of the span stator 2 achieved its Controlled Diffusion Airfoil pressure distribution, and even at 5 percent span, only a minor boundary layer separation is present at 90 percent chord (Fig. 7).

A third application of this technique is in the development of a model of a multistage compressor's internal aerodynamics, using leading edge probe data and casing static pressure data. This model is needed to assess the performance of the compressor's rotors and stators independently, for use in the development process and to assess the compressor's stage matching. Stator leading edge kiel probes, measuring total pressure and temperature, and casing static pressure taps (Fig. 8) provide data used to define stator–rotor stage characteristics, used to assess stage performance relative to design intent. However, this information is insufficient to uniquely define the rotor and stator performance individually. To do this, a throughflow analysis, solving the continuity, radial equilibrium, and energy equations, is used to deduce the internal aerodynamic variables. This analysis is used to match the leading edge and casing pressure and temperature data by assuming loss splits between rotors and stators and by varying distributions of blockage. The results of this analysis include distributions of flow angle and Mach number at the leading and trailing edges of all blade rows, and the total pressures at the rotor exit planes.

Acquisition of stator surface static pressure data permits a less arbitrary alternative procedure to deduce the compressor internal aereodynamics, more closely founded in the test results. The analytical procedure is used to match the stator

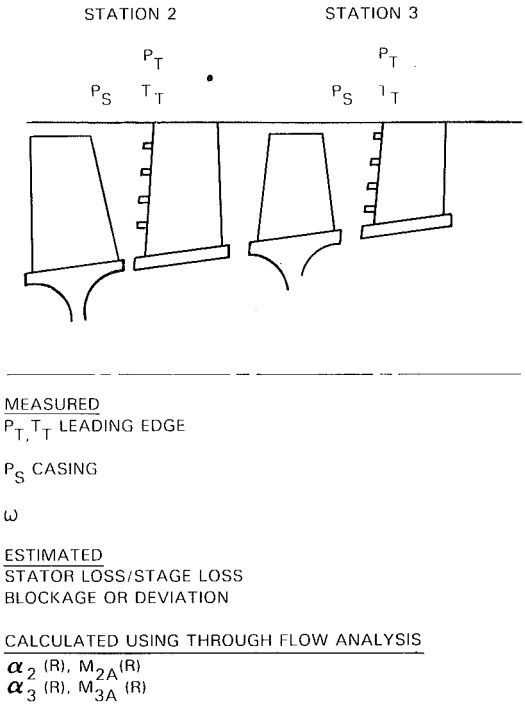

Fig. 8 Standard compressor stage data are used in a throughflow analysis to determine the compressor internal aerodynamics

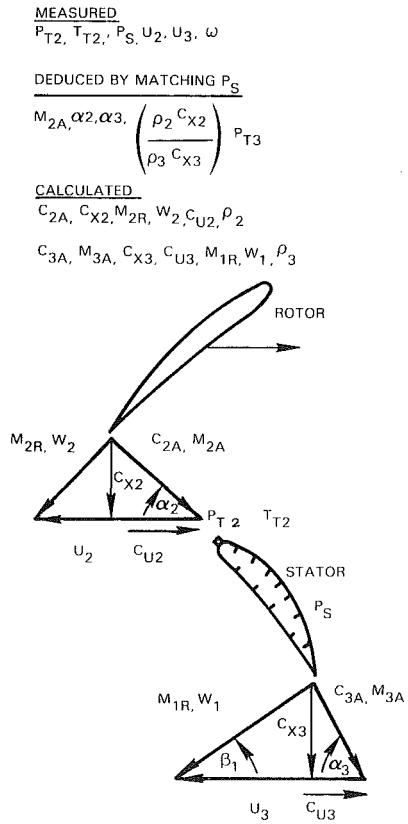

Fig. 9 Stator static pressure data can be used in a throughflow analysis to determine the compressor internal aerodynamics

static pressure data in order to deduce the stator inlet angle and Mach number, exit angle, and the streamtube contraction. The boundary layer analysis, wake mixing, and base pressure calculations are used to estimate the stator loss. Loss is calculated using a modification of the analysis of Stewart [9], which relates the downstream loss to the trailing edge

Downloaded 01 Jun 2010 to 171.66.16.57. Redistribution subject to ASME license or copyright; see http://www.asme.org/terms/Terms_Use.cfm

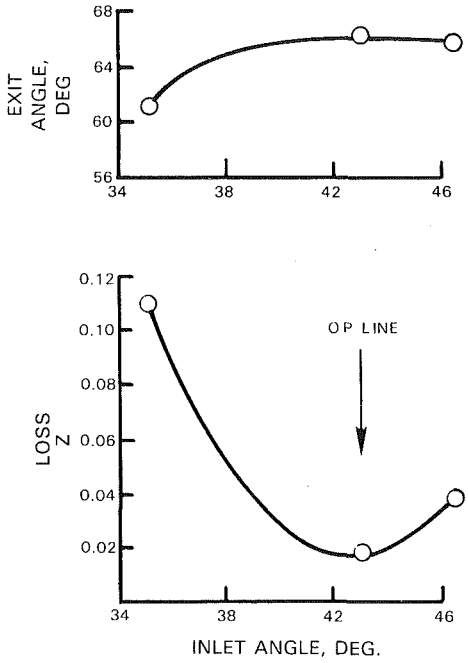

Fig. 10 Loss and turning characteristics for the 20 percent span section of stator 2 of a three-stage research compressor, as deduced by matching static pressure data

boundary layer characteristics. This procedure includes a base pressure loss correlation for thick trailing edges. Using the leading edge total pressure and temperature data, the deduced quantities can be used to completely define the stage velocity triangles (Fig. 9). Some of these quantities are redundant to those determined by the energy or continuity equations, providing an opportunity for corroboration of the analysis or an evaluation of the data accuracy. An example of this redundancy can be seen in the rotor discharge/stator inlet velocity triangle of Fig. 9, in which the swirl component C_{U2} can be defined both by the static pressure deduced stator inlet angle and Mach number and by the energy equation applied to the rotor, using the measured total temperatures.

In reconciling any differences between the internal aerodynamics deduced from theses two approaches, consideration must be given to the uncertainties in the temperature and pressure measurements, the quality of the stator surface static pressure matching, and the differences between the streamtube contractions across the stators used in the throughflow analysis and that deduced in the matching procedure. The effects of mixing must be considered as well in transferring quantities from blade row trailing edges to the following leading edges. In this highly complex reconstruction of the compressor internal aerodynamic flow field, attempting to satisfy simultaneously the throughflow analysis and the stator static pressure data, engineering judgment is still a very necessary ingredient. The input provided by the stator surface static pressure data brings this modeling procedure one step closer to the physical reality. Use of this procedure for a variety of configurations has led to improved understanding of the endwall blockage and loss development in multistage compressors and of the effectiveness of blading in the endwall region. This has resulted in improved compressor design procedures, modeling the endwall aerodynamics, and improving techniques for the full span design of compressor blading [10].

Finally, the procedure can be used to assess the compressor's off-design matching. The stator surface pressure data, acquired at several compressor test conditions in fixed stator testing, can be processed to provide stator loss and turning characteristics as a function of inlet angle for each speed line. Since the stage characteristics are also available, this permits the deduction of the rotor characteristics. Analysis of the rotor and stator characteristics can provide the designer with information needed to rematch the compressor to optimize performance or satisfy some off-design performance requirement.

For example, the current analysis was used to deduce the loss and turning of the 20 percent span section of the second stator of a three-stage research compressor, at design speed, as functions of inlet angle (Fig. 10). It can be seen that the stator minimum loss and maximum turning angle are near the compressor operating line incidence angle, indicating that this stator section was well matched. The wide incidence range of this stator could be used to modify the compressor to suit some off-design requirement, without significant increase in loss or deviation, thus not compromising design point performance.

Conclusions

The analysis of stator surface static pressure data has been shown to be a useful supplement to standard compressor instrumentation in the development process for multistage compressors. In particular, this analysis has been shown to assist in the optimization of compressor performance using variable stators, in the evaluation of compressor stator row performance relative to design intent, in the development of models of the compressor aerodynamic flow field, and in the assessment of off-design matching of rotor and stator rows. In all these applications, analysis of the stator surface static pressure data provides an improved understanding of the detailed aerodynamics, permitting a higher level of certainty in the conclusions reached. An analytical matching procedure has been developed which permits a formalized approach to the analysis of static pressure data to deduce the inlet and exit aerodynamic variables.

References

1 Behlke, R. F., Brooky, J. D., and Canal, E., "Study of Blade Aspect Ratio on a Compressor Front Stage," NASA CR-159556, Nov. 1980.

2 Caspar, J. R., Hobbs, D. E., and Davis, R. L., "The Calculation of Two-Dimensional Compressible Potential Flow in Cascades Using Finite Area Techniques," *AIAA Journal*, Vol. 18, No. 1, Jan. 1980.

3 Hobbs, D. E., and Weingold, H. D., "Development of Controlled Diffusion Airfoils for Multistage Compressor Application," ASME JOURNAL ENGINEERING FOR GAS TURBINES AND POWER, Vol. 106, Apr. 1984, pp. 271-278.

4 McNally, W. D., "Fortran Program for Calculating Compressible Laminar and Turbulent Boundary Layers in Arbitrary Pressure Gradients,' NASA TND-5681, May 1970.

5 Masden, L. E., and Vanderplaats, G. N., "COPES—a Fortran Control Program for Engineering Synthesis," NPS 69-81-003, Mar. 1982.

6 Vanderplaats, G. N., "CONMIN—a Fortran Program for Constrained Function Minimization: Users Manual," NASA TMX-62282, Aug. 1973.

7 Stephens, H. E., and Hobbs, D. E., "Design and Performance Evaluation of Supercritical Airfoils for Axial Flow Compressors," Final Report Contract N00019-77-C-0546, Pratt & Whitney Report FR *11355*, Feb. 1979.

8 Behlke, R. F., Brooky, J. D., and Canal, E., "Study of Controlled Diffusion Stator Blading. II. Final Report," NASA CR-167995, Mar. 1983.

9 Stewart, W. L., "Analysis of Two-Dimensional Compressible Flow Loss Characteristics Downstream of Turbomachine Blade Rows in Terms of Basic Boundary Layer Characteristics," NACA TN3515, July 1955.

10 Behlke, R. F., "The Development of a Second Generation of Controlled Diffusion Airfoils for Multistage Compressors," ASME JOURNAL OF ENGINEERING FOR GAS TURBINES AND POWER (in press).

Downloaded 01 Jun 2010 to 171.66.16.57. Redistribution subject to ASME license or copyright; see http://www.asme.org/terms/Terms_Use.cfm

Aircraft Turbofan Noise

J. F. Groeneweg

E. J. Rice

National Aeronautics and Space Administration, Lewis Research Center, Cleveland, OH 44135

Recent advances in the understanding of turbofan noise generation and suppression in aircraft engines are reviewed with particular emphasis on NASA research. The review addresses each link in the chain of physical processes which connect unsteady flow interactions with fan blades to far field noise. Mechanism identification and description, duct propagation, radiation, and acoustic suppression are discussed. Recent advances in the experimental technique of fan inflow control assure that in-flight generation mechanisms are not masked by extraneous sources in static tests. Rotor blade surface pressure and wake velocity measurements aid the determination of the types and strengths of the generation mechanisms. Approaches to predicting or measuring acoustic mode content, optimizing treatment impedance to maximize attenuation, translating impedance into porous wall structure, and interpreting far field directivity patterns are illustrated by comparisons of analytical and experimental results. A persistent theme of the review is the interdependence of source and acoustic treatment design to minimize far field noise. Areas requiring further research are discussed and the relevance of aircraft turbofan results to quieting other turbomachinery installations is addressed.

Introduction

Over the past decade the noise generated by the fan component of aircraft turbofan engines has been the subject of vigorous research. The emphasis on the fan reflects the fact that, for the high-bypass engines which dominate the world fleet of large commercial transports, the fan controls flyover noise on landing approach and is a strong contributor along with jet noise on takeoff. Indeed, for the next generation of turbofan engines the prominent contribution of the fan to propulsion system noise is projected to continue. Figure 1 shows the results of a system noise prediction done as part of an energy efficient engine design study [1]. Component noise levels in terms of tone-corrected perceived noise decibels are given at takeoff and approach conditions. The fan controls the totals at both conditions even with the suppression provided by substantial use of acoustic treatment. Similar conclusions about the importance of fan noise have been drawn in other studies [2, 3]. The purpose of this paper is to review recent results of research on fan noise generation and suppression, and to identify significant gains and remaining gaps in our understanding and ability to predict and control this annoying source.

The scope of this review is limited to results drawn mainly from NASA-initiated work carried out in roughly the last five years. We believe that this definition of scope, relaxed and supplemented in specific areas, leads to a reasonably accurate picture of the state of the art while not attempting to exhaustively cover parallel efforts and results. Several existing reviews provide extensive bibliographies and summarize earlier results in turbomachinery noise [4], flight effects [5], and suppressors [6, 7]. Our review builds upon, but primarily extends and updates these earlier efforts to cover significant advances in experimental flight simulation techniques, diagnostic measurements, theoretical modeling, and computation.

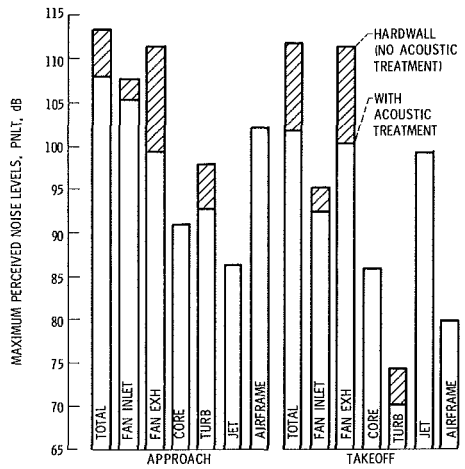

Fig. 1 Flyover component noise levels for an advanced turbofan [1]

The flow chart in Fig. 2 illustrates the chain of physical processes which links unsteady aerodyanamics of the fan flow field to the resultant far field acoustic signature. Elements in ovals are inputs to, or outputs of, the processes in the rectangles. The four processes – (*i*) blade unsteady aerodynamic response, (*ii*) coupling to the duct, (*iii*) propagation in the duct which may have acoustically treated walls, and (*iv*) acoustic coupling (radiation) to the far field – have each been studied and modeled separately as convenient subdivisions of the overall problem. A knowledge of the inputs and outputs – (*i*) unsteady flow field disturbances, (*ii*) blade surface pressure distributions, (*iii*) duct acoustic mode content at the entrance, and (*iv*) exit of the duct – is required to link the processes and arrive at the final output which is far field directivity (and spectra). Of course, from an experimental viewpoint, the in-

Contributed by the Gas Turbine Division for publication in the JOURNAL OF TURBOMACHINERY. Manuscript received at ASME Headquarters March 4, 1986. Paper No. 83-GT-197.

Copyright © 1987 by ASME

Downloaded 01 Jun 2010 to 171.66.16.57. Redistribution subject to ASME license or copyright; see http://www.asme.org/terms/Terms_Use.cfm

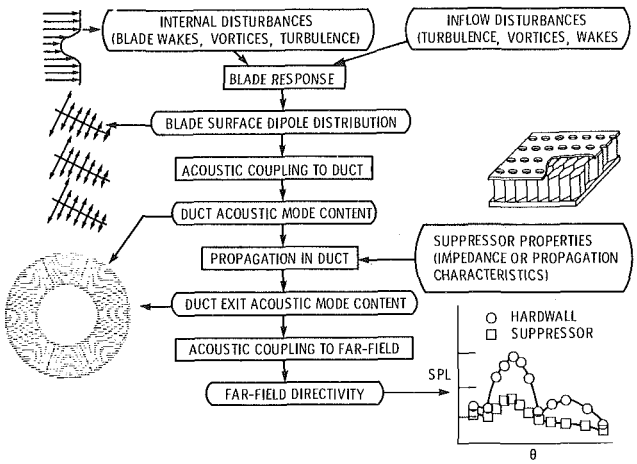

Fig. 2 Elements of fan noise generation and suppression

termediate inputs or outputs are often missing; only acoustic measurements in the far field are available. In fact, one of the greatest hindrances to applying the theories for the individual processes to practical situations has been the lack of definition of the key input/output quantities at the interfaces. Recent diagnostic measurements and analyses have begun to correct this deficiency. This review is organized around the elements of Fig. 2.

Generation Processes

Mechanism Identification. The primary input to the fan noise generation process at subsonic tip speeds is a description of the unsteady aerodynamic fluctuations encountered by a blade row. In spectral terms, random fluctuations produce broadband or narrowband (tonelike) random noise while periodic fluctuations produce tones at multiples of the blade passing frequency. At supersonic tip speeds the added phenomenon of multiple pure tones associated with rotor-locked leading edge shocks comes into play at multiples of shaft rotation frequency. The initial task of fan noise description is to identify the dominant mechanisms in terms of the origin of the responsible flow disturbance and the blade row with which it interacts. On the engine cross section in Fig. 3, some of the candidate turbofan mechanisms are labeled with flow disturbances grouped according to the blade row with which they interact. Sample narrowband spectra which identify the components associated with subsonic and supersonic tip speeds are also shown. Most progress has been made in understanding the generation of tones which usually dominate the spectrum levels; the relative importance of potential broadband generation mechanisms such as those associated with inlet boundary layer or wake turbulence remains vague.

Flow disturbances are divided into two categories in Fig. 2: those originating external to the engine but drawn into the inlet, and those originating inside the engine. While it has long been recognized that ingested external disturbances may control fan noise generation [8], it was the high-bypass engine flyover noise data, acquired in connection with noise certification requirements, which established that ground test tone levels were controlled by extraneous inflow disturbances unrepresentative of flight [5]. In fact, the practicality of the concept of choosing vane-blade ratio for cutoff [9, 10] to greatly reduce the fundamental tone was first demonstrated in rig tests [9], and later conclusively confirmed in flight and in wind tunnels as shown by the examples in Fig. 4.

Flight Simulation. The approach to controlling the inflow for flight simulation in static tests has evolved around the concept of inlet honeycomb – grid flow conditioners which must be acoustically transparent over the frequency range of interest. Figure 5 shows the range of inflow control devices

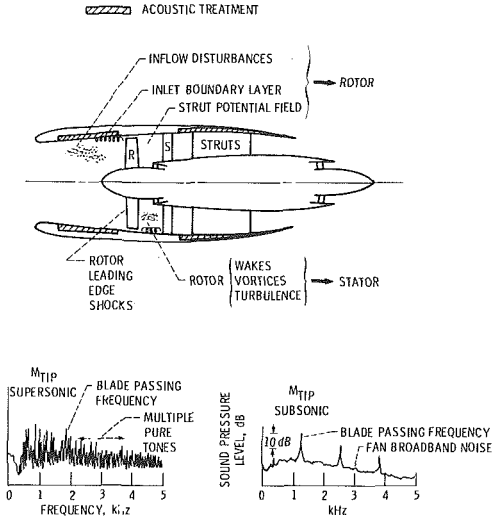

Fig. 3 Turbofan noise generation mechanisms and spectra

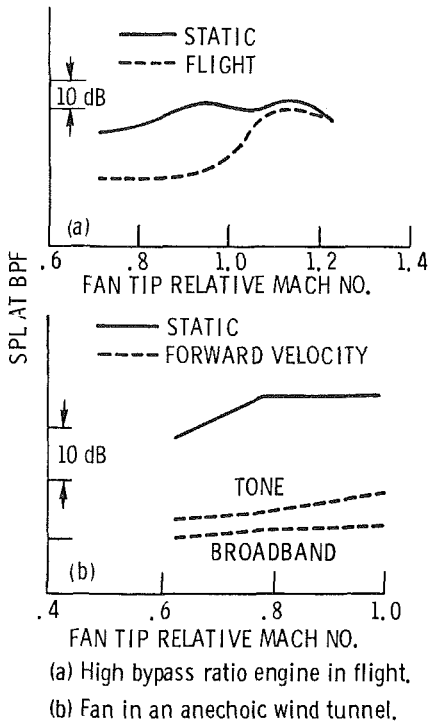

Fig. 4 Effect of forward velocity on the fan blade passing tone in the inlet duct [5]

(ICD's) investigated at NASA Lewis [11–14]. The sizes of the external devices, shown in Figs. 5(*a*) and (*b*), ranged from roughly 4 to 2 fan diameters. An induct honeycomb (Fig. 5*c*) was found to be aerodynamically effective but unacceptable from an acoustic transmission standpoint. The first generation design (Fig. 5*a*), drew on flow conditioning work for turbulence reduction [15] to arrive at the screen-honeycomb composite structure. The most recent version (Fig. 5*b*) is reduced in size, uses honeycomb only, and employs thinner support ribs with more carefully bonded joints and cleaner attachment to the inlet lip. The shape conforms to an equipotential surface.

Acoustic results for a JT15D engine in terms of fundamental blade passing tone and broadband directivities are shown in Fig. 6 for the two ICD's. Residual tone levels with inflow control approach the broadband over much of the angle range at these low fan speeds. Interestingly, the broadband levels remain essentially unchanged with inflow control indicating that

Downloaded 01 Jun 2010 to 171.66.16.57. Redistribution subject to ASME license or copyright; see http://www.asme.org/terms/Terms_Use.cfm

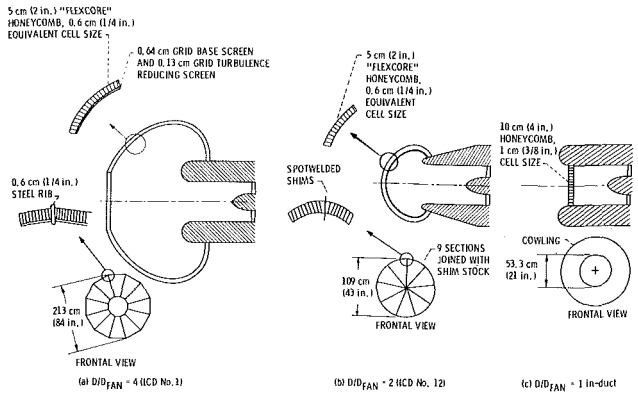

Fig. 5 Inflow control devices for flight fan noise simulation tested at Lewis Research Center [12]

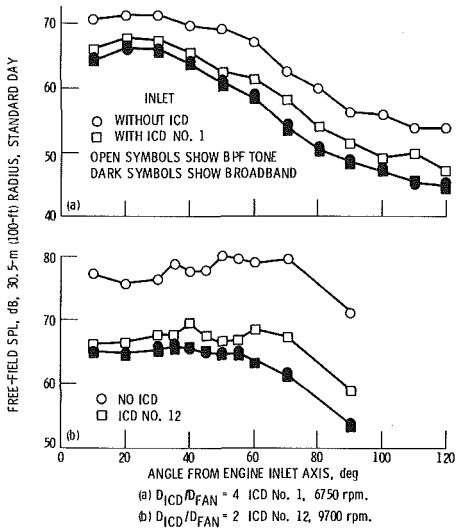

Fig. 6 Far-field directivity with inflow control devices in JT15D engine, $\Delta f = 25$ Hz [12]

another mechanism, probably internal to the fan, controls this spectral component. Tone levels for the two ICD's were generally comparable, but ICD 12 showed somewhat lower tone levels at forward angles. That feature, coupled with its smaller size, made it the design of choice [16].

Flight data from the JT15D on an OV-1 test-bed aircraft [14] confirm the effectiveness of the ICD of Fig. 5(*b*) as shown in Fig. 7. The fundamental tone directivity with inflow control agrees well with the flight data except at the most forward angles where the signal-to-noise ratio is low for flight.

Blade surface pressure measurements have proved to be a valuable diagnostic tool in evaluating the quality of inflow to the fan and, with inflow control, in determining the residual internal sources controlling flight levels. Miniature pressure transducers mounted near the fan blade leading and trailing edges at several spanwise locations are used in conjunction with a telemetry system [8, 12, 17] to continuously survey the circumferential variation of unsteady blade pressures. This technique originally identified longitudinally persistent, circumferentially localized disturbances attributed to atmospheric turbulence elongated by the streamtube contraction in the inflow [8]. Such disturbances, which may also be caused by ingested vortices, wakes, and instabilities associated with flow around the inlet lip, produce strong narrowband random tones.

Figure 8 compares narrowband blade pressure spectra without and with inflow control. Without an ICD, (Fig. 8*a*), the spectrum shows strong harmonic content at all multiples of shaft rotation frequency resulting from multiple encounters of the blade transducer with circumferentially varying flow

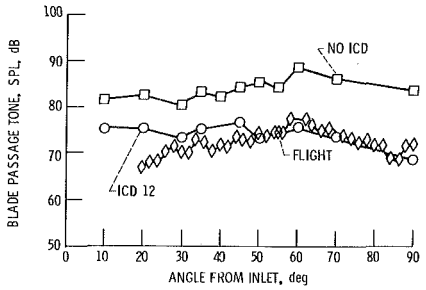

Fig. 7 Effectiveness of inflow control for flight fan tone simulation [14]

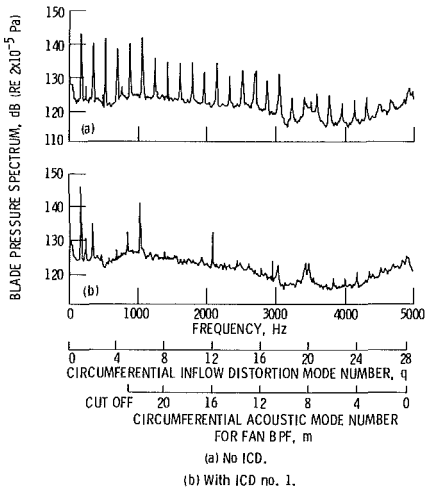

Fig. 8 Narrowband blade pressure spectra, pressure side transducer 1.9 cm from tip, JT15D engine, 10,500 rpm [12]

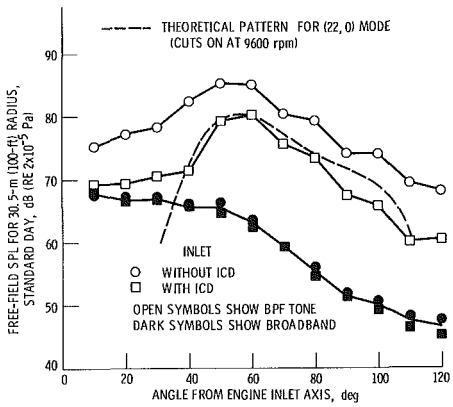

Fig. 9 Directivity pattern indicating presence of 22-lobed circumferential mode due to rotorstrut interaction, JT15D fan, 10,500 rpm [12]

disturbances. The additional scales on the abscissa are distortion number (multiple of shaft frequency) and the circumferential acoustic mode number corresponding to blade number minus distortion number. Inflow control eliminates the randomly varying disturbances and the corresponding bulk of the shaft harmonics as illustrated in Fig. 8(*b*). Those distortion numbers that remain are associated with periodic, internally generated flow disturbances which are fixed in space or have fixed rotation rates with respect to the rotor. As a result, clues to the mechanisms governing flight levels are found from the prominent residual peaks.

Substantial effort has also been applied to the inflow control problem by industry [17–24] including flyover level comparisons to static projections [23] and development of ICD design procedures [24]. The first generation of large engine ICD's, roughly 3 fan diameters in size, is currently in use. Although the quantitative agreement of inflow control and

Downloaded 01 Jun 2010 to 171.66.16.57. Redistribution subject to ASME license or copyright; see http://www.asme.org/terms/Terms_Use.cfm

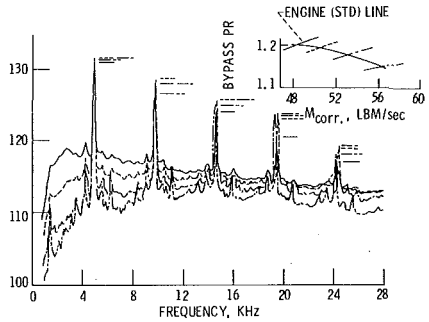

Fig. 10 Variation of broadband levels with fan operating point, JT15D fan in anechoic chamber, $\Delta f = 80$ Hz, 10,500 rpm

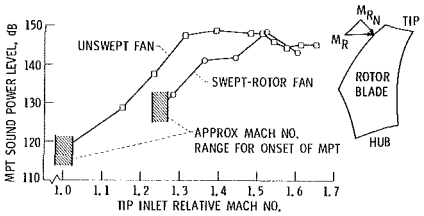

Fig. 11 Effect of rotor leading edge sweep on multiple pure tone generation [33]

flight data is still subject to some improvement, the current state of the art of static testing with inflow control does allow the study of bona fide internal sources controlling fan noise generation in flight. An alternative to ICD's is the anechoic wind tunnel [25, 27] which has also been found to eliminate the bulk of the extraneous inlet disturbances.

In-Flight Sources. Once the study of internal mechanisms is made possible by inflow control, the task becomes one of identifying the interactions responsible for the tone levels observed over the range of engine speeds. Rotor wake-stator interaction remains a prime mechanism, but even with the blade-vane ratio chosen to prevent fundamental tone propagation, other interactions may come into play. For example, the JT15D engine exhibits a strong fan fundamental tone which appears at a speed corresponding to the start of propagation of the 22-lobed acoustic mode as shown in Fig. 9 [12]. The source of the 22-lobed acoustic mode is the interaction between the 28 fan blades and the six structural support struts downstream of the fan stator. The blade pressure spectrum in Fig. 8(*b*) shows that a strong 6-per-revolution disturbance is sensed on the rotor. The strength of the rotor–strut interaction decreases with increased spacing between rotor and struts [28]. A prime candidate for the interaction mechanism is a strut potential field extending upstream through the stators and interacting with the rotor. An alternative explanation would be the interaction of residual rotor wakes with the six engine struts generating the 22-lobed spinning acoustic mode which is sensed on the rotor as a 6-per-revolution disturbance. Existing large high-bypass turbofans also contain downstream struts. Many of the next generation of engines will incorporate integral strut–stator vane assemblies with a potential for still more complicated interactions [29].

As mentioned earlier, the random disturbances responsible for broadband generation appear to be internal. Broadband levels vary strongly with fan operating point (rotor incidence angle or loading) as shown in Fig. 10. Fan blade suction surface flow separation and interaction with the trailing edge, blade tip interaction with the casing boundary layer, and rotor wake turbulence (midspan or tip) interaction with the stator are candidate mechanisms although the latter seems to be discounted by rotor-alone experiments [30].

While the multiple pure tone (MPT) generation mechanism is clearly associated with the rotor leading edge shocks and

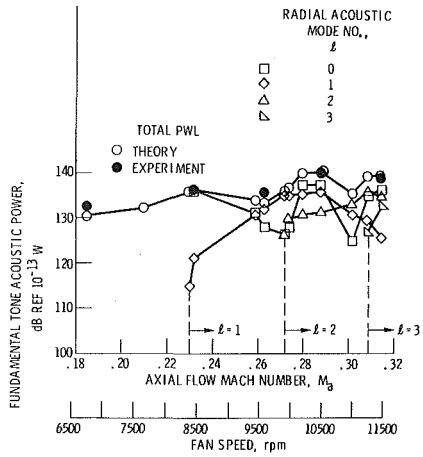

Fig. 12 Speed dependence of inlet fundamental tone modal power generated by 41 rod wakes interacting with a JT15D fan [43]

their blade-to-blade nonuniformity, quantitative descriptions of the source are lacking. Two aspects of the process have been investigated in connection with concepts to reduce this strong inlet source at takeoff fan speeds. First, a radical fan with compound leading edge sweep was designed to keep the normal component of blade inlet relative Mach number subsonic over the entire span [32]. Except for blade end effects and the sweep reversal point, a major portion of the strong leading edge shock system was expected to be eliminated. Figure 11 shows the measured MPT power results obtained with the swept design compared to a conventional, unswept fan [33]. Sweep delayed the onset of MPT's and reduced the levels over a large portion of the tip-speed range including takeoff. The second aspect of inlet noise generation at supersonic tip speeds concerned the observation that total tone power peaks beyond the transonic speed and then falls off. A fan designed for unusually high specific flow, 220 kg/s•m^2, at high tip speed, 553 m/s, exhibited a marked tone power decrease at design [34] although not qualitatively different from other high tip speed designs. The phenomenon appears to be only partially attributable to propagation inhibiting effects of elevated inlet Mach numbers and may be associated with nonlinear propagation characteristics in combination with the angle and associated strength variations of the leading edge shocks [35].

Mechanism Description

Ducted Cascade Response. Considerable effort has been expended within the last five years to model the noncompact compressible response of a ducted cascade of blades to unsteady upwash velocities. Perhaps the most complete description available is the three-dimensional lifting surface theory [36] for a rotating cascade in an annular duct. This blade response and duct coupling analysis is the heart of specialized studies of rotor-inflow distortion [37] and rotor–stator interaction [38]. These linear analyses are for the dipole-type sources at the surface of a cascade of thin (in some cases twisted) blades and represent exact solutions to the linearized continuity and momentum equations [39, Chap. 5].

Three features of these analyses are considered to be important advances. First, the three-dimensional approach makes possible the calculation of the circumferential and radial content of acoustic modes in annular or cylindrical ducts; the complete description of modal content is precisely the input required for successive propagation analyses. Second, cascade analysis predicts chordwise unsteady pressure distributions and integrated responses which differ substantially from single blade results [40, 41] that ignore blade-to-blade interactions (solidity) and the interblade phase angle of the disturbance. Third, source noncompactness, retained by calculating chord-

Downloaded 01 Jun 2010 to 171.66.16.57. Redistribution subject to ASME license or copyright; see http://www.asme.org/terms/Terms_Use.cfm

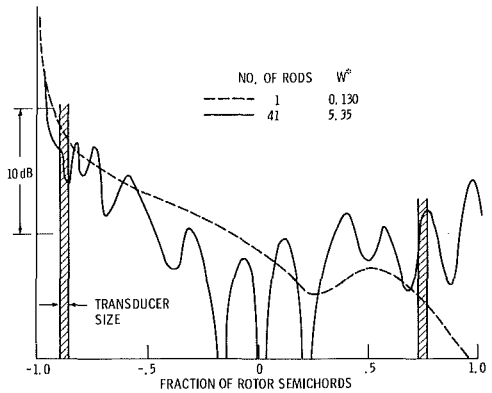

Fig. 13 Calculated chordwise variation of the fundamental component of rotor blade pressure generated by wakes from upstream rods

wise in addition to spanwise pressure fluctuations, has been shown to produce significant differences in calculated power compared to compact analyses. The magnitudes of the differences, which depend on incident disturbance shape and propagation direction with respect to the mean flow, are highest for single distortion modes [40]. For realistic distortion profiles represented by a combination of distortion modes, the effects of noncompactness are less dramatic with a tendency for the compact analysis to underestimate fundamental tone power for upstream propagation and overestimate the power propagating downstream [37].

Since full three-dimensional calculations are complex and lengthy, a quasi-three-dimensional analysis, which uses two-dimensional (strip) theory for aerodynamic response but annular duct acoustics for modal prediction, was investigated [37]. The results indicated that the quasi-three-dimensional approach produced relatively small errors in power, greatly reduced computation time, and fulfilled the requirement to predict annular duct acoustic modes. Consequently, the quasi-three-dimensional approach was adopted in the development of a computer program [42] which considered three types of flow disturbances: inlet turbulence, rotor mean wakes, and rotor wake turbulence. This quasi-three-dimensional approach is still being evaluated by data-theory comparisons.

The three-dimensional lifting surface tone power predictions have been compared to fan noise data [43] where the controlled source consisted of the fan interacting with an array of inlet distortion rod wakes. Figure 12 shows excellent agreement between the predicted total inlet fundamental tone power as a function of fan speed and the measured narrow-band tone power obtained from far-field measurements. Note the changing mix of radial mode contributions to the totals and the nonmonotonic increase with speed in both theory and data.

The intermediate quantity between blade response and duct coupling is blade pressure (Fig. 2). The cascade response portion of the code in [42] was used to calculate the chordwise magnitude of the unsteady blade pressures due to interaction with Gaussian wakes produced by upstream radial rods. As shown in Fig. 13, the high disturbance frequency associated with many (41) rod wakes is predicted to produce many rapid changes in pressure along the chord. Typical miniature transducer sizes are indicated near the leading and trailing edges. For high disturbance frequencies the analysis indicates that measured blade pressure amplitudes are subject to uncertainty due to finite transducer size and sensitivity to transducer location. However, experimental checks of the cascade response analysis using carefully controlled flow disturbances are needed.

Rotor-Stator Interaction. To apply the cascade response analyses just described to one of the main tone noise generation mechanisms, rotor-stator interaction, a thorough description of the rotor produced disturbance flow field is required. The need to describe blade wakes has long been recognized and a large body of wake data including mean and turbulence properties has been accumulated on laboratory fans (e.g., [44, 45]). In addition to midspan wakes, secondary flows such as tip vortices have been recognized as potential noise contributors [46]. Therefore, a linear cascade analysis including spanwise gust components has been developed to allow the relative noise contributions of tip vortices and midspan wakes to be determined [47]. What is lacking is a thorough model of the total rotor downstream flow field which is linked to fan design parameters and is validated by experimental data.

Some wake data have been obtained as functions of downstream distance on a fan operated with forward velocity in an anechoic wind tunnel [48]. Mean wake stator upwash velocity profiles are shown in Fig. 14 as a function of spanwise

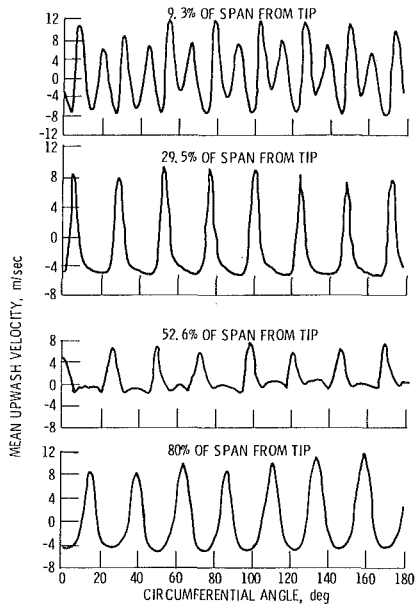

Fig. 14 Rotor mean wake velocity profiles as a function of spanwise location, 1.23 rotor chords downstream, 80 percent speed, tunnel velocity = 41 m/s [48]

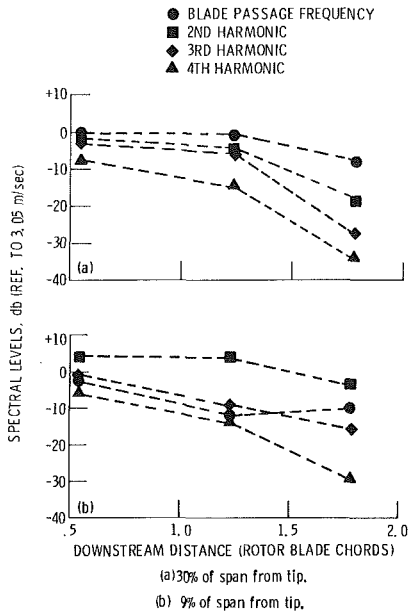

Fig. 15 Mean wake harmonic levels from ensemble average spectra, 80 percent design speed, upwash component, tunnel velocity = 41 m/s [48]

Downloaded 01 Jun 2010 to 171.66.16.57. Redistribution subject to ASME license or copyright; see http://www.asme.org/terms/Terms_Use.cfm

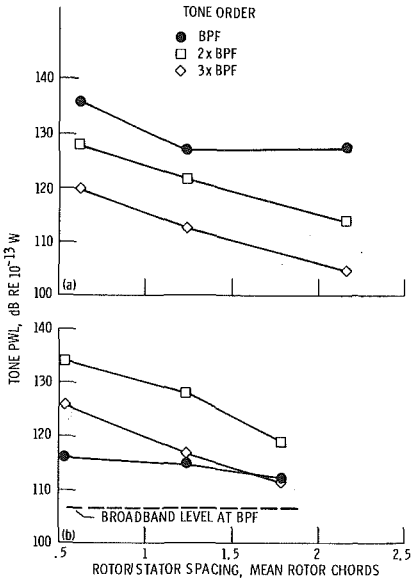

(a) 11-vane stator.
(b) 25-vane stator.

Fig. 16 Variation of narrowband tone harmonic power levels with rotor-stator spacing, 80 percent design speed, 15 rotor blades, tunnel velocity = 41 m/s [49]

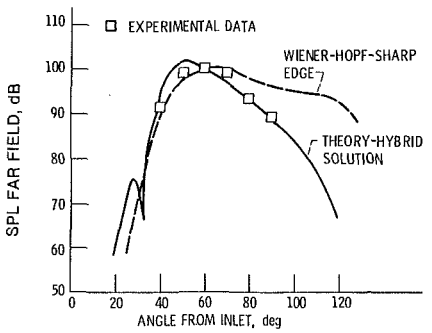

Fig. 17 Single mode inlet directivity comparison of theory with experiment 3150 Hz, (13, 0) mode, 6750 rpm [91]

position. The magnitudes vary substantially with radial location, but most significantly the profile near the tip is characterized by an extra upwash cycle between successive blades corresponding to strong secondary flows, probably a tip vortex. The variation of stator upwash harmonics, the required input to generation analyses, is shown in Fig. 15 as a function of downstream distance. From the complex variations observed, it must be concluded that simple Gaussian profiles which decay and spread monotonically with distance are an inadequate description of this flow field.

Acoustic data are available from rotor–stator spacing experiments on the same fan as was used for the wake measurements just described. Two stator vane-rotor blade ratios were examined: one for propagating and the other for cutoff fundamental tones. Figure 16 shows the inlet narrowband tone harmonic power level variation with rotor-stator spacing. Residual levels of the fundamental for the cutoff case (25 vanes) are nearly constant suggesting that a weak inflow disturbance–rotor interaction governs in this case rather than a rotor–stator interaction due to stator blade nonuniformities sufficient to generate other propagating modes [50]. Note that 25-vane second and third harmonic levels are higher than corresponding harmonics generated by the 11-vane set indicating a difference in the response and/or coupling to acoustic modes of the two stators. The 11-vane stator had longer chords than the 25-vane stator in order to maintain the same solidity.

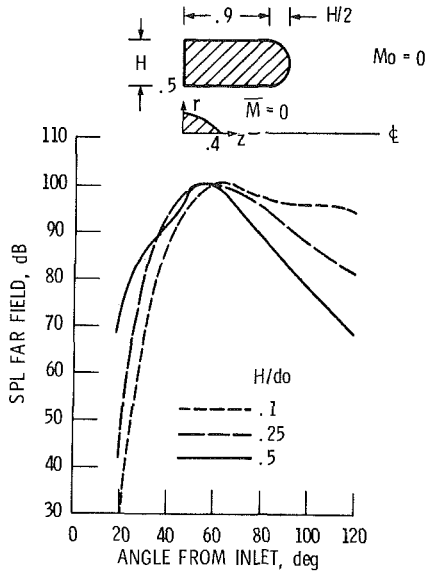

Fig. 18 Effect of inlet lip thickness on single mode directivity, $M_D = 0$, 3150 Hz, (13, 0) mode, (theory normalized to 100 dB at 60 deg) [91]

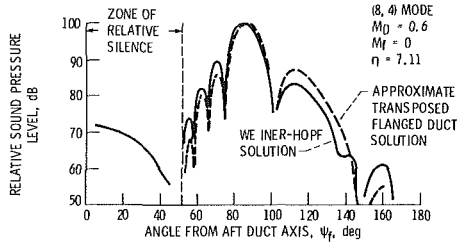

Fig. 19 Comparison of approximate and exact single mode aft directivity patterns [80]

Comparisons between the measurements and theory in [42] are in progress using the corresponding wake measurements as input. Tone powers measured in rotor-stator spacing and vane-blade ratio experiments in an anechoic chamber using inflow control have been compared to a two-dimensional (strip) model with encouraging results [52]. Wake data were not acquired so a wake model was used. While two-dimensional theory may do relatively well for power predictions, calculating far-field directivity and, therefore, acoustic mode content requires more sophistication in handling duct geometry and, probably, in describing the wake/vortex flow field. A semi-empirical wake/vortex model has been developed [53] specifically for use in rotor–stator noise calculations.

Source Modal Content. Both the magnitudes and phases of all the acoustic modes generated are the fundamental inputs to propagation analyses. To date, most available mode information is much less complete. For tone sources circumferential mode numbers may be determined from rules about blade row interactions [54]. No such simple rules exist for radial mode numbers. For example, in rotor-stator interactions the rotor wakes become increasingly radially skewed with downstream distance; one wake may simultaneously intersect several blades with the intersection points sweeping radially with time. In multimodal situations corresponding to random flow excitation, all possible modes that the duct can support are candidates.

Experimentally, two approaches to mode identification have been used. In the first, modal content is inferred from far-field directivity. Individual principal mode shapes obtained from radiation theory are matched to the observed lobe shapes [55, 56]. This method ignores any phasing effects be-

Downloaded 01 Jun 2010 to 171.66.16.57. Redistribution subject to ASME license or copyright; see http://www.asme.org/terms/Terms_Use.cfm

tween modes in the far field, depends on the accuracy of the radiation model, and breaks down for individual modes as the number of propagating modes increases. In the limit where a large number of modes propagate and a smooth directivity pattern results, either equal amplitude or equal energy modal distributions have been assumed and compared to data. One such study indicated that the equal energy assumption produced a better fit to inlet tone directivities than equal amplitude [57]; in another study [58] the equal energy assumption gave fair fits to the multimodal directivities in some cases but poorer results in others, particularly at aft angles.

The second experimental approach has involved attempts at direct mode determination from in-duct microphone measurements. Techniques range from matrix inversion of N selected wall pressure measurements to deterministically solve for N preselected modes [59], to a least-squares approach where the number of measurements is at least twice the number of modes [60]. Formidable practical difficulties exist: Radial measurements upstream of the fan introduce distortions and their associated extraneous modes, and measurements on the wall alone require large numbers of microphones distributed axially and circumferentially. An upstream rotating microphone technique has been formulated to overcome the problem of distortion mode generation by the probe and reduce the number of microphones required [61]. With the exception of an experiment using a wall-mounted array on an actual JT15D engine [62], demonstrations of the techniques have been limited to relatively low speed fans with conditions rather far removed from the turbofans of interest. Direct measurement techniques require additional development and still fall in the category of research efforts, not routine tools. Thus, results from three-dimensional or quasi-three-dimensional analyses [37, 38, 42, 43] are presently the main source of detailed modal information.

Propagation and Radiation – Unlined Ducts

In this section we deal with propagation in and radiation from ducts with hard walls. Untreated cases are important for carrying generation predictions to the far field to compare with experiments. Treated ducts will be discussed in the next section.

Blade Row Transmission. Sound generated by pressure fluctuations on the stator can only propagate upstream by traversing the rotor and vice versa. Inlet levels of propagating rotor–stator interaction tones sometimes display low sensitivity to rotor–stator spacing [55, 63] indicating substantial rotor attenuation. Stator generated modes incident on the rotor may be scattered into modes at other blade passing harmonics [64] or sum and difference tones in multistage arrangements [65], and are more highly attenuated if they are rotating opposite to the rotor. While actuator disk [66] and cascade analyses [67] exist, quantitative experimental verification has been limited to two-dimensional approximations [68]. The existing analytical frame-work remains to be applied to three-dimensional transmission in annular ducts for practical cases where the tone wavelengths of interest are often equal to or less than the blade chords.

Inlet Radiation. Assuming any blade row transmission effects have been accounted for, the modal content propagates to the far field through variable area ducts carrying flow and radiates from duct openings through nonuniform flow fields. For inlet radiation two distinct flow fields are of interest: largely radial potential flow in the static test case, and an inlet stream tube only slightly larger than the inlet diameter in the flight case. The Weiner–Hopf technique, applicable only to inlet lips of negligible thickness, has been applied to two idealized cases. One is uniform external and internal flow at the same Mach number, and the other is a constant Mach number external flow bounding a cylinder of higher uniform Mach number extending out of the inlet. The former is an approximation to the flight case but the latter is unrepresentative of any real inlet flow. Two other approaches to analyzing inlet radiation have been followed. The first uses simplifying assumptions based on ray acoustics while the second uses a fully numerical solution incorporating the actual flow field and inlet lip geometry.

Ray Acoustics in Terms of Cutoff Ratio. Approximate expressions for inlet radiation have been developed in terms of mode cutoff ratio $\xi = \pi\eta/\alpha_{mn}\sqrt{1-M_D^2}$ where the dimensionless frequency $\eta = fD/c$; using the eigenvalue of the (m, n)th mode α_{mn}; duct diameter D; duct Mach number M_D; and speed of sound c. The key simplification realized by the cutoff ratio formulation is that modes with the same ξ and η propagate similarly to the far field. This has been demonstrated for radiation from a flanged duct without flow [69] and is fairly accurate for principal lobe radiation [70]. Two important duct mode propagation angles, ϕ_x and ψ_x, are defined in (71) as

$$\cos\phi_x = \frac{-M_D + S}{1 - M_D S} \tag{1}$$

and

$$\cos\psi_x = \frac{S\sqrt{1-M_D^2}}{\sqrt{1-M_D^2 S^2}} \tag{2}$$

where

$$S = \sqrt{1 - 1/\xi 2} \tag{3}$$

Here, ϕ_x and ψ_x are the angles which the vector normal to the wave front and the group velocity vector, respectively, make with the duct axis. The duct mode angle ψ_x, given by equation (2), has been shown to closely approximate the angular location of the principal lobe in the far field [71]. This conclusion was reached by inspection of the directivity coefficient appearing in the Wiener–Hopf solution for the case of uniform flow everywhere [72]; an expression for the principal lobe angle identical to equation (2) was obtained. The approximate equality of in-duct propagation angle and far field principal lobe radiation angle suggests that ray acoustic arguments can be used to link the two angles for cases where the flow is not uniform.

For example, ray acoustic ideas have been applied to the case where far-field velocity is substantially less than inlet duct velocity, the limit being the static case where far-field velocity is zero. Based on a ray acoustic analysis which showed that refraction in a potential flow is second order with respect to Mach number [73], the wavefronts were assumed to be unbent going from duct to far field. That is, ϕ_x was assumed to be unchanged. Since ϕ_x and ψ_x are identical if Mach number is zero, the group velocity in the far field was assumed to have been shifted. At $M_D = -0.4$ and $\xi \approx 1$ (near cutoff), the calculated radiation peak is at 66 deg while the group velocity in the duct propagates at $\psi_x = 90$ deg. A peak near 66 deg was observed in the far field for a nearly cutoff mode generated by a controlled fan source [56]. However, the agreement of this observed peak with the theory which neglects lip shape may be misleading. A propagation phenomenon associated with the very thick inlet lip used in the experiment may have controlled the principal lobe location. An analysis of propagation in a variable area duct with gentle area variation shows that mode identity is preserved [74, 75] (i.e., no scattering occurs). Thus, as a mode propagates from the inlet throat to the highlight, ξ increases causing ϕ_x and ψ_x to decrease. Recent extensions of ray theory for propagation through an irrotational flow [76, 77] imply that it is the group velocity vector which is unchanged, not the normal to the wavefronts. The difference between the two assumptions is significant; e.g., 66 versus 90 deg peak near cutoff, and current evidence points to preservation of group

Downloaded 01 Jun 2010 to 171.66.16.57. Redistribution subject to ASME license or copyright; see http://www.asme.org/terms/Terms_Use.cfm

velocity as the better approach. Controlled experiments and possibly numerical simulations are needed to settle this issue.

Numerical Model. A hybrid numerical program has been developed [78] and exercised [79] to calculate both the internal and external sound propagation for actual engine inlet geometry and flow conditions. It is a hybrid program in the sense that a finite element method is used within the duct and in the near field and an integral radiation method handles the far field. Iteration is required to match the two solutions at the interface. A potential flow program is used to generate the steady flow for the actual inlet geometry; boundary layers are not included. The input to the program is the pressure profile for a given mode in the annulus at the fan source. While the program cannot handle the combination of high Mach number and high frequency due to computer storage limitations, some inlet geometry effects have been studied which were previously impossible to analyze.

Figure 17 compares the numerically predicted inlet tone directivity to the measured levels generated by the same controlled source mentioned previously – a JT15D engine with inlet rods [56]. A single (13, 0) mode propagates at the fan speed shown. The excellent agreement between the hybrid solution and the data is in contrast to the Wiener–Hopf solution for an infinitely thin lip, which is also shown. The thick lip used in the experiment (thickness-to-diameter ratio of 0.5) shifts the radiation peak toward the axis, as discussed in the preceeding section, and acts as a shield to reduce the levels in the aft quadrant. The dependence of the directivity on inlet lip thickness is illustrated in Fig. 18 where the shielding effect is also clearly evident. The numerical results show that the radiation peak moves aft as the lip gets thinner. At a thickness-to-diameter ratio of 0.1, the radiation pattern agrees very well with the Wiener–Hopf (zero thickness) result shown in Fig. 17. The hybrid program is a powerful tool for the solution of "real-world" inlet radiation problems.

Exhaust Radiation. In contrast to the complex inlet flow field, the exhaust flow, neglecting mixing, is much simpler. The fan exhaust may be approximated as an emerging cylindrical flow at Mach number M_D surrounded by a uniform flow at Mach number M_f which fits the requirements for an exact Wiener–Hopf radiation solution. The ray acoustic, mode cutoff ratio approach to an approximate solution can also be applied with more confidence to the aft slip layer. Starting from the zero-flow flanged duct radiation equation, a coordinate transformation was applied to account for the duct flow, and ray acoustics arguments were applied across the slip layer [80]. Single mode aft directivity from the approximate expression is compared to the full Wiener–Hopf solution [81] in Fig. 19. The good agreement builds confidence in the simplifications used to generate the approximate solution. The Wiener–Hopf solution gives finite levels in the zone of silence in contrast to the ray acoustics result although the particular values from [81] are believed to be incorrect.

The location of the principle lobe in the far field ψ_{fp} is found from the approximate theory [80] to be

$$\cos \psi_{fp} = \frac{-M_D + \xi\sqrt{\xi^2 - 1}(1 - M_D^2)}{\xi(1 - M_D^2)(\xi + M_D\sqrt{\xi^2 - 1})} \tag{4}$$

for the static case ($M_f = 0$). For $M_D = +0.6$ and $\xi = 1$, $\psi_{fn} = 160$ deg measured from the exhaust axis indicating that modes near cutoff radiate to the inlet quadrant. The analogous inlet analysis, equation (2), indicated that near cutoff mode peaks remain in the inlet quadrant. Thus, the inlet quadrant contains the near cutoff mode peaks no matter where the sound originated.

Suppression – Lined Ducts

Ducts between the turbomachinery components and the observer can be lined with sound absorbing materials to greatly reduce the radiated noise. Early workers [83] on suppressors considered the use of splitter rings in the duct to increase treated area and decrease the distance between treated surfaces.

Current emphasis is on the optimization of wall treatment alone to minimize aerodynamic losses and weight penalties in aircraft applications. The attenuation achieved is very sensitive to the source modal characteristics used as input [84, 85]. Input cases of interest range from a limited number of modes associated with tone noise from periodic blade row interactions, to multimodal situations associated with random processes exciting all the modes the duct can support. The latter number may be very large. At high frequencies considering modes spinning in one direction, the number can be estimated from [86] as $N = \pi^2\eta^2/8(1 - M_D^2)$. For typical values of $M_D = -0.4$ and $\eta = 20$ at blade passing frequency, $N \approx 600$. In such cases, some method of handling the modal distribution as a continuum subject to a simple rule describing the energy distribution is desirable.

The status of three aspects of suppressor research will be discussed: analytical propagation approaches including the cutoff ratio method, numerical propagation programs, and suppressor materials characterization.

Duct Acoustics – Analytical. Much analytical effort has gone into describing propagation of acoustic modes in simple geometries such as cylindrical and rectangular ducts lined with sound absorbing materials. A complex acoustic impedance (resistance and reactance) is used to specify the wall boundary condition for point reacting liners. Solution of the wave equation in the duct results in a complex eigenvalue and wave number for each mode. The real part of the wave number defines the attenuation while the imaginary part defines the axial wave speed.

From such single-mode solutions, attenuation contours plotted in the impedance plane, as shown in Fig. 20, reveal an optimum impedance for which the maximum possible attenuation is obtained. The important parameters are duct Mach number, boundary layer thickness, and frequency. Studies of optimum impedance led to the discovery [87] that mode cutoff ratio was a key correlating parameter for inlets: Modes with similar cutoff ratios propagate in a similar fashion. Figure 21 shows the correlation of optimum resistance as a function of cutoff ratio for different boundary layer thicknesses. Each point represents a single mode calculation. The curves through the points are from a correlation equation reported in [88] which also contains correlations for maximum possible attenuation and optimum reactance. Highest attenuation occurs near cutoff and drops rapidly with increasing cutoff ratio. Cutoff ratio correlations have been found for far field directivity [69] duct termination loss [69] and transmission loss through a variable area duct based on ξ at the throat [74, 75].

Multimodal cases, such as the example of $N = 600$ cited above, can be handled as a continuum in cutoff ratio. The modal number density function in a duct is given in [86] by

$$\frac{1}{N}\frac{dN}{d\xi} \approx \frac{2}{\xi^3} \tag{5}$$

The number density is converted into a modal power density by multiplying by a weighting function which must then be estimated by a technique such as a least-squares fit to experimental hardwall directivity patterns as described in [6].

The goal of these approximate suppressor analyses is to predict the suppressed far-field directivity. Additional work is needed to improve the quantitative results by including modal scattering at the hard-soft liner interface, refraction around the inlet lip at high Mach number, and redirection of sound by the inlet lip contour. Analogous optimum impedance and attenuation correlations remain to be derived for the aft duct case.

Downloaded 01 Jun 2010 to 171.66.16.57. Redistribution subject to ASME license or copyright; see http://www.asme.org/terms/Terms_Use.cfm

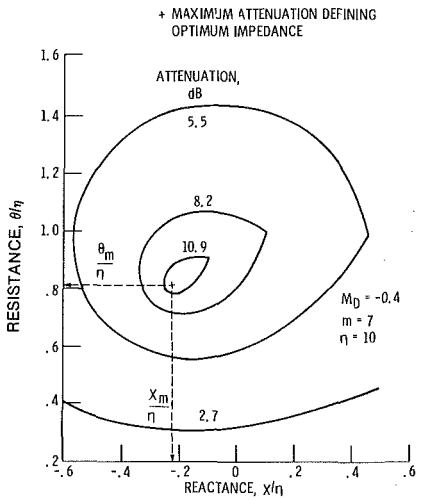

Fig. 20 Sound attenuation contours, boundary layer thickness $\epsilon = 0$; liner length/passage height, $L/H = 1.0$ [88]

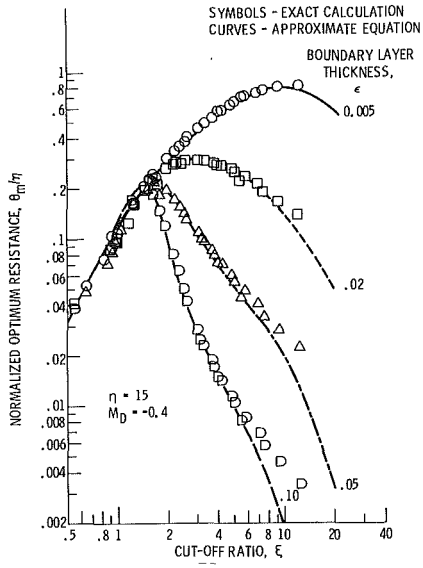

Fig. 21 Optimum wall resistance as a function of mode cutoff ratio for various inlet wall boundary layer thicknesses [88]

Duct Acoustics – Numerical. Recent reviews of the application of numerical methods to duct acoustics appear in [89, 90]. The hybrid numerical program in the "Inlet Radiation" section also handles the case of acoustically treated inlet walls and includes modal scattering effects at liner interfaces. Comparisons of the calculated and measured suppression for a series of very short inlet liners ($L/D = 0.15$) are shown in Fig. 22 [91]. The experiment again used a JT15D engine configured to produce a single (13, 0) mode. Three different liner resistances were tested [92]. For a single mode the attenuation is independent of angle. Therefore, at each resistance, data points are plotted for angles between 50 and 80 deg where the single mode at blade passing frequency dominates the levels. The calculated values agree well with the data which vary less than 5 dB with angle.

The hybrid program has been used to calculate attenuation contours in the impedance plane and thus define the optimum impedance [91] for the single mode as shown in Fig. 23. Optimum values of resistance and reactance are 0.6 and 0.85 compared to values of 1.14 and 0.5 calculated for a single (13, 0) mode in the soft-walled duct. Corresponding maximum possible attenuations differ by 20 dB (50 dB numerical versus 30 dB single mode). These comparisons show the importance of the inclusion in the hybrid program of modal scattering at the hard-soft interface, particularly for a near cutoff mode

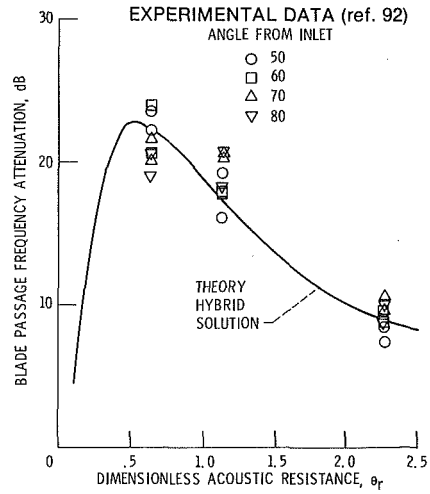

Fig. 22 Comparison of numerical suppression/radiation analysis to experiment as a function of liner resistance, (13.0) mode, 3150 Hz, $\chi = 0.5$ [91]

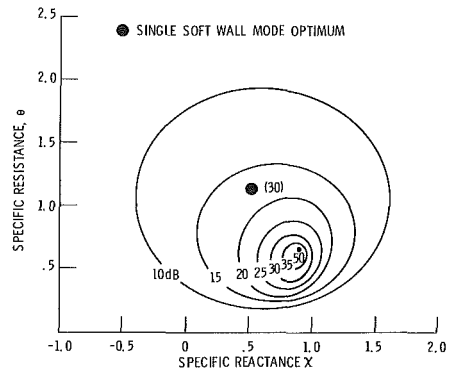

Fig. 23 Calculated optimum impedances from a hybrid numerical solution with scattering compared to the single soft wall mode solution, 3150 Hz, (13.0) mode, liner $L/d_0 = 0.15$ [91]

entering a short liner. As the liner is lengthened, the numerical calculation approaches the analytical result which neglects scattering. A semi-empirical correction was applied in [92], but explicit inclusion of scattering in the analysis is preferable.

The challenge in applying the numerical approach is to remove the limitations on frequency and Mach number ranges imposed by computer storage and run time. One possibility is to develop a transient solution method which can potentially cut storage requirements by several orders of magnitude [93, 94].

Suppressor Materials. In order to realize the attenuations calculated by the propagation analyses, the duct boundary conditions expressed as acoustic impedance must be translated into liner construction parameters, e.g., treatment thickness, wall porosity, fiber sizes and bulk densities, etc. For extended reaction liners, normal wall impedance is inappropriate and coefficients in the wave equation describing propagation in the liner itself must be related to real bulk absorbing material properties. The following discussion will briefly summarize the physics of the various dissipation mechanisms involved and some recent modeling efforts to link the suppressor construction details to the global properties needed for propagation analysis.

Impedance – Point Reacting Materials. Helmholtz resonator arrays formed by bonding a perforated plate to honeycomb have been widely used to acoustically treat aircraft engine ducts. Variants of the single-layer resonator designs add multiple honeycomb layers separated by perforated septa with grazing flow effects, of course, limited to the perforate exposed directly to the flow. In the absence of the grazing flow

Downloaded 01 Jun 2010 to 171.66.16.57. Redistribution subject to ASME license or copyright; see http://www.asme.org/terms/Terms_Use.cfm

present in engine applications, these suppressors are extremely nonlinear, i.e., resistance depends on sound pressure level because the oscillatory orifice flow is governed by the Bernoulli equation. However, at high grazing flows the resistance is proportional to free stream Mach number and is independent of sound pressure level. The control of resistance by grazing flow is due to orifice blockage which occurs as the mean flow is periodically turned into the orifices and then separates, reducing the discharge coefficients or the effective open area ratio of the perforated plate [95]. Acoustic dissipation occurs as the kinetic energy of the hydrodynamic jetlike flow induced in the orifices is dissipated in the surrounding fluid with little pressure recovery. Actually, boundary layer properties must also be considered since the orifices ingest flow from distances of the order of one orifice diameter. Acoustic resistance models have been published [92, 96] as a function of free stream Mach number and boundary layer thickness based on a 1/7th power profile. Recently, a model using friction velocity as the controlling parameter has been formulated [97] to handle the more general case of a boundary layer thickened by diffusion or altered in a way which divorces near-wall velocities from free stream conditions.

Perforated plate-honeycomb treatment has cost and load carrying advantages, but its acoustic design is complicated by the requirement to know local flow conditions which vary with engine speed. (The associated resistance variation is favorable in an inlet but detrimental in the exhaust.) To overcome the sensitivity of resistance to flow conditions and maintain acoustic linearitiy, treated surfaces having very small pores formed by densely packed wires or extremely fine screens have been used. In this case, the dissipation mechanism is viscous pressure loss in the fine pores as nearly stagnant fluid very near the wall is ingested. An impedance model for square weave screens supported by perforated plate has been developed [98]. Mechanical problems associated with fine screens have been addressed. Corrosion at the bonds with dissimilar metals can be prevented with coatings. Contamination is prevented by the self-cleaning action of the oscillatory velocities induced in the pores. Aside from the increased in situ impedance predictability, fine-pored materials have no acoustic advantage over perforated plate when used in a honeycomb-backed wall treatment.

Bulk Absorbers. Extended reaction liners formed by an uninterrupted layer of densely packed fibers retained by a high porosity face sheet do offer definite acoustic advantages. The distributed dissipation damps back cavity resonances which smooths the reactance as a function of frequency and increases high frequency absorption.

At low frequencies the speed of sound in the fiberous matrix is decreased, giving a greater apparent treatment depth and enhancing low frequency absorption. Beyond these inherently point reacting arguments, the possibility that axial and circumferential wave travel in the material may be used to advantage is being investigated [99]. Studies of the effects of high sound intensities on bulk absorber properties have been completed [100] and models for a range of bulk absorber types are under development [101].

There are mechanical difficulties associated with extended reaction liners which must be overcome. Absorption of liquids will destroy the acoustic effectiveness and can pose a safety problem. Nonwetting coatings may solve the problem for some liquids and allow removal of others using compatible solvents. To provide structural strength while preserving extended reaction, porous (acoustically transmitting) axial and circumferential face plate supports may be required.

Concluding Remarks

Status and Outlook. This review has addressed the links in the chain of aeroacoustic processes which connect turbofan noise generation and suppression to the observed far field noise. Although the theoretical outlines and a body of often flawed empirical data have been in hand for a decade or more, the unified application of theory and controlled experiment to practical cases is just now occurring. This productive development was delayed by contaminated data and theoretical complexity whose physical implications were inadequately communicated to or assimilated by applied noise researchers. During the past half decade, key advances have been made in experimental technique and theoretical application which open the way to a much broader understanding and control of turbofan noise.

With respect to generation, the development of effective inflow control techniques makes possible the conduct of definitive experiments on internally controlled blade row interactions. The initial round of such experiments, focused on rotor–stator tone generation, has highlighted the question of the relative importance of secondary flow disturbances (e.g., tip vortices) compared to midspan wakes. Both improved descriptions of the rotor-produced flow disturbances and the noise generation computer codes to use them are being developed to answer this question. With the help of rotor blade pressure measurements and inflow control, rotor interaction with struts downstream of the stator has been identified as a significant noise source. The experimental tools now exist to uncover other such mechanisms which set tone levels in specific engines. Computer codes which incorporate noncompact, cascade response to calculate the generated acoustic mode content are in the process of being validated by experiment. Tone power comparisons show good agreement. The next level of validation involves far field directivity which depends on a prediction of individual modes and their propagation behavior. At least a quasi-three-dimensional approach must be used to give both circumferential and radial mode content.

Pending the development of well-proven modal measurement techniques, confirmation of predicted mode content is intertwined with hardwall propagation and radiation analysis. The theoretical approaches discussed include approximate analyses, Wiener–Hopf techniques, and direct numerical solutions. Geometric acoustic approximations cast in terms of mode cutoff ratio have the advantage of producing relatively simple expressions and rules of thumb. The cutoff ratio combines individual mode identity (eigenvalue) with frequency and Mach number in a parameter which is particularly convenient for handling multimodal cases as a continuum. Aft fan radiation appears to be handled well by these techniques, but the geometric acoustics of the inlet lip and potential flow field requires additional work. On the other hand, the realistic inlet lip geometry and flow field can be accounted for by direct numerical methods such as the hybrid code. The challenge is to remove the computer storage limitations on combined frequency and flow range.

The approximate analytical and the full numerical approaches also bracket the range of suppressor analyses. Cutoff ratio is again a very useful parameter correlating the attenuation and optimum wall impedance in lined inlet ducts. The results from a full numerical solution, the hybrid code, have particularly emphasized the importance of modal scattering at the hard-soft interface for short treatment lengths. For the multimodal situation resulting from random generation processes, the key input to suppressor analysis is the modal energy distribution. While some broadband cases appear to follow equal energy, in general, the distribution must be inferred by empirical fits to data. The generation models now coming into use may provide some analytical guidance in this regard. The ability to specify acoustic treatment construction has been strengthened by improved understanding of the absorption physics which is concretely reflected in improved impedance models particularly for Helmholtz resonator arrays in flow en-

Downloaded 01 Jun 2010 to 171.66.16.57. Redistribution subject to ASME license or copyright; see http://www.asme.org/terms/Terms_Use.cfm

vironments. The quest for wider absorption bandwidth and enhanced low-frequency attenuation for a given treatment depth spurs the continued investigation of bulk absorbers in full extended reaction configurations.

Other Turbomachinery Installations. Several research results highlighted in this review are relevant to the noise control of stationary turbomachinery. The importance of reducing inflow disturbances to rotating blade rows, particularly for tone noise reduction, and the inflow control devices demonstrated for turbofans apply to stationary cases. In contrast to the turbofan testing constraint, in-duct honeycomb devies are an option. The recent finding that strong tones can be generated by downstream structural struts which interact with upstream rotors through intervening stators is another example of a mechanism likely to be generally operative. Blade pressure diagnostics represent a helpful tool for such mechanism identification. Duct acoustic treatment can be effectively applied to produce a compact suppressed installation. The approximate design methods based on cutoff ratio may be particularly helpful for multimodal situations that are likely to arise in complex, multistage machines.

References

1 Owens, R. E., "Energy Efficient Engine Propulsion System – Aircraft Integration Evaluation," NASA CR-159488, Mar. 1979.

2 Johnston, R. P., et al., "Energy Efficient Engine – Preliminary Design and Integration Study," NASA CR-135444, Sept. 1978.

3 Hodge, C. G., "Subsonic Transport Noise," AIAA Paper No. 80-0858, May 1980.

4 Cumpsty, N. A. "A Critical Review of Turbomachinery Noise," ASME *Journal of Fluids Engineering*, Vol. 99, No. 2, June 1977, pp. 278–293.

5 Feiler, C. E., and Groeneweg, J. F., "Summary of Forward Velocity Effects of Fan Noise," AIAA Paper No. 77-1319, Oct. 1977 (also NASA TM 73722).

6 Rice, E. J., and Sawdy, D. J., "A Theoretical Approach to Sound Propagation and Radiation for Ducts With Suppressors," presented at the 101st Meeting of the Acoustical Society of America, Ottawa, Ont., Can., May 1981 (also NASA TM 82612).

7 Dean, L. W., and Patrick, W. P., "Impedance Modeling of Acoustic Absorbing Materials for Aircraft Engine Applications," Paper No. X5, presented at the 101st Meeting of the Acoustical Society of America, Ottawa, Ont., Can., May 1981.

8 Hanson, D. B., "Spectrum of Rotor Noise Caused by Atmospheric Turbulence," *Journal of Acoustical Society of America*, Vol. 56, July 1974, pp. 110–126.

9 Tyler, J. M., and Sofrin, T. G., "Axial Flow Compressor Noise Studies," *SAE Transactions*, Vol. 70, 1962, pp. 309–332.

10 Sofrin, T. G., and McCann, J. F., "Pratt and Whitney Experience in Compressor-Noise Reduction," abstracted in *Journal of Acoustical Society of America*, Vol. 40, 1966, pp. 1248–1249.

11 Jones, W. L., McArdle, J. G., and Homyak, L., "Evaluation of Two Inflow Control Devices for Flight Simulation of Fan Noise Using a JT15D Engine," AIAA Paper No. 79-0654, Mar. 1979 (also NASA TM 79072).

12 McArdle, J. G., Jones, W. L., and Heidelberg, L. J., "Comparison of Several Inflow Control Devices for Flight Simulation of Fan Noise Using a JT15D Engine," AIAA Paper No. 80-1025, June 1980 (also NASA TM 81505).

13 Woodward, R. P., et al., "Effectiveness of an Inlet Flow Turbulence Control Device to Simulate Flight Fan Noise in an Anechoic Chamber," NASA TM 73855, Dec. 1977.

14 Chestnutt, D., ed., "Flight Effects of Fan Noise," NASA CP 2242, Sept. 1982.

15 Loehrke, R. I., and Nagib, H. M., "Control of Free Stream Turbulence by Means of Honeycombs: A Balance Between Suppression and Generation," ASME *Journal of Fluids Engineering*, Vol. 98, Sept. 1976, pp. 342–353.

16 Homyak, L., et al., "A Compact Inflow Control Device for Simulating Flight Fan Noise," AIAA Paper No. 83-0680, Apr. 1983 (also NASA TM 83349).

17 Rogers, D. F., and Ganz, U. W., "Aerodynamic Assessment of Methods to Simulate Flight Inflow Characteristics During Static Engine Testing," AIAA Paper No. 80-1023, Mar. 1980.

18 Kantola, R. A., and Warren, R. E., "Reduction of Rotor-Turbulence Interaction Noise in Static Fan Noise Testing," AIAA Paper No. 79-0656, Mar. 1979.

19 Ho, P. Y., and Smith, E. B., "An Inflow Turbulence Reduction Structure for Scale Model Fan Testing," AIAA Paper No. 79-0655, Mar. 1979.

20 Ginder, R. B., "Considerations for the Design of Inlet Flow Conditioners for Static Noise Testing," AIAA Paper 79-0657, Mar. 1979.

21 Ganz, U. W., "Analytical Investigation of Fan Tone Noise Due to Ingested Atmospheric Turbulence," NASA CR 3302, Aug. 1980.

22 Gedge, M. R., "A Design Procedure for Fan Inflow Control Structures," NASA CR 165625, Sept. 1980.

23 Atvars, Y., and Rogers, D. F., "The Development of Inflow Control Devices for Improved Simulation of Flight Noise Levels During Static Testing of a HBPR Turbofan Engine," AIAA Paper No. 80-1024, June 1980.

24 Perracchio, A. A., "Assessment of In-Flow Control Structure Effectiveness and Design System Development," AIAA Paper No. 81-2048, Oct. 1981.

25 Shaw, L. M., et al., "Inlet Turbulence and Fan Noise Measured in an Anechoic Wind Tunnel and Statically with an Inlet Flow Control Device," AIAA Paper No. 77-1345, Oct. 1977 (also NASA TM 73723).

26 Heidmann, M. F., and Dietrich, D. A., "Effects of Simulated Flight on Fan Noise Suppression," AIAA Paper No. 77-1334, Oct. 1977.

27 Holm, R. G., Langenbrunner, L. E., and McCann, E. O., "Forward Velocity Effects on Fan Noise and the Influence of Inlet Aeroacoustic Design as Measured in the NASA-Ames 40×80 Foot Wind Tunnel," NASA CR 152329, July 1981.

28 Woodward, R. P., and Balombin, J. R., "Tone Generation by Rotor-Downstream Strut Interaction," *AIAA Journal of Aircraft*, Vol. 21, No. 2, Feb. 1984, pp. 135–142.

29 Ho, P. Y., "The Effect of Fan-Frame Design on Rotor-Stator Interaction Noise," AIAA Paper No. 81-2034, Oct. 1981.

30 Ginder, R. B., and Newby, D. R., "An Improved Correlation for the Broadband Noise of High Speed Fans," *AIAA Journal of Aircraft*, Vol. 14, No. 9, Sept. 1977, pp. 844–849.

31 Gliebe, P. R., "The Effect of Throttling on Forward Radiated Fan Noise," AIAA Paper No. 79-0640, March 1979.

32 Hayden, R. E., et al., "Analysis and Design of a High Speed, Low Noise Aircraft Fan Incorporating Swept Leading Edge Rotor and Stator Blades," NASA CR 135092, Feb. 1978.

33 Lucas, J. G., Woodward, R. P., and MacKinnon, M. J., "Acoustic Evaluation of a Novel Swept-Rotor Fan," AIAA Paper No. 78-1121, July 1978.

34 Lucas, J. G., Woodward, R. P., and Michels, C. J., "Forward Acoustic Performance of a Model Turbofan Designed for a High Specific Flow (QF-14)," NASA TP 1968, Mar. 1982.

35 Mathews, D. C., and Nagel, R. T., "Inlet Geometry and Axial Mach Number Effects on Fan Noise Propagation," *AIAA Progress in Astronautics and Aeronautics*, Vol. 38, 1975, pp. 73–96.

36 Namba, M., "Three-Dimensional Analysis of Blade Force and Sound Generation for an Annular Cascade in Distorted Flows," *Journal of Sound and Vibration*, Vol. 50, Feb. 1977, pp. 479–508.

37 Kobayashi, H., "Three-Dimensional Effect on Pure Tone Fan Noise Due to Inflow Distortion," AIAA Paper No. 78-1120, July 1978 (also NASA TM 78885).

38 Schulten, J. B. H. M., "A Lifting Surface Theory for the Sound Generated by the Interaction of Velocity Disturbances With a Leaned Vane Stator," AIAA Paper No. 81-0091, Jan. 1981.

39 Goldstein, M. E., *Aeroacoustics*, McGraw-Hill, New York, 1976.

40 Kaji, S., "Noncompact Source Effect on the Prediction of Tone Noise From a Fan Rotor," AIAA Paper No. 75-446, 1975.

41 Fleeter, S., "Discrete Frequency Noise Reduction Modeling for Application to Fanjet Engines," *Journal of Acoustical Society of America*, Vol. 63, No. 3, Sept. 1980, pp. 957–965.

42 Ventres, C. S., Theobald, M. A., and Mark, W. D., "Turbofan Noise Generation," Vol. I: Analysis, NASA CR 167951 and Vol. II: Computer Programs, NASA CR 167952, July 1982.

43 Kobayashi, H., and Groeneweg, J. F., "Effects of Inflow Distortion Profiles on Fan Tone Noise," *AIAA Journal*, Vol. 18, No. 8, Aug. 1980, pp. 899–906.

44 Reynolds, B., and Lakshminarayana, B., "Characteristics of Lightly Loaded Fan Rotor Blade Wakes," NASA CR 3188, Oct. 1979.

45 Ravindranath, A., and Lakshminarayana, B., "Three Dimensional Mean Flow and Turbulence Characteristics of the Near Wake of a Compressor Rotor Blade," NASA CR 159518, June 1980.

46 Dittmar, J. H., "Interaction of Rotor Tip Flow Irregularities With Stator Vanes as a Noise Source," AIAA Paper No. 77-1342, Oct. 1977 (also NASA TM 73706).

47 Atassi, H., and Hamad, G., "Sound Generated in a Cascade by Three-Dimensional Disturbances Convected in a Subsonic Flow," AIAA Paper No. 81-2046, Oct. 1981.

48 Shaw, L. M., and Balombin, J. R., "Rotor Wake Characteristics Relevant to Rotor–Stator Interaction Noise Generation," AIAA Paper No. 81-2031, Oct. 1981 (also NASA TM 82703).

49 Woodward, R. P., and Glaser, F. W., "Effects of Blade-Vane Ratio and Rotor-Stator Spacing on Fan Noise With Forward Velocity," AIAA paper No. 81-2032, Oct. 1981 (also NASA TM 82690).

50 Sofrin, T. G., and Mathews, D. C., "Asymmetric Stator Interaction Noise," AIAA Paper No. 79-0638, March 1979.

51 Kantola, R. A., and Gliebe, P. R., "Effects of Vane/Blade Ratio and Spacing on Fan Noise," AIAA Paper No. 81-2033, Oct. 1981.

52 Gliebe, P. R., and Kantola, R. A., "Effects of Vane/Blade Ratio and Spacing on Fan Noise," Vol. I, Final Technical Report, NASA CR-174664, and Vol. II, Data Supplement, NASA CR-174665, Dec. 1983.

53 Majjigi, R. K., and Gliebe, P. R., "Development of a Rotor Wake/Vortex Model," Vol. I, Final Report, NASA CR-174849, and Vol. II, User's Manual for Computer Program, NASA CR-174850, June 1984.

Downloaded 01 Jun 2010 to 171.66.16.57. Redistribution subject to ASME license or copyright; see http://www.asme.org/terms/Terms_Use.cfm

54 Sofrin, T. G., "Some Modal-Frequency Spectra of Fan Noise," AIAA Paper No. 81-1990, Oct. 1981.

55 Cumpsty, N. A., "Tone Noise from Rotor-Stator Interaction in High Speed Fans," *Journal of Sound and Vibration*, Vol. 24, No. 3, 1972, pp. 393–409.

56 Heidmann, M. F., Saule, A. V., and McArdle, J. G., "Predicted and Observed Modal Radiation Patterns from JT15D Engine with Inlet Rods," *J. Aircraft*, Vol. 17, 1980, pp. 493–499.

57 Saule, A. V., "Modal Structure Inferred From Static Far-Field Noise Directivity," NASA TMS 71909, July 1976.

58 McArdle, J. G., Honyak, L., and Chrulski, D. D., "Turbomachinery Noise Studies of the AIResearch QCGAT Engine with Inflow Control," AIAA Paper No. 81-2049, Oct. 1981.

59 Pickett, G. F., Sofrin, T. G., and Wells, R. A., "Method of Fan Sound Mode Structure Determination, Final Report," NASA CR 135293, Aug. 1977.

60 Moore, C. J., "Measurement of Radial and Circumferential Modes in Annular and Circular Fan Ducts," *Journal of Sound and Vibration*, Vol. 62, No. 2, 1979, pp. 235–256.

61 Cicon, D. E., Sofrin, T. G., and Mathews, D. C., "Investigation of Continuously Traversing Microphone System for Mode Measurement," NASA CR-168040, Nov. 1982.

62 Joppa, P. D., "An Acoustic Mode Measurement Technique," AIAA Paper No. 84-2337, Oct. 1984.

63 Woodward, R. P., and Glaser, F. W., "Effect of Inflow Control on Inlet Noise of a Cut-on Fan," *AIAA Journal*, Vol. 19, No. 3, Mar. 1981, pp. 387–392.

64 Mani, R., and Horvay, G., "Sound Transmission Through Blade Rows," *Journal of Sound and Vibration*, Vol. 12, No. 1, 1970, pp. 59–83.

65 Cumpsty, N. A., "Sum and Difference Tones from Turbomachinery," *Journal of Sound and Vibration*, Vol. 32, No. 3, 1974, pp. 383–386.

66 Kaji, S., and Okazaki, T., "Propagation of Sound Waves Through a Blade Row. I. Analysis Based on the Semi-Acutator Disc Theory," *Journal of Sound and Vibration*, Vol. 11, No. 3, 1970, pp. 339–353.

67 Kaji, S., and Okazaki, T., "Propagation of Sound Waves Through a Blade Row. II. Analysis Based on the Acceleration Potential Method." *Journal of Sound and Vibration*, Vol. 11, No. 3, 1970, pp. 355–375.

68 Philpot, M. G., "The Role of Rotor Blockage in the Propagation of Fan Noise Interaction Tones," AIAA Paper No. 75-447, Mar. 1975.

69 Rice, E. J., "Multimodal Far-Field Acoustic Radiation Pattern Using Mode Cutoff Ratio," *AIAA Journal*, Vol. 16, 1978, pp. 906–911.

70 Saule, A. V., and Rice, E. J., "Far-Field Multimodal Acoustic Radiation Directivity," NASA TM 73839, 1977.

71 Rice, E. J., Heidmann, M. F., and Sofrin, T. G., "Modal Propagation Angles in a Cylindrical Duct With Flow and Their Relation to Sound Radiation," AIAA Paper No. 79-0183, Jan. 1979 (also NASA TM 70930, 1978).

72 Homicz, G. F., and Lordi, J. A., "A Note on the Radiative Directivity Patterns of Duct Acoustic Modes," *Journal of Sound and Vibration*, Vol. 41, 1975, pp. 283–290.

73 Landau, L. D., and Lifshitz, E. M., *The Classical Theory of Fluids*, rev. 2nd ed., Addison-Wesley, Reading, MA, 1962, Ch. 7.

74 Cho, Y. C., and Ingard, K. U., "Closed Form Solution of Mode Propagation in a Nonuniform Circular Duct," *AIAA Journal*, Vol. 20, No. 1, Jan. 1982, p. 39.

75 Cho, Y. C., and Ingard, K. U., "Mode Propagation in Nonuniform Circular Ducts With Potential Flow," AIAA Paper No. 82-0122, Jan. 1982 (also NASA TM 82776).

76 Cho, Y. C., and Rice, E. J., "High-Frequency Sound Preparation in a Spatially Varying Mean Flow," *Journal of Acoustical Society of America*, Vol. 70, No. 3, Sept. 1981, pp. 860–865.

77 Amiet, R. K., "Correction of Fan Noise for Effects of Forward Flight," *Journal of Sound and Vibration*, Vol. 89, No. 2, 1983, pp. 243–259.

78 Horowitz, S. J., Sigman, R. K., and Zinn, B. T., "An Iterative Finite Element-Integral Technique for Prodicting Sound Radiation from Turbofan Inlets in Steady Flight," AIAA Paper No. 82-0124, Jan. 1982.

79 Baumeister, K. J., and Horowitz, S. J., "Finite Element-Integral Simulation of Static and Flight Fan Noise Radiation from the JT15D Turbofan Engine," NASA TM 82936, Nov. 1982.

80 Rice, E. J., and Saule, A. V., "Far-Field Radiation of Aft Turbofan Noise," NASA TM 81506, 1980.

81 Savkar, S. D., and Edelfelt, I. H., "Radiation of Cylindrical Duct Acoustic Modes With Flow Mismatch," NASA CR 132613, 1975.

82 Savkar, S. D., "Radiation of Cylindrical Duct Acoustic Modes With Flow Mismatch," *Journal of Sound and Vibration*, Vol. 42, 1975, pp. 363–386.

83 Minner, G. L., and Rice, E. J., "Computer Method for Design of Acoustic Liners for Turbofan Engines," NASA TMX 3317, 1976.

84 Rice, E. J., "Spinning Mode Sound Propagation in Ducts with Acoustic Treatment," NASA TN D-7913, 1975.

85 Motsinger, R. E., Kraft, R. E., and Zwick, J. W., "Design of Optimum Acoustic Treatment for Rectangular Ducts with Flow," ASME Paper No. 76-GT-113, March 1976.

86 Rice, E. J., "Modal Density Function and Number of Propagating Modes in Ducts," NASA TMX 73539, 1976.

87 Rice, E. J., "Acoustic Liner Optimum Impedance for Spinning Modes With Mode Cut-Off Ratio as the Design Criterion," AIAA Paper No. 76-516, July 1976 (also NASA TMX 73411).

88 Rice, E. J., "Optimum Wall Impedance for Spinning Modes – A Correlation with Mode Cutoff Ratio," *Journal of Aircraft*, Vol. 16, 1979, pp. 336–343.

89 Baumeister, K. J., "Numerical Techniques in Linear Duct Acoustics – A Status Report," ASME *Journal of Engineering for Industry*, Vol. 103, Aug. 1981, pp. 270–281.

90 Baumeister, K. J., "Numerical Techniques in Linear Duct Acoustics – 1980–81 Update," NASA TM 82730, Nov. 1981.

91 Baumeister, K. J., "Utilizing Numerical Techniques in Turbofan Inlet Acoustic Suppressor Design," NASA TM 82994, Oct. 1982.

92 Heidelberg, L. J., Rice, E. J., and Homyak, L., "Acoustic Performance of Inlet Suppressors on an Engine Generating a Single Mode," AIAA Paper No. 81-1965 (also NASA TM 82697).

93 Baumeister, K. J., "Time Dependent Difference Theory for Noise Propagation in a Two-Dimensional Duct," *AIAA Journal*, Vol. 18, No. 12, Dec. 1980, pp. 1470–1476.

94 White, J. W., "A General Mapping Procedure for Variable Area Duct Acoustics," AIAA Paper No. 81-0094, Jan. 1981.

95 Walker, B. E., and Charwat, A. F., "Correlation of the Effects of Grazing Flow on the Impedance of Helmholtz Resonators," *Journal of Acoustical Society of America*, Vol. 72, No. 2, Aug. 1982, pp. 550–555.

96 Hersh, A. S., and Walker, B., "Effect of Grazing Flow on the Acoustic Impedance of Helmholtz Resonators Consisting of Single and Clustered Orifices," NASA CR 3177, Aug. 1979.

97 Kooi, J. W., and Sarin, S. L., "An Experimental Study of the Acoustic Impedance of Helmholtz Resonator Arrays Under a Turbulent Boundary Layer," AIAA Paper No. 81-1998, Oct. 1981.

98 Rice, E. J., "A Model for the Acoustic Impedance of Linear Suppressor Materials Bonded on Perforated Plate," AIAA Paper No. 81-1999, Oct. 1981, (also NASA TM 82716).

99 Hersh, A. S., Walker, B., and Dong, S. B., "Analytical and Experimental Investigation of the Propagation and Attenuation of Sound in Extended Reaction Liners," AIAA Paper No. 81-2014, Oct. 1981.

100 Kuntz, H. L., "High-Intensity Sound in Air Saturated, Fibrous Bulk Porous Materials," Ph.D. Thesis, The University of Texas at Austin, Aug. 1982 (also NASA CR 167979).

101 Lambert, R. F., "Acoustical Structure of Highly Porous Open-Cell Elastic Foams," *Journal of the Acoustical Society of America*, Vol. 72, No. 3, Sept. 1982, pp. 879–887.

Downloaded 01 Jun 2010 to 171.66.16.57. Redistribution subject to ASME license or copyright; see http://www.asme.org/terms/Terms_Use.cfm

Performance of Two Transonic Axial Compressor Rotors Incorporating Inlet Counterswirl

C. H. Law

A. J. Wennerstrom

Aero Propulsion Laboratory,
AFWAL/POTX,
Wright-Patterson AFB, OH 45433

A single-stage axial-flow compressor which incorporates rotor inlet counterswirl to improve stage performance is discussed. Results for two rotor configurations are presented, including design and experimental test data. In this compressor design, inlet guide vanes were used to add counterswirl to the inlet of the rotor. The magnitude of the counterswirl was radially distributed to maximize the overall stage efficiency by minimizing the rotor combined losses (diffusion losses and shock losses). The shock losses were minimized by simultaneously optimizing the rotor blade section geometry, through-blade static pressure distribution, and leading edge aerodynamic/geometric shock sweep angles. Results from both the design and experimental performance analyses are presented and comparisons are made between the experimental data and the analyses and between the performance of both rotor designs. The computation of the flow field for both rotor designs and for the analysis of both tests was performed in an identical fashion using an axisymmetric, streamline-curvature-type code. Results presented include tip section blade-to-blade static pressure distributions and rotor through-blade and exit distributions of various aerodynamic parameters. The performance of this compressor stage represents a significant improvement in axial compressor performance compared to previous attempts to use rotor inlet counterswirl and to current, more conventional, state-of-the-art axial compressors operating under similar conditions.

Introduction

This paper describes the results of the design and experimental tests of an advanced single-stage axial-flow compressor which incorporates rotor inlet counterswirl to improve stage performance. In this compressor design, inlet guide vanes were used to add counterswirl to the inlet of the rotor. The magnitude of the counterswirl was radially distributed to maximize the overall stage efficiency by minimizing the rotor diffusion losses without significantly increasing the shock losses. The rotor shock losses were minimized by simultaneously optimizing the rotor blade section geometry, through-blade static pressure distribution, and leading edge aerodynamic/geometric shock sweep angles. Two rotor designs were investigated, incorporating different section geometries to alter incidence, deviation, and overall work distributions and throat margin.

Inlet guide vanes which produce rotor inlet counterswirl have been used for many years on low-speed blowers and compressors to increase the head rise possible in a single stage. However, their use on transonic or supersonic stages has been extremely limited and has generally been associated with poor efficiency. The first example of their use known to the authors was reported by NACA [1], where guide vanes producing counterswirl were placed in front of an isolated transonic rotor which had been designed for axial inflow. The efficiency penalty was small leading to the conclusion that this was a feasible design option; however, the subject was not pursued further. The second example discovered by the authors was a supersonic stage reported by Pratt and Whitney Aircraft in 1966 [2]. This stage was designed to produce a pressure ratio of 2.75 with a rotor tip speed of only 968 ft/s (295 m/s). The measured stage isentropic efficiency did not exceed 70 percent at design speed. The last and most recent examples were reported by the Curtiss Wright Corporation in 1969 [3]. One stage, designed for a pressure ratio of 2.8 with a rotor tip speed of 1400 ft/s (426 m/s), developed a peak isentropic efficiency of 74.7 percent. Another stage, designed for a pressure ratio of 2.08 at the same rotor tip speed, achieved a peak isentropic efficiency of 78 percent at design speed. These were the only examples found by the authors in which inlet counterswirl was employed to substantially increase pressure rise in combination with a transonic or supersonic rotor. (Examples were not included in which minor counterswirl was introduced at the hub to reduce stator inlet Mach number.) Although the history of such designs does not lend itself to optimism, design technology applicable to higher Mach numbers has improved sufficiently since 1969 that the concept appeared worth re-examining. The performance of the stage reported herein represents a major improvement in efficiency with respect to the referenced examples. It also represents an im-

Contributed by the Gas Turbine Division and presented at the International Gas Turbine Conference and Exhibit, Dusseldorf, West Germany, June 8–12, 1986. Manuscript received by the Gas Turbine Division December 17, 1985. Paper No. 86-GT-33.

Copyright © 1987 by ASME

Downloaded 01 Jun 2010 to 171.66.16.57. Redistribution subject to ASME license or copyright; see http://www.asme.org/terms/Terms_Use.cfm

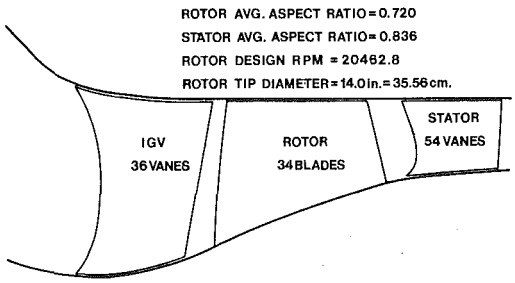

Fig. 1 First-stage geometric characteristics

provement in pressure ratio per stage capability relative to other designs operating at comparable levels of tip speed and efficiency. The application of rotor inlet counterswirl allowed diffusion levels to be set within the range of recent experience and high rotor solidity plus current methods of designing supersonic blade sections proved adequate to keep shock losses under control.

This paper describes the critical design features of the single-stage axial-flow compressor and design differences between the two rotor configurations investigated. The design goals for the stage were a total pressure ratio of 2.175 and an isentropic efficiency of 0.841 with a flow rate of 25.00 lb/s (11.34 kg/s) and a rotor tip speed of 1250 ft/s (381 m/s). The first rotor, rotor 1A, was designed to produce a total pressure ratio of 2.263 with an isentropic efficiency of 0.889, including the inlet guide vanes. The rotor 1A design was modified to produce the second rotor, rotor 1B, such that the second rotor had a larger throat margin, increased work level to make up for higher than originally anticipated inlet guide vane losses, and higher assumed deviation angles in the hub region. Rotor 1B was designed to produce a total pressure ratio of 2.264 with an isentropic efficiency of 0.868, including the inlet guide vanes. Otherwise, both rotors were geometrically identical in the meridional view, with similar solidity levels, thickness distributions, and nondimensional work distributions (radially and axially). The design of the second rotor (1B) was accomplished by the Garrett Turbine Engine Company under contract to take advantage of the three-dimensional CFD code NANCY developed by Dodge et al. Their three-dimensional aerodynamic analysis indicated that the first rotor (1A) might not be able to pass design flow at the design speed and that the design stage pressure ratio might not be met because originally assumed inlet guide vane losses were too low. The inlet guide vanes were analyzed with NANCY 1.0, a compressible three-dimensional viscous analysis program. This coupled with an auxiliary program allowed mixed-out losses to be calculated. The rotors were analyzed with NANCY 2.0 which is a compressible, three-dimensional inviscid rotational version of the code. Losses derived from axisymmetric analysis were input for rotor analysis.

This paper also describes specific results of the experimental tests of the single-stage axial-flow compressor with both rotor configurations (1A and 1B) and highlights differences in the performance of the two configurations. Comparisons are also made between the design and experimental analysis results for both configurations. Results of rotor tip dynamic static pressure measurements are presented in the form of tip section blade-to-blade contour plots of static pressure. Discussions are included which attempt to explain the differences between the design and test results and differences in the performance of the two rotors as associated with specific rotor design variants and methods used to calculate shock losses.

Single-Stage Compressor Design Objectives

The performance objectives for the single-stage compressor were derived from a preliminary design study of a multistage

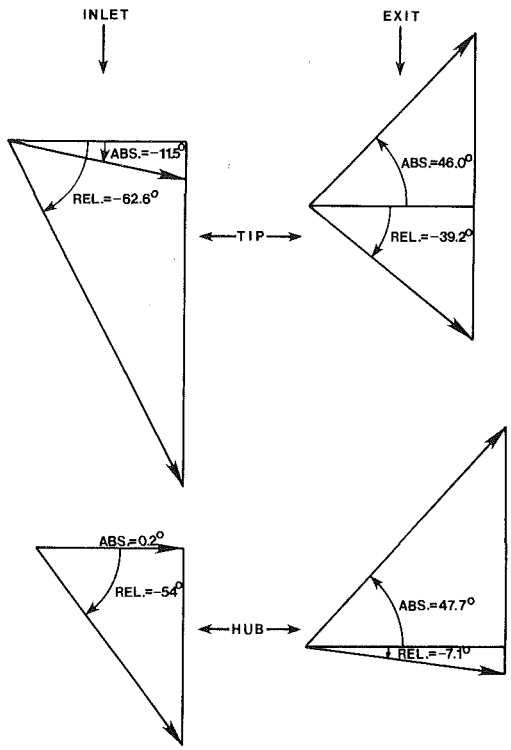

Fig. 2 First-stage rotor design velocity diagrams

core compressor for an advanced turbofan engine. The performance objectives of the multistage compressor were defined by inlet conditions provided by a two-stage, low-bypass ratio fan and exhaust conditions consistent with combustor designs under development. The two-stage fan was assumed to have a bypass ratio of 1:1, a pressure ratio of 3:1, and an efficiency of 85 percent. The compressor mechanical tip speed was designed for 1500 ft/s (457 m/s), or a corrected tip speed of 1250 ft/s (381 m/s) with standard inlet conditions at the compressor inlet. A hub/tip inlet radius ratio of 0.65 was specified at the outset as was the flow per unit inlet (to the first stage rotor) annulus area of 40.0 lb/s/sq.ft (195 kg/s/sq.m). Most of the rest of the compressor characteristics resulted from the overall objective of designing a compressor with a minimum number of stages consistent with the overall isentropic efficiency and pressure ratio goals. The design criteria finally chosen for the first stage were felt to represent the best compromise from the standpoint of the overall multistage compressor.

The detailed aerodynamic design of the multistage compressor was accomplished using the "streamline curvature" method of computation, and employed the same methods described in [4]. The computation assumed the flow to be axisymmetric with the flow being described by a series of concentric streamsurfaces across which no mass or momentum are transferred. A solution is obtained through an iterative numerical procedure to simultaneously satisfy the equations of momentum, continuity, and energy at each streamsurface/computing station intersection point. The form of the momentum equation used satisfies "full" radial equilibrium and includes the effects of streamline curvature, entropy gradients, and blade forces within each blade row. Solution of the continuity equation includes the effects of boundary layer blockage (to account for boundary layer development on both blades and annulus walls) and blade metal blockage within each blade row. The method of approach used for this design involved the specification of total enthalpy distributions through rotors and radius-times-swirl velocity distributions through the stators and inlet guide vane to produce sets of

Downloaded 01 Jun 2010 to 171.66.16.57. Redistribution subject to ASME license or copyright; see http://www.asme.org/terms/Terms_Use.cfm

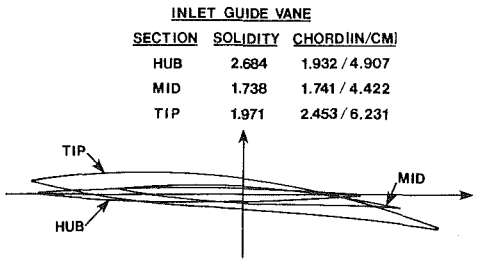

Fig. 3 Inlet guide vane section profiles and vane characteristics

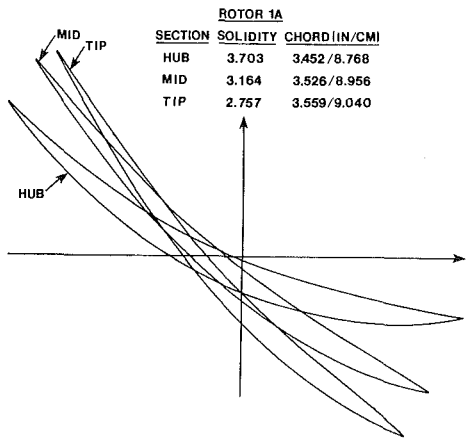

Fig. 4 Rotor 1A section profiles and blade characteristics

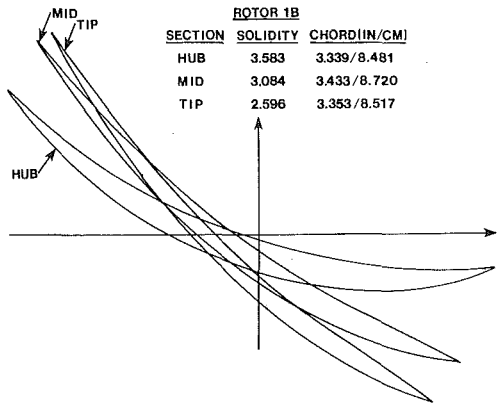

Fig. 5 Rotor 1B section profiles and blade characteristics

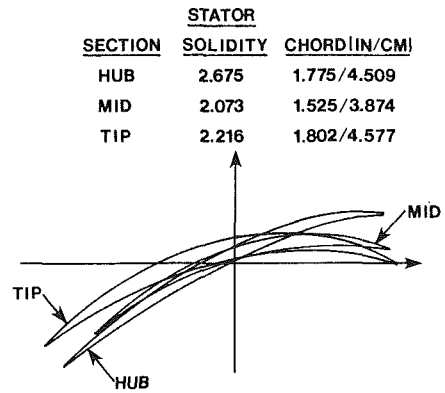

Fig. 6 Stator section profiles and vane characteristics

relative flow angle distributions along streamsurfaces. Camberline angles were defined on each streamsurface by specifying the incidence angle at the leading edge and the variation of deviation angle within the blade, then applying these corrections to the relative flow angles. The camberline angles thus defined the first derivative of the camberline at a number of points along its length. These points were spline fit and the resulting spline equations integrated to provide camberline coordinates. The streamsurface section surfaces were defined by applying a two-part cubic thickness distribution to each meanline, by specifying the location of the point of maximum section thickness and the magnitude of the section edge thicknesses and maximum section thickness. Since the computing stations chosen defined the meridional chord of the blade, an iterative process was employed to insure that the stacked blade matched the leading and trailing edge computing stations for the rotor and to insure that the deviation angle had converged to within an acceptable tolerance. This is required since deviation angle is a function of solidity and thus true chord which is only approximately known at the beginning of the design iterations.

The first-stage geometric characteristics are shown in Fig. 1. The inlet duct is configured to simulate the fan exit duct, or the inlet to a core compressor. This compressor stage is characterized by a constant casing diameter downstream of the inlet guide vane trailing edge. The first-stage aerodynamic design point characteristics were as follows:

Flowrate (lb/s) = 25.00
Flowrate (kg/s) = 11.34
Rotor total pressure ratio = 2.2631
Stage total pressure ratio = 2.1746
Rotor isentropic efficiency = 0.8893
Stage isentropic efficiency = 0.8409

A variety of rotor inlet swirl distributions was examined in the preliminary design phase to obtain the optimum compressor performance and stage matching characteristics. Included were distributions with maximum counterswirl at the hub to reduce stator hub inlet Mach numbers. However, it was determined that rotor inlet counterswirl distributions which varied linearly from hub to tip at all rotor inlets with zero counterswirl at the hub and maximum counterswirl at the tip produced the best predicted efficiency with acceptable velocity profiles. The resulting velocity diagrams for the first-stage rotor are shown in Fig. 2. The inlet guide vane was designed to provide the necessary counterswirl distribution. The resulting streamsurface section profiles and blade (or vane) characteristics for the inlet guide vane and first stage rotor 1A (original) and 1B (revised) and stator are shown in Figs. 3, 4, 5, and 6, respectively. Both rotor configurations were designed to meet the same compressor performance objectives listed above.

Rotor 1A and 1B Design Variations

First-stage rotors 1A and 1B were both designed to meet the same overall design point objectives listed above. Rotor 1B is the result of a redesign effort which was undertaken to provide an alternative rotor design, perhaps one that would provide a better chance to meet the stage design goals. A three-dimensional analysis of the original rotor design (1A) indicated the possibility that this rotor would not be able to pass the design flow at design speed. Analysis of the inlet guide vane also indicated that the original losses assumed for the inlet guide vane might be too low. Rotor 1A was, therefore, redesigned to provide a blade with greater throat margin and higher work levels to make up for higher inlet guide vane losses.

Since both rotors 1A and 1B were designed using the ar-

Downloaded 01 Jun 2010 to 171.66.16.57. Redistribution subject to ASME license or copyright; see http://www.asme.org/terms/Terms_Use.cfm

bitrary camberline blade design method, there were two ways to increase the throat margin: by increasing the through-the-blade variation of aerodynamic (surface boundary layer) blockage, and by increasing the through-the-blade variation of camberline deviation angle. Both of these techniques were used. While other variations, such as rotor meridional and exit radial work distributions, had some influence on throat margin, these variations were not as influential as blockage and camberline deviation changes. Figure 7 shows the original and revised throat margin distributions, defined as A/A^* downstream of a normal shock at the relative inlet Mach number.

The inlet guide vane and rotor trailing edge loss distributions were revised based on a viscous analysis and empirical correlations. To account for the revised losses, the rotor work was modified to provide the original inlet-to-rotor trailing edge total pressure distribution. The original rotor meanline incidence distribution resulted from a constant 2.0 deg suction surface incidence. The revised incidence model accounts for the influence of leading edge thickness blockage and bow-wave total pressure recovery on upstream inlet flow angle at supersonic inlet relative Mach numbers, and leading edge thickness blockage in the subsonic region of the blade. The original rotor exit deviation model was based on the NASA SP-36 deviation model with a +1.0 deg radially constant adder. The revised deviation model consists of a form of Carter's rule, modified to account for inlet-to-exit radius ratio and meridional velocity ratio, with an empirically based nonlinear adder of +4.0 deg at the hub to −2.0 deg at the tip.

The design of all blade rows including Rotor 1B was accomplished using the same Air Force-developed axisymmetric design code, which was furnished to Garrett for the benefit of the Rotor 1B design. However, all design decisions incorporated into Rotor 1B were based upon Garrett personnel's interpretation of the results of the NANCY code CFD calculations. Similarly, the revised empirical inputs incorporated into Rotor 1B were based upon correlations proprietary to Garrett. The reader should also be conscious of the fact that Rotor 1B was designed before Rotor 1A had been tested and so no guidance was available from Rotor 1A test results.

Experimental Test Results

The mass-averaged performance of the first stage with rotor 1A and rotor 1B is shown in Figs. 8 and 9, respectively. The mass-averaged performances of the rotors are compared in Fig. 10. These results indicate that both rotors exceeded design efficiency at design speed, that rotor 1B passed design flow, and rotor 1A passed 98.5 percent of design flow. The data points corresponding to peak efficiency were as follows:

	Design	Rotor 1A	Rotor 1B
Flow (lb/s):	25.000	24.554	25.095
Flow (kg/s):	11.340	11.138	11.383
Rotor total pressure ratio:	2.2631	2.2829	2.4102
Rotor isentropic efficiency:	0.8893	0.8831	0.9091
Stage total pressure ratio:	2.1746	2.2045	2.2921
Stage isentropic efficiency:	0.8409	0.8414	0.8508
Surge margin at design pressure ratio:	—	8.3%	10.6%
Surge margin at peak efficiency:	—	6.9%	4.9%

The data points at design speed closest to design flow and maximum efficiency were analyzed in detail by a through-blade aerodynamic analysis (described in [5]). Some of the results from these analyses are compared with design results for both rotors in Figs. 11–17. Figure 11 shows the radial variation of rotor incidence. Rotor 1B was operated at incidence angles approximately 2 to 3 deg less than rotor 1A across the span. Figure 12 shows the radial variation of rotor loss coefficient. Both rotors operated near design estimates,

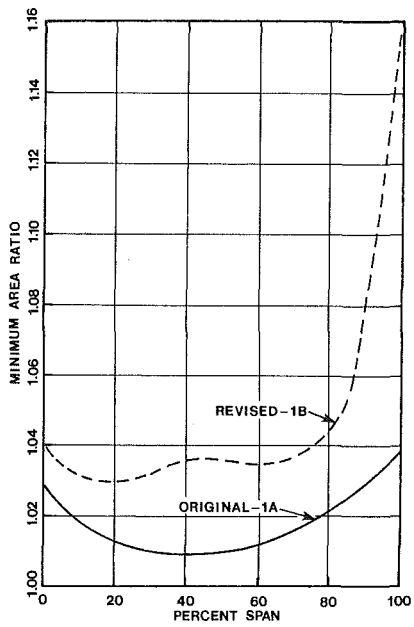

Fig. 7 Spanwise distributions of original and revised rotor throat margin

but rotor 1B generated less loss than rotor 1A across the span. Figure 13 shows the radial variation of rotor deviation. Both rotors operated at nearly the same average levels of deviation, but closer to the original predicted level than the revised predicted level. One result of this is substantial additional pressure ratio produced at the hub as shown in Fig. 14. The distributions of rotor inlet and exit meridional velocity are presented in Figs. 15 and 16 (all velocities are nondimensionalized by the speed of sound in still air at standard inlet conditions). Figure 17 shows the axial variation of midpassage aerodynamic blockage as determined from an axisymmetric through-flow analysis matching experimental values of time-averaged static pressure measured on the outer casing. Rotor 1B operated at significantly higher levels of aerodynamic blockage through the rotor. Both rotors exhibited a plateau in blockage near midchord. Based upon calculated and measured casing static pressures at the rotor inlet, it appeared that the original prediction of inlet guide vane losses was more accurate than the higher level predicted by the three-dimensional viscous CFD analysis. Hence, these values were used in reducing the data for both rotors since the close coupling between blade rows prevented actual measurement of inlet guide vane losses.

Dynamic pressure measurements were also made over the rotor tips at several operating points. Contour plots of the rotor tip static pressure distributions were generated from these data and the results are shown in Figs. 18 and 19 for the data points at design speed nearest design flow and maximum efficiency for rotors 1A and 1B, respectively. In these figures, lines of constant ratio of local static pressure to inlet static pressure are plotted through the rotor tip streamsurface section passage between two adjacent blades.

Downloaded 01 Jun 2010 to 171.66.16.57. Redistribution subject to ASME license or copyright; see http://www.asme.org/terms/Terms_Use.cfm

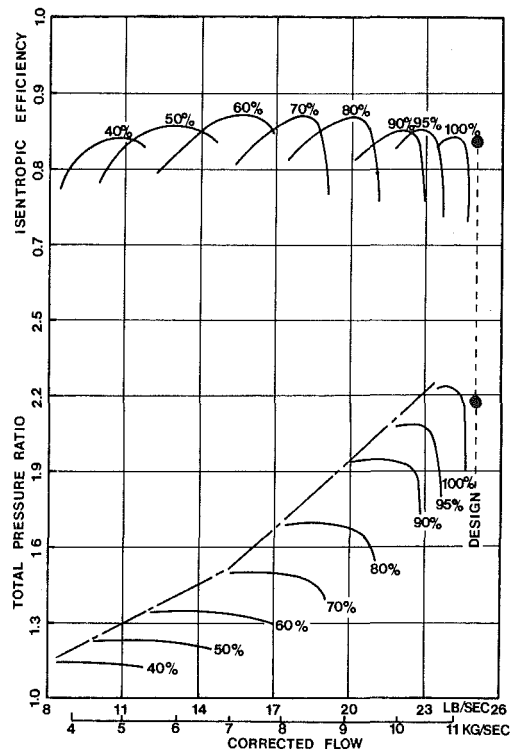

Fig. 8 First-stage compressor performance with rotor 1A

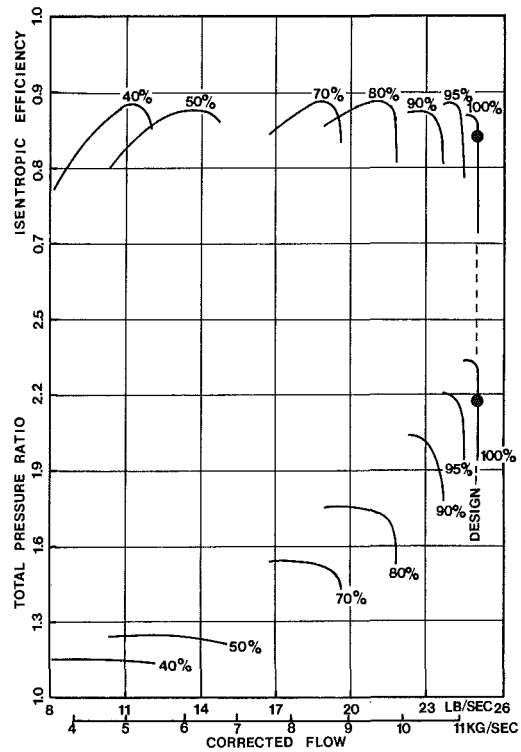

Fig. 9 First-stage compressor performance with rotor 1B

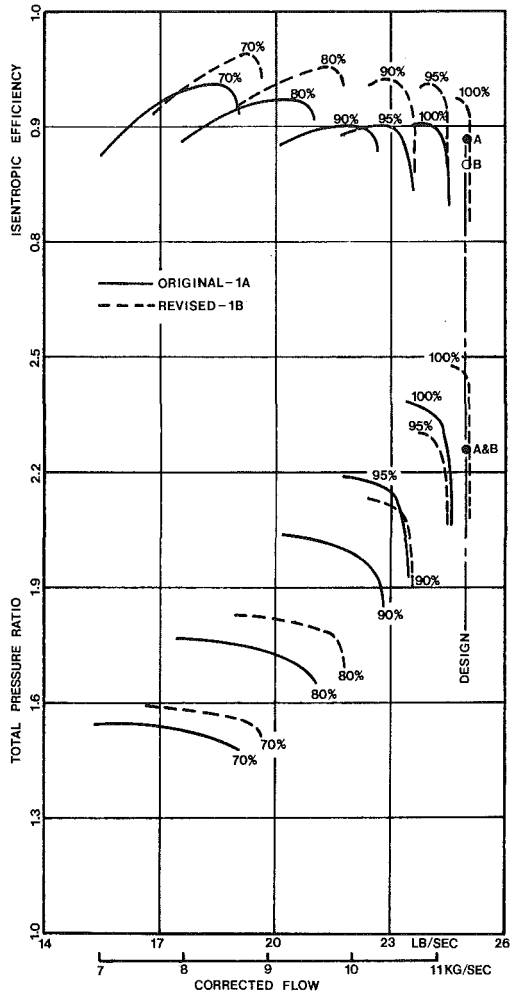

Fig. 10 Comparison of performances of rotors 1A and 1B

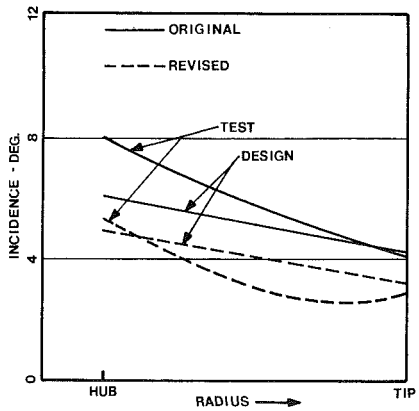

Fig. 11 Radial variation of rotor incidence

Discussion of Results

The revisions incorporated into rotor design 1B allowed the stage to achieve design flow and increased peak efficiency over the entire operating range. Figure 15 implies that the increased throat margin of rotor 1B, which reached a maximum at the tip, appears primarily responsible for most of the increase in flow of this rotor. This is somewhat puzzling since rotor 1A appeared primarily deficient in flow at the hub. However, the flow increased across the full span and this is some indication that the three-dimensional flow analysis performed for each blade row correctly assessed the rotor throat margin deficiency of the original design. The accuracy of the revised predictions for loss and deviation angle is more open to question. The extra loss predicted for the rotor tip of the redesign did not materialize. In fact, rotor 1B ran with less tip loss than either the design or experimental levels of rotor 1A, and substantially below the predicted level. The discrepancy with deviation angle was even larger, which led to the unexpected higher work of the 1B design. The large upsweep in deviation

Downloaded 01 Jun 2010 to 171.66.16.57. Redistribution subject to ASME license or copyright; see http://www.asme.org/terms/Terms_Use.cfm

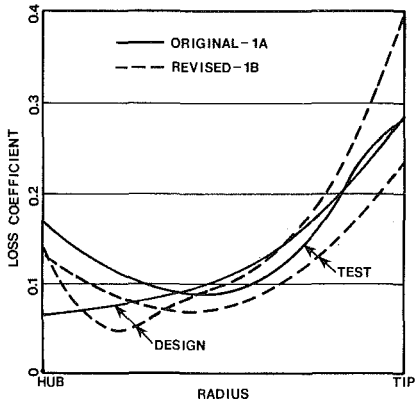

Fig. 12 Radial variation of rotor loss coefficient

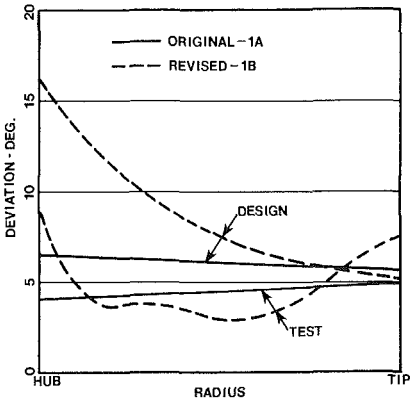

Fig. 13 Radial variation of rotor deviation

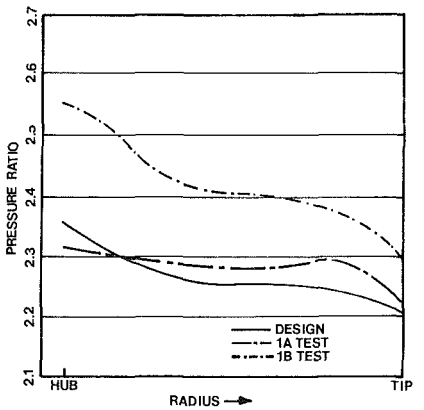

Fig. 14 Radial variation of total pressure ratio from inlet to rotor exit

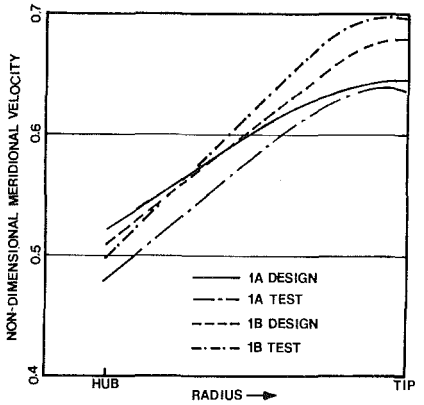

Fig. 15 Radial variation of rotor inlet nondimensional meridional velocity

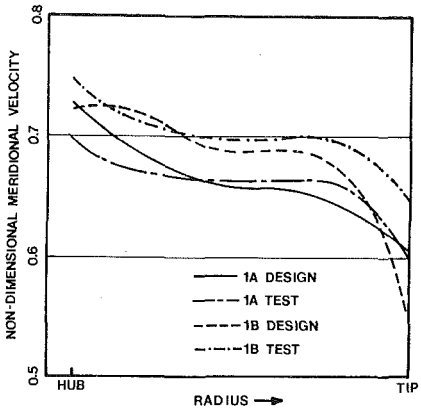

Fig. 16 Radial variation of rotor exit nondimensional meridional velocity

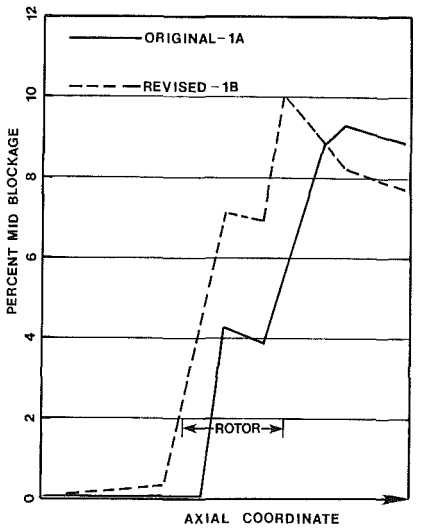

Fig. 17 Axial variation of midpassage blockage

predicted for the hub of the 1B design did not occur and the experimental result differed only slightly between the two rotors.

Since both designs were accomplished, a revised loss prediction scheme was published in [6]. This scheme incorporated a three-dimensional shock loss analysis in addition to a revised diffusion loss model. A prediction of the stage performance incorporating the 1B rotor was attempted using the revised loss prediction model. For this purpose, the experimental distribution of circumferentially averaged total temperature was employed in the stage exit plane to eliminate any error in predicting deviation angle as a factor in this comparison. Also, inlet guide vane losses were assumed equal to those predicted by the three-dimensional viscous analysis performed for the revised design 1B. The results of the prediction compared with the experimental peak efficiency point at design speed were as follows:

	Prediction	Experiment
Flow (lb/s):	25.000	24.957
Flow (kg/s):	11.340	11.320
Rotor total pressure ratio:	2.4050	2.4180
Rotor isentropic efficiency:	0.9100	0.9160
Stage total pressure ratio:	2.3090	2.3000
Stage isentropic efficiency:	0.8620	0.8580

The revised loss prediction scheme is seen to come much closer to the experimental results than either of the original predictions made for rotors 1A or 1B. The improvement in

Downloaded 01 Jun 2010 to 171.66.16.57. Redistribution subject to ASME license or copyright; see http://www.asme.org/terms/Terms_Use.cfm

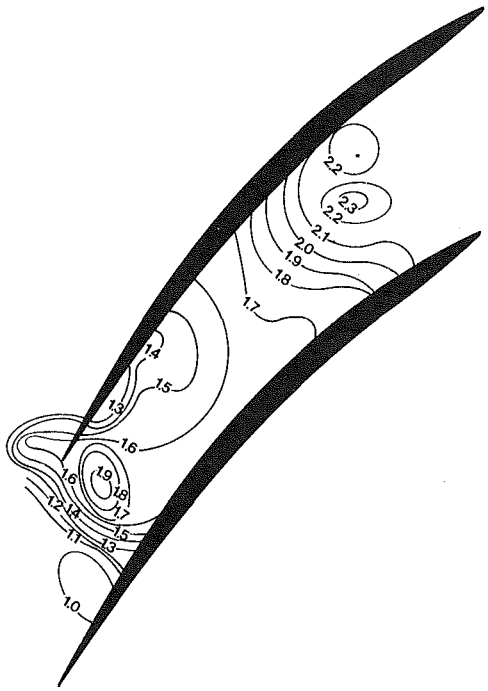

Fig. 18 Contour plot of rotor 1A tip section static pressure distribution

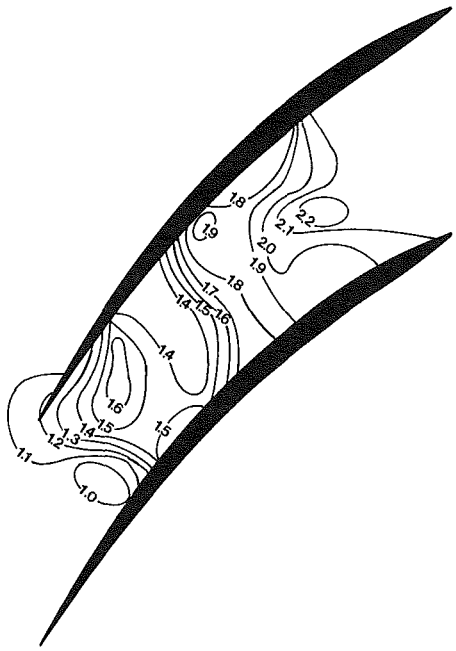

Fig. 19 Contour plot of rotor 1B tip section static pressure distribution

prediction accuracy for this stage is as much a result of the revised diffusion loss model as the three-dimensional shock loss model. Consideration of the spanwise sweep of the shock surface was worth 0.92 point in efficiency relative to considering the shock as purely normal on each streamsurface.

Static pressure distributions in the cascade plane at the rotor tip were constructed from ensemble averages of signals from eight high-frequency miniature pressure transducers mounted across the rotor in the outer casing. These are presented in Figs. 18 and 19 for rotors 1A and 1B, respectively, for the two cases analyzed at design speed near peak efficiency. Rotor 1A, which underflowed, is seen to have a single strong shock detached from the leading edge. Rotor 1B, which achieved its design flow, has a weaker, partially oblique bow shock followed by what appears to be a second weaker oblique shock about half way through the passage. These shock patterns are consistent with the lower losses recorded for rotor 1B. In both cases, the static pressure rise across the bow shock is less than one would expect from the inlet relative Mach number and shock angle, even when the spanwise shock obliquity is taken into account. However, this is not an uncommon occurrence and seems consistent with the observations of Prince [7].

Conclusions

The principal conclusion drawn from these results is that the use of counterswirl to raise rotor relative Mach number and reduce diffusion is a viable design concept for transonic and supersonic stages as well as subsonic stages. The poor results achieved with earlier designs of this type appear due primarily to the state of the art of design for higher Mach numbers at the time rather than any fundamental problem associated with this design approach. The moderate level of counterswirl employed permitted efficiencies in the mid to upper eighty percent bracket to be achieved over a wide operating range, coupled with very high pressure rise compared with production compressors, and introduced no unusual features in the characteristic map which might be expected to lead to engine operating problems.

A second conclusion is that the major contribution of the three-dimensional flow analysis performed in conjunction with the 1B rotor design was to guide the design in the correct way to achieve the design intent for flow. The original blade loading distributions were found to be relatively good and thus changed only slightly. The empirically guided modifications to rotor losses and deviation angle proved worse than the original predictions based upon older, also empirical, technology. However, the extra work which resulted was accomplished efficiently and can be used to advantage.

A third conclusion is that the loss model described in [6] proved quite accurate in predicting the performance of the stage including the 1B rotor. The accuracy was better than expected because the model follows the classical, and rather crude, format of combining an empirical diffusion loss with a calculated shock loss and was calibrated on a stage of substantially higher aspect ratio and lower hub/tip ratio.

References

1 Johnsen, L. J., and Fessler, T. E., "Experimental Investigation of Performance of Single-Stage Transonic Compressor With Guide Vanes Turning Counter to Direction of Rotor Whirl," NACA RM E57B04, Apr. 1957.

2 Final Report on Compressor Portion of Turboaccelerator Cycle Evaluation and Experimental Verification Program, PWA-2833, Pratt & Whitney Aircraft, June 1966.

3 Muller, C. H., and Cox, L. R., "Single Stage Axial Compressor Component Development for Small Gas Turbines. Volume III. Supersonic Compressor Stage Development," USAAVLABS Technical Report 68-90C, June 1969, AD857498.

4 Wennerstrom, A. J., "Experimental Study of a High-Through-Flow Transonic Axial Compressor Stage," ASME JOURNAL OF ENGINEERING FOR GAS TURBINES AND POWER, Vol. 106, No. 3, July 1984, pp. 552-560.

5 Law, C. H., "A Computer Program for Variable-Geometry Single-Stage Axial Compressor Test Data Analysis (UD0400)," AFWAL-TR-81-2078, Sept. 1981.

6 Wennerstrom, A. J., and Puterbaugh, S. L., "A Three-Dimensional Model for the Prediction of Shock Losses in Compressor Blade Rows," ASME JOURNAL OF ENGINEERING FOR GAS TURBINES AND POWER, Vol. 106, No. 2, Apr. 1984, pp. 295-299.

7 Prince, D. C., Jr., "Three Dimensional Shock Structures for Transonic/Supersonic Compressor Rotors," *Journal of Aircraft*, Vol. 17, No. 1, Jan. 1980, pp. 28-37.

Downloaded 01 Jun 2010 to 171.66.16.57. Redistribution subject to ASME license or copyright; see http://www.asme.org/terms/Terms_Use.cfm

Journal of Turbomachinery
Formerly Included in the Journal of Engineering for Gas Turbines and Power

Discussion

The Effect of Inlet Conditions on Heat Transfer in a Rotating Cavity With a Radial Outflow of Fluid[1]

John W. Chew.[2] Some interesting experimental results and comparisons between theory and measurements have been presented in this paper. Although the authors claim reasonable agreement between theory and experiment some discrepancies between the predicted Nusselt numbers and the measurements are apparent. For example, most of the experimental results in Long and Owen's Figs. 9, 10, and 11 show that for $a/b = 0.5$ the Nusselt numbers on the outer part of the disk are considerably lower than for $a/b = 0.1$; in contrast, the predictions for the two cases tend to converge at higher values of x.

Although the agreement between experiment and theoretical heat transfer results is probably as good as could be expected for $a/b = 0.1$ (where the measurements are affected by the wall jet in the source region) the level of disagreement for the case $a/b = 0.5$ is disappointing. At the higher radius ratio the inner shroud could be expected to produce a reasonably uniform inlet flow, which is closer to the mathematical model. If the fluid rotates at disk speed as it enters the cavity at $r/b = 0.5$, the convective heat transfer can be expected to be small at this radius. This effect is reflected in the theoretical Nusselt numbers, but, at high Reynolds numbers, the measurements show that the Nusselt number close to the inlet is of order half the peak measured value.

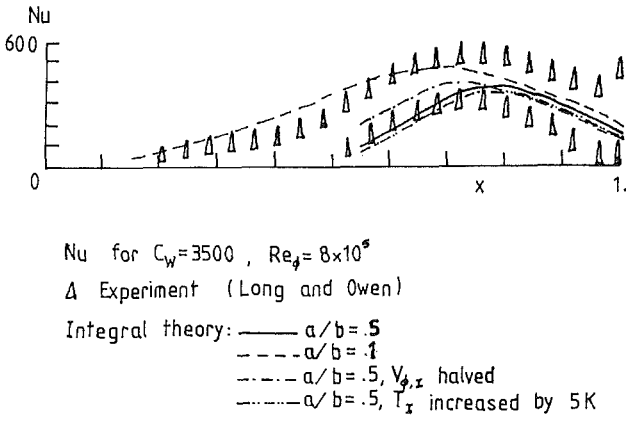

Fig. 12 Sensitivity of the predictions to inlet swirl and temperature

It is of interest to examine the sensitivity of the integral method predictions to inlet conditions. Figure 1 shows heat transfer predictions for $a/b = 0.5$, $C_w = 3500$, $\mathrm{Re} = 8 \times 10^5$ for different values of the temperature and tangential velocity of the fluid at inlet. These conditions correspond to Long and Owen's Fig. 9(*iii*). The integral method used here is described by Chew (1984) and differs only in some relatively minor aspects from that of Rogers used by Long and Owen. It appears that a 5K error in specifying the inlet temperature (which does not seem unlikely for this experiment) has little effect on the predictions. Reducing the inlet swirl from disk speed to half disk speed produces a considerable increase in Nusselt number in the source flow region.

The disparity between theory and experiment for the Nusselt number results for $a/b = 0.5$ is over 100 (compared to a peak Nusselt number of about 300). The question arises: Can this level of disagreement be attributed to experimental uncertainty, or should it be concluded that there are some shortcomings in the mathematical model?

I would like to thank Drs. Long and Owen for a preprint of their paper and for supplying their experimental data.

References

Chew, J. W., 1984, "An Integral Method for the Calculation of Flow and Heat Transfer in a Symmetrically Heated Rotating Cavity," Rolls-Royce report No. TSG0155.

Authors' Closure

The "experimental" Nusselt numbers were obtained using numerical differentiation of the computed temperature distribution within the heated disk. This is an error-prone process (Owen, 1979; Long, 1985), and the authors are pleased that the agreement between theory and experiment is as good as it is! In tests conducted on another rig in the Thermo-Fluid Mechanics Research Centre, where fluxmeters were used, the agreement is even better.

The question that should be asked is: Can these integral equations be used to predict, with acceptable accuracy, the temperatures of gas turbine disks? The authors [11] have shown that relatively crude approximations to the Nusselt numbers can produce "reasonable" estimates of the temperature distribution for plane disks, and Motoren- und Turbinen-Union [16] have produced acceptable results for compressor disks. It would appear, therefore, that the answer to the above question is yes.

References

Owen, J. M., 1979, "On the Computation of Heat Transfer Coefficients From Imperfect Temperature Measurements," *J. Mech. Eng. Sci.*, Vol. 21, p. 323.

Long, C. A., 1985, "The Effect of Thermocouple Disturbance Errors on the Measurement of Local Heat Transfer Coefficients," *Test and Transducer Conference*, Wembley, London, Vol. 3, p. 73.

[1] By C. A. Long and J. M. Owen, published in the July 1986 issue of the JOURNAL OF TURBOMACHINERY, Vol. 108, No. 1, pp. 145–152.

[2] Theoretical Science Group, Rolls-Royce plc, P.O. Box 31, Derby, United Kingdom.

Copyright © 1987 by ASME

Downloaded 01 Jun 2010 to 171.66.16.57. Redistribution subject to ASME license or copyright; see http://www.asme.org/terms/Terms_Use.cfm

The Effect of a Downstream Rotor on the Measured Performance of a Transonic Turbine Nozzle[1]

R. J. Roelke.[2] The authors have provided a very worthwhile and enlightening piece of experimental work. The data presented clearly illustrate the significant influence of the rotor on the flow field at the stator exit. As such, it provides an important insight to the interaction effects of adjacent blade rows. I am sure that work such as this will stimulate additional analysis and modeling efforts to more accurately predict interaction effects. It is unfortunate, however, that no stator surface static pressures were recorded during the tests, or if they were, were not reported in the paper. Surface static pressures would have provided additional information about the changing flow field.

[1] By R. G. Williamson, S. H. Moustapha, and J. P. Huot, published in the October 1986 issue of the JOURNAL OF TURBOMACHINERY, Vol. 108, No. 2, pp. 269–274.

[2] Aerospace Engineer, NASA Lewis Research Center, Cleveland, OH 44135.

Authors' Closure

The authors are grateful to Mr. Roelke for his discussion, and share his desire to investigate the effects of rotor interaction on the nozzle surface static pressure distributions. The "C" nozzle, to which the bulk of the data relate, was not instrumented for surface static pressures. Some very limited data obtained with the instrumented "S" nozzle suggest that the variations in the pressure distributions associated with rotor interaction effects were small. It is hoped that it may be possible to undertake additional work in this area.

Copyright © 1987 by ASME

Downloaded 01 Jun 2010 to 171.66.16.57. Redistribution subject to ASME license or copyright; see http://www.asme.org/terms/Terms_Use.cfm